Novel histamine H_3R and H_4R ligands for various applications

Inaugural-Dissertation

for the attainment of the title of doctor
in the Faculty of Mathematics and Natural Sciences
at the Heinrich-Heine-University Düsseldorf

presented by

Martin Moritz Stark
from Frankfurt am Main

Düsseldorf, August 2025

from the Institute of Pharmaceutical and Medicinal Chemistry
at the Heinrich-Heine-University Düsseldorf

Published by permission of the
Faculty of Mathematics and Natural Science at
Heinrich-Heine-University Düsseldorf

Supervisor: Prof. Dr. Dr. h.c. Holger Stark
Co-supervisor: Jun.-Prof. Dr. Jonathan Cramer

Date of the oral examination:

Affidavit

Ich versichere an Eides statt, dass die vorliegende Dissertation von mir selbstständig und ohne unzulässige fremde Hilfe unter Beachtung der Grundsätze zur Sicherung guter wissenschaftlicher Praxis an der Heinrich-Heine-Universität Düsseldorf erstellt worden ist.

Düsseldorf, August 2025

_____

Martin Moritz Stark

Für meine Familie – die nie ganz verstanden hat, was ich da eigentlich mache, aber trotzdem stolz ist.

Danksagung

An erster Stelle möchte ich mich bei Prof. Dr. Dr. h.c. Holger Stark für die Möglichkeit bedanken, meine Dissertation in seiner Arbeitsgruppe anfertigen zu dürfen. Für seine wissenschaftliche Betreuung, die Freiheit, eigene Ideen zu verfolgen, und die stets konstruktive Unterstützung bin ich sehr dankbar.

Mein besonderer Dank gilt Dr. Aleksandra Zivkovic für ihre fachkundige Unterstützung und die wertvollen wissenschaftlichen Impulse, die wesentlich zum Gelingen dieser Arbeit beigetragen haben.

Luisa Leitzbach und Tobias Werner danke ich herzlich für die zuverlässige und sorgfältige Durchführung der biologischen Testungen, die einen wesentlichen Beitrag zum Gelingen dieser Arbeit geleistet haben.

Dem gesamten Arbeitskreis Stark danke ich für die freundliche und offene Arbeitsatmosphäre, den fachlichen Austausch und den täglichen Humor im Labor, der vieles leichter gemacht hat. Besonders danke ich euch aber auch für die tollen sozialen Interaktionen außerhalb der Arbeit – sei es bei den Cocktailabenden, den mittäglichen Dartspielen oder dem legendären Beerpongturnier. Diese Momente haben nicht nur die Atmosphäre innerhalb des Arbeitskreises bereichert, sondern auch für viel Spaß und unvergessliche Erinnerungen gesorgt.

Ein herzliches Dankeschön an meine Familie, besonders an meine Eltern und meinen Bruder, für ihre unermüdliche Unterstützung seit dem Studium, ihre Geduld und ihr Vertrauen in mich. Auch wenn sie während meiner PhD Zeit oft dachten, ich würde mein Leben einfach nur chillen, nicht arbeiten und ständig nur Bier trinken – was natürlich auch stimmt – danke, dass ihr trotzdem immer hinter mir standet!

Ein herzliches Dankeschön geht an meine Freunde in Siena für die unvergessliche Zeit während meines Austauschs dort. Vielen Dank für die großartige Aufnahme in euren Arbeitskreis und für all die Unterstützung, die ich dort erfahren habe. Die Beziehungen, die ich dort geknüpft habe, sind für mich von unschätzbarem Wert und ich werde sie immer in bester Erinnerung behalten. Grazie mille ragazzi!

Meinen Freunden für ihre Unterstützung, ihr Verständnis in stressigen Zeiten und vor allem für die nötige Ablenkung, die geholfen hat, den Kopf frei zu bekommen.

Und schließlich danke ich meiner Freundin von Herzen für ihre Liebe, ihr Verständnis und ihre stete Unterstützung in allen Phasen dieses Projekts – und darüber hinaus.

List of publications

Paper:

1) Blankenburg, J.; Stark, M.; Frey, H. Oxidation-Responsive Polyether Block Copolymers Lead to Non-Ionic Polymer Surfactants with Multiple Amine N-Oxides. *Polym Chem* **2019**, *10* (13), 1569–1574. https://doi.org/10.1039/C9PY00093C.

2) Schwickert, M.; Fischer, T. R.; Zimmermann, R. A.; Hoba, S. N.; Meidner, J. L.; Weber, M.; Weber, M.; Stark, M. M.; Koch, J.; Jung, N.; Kersten, C.; Windbergs, M.; Lyko, F.; Helm, M.; Schirmeister, T. Discovery of Inhibitors of DNA Methyltransferase 2, an Epitranscriptomic Modulator and Potential Target for Cancer Treatment. *J Med Chem* **2022**, *65* (14), 9750–9788. https://doi.org/10.1021/acs.jmedchem.2c00388.

3) Schwickert, M.; Zimmermann, R. A.; Habeck, T.; Hoba, S. N.; Nidoieva, Z.; Fischer, T. R.; Stark, M. M.; Kersten, C.; Lermyte, F.; Helm, M.; Schirmeister, T. Covalent S-Adenosylhomocysteine-Based DNA Methyltransferase 2 Inhibitors with a New Type of Aryl Warhead. *ACS Med Chem Lett* **2023**, *14* (6), 777–787. https://doi.org/10.1021/acsmedchemlett.3c00062.

In Progress:

4) Stark, M.; Schultes, M.; Werner, T.; Leitzbach, L.; Zivkovic, A.; Louat, T.; Giret, M.; Carteret, J.; Nagmar, I.; Rouanet, S.; Calmels, T.; Jacob, C.; Stark, H. Multi-Target H3R Antagonists with D2R/D3R Activity: A Novel Approach to Parkinson's Disease Treatment. *Manuscript in progress.*

5) Stark, M.; Tardiolo, N.; Werner, T.; Böttger, E.; Papa, A.; Zivkovic, A.; Butini, S.; Stark, H. Structural fine tuning of multi-target compounds combining inhibition of the endocannabinoids' catabolizing enzymes with antagonism at H3 receptors. *Manuscript in progress.*

6) Stark, M.; Werner, T.; Leitzbach, L.; Zivkovic, A.; Roth, B., Stark, H. Novel dual-target ligands for narcolepsy: Merging H3 receptor antagonism with monoamine reuptake inhibition. *Manuscript in progress.*

7) Stark, M.; Werner, T.; Leitzbach, L.; Krenzer, J.; Zivkovic, A.; Müller, T.; Stark, H. Development of High-Affinity Tetrazine-based H3 Receptor Ligands: Enabling Next Generation GPCR Research Through Biorthogonal Chemistry. *Manuscript in progress.*

8) Stark, M.; Werner, T.; Leitzbach, L.; Krenzer, J.; Zivkovic, A.; Müller, T.; Stark, H. Expanding the molecular toolbox: Development of novel high-affinity fluorescent ligands for the H3 Receptor through optimized fluorophore integration strategies. *Manuscript in progress.*

Poster & Oral presentations:

1) Stark, M.; Leitzbach, L.; Stark, H. Synthesis of tetrazine-derived H3R ligands for Implementation in click chemistry. *Frontiers in Medicinal Chemistry* **2024**, Münich, Germany

2) Stark, M.; Leitzbach, L.; Stark, H. Development of novel H_3R ligands incorporating tetrazine-derived building blocks for application in click chemistry. *First joint meeting of European Histamine Research Society (EHRS) and the Histamine Research Society Europe (HRSE)* **2024**, Turin, Italy. (Winner of Best Flash Presentation Award)

Abstract

Histamine receptors ($H_{1-4}R$) represent significant therapeutic targets with diverse physiological roles. Particularly the H_3R has emerged as a promising target for neurological disorders, while the H_4R shows implications in inflammatory and allergic conditions. However, current single-target strategies often fail to address the multifaceted nature of complex H_3R-associated neurological disorders including Parkinson's disease and narcolepsy, necessitating new therapeutic approaches. Additionally, the molecular toolbox for investigating both receptors remains inadequate, evident for H_3R through the absence of ligands useful for bioorthogonal chemistry applications, which limits *in vivo* visualization techniques. H_4R research, on the other hand, lacks selective fluorescent ligands necessary to resolve the ongoing debate regarding its expression in brain tissues.

This thesis addresses these research gaps through the design and synthesis of novel ligands with applications ranging from potential therapeutic agents to specialized molecular research tools. In the therapeutic domain, two multitarget-directed ligand approaches were developed. The first project established dual-acting compounds combining H_3R antagonism with dopamine D_2/D_3 receptor agonism for Parkinson's disease treatment, yielding a lead compound with balanced receptor activities and favourable safety profiles, addressing dopaminergic stimulation and histaminergic regulation simultaneously. The second multitarget-directed approach focused on narcolepsy treatment by merging H_3R antagonism with norepinephrine-dopamine reuptake inhibition, resulting in compounds with promising pharmacological profiles likely capable of engaging multiple wake-promoting pathways, potentially offering improved efficacy while reducing polypharmacy-associated risks. Beyond therapeutic applications, this thesis pursued the expansion of the molecular toolbox for H_3R and H_4R research. The first approach yielded tetrazine-based H_3R ligands designed for metal-free click chemistry applications, with successful proof-of-concept conversion to a fluorescent ligand, adding bioorthogonal chemistry-capable ligands to the H_3R repertoire. The second molecular approach developed novel fluorescent H_3R ligands through systematic exploration of attachment strategies, identifying compounds that balance strong receptor binding with excellent fluorescent properties. The final project addressed the need for selective fluorescent H_4R ligands to investigate this receptor's controversially discussed presence in brain tissues, establishing strategic directions for future ligand development.

In summary, this work provides valuable insights for both therapeutic and basic research aspects of histamine receptor pharmacology, establishing foundations for innovative treatment strategies for complex neurological disorders while expanding the available methodology for investigating H_3R and H_4R function and distribution.

Zusammenfassung

Histamin-Rezeptoren ($H_{1-4}R$) stellen bedeutende therapeutische Targets mit vielfältigen physiologischen Funktionen dar. Insbesondere der H_3R hat sich als vielversprechende Zielstruktur für neurologische Erkrankungen erwiesen, während der H_4R Implikationen bei entzündlichen und allergischen Erkrankungen zeigt. Gegenwärtige Einzeltarget-Strategien können jedoch die vielschichtige Natur komplexer H_3R-assoziierter neurologischer Erkrankungen wie Parkinson und Narkolepsie nicht ausreichend bewältigen, was neue therapeutische Ansätze erforderlich macht. Zudem ist das molekulare Instrumentarium zur Untersuchung beider Rezeptoren unzureichend, beim H_3R erkennbar durch das Fehlen von Liganden für bioorthogonale Chemie, was fortschrittliche *in vivo* Visualisierungstechniken unzugänglich macht. Der H_4R-Forschung hingegen mangelt es an selektiven fluoreszenten Liganden zur Klärung der kontrovers diskutierten Expression in Hirngeweben.

Diese Dissertation adressiert diese Forschungslücken durch die Entwicklung neuartiger Liganden mit potentiellen Anwendungen als Therapeutika bis hin zu molekularen Forschungswerkzeugen. Im therapeutischen Bereich wurden zwei Multi-Target-Liganden-Ansätze entwickelt. Das erste Projekt etablierte dual-wirkende Verbindungen, die H_3R-Antagonismus mit Dopamin D_2/D_3-Rezeptor-Agonismus für die Parkinson-Behandlung kombinieren, was zu einer Leitstruktur mit ausgewogenen Rezeptoraktivitäten führte, die dopaminerge Stimulation und histaminerge Regulation gleichzeitig adressiert. Das zweite Projekt konzentrierte sich auf einen neuen Ansatz der Narkolepsie-Behandlung durch Kombination von H_3R-Antagonismus mit Noradrenalin-Dopamin-Wiederaufnahmehemmung, resultierend in Verbindungen mit vielversprechenden pharmakologischen Profilen, die mehrere wachheitsfördernde Signalwege ansprechen. Jenseits therapeutischer Anwendungen verfolgte diese Arbeit die Erweiterung des molekularen Instrumentariums für die H_3R- und H_4R-Forschung. Der erste Ansatz lieferte Tetrazin-basierte H_3R-Liganden für metallfreie Click-Chemie-Anwendungen mit erfolgreicher *Proof-of-Concept*-Umwandlung zu einem fluoreszenten Liganden. Im zweiten Projekt wurden neuartige fluoreszente H_3R-Liganden durch systematische Untersuchung verschiedener Verknüpfungsstrategien entwickelt. Das letzte Projekt adressierte den Bedarf an selektiven fluoreszenten H_4R-Liganden zur Untersuchung der kontrovers diskutierten Präsenz dieses Rezeptors in Hirngeweben und etablierte strategische Richtungen für zukünftige Liganden Entwicklung.

Zusammengefaßt verstärkt diese Arbeit signifikant sowohl therapeutische als auch grundlegende Forschungsaspekte der Histamin-Rezeptor-Pharmakologie und schafft Grundlagen für innovative Behandlungsstrategien komplexer neurologischer Erkrankungen bei gleichzeitiger Erweiterung der verfügbaren Methodik zur Untersuchung der H_3R- und H_4R-Funktion und -Verteilung.

Abbreviations

AA	arachidonic acid
AADC	L-amino acid decarboxylase
AC	adenylate cyclase
ACh	acetylcholine
AChE	acetylcholine esterase
ACN	acetonitrile
ADH	aldehyde dehydrogenase
ADHD	attention deficit hyperactivity disorder
ADME	absorption, distribution, metabolism and excretion
Akt	protein kinase B
AP1	activator protein-1
APCI	atmospheric pressure chemical ionization
Boc	*tert*-butyloxycarbonyl
BRET	bioluminescence resonance energy transfer
cAMP	cyclic adenosine monophosphate
CCL2	chemokine (C-C motif) ligand 2
CDI	1,1'-carbonyldiimidazole
cDNA	cyclic deoxyribonucleic acid
cGMP	cyclic guanosine monophosphate
CNS	central nervous system
COMT	catechol-O-methyltransferase
COPD	chronic obstructive pulmonary disease
CREB	cAMP response element-binding protein
CuAAc	copper(I)-catalyzed azide-alkyne cycloaddition
CV	cell viability
DA	dopamine
DAG	diacylglycerol
DAO	diamine oxidase
DAT	dopamine transporter
DC	dendritic cells
DCE	dichloroethane
DCM	dichloromethane
DEAD	diethyl azodicarboxylate
DIBAL	diisobutylaluminum hydride
DIPEA	*N*,*N*-diisopropylethylamine

DMF	*N*,*N*-dimethylformamide
DMP	Dess-Martin periodinane
DNA	deoxyribonucleic acid
DNRI	dopamine and norepinephrine reuptake inhibitor
DOPA	dihydroxyphenylalanin
D_1R	dopamine D_1 receptor
D_2R	dopamine D_2 receptor
D_3R	dopamine D_3 receptor
D_4R	dopamine D_4 receptor
D_5R	dopamine D_5 receptor
ECL	extracellular loop
EDS	excessive daytime sleepiness
EP	eosinophils
eq.	equivalent
ERK1/2	extracellular signal-regulated kinase 1/2
EWG	electron-withdrawing groups
5-FAM	5-carboxyfluorescein
FB	fibroblast
FRAP	fluorescence recovery after photobleaching
FRET	fluorescence resonance energy transfer
GABA	gamma-aminobutyric acid
GDP	guanosine diphosphate
Glu	glutamate
GPCR	G protein-coupled receptor
GRK	G protein kinases
GSK-3β	glycogen synthase kinase-3-beta
GTP	guanosine-5'-triphosphate
HATU	hexafluorophosphate azabenzotriazole tetramethyl uronium
HDC	histidine decarboxylase
HMT	histamine *N*-methyltransferase
HNMT	*N*-methyltransferase
HOAt	1-hydroxy-7-azabenzotriazole
HOMO	highest occupied molecular orbital
H_1R	histamine H_1 receptor
H_2R	histamine H_2 receptor
H_3R	histamine H_3 receptor

H_4R	histamine H_4 receptor
HRMS	high resolution mass spectrometry
5-HT	serotonin
IA	intrinsic activity
IEDDA	inverse electron-demand Diels-Alder
IgE	immunoglobulin E
IL1	Interleukin 1
IM	intermediate
IP_3	inositol 1,4,5-trisphosphate
IPRT	5'-phosphoribosyl transferase
LAH	lithium aluminium hydride
LC-DAD	liquid chromatography with diode array detector
LC-MS	liquid chromatography with mass spectrometry
LC-MS-DAD	liquid chromatography with mass spectrometry and diode array detector
LPS	lipopolysaccharide
LUMO	lowest unoccupied molecular orbital
MAO	monoamine oxidase
MAPK	mitogen-activated protein kinase
MC	mast cells
mCPBA	*meta*-chloroperoxybenzoic acid
MOC	monocyte
mRNA	messenger ribonucleic acid
MS	mass spectrometry
MTDL	multitarget-directed ligand
MT_1R	melatonin receptor 1
MT_2R	melatonin receptor 1
NAMH	*N*-methylhistamine
NanoBRET	nano-bioluminescence resonance energy transfer
NDRI	norepinephrine-dopamine reuptake inhibition
NE	norepinephrine
NET	norepinephrine transporter
NMP	*N*-methylpiperazine
NMR	nuclear magnetic resonance
NP	neutrophil
NPY	neuropeptide Y
NT	neurotransmitter

NT1	narcolepsy type 1
NT2	narcolepsy type 2
PBS	phosphate buffered saline
PD	Parkinson's disease
PDB	protein data base
PEG	polyethylene glycol
PET	positron emission tomography
PGE2	prostaglandin E2
PI3K	Phosphoinositide-3-kinase
PKA	protein kinase A
PKC	protein kinase C
PLA_2	phospholipase A2
PLC	phospholipase C
PWS	prader-willi syndrome
Py5	pyridine-based pentamethine cyanine dye
RA	rheumatoid arthritis
RAMH	(*R*)-α-methylhistamine
reg. TC	regulatory T cell
rf	reflux
RLS	restless legs syndrome
rt	room temperature
SAR	structure-activity relationship
SEM	standard error of the mean
SERT	serotonin transporter
SET	single electron transfer
sGC	soluble guanylate cyclase
SI	selectivity index
SM	starting material
S_N2	nucleophilic substitution type 2
S_NAr	aromatic nucleophilic substitution
SNc	substantia nigra pars compacta
SPAAC	strain-promoted azide-alkyne cycloaddition
SSRI	selective serotonin reuptake inhibitor
STAB	sodium triacetoxyborohydride
STAT	signal transducer and activator of transcription
TC	T cell

TCO	*trans*-cyclooctene
TEMPO	2,2,6,6-tetramethylpiperidinyloxyl
TFA	trifluoroacetic acid
Th	T helper cell
TH	tyrosine hydroxylase
THF	tetrahydrofuran
TIRF	total internal reflection fluorescence
TLC	thin layer chromatography
TM	transmembrane domain
TMN	tuberomamillary nucleus
TMS	tetramethylsilane
TNBS	2,4,6-trinitrobenzenesulfonic acid
TNFα	tumor necrosis factor alpha
TS	transition state
UV	ultraviolet
UV/Vis	ultraviolet-visible
VMAT2	vesicular monoamine transporter 2

Table of contents

1. Introduction

1.1 Histamine

The discovery of histamine (β-imidazolylethylamine) by Dale and Laidlaw in 1910 marked a turning point in the understanding of biological signalling molecules.[1] Initially identified for its potent vasodilatory and smooth muscle-contracting properties, histamine has since been recognized as a key regulator of numerous physiological and pathological processes, spanning the nervous, immune, gastrointestinal, and cardiovascular systems.[2–4]

The fundamental importance of histamine in biological processes is underscored by its remarkable evolutionary conservation as histamine signalling is one of the most conserved biological systems across species. Phylogenetic studies reveal its presence in organisms ranging from primitive invertebrates to humans,[5] highlighting its fundamental role in biological regulation. This evolutionary preservation extends to functional mechanisms, as evidenced by the conservation of histamine's role in photoreception from insects to vertebrates[6,7] and its involvement in immune response and gastric acid secretion across diverse species.[8,9] Most notably, the genes encoding histamine-synthesizing enzymes exhibit remarkable conservation, suggesting that histamine signalling emerged early in evolutionary history, likely predating the divergence of major animal phyla.[10]

1.1.1 Biosynthesis and metabolism

This deep evolutionary conservation accentuates the precision of histamine's biosynthesis, which operates through a precisely controlled enzymatic pathway. This process centres on histidine decarboxylase (HDC), a pyridoxal phosphate-dependent enzyme that catalyses the decarboxylation of L-histidine to produce the biogenic amine.[11] Mechanistically, the reaction is initiated when pyridoxal phosphate, initially bound to Lys305 of HDC, forms a Schiff base with L-histidine within the enzyme's active site. This binding triggers conformational changes that optimally position the α-carboxyl group for decarboxylation, followed by a coordinated electron transfer resulting in carbon dioxide release and histamine formation after hydrolysis (see Figure 1).[12]

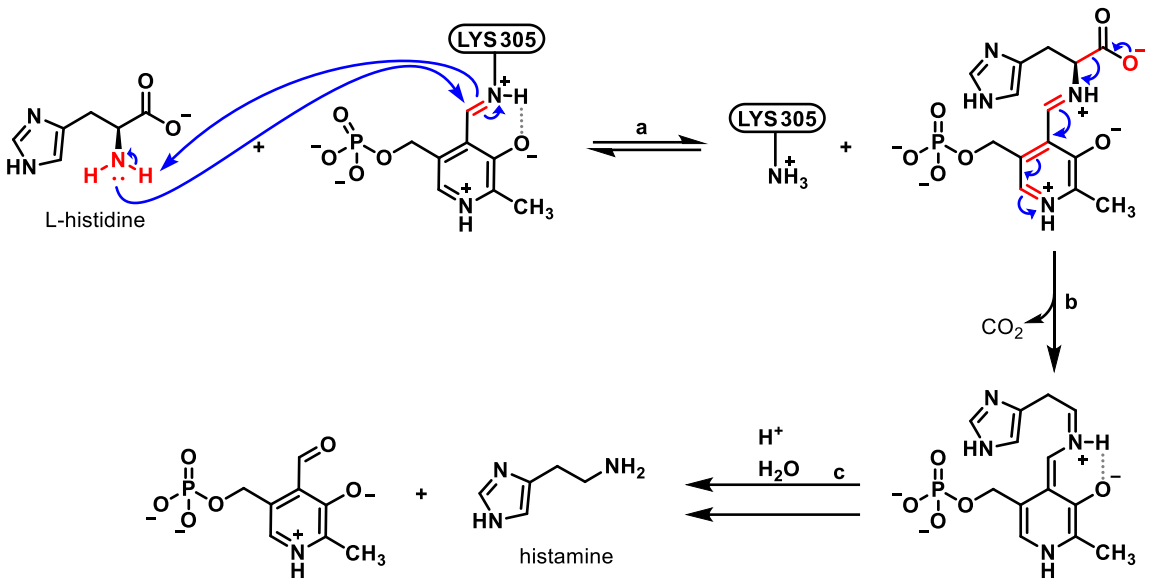

Figure 1: Mechanism of histamine biosynthesis through decarboxylation of histidine by HDC using pyridoxal phosphate as co-factor bound to the catalytic Lys305 of HDC. a) Schiff base formation b) Decarboxylation c) Hydrolysis.

Complementing this precise synthetic mechanism, histamine production is tightly regulated at multiple levels to ensure appropriate physiological responses. At the transcriptional level, HDC expression responds dynamically to diverse stimuli including inflammatory cytokines such as IL-1 and TNF-α, bacterial endotoxins like LPS, and epigenetic modifications through DNA methylation of promoter sequences.[13–15] Beyond transcriptional control, post-translational modifications, including phosphorylation and ubiquitination, provide rapid control over enzyme activity, fine-tuning histamine synthesis to meet diverse physiological demands across different cellular contexts.[16]

Once synthesized, histamine undergoes precise metabolic processing through two primary pathways (see Figure 2).[17] The first involves oxidative deamination by diamine oxidase (DAO), converting histamine into imidazole-4-acetaldehyde (**I**), which gets further metabolized to imidazole-4-acetic acid (**II**) by aldehyde dehydrogenase. This latter intermediate then gets conjugated with phosphoribosyl-pyrophosphate catalysed by 5'-phosphoribosyl transferase (IPRT), yielding after subsequent 5'-nucleotidase catalysed hydrolysis the imidazole acetic acid riboside (**III**).[18] The second pathway involves intracellular methylation by histamine *N*-methyltransferase (HNMT), which transfers a methyl group from *S*-adenosyl-L-methionine to histamine's imidazole ring, producing N^{tele}-methylhistamine (**IV**). This intermediate is further metabolized by monoamine oxidase B (MAO B) or DAO to N^{tele}-methylimidazole-4-acetaldehyde (**V**) and subsequently converted by aldehyde dehydrogenase to N^{tele} -methylimidazole acetic acid (**VI**). Both pathways are regulated through negative feedback loops, where the reaction products inhibit their respective enzymes, ensuring tight control over

histamine levels,[17] with HNMT predominantly regulating histamine concentrations in the brain while DAO exerts its main function in peripheral tissues, particularly the gastrointestinal tract.[19]

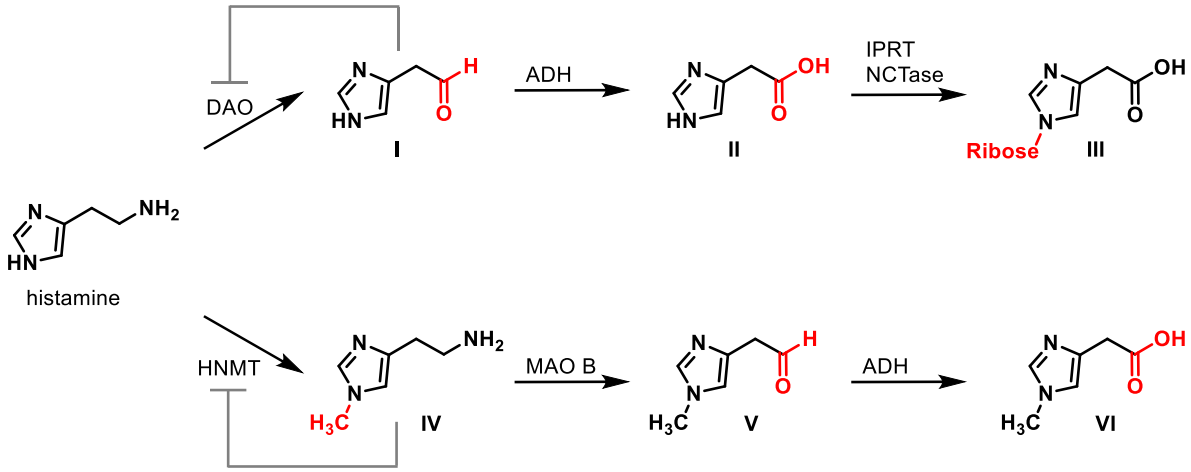

Figure 2: Metabolism pathways of histamine. DAO= diamine oxidase; ADH= aldehyde dehydrogenase; IPRT= 5'-phosphoribosyl transferase; NCTase= 5'-nucleotidase; HNMT= *N*-methyltransferase; MAO-B= monoamine oxidase B.

1.1.2 Storage and release

While metabolism controls histamine levels systemically, cellular storage mechanisms provide local control. Within individual cells, histamine is stored in specialized cellular compartments to enable rapid release upon stimulation. This storage system is particularly sophisticated in basophils and mast cells, which are the major source of histamine,[20] where it is concentrated in secretory granules through vesicular monoamine transporter 2 (VMAT2). These granules contain histamine bound to proteoglycans such as heparin and carboxylated proteases, maintaining high local concentrations essential for rapid release during immune responses.[21] While sharing the same VMAT2 transport mechanism, histaminergic neurons of the tuberomammillary nucleus employ synaptic vesicles rather than secretory granules for histamine storage, and release histamine in response to neuronal activation rather than immune signals.[22] Unlike other biogenic amines, histamine undergoes less reuptake, relying more on enzymatic degradation for signal termination. Throughout the body, tissue concentrations vary significantly, from high levels in skin mast cells and gastric mucosa to specialized distributions in different brain regions that reflect specific functional requirements.[23] Notably, immune cell histamine content fluctuates with their activation state, allowing dynamic responses to immunological challenges.[24] This distribution pattern allows precise control of histamine availability according to local tissue needs.

1.1.3 Physiological roles

Once released from these storage sites, histamine exerts diverse physiological effects, acting through four different G protein-coupled receptors (H_1R–H_4R) to regulate processes across multiple organ systems.[23] In the brain, histamine functions as a key neuromodulator, influencing critical functions from sleep-wake cycles and cognition to energy homeostasis, anxiety responses, and pain perception through complex interactions with other neurotransmitter systems, with alterations in this delicate balance contributing to various neurological disorders.[25–27] This intricate signalling extends to the immune system, where histamine coordinates both immediate and delayed immune responses through receptor-specific pathways, influencing various immune cell types and their functions in a complex system that, when disrupted, underlies many allergic and inflammatory conditions.[28–30] Beyond neural and immune regulation, histamine maintains gastrointestinal homeostasis by controlling acid secretion, mucosal integrity, and motility through precise interactions with multiple cell types, while disturbances in these pathways can lead to various digestive disorders.[4,31,32] These biological function further extends to the cardiovascular system, where histamine fine-tunes vascular permeability, blood flow, and cardiac function through coordinated effects on endothelial cells and smooth muscle, playing a crucial role in both physiological and pathological cardiovascular processes.[33–36]

1.1.4 Cellular networks

Building upon its diverse physiological roles, histamine's biological actions are intricately woven into a complex network of cellular signalling pathways. The integration with other neurotransmitter systems creates sophisticated regulatory mechanisms that fine-tune physiological responses. Particularly notable is the interaction between histaminergic and adrenergic systems, where receptor cross-talk influences both central and peripheral responses.[37] The serotonergic and dopaminergic systems demonstrate significant functional overlap with histamine pathways, especially in regulating arousal and cognitive functions.[38,39] At the molecular level, these interactions occur through receptor heterodimer formation, shared second messenger pathways, and convergent transcriptional regulation, creating complex feedback loops that maintain physiological homeostasis.[40,41] The intricate interplay of histamine with multiple signalling systems exemplifies its role as a master regulator of physiological function. This complexity is further enhanced by tissue-specific expression patterns of histamine receptors and their downstream effectors, creating highly specialized response networks.[42] Understanding these sophisticated regulatory networks has not only advanced our fundamental knowledge of biological systems but has also opened new ways for therapeutic intervention across multiple disease states.[43–46]

1.2 Histamine receptors as GPCRs

1.2.1 G protein-coupled receptors (GPCRs): Structure and function

Histamine mediates its various physiological effects through four distinct histamine receptor subtypes (H_1R-H_4R), which belong to the rhodopsin-like G protein-coupled receptor (GPCR) superfamily.[47] GPCRs constitute the largest and most versatile group of membrane receptors in eukaryotic cells, controlling numerous physiological processes, through their interaction with intracellular signalling molecules, primarily G proteins.[48] The fundamental importance of GPCRs in biological signalling was highlighted by the 2012 Nobel Prize in Chemistry, awarded to Robert Lefkowitz and Brian Kobilka for their pioneering work elucidating GPCR structure and function.[49] These receptors share a characteristic architectural organization consisting of seven transmembrane α-helices, connected by three extracellular loops that contribute to ligand recognition and three intracellular loops participating in signal transduction, with an extracellular N-terminus and intracellular C-terminus, the latter playing an important part in receptor regulation.[50] Their central role in cellular signalling makes them crucial therapeutic targets, with 30-50% of current marketed drugs modulating GPCR function.[51]

The molecular mechanisms underlying GPCR-mediated signal transduction involve complex pathways that can operate both through G protein-dependent and independent mechanisms. While G protein-independent signalling occurs through mechanisms involving G protein kinases (GRK), β-arrestins, and small GTPases, the traditional G protein-dependent pathway represents the main signalling mechanism.[52] In this well-characterized pathway, ligand binding triggers conformational changes in the GPCR that activate its pre-coupled heterotrimeric G protein, consisting of α, β, and γ subunits. This activation promotes the exchange of guanosine diphosphate (GDP) for guanosine triphosphate (GTP) on the α subunit of the G protein, causing the dissociation into an α subunit and a βγ complex (see Figure 3).[52] Both the α subunit and the βγ complex then act as independent signalling molecules, with the cellular response varying based on the specific G protein subtype ($G\alpha_s$, $G\alpha_{i/o}$, or $G\alpha_q$) involved.[53,54]

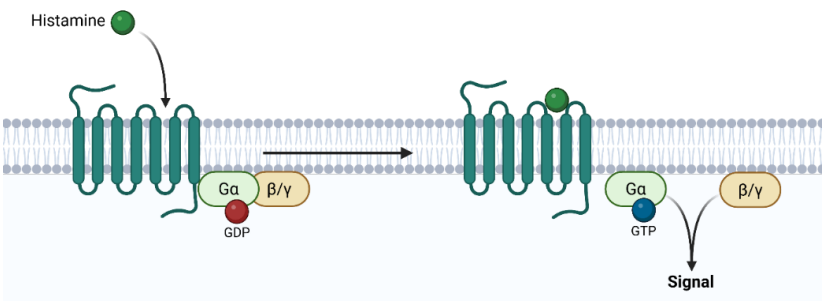

Figure 3: G protein activation after GPCR activation. GDP= guanosine diphosphate; GTP= guanosine triphosphate. Created in https://BioRender.com.

Accordingly, $G\alpha_s$ activates adenylate cyclase and the resulting increase in cyclic adenosine monophosphate (cAMP) levels triggers protein kinase A-dependent phosphorylation events, affecting multiple cellular targets and their functions (see Figure 4).[55] In contrast, $G\alpha_{i/o}$-coupled receptors reduce cellular cAMP levels through adenylate cyclase inhibition, leading to opposite physiological responses.[56] Independent of cAMP regulation, $G\alpha_q$ signalling operates through a different mechanism, activating phospholipase C (PLC) to generate second messengers inositol 1,4,5-trisphosphate (IP_3) and diacylglycerol (DAG). These molecules trigger calcium release from intracellular stores into the cytoplasm and activate protein kinase C (PKC), leading to phosphorylation of downstream effectors at serine/threonine residues, respectively.[57] Additionally, the liberated βγ subunits contribute to signal diversification by modulating different ion channels,[58,59] and activating several kinase cascades.[60–62]

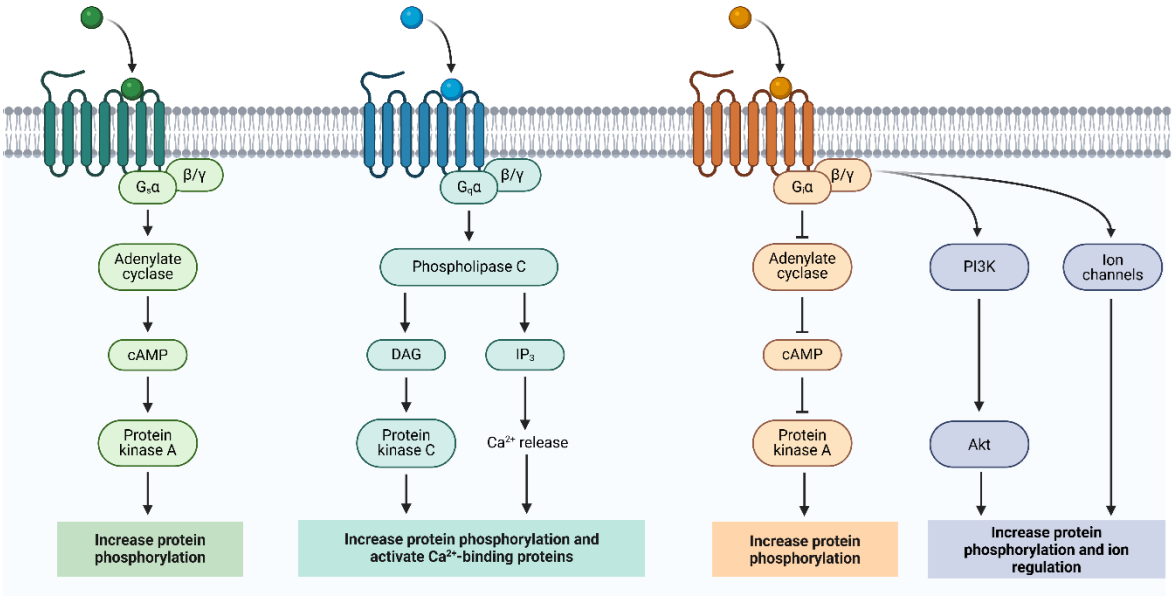

Figure 4: Main signalling pathways of the different G protein subunits after activation of the GPCR. cAMP= cyclic adenosine monophosphate ; DAG= diacylglycerol; IP_3= inositol 1,4,5 trisphosphate; PI3K= phosphoinositide 3-kinase; Akt= protein kinase B. Created in https://BioRender.com.

1.2.2 Histamine receptor evolution and diversity

All four histamine receptors share remarkable conservation across species, with H_1R and H_2R from an evolutionary perspective emerging earlier than H_3R and H_4R. Despite their shared ancestry, these receptors display surprisingly low sequence identities, with H_3R and H_4R sharing the highest sequence identity of around 42%.[63] These relatively low sequence similarities correlate with the receptors' differential recognition of their endogenous ligand histamine, which exhibits significantly higher binding affinities at H_3R and H_4R compared to H_1R and H_2R.[64] Regarding their GPCR signalling mechanisms, the four histamine receptor subtypes exhibit specific coupling preferences. Each histamine receptor subtype couples to different G proteins, determining their distinct cellular effects as H_1R signals mainly through $G\alpha_q$, H_2R

through $G\alpha_s$ or $G\alpha_q$, and both H_3R and H_4R through $Ga_{i/o}$.[42] This diversity in G protein coupling underlies the broad spectrum of histamine's physiological effects. Despite their diverse G protein coupling patterns, these receptors maintain common structural features, including an aspartate residue in transmembrane domain 3 (TM3) that forms crucial ionic interactions with histamine's amino group,[65] and the DRY motif at the cytoplasmic end of TM3, essential for G protein activation,[66] highlighting their evolutionary relationship. However, these receptors differ in their functional characteristics, including tissue expression patterns, constitutive activity levels, and regulatory mechanisms, as will be discussed in detail for each receptor subtype in the following sections.

1.3 Histamine H_1 receptor (H_1R)

1.3.1 Molecular structure and signalling pathways

The H_1 receptor (H_1R), first characterized in 1937 by Daniel Bovet,[67] represents the earliest discovered and most extensively studied histamine receptor subtype. This protein, comprising 487 amino acids and encoded by a single-exon gene on chromosome 3p25,[28] was further understood when its crystal structure, resolved in 2011 in complex with doxepin, provided crucial insights into the molecular architecture and ligand binding mechanisms of histamine receptors.[68] Detailed analysis revealed that the binding pocket contains several key residues, with Asp107 forming a crucial hydrogen bond with histamine's positive amino group, and Asn198, Tyr431 and Thr112 interacting with histamine's imidazole ring, playing essential roles in histamine recognition and receptor activation (see Figure 5).[69,70] Upon agonist binding, the molecular mechanism of receptor activation involves Ser113 acting as a rotamer toggle switch that initiates receptor activation through Asn298,[71] representing a conserved activation pathway in rhodopsin-like GPCRs. While agonist binding triggers this activation mechanism, antagonist recognition occurs through a distinct binding architecture consisting of multiple aromatic residues that create an essential lipophilic cavity,[72] complemented by a specific anion-binding region formed by Lys191 and Lys179[68] and with Asp107 playing a crucial role in antagonist binding as well.[69] Within this binding pocket, Lys200, unique to H_1R, plays a crucial role in antagonist selectivity through its ionic interactions.[73] Interestingly, studies on KW-4679, a selective H_1R antagonist, suggest the existence of an additional binding site that contributes to its selectivity. This binding site relies less on Asp107 interaction, which explains why ligands with strong Asp107 interactions often show poor receptor selectivity, as this residue is conserved across aminergic receptors.[74] Independent of these binding pockets, the receptor exhibits constitutive activity regulated by an Asn-cage mechanism, where Ile420 restrains Asn298 in its inactive conformation through a complex interaction network involving the DRY motif.[75]

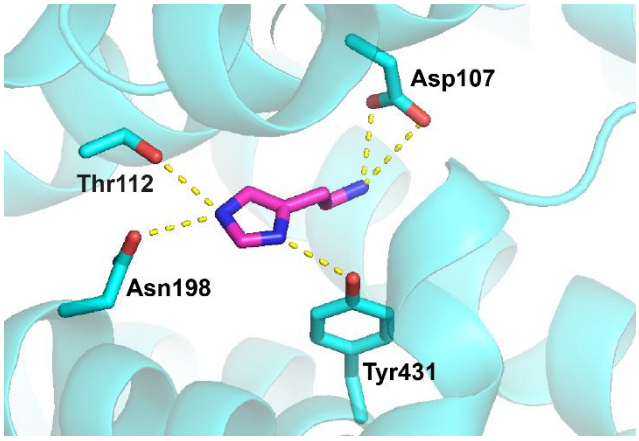

Figure 5: The ligand-binding pocket of histamine in the H_1R. (Crystal structure from PDB: 8YN2)[76]

Beyond its structural characteristics, H_1R shows widespread tissue distribution, with significant expression in smooth muscle, endothelial cells, neurons, and various immune cells.[77–79] This broad distribution pattern underlies its diverse physiological roles, from allergic responses to neurotransmission.[80,81] In these diverse tissues, the signalling cascade initiated by H_1R activation primarily involves $G\alpha_q$ protein coupling,[82] resulting through the second messenger pathway in calcium mobilization and PKC activation. Additionally, H_1R signals through $G\alpha_i/G\alpha_o$ proteins to activate phospholipase A2, leading to arachidonic acid production, while calcium-dependent NO synthase and NO-dependent guanylate cyclase generate nitric oxide and cGMP, respectively.[2] These diverse signalling pathways mediate cell-type specific responses depending on the receptor localization and translate into distinct physiological functions across different organ systems.

1.3.2 Tissue distribution and physiological roles

In smooth muscle cells, H_1R-mediated calcium mobilization triggers contraction, particularly evident in vascular and bronchial tissues,[83] causing bronchoconstriction in the latter.[84] The response in vascular tissue is more complex, exhibiting dual effects which include direct contraction, but also vasodilation mediated by upregulation of endothelial nitric oxide synthase and subsequent NO production in adjacent endothelial cells.[85] Beyond their role in vasodilation, endothelial cells respond to H_1R activation by regulating vascular permeability through cytoskeletal rearrangement and tight junction modulation.[86] Dysregulation of these mechanisms can lead to bronchial asthma and vascular disorders such as hypertension and migraine headaches.[87–89] Due to its presence in the central nervous system, particularly in regions controlling neuroendocrine function such as the hypothalamus, brainstem nuclei, thalamus, hippocampus and cortex,[90–94] H_1R also influences numerous neurological processes, including arousal, appetite regulation, circadian rhythms and multiple cognitive

functions through modulation of neuronal excitability.[95–97] The importance of H_1R in these processes is demonstrated by the occurrence of sleep disorders and vestibular disturbances when histamine signalling is dysregulated.[98,99] However, H_1R plays its most important role in immune responses involving multiple cell types. In mast cells and basophils, H_1R signalling contributes to the release of inflammatory mediators, while dendritic cells and T-lymphocytes express functional H_1R that modulate immune responses through antigen presentation, cytokine production, and T-cell differentiation.[81] This central role in both innate and adaptive immunity makes H_1R an important mediator in allergic diseases such as rhinitis, urticaria, and dermatitis.[100–102] Beyond allergies, H_1R dysregulation is also implicated in autoimmune disorders and chronic inflammatory conditions, demonstrating its broad impact on immune system homeostasis.[28,103]

1.3.3 Therapeutic implications

Based on the understanding of H_1R's physiological functions, therapeutic approaches were designed to inhibit receptor activity through antagonists or inverse agonists to address these pathophysiological conditions. Given H_1R's prominent role in allergic responses, this condition became the primary focus of drug development.[104] First-generation antihistamines like diphenhydramine (**R1**) and chlorpheniramine (**R2**) emerged, which, while effective in managing allergic conditions, showed considerable side effects due to their blood-brain barrier penetration.[105] This led to the development of second-generation compounds such as cetirizine (**R4**), fexofenadine (**R5**), and loratadine (**R6**) (see Figure 6), offering improved selectivity and reduced central nervous system effects.[106] These modern antihistamines additionally demonstrate improved safety profiles and act as inverse agonists rather than neutral antagonists to reduce both histamine-dependent and constitutive receptor activity.[107] The development continued with a newer group of antihistamines, which are in fact active metabolites of second-generation drugs, offering comparable therapeutic benefits while minimizing the cardiac toxicity concerns associated with earlier compounds.[108] Interestingly, the brain-penetrating properties of first-generation H_1R antagonists, initially considered a drawback, proved therapeutically valuable for other conditions. For example, diphenhydramine is commonly used as a sleep aid,[109] while meclizine (**R3**) effectively treats vestibular disorders such as vertigo and motion sickness,[110,111] reflecting H_1R's diverse biological functions across different tissues and organ systems.

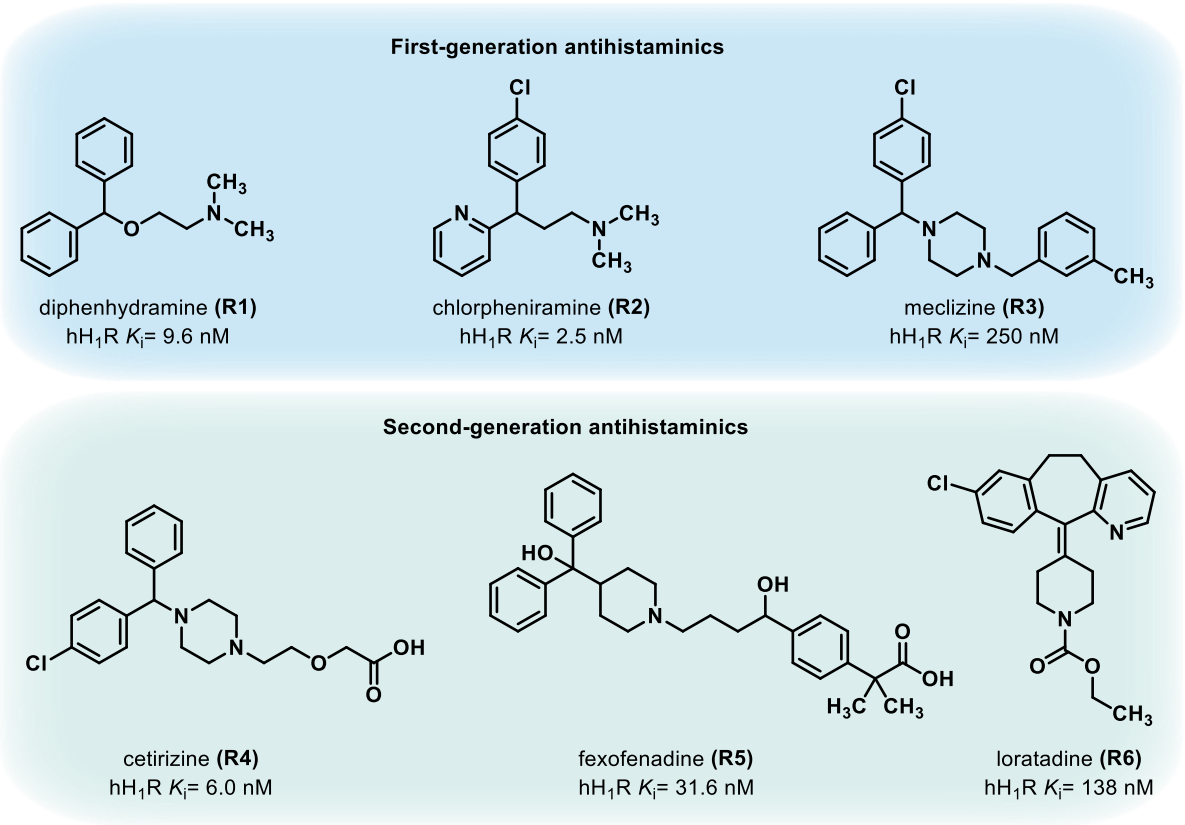

Figure 6: Selected H_1R antagonists of first-generation antihistamines (blue) and second-generation antihistamines (green). K_i values were compiled from published literature sources.[112–117]

1.4 Histamine H_2 receptor (H_2R)

1.4.1 Molecular structure and signalling pathways

The H_2 receptor (H_2R), discovered in 1972 by Black and colleagues,[118] represents a major breakthrough in GPCR research. Even though this 359-amino acid protein, encoded by a gene located on chromosome 5q35,[119] shares the basic seven-transmembrane architecture common to all histamine receptors, H_2R exhibits distinct structural features. Within its binding pocket, Asp98 serves as a counter anion for histamine's cationic amine moiety, while Asp186 and Tyr250 stabilize the imidazole ring (see Figure 7).[120,121] Together with Tyr182 and Thr190, which the latter influencing binding kinetics, these residues create a selective recognition system for H_2R ligands, with Asp186 particularly determining H_2-subtype selectivity.[122] For antagonist binding, Asp98 remains essential while additional residues including Val99 and Phe254 provide important hydrophobic interactions, with Asn159 and Asp186 contributing to complex stabilization.[123] Beyond these binding site characteristics, the receptor's DRY motif configuration plays a vital role in regulating constitutive activity levels, as mutations in this motif lead to increased basal activity but structural instability.[124] Even without stimulation, H_2R shows high constitutive activity even at low expression levels,[125] distinguishing it from other GPCRs including other histamine receptor subtypes. Structurally, this activity is mediated

through its second and third intracytoplasmic loops, which differentially activate both adenylate cyclase and GTP-dependent PLC signalling pathways through employing the respective G proteins.[126] $G\alpha_s$ coupling leads to activation of PKA through elevated cAMP levels, ultimately activating the cAMP response element-binding protein (CREB) transcription factor,[127] while the alternative pathway exert its effects through generating DAG and IP_3 as secondary messengers via PLC activation.

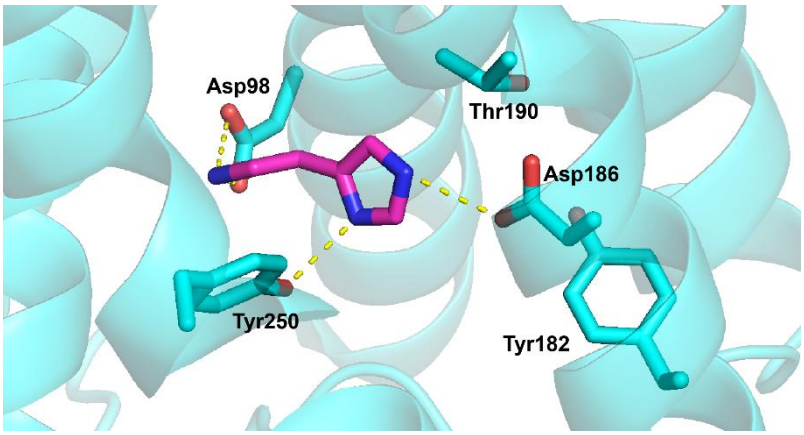

Figure 7: The ligand-binding pocket of histamine in the H_2R. (Crystal structure from PDB: 8YN3)[128]

1.4.2 Tissue distribution and physiological roles

These different signalling cascades and its distinct tissue distribution patterns with prominent expression in gastric parietal cells, but also cardiac tissue, brain regions, vascular smooth muscle, and immune cells, enables H_2R to exert its diverse tissue-specific effects.[3] In gastric tissue, H_2R localizes specifically to the basolateral membrane of parietal cells, where it co-localizes with H^+/K^+-ATPase to regulate acid secretion,[129] with its excessive activation leading to various gastrointestinal disorders like peptic ulcer disease and gastroesophageal reflux disease.[130] H_2R signalling role in gastric tissues is further evidenced by its control of parietal cell morphology and gastric mucosal homeostasis.[131] Beyond gastric functions, H_2R activation in cardiac tissues influences both heart rate and contractility through direct chronotropic and inotropic effects, while also increasing mitochondrial and endothelial permeability, which can exacerbate ischemia/reperfusion injury and heart failure.[132,133] Additionally, the receptor's presence in brain regions, particularly in glutamatergic neurons of the frontal cortex and medial septum, contributes to various neurological processes including cognitive function, learning, memory formation and appetite regulation, with dysregulation of H_2R signalling being implicated in schizophrenia and multiple sclerosis.[134–136] In the circulatory system, H_2R typically mediates vascular and gastric smooth muscle relaxation through NO/sGC pathways, opposing H_1R's contractile effects.[137] While less prominent than H_1R's pro-inflammatory role, H_2R exerts immunosuppressive effects across both innate and adaptive immune responses, regulating mast cell degranulation, dendritic cell function, T cell

proliferation, cytokine production, and B cell antibody responses through cAMP-dependent pathways,[138] with its dysfunction contributing to various inflammatory conditions, particularly gastric inflammation and mucosal injury.[139,140]

1.4.3 Therapeutic implications

Based on H_2R's main role in pathological gastric conditions, therapeutic approaches focused primarily on developing antagonists to inhibit excessive gastric acid secretion. The discovery of burimamide (**R7**) as the first H_2R antagonist by Black and colleagues marked a revolutionary advancement in receptor-targeted therapy, establishing a new paradigm in drug development through selective receptor targeting.[118] This breakthrough led to the development of more potent compounds like cimetidine (**R8**), which became the first blockbuster drug, revolutionizing ulcer treatment.[141,142] Further pharmaceutical advances produced improved agents such as ranitidine (**R9**) and famotidine (**R10**) (see Figure 8), which offered enhanced potency, better safety profiles, and longer duration of action.[143] These H_2R antagonists demonstrate exceptional receptor selectivity and transformed the treatment of acid-related disorders such as peptic ulcer disease and various inflammatory conditions, particularly gastric inflammation and mucosal injury.[144,145] Beyond their primary role in controlling gastric acid secretion, H_2R antagonists have proven valuable in treating immune-related conditions by enhancing immune responses through blocking H_2R's immunosuppressive effects,[138] as demonstrated by cimetidine's efficacy against viral infections like Varicella zoster and Herpes simplex.[146] Additionally, these agents have shown therapeutic benefits in combination with H_1R antagonists in central nervous system disorders, arthritic diseases, and cardiovascular conditions including heart failure,[147] highlighting the diverse physiological roles of histamine and its receptors in multiple organ systems.

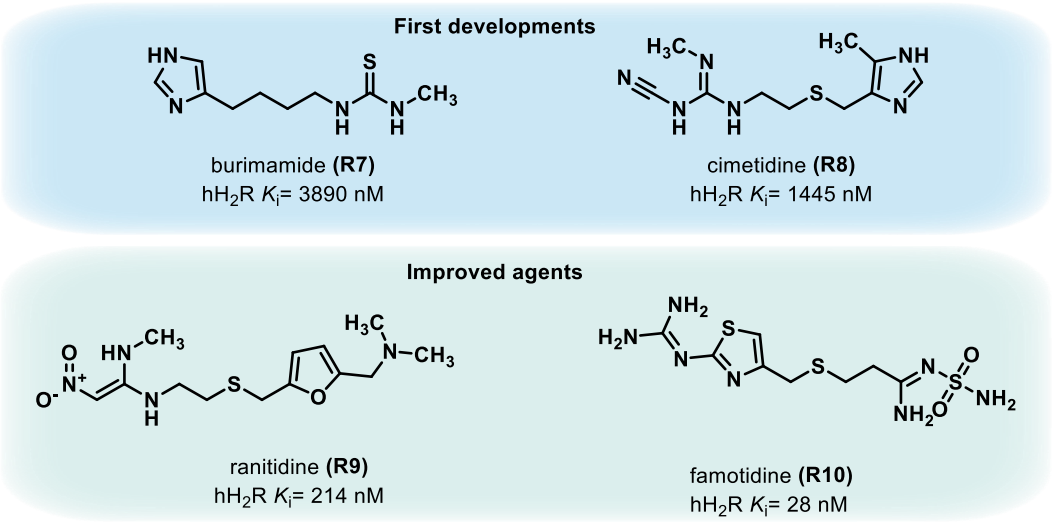

Figure 8: Selected H_2R antagonists: Early developed ligands (blue) and improved agents (green). K_i values were taken from Panula *et al.*.[42]

1.5 Histamine H_3 receptor (H_3R)

The histamine H_3 receptor (H_3R) was first identified and characterized in 1983 by Arrang and colleagues as a novel central nervous system autoreceptor regulating histamine synthesis and release.[148] This groundbreaking discovery established H_3R as an essential modulator of histamine release in the brain, functioning at both pre- and postsynaptic membranes of neuronal cells. Beyond its role as an autoreceptor controlling histamine synthesis and release, H_3R also functions as a heteroreceptor, regulating the release of various other neurotransmitters including acetylcholine,[149] dopamine,[150] noradrenaline[151] and serotonin,[38] therefore playing a major role in maintaining neurotransmitter balance.[152]

Despite its early pharmacological characterization, the molecular identity of H_3R remained elusive for over 15 years, due to its low sequence homology with the previously cloned histamine receptors.[153] The breakthrough came in 1999 when Lovenberg and colleagues successfully cloned the H_3R cDNA. The isolated clone encoded an open reading frame of 445 amino acids and, surprisingly, showed highest homology with M2 muscarinic acetylcholine receptors rather than other histamine receptors, showing only about 20% amino acid identity with H_1/H_2 receptors and around 42% with H_4 receptor.[63,154] Following this discovery, genetic mapping revealed that the human H_3R gene is located on chromosome 20q13.33. Structurally, the gene consists of either three exons and two introns or four exons and three introns, depending on the splice variant.[155,156] This complex genetic organization differs significantly from other histamine receptors and contributes to the generation of multiple receptor isoforms through alternative splicing[157] leading to isoforms that exhibit differences in their distribution, signalling properties, and constitutive activity levels.[158,159]

1.5.1 Molecular structure and networks

Complementing these genetic insights, structural studies have revealed the molecular basis of H_3R's ligand interactions, showing that the binding modes of H_3R ligands differ significantly between agonists and antagonists. H_3 receptor agonists, including the endogenous ligand histamine, usually bind in the cleft between TM2, TM3, TM6, and TM7.[160] A key element in this binding pocket is the conserved aspartic acid residue Asp114 in TM3, which interacts with the protonated ethylamine side chain of histamine.[161] The endogenic agonist binding is further stabilized as the imidazole ring of histamine functions as a hydrogen bond acceptor to glutamic acid Glu206 in TM5 (see Figure 9),[160] as demonstrated in H_3R homology models. Other agonists were also able to interact with Asp80 on TM2, which seems critical for receptor activation, as this amino acid contact triggers a conformational change in TM2 and TM7 that propagates to the intracellular domains, facilitating G protein coupling.[161] The binding pocket is further stabilized by interactions with Tyr115, Tyr374, and Trp371, which create an aromatic

network that properly orients agonists.[162] Notably, the presence of glutamic acid at position 206 in H_3R, rather than the asparagine Asn198 found in the H_1 receptor, enables stronger hydrogen bonding with histamine's imidazole ring, contributing to histamine's significantly higher affinity for H_3R compared to H_1R.[160]

In contrast to agonists, H_3 receptor antagonists exhibit distinct binding modes that exploit additional receptor pockets. While most H_3R antagonists maintain the critical interaction between their basic nitrogen and Asp114 in TM3, they typically extend into a hydrophobic cavity near TM5 formed by residues Tyr112, Leu175, Ala179, Leu199, and Ala202.[162] Unlike agonists, many antagonists do not require interaction with Glu206, as demonstrated by mutation studies showing that Glu206 substitution minimally affects certain antagonist binding.[162] Additionally, while Asp80 plays a crucial role in receptor activation by agonists, this interaction is not essential for antagonist binding, which primarily relies on contacts with Asp114 and the surrounding aromatic residues.[161] Instead, antagonists are stabilized by an aromatic cage formed by Tyr83, Phe368, and Trp371, which facilitates π-cation interactions with aromatic moieties of the ligands.[162] This structural arrangement accommodates the diverse chemical scaffolds found in H_3R antagonists. Notably, these binding interactions, initially predicted through homology modelling, have recently been confirmed by the high-resolution crystal structure of H_3R,[163] marking a significant breakthrough that came more than 20 years after the receptor's cloning, validating our understanding of the receptor's binding characteristics and providing definitive structural evidence for ligand-receptor interactions.

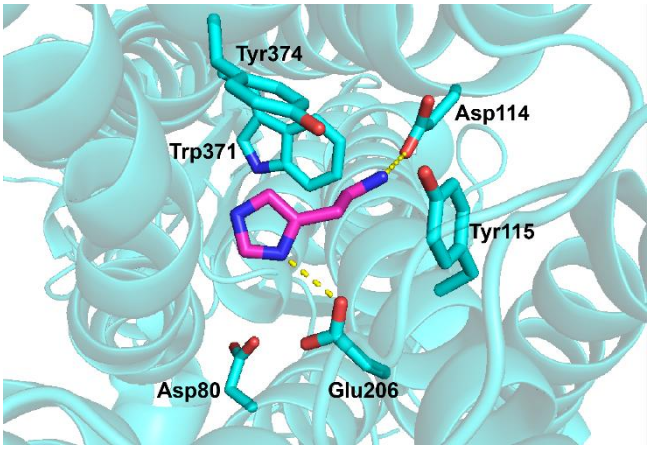

Figure 9: The ligand-binding pocket of histamine in the H_3R. (Crystal structure from PDB: 8YN5)[164]

A remarkable feature of H_3R is its high constitutive activity in the absence of agonist stimulation.[165] Structurally, this constitutive activity appears to be partly due to modifications in the carboxyl terminus of the third intracellular loop, as evidenced by functionally active H_3R

isoforms containing an extended amino acid sequence similar to that found in constitutively active β_2-adrenergic receptors.[166]

The complexity of H_3R pharmacology extends beyond its constitutive activity to include interactions with other receptors as it can form homo- and hetero-oligomers, providing additional regulatory mechanisms for receptor function. This oligomerization creates unique pharmacological properties distinct from the individual receptors. For example, H_3R forms heterodimers with dopamine D_1R and D_2R on GABAergic dynorphinergic and enkephalinergic neurons, with H_3R activation reducing the affinity of selective D_1R or D_2R agonists to their corresponding receptors.[167] This heterodimerization enables H_3R agonist-induced activation of a G_i protein that mediates MAPK activation.[168] Notably, D_1 and D_2 receptor-mediated activation of extracellular signal-regulated kinase 1/2 (ERK1/2) is absent in the striatum of H_3 receptor knockout mice, suggesting that normal dopamine receptor-mediated signalling requires histamine H_3 receptor.[169] The complex structural features of H_3R, including its unique binding pocket, constitutive activity, and ability to form oligomers, provide the molecular basis for its diverse physiological roles in the central and peripheral nervous systems.

1.5.2 Tissue distribution and physiological roles

These various functions are depended on the receptors distribution pattern, as H_3 receptors are predominantly expressed on neuronal cells, particularly on presynaptic terminal where they regulate neurotransmitter release. This neuronal expression pattern is consistent with their primary role in modulating synaptic transmission in both the central and peripheral nervous systems.[170,171] Within the central nervous system, the H_3 receptor is abundantly expressed in critical brain regions including the cerebral cortex, thalamus, caudate putamen, hippocampus, striatum, hypothalamus, histaminergic tuberomamillary nucleus (TMN), and noradrenergic neurons of locus coeruleus,[172] demonstrating H_3Rs major contribution to forming the extensive histaminergic network in the human brain (Figure 10). In the cerebral cortex, intense labelling of H_3R is found in layer V of most cortical areas, with human prefrontal cortex showing higher expression in layer V than other layers. This distribution pattern suggests a role in modulating cortical output, as layer V contains pyramidal neurons that project to subcortical structures.[173] Based on this anatomical mapping, the thalamocortical system and major parts of the limbic system constitute the primary elements of H_3 receptor-regulated systems. This means that H_3 receptors are strategically positioned to influence sensory processing, attention, and emotional responses by modulating the flow of information between the thalamus and cortex, as well as within limbic circuits involved in memory and motivation.[174] The localisation of H_3 receptors in the hypothalamus enables regulation of energy homeostasis and food intake by modulating the activity of neurons expressing

orexigenic peptides.[175] Additionally, H_3 receptors in the striatum play an important role in motor control through interactions with dopaminergic transmission, as evidenced by their effects on locomotor activity in experimental models.[167] The high expression of H_3 receptors in the TMN is particularly significant for arousal regulation, as histaminergic neurons projecting from this region promote wakefulness and cortical activation, with H_3 autoreceptor providing negative feedback control of this wake-promoting system.[176]

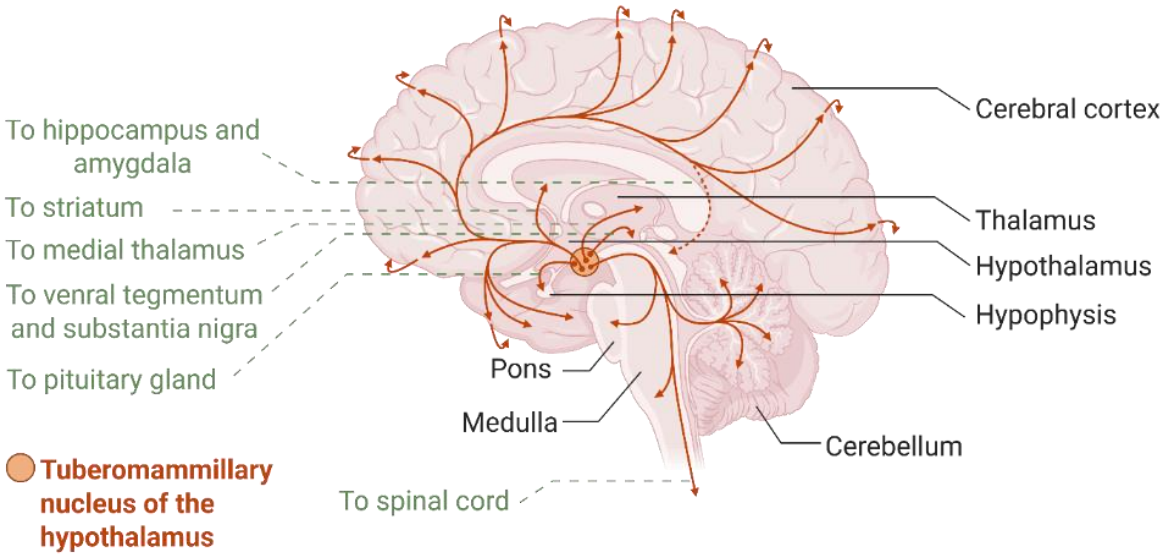

Figure 10: The histaminergic system in the human brain mainly regulated by H_3R due to its wide distribution pattern in different brain regions. Histaminergic projections (orange arrows) emanate from the tuberomammillary nucleus and branch throughout the whole central nervous system, innervating the major parts of the human brain, including cerebral cortex, amygdala, substantia nigra and striatum, with a descending pathway to the brain stem, cerebellum and the spinal cord. Adapted from Haas *et al.*[2] and created in https://BioRender.com.

Beyond its extensive presence in the central nervous system, H_3R is also expressed in the peripheral nervous system, regulating sympathetic neurotransmitter release in skin, dorsal root ganglia, superior cervical ganglia, and spinal cord, where it serves as a potential antinociceptive target for treating neuropathic pain by modulating sensory neurotransmission.[177,178] It's also expressed in different tissues in the cardiovascular system including saphenous vein, heart, and pulmonary artery where H_3R activation inhibits noradrenaline release from sympathetic nerve terminals, resulting in vasodilation and decreased cardiac contractility.[179,180] Additionally, evidence from guinea pig lung studies suggests that in the respiratory system, H_3 receptors are located on the smooth muscle of the trachea where they mediate bronchodilation when activated.[181]

1.5.3 Signalling pathways

The H_3 receptor exerts its diverse physiological effects through multiple signalling cascades (see Figure 11) beginning with its canonical coupling to $G\alpha_{i/o}$ proteins that directly inhibit adenylyl cyclase. This inhibition reduces cAMP production and decreases PKA activity, which leads to decreased phosphorylation of histidine decarboxylase and vesicular monoamine transporters, thereby reducing histamine synthesis and packaging into vesicles for release and ultimately to reduced neurotransmitter release in various brain regions.[182,183] Additionally, the inhibition of PKA modulates calcium homeostasis by decreasing K^+-induced calcium influx,[184] contributing to the inhibitory effect of H_3R activation on neurotransmitter release from nerve terminals. Beyond cAMP inhibition, H_3R activation stimulates phospholipase A2 via $G\alpha_{i/o}$ proteins, leading to the release of arachidonic acid and other metabolites.[185] These lipid mediators act as second messengers that modulate ion channel function and neuronal excitability, and can be further metabolized to produce prostaglandins and leukotrienes that influence inflammatory responses in the brain.[186] Through Gα16 activation, a less common signalling pathway compared to its canonical $G\alpha_{i/o}$ coupling, H_3R can increase cytosolic Ca^{2+} concentration through the PLC pathway, which triggers various calcium-dependent processes including neurotransmitter release and gene transcription.[187] The released Gβγ subunits trigger additional signalling pathways, including MAPK activation affecting neuronal plasticity and memory processes, particularly through ERK1/2 phosphorylation that regulates gene expression involved in long-term potentiation and memory consolidation.[185,188,189] The Gβγ subunits also activate the Akt/GSK-3β axis through PI3K, influencing neuronal migration and protection against apoptosis.[185] Akt activation leads to phosphorylation and inhibition of GSK-3β, which prevents tau hyperphosphorylation and promotes neuronal survival,[190] potentially explaining the neuroprotective effects observed with some H_3R ligands. Collectively, these various signalling pathways enable H_3R to exert both immediate effects on neurotransmission and long-term effects on neuronal function and viability, with each pathway showing differential constitutive activity and varying in intensity depending on the receptor isoform involved.[191]

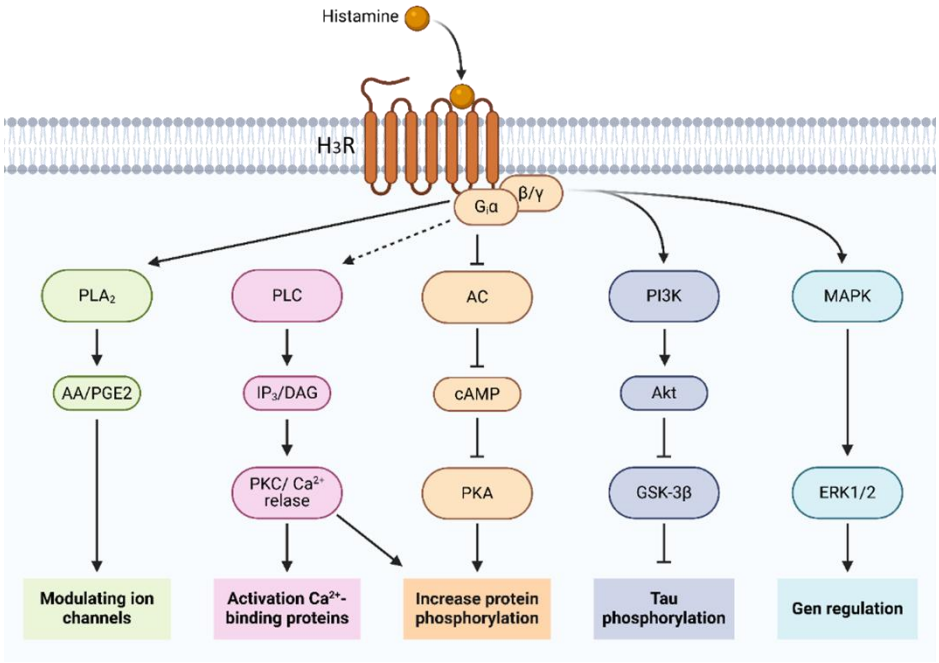

Figure 11: Overview of some of the different signalling pathways from histamine H_3 receptor after activation. PLA_2= phospholipase A2; AA= arachidonic acid; PGE2= prostaglandin E2; PLC= phospholipase C; IP_3= inositol-1,4,5-trisphosphate; DAG= diacylglycerol; PKC= protein kinase C; AC= adenylate cyclase; cAMP= cyclic adenosine monophosphate; PKA= protein kinase A; PI3K= phosphoinositide 3-kinases; Akt= protein kinase B; GSK-3β= glycogen synthase kinase-3-beta; MAPK= mitogen-activated protein kinase; ERK1/2= extracellular signal-regulated kinase 1/2. Created in https://BioRender.com.

1.5.4 Therapeutic relevance

The widespread distribution pattern and multifunctional role of neurotransmitter regulation explains why H_3R is implicated in a diverse spectrum of neurological, psychiatric and neuroendocrine disorders, ranging from Parkinson's disease, Alzheimer's disease, epilepsy and restless legs syndrome (RLS) to schizophrenia, attention deficit hyperactivity disorder (ADHD), depression, anxiety, narcolepsy, substance use disorders, obesity, and Prader-Willi syndrome (PWS).[175,192–199]

The role of H_3R in cognitive disorders is characterized by abnormal receptor signalling disrupting multiple neurotransmitter systems critical for cognitive function. In Alzheimer's disease, pathological receptor overactivation results in excessive inhibition of acetylcholine and glutamate release in cognitive centres of the brain. This dysregulation impairs CREB phosphorylation and GSK3β inhibition, leading to reduced synaptic plasticity and increased tau hyperphosphorylation, both key mechanisms underlying cognitive decline.[200] In ADHD and schizophrenia, H_3R dysfunction is present in the prefrontal cortex with distinct patterns of dysregulation. While ADHD involves altered H_3R modulation of multiple neurotransmitters essential for attention and executive function like dopamine, norepinephrine, and acetylcholine,[199] schizophrenia is characterized by H_3R upregulation that disrupts both

glutamatergic signalling in cortico-hippocampal circuits and dopamine release patterns, contributing to the positive symptoms and cognitive deficits characteristic of the disorder.[201] Similarly, in substance use disorders, H_3R dysfunction affects the prefrontal cortex and, additionally, the nucleus accumbens, disrupting normal dopaminergic transmission in these key regions of the reward circuit, thereby influencing both executive control over drug-seeking behaviours and reward processing, while also impacting the neuroplasticity changes that underlie addiction.[202] Furthermore, abnormal H_3R signalling contributes to depression and anxiety disorders by disrupting monoaminergic transmission in limbic structures, altering serotonin, norepinephrine, and dopamine levels essential for mood stability.[203] Additionally, H_3R dysregulation impairs hypothalamic-pituitary-adrenal axis function during stress responses, creating neuroendocrine imbalances that further exacerbate emotional dysregulation.[204] In Parkinson's disease, H_3R dysfunction manifests as receptor upregulation in the substantia nigra compared to normal control brains, disrupting the normal inhibitory control of neurotransmitter release. This dysregulation impairs the delicate balance between histaminergic and dopaminergic systems, exacerbating dopamine deficiency and contributing to the characteristic motor symptoms of the disease.[192] With arousal determined by the pacemaker firing frequency of TMN cells, H_3R is critically involved in sleep/wake regulation.[194] In narcolepsy, the loss of orexin neurons disrupts the normal inhibitory control that H_3R autoreceptor exert over histaminergic neuron activity in the TMN, creating an imbalance in the histaminergic system's regulation of wakefulness and contributing to the characteristic dysregulated sleep-wake transitions observed in narcolepsy patients.[176] In restless legs syndrome, H_3R dysfunction manifests as increased receptor expression in the striatum during iron deficiency, a common feature in RLS patients. This upregulation correlates positively with periodic limb movement severity, suggesting that abnormal histaminergic modulation of striatal dopamine transmission contributes to the sensorimotor symptoms characteristic of the disorder.[197] Another condition with prominent sleep disturbances, Prader-Willi syndrome, exhibits significant histaminergic involvement, as evidenced by the therapeutic response to H_3R modulation. The characteristic excessive daytime sleepiness, impaired nighttime sleep, reduced muscle tone, and cognitive deficits in PWS patients suggest dysregulated histaminergic neurotransmission affecting multiple brain circuits controlling arousal, motor function, and cognition.[198]

The histaminergic system also plays a critical role in seizure regulation through H_3R-mediated control of neuronal excitability, as evidenced by the regional imbalances observed in epileptic brains. Patients with mesial temporal lobe epilepsy exhibit a distinctive pattern of H_3R dysregulation characterized by reduced receptor function with elevated histamine in the

hippocampus alongside H_3R overactivation with decreased histamine in the temporal neocortex, disrupting the inhibitory control necessary for preventing abnormal neuronal firing and synchronization.[205] Furthermore, the histaminergic system exerts significant influence over energy homeostasis through H_3R located in hypothalamic centres, coordinating arousal states with feeding behaviour. This dual regulatory capacity allows H_3R to integrate novelty-induced attention, arousal, and satiety signals with the consolidation of temporal information associated with food consumption, creating a sophisticated neurochemical network that balances energy intake with expenditure and suggesting that H_3R dysregulation contributes to metabolic disorders like obesity through disruption of these finely tuned homeostatic mechanisms.[175,206] The H_3 receptor's involvement in this wide range of disorders (see Table 1) makes it a valuable therapeutic target, offering unique opportunities for both symptomatic relief and disease modification. This broad therapeutic potential has driven significant efforts to develop selective H_3 receptor ligands for clinical application.

Table 1: Disorder-specific effects of H_3R dysregulation: impacted neurotransmitter systems, brain regions, and pathophysiological outcomes. ADHD= attention deficit hyperactivity disorder; ACh= acetylcholine; Glu= glutamate; DA= dopamine; NE= norepinephrine; 5-HT= serotonin; GABA= gamma-aminobutyric acid; NPY= neuropeptide Y; NT= neurotransmitter; TMN= tuberomammillary nucleus. ↑= upregulation; ↓= downregulation; ↑↓= dysregulation.

H_3R-related disorder	**Dysregulated NT systems**	**Brain regions**	**Pathophysiological impact**
Alzheimer's diesease	ACh, Glu	Cognitive centres	Synaptic plasticity ↓
ADHD	DA, ACh, NE	Prefrontal cortex	Attention ↓
Schizophrenia	Glu, DA	Hippocampus	Cognition ↓
Substance abuse	DA	N. accumbens	Reward processing ↑↓
Depression/Anxiety	DA, NE, 5-HT	Limbic structures	Mood stability ↑↓
Parkinson's disease	DA	Substantia nigra	Motor function ↓
Narcolepsy	orexin	TMN cells	Arousal ↓
Restless leg syndrome	DA	Striatum	Motor activity ↑
Prader-Willi syndrome	GABA, 5-HT	Hypothalamus	Arousal, cognition ↓
Epilepsy	Glu, GABA	Hippocampus	Excitability ↑
Obesity	orexin, NPY	Hypothalamus	Energy balance ↓

1.6 Histamine H_3 receptor ligands

1.6.1 Agonists

1.6.1.1 Development

The first selective H_3 receptor agonists were developed based on modifications of the endogenous ligand histamine. (*R*)-α-methylhistamine (RAMH), initially synthesized in the 1980s, became the prototypical H_3R agonist with approximately 15-fold higher potency than histamine itself and excellent selectivity over the histamine receptor subtype H_1R and H_2R.[207] These valuable characteristic have made RAMH (**R11**) extensively used as a pharmacological tool to characterize H_3R function in various experimental settings.[208–210] Further structural refinements led to the development of imetit (**R12**), followed by immepip (**R13**), which both exhibit slightly higher potency and selectivity over H_1R and H_2R than RAMH.[211,212] Another significant advancement came with immethridine (**R15**), where the piperidine ring of immepip was replaced with a 4-pyridine ring (see Figure 12). Although immethridine shows similar affinity and functional activity at the human H_3 receptor compared to immepip, it demonstrates a better selectivity profile with approximately 300-fold selectivity over the human H_4R while maintaining no affinity towards H_1R and H_2R.[213] This favourable selectivity and affinity profile was also conserved by methimepip (**R14**), a methylation product of immepip, featuring a 4-methyl substituent on the imidazole ring that additionally significantly enhances CNS penetration.[214] These imidazole-containing agonists have been invaluable research tools, though their clinical utility is limited by potential interactions with cytochrome P450 enzymes due to their imidazole moiety.[215] Another notable compound is proxyfan (**R16**), which displays complex pharmacological properties as a protean agonist, meaning it can act as both an agonist and antagonist depending on the signalling pathway, receptor context, and concentration.[216] Different degrees of partial agonist properties were later also found in other series of non-amine imidazole derivatives like cipralisant (**R17**) that displayed the spectrum of pharmacological activities from full agonism to full antagonism.[65,217]

1.6.1.2 Therapeutic potential

The therapeutic potential of these H_3R agonists emerges from their ability to modulate neurotransmitter release in various physiological systems. In sleep regulation, compounds such as RAMH, imetit, and immepip have demonstrated sleep-promoting effects in preclinical models by inhibiting histaminergic neurotransmission, which plays a key role in arousal. These effects align with the known wake-promoting action of histamine, though translational outcomes have varied between studies and compounds.[218,219] The anti-inflammatory properties of H_3R agonists derive from their dual action on neurogenic inflammation and direct smooth muscle effects. RAMH has shown efficacy as a bronchodilator in guinea pig models,

relaxing airway smooth muscle under resting conditions.[220,221] This bronchodilatory effect, coupled with the ability of both RAMH and imetit to reduce endothelial permeability in pulmonary edema models, suggests potential utility in asthma and inflammatory airway conditions.[222] For migraine, the therapeutic rationale centres on neurogenic inflammation control. Immepip and related compounds have demonstrated efficacy in preclinical neurogenic vascular inflammation models,[223] while *N*-methylhistamine showed promising results in phase II clinical trials at remarkably low doses, significantly reducing the frequency and severity of migraine attacks.[224,225] These findings suggest that subtle modulation of histaminergic signalling may effectively interrupt the migraine cascade. In cardiovascular applications, the potential of H_3 agonists stems from their ability to regulate sympathetic outflow. By reducing norepinephrine release during ischemic conditions, these compounds may protect against arrhythmias and cardiac dysfunction associated with excessive sympathetic activation.[180,226] This cardioprotective mechanism represents a distinct therapeutic approach compared to conventional antiarrhythmic strategies.

Despite these promising therapeutic directions, no H_3R agonist has yet reached clinical use, often limited by pharmacokinetic restrictions, with compounds like RAMH showing poor oral bioavailability and rapid metabolism,[227] and immethridine, despite showing excellent selectivity and affinity in preclinical studies, having produced mixed results in early clinical trials, further limiting its current clinical application. These results highlight the need for improved drug delivery systems or novel chemical scaffolds to fully realize the therapeutic potential of H_3R agonists.

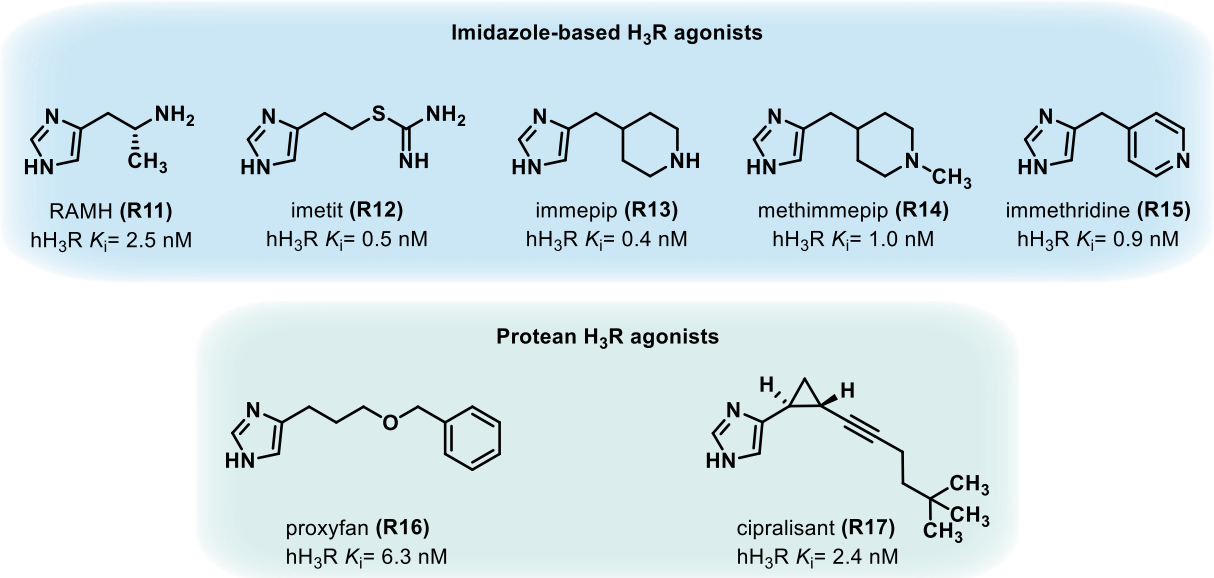

Figure 12: Selected H_3R ligands: imidazole-based agonists (blue) and protean agonists (green). K_i values were compiled from published literature sources.[42,213,228]

1.6.2 Antagonists and inverse agonists

1.6.2.1 Development

The journey toward developing selective histamine H_3R antagonists, which actually often function as inverse agonists due to the receptor's high constitutive activity, began in the late 1980s with a significant discovery, that the H_2R antagonist burimamide (**R7**) demonstrated unexpected antagonistic properties at H_3R.[148] This interesting finding provided researchers with a valuable lead compound for subsequent structural modifications and optimization. Research efforts initially concentrated on imidazole-based ligands, culminating in the synthesis of thioperamide (**R18**), which quickly established itself as the prototypical H_3R antagonist due to its high affinity and selectivity for the receptor.[207] Following thioperamide's success, additional imidazole-containing antagonists were developed, including clobenpropit (**R19**) and ciproxifan (**R20**), each with enhanced properties. While clobenpropit demonstrated improved receptor affinity compared to thioperamide, ciproxifan offered superior brain penetration, making it particularly valuable for *in vivo* studies investigating central nervous system functions regulated by H_3R.[229,230] Despite these advances, these first-generation imidazole-containing compounds faced considerable limitations. The subsequent discovery of the H_4R in the early 2000s revealed significant selectivity issues, as both clobenpropit and thioperamide exhibited potent activity at H_4R.[231] Additionally, further investigation revealed that each of these three compounds exhibited varying degrees of activity at other biogenic amine receptors, including 5-HT_3 receptors and α_2-adrenergic receptors.[232] More problematically, the imidazole moiety caused significant drug-drug interactions through cytochrome P450 inhibition, severely limiting their clinical potential.[65]

These challenges ultimately drove researchers to develop non-imidazole H_3R antagonists. This pivotal shift involved substituting the imidazole moiety with cyclic or tertiary amines, leading to a new generation of non-imidazole ligands with improved properties.[65] Computer modelling strategies for ligand docking and pharmacophore screening became increasingly important in this phase of development,[162,233] helping researchers identify essential pharmacophoric elements and resulting in a diverse array of novel ligands (see Figure 13). The resulting second-generation histamine H_3R antagonists, despite their structural variability, share a common feature as they replaced the imidazole ring with alternative basic moieties, such as azepine (GSK-189254 (**R21**)), pyrrolidine (ABT-239 (**R22**)), or morpholine (JNJ-31001074 (**R23**)).[234,235] These structural modifications maintain the ability of these antagonists to interact with Asp114 through hydrogen bonding in the receptor binding pocket, while their lipophilic substituents occupy hydrophobic pockets formed by transmembrane domains.[162] Beyond preserving crucial receptor interactions, these structural innovations yielded compounds with

significantly improved pharmacological profiles. The non-imidazole antagonists generally demonstrated improved brain penetration, reduced potential for drug-drug interactions, better oral bioavailability, and longer half-lives allowing for once-daily dosing,[215] which is why H_3R antagonist development continued in this direction.[236] A particularly notable development was pitolisant (**R24**), which incorporates a piperidine moiety in place of the imidazole group, demonstrating exceptional selectivity for H_3R and favourable pharmacokinetic properties.[237]

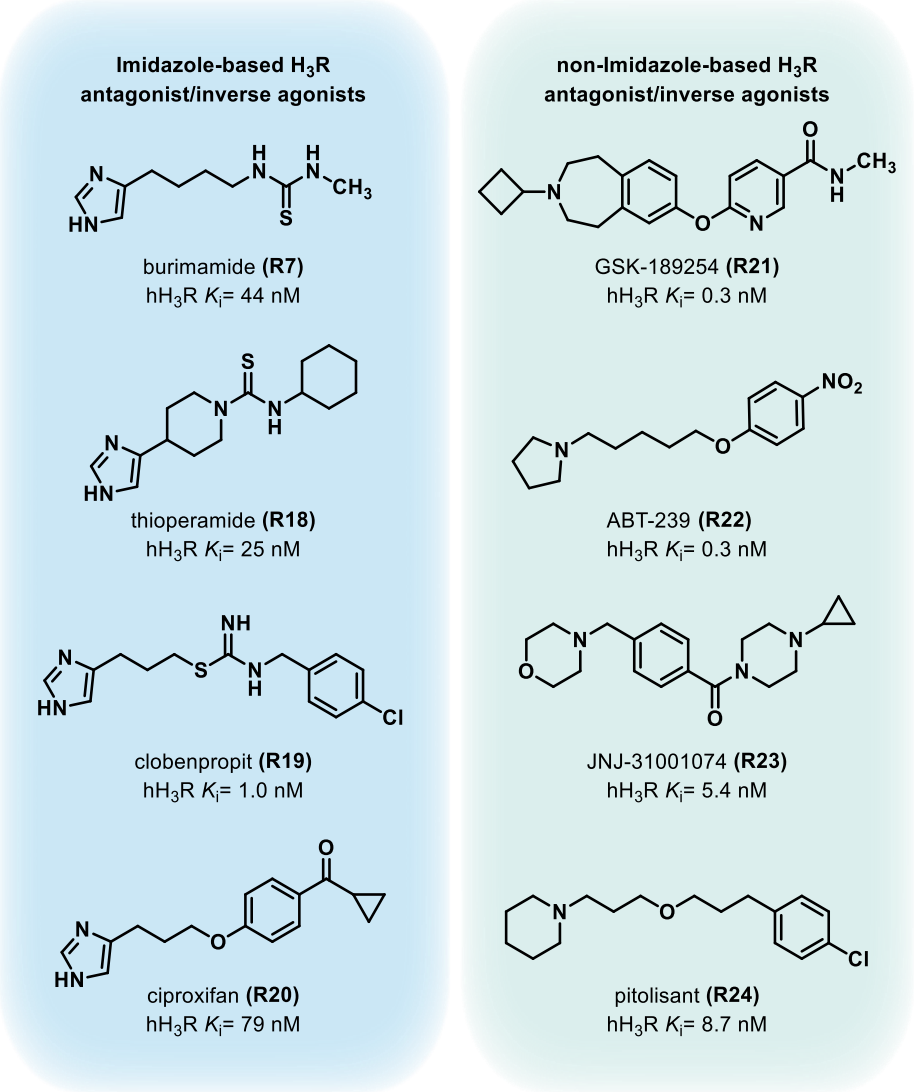

Figure 13: Selected H_3R ligands: imidazole-based antagonist/inverse agonists (blue) and non-imidazole-based antagonist/inverse agonists (green). K_i values were compiled from published literature sources.[42,177,235,238]

1.6.2.2 Pharmacophore

Over time, the H_3R pharmacophore evolved considerably from its original conception. What began as an imidazole moiety attached to a spacer system with an apolar group and a hydrophobic cap transformed as researchers synthesized and evaluated numerous non-imidazole ligands. This extensive exploration led to a refined pharmacophore model featuring alkylamine groups, preferably cyclic amines, connected to a central aromatic core

through a flexible spacer system, constituting the western portion of the molecule. The eastern portion demonstrated remarkable versatility, being able to accommodate different moieties like a second basic group, various polar functionalities, or lipophilic residues.[239] This structural refinement culminated in a generalized alkylamino-propoxyphenyl framework that became the scaffold for numerous potent H_3R antagonists, including DL-77 (**R25**) and JNJ-5207852 (**R26**), establishing a blueprint that continues to guide drug development efforts in this therapeutic area (see Figure 14).[239]

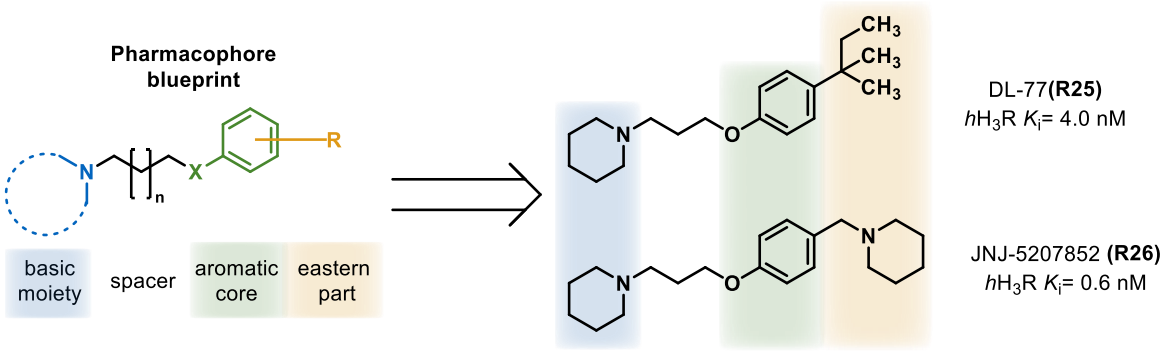

Figure 14: Pharmacophore blueprint of non-imidazole-based H_3R antagonists/inverse agonist, exemplified at DL-77 and JNJ-5207852. K_i values were compiled from published literature sources.[240]

1.6.2.3 Therapeutic potential

The pharmacological advantages of these structurally refined H_3R antagonists have enabled their progression into clinical development for a diverse range of conditions. Several compounds have advanced to Phase I, II, and even Phase III clinical trials for various indications including sleep disorders, cognitive impairments in schizophrenia, Alzheimer's disease, Parkinson's disease, ADHD, substance abuse, obesity, and epilepsy.[65] Early imidazole-containing H_3R antagonists demonstrated promising therapeutic potential in preclinical studies despite their pharmacokinetic limitations. Thioperamide showed efficacy in behavioural models of learning and memory as well as in epilepsy models.[241–243] It also demonstrated negative regulation of food intake in rodent models, suggesting therapeutic potential for obesity.[244] Similarly, clobenpropit and ciproxifan demonstrated activity in *in vivo* models of working memory, seizures, and Alzheimer's disease.[245,246] Non-imidazole H_3R antagonists show considerable therapeutic promise in the treatment of cognitive disorders. GSK-239512 was evaluated in clinical trials for cognitive impairment in Alzheimer's disease and schizophrenia, demonstrating improvements in attention and processing speed.[247,248] ABT-288 underwent clinical testing for cognitive dysfunction with mixed results. Notably, a randomized controlled trial found that ABT-288 failed to improve cognitive function in patients with schizophrenia despite promising preclinical data showing efficacy in multiple animal cognition models.[248–250] The benzofuran-containing ABT-239 demonstrated versatility as a

standard non-imidazole antagonist, showing high potency in models of attention, cognition, and Alzheimer's disease.[200,238] Beyond these cognitive applications, ABT-239 and other H_3R antagonists have shown efficacy in additional therapeutic areas. For instance, ABT-239 and GSK-189254 both demonstrated effectiveness in various pain models, particularly osteoarthritis pain, highlighting the potential of H_3R antagonists in pain management.[251,252] In addiction research, JNJ-39220675 and DL-77 were found to decrease voluntary ethanol intake in ethanol-preferring rats,[253] while DL-77 additionally demonstrated ethanol-induced conditioned place preference in mice.[254] DL-77 also showed promise in neurological disorders, exhibiting both anticonvulsant effects and improved cognitive performance, suggesting potential for treating memory impairment associated with epilepsy.[255] For attention disorders, JNJ-31001074 has been investigated in clinical trials for ADHD, with preliminary results suggesting improvements in attention and impulsivity measures.[256] Preclinical studies demonstrate that H_3R blockage enhance prefrontal cortex function and modulate dopaminergic transmission in ways that could address core ADHD symptoms.[257] However, the most successful clinical application to date has been in the treatment of sleep disorders. Pitolisant (Wakix®) has demonstrated significant efficacy in promoting wakefulness in both animal models and humans.[237] This culminated in its approval for narcolepsy treatment in Europe (2016) and the US (2019), representing the first H_3R antagonist to achieve regulatory approval.[258] Pitolisant significantly reduces excessive daytime sleepiness and cataplexy in narcolepsy patients without the addiction potential of traditional stimulants.[259,260] The compound's once-daily dosing regimen, made possible by its improved pharmacokinetic profile, has also established it as a treatment option for excessive daytime sleepiness in Parkinson's patients.[65]

With this milestone achievement in sleep medicine, H_3R antagonists have firmly established themselves as a promising class of therapeutic agents, with pitolisant's approval for narcolepsy marking the first successful clinical translation of H_3R pharmacology.[261] Despite this success, challenges remain in optimizing compounds for specific indications and patient populations. The complex pharmacology of H_3R, including its constitutive activity and heterodimer formation with other receptors, continues to influence drug development strategies.[42] Future directions include the development of biased ligands that selectively modulate specific signalling pathways, tissue-selective compounds that target H_3R in specific anatomical locations, and combination approaches that leverage H_3R antagonism alongside complementary mechanisms.[262] As our understanding of H_3R structure and function continues to evolve, so too will the therapeutic potential of compounds targeting this important receptor.

1.6.3 Current available H_3R molecular tools

Due to the significant therapeutic potential of histamine H_3R arising from their involvement in numerous neurological processes and disorders, they represent a highly interesting target for drug development.[236] Consequently, elucidating their signalling pathways, structure, and function is extremely valuable, which has led to the development of various molecular tools, including radio- and fluorescent-labelled tracers. For decades, the field has relied on radioligands such as [^{3}H]-thioperamide (**R59**), [^{3}H]NAMH (**R60**), and [^{125}I]iodoproxyfan (**R61**), which are commercially available and widely used in radio displacement assays for binding studies, allowing for scientific comparison across research groups. research groups.[42,64,263] However, working with radiolabelled ligands presents several disadvantages, including safety concerns, high costs, and specialized disposal requirements.[264] These limitations have prompted the development and increased use of fluorescent-labelled ligands, which not only address these issues but also enable a broader range of applications such as fluorescence imaging and fluorescence/bioluminescence resonance energy transfer techniques.[264,265] The initial advance focused on imidazole-based fluorescent H_3R ligands, such as BODIPY-FL-histamine (**R62**), which couples histamine to BODIPY-FL but shows only moderate binding to H_3R. Following a similar conjugation approach, clobenpropit-BODIPY-FL represents another fluorescent tool that links the BODIPY fluorophore to a known H_3R ligand, although its complete molecular structure has not been publicly disclosed.[263] Unfortunately, both ligands lack histamine receptor subtype selectivity due to their imidazole structure, limiting their applications in complex biological systems.[64,246,263] More recently, another series of imidazole-based fluorescent H_3R ligands was published, attaching histamine derivatives to Py-5 fluorophore, culminating in UR-DEBa242 (**R66**), which demonstrated high potency towards H_3R, but as expected, also lacked selectivity by showing significant inverse agonistic/antagonistic affinity for the H_4R.[266] Those limitations drove the transition from imidazole-based to non-imidazole fluorescent ligands, switching to the established H_3R antagonistic alkylamino-propoxyphenyl framework (see Figure 15).

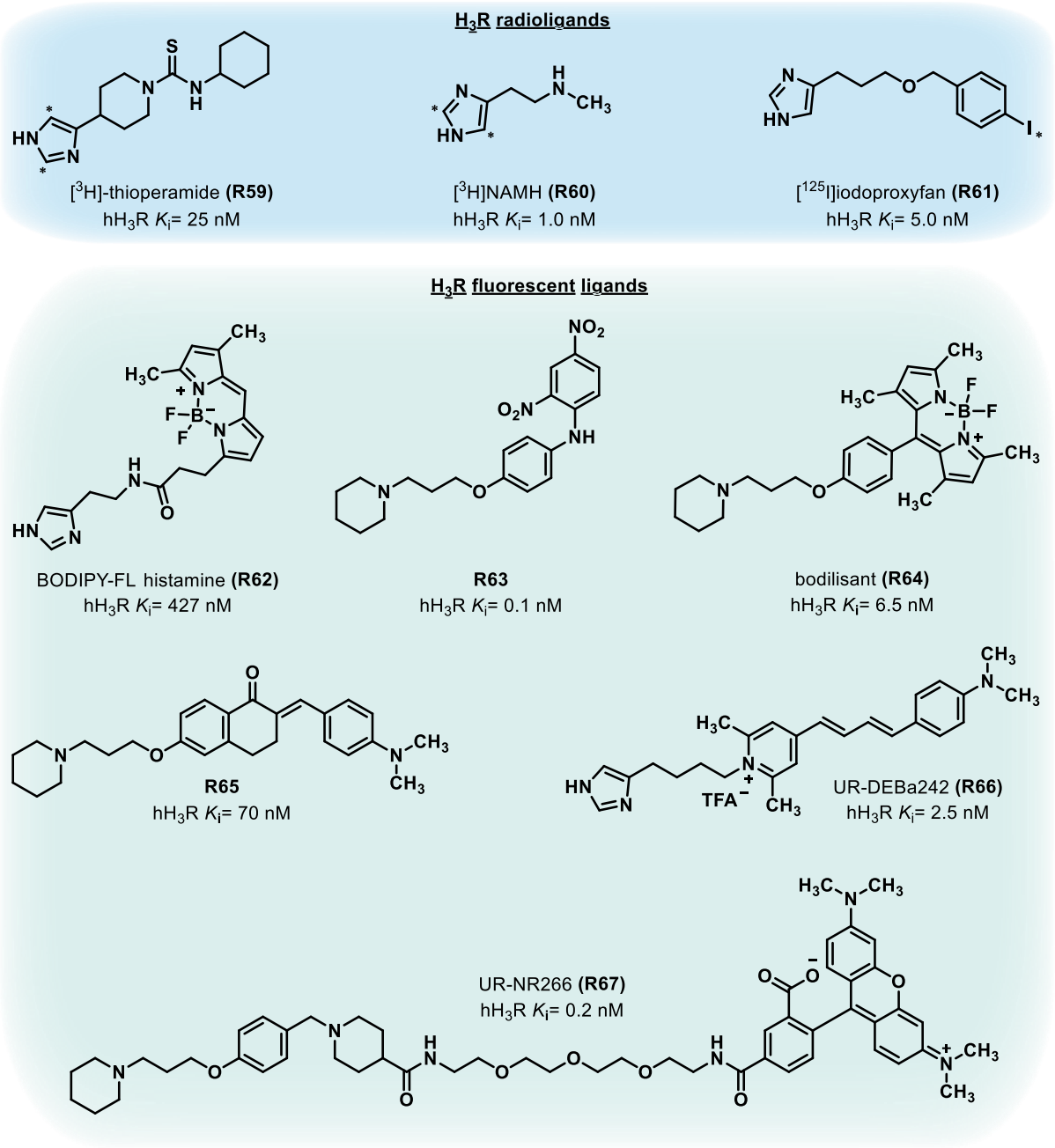

Figure 15: Selection of radioligands (blue) and fluorescent ligands (green) for the histamine H_3 receptor. K_i values were compiled from published literature sources.[42,263,266–271]

This strategic shift has yielded a series of potent fluorescent-tagged H_3R ligands, linking different small molecular fluorophores to the H_3R pharmacophore (**R63**).[270] Additionally, a series of fluorescent ligands was developed using an innovative attachment strategy that merged a chalcone-based fluorophore moiety with the aromatic part of the H_3R pharmacophore. These compounds (**R65**) demonstrated promising affinity, good subtype selectivity, and excellent fluorescent properties, as confirmed by *in vitro* cellular imaging.[269] A similar fluorophore integration approach was employed for the development of bodilisant (**R64**) by ingeniously extending the conjugated system of the employed BODIPY fluorophore

with the phenyl ring of the H_3R pharmacophore. This design offered improvements in both physicochemical and pharmacological properties over the chalcone derivatives, resulting in a highly potent and selective fluorescent H_3R ligand that has proven suitable for *ex vivo* receptor staining in tissues.[268] Most recently, the versatile sub-nanomolar fluorescent ligand UR-NR266 (**R67**) has been published. This compound couples a fluorescein analogue fluorophore via a linker system to the known H_3R antagonist pharmacophore, resulting in an exceptional selectivity profile within the histamine receptor family. The outstanding properties of UR-NR266 have enabled its successful application in NanoBRET binding studies as well as single-molecule microscopy, further expanding the toolkit available for investigating H_3R biology at unprecedented resolution.[271]

1.7 Histamine H_4 receptor (H_4R)

Research into histamine receptors expanded significantly in the early 2000s when multiple independent laboratories simultaneously identified the fourth member of this receptor family, the H_4R.[272–274] This discovery revealed a receptor predominantly expressed in cells of hematopoietic lineage that primarily functions as a chemotactic mediator, orchestrating immune cell migration toward inflammatory sites and regulating inflammatory mediator release, thus establishing its crucial role in immune system modulation.[81,275]

Molecular characterization of the newly discovered H_4R revealed a 390-amino-acid polypeptide with the characteristic seven-transmembrane domain structure of G protein coupled receptors. Interestingly, sequence comparisons demonstrated limited homology with H_1R and H_2R (approximately 19%), but substantial similarity to H_3R (37-43%), suggesting these receptors likely emerged from a common ancestral gene through duplication events.[276] To better understand the genetic basis of this receptor, researchers conducted detailed genomic studies that mapped the H_4R gene to chromosome 18q11.2, revealing its structural organization within the human genome. The gene's architecture includes three exons interrupted by two substantial introns exceeding 7800 and 17500 base pairs respectively, with these exons encoding discrete segments of the receptor protein.[277] Unlike the H_3R gene which generates multiple functional isoforms, the H_4R gene undergoes alternative splicing to produce truncated variants that cannot bind histamine but instead may regulate receptor function through dominant negative mechanisms and oligomerization with full-length receptors.[278]

1.7.1 Molecular structure and networks

Molecular studies of the H_4 receptor have identified key structural elements and binding determinants that underlie its pharmacological profile and distinguish it from other histamine receptor subtypes. The agonist binding pocket of the H_4R is defined by several critical amino acid residues that coordinate the binding of the endogenous agonist histamine and related compounds. Central to this interaction is a conserved acidic residue Asp94 in transmembrane domain 3, which forms a salt bridge with the protonated amine group of histamine (see Figure 16).[279] A distinctive feature of the H_4R is the presence of Glu182 in TM5, which serves as an anchor point for the imidazole ring of histamine through hydrogen bonding.[160,279] Since this glutamate is shared with the H_3R but absent in H_1 and H_2 receptors, this may account for the significantly higher binding affinity of histamine for H_4R compared to H_1R and H_2R.[64,160] The binding pocket is further defined by Trp316, which can adopt an "active" rotamer conformation by forming a hydrogen bond with Glu182, which is crucial for receptor activation.[280] Interestingly, the second extracellular loop (ECL2) has been identified as a determinant of ligand binding specificity, with Phe169 in this loop being responsible for species differences in histamine affinity between human and rodent H_4Rs.[281]

While maintaining the critical interaction with Asp94, antagonists typically extend into additional binding regions that are not accessed by agonists. Further structure-activity relationship studies have identified two distinct hydrophobic pockets that can accommodate antagonist molecules. One pocket is located close to Trp316 between TM3, TM4, TM5, and TM6, while another pocket extends toward the extracellular region between TM3, TM5, TM6, and the second extracellular loop (ECL2).[282] Additionally, antagonists can form hydrogen bonds with Thr178 and Ser179 in TM5, further stabilizing their binding and contributing to increased affinity.[283] These multiple interaction points allow for diverse chemical scaffolds to effectively block H_4R signalling, explaining the structural variety observed among H_4 receptor antagonists. While recent advances in cryo-electron microscopy have provided structures for all histamine receptor subtypes,[121] a high-resolution X-ray crystallographic structure of the H_4R has yet to be determined, which would further refine our understanding of its binding characteristics.

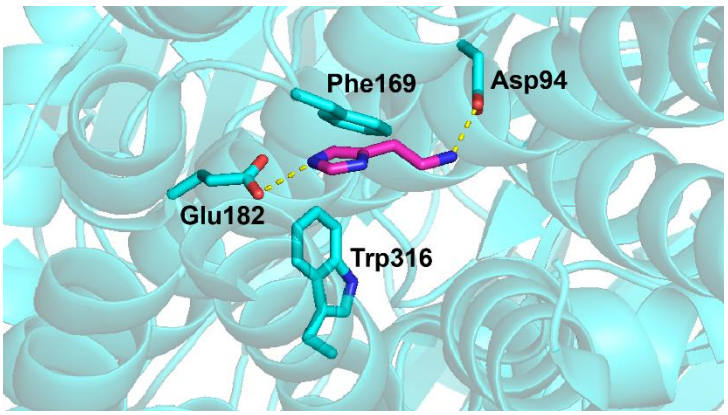

Figure 16: The ligand-binding pocket of histamine in the H_4R. (Crystal structure from PDB: 7YFC)[284]

Similar to the H_3R, the H_4R exhibits significant constitutive activity in the absence of ligand binding. This property is related to its structural features, particularly the absence of the classical "ionic lock" between the DRY motif at the end of TM3 and a negatively charged residue in TM6. Instead of the negatively charged residue typically found at position 6.30, the H_4 receptor contains an alanine, which prevents formation of the stabilizing ionic interaction that would maintain the receptor in an inactive state.[42,285] This structural difference likely contributes to the receptor's ability to spontaneously adopt an active conformation, even though mutation of this alanine to glutamate does not significantly reduce the constitutive activity, suggesting other structural elements are involved.[286] While constitutive activity affects the receptor's basal signalling state, oligomerization provides an additional layer of regulation at the structural level. Homo-oligomers, as confirmed through multiple experimental approaches, form constitutively at physiologically relevant expression levels, localize to the cell surface, and remain unaffected by ligand binding or receptor activation state.[287,288] Notably, H_4R oligomers have been detected not only in heterologous expression systems but also in native cells endogenously expressing H_4Rs, such as human phytohaemagglutinin blasts and spleen lysates.[288] The H_4R also participates in hetero-oligomerization, primarily with its own splice variants and this interaction may represent an endogenous regulatory mechanism, as these splice variants show differential expression across cell types.[278] Although H_1R-H_4R hetero-oligomers have been detected, they only form at non-physiological expression levels and likely result from random interactions rather than specific assembly.[288] The identification of these oligomeric structures adds yet another layer of complexity to H_4R pharmacology and may provide new insights into receptor regulation and function.

1.7.2 Tissue distribution and physiological roles

Next to its structural organization, H_4R's expression profile additionally provides valuable insights into its function, with the receptor exhibiting a distinctive distribution pattern primarily concentrated in cells of hematopoietic origin, suggesting its fundamental role in immune

system regulation. Extensive research has confirmed H_4R expression in numerous immune cell types including eosinophils, mast cells, basophils, neutrophils, dendritic cells, monocytes, and various T cell subsets (see Figure 17),[289–295] which aligns with the receptor's established functions in mediating chemotaxis, cytokine production, and cell activation within the immune system. Beyond circulating immune cells, H_4R expression extends to tissue-resident immune cells, including Langerhans cells in the skin and specialized immune populations in the gastrointestinal tract.[296,297] Importantly, H_4R expression is not static but dynamically regulated in response to the immunological microenvironment, with inflammatory mediators such as IFN-γ upregulating H_4R on monocytes and IL-4 increasing expression on T cells.[294,298] This inflammation-responsive expression pattern further supports the receptor's role in coordinating immune responses under different physiological and pathological conditions. The functional significance of H_4R in immune regulation is additionally supported by genetic studies revealing associations between H_4R polymorphisms and inflammatory conditions including atopic dermatitis, infection-induced asthma, and systemic lupus erythematosus.[299–301] While H_4R expression in the immune system is well-established, its presence in the central nervous system remains controversial. Some studies have reported H_4R mRNA expression in human brain regions including the amygdala, cerebellum, corpus callosum, cortex, hippocampus, and thalamus.[302] Additionally, immunohistochemical investigations have suggested H_4R localization in cortical layers I-VI in human samples, and in the thalamus, hippocampal CA4 stratum lucidum, and layer IV of the cerebral cortex in mice.[303] In rodent models, H_4R immunoreactivity has been detected in dorsal root ganglion neurons, spinal cord laminae, and vestibular nuclei, potentially indicating roles in sensory processing.[302,304] However, these CNS expression findings face significant scepticism within the scientific community for several reasons. First, many studies rely heavily on antibody-based detection methods, and rigorous control studies have demonstrated that several commercially available H_4R antibodies lack specificity.[305] Second, mRNA detection alone cannot confirm functional protein expression, and comprehensive quantitative mRNA analysis across mammalian CNS regions remains limited.[42] Third, the reported CNS expression patterns have not consistently been verified through parallel analyses of mRNA expression and protein detection.[302] These methodological limitations have led to ongoing debate regarding the extent and significance of H_4R expression in the nervous system, with the scientific consensus remaining that further research using multiple complementary approaches is needed to definitively establish the receptor's presence and function in the CNS.

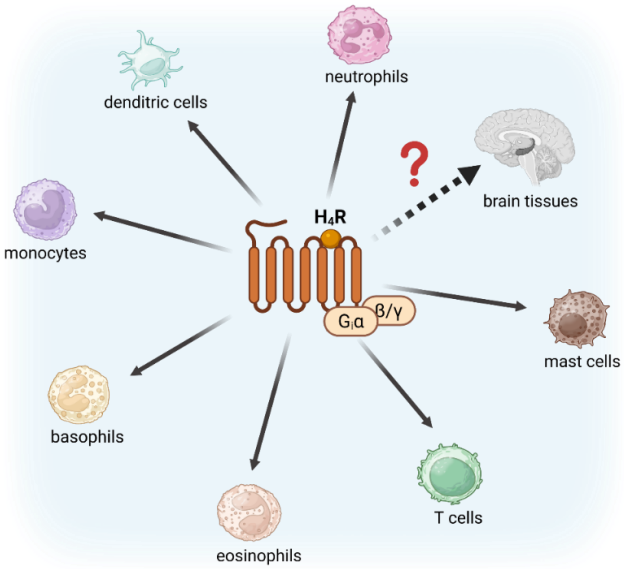

Figure 17: Overview of the expression profile of the human histamine H_4 receptor. Created in https://BioRender.com.

1.7.3 Signalling pathways

In contrast, the signalling mechanisms of H_4R in immune cells are well characterized, as the H_4R orchestrates cellular responses through multiple signalling mechanisms (see Figure 18), with its primary action occurring via $G\alpha_{i/o}$ protein coupling. Upon activation, H_4R inhibits adenylyl cyclase activity, resulting in decreased cAMP levels and through diminished PKA activation to reduced CREB-dependent gene transcription.[306] This inhibition leads to decreased expression of cAMP-regulated genes,[307] ultimately affecting cellular functions such as inflammatory mediator production and immune cell activation. A key downstream consequence of H_4R activation is intracellular calcium mobilization.[308,309] This process involves Gβγ subunits released from activated $G\alpha_{i/o}$ proteins, which stimulate phospholipase C to generate IP_3. The consequent binding of IP_3 to receptors on the endoplasmic reticulum triggers calcium release, initiating various calcium-dependent cellular processes.[308] This essential role of H_4R in calcium signalling has been established in multiple cell types, including human eosinophils and mast cells.[308–310] This calcium mobilization directly drives H_4R's effects on cytoskeletal dynamics and cellular migration, critical processes in immune cell function. In eosinophils and dendritic cells, the calcium flux following receptor activation rapidly induces actin polymerization within seconds, promoting cell shape changes and directional movement necessary for immune cell recruitment to inflammatory sites.[310,311] Additionally, the receptor activates multiple kinase pathways, including MAP kinases,[306] ERK, PI3K, and p38 MAPK, through both $G\alpha_{i/o}$-dependent mechanisms and Gβγ-mediated signalling pathways.[312–314] These kinase cascades contribute to transcriptional regulation, as exemplified by H_4R activation influencing AP-1 transcription factor activity.[314] Furthermore, H_4R signalling appears to suppress STAT1 activation, as receptor antagonism enhances STAT1α production and

phosphorylation, suggesting a role for H_4R in modulating cytokine-responsive gene expression and potentially influencing T helper cell differentiation.[315] Recent discoveries have revealed that H_4R signalling extends beyond traditional G protein pathways to include β-arrestin recruitment. Certain compounds classified as H_4R antagonists based on their ability to block G protein signalling can function as partial agonists for β-arrestin recruitment, exemplifying biased signalling. This β-arrestin pathway leads to delayed ERK phosphorylation with distinct temporal kinetics compared to G protein-mediated signalling, highlighting how different downstream pathways can be selectively engaged by specific ligands.[316] Together, these diverse signalling mechanisms enable the H_4R to exert complex effects across multiple cell types, with pathway engagement determined by factors including ligand properties, receptor expression levels, and the cellular environment.

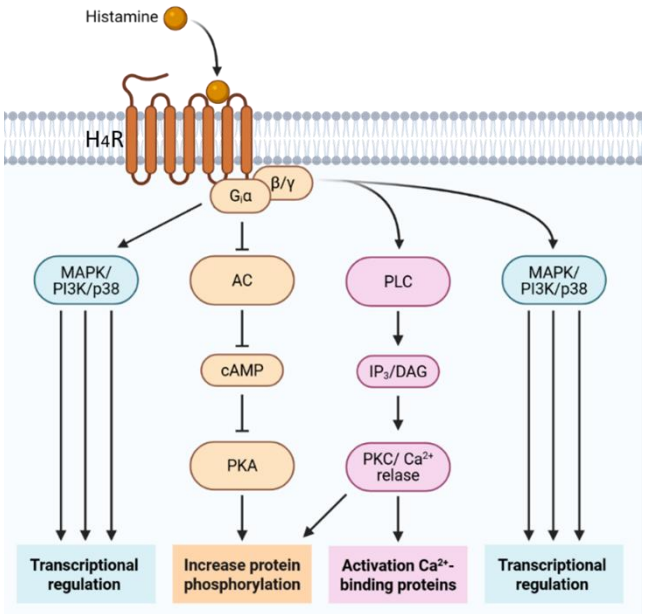

Figure 18: Overview of some of the different signalling pathways from histamine H_4 receptor after activation. PLC= phospholipase C; IP_3= inositol-1,4,5-trisphosphate; DAG= diacylglycerol; PKC= protein kinase C; AC= adenylate cyclase; cAMP= cyclic adenosine monophosphate; PKA= protein kinase A; PI3K= phosphoinositide 3-kinases; MAPK= mitogen-activated protein kinase. Created in https://BioRender.com.

1.7.4 Therapeutic relevance

Since the histamine H_4R is predominantly expressed on cells of the immune system, it plays a essential role in a diverse spectrum of inflammatory and immune-related disorders, including allergic conditions, autoimmune diseases, dermatological disorders, respiratory diseases and gastrointestinal inflammation. This involvement stems from its immunomodulatory properties demonstrated in its crucial part in immune cell chemotaxis, cytokine production, and inflammatory signalling pathways.[274,295]

In allergic disorders, H_4R dysfunction manifests as receptor overactivation on mast cells, eosinophils, and dendritic cells, leading to enhanced chemotaxis and inflammatory mediator release. This dysregulation creates a self-perpetuating cycle of immune cell recruitment and activation, particularly evident in allergic rhinitis where H_4R-mediated eosinophil and mast cell accumulation in affected tissues directly correlates with symptom severity.[311,317–319] Beyond chemotaxis, H_4R activation in mast cells triggers pro-inflammatory cytokine and chemokine production, degranulation, and leukotriene synthesis, which collectively exacerbate allergic symptoms and tissue inflammation.[291] Furthermore, studies in H_4R-deficient mice demonstrate significantly reduced allergic airway inflammation and decreased Th2 cytokine production, confirming the receptor's central role in orchestrating allergic responses through modulation of dendritic cell function and subsequent T cell polarization.[320] The contribution of H_4R to autoimmune diseases is characterized by abnormal receptor signalling disrupting immune tolerance mechanisms. In rheumatoid arthritis (RA), H_4R expression shows considerable variations in synovial cells that correlate with disease severity and duration,[321] suggesting that H_4R-mediated immune cell recruitment and activation contribute to joint inflammation and cartilage destruction.[322,323] Regarding multiple sclerosis research, studies using experimental autoimmune encephalomyelitis models demonstrate that H_4R deficiency exacerbates disease outcomes by compromising regulatory T cell migration and function.[324] In respiratory disorders, particularly asthma, H_4R dysfunction presents as receptor-mediated redistribution and recruitment of mast cells in the airway mucosal epithelium in response to allergens, amplifying allergic symptoms and maintaining chronic inflammation.[325] This amplification occurs through H_4R-mediated release of IL-16 from CD8+ T cells, which acts as a potent chemoattractant for CD4+ T cells, creating a self-reinforcing cycle of immune cell infiltration and cytokine production that sustains the inflammatory response in the airways.[326] Dermatological conditions, particularly chronic pruritus and atopic dermatitis, also involve significant H_4R-mediated pathology as the receptor's expression in skin mast cells, inflammatory dendritic epidermal cells, and dermal fibroblasts creates a complex network of H_4R-mediated inflammatory responses in the skin.[327–329] This network is characterized by H_4R-mediated inhibition of IL-12p40 and IL-12p70 release from inflammatory dendritic epidermal cells, downregulation of CCL2 production in Langerhans cells, and modulation of keratinocyte proliferation, collectively contributing to the chronic inflammatory state in dermatological disorders.[297,314,328,330] In gastrointestinal inflammatory disorders, H_4R dysfunction manifests as receptor-mediated immune cell recruitment and activation in the intestinal mucosa. Studies in rat models of subchronic colitis demonstrate H_4R involvement in inflammatory bowel diseases, as its blockage reduces macroscopic damage, mucosal and submucosal thickness, neutrophil infiltration, and inhibits colonic myeloperoxidase and TNF-α elevation.[331] Beyond its

peripheral inflammatory roles, behavioural studies of H_4R-deficient mice have fuelled the discussion of potential H_4R expression in the central nervous system as these mice exhibit anxiogenic-like behaviour and increased food intake, suggesting that neuronal H_4R stimulation may have anxiolytic effects and influence feeding behaviour.[332] Additionally, investigations indicate H_4R expression on microglia that may affect its migration and inflammatory mediators production, potentially influencing neuroinflammatory processes.[313] Furthermore, antinociceptive effects of H_4R antagonism were described in a rat model of carrageenan-induced inflammation, suggesting H_4R involvement in pain management.[333]

The H_4R significant involvement in this diverse array of inflammatory and immune-related disorders (see Table 2) positions it as a compelling therapeutic target, offering distinctive opportunities for intervention in conditions ranging from allergies and autoimmune diseases to dermatological and gastrointestinal disorders. This broad pathophysiological relevance has stimulated intensive research efforts to develop selective H_4R ligands with clinical potential.

Table 2: Disorder-specific effects of H_4R dysregulation: impacted (immune)cells, tissues, and pathophysiological outcomes. MC= mast cells; EP= eosinophils; DC= dendritic cells; Reg. TC= regulatory T cell; TC= T cell; FB= fibroblast; NP= neutrophil; MOC= monocyte. ↑= upregulation; ↓= downregulation; ↑↓= dysregulation.

H_4R-related disorder	**Dysregulated (immune) cells**	**Affected tissues**	**Pathophysiological impact**
Allergic disorders	MC, EP, DC	Nose, lung, skin	Inflammation↑
Rheumatoid arthritis	Synovial	Joints, cartilage	Immune infiltration ↑
Multiple sclerosis	Reg. TC	CNS	Immune regulation ↑↓
Asthma	MC, CD8+ TC	Airways	Inflammation↑
Atopic dermatitis	MC, DC, FB	Skin	Inflammation↑
Colitis	NP, MOC	Gut mucosa	Tissues damage ↑

1.8 Histamine H_4 receptor ligands

1.8.1 Agonists

1.8.1.1 Development

Due to the high sequence homology between H_3R and H_4R, many imidazole-containing H_3R agonists also bind to the H_4R, albeit with expected poor selectivity over H_3R.[64] The first developed H_4R agonists with modest selectivity were methylcyanoguanidine analogs, culminated by OUP-16 (**R25**), which demonstrated approximately 40-fold selectivity over H_3R but only moderate H_4R affinity.[334] 4-Methylhistamine (**R26**), initially developed as an H_2R ligand,

emerged as the first selective H_4R agonist with good binding affinity and moderate selectivity exceeding 100-fold over other histamine receptor subtypes.[64] A further development was compound VUF-6884 (**R27**), derived from clozapine, demonstrating even better selectivity over H_3R (>300-fold) while maintaining good affinity for the H_4R, representing an important advance in non-imidazole H_4R agonists.[335]

In more recent years, several new classes of H_4R agonists have been developed, showing that structurally diverse chemical scaffolds can maintain full agonist activity at the H_4R. For example, acylguanidine-based ligands, initially designed as H_2R agonists, emerged, demonstrating potent H_4R affinity and promising selectivity.[336] The subsequent exchange of the acyl group with a cyano group, resulting in cyanoguanidines like UR-PI376 (**R28**), further improved the H_4R selectivity over H_3R for this compound class.[337] Another promising class are the 2-arylbenzimidazoles, developed by Johnson & Johnson, with the lead compound **R29** (see Figure 19) demonstrating sub nanomolar H_4R affinity and more than 600-fold selectivity over other histamine receptor subtypes.[338] Interestingly, minor structural modifications in this series can shift the pharmacological profile from agonist to antagonist.[339] The development of ST-1006 (**R30**), featuring an aminopyrimidine scaffold, represents another highly potent H_4R agonist that has proven useful in *in vitro* studies and contributed to our understanding of H_4R pharmacology.[340,341]

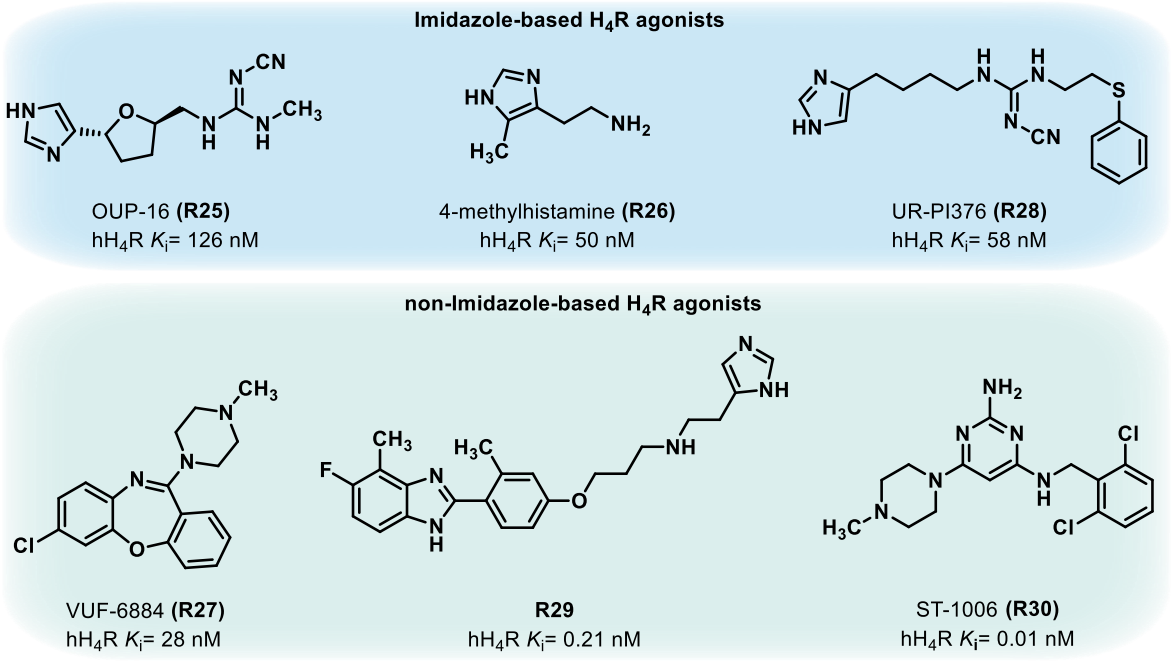

Figure 19: Selected H_4R ligands: imidazole-based agonists (blue) and non-imidazole-based agonists (green). K_i values were compiled from published literature sources.[334]

1.8.1.2 Therapeutic potential

The therapeutic potential of H_4R agonists stems from their ability to modulate immune responses and inflammatory processes, mainly through regulation of T cell function and suppression of pro-inflammatory cytokine production.[320] In asthma and allergic airway diseases, 4-methylhistamine has shown efficacy when administered intratracheally in mouse models, reducing airway inflammation through recruitment of regulatory T cells.[342] This effect suggests potential applications in conditions like allergic asthma, allergic rhinitis, and COPD, where selective immune suppression could provide therapeutic benefits.[81,320] H_4R agonists also show promise in autoimmune conditions, as the complex interplay between histamine signalling pathways observed in autoimmune encephalomyelitis models suggests that selective H_4R activation might provide therapeutic benefits in conditions such as multiple sclerosis and rheumatoid arthritis.[343] Additionally, ST-1006 and related compounds have demonstrated efficacy in preclinical models of inflammation by suppressing pro-inflammatory cytokine production, particularly IL-12p70 in human monocytes, which are associated with autoimmune disorders such as multiple sclerosis and rheumatoid arthritis.[341,344] Although H_4R agonists demonstrate promising results in preclinical research, to date, no H_4R agonists have yet advanced to clinical trials.

1.8.2 Antagonists

1.8.2.1 Development

The development of selective histamine H_4R antagonists began with the discovery of JNJ-7777120 (**R31**), the first potent and selective non-imidazole H_4R antagonist. Identified through high-throughput screening at Johnson & Johnson, this compound showed remarkable binding affinity and exceptional selectivity with greater than 1000-fold over other histamine receptors,[325] quickly becoming an essential pharmacological tool for investigating H_4R-mediated processes.[345] The initial success with JNJ-7777120 prompted extensive research into structurally related compounds to address its limitations, particularly its relatively short half-life in rats.[346] Subsequently, JNJ-10191584 (**R32**) emerged, a close analogue of JNJ-7777120 where the indole group was replaced with a benzimidazole moiety.[346,347] Although this compound maintained high potency and selectivity for H_4R, it failed to improve the short half-life.[346] From this structure, a series of 2-arylbenzimidazole H_4R antagonists was developed (see **R33** in Figure 20), exploring a longer distance between the benzimidazole moiety and the basic amine moiety through varying linkers.[348–350] These compounds showed reasonable H_4R affinity and structure-activity relationship studies established propoxy/propylamine linkers in para-position to the benzene ring as providing optimal binding affinity.[351] Through a fragment-based drug discovery project, a new class of quinoxalinone H_4R antagonists was developed, demonstrating potent affinity.[352] Subsequent scaffold hopping led to the discovery of

quinazoline-based H_4R inverse agonists, featuring different substituents at the 4-position, including an ethylene linker with terminal sulfonamide moiety (**R34**), that can accommodate different substituents without losing affinity.[353] Another important development was the disclosure of a novel scaffold of 2-aminopyrimidine compounds by Bayer, featuring a distinctive 4,6-position disubstitution pattern with an aryl moiety and a cyclic amine (**R35**).[354,355] This scaffold quickly served as a leading structure for modifications, resulting in the development of several variants with different substituents in positions 4 or 6. Structure-activity relationship studies revealed that while the aryl substituent is variable and can be even exchanged with alkyl groups, the cyclic amine remained essential for activity.[356–359] Based on this 2-aminopyrimidine family, which has become the most widely published H_4R antagonist scaffold,[65] researchers developed rotationally constrained analogues including benzofuropyrimidines (**R36**) and benzothienopyrimidines,[360–365] aiming to improve pharmacokinetic properties while maintaining the essential binding interactions with the receptor.

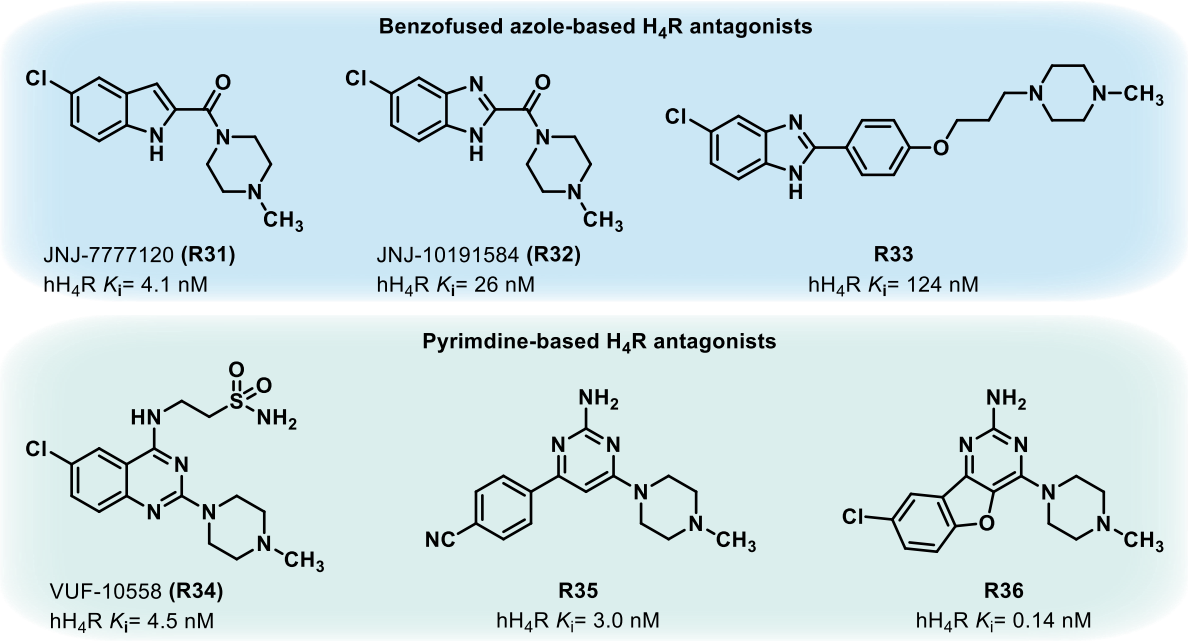

Figure 20: Selected H_4R ligands: benzofused azole-based antagonists (blue) and pyrimidine-based antagonists (green). K_i values were compiled from published literature sources.[325,346,353,366,367]

1.8.2.2 Pharmacophore

A general blueprint for H_4R antagonists can be postulated derived from these different structural classes, consisting of a lipophilic residue connected to a central hydrogen bond acceptor/donor system, and a basic motif attached to the opposite side of the core, especially cycloaliphatic or tertiary amines (see Figure 21). The hydrophobic residue is highly variable and structurally diverse, ranging from branched, straight, or even fused to the central core, which itself allows for many variations, particularly heteroaromatic systems. The basic moiety is

more restricted in its diversity, partly due to size constraints, with the most frequently encountered example being the *N*-methylpiperazine (NMP) group.[367,368]

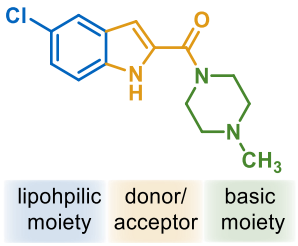

Figure 21: Pharmacophore blueprint for H_4R antagonists, demonstrated on widely used reference ligand JNJ-7777120.

1.8.2.3 Therapeutic potential

The development of selective H_4R antagonists has revealed their therapeutic potential in various pathophysiological conditions, including atopic dermatitis, chronic pruritus, asthma, allergic rhinitis, pain conditions and inflammatory bowel diseases.[325] One of the most promising therapeutic applications for H_4R antagonists is in the treatment of pruritus and atopic dermatitis, as demonstrated by the notable H_4R antagonist JNJ-7777120, showing significant reduction in pruritic response following challenges with allergen, substance P, and various haptens in multiple models[369–371] Its antipruritic effects in histamine-induced scratching behaviour in mice even proved superior to traditional antihistamines, suggesting a greater involvement of H_4R in pruritic response than of H_1R.[370] In a murine chronic allergic contact dermatitis model, JNJ-7777120 administration resulted in amelioration of eczematous lesions and decreased numbers of mast cells and eosinophils, further supporting the role of H_4R antagonists in treating dermatitis. Importantly, combination therapy with H_1R and H_4R antagonists proved significantly more effective than H_1R antagonist monotherapy, with greater reductions in serum IgE and Th2 cytokines.[372] Additionally, H_4R antagonists have shown promising results in asthma models. In a murine ovalbumin-induced inflammation model, JNJ-7777120 demonstrated significant anti-inflammatory responses during both the sensitization and effector phases, suggesting that H_4R antagonism remains efficacious even after allergen sensitization has occurred.[320] Further studies in this model showed that JNJ-7777120 administration resulted in reduced serum titters of ovalbumin-specific IgE, decreased inflammatory infiltrations in the lungs, and lower eosinophil counts in the bronchoalveolar lavage, confirming the receptor's important role in allergic airway inflammation.[373] H_4R antagonists have also shown efficacy in allergic rhinitis models. In mice, JNJ-7777120 demonstrated dose-dependent inhibition of nasal symptoms through both intranasal and oral administration, leading to significantly reduced serum IgE levels and altered cytokine profiles in nasal lavage fluid, indicating immunomodulatory effects.[333] Given

that multiple histamine receptors are involved in this condition, there is growing interest in developing combination approaches, potentially combining H_1R/H_4R, H_3R/H_4R, or even $H_1R/H_3R/H_4R$ antagonist activities in single molecules to address multiple aspects of allergic rhinitis pathophysiology.[367] H_4R's potential role in nociception has been further evidenced by studies showing that JNJ-7777120 and its benzimidazole analogue increase paw withdrawal latency in carrageenan-induced thermal hyperalgesia in rats.[333] This antinociceptive effect was substantiated in another study, demonstrating efficacy of H_4R antagonism against both inflammatory pain and neuropathic pain in a spinal nerve ligation model.[374] Furthermore, the benefit of H_4R antagonists in inflammatory bowel disease has been demonstrated as high doses of JNJ-7777120 reduced TNBS-induced colon damage, neutrophil influx, and myeloperoxidase levels in colonic tissue.[331]

Despite the promising preclinical data across a variety of inflammatory and immune-mediated conditions, no H_4R antagonist has yet been approved for clinical use, though several compounds have advanced to clinical trials for different disorders like atopic dermatitis, asthma and histamine-induced itch in rheumatoid arthritis. However, JNJ-7777120 stands out as the most widely used reference compound in preclinical studies, establishing the foundation for understanding H_4R pharmacology and its therapeutic potential.[65]

1.8.3 Current available H_4R molecular tools

Molecular tools for the histamine H_4R are essential for understanding its pharmacology, distribution, and physiological roles. Therefore, several radioligands have been developed, including [^{3}H]UR-DEBa176 (**R68**),[375] [^{125}I]iodophenpropit (**R69**),[64] and tritiated JNJ-7777120 (**R70**),[325] which are primarily used in displacement assays and binding studies. However, these radioligands present significant limitations, as some suffer from poor chemical stability and exhibit short half-life, and generally, they require relatively high amounts of both radioligand and receptor protein, making them resource-intensive and less suitable for detailed biological studies.[375] In contrast, fluorescent probes overcome these limitations while additionally offering significant advantages over radioligands, including higher spatial resolution, real-time visualization capabilities, and the ability to perform live-cell imaging without the hazards associated with radioactive materials.[264] These advantages, coupled with their versatility in various experimental applications, make fluorescent ligands particularly well-suited for resolving the ongoing discussion about central H_4R expression,[303,376,377] as selective fluorescent tools could provide crucial insights into the precise localization and potential function of this receptor in the central nervous system. Notably, since the H_3R, which shows high sequence homology to H_4R, is abundantly expressed in brain tissues,[172] the development of subtype selective fluorescent tools is particularly crucial. Unfortunately, all known fluorescent ligands

for H_4R (see Figure 22) up to date lack this crucial selectivity, as they were primarily developed for H_3R, but showing additional H_4R affinity. These include imidazole-based ligands such as BODIPY-FL-histamine (**R62**),[263] clobenpropit-BODIPY,[263] and Py-5-labeled 2-arylbenzimidazoles (**R71**).[378] Recently, another histamine-based Py-5-labeled compound UR-DEBa242 (**R66**) was developed, which due to its imidazole moiety lacks subtype selectivity as well, but proved suitable for H_4R localization and trafficking studies in live cells.[266]

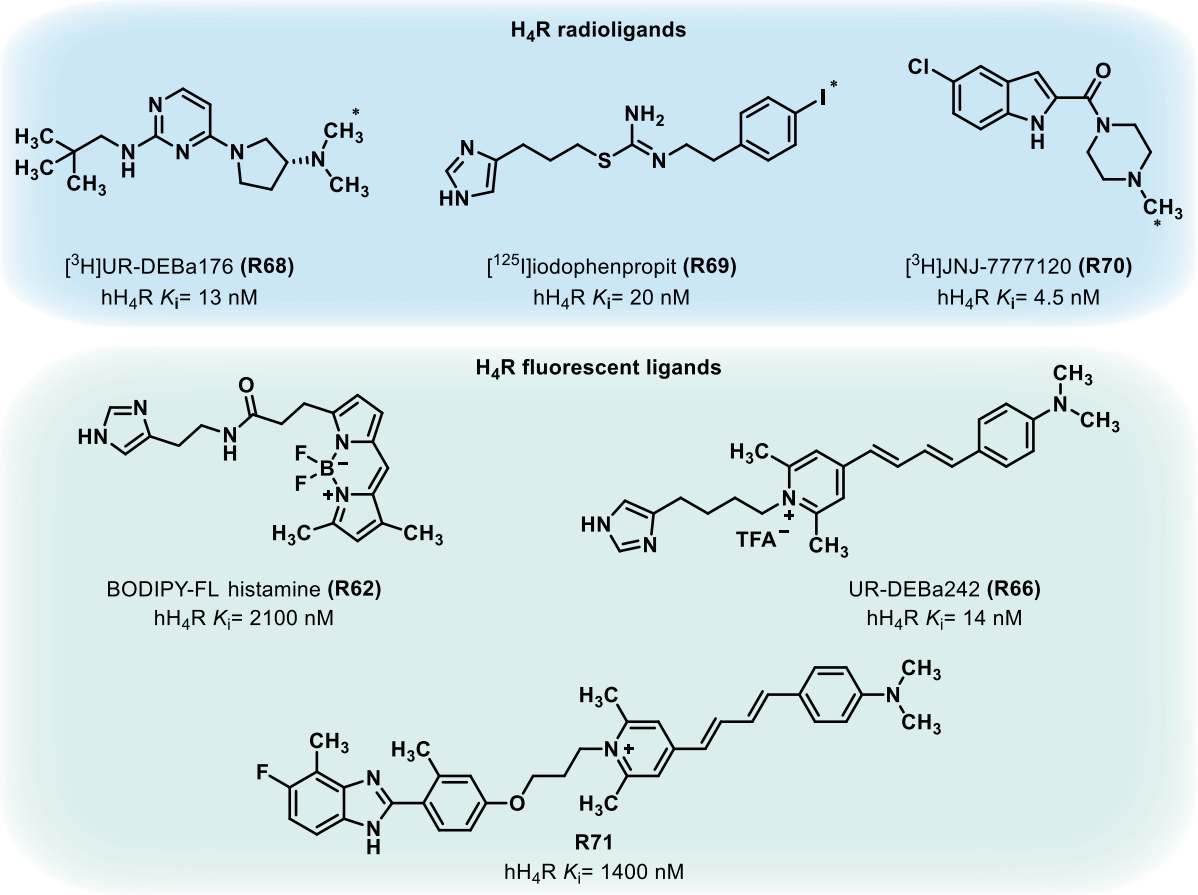

Figure 22: Selection of radioligands (blue) and fluorescent ligands (green) for the histamine H_4 receptor. K_i values were compiled from published literature sources.[64,266,325,375,378,379]

1.9 Dopamine and its receptors

Dopamine is a catecholamine neurotransmitter that serves as a critical signalling molecule in the central nervous system and peripheral tissues. This biogenic amine regulates diverse physiological processes including motor control, reward processing, cognition, and endocrine function, with its dysregulation implicated in numerous neurological and psychiatric disorders.[380,381] Its biosynthesis (see Figure 23) follows a tightly regulated enzymatic pathway beginning with the amino acid tyrosine (**VII**), which gets converted to L-DOPA (**VIII**) by tyrosine hydroxylase (TH).[382] Subsequently, aromatic L-amino acid decarboxylase (AADC) transforms L-DOPA to dopamine (**IX**) through decarboxylation.[383] Once synthesized, dopamine undergoes metabolism through two primary pathways. The first involves monoamine oxidase (MAO),

which catalyzes oxidative deamination to produce 3,4-dihydroxyphenylacetaldehyde (**X**), subsequently converted to 3,4-dihydroxyphenylacetic acid (**XI**) by aldehyde dehydrogenase. The second pathway utilizes catechol-*O*-methyltransferase (COMT), which transfers a methyl group to dopamine's catechol structure, producing 3-methoxytyramine (**XII**).[384] After its synthesis, dopamine is transported and stored in synaptic vesicles through the VMAT2, which concentrates dopamine against a gradient using proton antiport mechanisms.[385] This compartmentalization protects dopamine from cytosolic degradation and enables regulated release during neurotransmission, which occurs primarily through calcium-dependent exocytosis following action potentials.[381,386] This release manifests in two distinct neuronal firing patterns that serve complementary functions in dopaminergic signalling. Phasic firing, characterized by transient high-frequency bursts, is associated with reward prediction and motivational salience.[387] In contrast, tonic firing maintains baseline dopamine levels critical for motor function.[388] Once released into the synaptic cleft, extracellular dopamine concentrations are primarily regulated through reuptake by the dopamine transporter (DAT), a plasma membrane protein that actively transports dopamine back into the presynaptic neuron, thereby terminating dopaminergic signalling and allowing for neurotransmitter recycling.[389] During its presence in the synapse, dopamine exerts its effects through five distinct GPCRs classified into two families: D_1-like (D_1, D_5) and D_2-like (D_2, D_3, D_4) receptors.[390] These receptors share the characteristic seven-transmembrane domain structure of GPCRs but differ in their signalling mechanisms, biological function and anatomical distribution.[391]

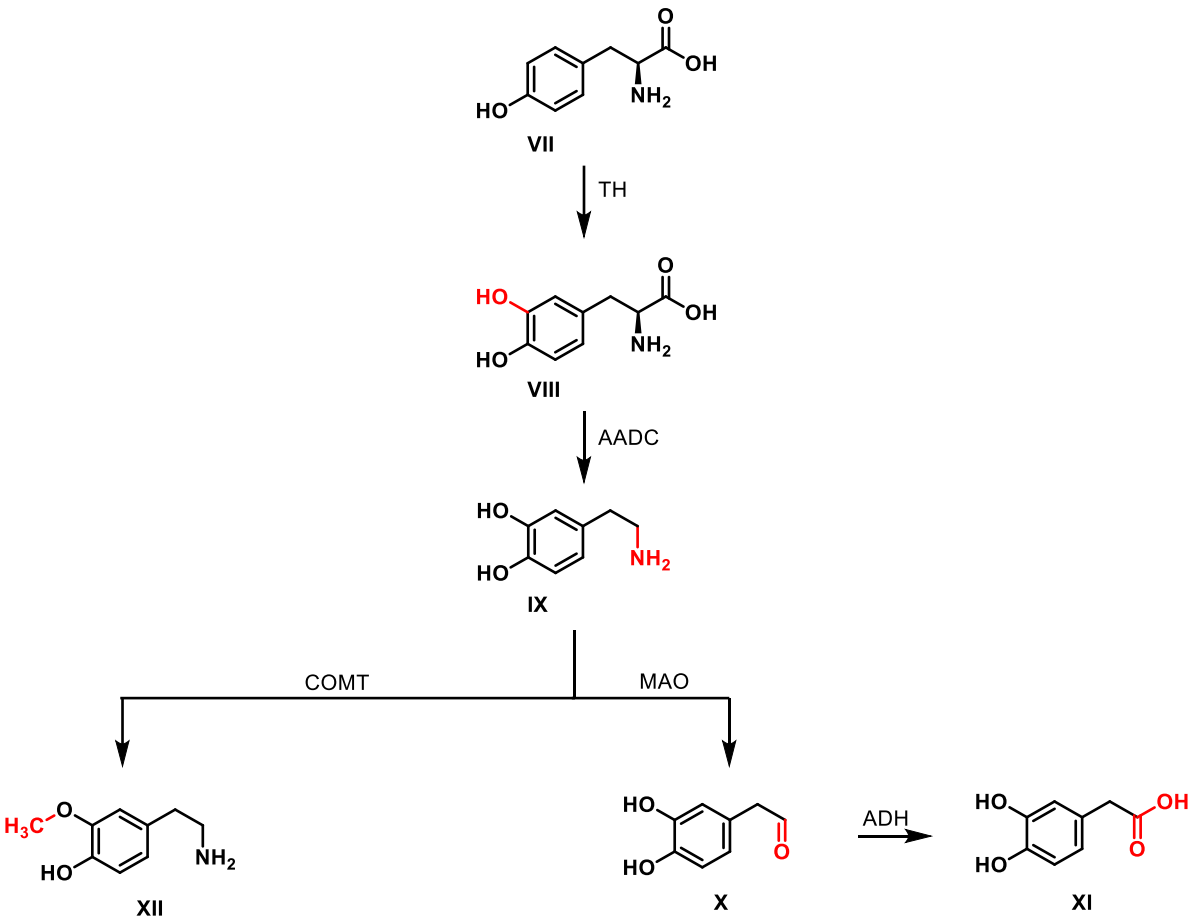

Figure 23: Biosynthesis and metabolism pathways of dopamine. TH= tyrosine hydroxylase; AADC= L-amino acid decarboxylase; MAO= monoamine oxidase; ADH= aldehyde dehydrogenase; COMT= catechol-*O*-methyltransferase.

1.9.1 Dopamine D_2 receptor

The dopamine D_2 receptor (D_2R), first cloned in 1988, represents one of the most extensively studied GPCRs in neuropharmacology. Its significance stems from its critical role in regulating motor control, reward processing, and cognitive functions, with its dysregulation implicated in numerous neuropsychiatric and movement disorders.[392–395] This central role in brain function is explained by D_2R's prominent expression throughout the central nervous system, particularly in the striatum, nucleus accumbens, and olfactory tubercle, with significant presence in the substantia nigra and ventral tegmental area where it functions mainly as an presynaptic autoreceptor regulating dopamine synthesis and release (see Figure 24).[396] Beyond the CNS, it also appears in the pituitary gland, regulating prolactin secretion, and in peripheral tissues including lymphocytes where it modulates immune responses and inflammatory signalling.[397,398] These diverse physiological effects of D_2R result from its signalling primarily through G_i/G_o proteins, inhibiting adenylyl cyclase and reducing cAMP production, while activating K^+ channels and inhibiting Ca^{2+} channels.[380] Beyond this canonical pathway, D_2R can signal through β-arrestin pathways independent of G protein activation.[399]

This dual signalling capability enables D_2R to regulate multiple downstream effectors, including the ERK pathway and the AKT/GSK3 signalling cascade, which are implicated in neuronal plasticity and cell survival.[400–402] Additionally, D_2R is known to form both homodimers and heterodimers with other receptors, including D_3R, adenosine A_{2A}, histamine H_3, and serotonin 5-HT_{2A} receptors, which significantly expands its signalling capabilities.[167,392,403–405]

In the nigrostriatal pathway, these signalling cascades lead to D_2R regulation of motor function through modulation of basal ganglia circuits, with receptor activation facilitating movement initiation and coordination.[406] Additionally, D_2R influences reward processing, motivation, and emotional responses within the mesocorticolimbic system, contributing to hedonic experiences and goal-directed behaviours.[407–409] D_2R also plays a critical role in cognitive functions, particularly working memory and cognitive flexibility, through its expression in prefrontal cortical regions.[410] Since age-related decline in D_2R density correlates with cognitive impairment, it suggest its importance in maintaining cognitive function throughout the lifespan.[411] Given these diverse physiological roles, D_2R dysfunction plays a crucial role in several neurological and psychiatric disorders. In schizophrenia, the "dopamine hypothesis" posits that excessive D_2R stimulation in mesolimbic pathways contributes to positive symptoms, while reduced D_2R activation in mesocortical pathways may underlie negative and cognitive symptoms.[412,413] This hypothesis is supported by the correlation between clinical efficacy of antipsychotics and their D_2R binding affinity.[414] D_2R also plays a significant role in addiction, where drug-induced alterations in receptor density and sensitivity contribute to reward processing dysregulation and compulsive drug-seeking behaviours.[415] Additionally, D_2R dysfunction is central to Parkinson's disease pathophysiology, where progressive loss of dopaminergic neurons leads to reduced D_2R stimulation in the striatum, resulting in the characteristic motor symptoms.[416,417] Postmortem and PET imaging studies have consistently demonstrated altered D_2R density and function in Parkinson's disease patients, correlating with disease progression.[418,419]

1.9.2 Dopamine D_3 receptor

The dopamine D_3 receptor (D_3R), cloned in 1990 shortly after the D_2R, also represents a critical target in neuropsychiatric pharmacology due to its involvement in modulating reward circuits, emotional responses, and specific aspects of motor function.[420,421] While sharing approximately 75% sequence homology with D_2R in transmembrane domains,[420] D_3R plays distinct physiological roles that make it particularly relevant for treating impulse control disorders, addiction, and non-motor symptoms of Parkinson's disease.[421–423] Unlike the more widely distributed D_2R, D_3R shows a more restricted expression pattern, with highest concentrations in limbic regions including the nucleus accumbens, islands of Calleja, and

olfactory tubercle, with moderate expression in the substantia nigra, ventral tegmental area, and hippocampus (see Figure 24).[424] This preferential localization in limbic structures explains D_3R's predominant role in reward processing and emotional regulation rather than broad motor control.[425] The D_3R exhibits a more limited peripheral distribution compared to the D_2 receptor, with notable expression in the kidneys, regulating sodium excretion and blood pressure.[426]

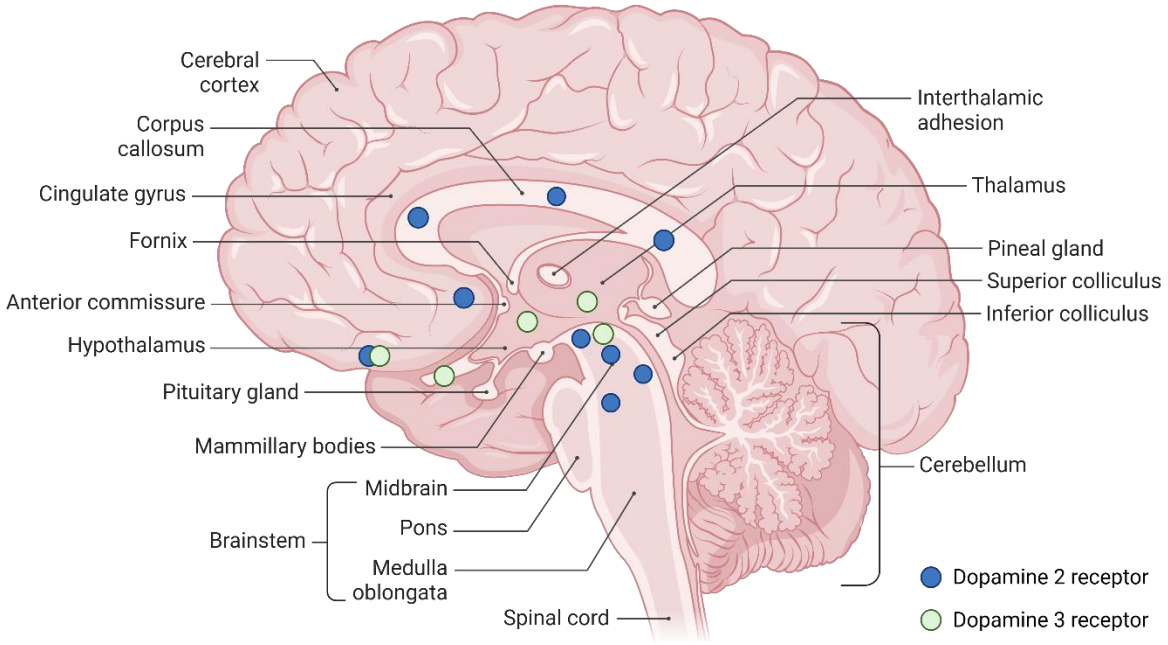

Figure 24: Expression patterns of the D_2R (blue) and D_3R (green) in the human brain. Created in https://BioRender.com.

Similar to D_2R, the primary signalling mechanisms of D_3R involve coupling to G_i/G_o proteins, inhibiting adenylyl cyclase and reducing cAMP production, but with important distinctions.[427] Notably, D_3R exhibits approximately 20-fold higher affinity for dopamine than D_2R, allowing it to respond to lower dopamine concentrations and potentially serve as a more sensitive modulator of dopaminergic transmission.[420] While both receptors engage β-arrestin pathways, D_3R recruitment of β-arrestin leads to preferential activation of ERK1/2 signalling with slower kinetics and greater persistence compared to D_2R-mediated responses.[380,428] D_3R also modulates ion channel function, inhibiting calcium currents and activating potassium channels, thereby reducing neuronal excitability.[429,430] Through these signalling mechanisms, D_3R functions both as a postsynaptic receptor mediating dopamine's effects on target neurons and as an autoreceptor on dopaminergic neurons themselves, where it provides inhibitory feedback to regulate dopamine synthesis and release, particularly in mesolimbic pathways.[431] This dual pre- and postsynaptic localization allows D_3R to fine-tune dopaminergic transmission according to physiological demands.

Due to its localization and signalling mechanism, D_3R exerts diverse physiological effects across neural circuits. In the mesolimbic system, D_3R activation modulates reward processing and motivated behaviours, with receptor stimulation generally enhancing the rewarding properties of natural reinforcers and drugs of abuse.[432,433] Its more limited role in motor function primarily involves modulation of fine motor control and specific aspects of locomotor activity rather than gross movement initiation.[434] Cognitively, D_3R influences functions related to impulsivity, behavioural flexibility, and social cognition through its expression in frontal cortical regions and the amygdala.[435] The involvement of D_3R in neuropsychiatric conditions is substantial but distinct from D_2R. Substance use disorders feature elevated D_3R expression following chronic drug exposure, contributing to drug craving and relapse vulnerability.[436] This receptor upregulation makes D_3R an attractive target for addiction pharmacotherapies. Regarding schizophrenia, D_3R dysfunction may specifically contribute to cognitive and negative symptoms through altered prefrontal cortical function and emotional processing, complementing D_2R's role in positive symptom manifestation.[437] For Parkinson's disease patients, D_3R has emerged as a crucial therapeutic target alongside D_2R. While nigrostriatal dopamine depletion primarily affects motor function through D_2R, the concurrent impact on D_3R signalling in limbic regions contributes to non-motor symptoms such as depression, anxiety, and impulse control disorders.[438–440] The therapeutic relevance of D_3R in Parkinson's disease extends beyond symptom management, as D_3R activation appears to offer neuroprotective effects by promoting neuronal survival, stimulating endogenous neurogenesis, and reducing inflammatory responses in the substantia nigra.[441–443] These properties may contribute to disease-modifying effects that could potentially slow progression.

These therapeutic benefits have driven the development of selective D_3R ligands. However, this has been proven challenging due to the high sequence homology with D_2R, though structural differences in the binding pockets, particularly in the extended binding pocket region, have enabled the creation of compounds with increasing D_3R selectivity.[444] Pramipexole, a D_3R-preferring dopamine agonist used in Parkinson's disease treatment, exemplifies how receptor selectivity can be partly achieved despite these structural similarities between D_2-like receptors. Its preferential D_3R activity not only addresses motor symptoms through sufficient D_2R activation but may also improve non-motor symptoms and potentially offer neuroprotective benefits through D_3R-mediated mechanisms.[443,445,446]

1.10 Parkinson's disease

Parkinson's disease (PD), first described by James Parkinson as "shaking palsy", represents the second most common neurodegenerative disorder worldwide, characterized by progressive degeneration of dopaminergic neurons in the substantia nigra pars compacta (SNc).[447,448] This neurodegeneration leads to striatal dopamine depletion and the formation of intracellular protein aggregates known as Lewy bodies, containing misfolded α-synuclein.[449] The resulting dopamine deficiency disrupts the delicate balance between the direct and indirect pathways of the basal ganglia motor circuits, leading to excessive inhibitory output from the globus pallidus interna and substantia nigra pars reticulata to the thalamus, thereby impairing movement initiation and selection.[450] While dopaminergic dysfunction is central to PD pathophysiology, other neurotransmitter systems are also affected. Noradrenergic, serotonergic, and cholinergic neurons undergo degeneration, contributing to non-motor symptoms.[449,451] Notably, histaminergic neurons are relatively preserved, with elevated histamine levels observed in the basal ganglia of PD patients, potentially influencing neuroinflammatory processes and compensatory mechanisms.[452]

At diagnosis, approximately 60-80% of dopaminergic neurons have already degenerated due to compensatory mechanisms that initially mask symptoms.[453,454] These adaptive processes include decreased dopamine reuptake, increased turnover in remaining neurons, and upregulation of postsynaptic dopamine receptors.[455] However, disease progression is gradual and relentless, with symptoms exacerbating over time, potentially accelerated by infections or emotional stress, eventually overwhelming these compensatory mechanisms.[456] After manifestation of the disease, PD clinically presents with both motor and non-motor symptoms (see Figure 25). The cardinal motor features include bradykinesia, rigidity, and tremor, while non-motor manifestations encompass sleep disturbances, depression, and cognitive impairment. Especially these non-motor symptoms significantly impact quality of life and often precede motor symptoms by years,[453] thereby potentially offering a window for earlier diagnosis.[457]

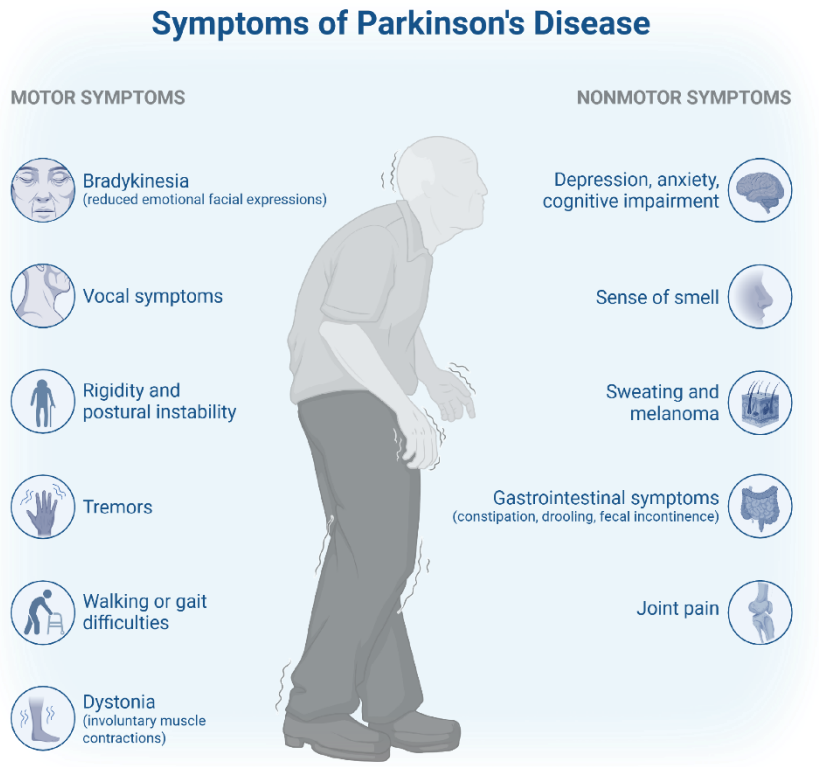

Figure 25: Symptoms of Parkinson's disease. Created in https://BioRender.com.

1.10.1 Therapeutic approaches

Despite advances in understanding PD pathophysiology, current therapeutic approaches remain primarily symptomatic, focusing on restoring dopaminergic neurotransmission to alleviate motor symptoms. Levodopa (**R49**), the dopamine precursor, continues to be the gold standard therapy, providing the most effective relief of motor symptoms but frequently leads to motor complications with long-term use, including dyskinesias and response fluctuations associated with direct pathway overactivation.[458] Other dopamine-restoring approaches include enzyme inhibitors that prolong dopamine half-life (see Figure 26) such as MAO-B inhibitors (**R50**), preventing the breakdown of dopamine in the synaptic cleft, or COMT inhibitors (**R51**), which block the peripheral metabolism of levodopa, increasing its availability to the brain.[459–461] Additionally, there are non-dopaminergic approaches including anticholinergics and glutamatergic agents like amantadine (**R52**) that address specific symptoms such as tremor and dyskinesias, or complications of dopaminergic therapy.[462]

Direct agonistic stimulation of dopamine receptors, mimicking the natural neurotransmitter's effects, represents another important therapeutic strategy. These agonists, particularly those selective for D_2 and D_3 receptors like pramipexole (**R53**), which shows preferential selectivity for D_3 over D_2 receptors, serve as valuable treatment options either as monotherapy in early disease or as adjuncts to levodopa in advanced stages.[463] Next to clinical efficacy in reducing motor fluctuations, those D_2R/D_3R agonists also are shown to exhibit antidepressant effects.[464]

The activation of D_3 receptors may be particularly beneficial, as D_3R stimulation appears to attenuate disease progression in early stages and reduce levodopa- induced dyskinesias.[438] Additionally, preclinical studies suggest potential neuroprotective effects of pramipexole, possibly mediated through its antioxidant properties and effects on mitochondrial function.[465,466] However, dopamine agonists share common adverse effects including impulse control disorders, sleep disturbances, hallucinations, and cognitive impairment, which can limit their clinical utility in certain patient populations.[467]

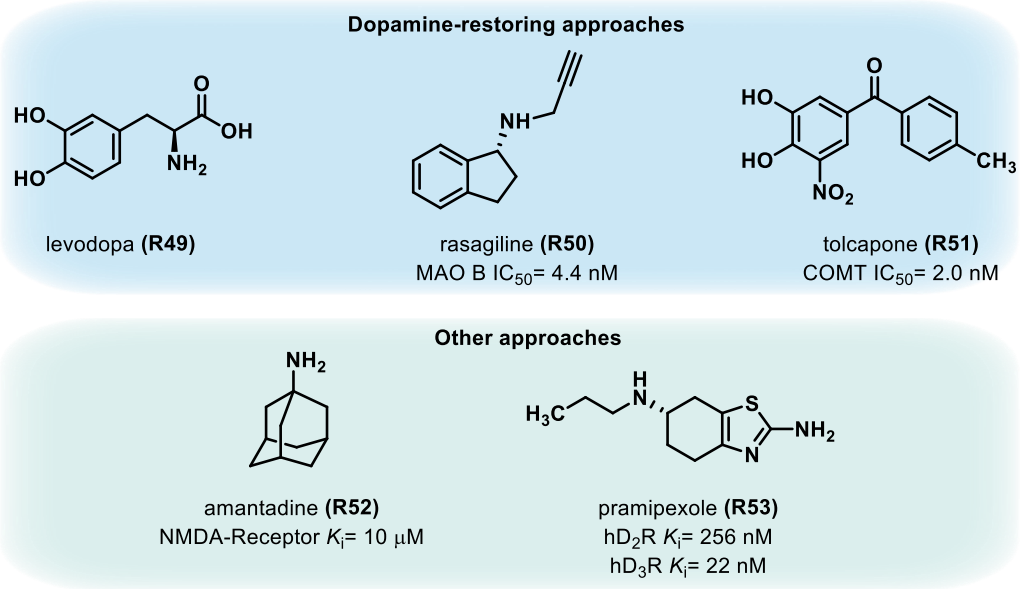

Figure 26: Selection of drugs used for treatment of Parkinson's disease following a dopamine restoring approach (marked in blue) and other approaches (marked in green). Pharmacological values were compiled from published literature sources.[468–470]

Beyond the dopamine-regulating approaches described above, the histamine H_3R represents a promising therapeutic target for addressing multiple aspects of PD, including the adverse effects of D_2R/D_3R agonists such as sleep disturbances.[471] H_3Rs are present on dopaminergic neurons projecting from the substantia nigra pars compacta to the striatum, where they, as a heteroreceptor, modulate various neurotransmitter systems, including dopamine release and synthesis.[39] Blockade of this receptor can enhance neurotransmitter release, potentially complementing traditional dopaminergic therapies and counteracting the dopamine deficiency characteristic of PD manifestation. This has been demonstrated with the H_3R inverse agonist thioperamide, which enhances release from glutamatergic neurons in the cortex and thalamus that directly stimulate the striatum.[472,473] Additionally, H_3Rs co-localize and in part heterodimerize with D_1 and D_2 receptors in medium spiny neurons in the striatum, influencing dopaminergic signalling in both pathways.[152] In the indirect pathway, H_3Rs functionally interact with D_2 receptors, reducing D_2R agonist binding affinity and modulating

motor control.[474] Consistent with this interaction, the H_3R inverse agonist thioperamide enhances locomotor responses to both D_1 and D_2 receptor stimulation.[167] Furthermore, H_3R antagonism offers benefits beyond dopaminergic effects. It may modulate neuroinflammatory processes involved in PD progression,[475] improve cognitive function,[234] and address sleep-wake cycle disturbances that frequently accompany PD.[476] For example, pitolisant, the first marketed H_3R antagonist/inverse agonist, has demonstrated efficacy in treating excessive daytime sleepiness in narcolepsy patients,[258] suggesting potential applications for similar symptoms in PD patients.

1.11 Narcolepsy

Narcolepsy represents a chronic neurological disorder characterized by excessive daytime sleepiness (EDS) and dysregulation of the sleep-wake cycle, affecting approximately 1 in 2,000 individuals worldwide.[452] The condition is primarily classified into two types: narcolepsy type 1 (NT1), characterized by the occurrence of cataplexy, which is a sudden loss of muscle tone triggered by strong emotions while consciousness remains intact, and narcolepsy type 2 (NT2), which normally lacks cataplexy.[477] These two subtypes not only differ in their clinical presentation but also in their underlying pathophysiology, which for NT1 has been extensively elucidated, while NT2 mechanisms remain more elusive.[478] Pathological studies have consistently demonstrated that NT1 centres on the selective loss of orexin-producing neurons in the lateral hypothalamus, with up to 85-95% reduction in these neurons.[479] This neuronal loss appears to have an autoimmune etiology, with genetic predisposition and environmental triggers implicated in disease development.[480] In contrast, NT2's underlying pathophysiology remains less well-defined. While NT2 patients can have normal cerebrospinal fluid orexin levels,[481] some exhibit a partial loss of orexin neurons with below 50% of normal levels.[482] Such partial deficiency appears sufficient to cause excessive daytime sleepiness but not severe enough to trigger cataplexy, suggesting a potential continuum between NT1 and NT2 pathophysiology. This hypothesis is supported by animal models where partial orexin loss produces EDS without cataplexy,[483] though this mechanism likely explains only a subset of NT2 cases, with other neurobiological factors remaining to be identified.[484] The pathophysiological consequences of orexin neuron loss become apparent when considering orexins' role as master regulators of the brain's arousal network. Orexins are hypothalamic neuropeptides that act primarily as excitatory neurotransmitters through their respective GPCRs, playing a crucial role in maintaining wakefulness by projecting to multiple wake-promoting neurotransmitter systems.[478] These include noradrenergic neurons in the locus coeruleus, serotonergic neurons in the raphe nuclei, cholinergic neurons in the basal forebrain, and histaminergic neurons in the tuberomammillary nucleus, all of which receive excitatory input from orexin neurons to

stabilize wakefulness through their respective neurotransmitter signalling pathways.[485,486] Particularly, the histaminergic signalling system, which is tightly regulated by the H_3R functioning as a presynaptic inhibitory autoreceptor, represents one of the key targets of orexin excitatory influence. In narcolepsy, the loss of excitatory orexin input to these histaminergic neurons contributes to reduced histaminergic tone and subsequent dysregulation of arousal pathways, leading to destabilization of sleep-wake boundaries and excessive sleepiness,[478] making H_3R a promising therapeutic target for narcolepsy.[487] These neurochemical imbalances resulting from orexin deficiency manifest clinically as a spectrum of sleep-wake symptoms, with EDS representing the cardinal and universal symptom, characterized by an overwhelming urge to sleep during inappropriate times.[478] Additional primary symptoms include sleep paralysis, hypnagogic/hypnopompic hallucinations, disrupted nocturnal sleep with frequent awakenings, and cataplexy, though the latter occurs exclusively in NT1 (see Figure 27).[488] Beyond these classic features, narcolepsy patients frequently suffer from cognitive impairment, metabolic disturbances, and mood disorders, particularly depression and anxiety, further compromising quality of life,[480] underscoring the need for comprehensive therapeutic approaches that address both primary symptoms and comorbidities.

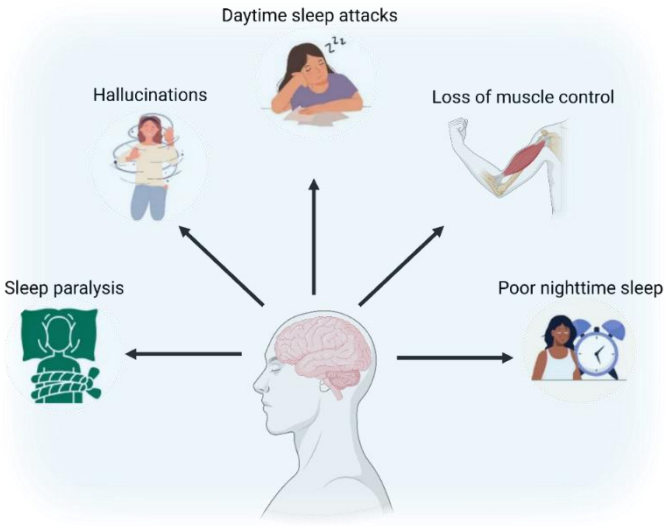

Figure 27: Overview of the typical symptoms of narcolepsy disorder. Created in https://BioRender.com.

1.11.1 Therapeutic approaches

Building upon our understanding of narcolepsy's pathophysiology, different therapeutic approaches have evolved to target the neurochemical imbalances resulting from orexin deficiency. Initially, treatment strategies focused on direct stimulation of arousal systems, represented by traditional stimulants like amphetamines (**R54**) and methylphenidate (**R55**),[489] which primarily function by increasing monoamine release and thereby triggering their awakening effects.[490] They have long been used to combat EDS but carry significant risks of

cardiovascular effects and abuse potential.[491] Sodium oxybate (**R56**) represents an alternative therapeutic approach, likely acting as a GABA-B receptor agonist suppressing dopaminergic neuronal activity, which leads to increased sleep efficiency, even though its mode of action is not fully elucidated.[492] Despite its efficacy in reducing cataplexy and excessive daytime sleepiness, it can cause side effects including dizziness, nausea, parasomnias, and neuropsychiatric symptoms.[493] To mitigate these side effects, newer pharmacological strategies have shifted toward modulating monoamine reuptake transporters (see Figure 28) rather than directly stimulating their release, leading to prolonged neurotransmitter presence in the synaptic cleft and therefore extended signalling effects.[494] This approach led to the development of modafinil (**R57**), a wake-promoting agent that selectively inhibits the dopamine reuptake transporter with minimal effects on norepinephrine and serotonin reuptake, offering improved tolerability compared to traditional stimulants.[495] Following the same strategy, solriamfetol (**R58**), a selective dopamine and norepinephrine reuptake inhibitor, emerged as another treatment option.[496] While its precise mechanism of action is not fully elucidated, the efficacy of solriamfetol in reducing EDS has been demonstrated in clinical studies, which showed dose-dependent improvements in wakefulness measured by Maintenance of Wakefulness Test and reductions in subjective sleepiness.[497] Regarding safety considerations, solriamfetol presents a beneficial safety and tolerance profile, including only common adverse effects such as headache, decreased appetite, anxiety, as well as some modest doses-dependent cardiovascular effects, like increases in blood pressure and heart rate.[498,499] Importantly, solriamfetol demonstrates a favourable risk-benefit profile with substantially lower abuse potential than traditional stimulants,[500] though regulatory agencies still classify it as a controlled substance due to its dopaminergic activity. In contrast to these monoaminergic approaches, a fundamentally different therapeutic strategy emerged by targeting the histaminergic system, which plays a crucial role in arousal regulation.[501] By antagonizing the H_3R autoreceptor, the natural brake on histamine release and synthesis is removed, leading to enhanced histaminergic neurotransmission and promotion of wakefulness. This innovative approach culminated in the development of pitolisant (**R24**), the first selective H_3R antagonist/inverse agonist approved for clinical use in narcolepsy patients.[487] The unique mechanism of action of pitolisant also confers several advantages as it has only minimal abuse potential,[502] with no evidence of withdrawal symptoms upon discontinuation, and does not disrupt nighttime sleep architecture.[259] Additionally, patients generally tolerate pitolisant well, with most adverse effects including headache, insomnia, and nausea being mild to moderate and typically resolving with continued treatment.[261]

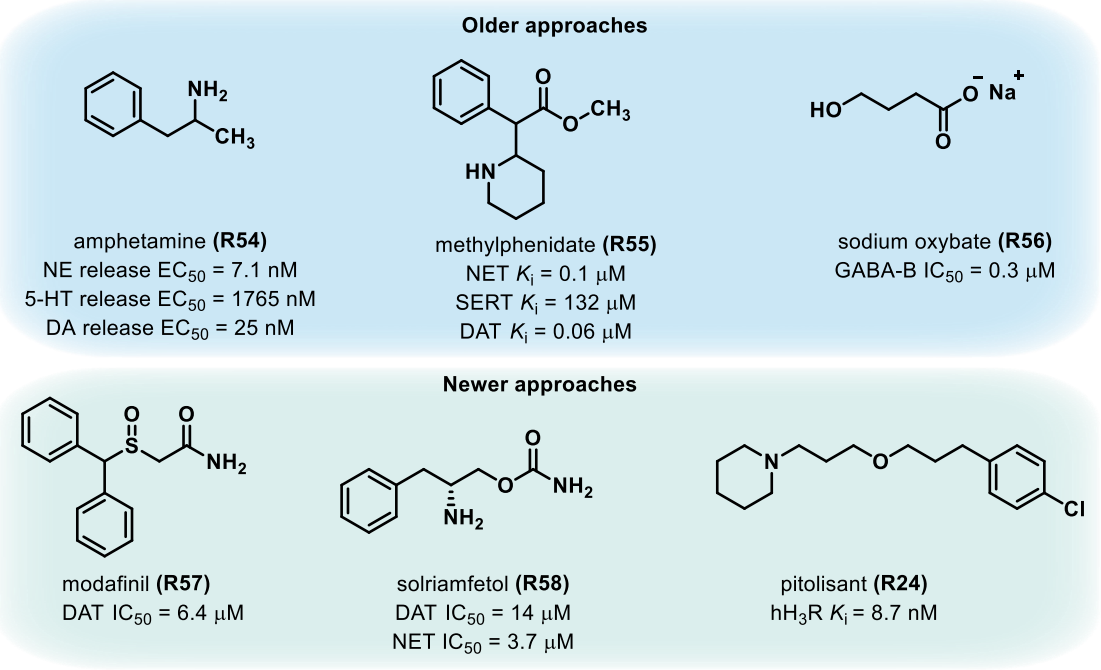

Figure 28: Selection of drugs used for the treatment of narcolepsy following older approaches (marked in blue) and newer approaches (marked in green). Pharmacological values were compiled from published literature sources.[503–506]

1.12 Multitarget-directed ligands (MTDLs)

The traditional approach to drug discovery has long been dominated by the "one disease, one target, one drug" paradigm, inspired by Paul Ehrlich's "magic bullet" concept.[507] Although this reductionist approach has resulted in numerous drugs currently in use, it has shown significant limitations, particularly for complex disorders with multifactorial pathologies. In response, a paradigm shift has occurred toward multitarget-directed ligands (MTDLs), compounds designed to modulate multiple biological targets simultaneously.[508] This shift was partly driven by the retrospective recognition that many clinically effective drugs, once criticized as "dirty" or "promiscuous," actually derive their therapeutic efficacy from interactions with multiple targets.[508,509] This polypharmacology can be deliberately exploited to achieve superior therapeutic outcomes in diseases with complex etiologies, particularly CNS disorders including Alzheimer's disease, Parkinson's disease, and narcolepsy, which often involve dysregulation of multiple neurotransmitter systems and signalling pathways.[509]

1.12.1 Design

In practice, the development of MTDLs begins with strategic target selection, as targets are typically chosen based on their involvement in complementary or synergistic pathways relevant to the disease pathology. For CNS disorders, this often involves targeting multiple neurotransmitter systems, enzymes involved in neurotransmitter metabolism or transport, or combinations of receptors and enzymes that contribute to disease manifestation.[510–512] Once

appropriate targets are identified, MTDL design is normally conducted either through knowledge-based methods utilizing established pharmacophores or through screening approaches when target information is limited. The subsequent chemical realization of the designed MTDLs typically follows three main strategies: linking, fusing, or merging of pharmacophores (see Figure 29).[513] The linking approach connects two distinct pharmacophores via a chemical tether, which can be either metabolically stable or cleavable. While this method preserves the individual binding properties of each pharmacophore, it often results in high molecular weight compounds with potential pharmacokinetic limitations.[513] In contrast, the fusing strategy overlaps two pharmacophores at compatible structural elements, reducing molecular weight while maintaining key binding features, though potentially sacrificing optimal interaction with each individual target.[513] Lastly, the merging approach represents the most sophisticated strategy by integrating essential pharmacophoric elements of multiple ligands into a single, compact structure, often achieving the most favourable balance between multitarget activity and drug-like properties, though requiring advanced design expertise.[514]

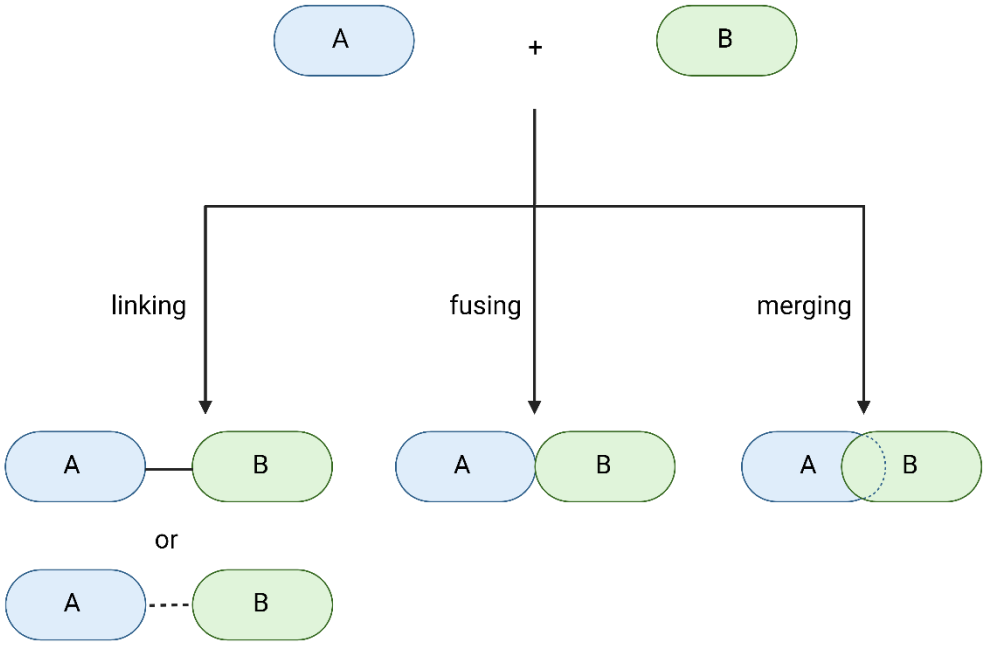

Figure 29: Three main strategies for MTDL design: linking, fusing, and merging. Linking can involve either a metabolically stable linker (solid line) or a cleavable linker (dotted line).

1.12.2 Challenges and advantages

However, each of these approaches faces unique challenges, as MTDLs must navigate a more constrained chemical space, satisfying the binding requirements of multiple targets while maintaining both favourable physicochemical properties and acceptable ADME profiles.[515] Consequently, the optimization process for MTDLs requires careful monitoring of both

physicochemical parameters and pharmacokinetic behaviour alongside biological activity at each target of interest. Beyond these physicochemical considerations, MTDL development presents further considerable challenges, as pharmacological characterization against multiple targets needs extensive screening and validation. Optimizing activity across multiple targets while minimizing off-target effects represents a complex balancing act, often requiring iterative cycles of design, synthesis, and testing.[513] Additionally, regulatory considerations also present hurdles, as current approval frameworks are primarily designed for single-target drugs with well-defined mechanisms of action, requiring more comprehensive mechanistic studies to secure approval for MTDLs.[509]

Despite these challenges, MTDLs offer several distinct advantages over both selective single-target drugs and combination therapies. They present a unified pharmacokinetic profile, eliminating the variable pharmacokinetics associated with drug combinations and simplifying dosing regimens which can help improve patient compliance, particularly valuable for CNS disorders where adherence is often problematic. Additionally, MTDLs also circumvent potential drug-drug interactions that may occur with polypharmacy approaches, which is especially relevant for recipients of multiple medications for comorbid conditions.[509] Perhaps most significantly, MTDLs offer the potential for synergistic or additive therapeutic effects through simultaneous modulation of complementary pathways. This network pharmacology approach may achieve therapeutic outcomes unattainable through single-target intervention, particularly for diseases with multiple parallel pathological mechanisms.[516]

1.12.3 H_3R-directed MTDLs

The histamine H_3R, due to its unique auto- and heteroreceptor functionality, is involved in the regulation of multiple neurotransmitter systems and signalling pathways throughout the central nervous system, which has positioned it as an attractive target for developing MTDLs to address complex CNS disorders.[517] For psychiatric disorders such as schizophrenia, H_3R/dopamine receptor ligands have been developed by merging the H_3R pharmacophore with known neuroleptic scaffolds. These hybrid molecules (**R37**) combine H_3R antagonism with D_2R affinity while reducing unwanted H_1R interactions, resulting in improved antipsychotic profiles with reduced extrapyramidal symptoms and weight gain side effects.[518] In the realm of neurodegenerative disorders, particularly Alzheimer's disease, several MTDL approaches have shown promise (see Figure 30). Through pharmacophore-based virtual screening, H_3R/serotonin receptor dual-targeting compounds were identified (**R38**), demonstrating significant cognitive enhancement, successfully reversing scopolamine-induced memory impairment in spatial working memory tests.[519] Building on this neuroprotective strategy, researchers have also designed H_3R/melatonin receptor ligands by connecting the imidazole-

containing H_3R antagonist pharmacophore with melatonin's core structure (**R39**). The resulting compounds simultaneously target H_3R, MT_1R, and MT_2R, leveraging the complementary neuroprotective and antioxidant effects of both systems for treating cognitive disorders.[520] Beyond targeting multiple GPCRs, combining H_3R antagonism with transporter inhibition has also been explored, demonstrated by the development of H_3R/SERT inhibitors to address mood disorders like depression. These dual-acting compounds (**R40**) combine the wakefulness-promoting effects of H_3R antagonism with serotonin reuptake inhibition, potentially providing faster symptom relief and cognitive benefits compared to traditional SSRIs.[521–523] Another transporter-targeting approach has focused on addressing pain conditions through H_3R/NET inhibitors (**R41**), designed by linking H_3R pharmacophores to duloxetine analogues. The resulting structures have demonstrated efficacy in neuropathic and osteoarthritis pain models by simultaneously modulating histaminergic and noradrenergic systems, with impressive efficacy of 70-93% in rat models.[524] In addition to GPCRs and transporters, enzymes have also been explored as additional targets for H_3R-adressing MTDLs. For example, H_3R/HMT dual inhibitors (**R42**) were created through different linkage strategies, resulting in compounds that increase central histamine levels through complementary mechanisms.[525,526] Similarly, H_3R/AChE inhibitors combining different AChE inhibitor structures with H_3R pharmacophores were developed, which can interact with both the catalytic site or the peripheral anionic site of AChE while maintaining H_3R antagonism, showing promise for Alzheimer's disease treatment.[527–531] A notable example is Contilisant (**R43**), a permeable, antioxidant, and neuroprotective agent that combines H_3R antagonism with inhibition of cholinesterases and monoamine oxidases, as well as potent sigma-1 receptor agonism, demonstrating strong efficacy in preclinical Alzheimer's models.[532] Further innovative approaches also include H_3R antagonists with NO-releasing properties (**R44**), created by coupling H_3R antagonists with furoxan systems capable of releasing nitric oxide under physiological conditions. These resulting dual-mechanism compounds offer synergistic benefits for memory and learning disorders through complementary pathways.[533–535] Collectively, these diverse H_3R-based multitarget-directed approaches highlight the versatility of the histaminergic system as a foundation for developing novel therapeutics that can simultaneously modulate multiple disease-relevant pathways, potentially offering improved efficacy and reduced side effects compared to single-target approaches for complex CNS disorders.

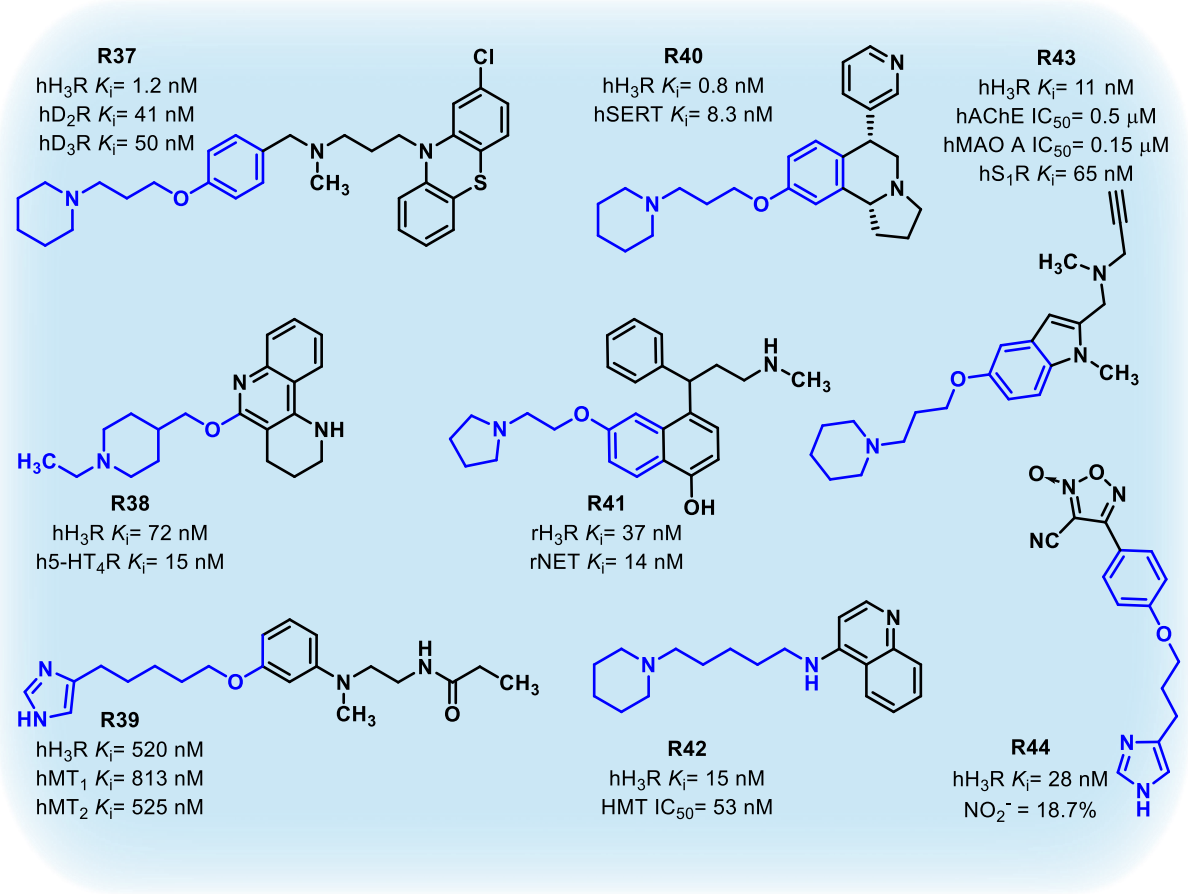

Figure 30: Selection of diverse H_3R-directed MTDLs with the H_3R pharmacophore marked in blue. K_i *and* IC_{50} values were compiled from published literature sources.[518–521,524,525,529,535]

1.13 Click chemistry

Click chemistry has revolutionized molecular assembly strategies across scientific disciplines, particularly in drug discovery and development. Recognized with the 2022 Nobel Prize in Chemistry, this concept offers reliable and selective methods for molecular building block connection characterized by high yields, stereospecificity, simple reaction conditions, and rapid kinetics.[536,537] In the early 2000s, click chemistry was pioneered by Sharpless and Meldal independently with the discovery of the copper(I)-catalyzed azide-alkyne cycloaddition (CuAAC). This reaction served as the prototype click reaction, enabling efficient formation of 1,2,3-triazoles under mild conditions.[538,539] However, the cytotoxicity of the necessary copper catalysts significantly limited its applications in biological systems.[540] This limitation prompted the development of strain-promoted azide-alkyne cycloaddition (SPAAC), which eliminated the need for copper catalysts and enabled click chemistry in living systems. This advancement opened the door for bioorthogonal applications, a term coined by Carolyn Bertozzi in the early 2000s to describe chemical reactions that occur inside of living organisms without interfering with native biochemical processes.[541] Building upon these advances, the inverse electron-demand Diels-Alder (IEDDA) reaction between dienes and strained dienophiles has emerged

as a superior bioorthogonal reaction, as it offers unprecedented reaction kinetics and excellent biocompatibility, making it particularly valuable for biological applications .[542,543]

1.13.1 IEDDA

A key advantage of IEDDA reactions is their exceptionally fast reaction rates, often orders of magnitude higher than other bioorthogonal reactions, allowing labelling at very low concentrations of biomolecules.[544,545] Among the various components used in IEDDA chemistry, tetrazines have become central to its success, serving as the predominant diene component.[546] Their exceptional utility stems from their electron-deficient nature, which significantly lowers the LUMO energy level, thereby reducing the $HOMO_{(dienophile)}$-$LUMO_{(diene)}$ energy gap and enabling rapid cycloaddition with dienophiles. This reactivity can be finely tuned through substitution patterns, with electron-withdrawing groups (EWGs) further enhancing reactivity by additionally lowering the LUMO energy of the tetrazine.[547] Both electron-rich dienophiles and those with ring strain like trans-cyclooctene (TCO) perform exceptionally well in these reactions, since both properties significantly contribute to reaction acceleration by raising the dienophile's HOMO energy and providing favourable orbital overlap.[547–549] Mechanistically, as depicted in Figure 31, the reaction initiates through an orbital-controlled coordination of both components, proceeding through a [4+2] cycloaddition followed by a retro-Diels-Alder reaction with nitrogen release, resulting in stable dihydropyridazine isomers that can undergo oxidation to form the final pyridazine product.[547]

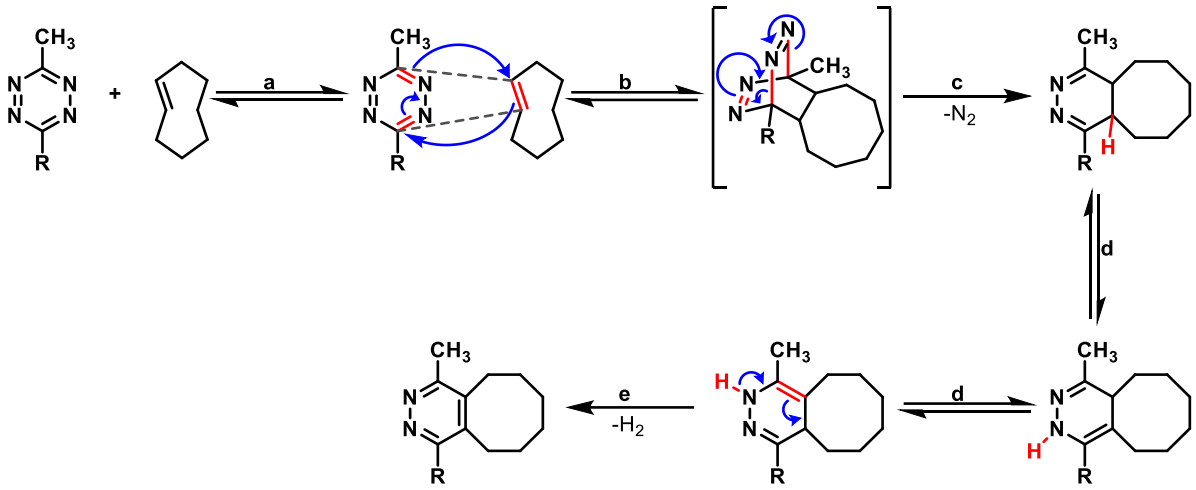

Figure 31: Mechanism of IEDDA click reaction exemplified for TCO as the ring-strained alkene and a methyltetrazine as the dienophile component. a) Orbital-controlled coordination b) [4+2]-Cycloaddition c) Retro Diels-Alder d) Isomerisation e) Oxidation.

The application of tetrazines in IEDDA reactions has enabled numerous advances in medicinal chemistry and drug development, with these reactive moieties being successfully incorporated into various applications including targeted drug delivery systems, prodrug

activation strategies, small molecule-protein conjugates, protein modification, antibody-drug conjugates and molecular imaging.[542] In the field of fluorescent labelling, tetrazines offer particularly versatile strategies. Beyond conventional approaches where tetrazines are directly conjugated to fluorophores, they enable innovative "turn-on" fluorogenic systems.[550] In these systems, the tetrazine quenches a nearby fluorophore until it reacts with a dienophile, resulting in fluorescence activation only after the click reaction occurs, providing exceptional signal-to-noise ratios.[551] Recent studies have demonstrated the power of bioorthogonal labelling approaches for GPCR targets using tetrazine-based IEDDA click chemistry, providing valuable insights into receptor dynamics and interactions.[552,553] These successes suggest a promising application of this methodology for further investigation of the histamine H_3R.

1.14 Fluorescent ligands as molecular tools

Since GPCRs serve as targets for approximately 30-50% of all marketed drugs,[554] the study of these receptors has evolved significantly over the decades, from early radioligand binding assays to sophisticated fluorescence-based techniques that allow real-time visualization of receptor-ligand interactions, helping our understanding of receptor pharmacology.[555] This transition from radioactive to fluorescent methodologies represents not only a safer approach but also offers enhanced spatial and temporal resolution for investigating receptor function.[264,265,556] This enhanced resolution achieved with fluorescent techniques derives directly from the fundamental principles of fluorescence, which is a photophysical phenomenon that occurs when a molecule absorbs light at a specific wavelength and subsequently emits light at a longer wavelength. This process involves the excitation of electrons from the ground state to an excited state, followed by relaxation and emission of a photon as the electron returns to its ground state.[557] A key aspect of this process is the difference between excitation and emission wavelengths, known as the Stokes shift, which is a important parameter that determines the practical utility of fluorophores in biological applications by allowing separation of excitation and emission signals.[558] Another crucial characteristic that defines fluorophore performance is the quantum yield, which gives the ratio of photons emitted to photons absorbed and determines brightness, while the signal intensity is affected by the molar extinction coefficient, which gives the capacity of a molecule to absorb light at a given wavelength.[557] Additionally, minimal environmental sensitivity and good photostability are essential properties for effective fluorophores. [558,559] These important parameters guide the selection of appropriate fluorophores for biological applications, which requires careful consideration of these properties, as well as factors such as size, hydrophilicity/hydrophobicity, and potential interactions with biological systems.[264,559]

1.14.1 Key fluorophores

Due to their ability to meet many of these critical criteria, two classes of fluorescent compounds have become particularly prominent in GPCR research with fluorescein derivatives and BODIPY (boron-dipyrromethene) compounds.[560] Fluorescein, first synthesized in 1871, has long been used as a standard fluorescent ligand but has undergone extensive modification to address limitations such as pH sensitivity, photobleaching, and self-quenching at high concentrations.[561–564] These improvements have led to derivatives like rhodamine, in which the hydroxyl groups of fluorescein are replaced by amine functionalities, Oregon Green and carboxyfluoresceins (**R45**) that offer improved stability and brightness for fluorescent ligand development.[565–567] Complementing the fluorescein-based fluorophores, BODIPY fluorophores have emerged as particularly valuable tools for GPCR research due to their exceptional versatility and favourable properties. These compounds (see **R46** in Figure 32) typically exhibit high quantum yields, narrow emission bands, good photostability, and relative insensitivity to solvent polarity.[568] Most interestingly, the BODIPY core structure can be readily modified to tune spectral properties, enabling the development of derivatives spanning the visible spectrum from green to near-infrared.[569] Additionally, the relatively small size and hydrophobic nature of BODIPY fluorophores can be advantageous for maintaining ligand binding properties, particularly for lipophilic binding pockets.[570]

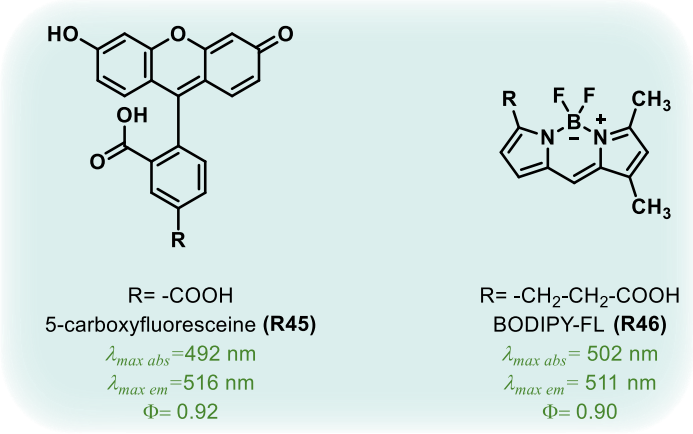

Figure 32: Fluorophore core structures of fluorescein and BODIPY, as represented in the structures of 5-carboxyfluorescein (**R45**) and BODIPY-FL (**R46**), along with their respective photophysical properties.[565,571]

1.14.2 Design

Next to the selection of fluorophore, the development process of fluorescent ligands requires also careful consideration of how and where to attach the fluorescent moiety to the pharmacophore, as this represents a delicate balance between maintaining pharmacological activity and incorporating suitable fluorescent properties. Structure-activity relationship (SAR) studies are essential in this process, guiding researchers to identify positions on the ligand

where modification will minimally disrupt receptor binding while preserving the fluorophore's spectral properties.[560] However, successful design must consider not only the attachment point but also the nature of the linker connecting the pharmacophore to the fluorophore, as linker length, flexibility, and chemical composition significantly influence both pharmacological and photophysical properties of the resulting conjugate.[264] Therefore, similar to MTDL design, three main approaches exist for creating fluorescent ligands: direct incorporation of the fluorophore into the pharmacophore structure, where it may directly contribute to receptor binding, direct attachment of the fluorophore to the pharmacophore without a spacer, or attachment via a linker to a pharmacophore position that tolerates modification (see Figure 33).[560]

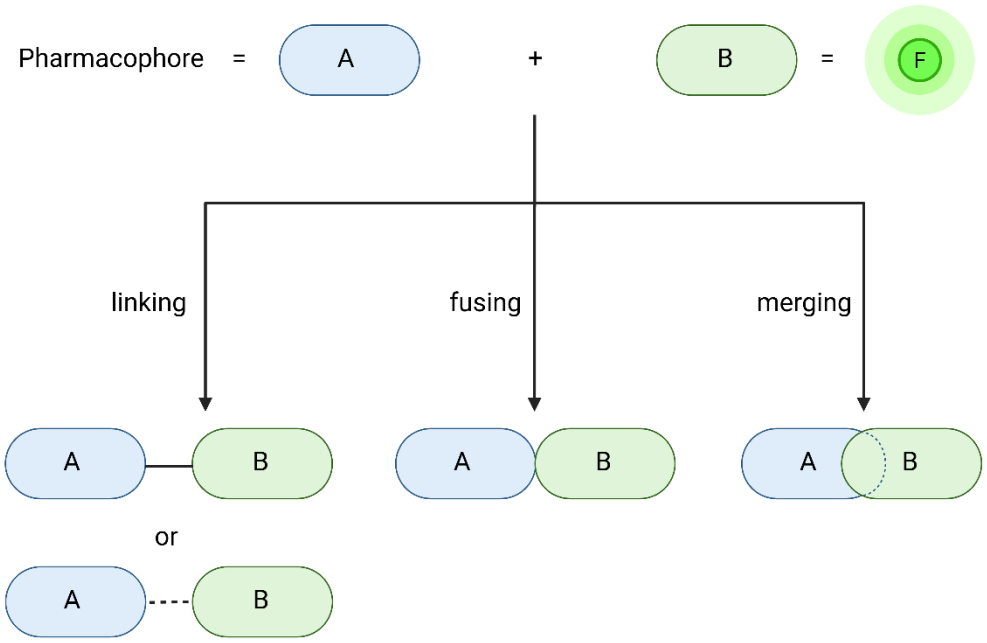

Figure 33: Three main strategies for fluorescent ligand design: linking, fusing, and merging. Linking can involve either a metabolically stable linker (solid line) or a cleavable linker (dotted line).

1.14.3 Application potential

Building on these design strategies, fluorescent ligands have revolutionized multiple aspects of GPCR research, from basic pharmacological characterization to complex studies of receptor dynamics and signalling. Their applications span a broad spectrum of methodologies, ranging from high-throughput screening through displacement assays for novel GPCR ligand identification, to advanced visualization techniques.[572,573] Imaging technologies like confocal microscopy and total internal reflection fluorescence (TIRF) allow high resolution visualization of receptor distribution and trafficking,[574,575] while emerging super-resolution microscopy techniques overcome the diffraction limit, enabling visualization of receptor organization at nanoscale resolution.[576] Expanding beyond static imaging, resonance

energy transfer approaches utilize fluorescent ligands to study receptor interactions and conformational changes, providing insights into the molecular mechanisms of receptor function.[577] These fluorescent tools also enable dynamic studies of receptor behaviour, from tracking internalization, recycling, and degradation to following individual receptor movements within cell membranes through single-molecule tracking approaches and techniques such as fluorescence recovery after photobleaching (FRAP), offering new insights about receptor mobility and clustering.[578,579] Recent advances continue to expand these capabilities, as photoactivatable and photoswitchable fluorophores enable precise spatiotemporal control of receptor activation and visualization,[580,581] while environment-sensitive fluorophores, that change their spectral properties upon receptor binding, provide new insights into ligand-receptor interactions.[582] In summary, fluorescent ligands represent a transformative technology in GPCR research, offering unprecedented versatility and resolution for investigating receptor structure, function, and dynamics. This holds particular promise for multifunctional receptors involved in various physiological roles and implicated in numerous disease states, such as the histamine H_3 and H_4 receptors, where fluorescent tools could provide crucial insights not only into receptor structure and function but also into their specific roles in pathological conditions.

2. Scope of thesis

Histamine receptors ($H_{1-4}R$) represent important therapeutic targets across various physiological systems. Among these, the histamine H_3 and H_4 receptors have emerged as particularly promising targets for therapeutic intervention and fundamental research. The histamine H_3 receptor, predominantly expressed in the central nervous system, represents a particularly versatile therapeutic target due to its multifaceted role in various neurological disorders, including Parkinson's disease,[452] narcolepsy,[583] and cognitive disorders.[584] Its unique ability to modulate multiple neurotransmitter systems[170] makes it an attractive candidate for multi-target ligand approaches, as its involvement in diverse pathological conditions enables beneficial combinations with various therapeutic agents.[585] In contrast, the H_4R, initially identified primarily in immune cells, has been implicated in inflammatory and allergic conditions,[275] though its complete expression pattern remains controversial, with emerging evidence suggesting potential presence in brain tissues.[303]

Despite their significant potential, the current landscape of H_3R and H_4R receptor research reveals several limitations in both therapeutic approaches and research tools. Therapeutically, single-target strategies often fail to address the multifaceted nature of complex, H_3R-associated neurological disorders like Parkinson's disease and narcolepsy.[492,586] Consequently, patients are frequently required to manage multiple medications simultaneously, facing increased risks of drug interactions, reduced compliance, and greater side effect burden, highlighting the need for more integrated therapeutic approaches.[587] From a research perspective, the available molecular tools for investigating H_3R and H_4R function and distribution remain limited. While the molecular toolbox for H_3R mainly lacks diversity in fluorescent ligands, there is a notable absence of ligands designed for bioorthogonal chemistry applications that could enable advanced visualization techniques,[540] helping further elucidate this important receptor. In contrast, the H_4R research toolkit critically lacks a highly selective fluorescent ligand capable of unambiguous receptor identification in tissues where multiple histamine receptor subtypes are expressed, a tool that would be invaluable for resolving the ongoing debate regarding H_4R localization in brain tissues.[588]

To address these research gaps, the focus of this thesis lies on the development of novel histamine H_3 and H_4 receptor ligands for diverse applications ranging from potential therapeutic agents to molecular research tools. Through systematic exploration of different design strategies and synthetic approaches, this work aims to help expanding the current understanding of these receptor systems as well as to establish new therapeutic opportunities involving these targets. Building on this rational, the first project aimed to develop novel multi-

targeting ligands that simultaneously address dopaminergic deficiency and histaminergic modulation in Parkinson's disease by combining H_3R antagonism with D_2/D_3 receptor agonism in a single molecule. This approach seeks to provide more comprehensive symptom management by addressing both motor and non-motor symptoms simultaneously, potentially offering improved therapeutic efficacy compared to current monotherapeutic methods through the synergistic combination of dopaminergic stimulation and histaminergic modulation,[167] while minimizing the side effects and drug interactions that typically result from administering multiple single-target therapies. Similarly, the second project pursued an enhanced approach to narcolepsy treatment by developing novel dual-target ligands through rational design that combines the pharmacophores of two clinically validated narcolepsy medications, pitolisant and solriamfetol, integrating H_3R antagonism with norepinephrine-dopamine reuptake inhibition. This strategy was designed to create single-molecule therapeutics capable of engaging multiple wake-promoting pathways, potentially offering improved symptom management while reducing the need for complex combination therapies.[589]

Beyond therapeutic applications, this work additionally focused on advancing the understanding of H_3R function through the development of sophisticated molecular tools. To this end, the next project pursued to expand the existing molecular toolbox for H_3R by developing tetrazine-based H_3R ligands, designed to engage in metal-free click chemistry. These novel tools exhibit the capabilities for biorthogonal cross-linking reactions,[590] allowing for unique imaging applications in living systems that were previously unattainable with conventional H_3R molecular tools. Complementing these click chemistry tools, the development of novel fluorescent H_3R ligands was planned in the next project to expand the diversity of the available molecular toolbox for receptor visualization and characterization even further. Therefore, different pharmacophore-fluorophore attachment strategies were explored to optimize the balance between maintaining strong receptor affinity and selectivity while achieving excellent fluorescent properties.[560]

Building on this experience with fluorescent H_3R ligands, this thesis encompasses another project dedicated to developing selective H_4R fluorescent ligands, addressing the critical need for tools to investigate this receptor's precise function and controversially discussed distribution pattern, particularly regarding its potential presence in brain tissues.[588] Through systematic exploration of multiple design strategies based on established H_4R ligands, this project aimed to develop H_4R affine and selective fluorescent tools enabling receptor visualization and localization studies, ultimately working to bridge this significant gap in H_4R research and shed light on this ongoing scientific debate. Collectively, these multifaceted

projects seek to advance the field of histamine receptor research on multiple fronts. The therapeutic projects aim to develop innovative multi-target approaches for neurological disorders, potentially offering improved efficacy and reduced side effect profiles compared to current treatments, while the molecular tool development projects address critical gaps in the available methods for investigating H_3R and H_4R function and distribution, potentially enabling new insights into these receptors' roles in health and disease.

The successful completion of these projects would not only expand the arsenal of available compounds for histamine receptor research but could also provide valuable leads for future therapeutic development.

Part I

H_3R-based MTDLs

3. Development of H_3R-based MTDLs for Parkinson's disease

This chapter describes the design, synthesis and biological evaluation of novel MTDLs combining H_3 receptor antagonism with D_2/D_3 receptor agonism as potential therapeutic agents for the treatment of Parkinson's disease.

3.1 Rational design

Despite promising therapeutic approaches, current single-target strategies often fail to address the multifaceted nature of PD, with each approach limited by either insufficient efficacy across the symptom spectrum or problematic side effect profiles.[586] Additionally, the complex pharmacokinetic interactions and polypharmacy burden associated with administering multiple single-target drugs simultaneously can lead to reduced patient compliance and increased risk of adverse events.[591] Therefore, Parkinson's disease management remains a complex therapeutic challenge, requiring innovative approaches to address both motor and non-motor symptoms.[592] Therefore, the development of MTDLs simultaneously addressing dopaminergic deficiency and histaminergic modulation in PD represents a promising strategy. This approach aims to provide more comprehensive symptom management while potentially reducing side effects associated with multiple single-target therapies, by designing and synthesizing novel MTDLs combining D_2/D_3 receptor agonism with H_3 receptor antagonism. The therapeutic rationale for this dual-targeting approach is substantiated by the intricate interplay between these receptor systems in the central nervous system.[593] While direct dopamine agonism addresses the fundamental dopaminergic deficit in Parkinson's disease,[594] H_3 receptor antagonism enhances dopaminergic signalling through multiple mechanisms like direct upregulation of dopamine release, modulation of postsynaptic responses, and formation of functional H_3-D_2 receptor heterocomplexes in the striatum.[167] To achieve this dual-targeting profile, a molecular merger approach was employed by combining the pharmacophores of established ligands: the H_3R antagonist **JNJ-5207852**[595] and the clinically approved D_2R/D_3R agonist **pramipexole**.[596] Two potential pharmacophore connection strategies were identified, namely through the aromatic amine or via the aliphatic secondary amine of **pramipexole** (see Figure 34). Previous work in our research group explored the aromatic amine connection, resulting in compounds that showed high H_3R affinity but lost dopaminergic activity. Therefore, this project investigated the aliphatic amine connection strategy, hypothesizing that preserving the free aromatic aminothiazole moiety might be crucial for maintaining dopamine receptor activity.

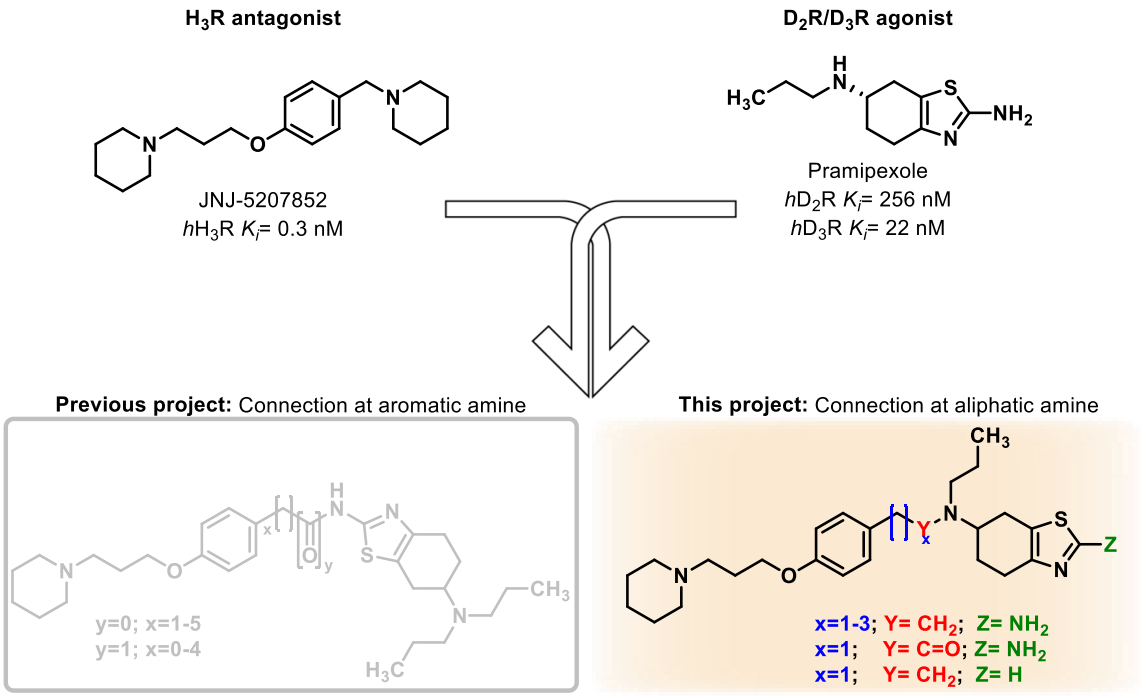

Figure 34: Employed pharmacophore merging strategies leading to novel MTDLs for Parkinson treatment. Connection at **pramipexole's** aliphatic amine (highlighted in orange) yielded the current series, while previous work explored connection at the aromatic amine (shown in grey).

3.2 Synthesis

3.2.1 First synthetic approach

A small series of three MTDLs was outlined with varying linker lengths (methylene to trimethylene) between the combined pharmacophores. The synthetic route (see Figure 35) was designed to begin with building the H_3R pharmacophore from the respective aldehydes **1a-c**, each containing different linker lengths between the aldehyde function and the phenol ring. Alkylation of the phenolic group with 1-(3-chloropropyl)piperidine hydrochloride would yield compounds **2a-c**, establishing the H_3R pharmacophore. The resulting aldehydes **2a-c** were planned to be connected to the **pramipexole** core structure **4**, which would be previously prepared by reductive amination of compound **3** with propylamine, producing the prefinal compounds **5a-c**. In the final step, a one-pot synthesis comprising acetal cleavage, α-bromination, and Hantzsch thiazole synthesis would form the **pramipexole** pharmacophore, yielding the final MTDLs **P1a-c**.

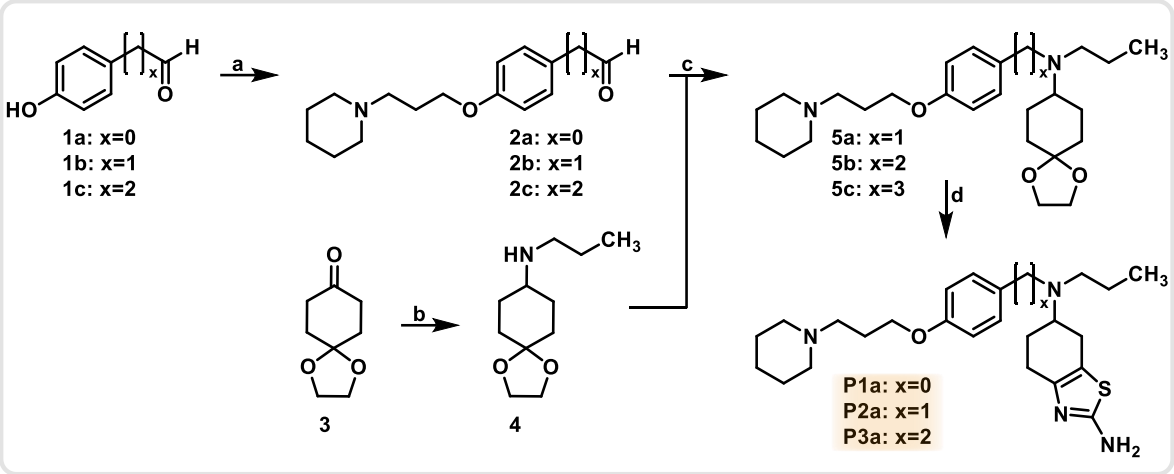

Figure 35: Planned synthetic route for the preparation of the MTDLs combining H_3R antagonist and D_2R/D_3R agonist pharmacophores. Reaction conditions: a) KI, K_2CO_3, 1-(3-chloropropyl)piperidine hydrochloride, acetone, reflux, 24 h. b) propylamine, acetic acid,STAB, DCE, room temperature, 24 h. c) acetic acid,STAB, DCE, reflux, 20 h. d) i) HBr, 0 °C, 1 h ii) bromine, 0 °C, 4 h iii) thiourea, reflux, 17 h.

The synthetic route for the MTDL with the shortest methylene linker (**P1a**) began with introducing the H_3R pharmacophore warhead through alkylation of para-hydroxybenzaldehyde (**1a**) with 1-(3-chloropropyl)piperidine hydrochloride (**SM1**). This transformation was performed as a Williamson ether synthesis under Finkelstein conditions[597] at reflux for 24 hours, yielding compound **2a** in 80%.[598] The reaction mechanism, shown representatively in Figure 36, proceeds via initial deprotonation of the weakly acidic phenol by potassium carbonate to generate the nucleophilic phenolate (**IM2**). The addition of potassium iodide in acetone facilitates an in situ halogen exchange, generating the more reactive alkyl iodide (**IM1**).[597] The formation of insoluble potassium chloride in acetone drives the equilibrium toward the product.[599] The phenolate then attacks the alkyl halide via an S_N2 mechanism[600], passing through a five-membered transition state,[601] establishing the ether linkage and introducing the H_3R pharmacophore.

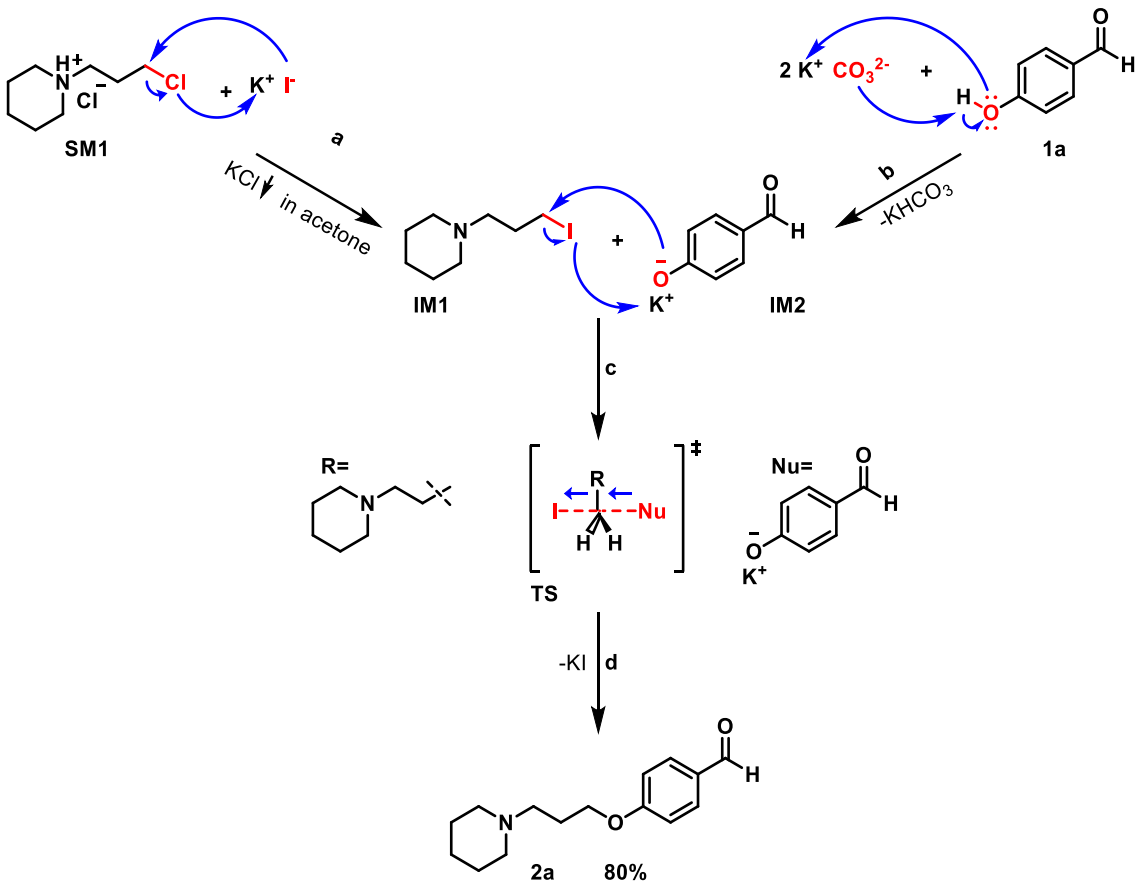

Figure 36: Mechanism of Williamson ether synthesis under Finkelstein conditions, exemplarily shown for the synthesis of compound **2a**. a) Nucleophilic substitution b) Phenol deprotonation c) Nucleophilic attack d) Elimination.

The next step in the proposed synthetic route was the formation of compound **4**, which serves as the core building block of the pramipexole pharmacophore. Starting from cyclohexanedione monoethylene ketal **3**, reductive amination with propylamine was performed at room temperature for 24 h, yielding compound **4** in 78%.[602] The reaction mechanism, shown in Figure 37, proceeds through initial ketone activation via protonation by acetic acid, creating an electrophilic centre (**TS1**). This activated carbonyl is then attacked by propylamine as the nucleophile forming a hemiaminal (**TS2**). Intramolecular proton transfer leads to **TS3**, which converts to the protonated imine (**TS4**) via elimination of water. In the final step, sodium triacetoxyborohydride (STAB) delivers a hydride to the imine, generating the secondary amine **4**[603] This irreversible reduction step drives the equilibrium toward product formation.[599] STAB's selective reduction of imine over ketones also enables an efficient one-pot reductive amination, making it the reducing agent of choice for this transformation.[604]

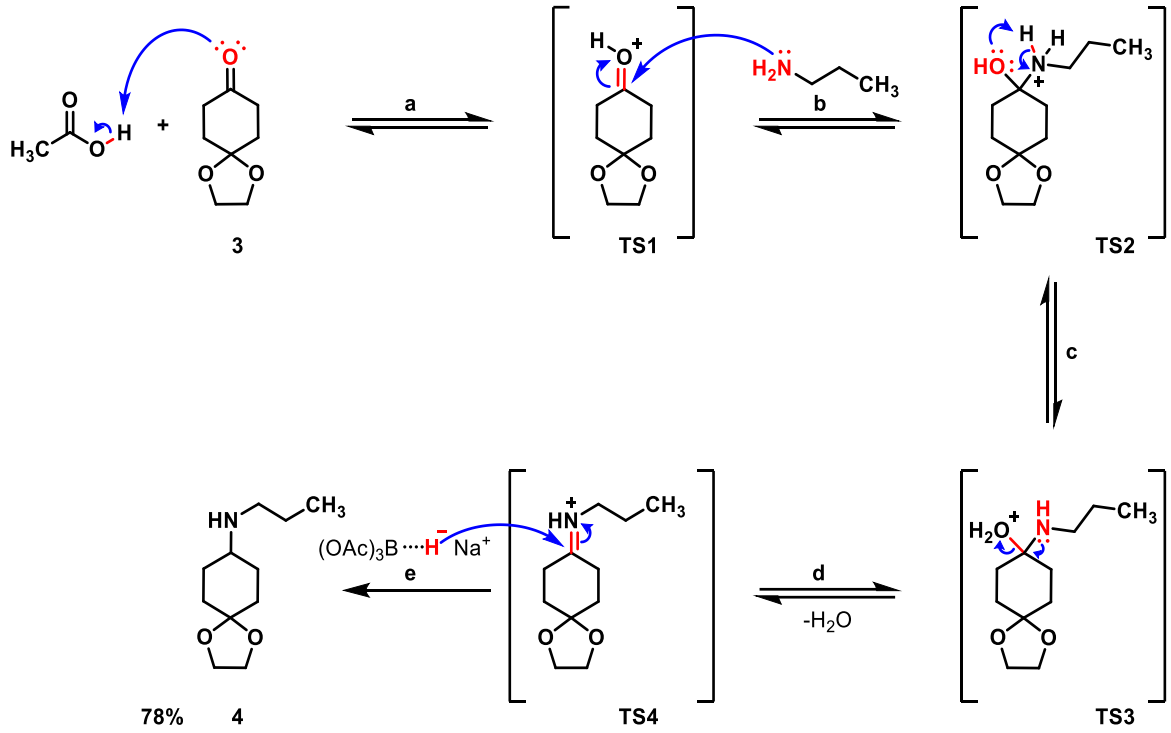

Figure 37: Mechanism of reductive amination, exemplarily shown for the synthesis of compound **4**. a) Ketone protonation b) Nucleophilic attack c) Intramolecular proton transfer d) Imine formation e) Imine reduction.

The secondary amine **4** underwent a following reductive amination with aldehyde **2a**, containing the previously synthesized H_3R pharmacophore, establishing the connection between the two pharmacophores to be merged. The reaction followed the same mechanism as shown in Figure 37 and yielded the prefinal compound **5a** in 36% after heating under reflux for 20 h (see Figure 38).[602] The moderate yield can be attributed to several factors: the use of a sterically hindered secondary amine as nucleophile, which leads to the formation of the less favourable iminium ion compared to an imine,[605] and the inherent stability of the aromatic aldehyde due to the electron-donating ether substituent in *para*-position, which decreases the electrophilicity of the aldehyde group.[606] Furthermore, the reversible nature of iminium ion formation under the reaction conditions and potential hydrolysis of the intermediate iminium species could potentially contribute to the moderate yield.[607]

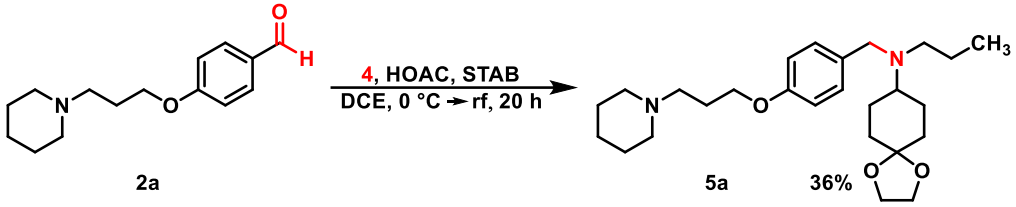

Figure 38: Reaction of the second reductive amination of **2a** with **4** yielding the prefinal compound **5a**.

The formation of the **pramipexole** pharmacophore from prefinal **5a** to the final MTDL progresses through an elegant three-step one-pot synthesis (see Figure 39).[608] Starting at 0 °C,

the initial transformation involves acetal hydrolysis[609] in hydrobromic acid for one hour, where the acid protonates the acetal (**TS1**). This protonation initiates an intramolecular bond cleavage (**TS1**), followed by nucleophilic attack of water on the resulting carbenium ion (**TS2**) to form a hemiacetal intermediate (**TS3**). Subsequent intramolecular proton transfer (**TS4**) and elimination of ethylene glycol reveals the carbonyl functionality, yielding intermediate **IM1**. Maintaining the temperature at 0 °C, the exposed ketone **IM1** then undergoes α-bromination through addition of bromine over four hours in the second step.[610] This transformation proceeds through keto-enol tautomerism, where the enol form experiences electrophilic attack by bromine (**TS5**). The residual bromide ion acts as a base, abstracting the proton from the carbonyl to produce the α-brominated ketone **IM2**. In the final step, thiourea is added and the mixture is heated for two hours, followed by stirring at room temperature for 17 hours to perform the Hantzsch thiazole synthesis to construct the aminothiazole ring.[611] The reaction sequence begins with nucleophilic attack by the sulfur atom of thiourea at the α-position of the ketone, displacing the bromide (**TS6**). The released bromide serves as a base, deprotonating the thiourea. Then Ring closure occurs through intramolecular nucleophilic attack by the free amine of the thiourea on the ketone (**TS7**). The aminothiazole ring formation completes through intramolecular proton transfer and water elimination (**TS8**). This efficient one-pot synthetic sequence delivers the final MTDL **P1a** in 16% overall yield, with the low yield likely attributed to competing side reactions during the α-bromination step[612] and potential hydrolysis of intermediates under the acidic conditions.[613] Nevertheless, the methodology effectively combines three synthetic transformations in a single reaction vessel, representing a streamlined approach to the pramipexole pharmacophore that minimizes handling steps and purification procedures.

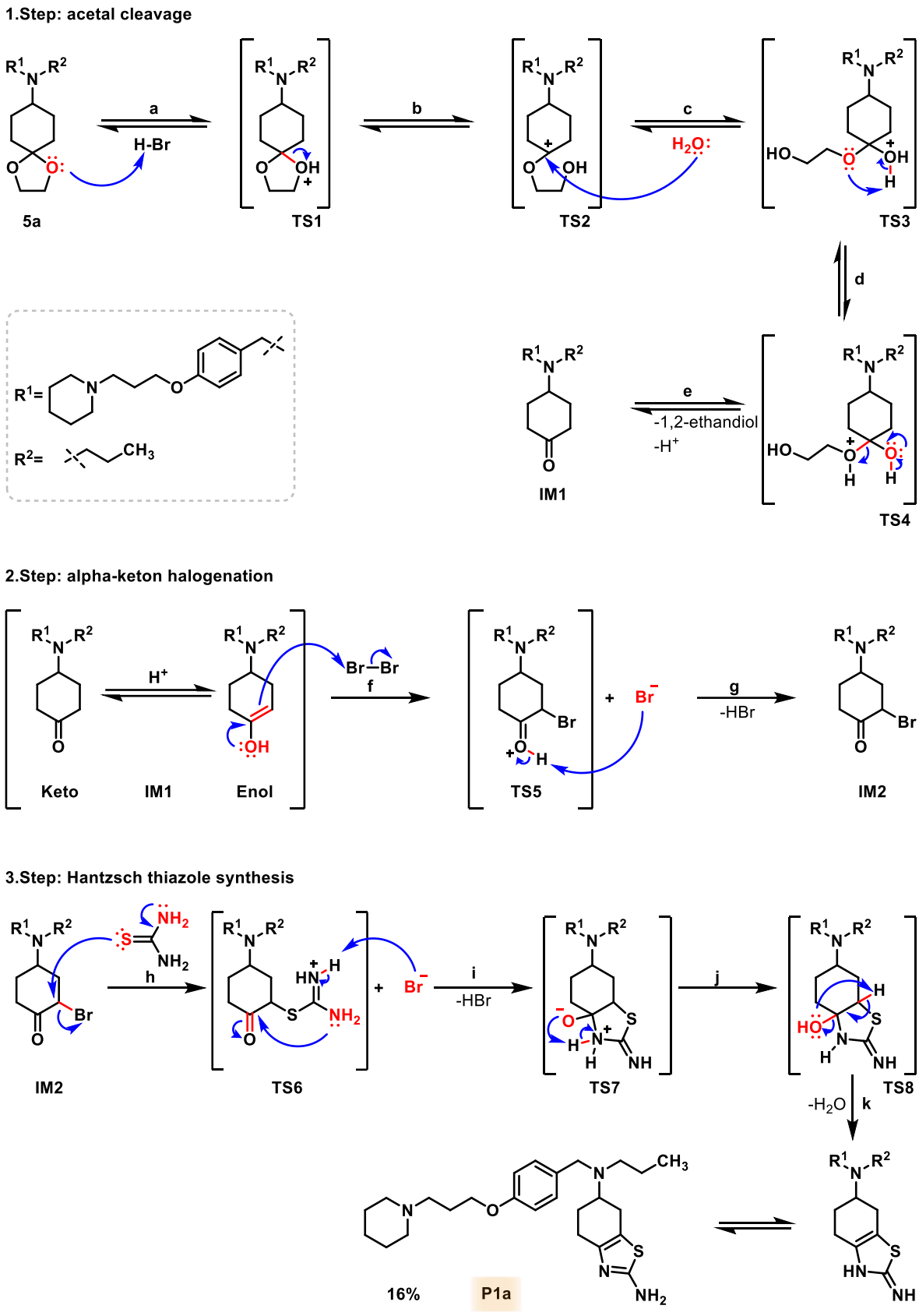

Figure 39: Mechanism of the individual steps in the one-pot synthesis exemplarily shown for the synthesis of MTDL **P1a**. a) Protonation b) Formation of carbenium ion c) Hemiacetal formation d) Intramolecular proton transfer e) Alcohol elimination f) Bromination in α-position g) Deprotonation h) Nucleophilic attack i) Deprotonation and ring formation j) Intramolecular proton transfer k) Water elimination.

3.2.2 Second synthetic approach

The derivatives with extended linker chains were initially planned to follow the same reaction route (see Figure 35). Since the corresponding aldehydes **1b,c** were not commercially available, their synthesis was attempted through oxidation of the respective alcohols **6a,b** (see Figure 40). Various oxidation methods were investigated, including DMP oxidation,[614] Swern oxidation,[615] and TEMPO-catalyzed oxidation.[616] Despite the broad range of oxidation conditions explored, the desired aldehydes could not be obtained in sufficient yields, reflecting the characteristic reactivity of aliphatic aldehydes, which presented interesting synthetic challenges, particularly due to their inherent instability.[617] These properties often lead to self-condensation reactions,[618] rapid air oxidation to carboxylic acids,[619] and formation of hydrates in the presence of traces of water.[620]

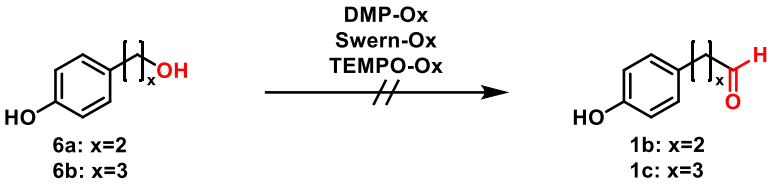

Figure 40: Reaction for various oxidation attempts of alcohols **6b,c** to synthesize aldehydes **1b,c**.

This chemical behaviour provided valuable insights, leading to an alternative synthetic strategy where the two pharmacophores should be connected via alkylation of the aliphatic amine rather than reductive amination (see Figure 41). This approach would begin again with the Williamson ether synthesis of 4-hydroxyphenylalcohols **6a,b** using 1-(3-chloropropyl)piperidine hydrochloride to construct the H_3R pharmacophore. Instead of oxidizing to aldehydes, the alcohols **7a,b** would be converted to the corresponding chlorides **8a,b**, establishing a suitable leaving group for subsequent alkylation. These organochlorides would then be subjected to alkylation under Finkelstein conditions with secondary amine **4** to achieve the pharmacophore linkage. The final step would employ the established one-pot synthesis to construct the aminothiazole ring system, yielding the final MTDLs **P1b,c**.

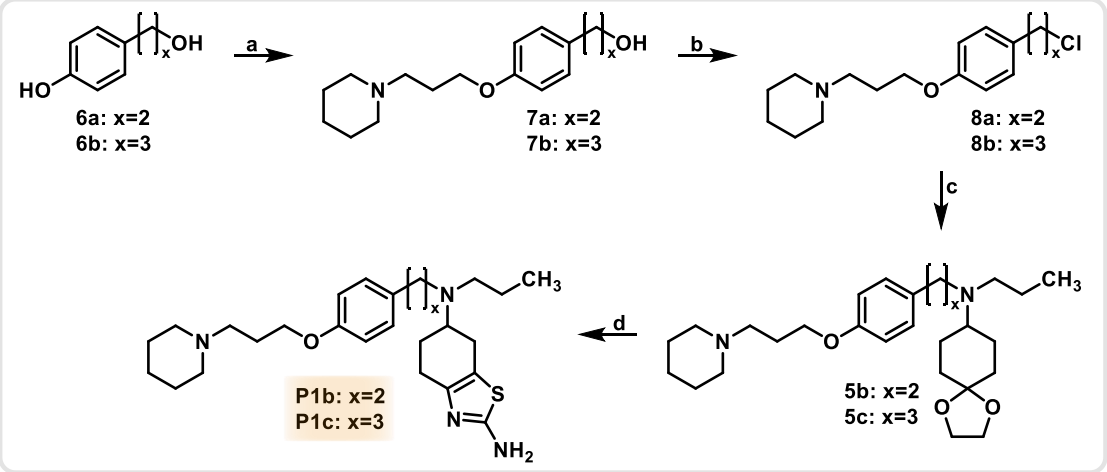

Figure 41: Second synthetic approach for the preparation of the MTDLs **P1b,c**. Reaction conditions: a) **SM1**, KI, K_2CO_3, acetone, reflux, 48 h. b) thionylchloride, THF, reflux, 16 h. c) compound **4**, KI, K_2CO_3, acetone, reflux, 24 h. d) i) HBr, 0 °C, 1 h ii) bromine, 0 °C, 4 h iii) thiourea, reflux, 17 h.

Initially, the 4-hydroxyphenyl alcohols **6a,b** were alkylated with the H_3R warhead 1-(3-chloropropyl)piperidine **SM1**, previously synthesized in-house according to an established procedure,[598] via Williamson ether synthesis under Finkelstein conditions to establish the H_3R pharmacophore (see Figure 42). The reaction proceeded according to the mechanism described in Figure 36, yielding 66-75% of product **7a,b** after refluxing for 48 hours.[598]

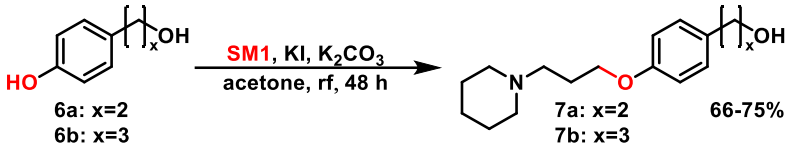

Figure 42: Reaction showing the Williamson ether synthesis under Finkelstein conditions from alcohols **6a,b** yielding the alkylated products **7a,b**.

In the second step, the free alcohol groups of compounds **6a,b** were converted to their corresponding chlorides to create suitable leaving groups for the subsequent alkylation, enabling the linkage of both pharmacophores. The chlorination was performed using thionyl chloride as the chlorinating reagent, which allowed for quantitative conversion under optimized conditions where the reaction mixture in THF was first refluxed for 30 minutes, followed by stirring at room temperature for 16 hours.[621] The chlorination mechanism[603] (see Figure 43) proceeds via an internal nucleophilic substitution and begins with the alcohol group performing a nucleophilic attack with its lone pair on the sulphur atom of thionyl chloride, which transforms the sulfoxide double bond into a single bond (**TS1**). Through intramolecular proton transfer and reformation of the sulfoxide double bond, hydrogen chloride is eliminated. The resulting intermediate (**IM1**) now bears a good leaving group, which is then displaced

through nucleophilic attack of the generated chloride at the alpha carbon position. This leads to the elimination of sulphur dioxide and chloride, yielding the final alkyl chlorides **8a,b**.

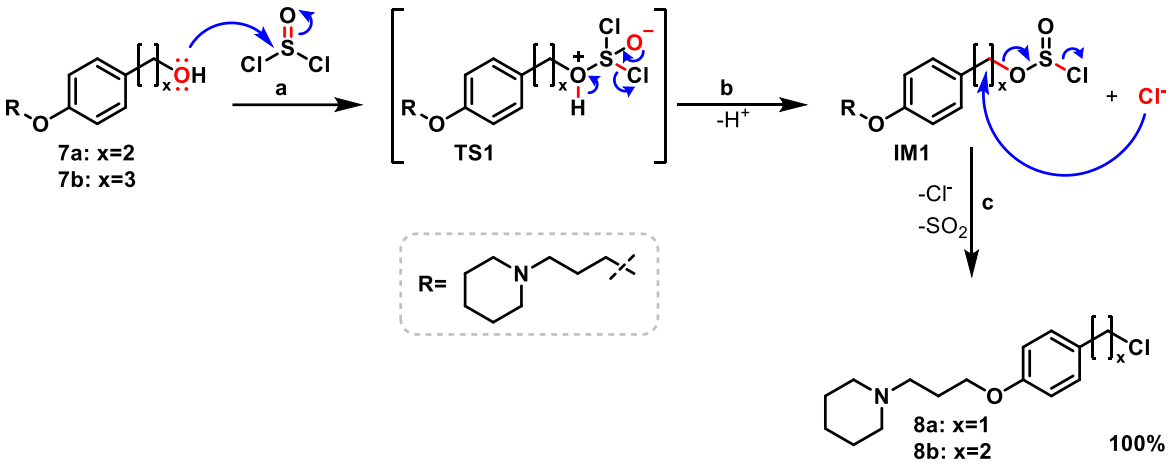

Figure 43: Mechanism of the alcohol chlorination with thionyl chloride, exemplified by the synthesis of compounds **8a,b.** a) Nucleophilic attack b) Elimination of hydrogen chloride c) Nucleophilic attack and elimination of sulphur dioxide and chloride.

Amine **4** was subsequently alkylated under Finkelstein conditions with compounds **8b,c** to achieve the combination of the H_3R pharmacophore and the **pramipexole** pharmacophore, with **4** representing the core structure of the latter. The alkylation of compound **8c** was conducted in acetone under reflux conditions for 24 hours, delivering the desired product **5c** in 41% yield (see Figure 44).[622] The reaction proceeds via the S_N2 mechanism illustrated in Figure 36. The moderate yield, when compared to the described Williamson ether syntheses, can be rationalized through several factors. The secondary amine **4** can undergo double alkylation,[603] forming tertiary ammonium salts that are removed during the purification process. Furthermore, the presence of an additional tertiary amine in molecule **8c** provides another nucleophilic centre that can participate in alkylation reactions, leading to quaternary ammonium salt formation, resulting in the observed yield.

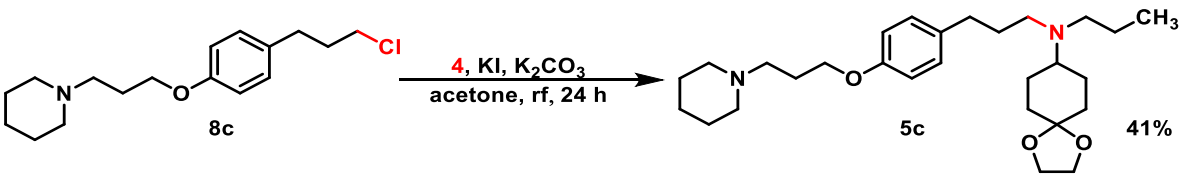

Figure 44: Reaction of the alkylation of secondary amine **4** with **8c** under Finkelstein conditions, yielding compound **5c**.

While the alkylation with **8c** proceeded as planned, the reaction with compound **8b** proved more challenging. During the alkylation of secondary amine **4** with compound **8b**, no product could be obtained in sufficient yields. The reason for this is the competitive E2 elimination

reaction that competes with the S_N2 reaction under these conditions.[622,623] Due to the formation of a stable styrene derivative where the resulting double bond is conjugated with the aromatic system, the E2 reaction is favoured,[624] yielding mainly the undesired elimination product **5b$_E$**, which could be detected by NMR and LC-MS but was not isolated. This competitive elimination does not occur as much during the alkylation with **8c**, since its elimination product would not be conjugated with the aromatic ring, making the E2 pathway less favourable. Both competing mechanisms are shown in Figure 45. The S_N2 mechanism involves a nucleophilic attack at the alpha C-atom, forcing the chloride to leave the molecule through a 5-membered transition state (**TS1**).[625] The elimination proceeds through deprotonation of the beta carbon, which leads to double bond formation between the alpha and beta carbons, causing the chloride to be eliminated from the molecule, also through a 5-membered transition state (**TS2**).[626]

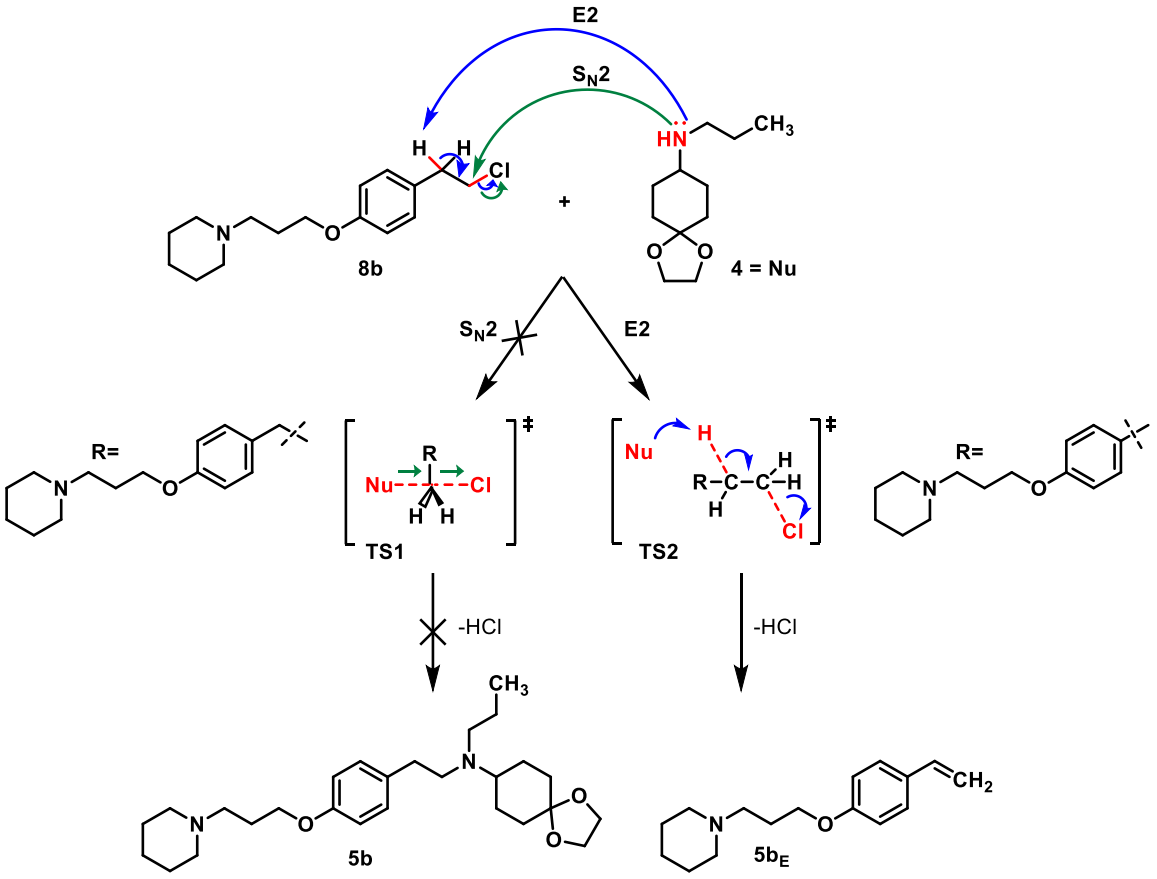

Figure 45: Mechanisms of both competing reactions (S_N2 and E2) during the attempted alkylation of **4** with **8b**, leading to the main formation of styrene derivative **5b$_E$**.

Despite these challenges with compound **8b**, the successful synthesis with **8c** was carried forward. In the final step, the one-pot three-step synthesis was performed, forming MTDL **P1c** from **5c**, incorporating acetal cleavage, alpha bromination, and lastly thiazole synthesis following Hantzsch conditions (see Figure 46).[608] The reaction sequence followed the same

mechanism and protocol as previously described in Figure 39. The low yield can likely be attributed to decomposition of the intermediates under the harsh conditions,[613] as well as to side reactions, especially during the bromination step[612] as already discussed earlier. However, the streamlined synthesis and reduced purification steps make the lower yields acceptable.

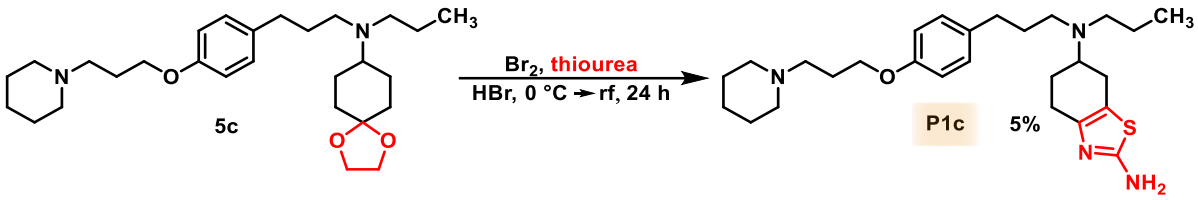

Figure 46: Reaction of the three-step one-pot synthesis of MTDL **P1c**.

3.2.3 Third synthetic approach

Since neither the alkylation nor the reductive amination route was successful as a pharmacophore-connecting step, a new synthetic route for MTDL **P1b** had to be designed, as shown in Figure 47. In this approach, the pharmacophore connection would be performed first, before building the H_3R pharmacophore. This would allowed the use of tyramine **9** as starting material, which normally could undergo undesired alkylation at the primary amine instead of the phenolic hydroxyl group during the H_3R warhead introduction. By first connecting the pharmacophores through a double reductive amination of tyramine **9** with cyclohexanedione monoethylene ketal **3** and propanal, the primary amine would be converted to a tertiary amine **10**, avoiding this competing reaction. The alkylation with the H_3R warhead could then be performed selectively at the phenol position, yielding compound **5b**. The following three-step one-pot synthesis would deliver the final MTDL **P1b**.

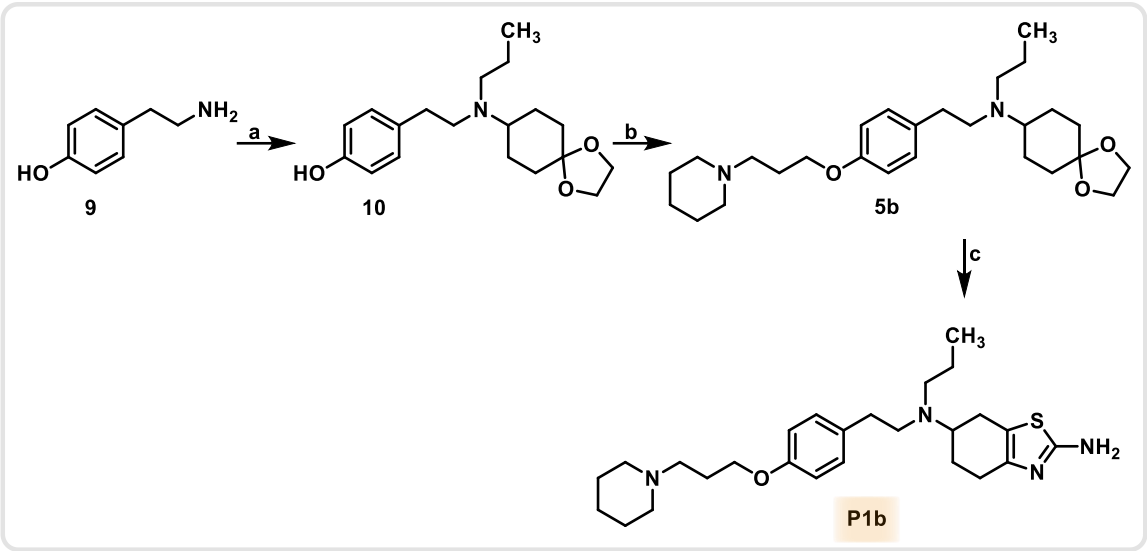

Figure 47: Third synthetic approach for the preparation of the MTDL **P1b.** Reaction conditions: a) acetic acid, compound **3**, propanal, STAB, DCE, room temperature, 24 h. b) **SM1**, KI, K_2CO_3, acetone, reflux, 24 h. c) i) HBr, 0 °C, 1 h ii) bromine, 0 °C, 4 h iii) thiourea, reflux, 17 h.

The synthesis commenced with a one-pot sequential double reductive amination, establishing the pharmacophore connection in the first step (see Figure 48). Initially, cyclohexanedione monoethylene ketal **3** was reacted with tyramine in dichloroethane (DCE) at room temperature using acetic acid as catalyst and STAB as reducing agent. The addition of STAB was performed at 0 °C, after which the reaction mixture was allowed to warm to room temperature and stirred for 20 hours.[627] The resulting secondary amine intermediate was then subjected *in situ* to a second reductive amination with propanal, again using STAB as reducing agent, to provide the desired tertiary amine **10**. Both reductive amination steps proceeded according to the mechanism shown in Figure 37. This one-pot strategy proved efficient, delivering the product in 36% yield over two consecutive reductive amination steps without intermediate purification (see Figure 48). The moderate yield is well justified by the significant advantages of the one-pot approach, particularly the reduced handling steps.

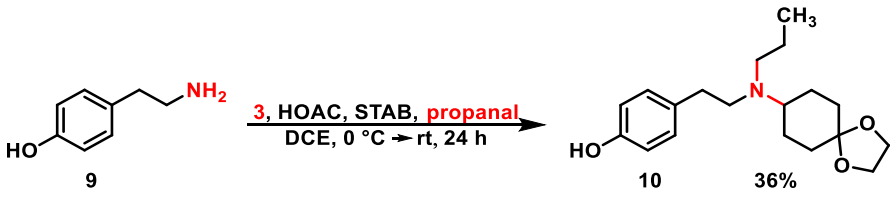

Figure 48: Reaction of the one-pot double reductive amination of tyramine **9** with cyclohexanedione monoethylene ketal **3** and propanal, yielding compound **10**.

In the following step, the H_3R pharmacophore was formed by introducing the H_3R warhead through alkylation of the phenol **10** with 1-(3-chloropropyl)piperidine hydrochloride **SM1** (see Figure 49). The alkylation was performed under Finkelstein conditions, following the

mechanism shown in Figure 36, for 24 hours under reflux, yielding compound **5b** in 52%.[598] Again the yield reduction can be attributed to quaternary ammonium salt formation through overalkylation at the tertiary amine site.[603]

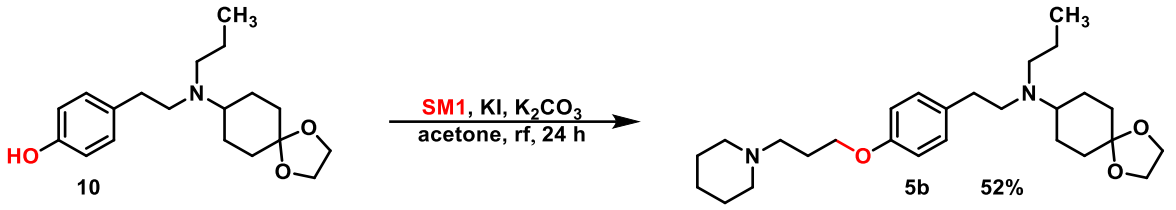

Figure 49: Reaction of the alkylation of compound **10** with **SM1** under Finkelstein conditions, yielding compound **5b**.

Lastly, compound **5b** was subjected to the three-step one-pot synthesis[608] to form the **pramipexole** pharmacophore, following the mechanism and protocol described in Figure 39. The synthesis delivered MTDL **P1b** in 4% yield (see Figure 50), reflecting the challenging nature of the consecutive transformations under one-pot conditions as discussed above. Ultimately, this revised synthetic strategy successfully provided access to the target compound MTDL **P1b** after the previous two synthetic routes had proven unsuccessful.

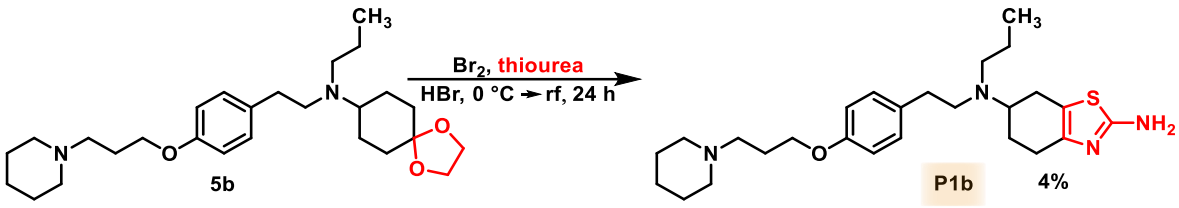

Figure 50: Reaction of the three-step one-pot synthesis of MTDL **P1b**.

3.3 Binding profile assessment

Following their successful synthesis, the three MTDLs **P1a-c** were examined for their pharmacological profiles to evaluate whether the aliphatic linkage approach connecting the two pharmacophores was successful and whether it is reasonable to continue pursuing this attachment strategy. Therefore, the MTDLs **P1a-c** were subjected to binding affinity studies against their target receptors H_3R, D_2R, and D_3R, which were performed in collaboration with colleagues and are described in detail in the experimental section. As shown in Table 3, all compounds exhibited excellent H_3R binding affinity, in a single-digit nanomolar range, with some representatives even in subnanomolar range with K_i values of 0.78-5.14 nM, approaching the affinity of reference compound **JNJ-5207852** (K_i = 0.3 nM),[595] demonstrating the robustness of the H_3R pharmacophore across structural modifications.[595,628] Additionally, they showed selectivity for H_3R over the other investigated histamine receptor subtypes H_1R and H_4R, being crucial for avoiding potential side effects that could arise from interactions with other

histamine receptor subtypes.[215,629] Structure-activity relationship analysis revealed several significant insights for the binding to the dopamine receptors. The extension of the aliphatic linker influenced D_3R affinity, with compounds **P1b** and **P1c** demonstrating notable receptor activity (K_i = 16.7 nM and 54.4 nM respectively), matching the affinity of parent ligand **pramipexole**, while **P1a** showed moderate affinity (K_i = 695 nM). All three compounds displayed moderate affinity towards D_2R (K_i = 361-511 nM) similar to the reference ligand. The data demonstrates that a linker length of at least two methylene groups is necessary for enhanced D_3R binding,[630] as evidenced by the significantly lower affinity of **P1a** compared to both **P1b** and **P1c**. While **P1b** showed numerically higher D_3R affinity, the overlapping confidence intervals with **P1c** prevent a definitive conclusion about their relative potencies. However, **P1b's** superior D_2R/D_3R selectivity ratio of 21.6, even superior to the parent ligand **pramipexole**, establishes it as the lead compound for further development. The potentially superior binding profile of **P1b** might result from an optimal spatial orientation of its ethylene linker, which adopts a different conformation compared to the methylene and propylene linkers, allowing optimal positioning of both pharmacophores in their respective binding pockets and maximizing key receptor interactions.[631] Molecular docking studies and the synthesis of a butylene-linked derivative, which should adopt a similar spatial orientation as **P1b**, could help validate this hypothesis,

Notably, these results represent an improvement over previous pharmacophore connection strategies explored in our group, where the connection via the aromatic amine led to an almost complete loss of dopamine receptor activity. The current approach of maintaining the intact aminothiazole moiety of the **pramipexole** pharmacophore successfully preserved D_3R affinity while simultaneously incorporating the H_3R pharmacophore, thereby retaining affinity for both receptors.

Table 3: Dopamine D_2 and D_3 receptor and histamine H_1, H_3 and H_4 receptor affinity of MTDLs **P1a-c** and **pramipexole** as a reference.

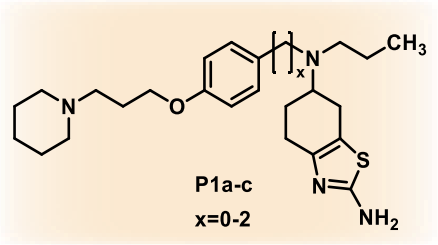

Compound	x	hH_1R K_i (nM) [95% CI]	hH_3R K_i (nM) [95% CI]	hH_4R K_i (nM) [95% CI]	hD_2R K_i (nM) [95% CI]	hD_3R K_i (nM) [95% CI]	Selectivity (D_2/D_3)
P1a	1	>5000	**0.78** [0.16; 3.74]	>5000	**475** [256; 881]	**695** [376; 1286]	-
P1b	2	>5000	**2.37** [0.47; 12.0]	>5000	**361** [151; 862]	**16.7** [3.6; 78]	22
P1c	3	>5000	**5.14** [3.51; 7.51]	>5000	**511** [223; 1172]	**54.4** [21.8; 136]	9
Pramipexole		n.d.	**> 10000**	n.d.	**256** n=2	**21.6** [9.97; 47.0]	12

n.d.= not determined

3.4 Lead compound optimization

Given that only the *S*-enantiomer of the reference compound pramipexole represents the active form, it was logical to next prepare the enantiomerically pure derivative of the lead compound **P1b** to investigate whether activity could be further improved, especially since its racemic mixture already showed comparable potency to **pramipexole**. Furthermore, improvements in pharmacokinetic properties were proposed by deaminating the aminothiazole moiety, which also examines its necessity in maintaining dopamine affinity. Moreover, the flexible ethylene amine linker was replaced with a more rigid amide bridge. This latter modification explores how introducing a conformationally restricted amide group between the pharmacophores alters their spatial arrangement and thereby influences receptor binding. These modifications will help expanding our understanding of the structure-activity relationships and guide further optimization of the multi-targeting compounds.

3.4.1 Synthesis

To synthesize these variations of the lead compound **P1b**, scale-up production was required. Given the low yields in the final three-step one-pot aminothiazole ring formation, a new synthetic strategy was designed that circumvents the challenging ring construction by directly connecting the complete **pramipexole** pharmacophore with the H_3R pharmacophore. The new scheme is shown in Figure 51. The synthetic route was designed to begin with methyl 2-(4-hydroxyphenyl)acetate **11**, which should be alkylated with the H_3R warhead 1-(3-chloropropyl)piperidine hydrochloride **SM1** to incorporate the H_3R pharmacophore. From this intermediate **12**, the synthesis scheme was planned to branch into two paths to obtain the amide derivative **P3$_S$** and the deaminated derivative **P2$_S$**. For the latter derivative **P2$_S$**, the key step would involve reductive amination between **pramipexole** and the H_3R building block. This would require the aldehyde intermediate **13**, which was not accessible through alcohol oxidation as shown in Figure 40. In this approach, the aldehyde is supposed to be generated through controlled DIBAL reduction of the ester, which selectively stops at the aldehyde stage under optimized conditions.[632] Subsequent reductive amination with **pramipexole** (**15**) should yield the *S*-enantiomer **P1b$_S$** of lead compound **P1b**, which should undergo final deamination via a diazotization step to deliver compound **P2$_S$**. For the amide derivative **P3$_S$**, the pharmacophore linkage was designed to be achieved through a coupling reaction. This would require basic hydrolysis of the ester **12** to the corresponding carboxylate **14**, followed by HATU-mediated coupling with **pramipexole 15** to yield the final MTDL **P3$_S$**.

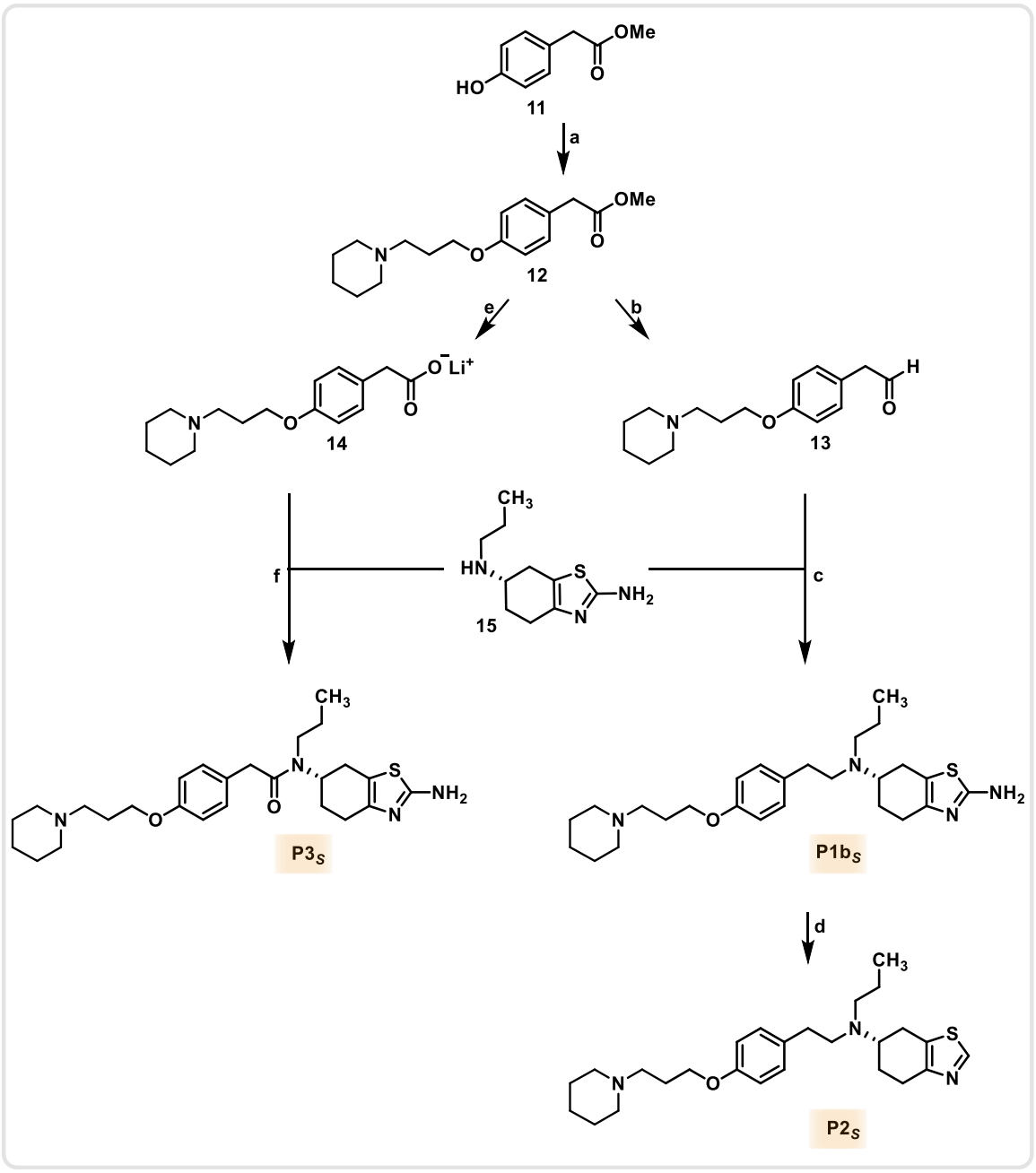

Figure 51: Planned synthetic route to yield the deaminated derivative **P2*s*** and amide derivative **P3s** of lead compound **P1b**, as well as its enantiomerically pure *S*-enantiomer **P1bs**. Reaction conditions: a) **SM1**, KI, K_2CO_3, acetone, reflux, 48 h. b) DIBAL, toluene, -78 °C, 5 h. c) acetic acid, STAB, DCE, room temperature, 20 h. d) $NaNO_2$, H_3PO_2, HCl, -30 °C, 24 h. e) LiOH, THF/water (1:1), room temperature, 20 h. f) HATU, DIPEA, DMF, room temperature, 24 h.

In the first step, the H_3R pharmacophore was formed through a Williamson ether synthesis under Finkelstein conditions, combining methyl 2-(4-hydroxyphenyl)acetate **11** with the H_3R warhead 1-(3-chloropropyl)piperidine hydrochloride **SM1** (see Figure 52). The reaction was performed under reflux conditions for 48 hours, yielding the desired product **12** in 59%,[598] following the mechanism described in Figure 36.

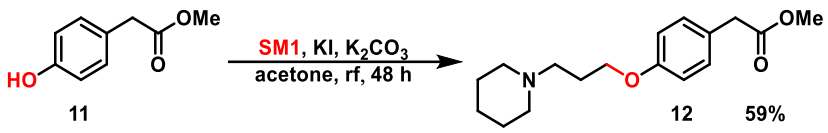

Figure 52: Reaction of the Williamson ether synthesis of methyl 2-(4-hydroxyphenyl)acetate (**11**) with 1-(3-chloropropyl)piperidine hydrochloride (**SM1**) under Finkelstein conditions to yield product **12**.

In the next step of the synthesis route towards the deaminated MTDL **P2$_S$**, ester **12** was converted to an aldehyde to enable a reductive amination for the pharmacophore linkage. The ester was reduced under mild conditions at -78 °C in toluene for five hours using DIBAL,[633] which after quenching and aqueous workup yielded the aldehyde with high chemo selectivity and quantitative conversion (see Figure 53). The low temperature is crucial as it allows the reaction to be stopped at the aldehyde stage, since at this temperature a second hydride addition is kinetically unfavourable.[603,634] The reaction mechanism[603] begins with DIBAL acting as a Lewis acid, coordinating the carbonyl oxygen to increase the electrophilicity of the carbonyl carbon.[635] This molecular approach enables hydride transfer to the carbonyl carbon, leading to the cleavage of the carbonyl double bond (**TS1**). The resulting hemiacetal then eliminates methanol while reforming a carbonyl double bond (**TS2**). At this stage, the aluminium species remains coordinated to the oxygen, preventing further reduction. During the aqueous workup, the remaining aluminium species is removed. Water attacks nucleophilically at the carbonyl carbon (**TS3**), and through proton transfer, a geminal diol is formed (**TS4**). Finally, this intermediate reforms the carbonyl bond with the elimination of an aluminium hydroxide species, yielding the aldehyde **13**.

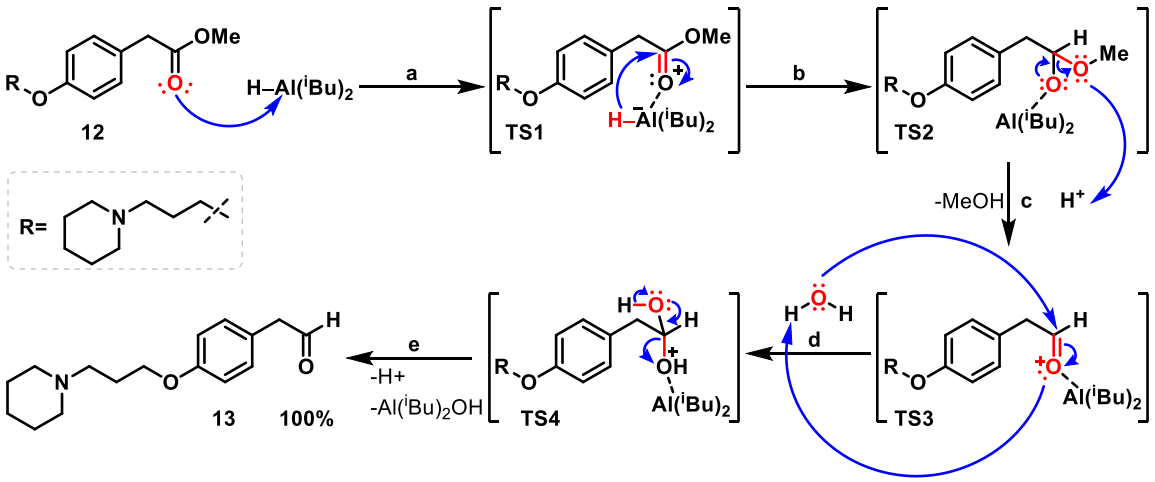

Figure 53: Reaction mechanism of the DIBAL-mediated reduction of ester **12**, yielding aldehyde **13**. a) Lewis-acid coordination b) Hydride transfer c) Methanol elimination d) Aqueous work up e) Elimination of aluminium species.

Due to the susceptibility of aldehydes to degradation,[617–619] the prepared aldehyde **13** was immediately subjected to reductive amination with **pramipexole 15**, following the mechanism

described in Figure 37 to establish the pharmacophore connection. The reaction was carried out with acetic acid as a proton source and STAB as reducing agent in DCE. The reaction mixture was kept at 0 °C during STAB addition and then warmed to room temperature for 20 hours,[602] delivering the enantiomerically pure (*S*)-enantiomer **P1b$_S$** of the lead compound **P1b** in 45% yield (see Figure 54). This yield represents a significant improvement over the previously reported three-step one-pot synthesis (4-17%). The new synthetic route (see Figure 51) proves superior by reducing the number of steps from four to three required to achieve the final product, while gaining the advantage of obtaining enantiomerically pure compounds.

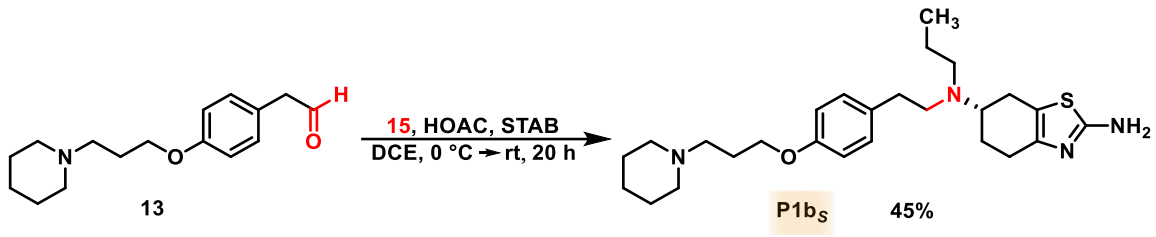

Figure 54: Reaction for the reductive amination of aldehyde **13** with **pramipexole 15**, yielding the enantiomerically pure (*S*)-enantiomer **P1b$_S$** of the lead compound **P1b**.

In the final step, MTDL **P1b$_S$** was deaminated to investigate how modifications of the **pramipexole** pharmacophore affect dopamine receptor affinity. The deamination proceeds through formation of a diazonium intermediate via diazotization, which is then reduced to the thiazole. The reaction sequence was carried out in hydrochloric acid as solvent at -30 °C, using sodium nitrite for the diazotization and phosphinic acid as the reducing agent, yielding the product in 54%.[636] The mechanism[637–639] (see Figure 55) begins with the formation of the nitrosyl cation (**TS3**) from sodium nitrite **16** through double protonation (**TS1**), internal electron redistribution and water elimination (**TS2**). The electrophilic species is then attacked nucleophilically by the primary aromatic amine of **P1b$_S$**, forming a *N*-nitrosamine species (**TS4**). Through intramolecular proton transfer and internal electron redistribution, a diazohydroxide intermediate (**TS5**) is formed, which undergoes protonation (**TS6**) and water elimination to generate the diazonium cation (**IM1**). Finally, in a radical process,[640] the diazonium intermediate **IM1** eliminates molecular nitrogen to form an aryl radical (**TS7**). This radical then accepts an electron and hydrogen from phosphinic acid, which is oxidized to phosphoric acid in the process, leading to the formation of the deaminated MTDL **P2$_S$**.

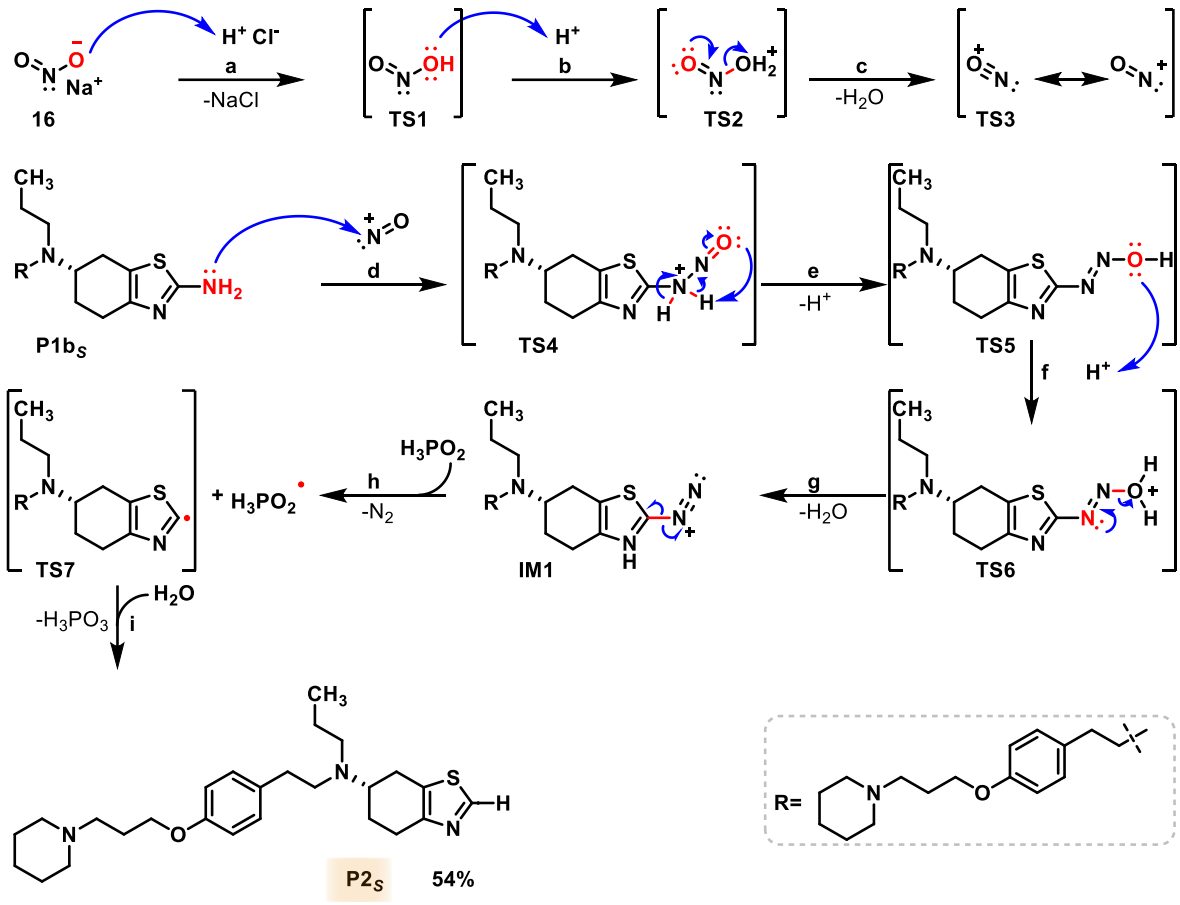

Figure 55: Reaction mechanism for the deamination of MTDL **P1b$_S$** through diazotization followed by reduction of the diazonium intermediate (**IM1**) to yield the deaminated MTDL **P2$_S$**. a) Protonation b) Protonation c) Water elimination d) Nucleophilic attack e) Intramolecular proton transfer and internal electron redistribution f) Protonation g) Water elimination h) Nitrogen elimination i) Reduction.

For the synthesis of the amide derivative MTDL **P3$_S$**, the next step in the synthetic route following the formation of compound **12** involved ester cleavage under basic conditions (see Figure 56). Using lithium hydroxide as a base in a THF/water (1:1) mixture at room temperature for 20 hours yielded the lithium carboxylate salt **14** quantitatively.[641] The reaction mechanism[642] is initiated with the nucleophilic attack of an hydroxide ion at the carbonyl carbon, leading to cleavage of the carbonyl double bond, with the resulting negatively charged carbonyl oxygen coordinating to the lithium counterion (**TS1**). Through reformation of the carbonyl bond, lithium methoxide is eliminated (**TS2**), which, due to its higher basicity,[643] deprotonates the newly formed carboxylic acid group, yielding methanol and the desired lithium carboxylate salt **14**.

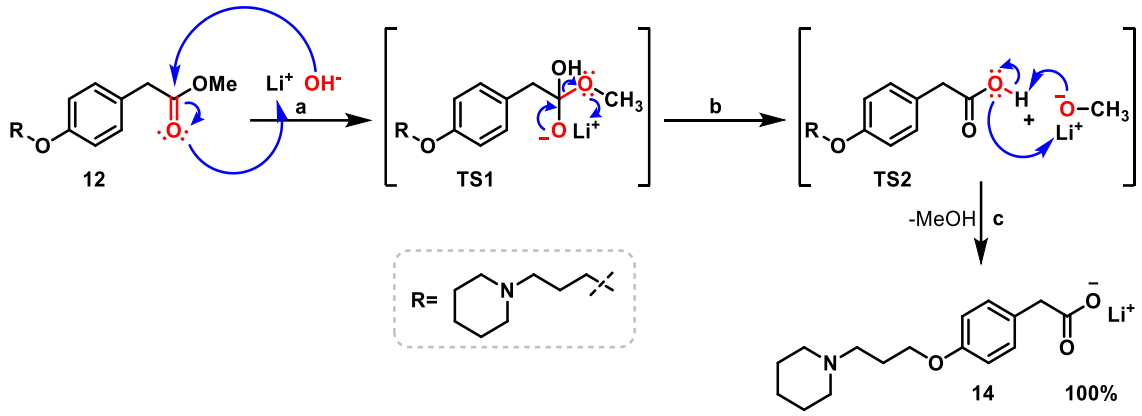

Figure 56: Mechanism of base-catalysed ester cleavage, exemplarily shown for the synthesis of compound **14**. a) Nucleophilic attack b) Methanolate elimination c) Deprotonation.

In the final step, the carboxylate salt **14** was coupled with **pramipexole 15** to establish the pharmacophore linkage through a rigid amide linker (see Figure 57). The coupling was performed using HATU as a coupling reagent in DMF at room temperature for 24 hours, affording the final MTDL **P3$_S$** in a 32% yield.[644] The moderate yield could likely be attributed to the hydrolysis of the during the coupling formed intermediates due to moisture,[645] particularly given the hygroscopic properties of the carboxylate salt starting material, as well as to product losses during the purification process. Mechanistically,[603,645] the reaction begins with the nucleophilic attack of the carboxylate anion of **14** on the guanidinium cation of HATU **16**, which after internal electron redistribution releases the 1-hydroxy-7-azabenzotriazole (HOAt) anion and forms a mesomerically stabilized *O*-acyl uronium species (**TS1**). The liberated HOAt anion then attacks nucleophilically at the carbonyl carbon, eliminating *N*,*N*-tetramethyl urea in a transesterification. The resulting HOAt ester intermediate **IM1** is now primed[646] for the nucleophilic attack by the amine, in this case **pramipexole 15**. This nucleophilic addition leads to the cleavage of the carbonyl double bond (**TS2**) and, under reformation of the carbonyl bond leading to elimination of HOAt, yields the desired amide-linked MTDL **P3$_S$**.

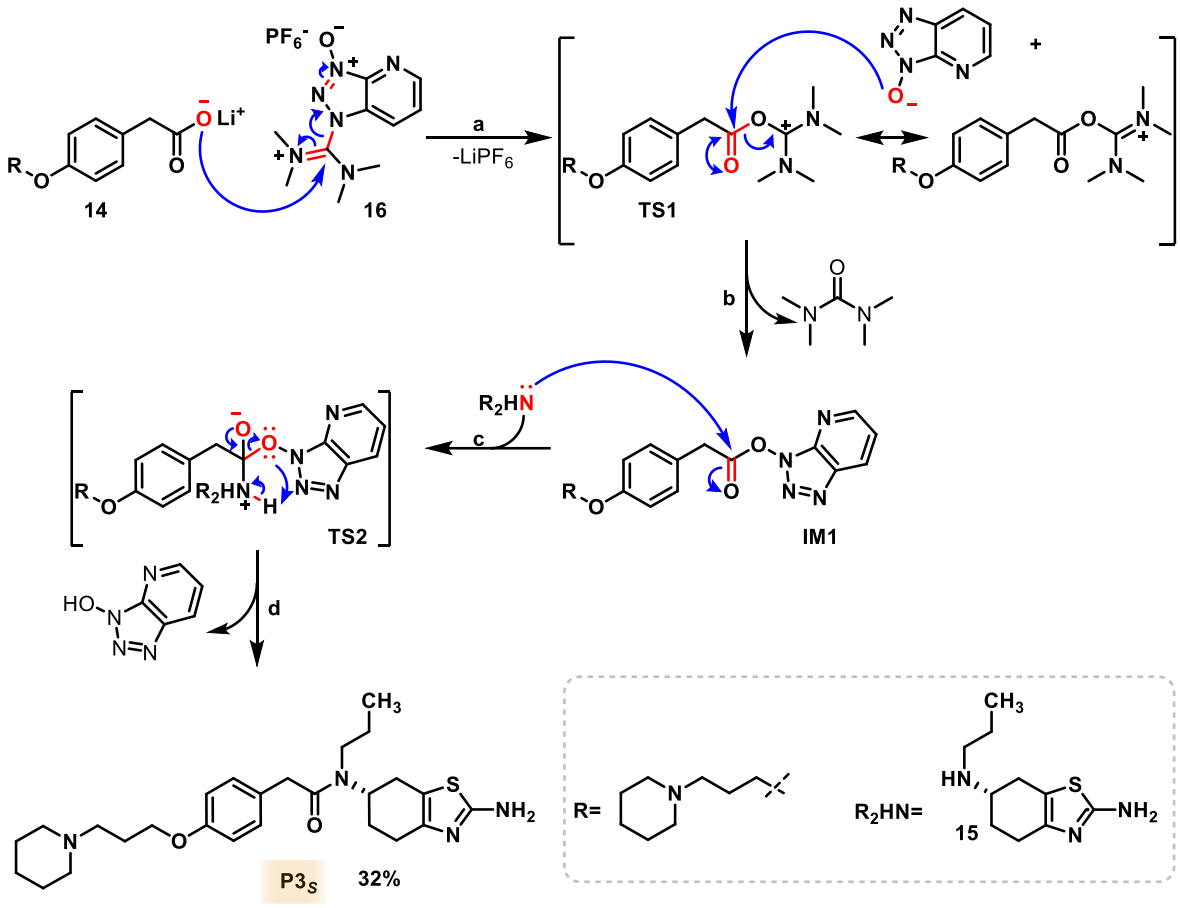

Figure 57: Mechanism of HATU-mediated amide coupling between the carboxylate **14** and **pramipexole 15** as the amine, exemplarily shown for the synthesis of MTDL **P3s**. a) Formation of *O*-acyl uronium species b) Transesterification c) Nucleophilic attack d) HOAt elimination.

3.4.2 Binding profile assessment

To investigate structure-activity relationships regarding the necessity of a primary aromatic amine of the aminothiazole for D_2R affinity, the impact of a rigid amide linker between the pharmacophores, and the influence of absolute configuration, the synthesized MTDLs **P1b$_S$**, **P2$_S$** and **P3$_S$** were subjected to binding affinity studies against their target receptors H_3R, D_2R, and D_3R, as well as histamine receptor subtypes H_1R and H_4R to prove selectivity for H_3R. As shown in Table 4, all three compounds display excellent low nanomolar affinities at the H_3R receptor, which was expected since the introduced structural modifications did not affect the H_3R pharmacophore but rather the **pramipexole** portion and the linker region. The H_3R affinities remain in the range of the reference compound **JNJ-5207852** (K_i = 0.3 nM),[595] and even though all compounds show slightly higher H_1R affinity compared to **P1a-c**, these values remain negligible relative to their potent H_3R binding, preserving the desired selectivity profile. Compound **P1b$_S$**, featuring the defined absolute configuration in the **pramipexol** pharmacophore, maintains the affinity pattern of its racemic predecessor **P1b**, with potent H_3R and D_3R affinities while showing only moderate D_2R binding, perfectly matching **pramipexol's**

binding profile (see Table 3). Notably, the D_3R/D_2R selectivity ratio is slightly enhanced compared to the racemic derivative, reflecting the characteristic eutomer discrimination known for pramipexol.[596] The deaminated compound **P2$_S$** surprisingly shows no decrease in affinity towards the dopamine D_3 receptor (K_i = 16.8 nM) compared to lead compound **P1b** (K_i = 16.7 nM). The obtained result was unexpected based on the previous project where the linking of pharmacophore with aromatic amine (see Figure 34) resulted in complete loss of D_3 receptor affinity. This led to the hypothesis that the primary amine of the aminothiazole group might be crucial for affinity. However, these results demonstrate that this is not necessarily the case. In contrast to the lead compound **P1b**, which showed D_2/D_3 selectivity with a ratio of 21.6, **P2$_S$** shows reduced selectivity between the two dopamine receptors, with a D_2/D_3 selectivity ratio of 9.5, as it also binds well to D_2R with an affinity of K_i = 160 nM. While this reduced selectivity identifies **P1b** as the more promising compound for D_3R-selective targeting, the successful deamination in **P2$_S$** opens up interesting optimization possibilities. The tolerated deamination suggests that further modifications at this position, such as halogenation with chlorine or bromine via diazotization,[647,648] could be valuable to explore. Such modifications could potentially enhance both the compound's pharmacokinetic properties and blood-brain barrier permeability[649] while maintaining the desired receptor affinity. This approach could lead to compounds combining the favourable D_3-selectivity of **P1b** with improved drug-like properties. The amide derivative **P3$_S$**, which was designed to rigidify the linker between the pharmacophores, shows, as expected, almost no affinity to either D_2R (K_i = 4462 nM) or D_3R (K_i = 1472 nM). This can be attributed to several factors: the reduced basicity and lipophilicity of the amide group,[650] conformational constraints limiting spatial orientation and flexibility,[651] altered hydrogen bonding patterns,[652] and potential changes in the overall electronic distribution of the molecule.[653] The amide's planar geometry might also create unfavourable interactions within the binding pocket.[654]

Table 4: Dopamine D_2 and D_3 receptor and histamine H_1, H_3 and H_4 receptor affinities of MTDLs **P1b$_S$**, **P2$_S$** and **P3$_S$.**

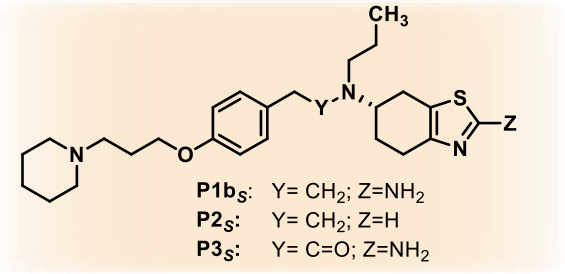

Compound	hH_1R K_i (nM) [95% CI]	hH_3R K_i (nM) [95% CI]	hH_4R K_i (nM) [95% CI]	hD_2R K_i (nM) [95% CI]	hD_3R K_i (nM) [95% CI]	Selectivity (D_2/D_3)
P1b$_S$	**2615** [1424; 4804]	**4.10** [0.84; 20.0]	**>10000**	**285** [199; 408]	**8.73** [3.88; 19.7]	33
P2$_S$	**1331** [574; 3087]	**3.97** [1.34; 11.7]	**>10000**	**160** [121; 212]	**16.8** [9.55; 29.4]	10
P3$_S$	**3515** [1606; 7693]	**11.0** [3.87; 31.1]	**>10000**	**4462** [1788; 11134]	**1472** [704; 3079]	3.

3.4.3 Binding mode assessment

To confirm the suitability of these promising ligands for potential PD treatment, their respective binding modes on the target receptors needed to be determined, which was conducted in cooperation with Bioprojet Biotech. The results (see Table 5 and Figure 58) of these functional assays, which are described in detail in the experimental section, confirm that all tested compounds act as strong H_3R antagonists/inverse agonists, as suggested by the underlying **JNJ-5207852** pharmacophore.[595] Additionally, four out of five compounds act as the envisioned full agonists (IA > 1) for the hD_3R and hD_2R with EC_{50} values in the low nanomolar range, matching the properties of their lead pharmacophore **pramipexole**[596] and therefore aligning with the initial expectations. An exception is the short-linker compound **P1a**, which presents only a partial agonist binding mode (IA < 1) for hD_3R. and hD_2R. Nevertheless, these determined binding modes are crucial for the potential therapeutic application of those MTDLs in PD treatment,[655,656] as this multi-targeting approach successfully combined the symptomatic benefits of dopamine receptor agonism with the cognitive improvements associated with H_3R antagonism/inverse agonism in a single molecule. It should be noted that the GTPγ[^{35}S] functional assay used in this study, whose detailed procedure can be found in the experimental section, does not directly distinguish between H_3R antagonism and inverse agonism, but rather

measures the compounds' ability to reverse the activity of a reference agonist. Additionally, all compounds present only weak affinity to hERG channels, demonstrating low cardiotoxicity and therefore further strengthening their potential clinical use.

Table 5: Functional GTPγ[^{35}S] assay data for the dopamine D_2 and D_3 receptor and the histamine H_3 receptor of MTDLs **P1a**, **P1b**, **P1b$_S$**, and **P2$_S$**, as well as their affinity towards hERG channel.

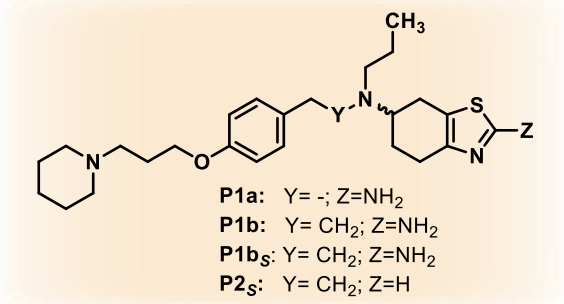

Compound	hD_2R EC_{50}(nM)*	hD_2R IA*	hD_3R EC_{50}(nM)*	hD_3R IA*	hH_3R K_i(nM)*	hERG K_i(μM)*
P1a	33.9	0.24	22.6	1.15	0.13	3.88
P1b	17.9	1.15	1.81	1.07	0.24	5.12
P1b$_S$	15.0	1.23	0.66	1.07	0.26	5.77
P2$_S$	13.9	1.21	0.86	1.00	0.24	3.80
Pramipexole	185	1.01	2.38	0.90	n.d.	6.58

*All compounds were assessed in technical duplicates, in six points dose-responses. The mean of two independent biological experiments is displayed. IA= intrinsic activity; n.d.= not determined.

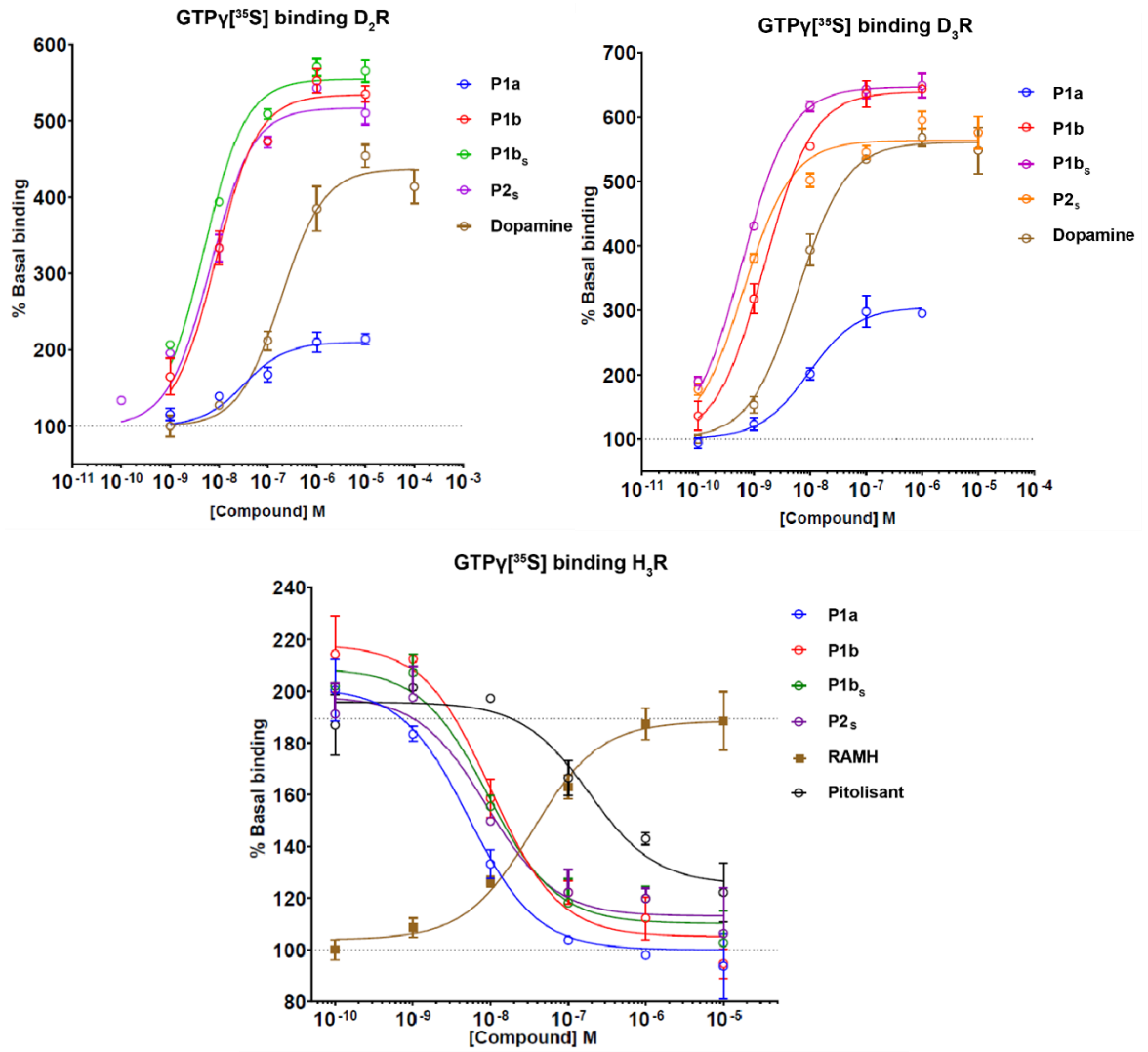

Figure 58: Binding curves of the functional GTPγ[^{35}S] assay determining the binding modes of compounds **P1a**, **P1b**, **P1b$_S$** and **P2$_S$** at D_2R (left), D_3R (right) and H_3R (down).

3.4.4 Cytotoxicity

Additionally to the binding studies, the most promising MTDLs **P1b$_S$**, **P1b**, and **P2$_S$** were tested for cytotoxicity according to the procedure described in the experimental part. The results demonstrate that all three compounds (**P1b$_S$**, **P1b**, and **P2$_S$**) maintained 100% cell viability at 100 µM in the SH-SY5Y cell line, representing a promising initial cytotoxicity assessment (see Figure 59). This promising finding, showing complete cell survival at a relatively high concentration, meets essential requirements for their development as MTDLs in Parkinson's disease treatment.

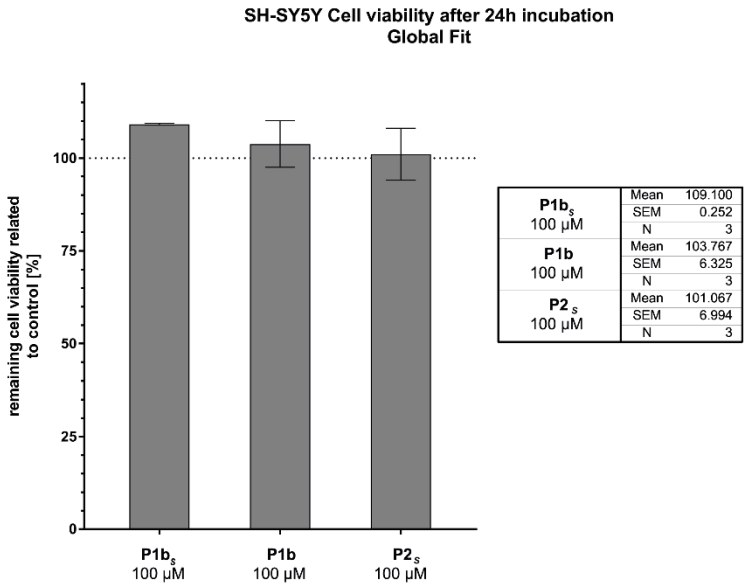

Figure 59: Cell viability of SH-SY5Y cell line after 24 h incubation with the three main compounds **P1b$_S$**, **P1b** and **P2$_S$** at a concentration of 100 µM.

3.4.5 Therapeutic relevance

The novel MTDLs developed in this work, especially **P1b$_S$** and **P2$_S$**, exhibit promising therapeutic potential for Parkinson's disease by combining dopamine D_2/D_3 receptor agonism with histamine H_3 receptor antagonism in a single molecule. This multi-targeting strategy enables these compounds to address both motor symptoms, via dopamine receptor activation, and cognitive impairments, through H_3 receptor antagonism, two significant clinical challenges in PD management. In comparison to established Parkinson's medications such as levodopa, MAO-B inhibitors, or COMT inhibitors, these MTDLs offer a potentially more integrated approach by simultaneously targeting multiple pathways involved in disease symptoms. While levodopa remains the most effective agent for motor symptom relief, its long-term use is associated with motor fluctuations and dyskinesias.[657] Dopamine agonists like **pramipexole** are often used as adjunct therapy or in early-stage PD to delay levodopa initiation but lack effects on cognitive symptoms.[657] The D_2R/D_3R agonist and H_3R antagonist profile of these MTDLs may provide symptomatic relief while also addressing non-motor aspects of the disease such as cognitive decline. Compared to the parent compound **pramipexole**, the lead compounds **P1b$_S$** and **P2$_S$** demonstrate comparable or even superior affinities for dopamine receptors, with an improved D_3R/D_2R selectivity ratio. Importantly, the inclusion of potent H_3R antagonism is expected to contribute cognitive benefits not provided by current dopamine agonists. Moreover, the deamination of the aminothiazole moiety (**P2$_S$**) resulted in a compound that retained pharmacological activity while exhibiting improved pharmacokinetic properties, such as enhanced lipophilicity, which may contribute to better bioavailability, blood-brain barrier penetration, and metabolic stability. These factors could

lead to improved drug exposure, longer duration of action, and potentially reduced side effects, highly desirable features for chronic Parkinson's disease treatment. Additionally, initial safety data demonstrating low cardiotoxicity risk and excellent cell viability further support the potential clinical suitability of these compounds. Overall, this multi-targeting approach represents a promising advancement in PD therapy, potentially offering enhanced symptomatic relief by simultaneously modulating motor and cognitive pathways with a single agent, while also potentially improving patient compliance and quality of life compared to polypharmacy approaches. Furthermore, since pramipexole is an approved treatment for RLS, a condition often comorbid with PD,[658] the developed MTDLs **P1b$_S$** and **P2$_S$**, given the structural and pharmacological similarities, might also hold therapeutic potential for RLS.

3.5 Summary

The successful design, synthesis, and biological evaluation of novel MTDLs combining D_2/D_3 receptor agonism with H_3 receptor antagonism in one single molecule for potential Parkinson's disease treatment is described in this chapter. Through systematic exploration of different synthetic routes, we successfully developed an efficient approach to merge the pharmacophores of H_3R antagonist **JNJ-5207852** and D_2/D_3 agonist **pramipexole**. The key findings demonstrate several significant achievements in synthetic methodology, where multiple synthetic routes were investigated. Initial approaches revealed valuable insights through specific challenges as the oxidative synthesis of the required aldehyde intermediate needed for the pharmacophore connection proved unsuccessful while the alternative alkylation strategy for connecting the pharmacophores was complicated by competing elimination reactions. Additionally, the one-pot synthesis constructing the **pramipexole** ring system delivered insufficient yields. This systematic exploration ultimately led to the identification of a successful synthetic pathway where the aldehyde synthesis was achieved through controlled ester reduction, and the pharmacophores were connected in a reductive amination step through the aliphatic amine of **pramipexole** by directly utilizing the complete **pramipexole** pharmacophore, thereby avoiding the challenging ring formation step. Following binding studies revealed that all compounds demonstrated excellent H_3R affinity. Analysis of dopamine receptor binding showed that a minimum linker length of two methylene groups was required for D_3R affinity, as only the compounds with longer linkers (**P1b** and **P1c**) displayed good D_3R affinity while all three compounds exhibited moderate D_2R binding, matching the binding profile of parent ligand **pramipexole**. Among these, the ethylene-linked compound **P1b** emerged as the lead compound, demonstrating a similar pharmacological profile to the parent compound **pramipexole** but exhibiting superior D_2R/D_3R selectivity (ratio 21.6).Importantly, all compounds maintained selectivity for H_3R over other histamine

receptor subtypes. Further structural modifications explored the importance of key molecular features, revealing that deamination of the pramipexol pharmacophore preserved dopamine receptor affinity (**P2*S***), while improving the compounds pharmacokinetic properties. However, the introduction of a rigid amide linker (**P3*S***) led to loss of dopamine receptor binding. Additional investigation of absolute stereochemistry of the **pramipexole** pharmacophore demonstrated that the defined configuration not only maintained the favourable binding profile (**P1b*S***) but also showed enhanced receptor subtype selectivity, reflecting the characteristic eutomer discrimination known for **pramipexole**.[596] Initial safety assessment demonstrated promising results with all tested compounds showing 100% cell viability at 100 µM and only low hERG channel affinity. Furthermore, the functional evaluation of these novel MTDLs at their respective receptors confirmed their therapeutic potential, demonstrating strong H_3R antagonism/inverse agonism and the necessary D_3R and D_2R full agonism for most of the tested compounds. These findings establish a valuable foundation for further development of multi-targeting therapeutic agents for Parkinson's disease, with compounds **P1b*S*** and **P2*S*** representing particularly promising candidates for clinical development.

4. Development of H_3R-based MTDLs for narcolepsy

This chapter describes the design, synthesis and biological evaluation of novel **solriamfetol**-like multi-targeting compounds combining H_3 receptor antagonism with dopamine-norepinephrine reuptake inhibition (NDRI) as potential therapeutic agents for the treatment of narcolepsy.

4.1 Rational design

Despite recent therapeutic advances in narcolepsy treatment,[659–661] substantial therapeutic gaps persist, particularly regarding comprehensive symptom management and treatment-resistant cases.[662] Notably, current monotherapies' limitations often necessitate complex combination treatments that can negatively impact patient compliance and quality of life.[663,664] To address these limitations, this project pursued the development of novel MTDLs through a rational design approach combining the pharmacophores of two clinically validated narcolepsy medications, **pitolisant**[258] and **solriamfetol**.[665] This molecular merger strategy aims to create single-molecule therapeutics that simultaneously engage multiple wake-promoting pathways, complementing our group's parallel project exploring combining H_3R antagonism with modafinil.[666] The selection of these specific pharmacophores is strategically founded on their distinct mechanisms of action.[667,668] **Pitolisant** enhances wakefulness through H_3 receptor antagonism/inverse agonism, leading to both direct activation of histaminergic neurons and indirect stimulation of other wake-promoting neurotransmitters via heteroreceptor modulation.[667] **Solriamfetol**, conversely, acts as a selective dopamine and norepinephrine reuptake inhibitor, increasing the levels of these monoamines in the synaptic cleft, thereby enhancing their wake-promoting effects.[668] Consequently, the combination of these individual mechanisms may offer potential synergistic effects on alertness and wakefulness.

Building upon this rationale, a molecular design strategy was developed, that involved attaching the H_3R antagonist warhead of **pitolisant**[669] to the phenyl ring of **solriamfetol** (see Figure 60), forming the **JNJ-5207852** derived H_3R pharmacophore (see Figure 14), while preserving **solriamfetol's** core framework.[665] This design approach capitalizes on the well-documented robustness of the H_3R pharmacophore[595,628] while enabling systematic exploration of structure-activity relationships through strategic modifications of the **solriamfetol** component.

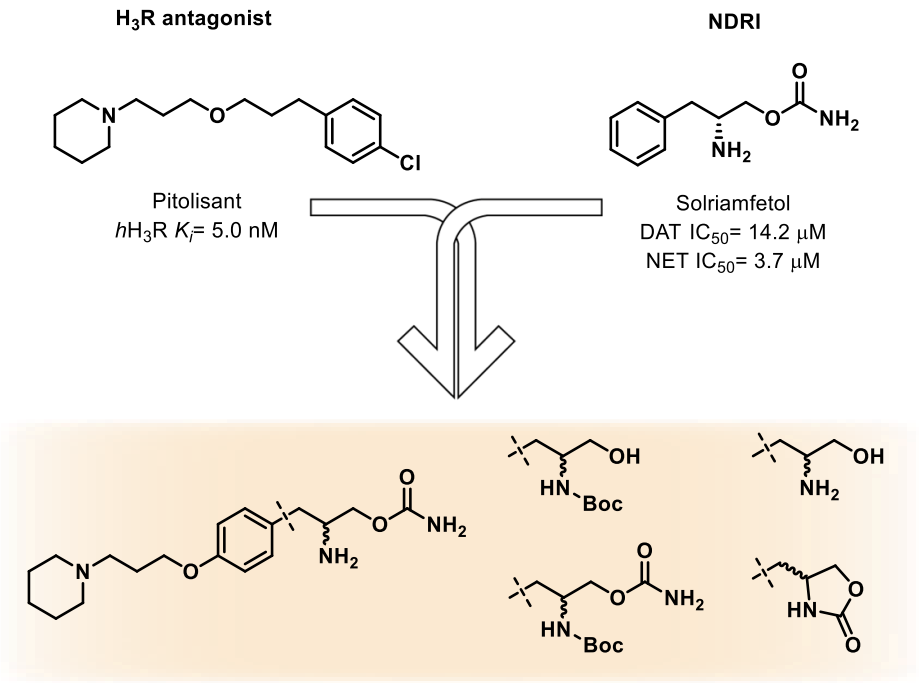

Figure 60: Molecular design strategy merging the pharmacophores of **pitolisant** (H_3R antagonist) and **solriamfetol** (NDRI) to generate novel MTDLs for potential narcolepsy treatment, including systematic SAR exploration.

4.2 Synthesis

4.2.1 *R*-enantiomeric series

To implement this design strategy, a synthetic route toward the target compounds as displayed in Figure 61 was developed. The scheme was designed to start with enantiomerically pure Boc-D-tyrosine-methylester **17**, chosen to match the *R*-configuration of the pharmacologically active **solriamfetol** enantiomer.[670] The initial step would involve its alkylation with 1-(3-chloropropyl)piperidine hydrochloride, introducing the H_3R antagonist warhead to form compound **18**. Subsequent reduction of the ester would generate the corresponding alcohol **P4**, our first product for SAR exploration. **P4** would then undergo transformation to a primary carbamate structure through CDI coupling followed by *in situ* aminolysis to give compound **P5**, the second product for our SAR studies. The final step would involve Boc deprotection to obtain

the lead compound **P6**, which combines the H_3R pharmacophore with the full unaltered **solriamfetol** pharmacophore.

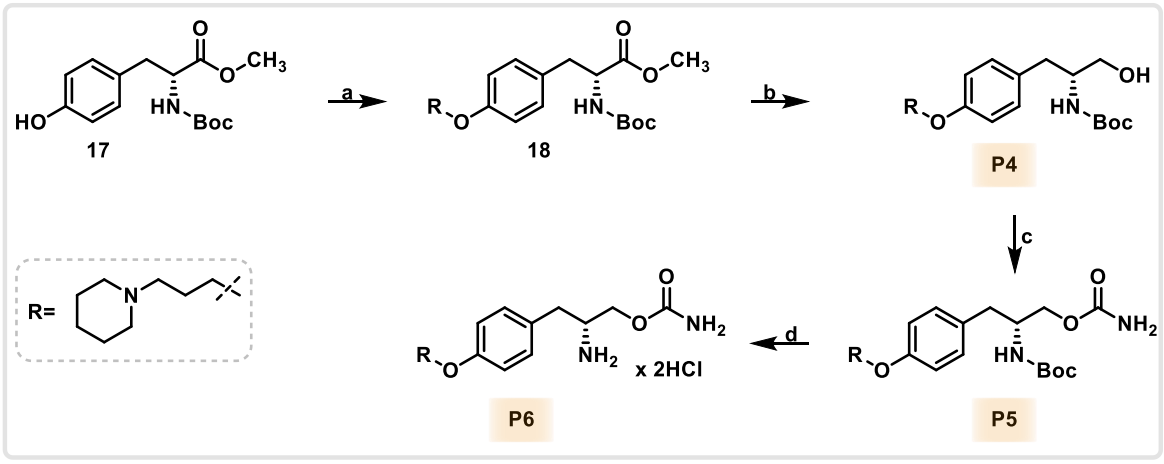

Figure 61: Planned synthetic route for the preparation of MTDLs combining the pharmacophores of **pitolisant** and **solriamfetol**, with **P4**, **P5** and lead compound **P6** (all highlighted in orange) for SAR exploration. Reaction conditions: a) **SM1**, KI, K_2CO_3, acetone, reflux, 24 h. b) LAH, THF, -78 °C, 2 h. c) CDI, ammonium chloride, toluene, room temperature, 3 d. d) HCl, methanol, room temperature, 3 d.

Implementing this strategy, the first step of the synthetic route started with Boc-D-tyrosine-methylester **17**, which serves as the core frame of the **solriamfetol** pharmacophore for the MTDLs. Switching from phenylalanine, which normally forms the structural foundation of **solriamfetol**, to tyrosine as the underlying amino acid, provides a phenolic hydroxyl group. This group can be readily alkylated in a Williamson ether synthesis with 1-(3-chloropropyl)piperidine hydrochloride **SM1** to form the desired H_3R antagonist pharmacophore. Based on this rationale, the alkylation was performed under Finkelstein conditions for 24 hours[598] following the mechanism described in Figure 36, delivering the desired enantiomeric pure product **18** with a satisfactory yield of 68% (see Figure 62).

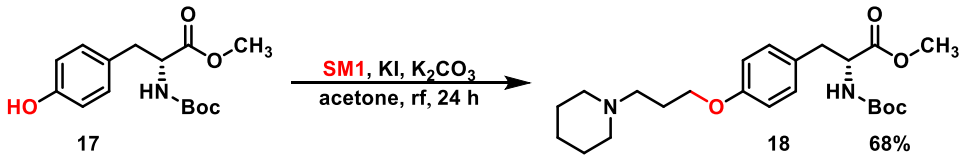

Figure 62: Reaction of the alkylation of **17** with **SM1**, yielding compound **18.**

In the following step, ester **18** was reduced to the alcohol to provide the free hydroxyl group, which could then be transformed into the carbamate structure present in the **solriamfetol** pharmacophore. The reduction was performed in THF with excess of LAH as reducing agent under mild conditions at -78 °C for two hours, leading to the desired enantiomerically pure alcohol **P4** with 90% yield.[671] The mechanism[603] (see Figure 63) is initiated by a hydride attack, donated by the reducing agent LAH, at the carbonyl group, leading to the breaking of the

carbonyl double bond and formation of a lithium-coordinated hemiacetal transition state (**TS1**). Through reformation of the carbonyl bond leading to the elimination of lithium methoxide, the aldehyde (**IM1**) is formed, which is further reduced to the alcohol. Again, hydride nucleophilically attacks the carbonyl group, leading to the breaking of the carbonyl double bond and formation of a lithium alkoxide complex (**TS2**). This alkoxide then undergoes coordination exchange to form the aluminium alkoxide species (**TS3**), which upon aqueous workup is cleaved to deliver the desired alcohol **P4**.

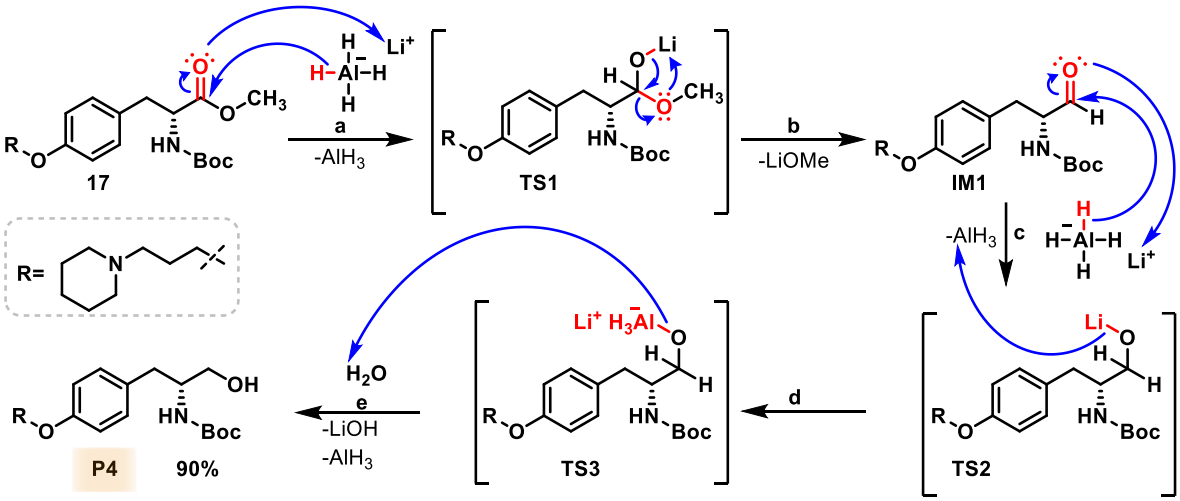

Figure 63: Mechanism of the ester reduction from compound **18** to its respective alcohol **P4** using LAH. a) Hydride transfer b) Elimination of lithium methanolate c)Hydride transfer d) Coordination exchange e) Aqueous workup.

Having established the alcohol functionality, the next synthetic step focused on introducing the primary carbamate group present in **solriamfetol**. The free alcohol of compound **P4** underwent coupling with CDI, forming an active carbamate species. This intermediate can then be cleaved through the addition of ammonia to form the desired primary carbamate **P5**, resembling the Boc-protected **solriamfetol** pharmacophore. The coupling was performed in THF with CDI for four hours at room temperature, forming the active intermediate. Through addition of aqueous ammonia solution, its aminolytic cleavage was carried out at room temperature for three days, yielding the enantiomerically pure product **P5** in 92%.[672] Mechanistically, the coupling proceeds through several distinct steps (see Figure 64).[603,673] The mechanism starts with the nucleophilic attack of the hydroxyl group of **P4** at the carbonyl group of CDI, leading through the breaking of the carbonyl double bond to a hemiaminal-containing transition state (**TS1**). Reestablishment of the carbonyl group leads to elimination of one imidazole moiety, yielding the activated carbamate structure (**IM1**). Due to nucleophilic attack of ammonia at the carbonyl group, again a hemiaminal-comprising transition state (**TS2**) is formed, which through reformation of the carbonyl group and elimination of the other imidazole moiety is transformed to the desired product **P5**.

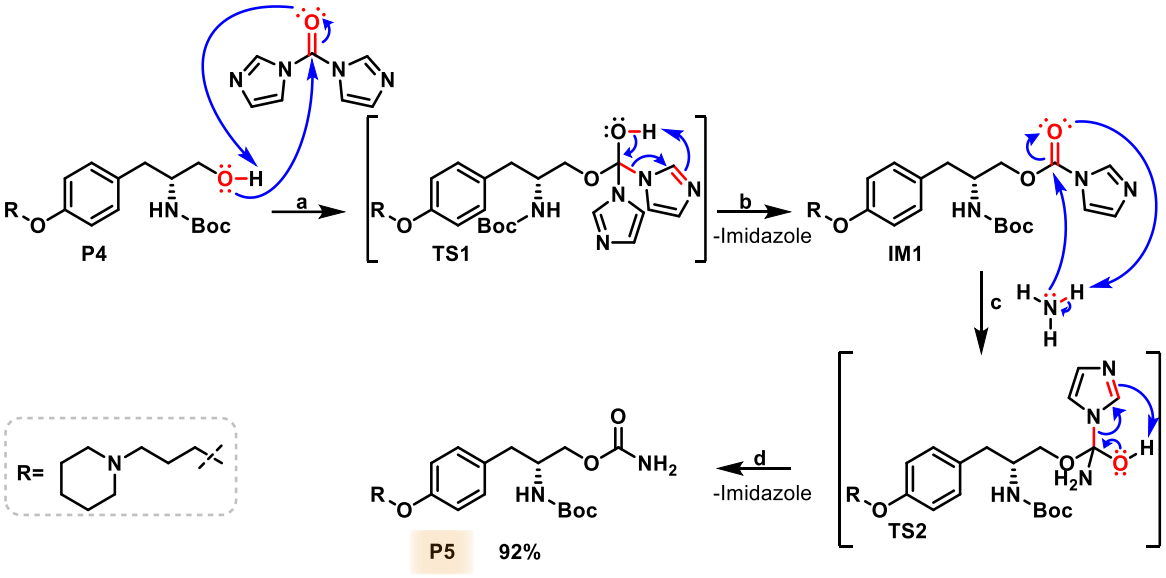

Figure 64: Mechanism of the carbamate formation from alcohol **P4** using CDI, followed by aminolysis, exemplarily shown for the formation of compound **P5**. a) Nucleophilic attack of the alcohol b) Elimination of imidazole c) Nucleophilic attack of ammonia d) Elimination of imidazole.

In the final step of the synthetic route, the Boc protecting group was cleaved to release the full unaltered **solriamfetol** pharmacophore. The cleavage was performed under acidic conditions by adding concentrated HCl to the product dissolved in methanol under ice cooling, followed by stirring at room temperature for three days, yielding the enantiomerically pure lead compound **P6** in 92% as a double hydrochloride salt.[674] Mechanistically,[643] the reaction starts with the protonation of the carbonyl oxygen of the Boc carbamate ester (**TS1**). This leads to the formation of a carbamic acid intermediate (**IM1**) under liberation of the stabilized *tert*-butyl cation.[675] The resulting intermediate then undergoes deprotonation, resulting in decarboxylation to afford the unprotonated product **IM2**. Under the acidic conditions, the newly formed primary amine becomes protonated, while the tertiary amine of the H_3R pharmacophore portion exists in its protonated form throughout the mechanism, leading to the dihydrochloride salt form of product **P6** (see Figure 65).

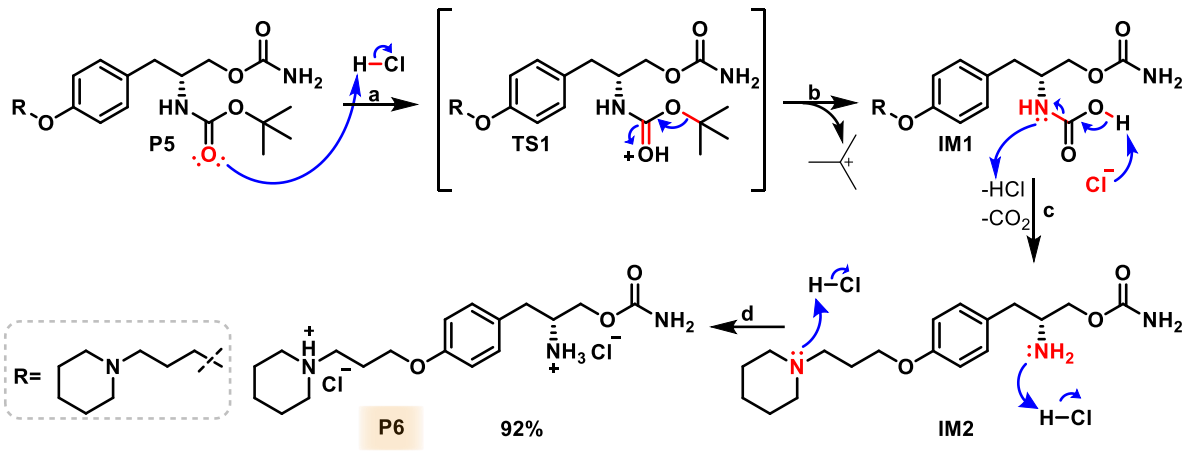

Figure 65: Mechanism of the Boc deprotection, exemplarily shown for the formation of compound **P6**. a) Protonation b) Elimination of *tert*-butyl cation c) Deprotonation and decarboxylation d) Salt formation.

4.2.2 *S*-enantiomeric series

To achieve a comprehensive SAR evaluation, the complementary *S*-enantiomer compounds were planned to be investigated and therefore had to be synthesized. This study aimed to test if the addition of the H_3R pharmacophore might alter the **solriamfetol** pharmacophore's properties,[513] possibly by forcing a different positioning in the binding pocket, potentially making these *S*-enantiomers tolerated in the described MTDLs, in contrast to **solriamfetol** alone, which is only active as *R*-enantiomer.[670,676]

To accomplish this goal, a synthetic route (see Figure 66) for the *S*-enantiomer series was designed, which could be shortened by one step since Boc-L-tyrosinol, derived from the natural amino acid, is commercially available. This would eliminate the need for the ester intermediate and consequently the reduction step (see Figure 61). The synthesis was designed to start with the alkylation of Boc-L-tyrosinol with 1-(3-chloropropyl)piperidine hydrochloride (**SM1**) to form the desired H_3R antagonist pharmacophore, yielding the *S*-enantiomeric product **P7**. With the aliphatic alcohol group already present, the synthesis could proceed directly to carbamate formation through CDI coupling followed by aminolysis to obtain the *S*-enantiomer **P8**. Final Boc deprotection would lead to the dihydrochloride salt form of the *S*-enantiomeric product **P9**.

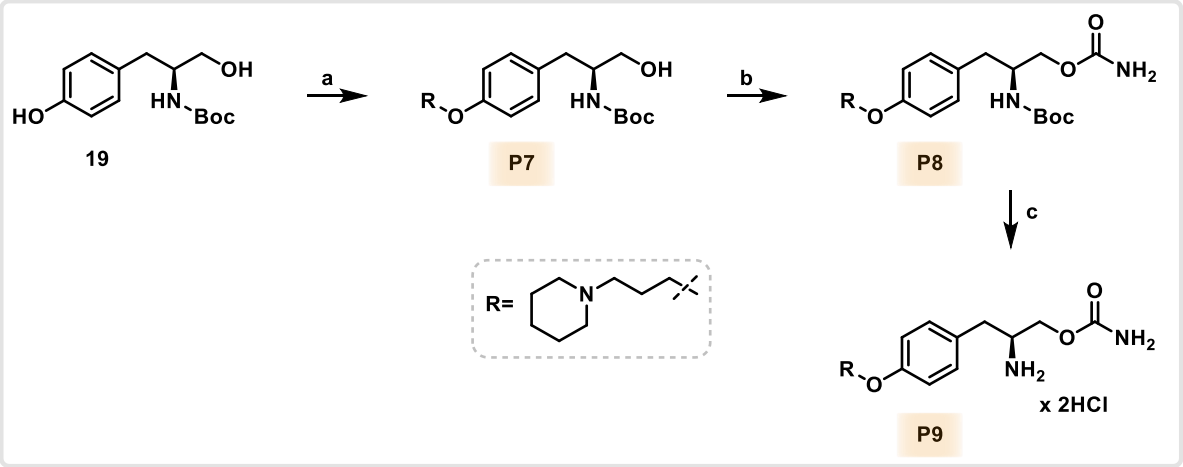

Figure 66: Planned synthetic route for the preparation of the *S*-enantiomeric MTDL series, complementing the SAR evaluation with compounds **P7**, **P8** and lead compound **P9** (all highlighted in orange). Reaction conditions: a) **SM1**, KI, K_2CO_3, acetone, reflux, 48 h. b) CDI, ammonium chloride, THF, room temperature, 3 d. c) HCl, methanol, room temperature, 3 d.

Following this synthetic plan, the first step involved the alkylation of Boc-L-tyrosinol **19** with the H_3R warhead 1-(3-chloropropyl)piperidine hydrochloride (**SM1**) to introduce the H_3R pharmacophore. The Williamson ether synthesis was carried out under Finkelstein conditions for 48 hours, yielding enantiomerically pure **P7** with 36% yield (see Figure 67),[598] following the mechanism described in Figure 36. The moderate yield can be attributed to the presence of the aliphatic alcohol group, which can compete as a nucleophile in the alkylation reaction,[643] as well as to potential over-alkylation products at the tertiary amine.[603]

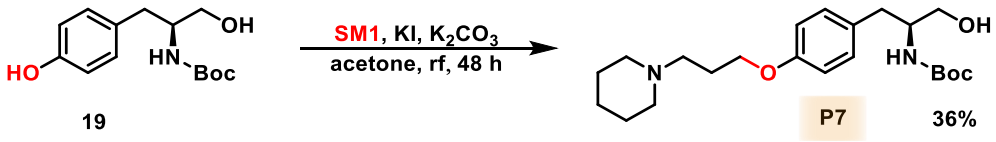

Figure 67: Reaction of the alkylation of **19** with **SM1**, yielding compound **P7**.

The resulting alcohol **P7** was then converted into the primary carbamate structure through CDI coupling followed by aminolysis of the formed active carbamate intermediate. The reaction was carried out, according to the mechanism described in Figure 64, for three days at room temperature, leading to the formation of the *S*-enantiomeric product **P8** with 82% yield,[672] as shown in Figure 68.

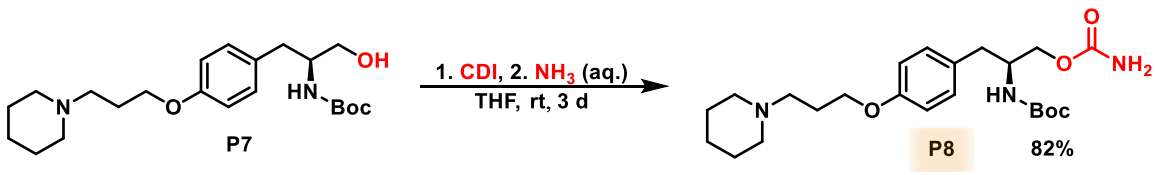

Figure 68: Reaction of the carbamate formation from **P7** with CDI and aminolysis, yielding compound **P8**.

Lastly, the Boc cleavage was performed to obtain the *S*-enantiomer of the lead compound. The deprotection, proceeding mechanistically as shown in Figure 65, was conducted for three days at room temperature, with initial addition of hydrochloric acid at 0 °C, yielding the dihydrochloride salt of the *S*-enantiomeric product **P9** in 76% yield (see Figure 69).[674] The slightly diminished yield of 76%, which is lower than the typically observed quantitative yields of Boc deprotections,[677] can be attributed to product loss during purification.

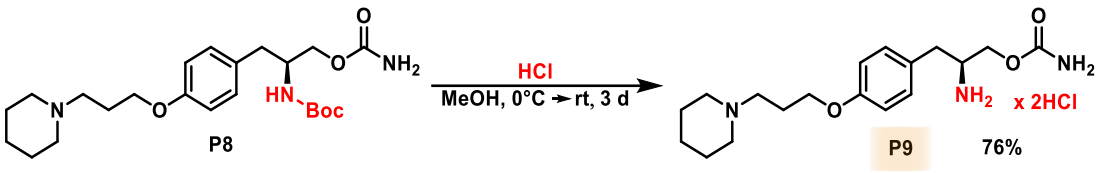

Figure 69: Reaction of the Boc deprotection of compound **P8**, yielding compound **P9**.

The optical purity of all synthesized compounds was confirmed by polarimetry. The measured specific rotations showed the expected opposite signs for the *R*- and *S*-enantiomers, supporting the assumption of high enantiomeric purity throughout the synthetic process.

4.2.3 Further SAR exploration

To further explore the SAR of these MTDLs, potential variations of the **solriamfetol** pharmacophore were investigated for both enantiomeric forms, focusing on possible transformations arising from its primary carbamate structure. One potential chemical alteration involves hydrolysis of the carbamate[678] followed by decarboxylation, resulting in the regeneration of the aliphatic hydroxyl group. To mimic this envisioned transformation product, compounds **P4** and **P7**, which already contained this free hydroxyl group, could be deprotected to obtain compounds **P10** and **P11**, respectively. The second potential reaction pathway engages an intramolecular attack of the primary amine at the carbamate, leading to oxazolidinone ring formation.[679,680] This structural motif could likewise be accessed starting from **P4** and **P7** through deprotonation of the alcohol group, which initiates a nucleophilic attack of the resulting alkoxide at the carbamate structure of the Boc group, leading to the desired oxazolidinone-containing derivatives as shown in Figure 70.

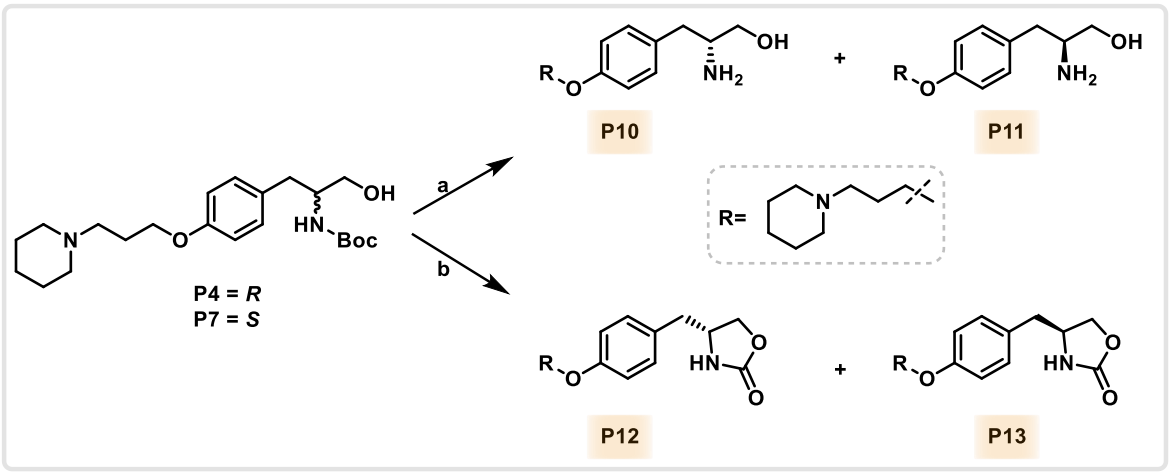

Figure 70: Planned synthetic route for expansion of the SAR evaluation of the **solriamfetol** pharmacophore, investigating potential chemical transformation products **P10-13** for both enantiomeric forms (all highlighted in orange). Reaction conditions: a) HCl, methanol, room temperature, 7 d. b) NaH, THF, room temperature, 2 d.

Beginning with the first possible transformation pathway, compounds **P4** and **P7** underwent Boc deprotection. The reactions were carried out using hydrochloric acid as cleavage reagent for seven days at room temperature, yielding the products in 89% and 95% yield, respectively (see Figure 71).[674] The mechanism proceeded as previously described (see Figure 65). However, during purification normal phase column chromatography was performed using basic additives, delivering the free base forms of products **P10** and **P11** rather than the dihydrochloride salts formed during the reaction.

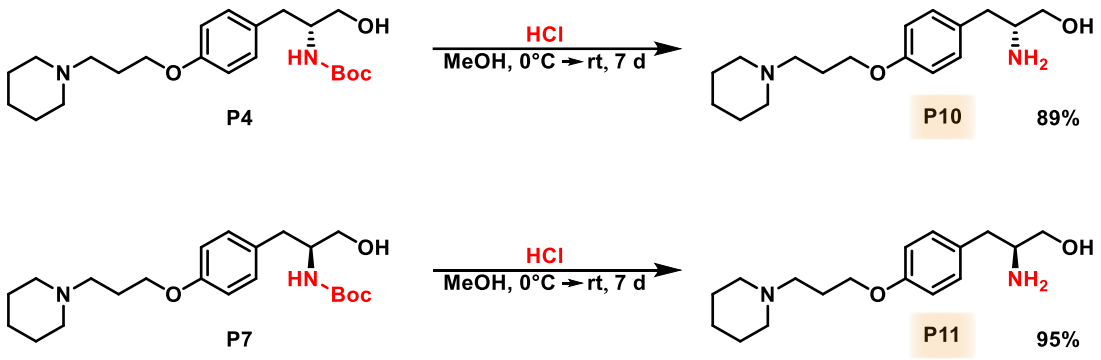

Figure 71: Reactions of the Boc deprotections of compound **P4** and **P7**, yielding the hydrolysis transformation mimic compounds **P10** and **P11**.

The second envisioned transformation products were accessed by deprotonating the hydroxyl groups of **P4** and **P7**, respectively, leading through an intramolecular nucleophilic attack of the resulting alkoxides at the Boc group to oxazolidinone ring formation. The reaction was performed in THF using sodium hydride as base, which is sufficiently strong to deprotonate aliphatic alcohols.[643] The reactions were carried out for two days at room temperature, with base addition at 0 °C, yielding the cyclic products in almost quantitative yields of 98% (see

Figure 72).[681] Mechanistically,[603] the reaction begins with deprotonation of the alcohol group by sodium hydride, forming the sodium alkoxide (**IM1**). This intermediate then performs a nucleophilic attack at the carbonyl group of the Boc carbamate, forming an acetal-containing transition state (**TS1**). Through reformation of the carbonyl bond, sodium *tert*-butoxide is eliminated and ring formation is completed, leading to the final products **P12** and **P13**.

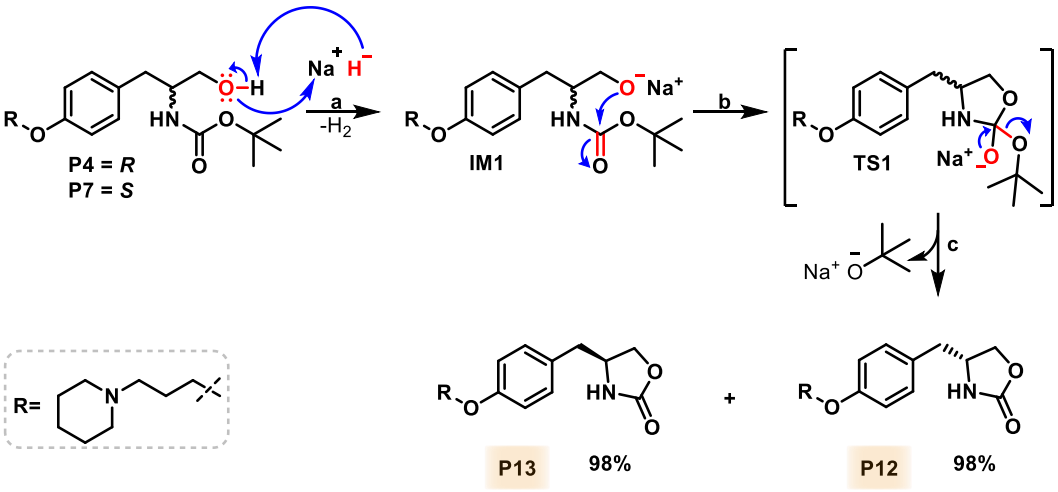

Figure 72: Mechanism of the oxazolidinone ring formation, yielding the second potential transformation mimic compounds **P12** and **P13**. a) Deprotonation b) Nucleophilic attack from the alkoxide c) Elimination of sodium *tert*-butoxide.

4.3 Biological evaluation

4.3.1 Binding profile

The synthesized MTDLs **P4-P13** were subjected to H_3R affinity testing and the results (shown in Table 6) demonstrated significant H_3R binding affinity, with K_i values ranging from 16.9 to 211 nM. All compounds exhibited very high affinity towards H_3R, with the exception of compounds **P4** and **P5** showing moderately reduced binding (K_i = 211 nM and 203 nM, respectively), confirming once again the effectiveness and robustness of the H_3R pharmacophore design.[595,628] Notably, **solriamfetol** itself showed no H_3R affinity (K_i > 10000 nM), validating that the introduced 3-(piperidin-1-yl)propoxy warhead, a key structural element shared with **pitolisant** (K_i = 0.16 nM),[258] is essential for H_3R binding. Structure-activity relationship analysis revealed interesting stereochemical influences on receptor affinity. The *R*-enantiomers **P4** and **P5**, both containing Boc-protecting groups at the stereogenic amino group, showed moderately reduced H_3R affinity compared to their *S*-enantiomeric counterparts **P7** and **P8** (K_i = 51.4 nM and 33.3 nM). This stereoselective difference in binding affinity was uniquely observed for the Boc-containing compounds, suggesting that the bulky Boc group may create unfavourable steric interactions within the binding pocket when in *R*-configuration. This assumption is consistent with studies on stereochemistry-dependent H_3R binding that

highlight the critical role of stereochemistry in receptor affinity and selectivity.[682,683] The remaining enantiomeric pairs (**P6/P9**, **P10/P11**, and **P12/P13**) demonstrated comparable high affinities, both between different pairs and within each enantiomeric pair, with overlapping confidence intervals. This common binding profile further supports the hypothesis that the observed stereoselectivity is specific to the synthesized Boc-containing compounds due to steric hindrance.

While binding studies have demonstrated excellent H_3R affinity and selectivity, functional characterization would provide valuable insights into the compounds' pharmacological profiles. Based on the employed H_3R pharmacophore, which incorporates the 3-(piperidin-1-yl)propoxy warhead of **pitolisant**[669] and through merging with **solriamfetol** resulted in the **JNJ-5207852** underlying pharmacophore,[595] these compounds are designed to act as H_3R antagonists. However, for definitive confirmation of their H_3R antagonistic properties and consequently their wake-promoting effects through histaminergic pathway modulation, functional assays are needed to fully establish the first component of their multi-mechanism approach for narcolepsy treatment.

As for the second component, the evaluation of these compounds' effects on norepinephrine, dopamine, and serotonin reuptake transporters to validate their multi-target design has yielded preliminary results in collaboration with the team of Prof. Bryan Roth at the University of North Carolina. The data from single-point screening at 10 µM, which is described in detail in the experimental section, revealed varying degrees of transporter inhibition across the compound series, with **P6** demonstrating the most promising profile. This *R*-enantiomer exhibited substantial inhibition of NET (51.6%), SERT (44.9%), and DAT (35.1%), confirming that the **solriamfetol** pharmacophore maintains significant transporter inhibition activity when incorporated into the multi-target design. Interestingly, **P6** showed more balanced inhibition across all three transporters compared to **solriamfetol** itself (see Table 6), which displayed expectedly strong DAT inhibition (73.1%) and moderate NET inhibition (29.0%) and no NET activity (-9.6%). While **P6's** DAT inhibition is lower than that of **solriamfetol**, its broader and more balanced inhibition profile across DAT, NET, and SERT may offer therapeutic advantages by modulating multiple neurotransmitter systems implicated in narcolepsy.

Table 6: Histamine H_3 receptor affinities of MTDLs **P4-P13**, as well as their inhibition of the different transporters DAT, SERT, NET.

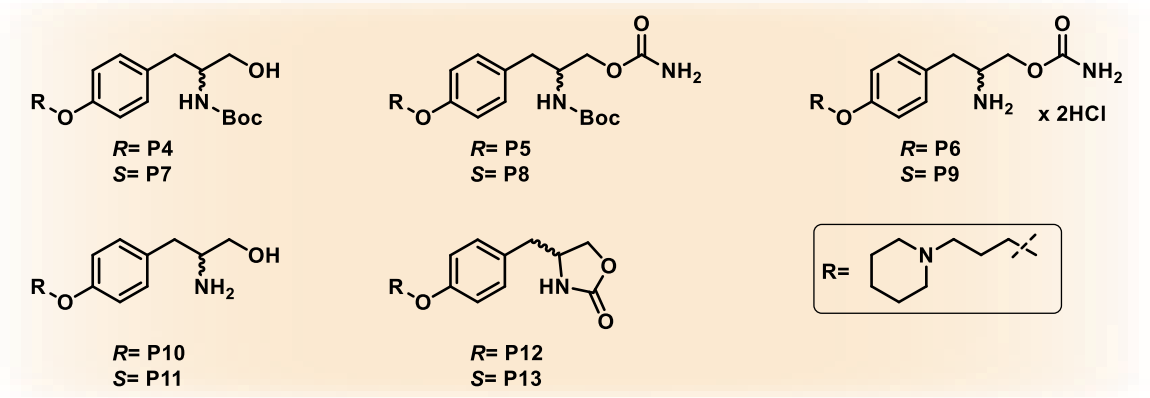

Compound	Enantiomer	hH_3R K_i (nM) [95% CI]	NET* %inhib ± SEM	DAT* %inhib ± SEM	SERT* %inhib ± SEM
P4	*R*	**211** [122; 366]	**6.8** ± 6.9	**-10.1** ± 6.2	**15.9** ± 1.1
P7	*S*	**51.4** [26.3; 101]	**13.5** ± 8.9	**10.9** ± 8.3	**4.3** ± 3.9
P5	*R*	**203** [96.1; 430]	**12.8** ± 2.8	**10.1** ± 3.4	**6.2** ± 4.3
P8	*S*	**33.3** [11.9; 93.4]	**12.5** ± 7.7	**7.6** ± 8.5	**7.0** ± 9.0
P6	*R*	**46.0** [21.5; 98.3]	**51.6** ± 2.7	**35.1** ± 2.8	**44.9** ± 7.3
P9	*S*	**16.9** [9.5; 30.2]	**28.9** ± 8.4	**11.1** ± 5.0	**-2.7** ± 2.9
P10	*R*	**26.6** [16.2; 43.7]	**19.9** ± 5.2	**15.9** ± 2.4	**8.5** ± 3.2
P11	*S*	**31.5** [20.2; 49.0]	**16.3** ± 3.3	**0.3** ± 11.8	**4.8** ± 3.8
P12	*R*	**20.9** [7.8; 56.0]	**17.3** ± 4.9	**36.6** ± 3.0	**4.0** ± 2.1
P13	*S*	**49.0** [41.4; 58.0]	**8.7** ± 3.2	**-0,7** ± 10.1	**4.9** ± 1.5
Solriamfetol	*R*	**>10000**	**29.0** ± 1.3	**73.1** ± 3.4	**-9.6** ± 4.6

*Single-point inhibition at 10 µM (n=4)

The other compounds in the series showed generally modest transporter inhibition as expected, since they feature more substantial modifications to the **solriamfetol** pharmacophore than **P6**, with **P9** demonstrating the second-highest NET inhibition (28.9%) while **P12** showed notable DAT inhibition (36.6%). Compound **P12** is of particular interest since it exhibits a transporter inhibition profile comparable in selectivity to **solriamfetol**, albeit with lower potency. This similarity in transporter selectivity, combined with the added H_3R antagonist activity, positions **P12** as a promising candidate for future development, potentially offering a multi mechanism of action with a transporter inhibition profile close to the clinically validated **solriamfetol**. The data also suggest that stereochemistry plays an important role in transporter binding, with *R*-enantiomers generally exhibiting stronger inhibition profiles than their *S*-counterparts, particularly evident in the **P6/P9** pair. This stereochemical preference aligns with the established activity profile of **solriamfetol**, where the *R*-enantiomer represents the eutomer with superior pharmacological activity.[665]

While these results are preliminary, they lay a solid foundation for confirming the transporter-related aspect of the multi-target approach. For compounds showing more than 50% inhibition in the initial screening, full IC_{50} determinations were performed to precisely quantify transporter affinity. Notably, compound **P6** demonstrated an IC_{50} of 4934 nM at the norepinephrine transporter, confirming its effective inhibition. With balanced activity across DAT, NET, and SERT, **P6** emerges as the leading candidate, potentially offering a well-rounded multi-target therapeutic profile for the treatment of narcolepsy.

4.3.2 Selectivity

To confirm the suitability of the lead compound **P6** and its enantiomeric partner **P9** for use as MTDLs for narcolepsy treatment, their selectivity toward related GPCRs was evaluated as shown in the results in Table 7. As expected, the H_3R pharmacophore used for the design of these MTDLs showed no reasonable affinity toward other histamine or dopamine receptors, establishing the selectivity needed for therapeutic application.

Table 7: Results of selectivity screening for MTDLs **P4-P13.**

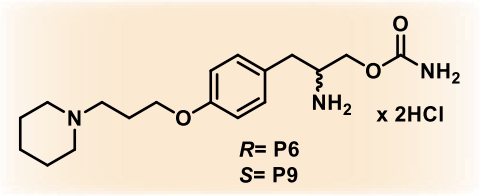

Compound	hH_1R K_i (nM) [95% CI]	hH_4R K_i (nM) [95% CI]	hD_2R K_i (nM) [95% CI]	hD_3R K_i (nM) [95% CI]
P6	**> 10,000**	**>10000**	**4337** [3220; 5841]	**>10000**
P9	**3183** [2643; 4114]	**>10000**	**>10000**	**>10000**

4.3.3 Cytotoxicity

All MTDLs were further tested for cytotoxicity on a SH-SY5Y cell line for an initial safety evaluation (see Figure 73). Every compound maintained 100% cell viability at 100 µM, with the exception of **P4** which exhibited mild cytotoxicity with approximately 70% cell viability. Given that this assessment used concentrations several orders of magnitude higher than those required for biological activity (100 µM versus nanomolar range), also compound **P4** is likely to maintain acceptable safety margins at therapeutically relevant concentrations. Importantly, the lead compounds **P6** and **P9** demonstrated complete cell survival at these concentrations, fulfilling a crucial criterion for their potential application as MTDLs in narcolepsy treatment.

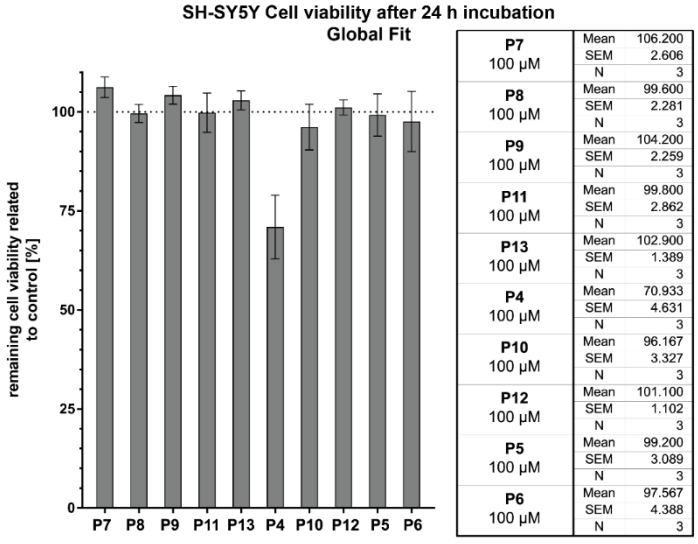

Figure 73: Cell viability of SH-SY5Y cell line after 24 h incubation with MTDLs **P4-P13** at a concentration of 100 µM.

4.3.4 Therapeutic relevance

The novel MTDL **P6** developed in this study, exhibit promising therapeutic potential for narcolepsy by simultaneously modulating histamine H_3 receptor and monoamine transporters DAT, NET and SERT. Unlike established wake-promoting agents such as modafinil, which primarily acts as a DAT inhibitor and **solriamfetol**, which selectively inhibits DAT and NET, this compound shows a more balanced transporter inhibition profile. This more evenly distributed activity may help reduce overstimulation of any single neurotransmitter system, thereby potentially lowering risks such as cardiovascular issues, dependence, or neurotoxicity that have been associated with the more selective DAT inhibitors.[684] Additionally, the inclusion of strong H_3R antagonism offers a complementary wake-promoting mechanism that may improve cognitive function and reduce excessive daytime sleepiness through enhanced histamine release. Furthermore, H_3R antagonism could potentially mitigate some stimulant-related side effects, such as insomnia or jitteriness, by modulating histaminergic tone and promoting a more physiologically balanced arousal state.[2] Moreover, compound **P6** demonstrates high selectivity for its targets and have shown no cytotoxic effects in preliminary safety assessments, further encouraging its potential clinical suitability.

Pharmacokinetic considerations also supports the potential advantages of these new MTDLs, as demonstrated by Compound **P12**, which shows a transporter inhibition profile comparable to **solriamfetol**, albeit with lower potency, but offers potentially improved pharmacokinetic properties due to decreased polarity and reduced hydrogen bonding capacity. This structural modification likely enhances blood-brain barrier penetration and oral bioavailability, while potentially increasing metabolic stability, key factors for effective central nervous system drug action. Moreover, the ring-closed scaffold in **P12** may serve as a prodrug-like structure, allowing *in vivo* conversion back to **P6**, thereby offering a strategic balance between pharmacokinetic stability and pharmacodynamic activity.

Overall, these MTDLs represent a promising advancement over current narcolepsy treatments by offering a multi-faceted pharmacological approach, improved pharmacokinetic characteristics, and potentially better safety and tolerability profiles.

4.4 Summary

This chapter presents the successful development of novel potential MTDLs designed for enhanced treatment of narcolepsy. The rational design strategy aimed to merge the pharmacophores of two clinically approved narcolepsy drugs by combining **pitolisant's** H_3R antagonist warhead[669] with **solriamfetol's** NDRI pharmacophore.[665] The envisioned MTDLs are expected to exert their wake-promoting effects through two complementary pathways,

combining histaminergic activation[667] via the **pitolisant**-derived H_3R antagonist moiety and dopaminergic stimulation[668] through the preserved NDRI functionality. To achieve those MTDLs, a robust synthetic route was established to deliver the *R*-enantiomerically pure intended MTDL **P6**, which serves as the lead compound, representing the biologically active stereoisomer of the **solriamfetol** pharmacophore.[670] Beyond merging both unaltered pharmacophores, the project explored SAR through strategic modifications of the **solriamfetol** component, represented in compounds **P4** and **P5**. For comprehensive SAR analysis, the corresponding *S*-series compounds were synthesized to investigate whether the merger with the H_3R pharmacophore might alter the established stereochemical requirements of the **solriamfetol** moiety for NDRI activity. Additionally, potential transformation products of the **solriamfetol** moiety were synthesized for both enantiomers, specifically compounds mimicking carbamate hydrolysis[678] and intramolecular cyclization products.[679,680] Following successful synthesis, biological evaluation of the MTDLs demonstrated excellent H_3R binding affinities (K_i = 16.9-211 nM) for all compounds. While most compounds maintained strong H_3R binding, the Boc-protected *R*-enantiomers **P4** and **P5** exhibited moderately reduced affinity, likely due to unfavourable steric interactions within the binding pocket caused by the spatial orientation of the bulky protecting group. In contrast, the unprotected lead compounds **P6** and **P9** not only showed high H_3R affinity (K_i = 46.0 nM and 16.9 nM), but also demonstrated excellent target selectivity in an additional GPCR screening. Furthermore, initial cytotoxicity studies showed excellent results, with all tested compounds maintaining high cell viability even at high concentrations of 100 µM. Building on these promising H_3R binding and safety findings, preliminary results of the ongoing monoamine reuptake inhibition evaluation have confirmed significant activity of lead compound **P6**, demonstrating a more balanced profile across all three tested transporters (DAT, SERT, NET) compared to **solriamfetol** itself. This was validated by IC_{50} determinations, supporting **P6** as a promising therapeutic candidate for narcolepsy treatment, as it offers enhanced wake-promoting effects through the synergistic combination of H_3R antagonism and triple monoamine reuptake inhibition, while potentially reducing side effects caused by overstimulation of a single neurotransmitter pathway. Moreover, compound **P12** emerged as an interesting candidate for further development in narcolepsy treatment, mimicking the pharmacological profile of the parent pharmacophore **solriamfetol** with lower potency but exhibiting a favourable pharmacokinetic profile due to structural modifications that likely improve blood-brain barrier penetration, oral bioavailability, and metabolic stability.

Part II

H_3R-based molecular tools

5. Development of H_3R molecular tools for click chemistry

This chapter describes the design, synthesis and biological evaluation of novel tetrazine-based H_3R ligands, designed to enable inverse electron-demand Diels-Alder (IEDDA) click chemistry reactions. These specialized molecular tools complement the existing molecular toolbox for H_3R research by offering potential use in biorthogonal cross-linking reactions for chemical biology and advanced imaging applications.

5.1 Rational design

While current H_3R research tools already encompass a wide range of ligand classes for receptor visualization and characterization, including fluorescent ligands and isotope-labelled radiotracers,[268–270,685] the toolbox is notably lacking ligands containing reactive groups suitable for bioorthogonal chemistry that would enable selective labelling in complex biological environments and *in vivo* applications. To date, click chemistry in H_3R research has been limited to use as a synthetic tool for ligand preparation, specifically using CuAAC,[621,686] with no reported H_3R ligands designed for post-binding bioorthogonal reactions such as IEDDA chemistry, despite their demonstrated potential for advanced receptor visualization studies.

This project aims to close this gap in H_3R research by developing of a new class of click chemistry-capable H_3R ligands that can engage in metal-free IEDDA click reactions, complementing the existing molecular toolbox for H_3R research. These novel ligands feature a methyl tetrazine moiety connected to the well-established **JNJ-5207852**-derived H_3R pharmacophore,[595] designed to maintain the essential H_3R affinity and selectivity while enabling tetrazine-based IEDDA click chemistry capabilities.[687] The presented IEDDA-based approach addresses current limitations in H_3R visualization tools where conventional, bulky, directly-attached probes may interfere with receptor function.[688] By utilizing a small tetrazine modification, this design seeks to enable biorthogonal, sequential labelling, where probes are selectively attached only after the ligand has bound to the receptor, thus minimizing interference throughout the entire process.[590] Additionally, these tetrazine-containing H_3R ligands are intended to not only offer superb reaction kinetics[689] and biocompatibility for efficient labelling under physiological conditions,[690] but also to enable the versatile attachment of various probes, including fluorophores,[691] radiotracers,[692] and protein labels,[693] substantially adding to the available toolset for H_3R research and visualization methods. Building upon this rationale, the methyl tetrazine click moiety was attached to the **JNJ-5207852**-derived H_3R pharmacophore,[595] both directly and through a series of alkyl phenol ethers with varying aliphatic chain lengths (see Figure 74). This systematic variation of linker presence and length was implemented to explore whether and what distance between the

pharmacophore and tetrazine would be necessary to maintain H_3R affinity while ensuring the tetrazine ring remains accessible for click reactions.

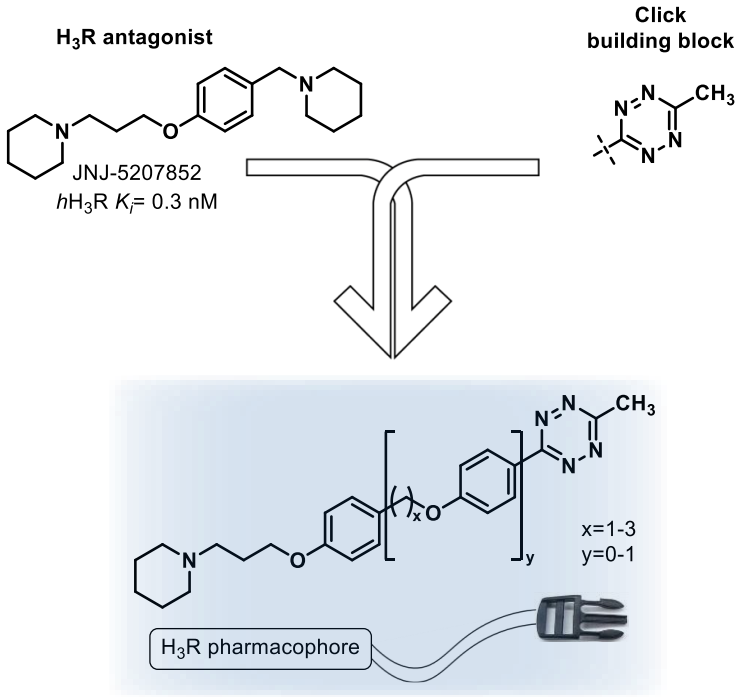

Figure 74: Rational design strategy linking a methyl tetrazine click building block to the pharmacophore of **JNJ-207852** (H_3R antagonist) through varying linker lengths to generate novel IEDDA-capable H_3R click chemistry tools.

5.2 Synthesis

Following this design concept, a small series of three H_3R ligands with a linkage system between the H_3R pharmacophore and the tetrazine click moiety was synthesized, with the envisioned synthetic route shown in Figure 75. The synthesis was designed to start from a series of 4-hydroxyphenyl alcohols **20,6a-b**, differing in their primary alcohol chain length from methanol to propanol, introducing the H_3R pharmacophore through alkylation of the phenolic hydroxyl group with 1-(3-chloropropyl)piperidine hydrochloride **SM1**. The resulting alcohols **21,7a-b** would then undergo a Mitsunobu reaction with 4-cyanophenol to form compounds **22a-c**, establishing both the varying alkyl phenol ether linkers and introducing the tetrazine precursor fragment. To complete the synthesis, these compounds would subsequently be subjected to a final ring formation reaction using hydrazine and a zinc catalyst to generate the desired methyl tetrazine containing compounds **P14a-c**.

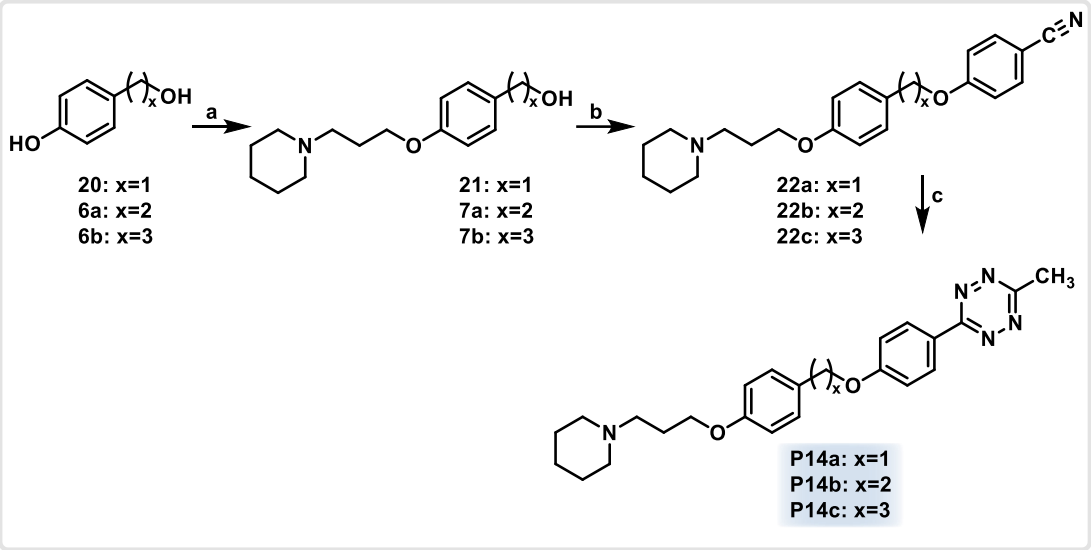

Figure 75: Planned synthetic route for the novel linker-containing tetrazine-based H_3R ligands **P14a-c** (highlighted in blue), designed for their capability to undergo IEDDA click chemistry. a) **SM1**, KI, K_2CO_3, acetone reflux, 48 h. b) DEAD, PPh_3, ,4-cyanophenol, THF, room temperature, 48 h. c) $Zn(OTf)_2$, hydrazine, acetonitrile, 60 °C, 48 h.

To start the synthetic route, the 4-hydroxyphenyl alcohols **20, 6a-b** were alkylated with 1-(3-chloropropyl)piperidine hydrochloride (**SM1**) in a Williamson ether synthesis under Finkelstein conditions to form the H_3R pharmacophore. The reaction was performed for 48 hours under reflux, following the mechanism described in Figure 36, yielding the respective products **21,7a-b** in 43-74% yield (see Figure 76).[598] The lower yield range of 43% can likely be attributed to competing side reactions, with the aliphatic alcohol group acting as an additional nucleophile in the alkylation reaction[643] or potential over-alkylation occurring at the tertiary amine position.[603]

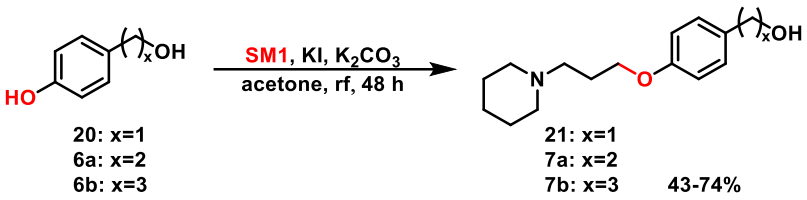

Figure 76: Reaction of the Williamson ether synthesis under Finkelstein conditions from alcohols **20, 6a-b** yielding the alkylated products **21, 7a-b**.

In the next step, compounds **21, 7a-b** were transformed in a Mitsunobu reaction with 4-cyanophenol to form alkyl phenyl ethers **22a-c**, establishing the linkage between the H_3R pharmacophore and click moiety while simultaneously incorporating the tetrazine precursor. The reaction was performed using diethyl azodicarboxylate (DEAD) and triphenylphosphine as the Mitsunobu system at room temperature for 48 hours, yielding the products in 35-76% yield.[694] The moderate yield of 35% can likely be attributed to the moisture sensitivity of DEAD,[695] which could be overcome by working under an inert atmosphere. While many

different mechanisms have been proposed for the Mitsunobu reaction over the years,[696,697] a possible one is depicted in Figure 77. Initially, triphenylphosphine nucleophilically attacks the DEAD azo function, cleaving the N=N double bond (**TS1**). The resulting DEAD anion then abstracts the proton from the phenolic group of 4-cyanophenol, generating a phenolate ion that serves as a nucleophile in subsequent steps. Next, the aliphatic alcohol (**21** or **7a-b**) attacks the positively charged phosphorus atom of the phosphine imide species (**TS2**), leading to a deprotonated, reduced form of DEAD and a protonated phosphinite species (**TS3**). A subsequent proton transfer produces the phosphinite intermediate (**TS4**) and releases the reduced DEAD. The phenolate then performs a nucleophilic attack at the alpha carbon atom of the phosphinite, producing triphenylphosphine oxide and the desired alkyl phenyl ethers (**22a-c**). This transformation is particularly efficient due to the formation of the thermodynamically favourable phosphorus-oxygen double bond in the triphenylphosphine oxide byproduct, which serves as the primary driving force for the overall reaction.[643,695]

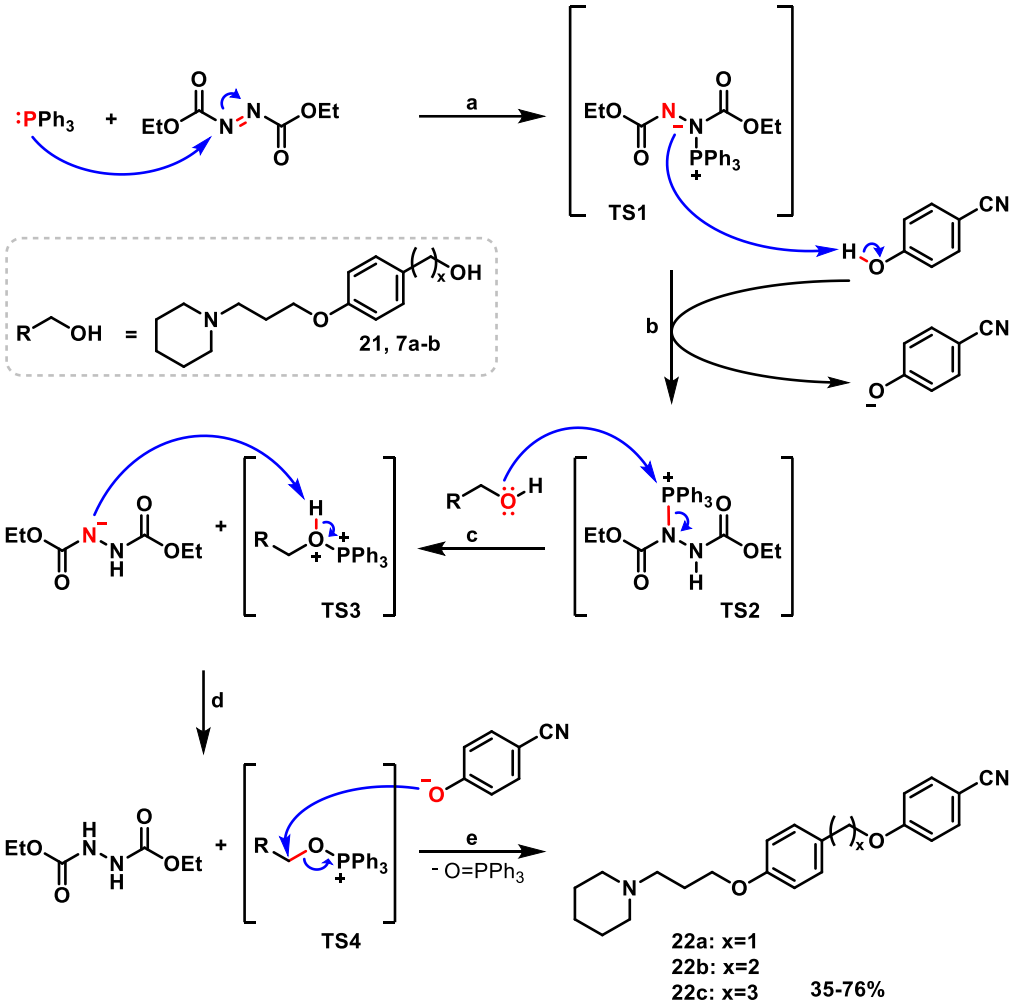

Figure 77: Mechanism of the Mitsunobu reaction of the alcohols **21, 7a-b** with 4-cyanophenole, yielding the alkyl phenol ethers **22a-c**. a) Nucleophilic attack of the triphenylphosphine b) Deprotonation of the phenol c) Nucleophilic attack of the alcohol d) Proton transfer e) Nucleophilic attack of the phenolate.

To form the final IEDDA-capable H_3R ligands, the terminal nitrile groups of compounds **22a-c** were transformed into the respective methyl tetrazines **P14a-c** through ring formation. The reaction was performed under zinc(II)triflate catalysis with acetonitrile and hydrazine at 60 °C for two days, yielding the desired tetrazines **P14a-c** as pink solids in yields of 5-17%.[698] The relatively low yields of the ring formation are consistent with the generally modest yields reported for unsymmetrical tetrazines in the literature.[698–700] In this case, the yields were particularly impacted by multiple side products, largely attributed to potential dimerization reactions,[701] making purification challenging. Additionally, incomplete oxidation of the dihydrotetrazine intermediates to the desired tetrazines further contributed to the modest yields. These reduced byproducts **BP14a-c** were isolated during the purification process in 14-27% yield as colourless solids. The mechanism,[698,702] as shown in Figure 78, begins with the association of the zinc triflate catalyst to the nitrile group of compounds **21a-c**, activating it through its Lewis acid properties for nucleophilic attack (**TS1**). Coordination of hydrazine (**TS2**) brings it into spatial proximity for a nucleophilic attack on the nitrile group, leading to a zinc-coordinated hydrazide (**TS3**). This latter then attacks the nitrile group of acetonitrile, forming the zinc-coordinated bisamidine species **TS4**. Nucleophilic attack of another hydrazine molecule on one of the amidine groups leads to formation of a hydrazine species (**TS5**), which can then undergo an intramolecular nucleophilic attack on the second amidine, resulting in ring closure (**TS6**). Elimination of ammonia stabilizes the ring, forming the dihydrotetrazines. The subsequent oxidation step using sodium nitrite and HCl yielded both the desired tetrazines **P14a-c** and the incompletely oxidized dihydrotetrazines **BP14a-c**.

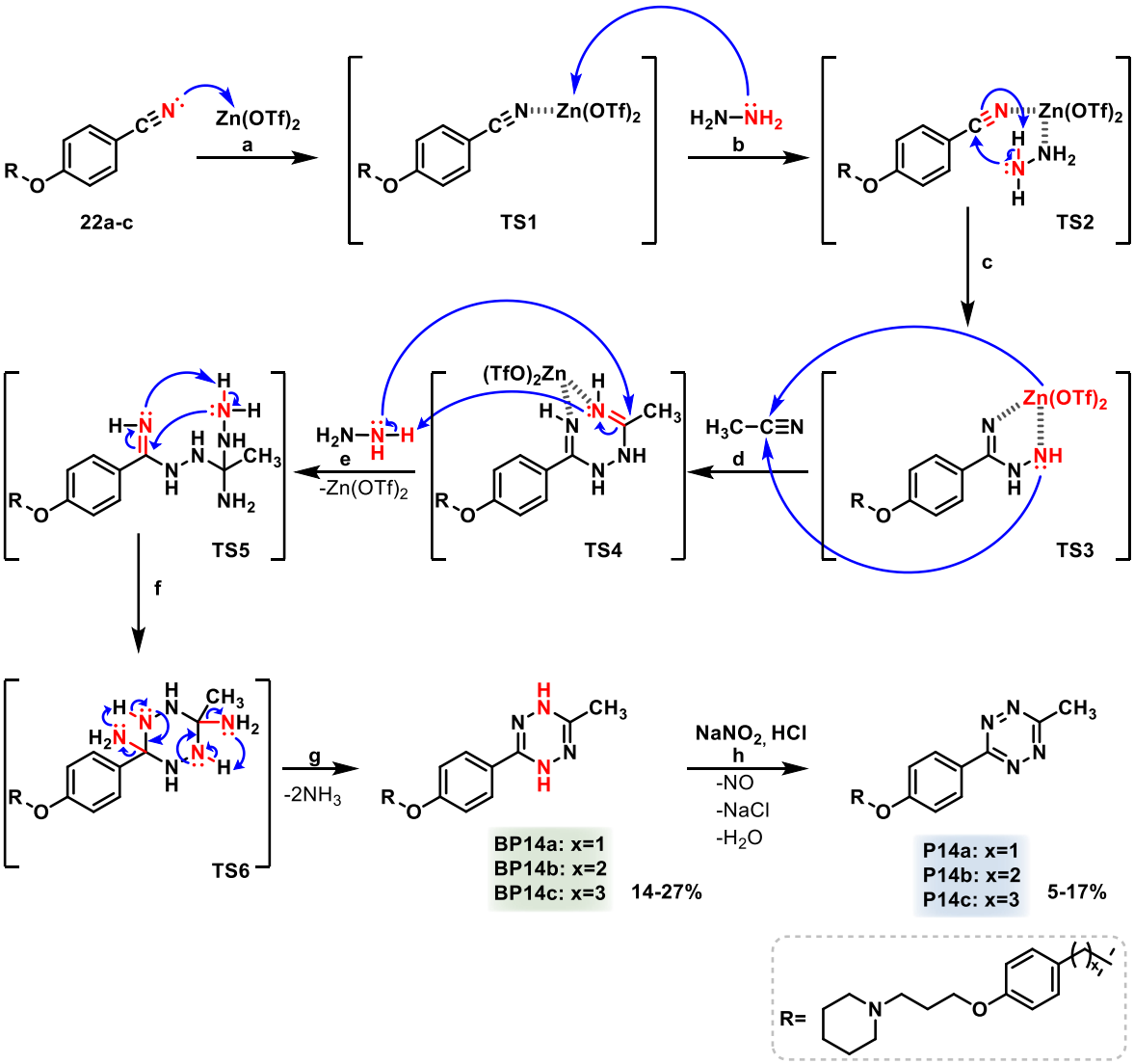

Figure 78: Mechanism of the tetrazine ring formation of the alcohols **22a-c**, yielding the desired tetrazines **P14a-c** (highlighted in orange), as well as the incompletely oxidized dihydrotetrazines **PB14a-c** (highlighted in green). a) Lewis acid acitivation b) Hydrazine coordination c) Nucleophilic attack of the hydrazine d) Nucleophilic attack of the amidine e) Nucleophilic attack of another hydrazine molecule f) Intramolecular ring closure g) Ammonia elimination h) Oxidation.

Complementary to the approach of introducing a linker system between H_3R pharmacophore and click moiety, a compound with the direct attachment of the tetrazine onto the pharmacophore was planned to be synthesized. This direct attachment strategy would later allow evaluation of whether a linker system is necessary for maintaining H_3R affinity and ensuring tetrazine ring accessibility for labelling reactions. The synthetic route was designed to start with the alkylation of 4-cyanophenol (**22**) with 1-(3-chloropropyl)piperidine hydrochloride (**SM1**), forming the H_3R pharmacophore represented in compound **23**. Its terminal nitrile group can then undergo tetrazine ring formation synthesis, that would lead to the final tetrazine **P15** (see Figure 79).

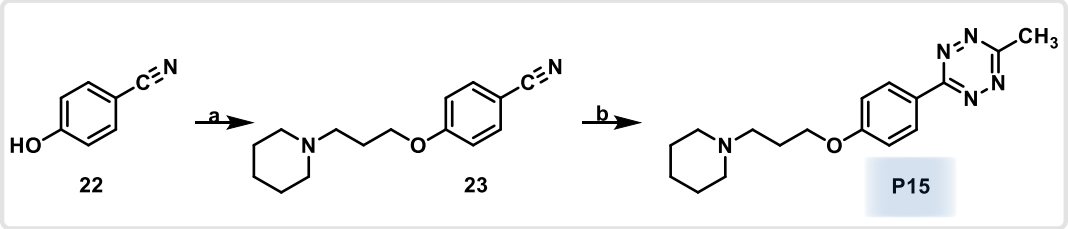

Figure 79: Planned synthetic route for the tetrazine-based H_3R ligand **P15** (highlighted in orange), exploring the direct attachment of the click moiety onto the H_3R pharmacophore. Reaction conditions: a) **SM1**, KI, K_2CO_3, acetone, reflux, 48 h. b) $Zn(OTf)_2$, hydrazine, acetonitrile, 60 °C, 48 h.

Firstly, the H_3R pharmacophore formation was achieved through a Williamson ether synthesis under Finkelstein conditions using 1-(3-chloropropyl)piperidine hydrochloride (**SM1**) as the alkylating agent for 4-cyanophenol (**22**). The reaction followed the mechanism depicted in Figure 36, and was performed for 48 hours under reflux conditions, yielding compound **23** in 72% yield (see Figure 80).[598]

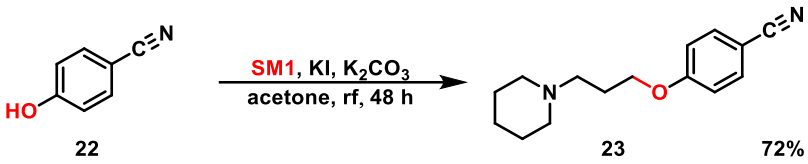

Figure 80: Reaction of the Williamson ether synthesis of 4-cyanophenol (**22**) with **SM1**, yielding compound **23**.

Subsequently, compound **23** underwent a tetrazine ring formation reaction to yield compound **P15**, where the tetrazine moiety is directly attached to the H_3R pharmacophore. The reaction was performed, following the mechanism discussed in Figure 78, under zinc catalysis with hydrazine in acetonitrile at 60 °C for 48 hours (see Figure 81).[698] The tetrazine product **P15** was obtained in 17% yield, reflecting the previously discussed challenges of tetrazine formation including dimerization[701] and the generally moderate-yielding nature of this tetrazine synthesis protocol.[698–700] Additionally, because of incomplete oxidation, the dihydrotetrazine **BP15** was again obtained and isolated during purification in 19% yield.

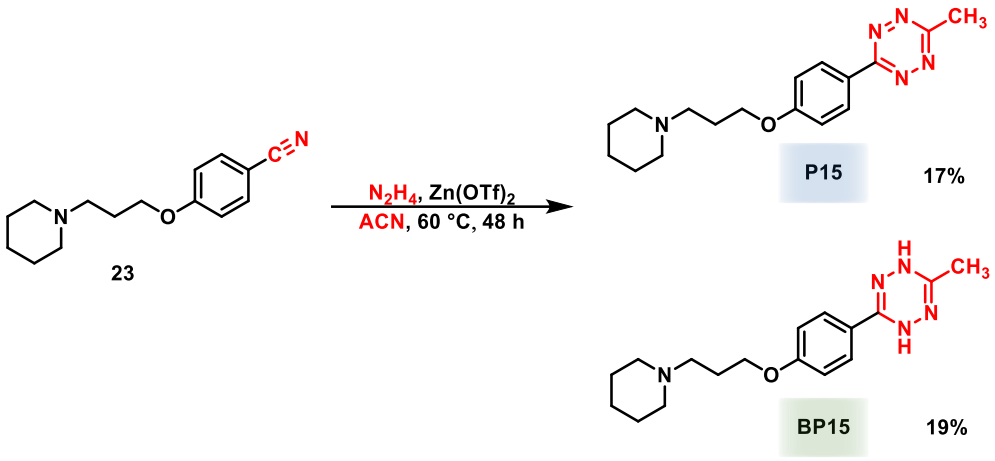

Figure 81: Reaction of the tetrazine ring formation of compound **23**, yielding tetrazine ligand **P15** and dihydrotetrazine byproduct **BP15**.

5.3 Binding profile assessment

All four synthesized tetrazine-containing compounds (**P14a-c, P15**) and their reduced dihydrotetrazine counterparts (**BP14a-c, BP15**) were subjected to H_3R affinity measurements to establish their binding properties (see Table 8). While the dihydrotetrazines are not capable of undergoing click chemistry reactions, they were still included in the binding studies to evaluate their potential as H_3R ligands. Notably, they showed high affinities with K_i values ranging from 6.8 to 38.3 nM, establishing them as potent H_3R ligands. The tetrazines, designed as molecular tools for click chemistry applications, displayed strong binding properties as well with K_i values ranging from 18.2 to 94.6 nM. The results demonstrate that the linker length between H_3R pharmacophore and methyl tetrazine click moiety does not influence receptor binding, with all linker-containing compounds having overlapping confidence intervals. As shown by compound **P15** (K_i = 32.2 nM), the presence of a linker is not even necessary for maintaining high H_3R affinity, once again demonstrating the robustness of the selected pharmacophore.[595,628] Having established that neither linker length nor presence affects H_3R binding, these compounds already meet a key requirement as molecular tools through their high receptor affinity. The tetrazine moiety's accessibility for click reactions, representing the second key feature for their application, would require further evaluation through labelling experiments to determine both the necessity and optimal length of the linker system for efficient biorthogonal labelling.

Table 8: Affinity of the tetrazine compounds **P14a-c** and **P15**, as well as their dihydrotetrazines counterparts **BP14a-c** and **BP15** for the histamine H_3 receptor.

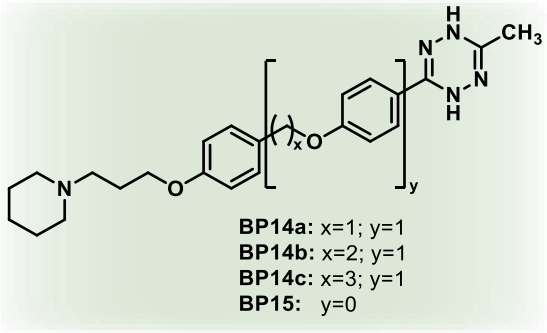

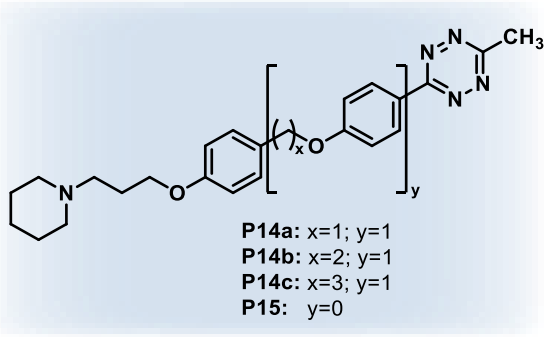

Class	Compound	Linker	hH_3R K_i (nM) [95% CI]
Dihydrotetrazines	**BP14a**	y=1; x=1	**30.4** [10.6; 87.1]
	BP14b	y=1; x=2	**38.3** [19.6; 74.9]
	BP14c	y=1; x=3	**14.7** [4.90; 43.4]
	BP15	y=0	**6.8** [5.5; 8.4]
Tetrazines	**P14a**	y=1; x=1	**18.2** [5.60; 59.8]
	P14b	y=1; x=2	**94.6** [39.5; 227]
	P14c	y=1; x=3	**32.2** [9.10; 114]
	P15	y=0	**25.6** [10.5; 62.1]

5.4 Proof-of-concept

After establishing the high-affinity binding profile for the H_3R receptor, the next step involved investigating the capability of these novel ligands to undergo IEDDA click reactions in chemical batch reaction, thereby confirming their potential for biorthogonal click chemistry applications. Compound **P15** was selected as a representative example for these studies due to its straightforward structure without a linker, eliminating variables such as conformational flexibility[703] and potential electronic effects.[704] This simplified structure allowed for clear interpretation of results and establishment of a proof-of-concept for the click chemistry approach. Additionally, its more direct synthesis route and higher yields made it the most practical choice for obtaining sufficient material for comprehensive method development studies.

5.4.1 Click chemistry

For proof-of-concept, a synthetic route was designed to generate a fluorescent ligand from compound **P15** using click chemistry, thereby demonstrating the tetrazine ligands' click chemistry capability (see Figure 82). First, **P15** would undergo an IEDDA click reaction with a ring-strained amino-functionalized norbornene derivative (**24**), yielding a constitutional isomer mixture of click products **25a/b**, depending on the norbornene derivative's orientation during the reaction. Subsequently, the primary amino function would get coupled to a commercially available fluorophore via HATU-mediated amide formation, resulting in the respective isomer mixture **P16a/b**. For this fluorescent labelling approach, BODIPY-FL was selected as the fluorophore due to its favourable properties, including high quantum yield, photostability, and small molecular size.[705] The reaction sequence itself was strategically designed to maximize efficiency with valuable reagents and does not reflect physiological cellular conditions in the second step. While direct labelling with fluorophore-modified dienophiles would be the method of choice for labelling experiments,[706] where only nano- to micromolar quantities are needed, the selected two-step approach proved optimal for batch synthesis scale. This strategy minimizes both the risk of losing expensive fluorophore-modified compounds and avoids potential loss of material during an initial fluorophore coupling step. Although this sequence differs from labelling protocols, it effectively demonstrates the click chemistry capability of the synthesized tetrazine ligands.

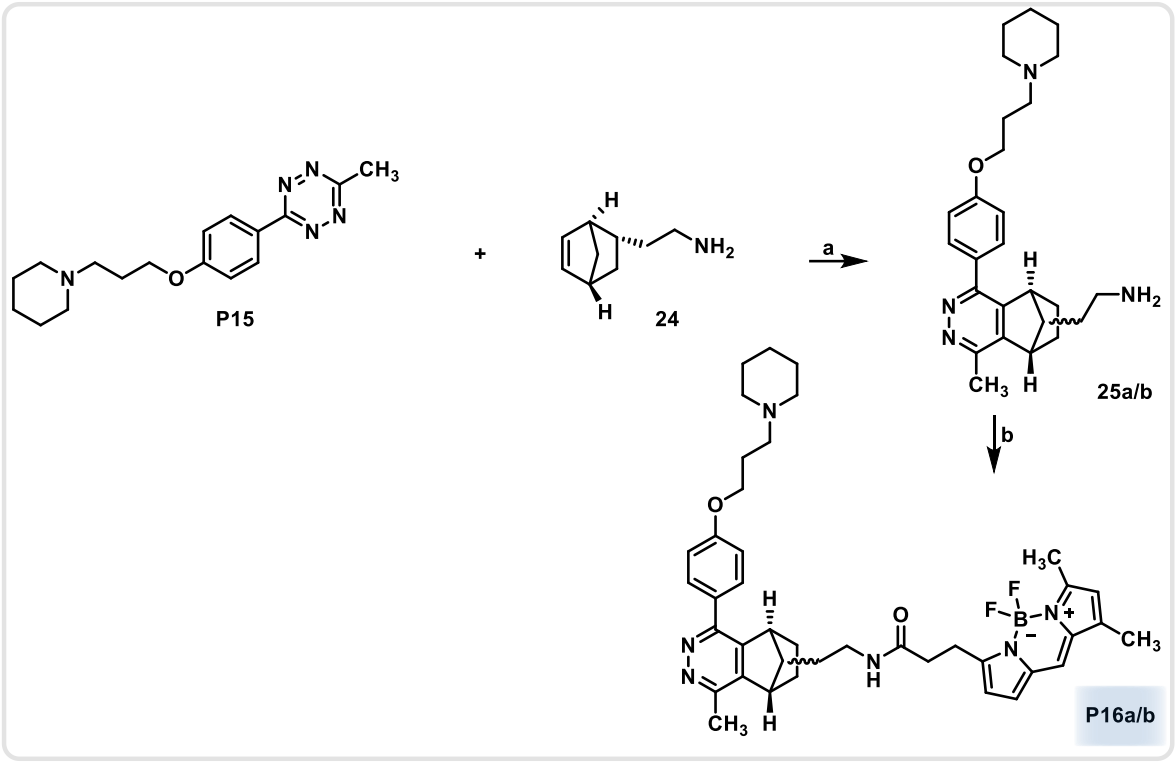

Figure 82: Planned synthetic route for the synthesis of fluorescent H_3R ligand **P16a/b** via IEDDA click reaction with **P15** for proof-of-concept. Reaction conditions: a) PBS, 37 °C, 24 h. b) HATU, DIPEA, BODIPY-FL, DMF, room temperature, 20 h.

In executing this strategy, the initial IEDDA reaction between **P15** and norbornene derivative **24** was performed in PBS buffer at 37 °C to simulate *in vivo* conditions (see Figure 83).[707] Following the mechanism[708] described and discussed in Figure 31 the reaction yielded a constitutional isomer mixture of the product (**25a/b**) in a ratio of 70:30, with the predominant isomer (**25b**) showing the ethylamine linker pointing away from the H_3R pharmacophore, reflecting the preferred orientation of the dienophile during the IEDDA reaction due to minimized steric hindrance.

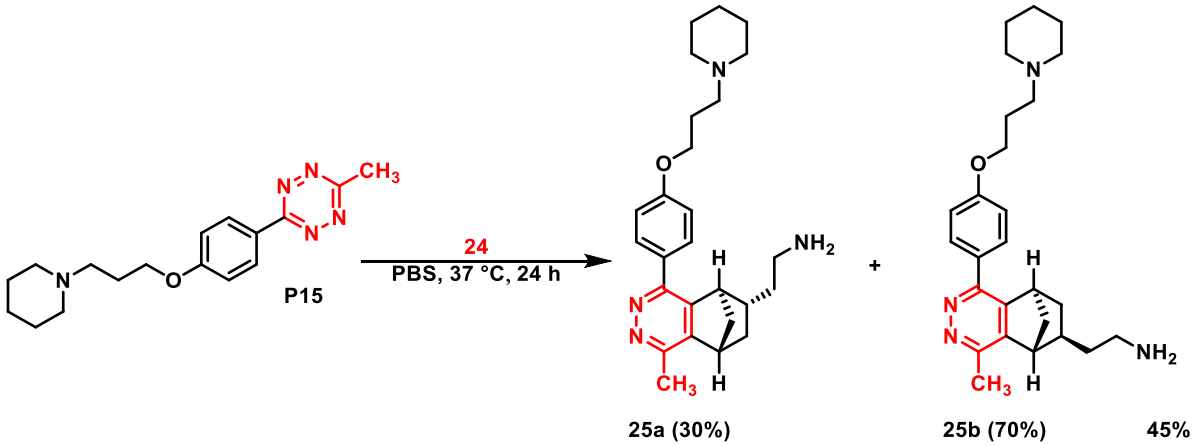

Figure 83: Reaction of the IEDDA reaction between **P15** and norbornene derivative **24** for proof-of-concept, yielding the constitutional isomer mixture of products **25a/b**.

5.4.2 Reaction control

The reaction progress was monitored by LC-MS (see Table 9) to gain deeper insights into the click reaction kinetics. The analysis revealed complete consumption of the tetrazine starting material **P15** after 24 hours. While the initial rapid product formation of 23% after just 30 minutes demonstrated the viability of the click reaction, the yield reached a plateau of approximately 50% between three to seven hours, showing even a slight decrease to 45% after 24 hours, likely due to minor product degradation over the extended reaction times. During this period, also several side products were formed, first detected after three hours with their concentrations increasing over time, which correlates with the observed product plateau. These byproducts showed a clear progression from 14% at three hours to 40% by 24 hours, likely originated from tetrazine degradation processes, such as photoinduced dimerization/oligomerization[709] or hydrolysis[710] due to the aqueous medium. The detection of unreacted norbornene derivative (**24**), remaining at 15% after 24 hours despite complete tetrazine consumption, further supported this degradation hypothesis, indicating incomplete conversion in the click reaction and suggesting competition between tetrazine decomposition and the IEDDA transformation.

These experimental constraints primarily stemmed from the high concentrations required for this batch synthesis, which necessitated extended reaction times and additionally led to solubility issues in the PBS medium. To address these challenges, the use of a more reactive dienophile like TCO,[711] commonly employed in tetrazine chemistry,[712] would significantly enhance reaction kinetics and therefore reduce reaction times, though its high cost precluded its utilization in this batch scale synthesis. Meanwhile, the degradation complications could be minimized by protecting the reaction from light to prevent photodegradation of the tetrazine,[709] and optimizing reagent stoichiometry,[713] particularly ensuring excess norbornene to promote complete consumption of **P15** before degradation pathways become significant.

While these challenges were significant for the proof-of-concept batch synthesis, they should not affect the intended labelling applications of these ligands. At the significantly lower concentration ranges typical for labelling experiments, solubility issues and thus reactant availability should be considerably improved, leading to shorter reaction times. Although the tetrazine accessibility in receptor-bound states still requires further investigation, this proof-of-concept batch synthesis successfully demonstrated the fundamental click chemistry capability of these tetrazine-based ligands under physiological conditions, with the observed rapid initial product formation being particularly promising for future labelling applications.

Table 9: Results of the LC-MS monitoring of the IEDDA click reaction between compound **P15** and dienophile **24**, mimicking physiological conditions.

Time (h)	Tetrazine **P15** (%)	Dienophile **24** (%)	Side products (%)	Product **25a/b** (%)
0	55	45	-	-
0.5	44	33	-	23
3	20	21	14	45
5	9	17	25	49
7	8	15	27	50
24	0	15	40	45

In addition to the LC-MS monitoring, the reaction progress can be conveniently monitored through visual observation, as the characteristic bright pink colour of the tetrazine ligand **P15** gradually fades during the reaction (see Figure 84). While this colour change provides a useful initial indicator of tetrazine consumption, complementary analytical techniques like LC-MS are necessary, as they enable accurate quantification of product formation and detection of colourless side products. Nevertheless, the visual monitoring serves as an excellent practical tool, offering immediate feedback during the reaction process.

Figure 84: Colour progression of the IEDDA click reaction between compound **P15** and dienophile **24**,

5.4.3 Fluorophore attachment

To finalize the synthesis of the envisioned fluorescent H_3R ligand, the crude isomeric mixture of click product **25a/b** was coupled with a commercially available carboxy-functionalized BODIPY-FL fluorophore (see Figure 85). The coupling reaction employed HATU in DMF at room temperature for 20 hours, following the mechanism described in Figure 57, to form the amide-linked fluorescent H_3R ligand **P16a/b** as an constitutional isomer mixture (70:30) in 36% yield. The moderate yield can be attributed to the low purity of the starting material (45% by LC-MS,

see Table 9), which likely affected the coupling efficiency through side product interferences and complicated the final purification process, resulting in additional product losses.

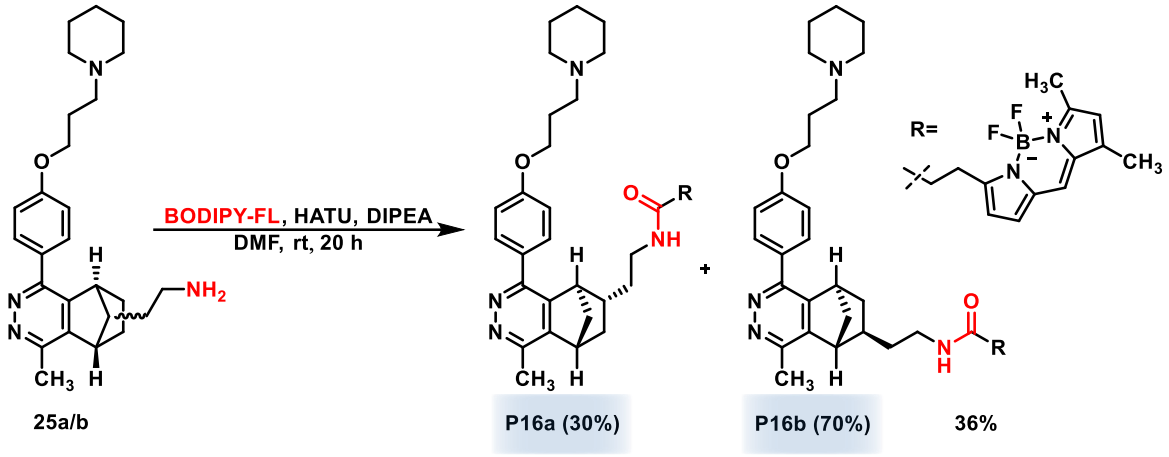

Figure 85: Reaction equation of the HATU-mediated coupling of click product **25a/b** with BODIPY-FL, yielding the desired fluorescent H_3R ligand **P16a/b**.

5.5 Characterisation as molecular tools

5.5.1 Binding profile

The successfully synthesized isomeric mixture of fluorescent ligand **P16a/b** was subsequently evaluated for H_3R binding affinity to assess its utility use as a fluorescent molecular tool. Since the fluorophore attachment occurred at the tetrazine moiety, leaving the H_3R pharmacophore unmodified, preservation of high H_3R affinity was anticipated, despite potential steric effects of the introduced bulky group.[714] This expectation was confirmed by the performed binding studies (see Table 10), which revealed that **P16a/b** maintains potent affinity for *h*H_3R (K_i = 11.1 nM). This observation indicates that the tetrazine moiety is likely positioned outside the binding pocket, as demonstrated by the maintained potent binding despite the bulky modification, since such alterations would likely cause steric interference if located within the receptor cavity. However, definitive conclusions about the accessibility of the tetrazine moiety would require further investigation through labelling studies.

5.5.2 Fluorescence properties

Having established the high H_3R affinity, the fluorescent properties of **P16a/b** were characterized as the second key feature of an effective fluorescent molecular tool. These evaluations were conducted in collaboration with Julius Krenzer from the working group of Prof. Müller (HHU, Düsseldorf), with detailed experimental procedures provided in the experimental section. Fluorescence characterization revealed an absorption maximum at 504 nm, closely matching that of the parent BODIPY-FL fluorophore (503 nm). Similarly, both compounds showed emission maxima at 511 nm, resulting in Stokes shifts of 7 cm^{-1} (**P16a/b**) and 8 cm^{-1} (BODIPY-FL), respectively (see Table 10, Figure 86). These spectral characteristics align well

with literature values[571] for unmodified BODIPY-FL, validating the experimental setup, while the nearly identical values observed for **P16a/b** confirm that this specific ligand conjugation preserves the fluorophore's photophysical properties. Notably, **P16a/b** exhibited an excellent quantum yield (Φ = 0.95) when excited at 475 nm, comparable to BODIPY-FL literature values, further strengthening its profile as a promising fluorescent H_3R ligand. Additionally, **P16a/b** has enabled the establishment and validation of a fluorescence displacement binding assay for H_3R that could potentially replace the typically used in-house radio displacement assay, further highlighting the utility of this fluorescent compound. The combination of strong H_3R affinity and excellent fluorescent properties not only establishes **P16a/b** as a valuable molecular tool for H_3R-targeted fluorescence studies, but its synthesis also provides proof-of-concept for the novel tetrazine-based H_3R ligands (**P14a-c**,**P15**) as versatile scaffolds for metal-free IEDDA click chemistry in biorthogonal crosslinking applications. Indeed, fluorescence labelling studies with these compounds are currently ongoing.

Table 10: Summary of the photophysical properties of **P16a/b** and BODIPY FL (determined values/literature values[571]), as well as the affinity of **P16a/b** for hH_3R.

Compound	hH_3R (nM) [95% CI]	Solvent	$\lambda_{max(Abs.)}$ (nm)	$\lambda_{max(Em.)}$ (nm)	Δλ (cm^{-1})	Φ_f
P16a/b	**11.1** [4.32; 28.3]	PBS buffer	504	511	7	0.95*
BODIPY-FL	-	PBS buffer	503/502	511/511	8/9	-/0.90

*λ_{exc} = 475 nm

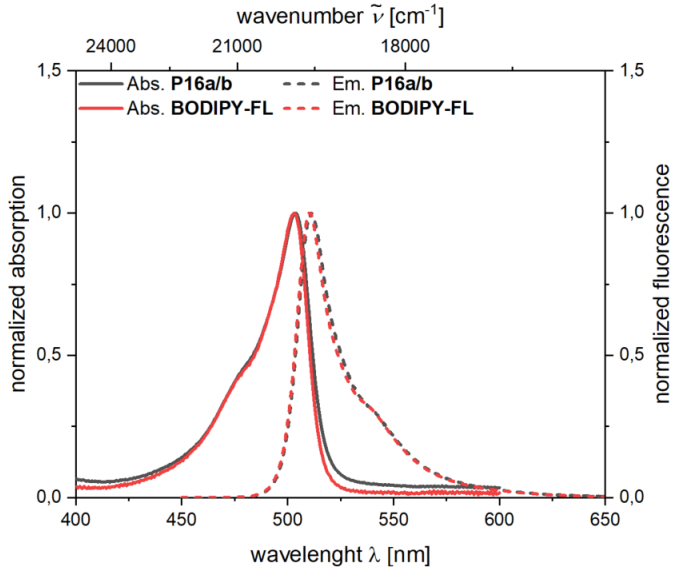

Figure 86: Normalized absorption and emission spectra of fluorescent H_3R ligand **P16a/b** and reference compound BODIPY-FL in PBS buffer.

5.5.3 Selectivity

The synthesized tetrazine-based ligands **P14a-c** and **P15** demonstrated excellent H_3R affinity and proved their click reaction capabilities, as exemplified by compound **P15**, fulfilling the two key requirements for their use as molecular tools in biorthogonal click applications. However, selectivity is crucial for successful *in vitro* and *in vivo* crosslinking applications to avoid off-target effects. Therefore, comprehensive selectivity studies were conducted with **P15** against related GPCRs to validate its practical utility. Additionally, the selectivity of the highly potent fluorescent ligand **P16a**/b was investigated. The results (see Table 11) revealed that both compounds exhibit great selectivity for H_3R. While they show almost no interaction with most tested receptors, including D_2R which is particularly relevant due to its potential to form heterodimers with H_3R,[167] only slight H_1R binding was detected. However, these H_1R affinities remains inconsequential when compared to the compounds potent H_3R activities (K_i = 32.2 nM for **P15** and K_i = 11.1 nM for **P16a/b**). This favourable selectivity profile, combined with the strong H_3R affinity and proven click capability demonstrated by **P15**, establish this novel ligand as a valuable molecular tool in metal-free IEDDA click chemistry mediated biorthogonal crosslinking applications investigating H_3R. Additionally, compounds **P16a/b** potent H_3R affinity and excellent selectivity profile validate its potential use as a fluorescent probe for H_3R investigation.

Table 11: H_1 and H_4 receptor and dopamine D_2 and D_3 receptor affinities of lead compounds **P15** and fluorescent ligand **P16a/b** for selectivity evaluation.

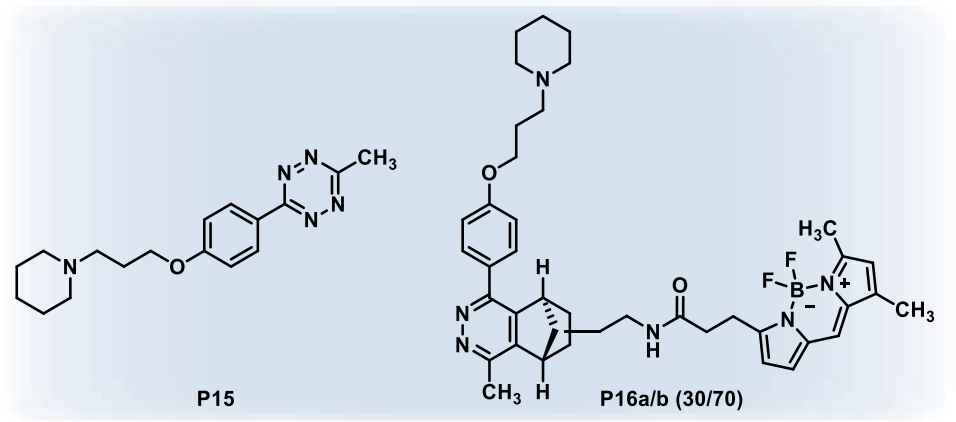

Compound	hH_1R (nM) [95% CI]	hH_4R (nM) [95% CI]	hD_2R (nM) [95% CI]	hD_3R (nM) [95% CI]
P15	**609** [424; 875]	**>10000**	**>10000**	**>10000**
P16a/b	**1382** [411; 4653]	**>10000**	**5048** [1576; 16173]	**5537** [1837; 16363]

5.6 Summary

This chapter presented the successful development of novel tetrazine-based H_3R ligands designed for metal-free IEDDA click chemistry applications. To achieve this goal, the rational design strategy focused on incorporating an IEDDA-capable methyl tetrazine click moiety[715] into the **JNJ-5207852**-derived H_3R pharmacophore,[595] both directly and through an alkyl phenol ether linkage system with varying alkyl chain lengths. Following this design concept, a robust synthetic route was established to deliver compounds **P14a-c** and **P15**, along with their respective IEDDA-incapable dihydrotetrazine byproducts (**BP14a-c** and **BP15**).In pharmacological evaluation, both the tetrazines and their dihydrotetrazine counterparts demonstrated excellent H_3R binding affinities (K_i = 18.2-94.6 nM and 6.8-38.3 nM, respectively), with the linker length showing no significant impact on receptor binding, establishing all compounds as potent H_3R ligands regardless of their click chemistry capabilities. As proof-of-concept for the IEDDA approach, the click chemistry capability of the tetrazine-based ligands was successfully validated using **P15** as a representative example, leading to the synthesis of a fluorescent H_3R ligand (**P16a/b**) that demonstrated both strong receptor affinity (K_i = 11.1 nM) and selectivity, as well as excellent fluorescent properties. Its value as a H_3R molecular tool in its own right was proved by establishing and validating a fluorescence displacement binding

assay for H_3R, highlighting the utility of fluorescent compound **P16a/b**. Completing **P15**'s profile as a potential valuable H_3R molecular tool for biorthogonal crosslinking applications, comprehensive selectivity studies revealed outstanding H_3R specificity, showing no observable binding towards related histamine and dopamine receptors. Building on these promising findings, the accessibility of the tetrazine moiety for click chemistry in a receptor-bound state remains a key question that requires further investigation through labelling studies. While the preserved H_3R affinity of the synthesized fluorescent ligand **P16a/b** suggests favourable positioning of the tetrazine outside the binding pocket, as steric interference from the bulky moiety would likely have led to reduced binding if located within the receptor cavity, labelling experiments are necessary to provide definitive confirmation.

Combined with their excellent H_3R affinity, click chemistry capability, and selectivity, the successful validation of tetrazine accessibility through the currently ongoing labelling experiments would ultimately establish these compounds, particularly **P15**, as valuable molecular tools for studying H_3R dynamics and interactions in biological systems through metal-free IEDDA click chemistry-mediated biorthogonal crosslinking applications.

6. Development of novel fluorescent H_3R molecular tools

This chapter describes the design, synthesis and biological evaluation of novel H_3R fluorescent ligands, exploring different fluorophore variations and H_3R pharmacophore attachment strategies, thereby expanding the molecular toolbox available for investigating this therapeutically relevant receptor.

6.1 Rational design

Despite advances in the development of fluorescent H_3R ligands, the limited diversity of available probes with varied photophysical properties highlights the need for an expanded molecular toolbox to enable comprehensive investigation of this therapeutically relevant receptor. This project aimed to address those limitations by developing novel H_3R fluorescent ligands, building upon the previous success with the potent fluorescent H_3R ligand **P16a/b**, to expand the existing toolbox for H_3R research even further, providing more options for receptor visualization and characterization studies. Since the development of fluorescent molecular tools represents a complex challenge, balancing the preservation of pharmacological activity of the chosen pharmacophore with excellent fluorescent properties,[560] this design approach focused on exploring different pharmacophore-fluorophore attachment strategies. To establish a strong pharmacological foundation, the H_3R antagonist **JNJ-5207852** was chosen to serve as the pharmacophore template to ensure high H_3R affinity, as this structure has demonstrated its robustness across different structural modifications.[595,628] Building upon this basis, BODIPY-based and fluorescein-based fluorophores were selected for the attachment strategies, standing out with their exceptional brightness, photostability, and versatile conjugation chemistry, properties that enable sophisticated applications from single-molecule tracking[716] to super-resolution imaging[717] and flow cytometry studies.[718]

In this study, two different pharmacophore-fluorophore attachment strategies were explored through direct merging of the pharmacophore with the fluorophore and connection of both moieties via linkers (see Figure 87). Following this concept, Set A investigated the merging approach by attachment of the 3-(piperidin-1-yl)propoxy H_3R warhead[669] onto fluorescein's xanthene structure, resulting in a merged structure, where the chromophore ring becomes an integral part of the H_3R pharmacophore, building on a design concept previously demonstrated with fluorescent H_3R ligand bodilisant.[268] In contrast, Set B pursued the linking approach by connecting both fluorescein-based and BODIPY-based fluorophores to the **JNJ-5207852**-derived pharmacophore[595,628] via linkers, leaving both structural elements unaltered. This dual strategy allows systematic exploration of the balance between H_3R affinity

and fluorescent properties through different chemical connectivity approaches of the respective structural components.

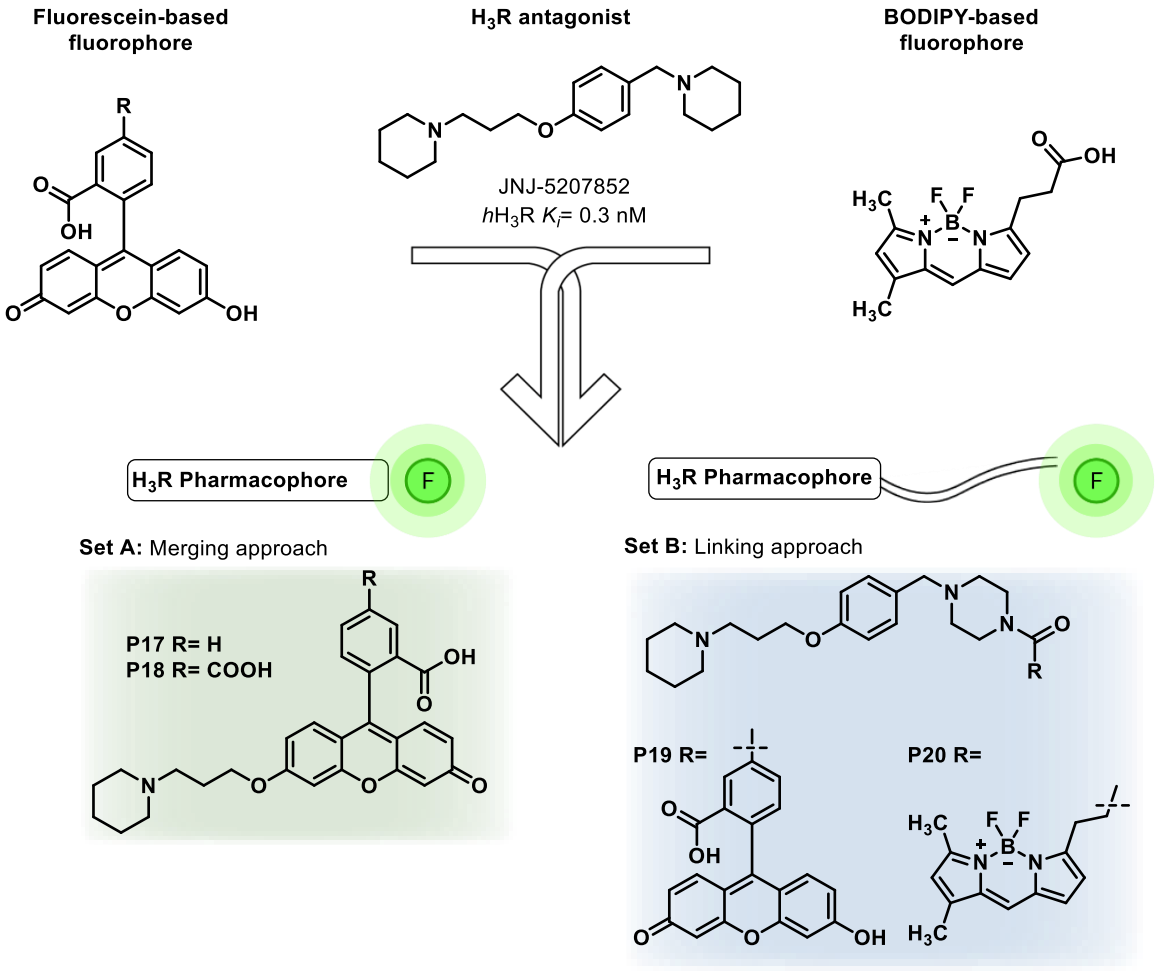

Figure 87: Rational design strategy for novel fluorescent H_3R ligands based on **JNJ-5207852** through two distinct attachment approaches: Set A (green) illustrating direct merging of pharmacophore and fluorophore and Set B (blue) displaying the linking strategy.

6.2 Synthesis

6.2.1 Merging approach

To establish the first set of compounds, merging the H_3R pharmacophore with fluorescein's chromophore was achieved through a simple alkylation reaction. The aromatic hydroxyl group of fluorescein's xanthene ring was alkylated with 1-(3-chloropropyl)piperidine hydrochloride **SM1**, resulting in the attachment of the H_3R antagonist warhead[669] on to the fluorophore. Within this merged design, the xanthene ring partially becomes an integral part of the H_3R pharmacophore by replacing the phenyl ring of the original **JNJ-5207852**-derived pharmacophore,[595] maintaining the essential aromatic moiety needed for π-π stacking interactions in the receptor's binding pocket.[163]

Central to this merging approach are fluorescein's phenolic groups at the xanthene structure, which are crucial for its photophysical properties since they modulate fluorescence through electron-donating effects and pH responsiveness.[565] Selective mono-alkylation of these groups, however, typically maintains the fundamental fluorescent functionality, resulting only in minimal, if any, changes to emission profiles and quantum efficiency,[719] thus supporting our merging strategy of attaching the H_3R pharmacophore through alkylation of the xanthene hydroxyl group. Based on these considerations, the alkylation reaction was performed using potassium carbonate in DMF under microwave conditions at 80 °C for 30 minutes, yielding fluorescent ligand **P17** (see Figure 88),[720] which was isolated as its acetate salt in 70% yield after reverse-phase flash chromatography using a water/acetonitrile gradient with acid additive. The reaction mechanism follows the same S_N2 pathway as depicted in Figure 36, with one key difference that no Finkelstein conditions were employed, thus no reactive alkyl iodide intermediate was formed *in situ* to facilitate the substitution.[597] Instead, the reaction proceeds through direct nucleophilic attack of the deprotonated hydroxyl group of fluorescein's xanthene ring on the alkyl chloride.

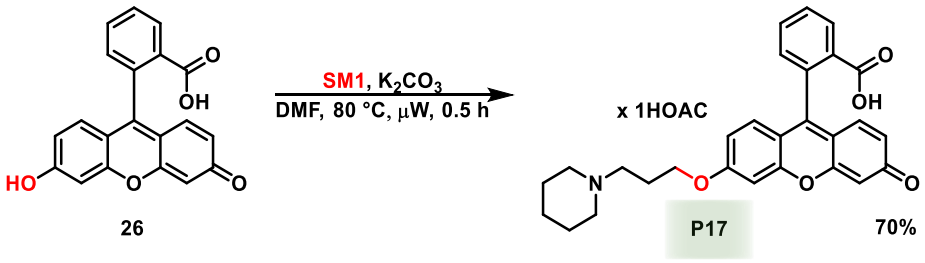

Figure 88: Reaction of the alkylation of fluorescein with 1-(3-chloropropyl)piperidine hydrochloride (**SM1**) under microwave conditions, yielding fluorescent H_3R ligand **P17**.

The second and final compound of Set A was synthesized following the same principle using 5-carboxyfluorescein (5-FAM) as fluorophore, which bears an additional carboxylic acid function at the 5-position of the phenyl ring (see Figure 89). Following the established protocol,[720] the alkylation was conducted under identical microwave conditions (80 °C, 30 minutes) using potassium carbonate as base in DMF, following the S_N2 mechanism shown in Figure 36, with the same key difference described for compound **P17**, yielding product **P18** in 45% yield. This relatively moderate yield can be attributed to competing alkylation at both the tertiary amine[603] and the carboxylic group in 5-position as well as to loss during the challenging purification due to the presence of both basic and acidic centres leading to zwitterionic forms.

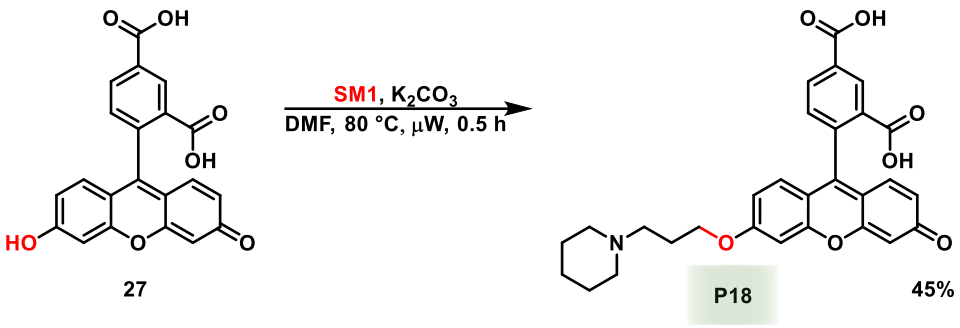

Figure 89: Reaction of the alkylation of 5-FAM with 1-(3-chloropropyl)piperidine hydrochloride (**SM1**) under microwave conditions, yielding fluorescent H_3R ligand **P18**.

6.2.2 Linking approach

In contrast to Set A, the ligands of Set B were designed to investigate a linking approach between fluorophore and H_3R pharmacophore, aiming to preserve the functionality of both components. This strategy required initial synthesis of an amino-functionalized H_3R pharmacophore that could subsequently be coupled to both BODIPY-FL and 5-FAM at its non-chromophoric 5-position carboxyl group.[565,721] Accordingly, the synthetic route was designed to start with alcohol **21**, which was previously synthesized as shown in Figure 76 and already contains the H_3R pharmacophore. From this starting point, the synthesis would proceed through chlorination of the hydroxyl group (**28**) to provide a better leaving group for subsequent nucleophilic substitution with Boc-piperazine (**29**). This step would introduce a cyclic amine-containing linker, while simultaneously demonstrating structural similarity to **JNJ-5207852**.[595] With the linker in place, deprotection would yield the free amine **30**, which then used for coupling with both fluorophores BODIPY-FL and 5-FAM to achieve the linker-containing fluorescent ligands **P19** and **P20** (see Figure 90).

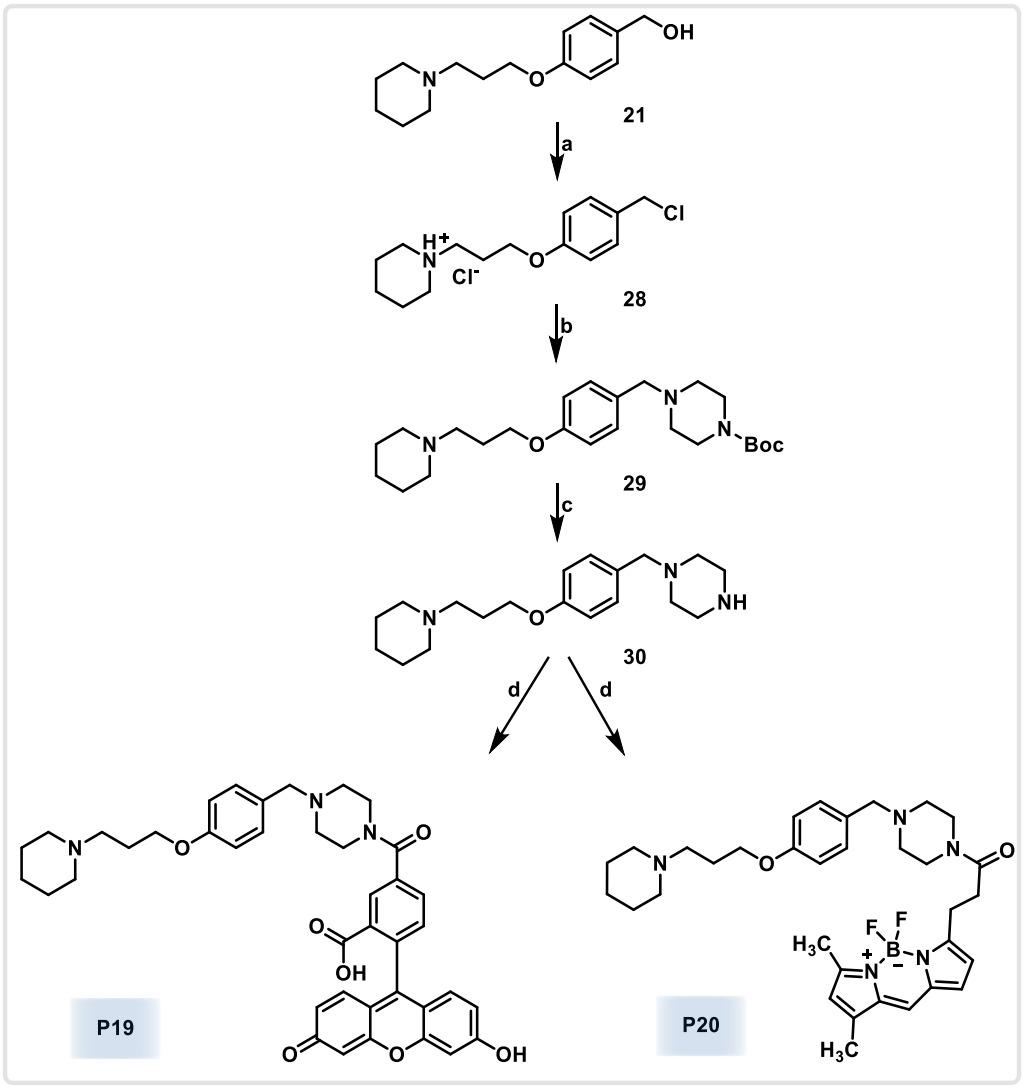

Figure 90: Planned synthetic route to fluorescent H_3R ligand **P19** and **P20** of Set B exploring the linking approach. Reaction conditions: a) thionyl chloride, THF, reflux, 2 h. b) 1-Boc-piperazine, KI, K_2CO_3, acetone, reflux, 48 h. c) HCl, methanol, room temperature, 20 h. d) HATU, DIPEA, 5-FAM/BODIPY-FL, DMF, room temperature, 20 h.

In the first step of the amino-functionalized H_3R pharmacophore synthesis, alcohol **21** was converted to the corresponding alkyl chloride **28** using thionyl chloride as chlorination reagent, introducing a better leaving group to facilitate subsequent linker installation via substitution. The reaction was conducted in THF at reflux for two hours, following the mechanism shown in Figure 43, yielding the product **28** quantitatively as hydrochloride salt (see Figure 91).[621]

Figure 91: Reaction of the chlorination of compound **21**, yielding compound **28**.

With the activated chloride in hand, the **JNJ-5207852**-inspired cyclic amine linker was introduced to the pharmacophore through substitution of the chloride in compound **28** with

1-Boc-piperazine serving as the nucleophile. The alkylation was performed under Finkelstein conditions for 48 hours, following the mechanism shown in Figure 36, delivering compound **29** in 79% yield (see Figure 92).[598]

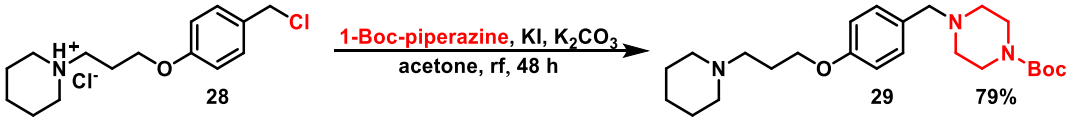

Figure 92: Reaction of the alkylation of compound **28** with 1-Boc-piperazine, yielding compound **29**.

Lastly, compound **29** was deprotected to yield the H_3R pharmacophore with its unprotected cyclic amine linker. The reaction followed the mechanism as depicted in Figure 65 and was conducted in methanol at room temperature using hydrochloric acid as proton source for 20 hours,[674] yielding the free base of compound **30** quantitatively after basic workup, providing the key intermediate for fluorophore attachment via the linking approach (see Figure 93).

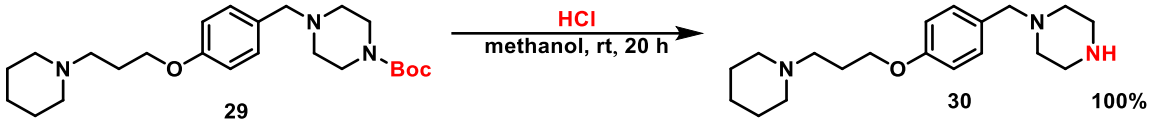

Figure 93: Reaction of the Boc deprotection of compound 29, yielding compound 30.

Taking advantage of the free amine, the H_3R pharmacophore building block **30** was coupled with 5-FAM (**27)** at its non-chromophoric 5-position carboxyl group,[721] implementing the linking strategy while preserving the structural integrity of both components, thereby aiming to maintain their respective properties. Following the mechanism depicted in Figure 57, the coupling was performed using HATU in DMF with DIPEA as base at room temperature for 20 hours, yielding the fluorescent H_3R ligand **P19** in 25% yield (see Figure 94).[644] The relatively low yield can be attributed to purification challenges arising from zwitterion formation due to the presence of both basic and acidic centres in the molecule.

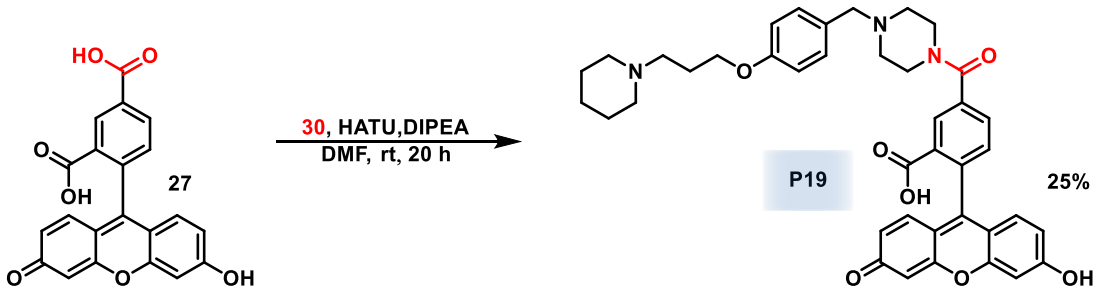

Figure 94: Reaction of the HATU-mediated coupling of 5-FAM (**27**) with compound **30**, yielding fluorescent H_3R ligand **P19**.

Completing the linking strategy, compound **30** was coupled with BODIPY-FL (**31**) to achieve the final compound of Set B. The HATU-mediated amide formation in DMF with DIPEA at room

temperature for two hours yielded fluorescent H_3R ligand **P20** in 45% yield (see Figure 95).[644] While the moderate yield is likely attributed to BODIPY's slight base sensitivity,[722] basic conditions are essential for successful amide formation via the HATU coupling mechanism[603,645] (see Figure 57). Although compound **30**'s inherent basicity could theoretically facilitate the required carboxylate activation, this leads to the formation of an ammonium carboxylate salt, necessitating the addition of base to prevent precipitation and assure solubility, as evidenced by unsuccessful coupling attempts without basic additive with this system.

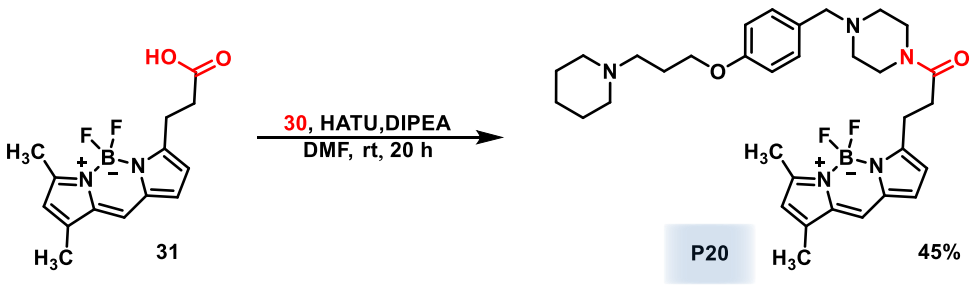

Figure 95: Reaction of the HATU-mediated coupling of BODIPY-FL (**31**) with compound **30**, yielding fluorescent H_3R ligand **P20**.

6.3 Characterisation as molecular tools

6.3.1 Binding profile

To evaluate the two different pharmacophore-fluorophore attachment approaches and their influence on preserving structural component properties, all four ligands (**P17-P20**) were subjected to affinity measurements towards the H_3R. The results revealed distinct differences between the two design strategies, providing valuable insights into optimal fluorescent ligand development. The merging approach (Set A), where the H_3R pharmacophore was partially integrated into the fluorescein chromophore by attaching the H_3R antagonist warhead[669] to the hydroxyl group of the xanthene core structure, resulted in only moderate to poor affinities (see Table 12). This reduced binding efficiency may be attributed to the replacement of the *para*-substituted phenyl ring of the parent pharmacophore with the bulky xanthene core structure of the fluorescein fluorophore, which could not only cause steric interference but also disrupt the phenyl ring's crucial π-π stacking interactions typically occurring within the aromatic cage of the binding pocket.[163] Moreover, the rigid annulated system may force the molecule into a different spatial orientation compared to the more flexible parent compound, potentially causing unfavourable positioning within the binding pocket. While these structural features affect both compounds of Set A, the significant difference in affinity between **P17** and **P18** can likely be explained by **P18**'s free carboxylic acid in the 5-position. This structural feature alters key physicochemical properties such as lipophilicity[723] and solubility,[724]

potentially affecting **P18**'s binding properties. Additionally, the deprotonated carboxylic acid function at physiological pH may disrupt binding pocket interactions through unfavourable electrostatic interactions and interference with essential hydrogen bonding networks.[725]

In contrast, Set B compounds, employing the linking approach, demonstrated excellent H_3R affinities (K_i = 21.1 - 30.1 nM). This superior affinity profile can likely be attributed to the preservation of the complete pharmacophore structure,[595,628] therefore maintaining its optimal binding characteristics.[726] The increased spatial separation between the fluorophore and pharmacophore through the incorporated linker may enable the bulky fluorescent moieties to position themselves either outside or at the surface of the binding pocket, minimizing interference with the typical binding mode. This hypothesis is supported by the observation that both fluorophore-containing compounds yield excellent affinities despite their different steric demands and molecular shapes.

Based on these promising results, Set B compounds were subsequently evaluated for their selectivity against related GPCRs (see Table 12). Gratifyingly, both **P19** and **P20** showed good selectivity with only insignificant binding to related GPCRs, including histamine receptors (H_1R, H_4R) and dopamine receptors (D_2R, D_3R), negligible compared to the strong binding towards H_3R (K_i = 21.1 - 30.1 nM), validating their potential as new fluorescent H_3R molecular tools.

Table 12: Histamine H_3 receptor affinities of ligands **P17-P20**, as well as H_1 and H_4 receptor and dopamine D_2 and D_3 receptor affinities of Set B compounds **P19** and **P20** for selectivity evaluation.

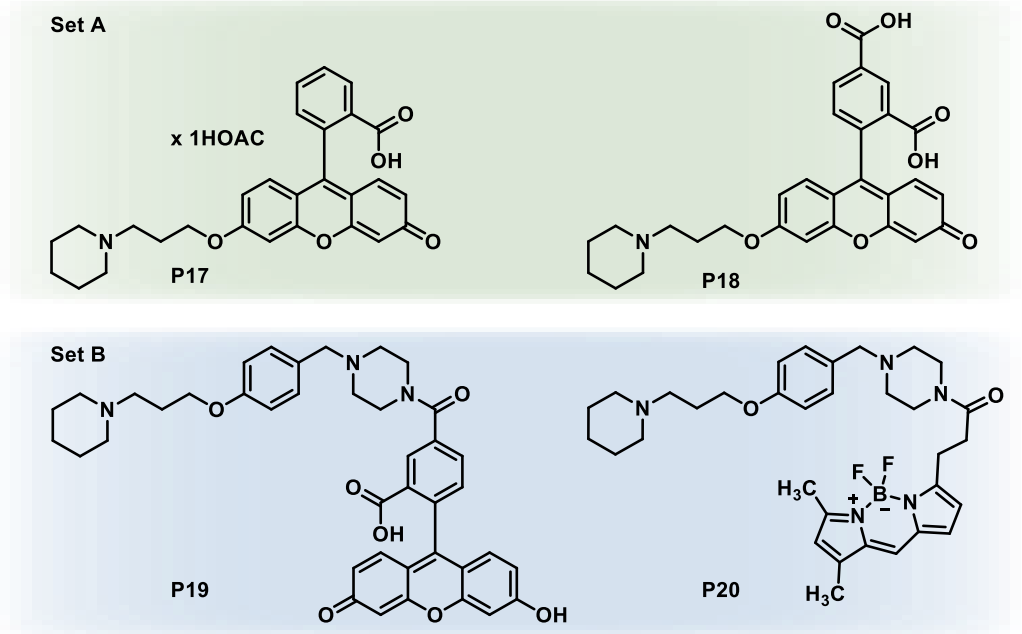

Set	Compound	hH_3R K_i (nM) [95% CI]	hH_1R K_i (nM) [95% CI]	hH_4R K_i (nM) [95% CI]	hD_2R K_i (nM) [95% CI]	hD_3R K_i (nM) [95% CI
Set A	**P17**	**608** [203; 1823]	**n.d.**	**n.d.**	**n.d.**	**n.d.**
	P18	**5175** [2444; 10956]	**n.d.**	**n.d.**	**n.d.**	**n.d.**
Set B	**P19**	**30.1** [12.8; 70.8]	**4786** [2116; 10824]	**>10000**	**7168** [5082; 10109]	**>10000**
	P20	**21.1** [7.88; 56.6]	**873** [575; 1326]	**>10000**	**2740** [904; 8309]	**4662** [1244; 17471]

*n.d.= not determined

6.3.2 Cytotoxicity

Having demonstrated both excellent affinity and selectivity profiles, the Set B compounds were further evaluated for their cytotoxic properties on a SH-SY5Y cell line (see Figure 96). While compound **P19** showed 100% cell viability at 100 µM, compound **P20** exhibited only 4% cell survival at this concentration. However, when evaluated at 10 µM, compound **P20** also demonstrated 100% cell viability. Given that this concentration range (10 µM) is still several

orders of magnitude higher than the nanomolar concentrations required for its intended biological applications, both compounds can be considered non-cytotoxic, fulfilling yet another key requirement for their envisioned use in fluorescence-based H_3R studies.

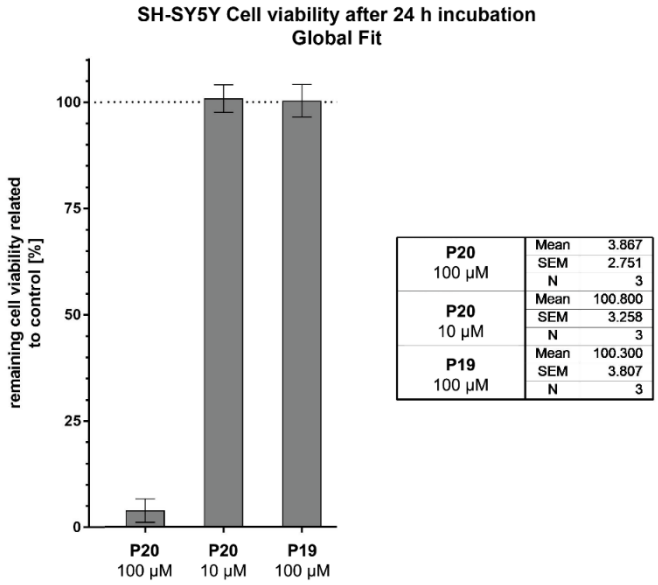

Figure 96*:* Cell viability of SH-SY5Y cell line after 24 h incubation with the fluorescent ligands **P19** and **P20** at a concentration of 100 µM and 10 µM.

6.3.3 Fluorescence properties

Having established the excellent pharmacological profiles of Set B compounds **P19** and **P20**, their fluorescent properties were subsequently investigated in collaboration with Julius Krenzer from the working group of Prof. Müller (HHU, Düsseldorf), to validate their potential as molecular imaging tools. The spectroscopic characterization revealed that both compounds largely maintain the excellent photophysical properties of their parent fluorophores. The absorption and emission maxima closely match those of the unmodified fluorescent scaffolds (see Figure 97), and together with the Stokes shifts also align well with literature values,[565,571] validating the experimental setup. This preservation of spectral characteristics expectedly confirms that the attachment of the H_3R pharmacophore through the linking strategy does not interfere with the fluorophores' electronic properties. However, the quantum yields measured in PBS buffer showed a slight decrease compared to their parent compounds, retaining 83% and 67% of the original values, respectively (see Table 13). This reduction can likely be attributed to additional molecular flexibility introduced by the linker region, enabling non-radiative relaxation pathways.[727] Nevertheless, both compounds exhibit robust fluorescent properties under physiological conditions, supporting their suitability as fluorescent tools in H_3R targeted imaging studies, thus successfully completing the envisioned design of these H_3R fluorescent ligands.

Table 13: Summary of the photophysical properties of **P19** and **P20** with BODIPY FL and 5-FAM as references (determined values/literature values,[565,571]).

Compound	Solvent	$\lambda_{max(Abs.)}$ (nm)	$\lambda_{max(Em.)}$ (nm)	Δλ (cm^{-1})	Φ_f	Φ_f/Φ_{f0}
P19	PBS buffer	493	520	27	0.76*	83%
5-FAM	PBS buffer	492/492	518/516	26/24	0.92	-
P20	PBS buffer	503	511	8	0.60*	67%
BODIPY-FL	PBS buffer	503/502	511/511	8/9	-/0.90	-

*λ_{exc} = 475 nm

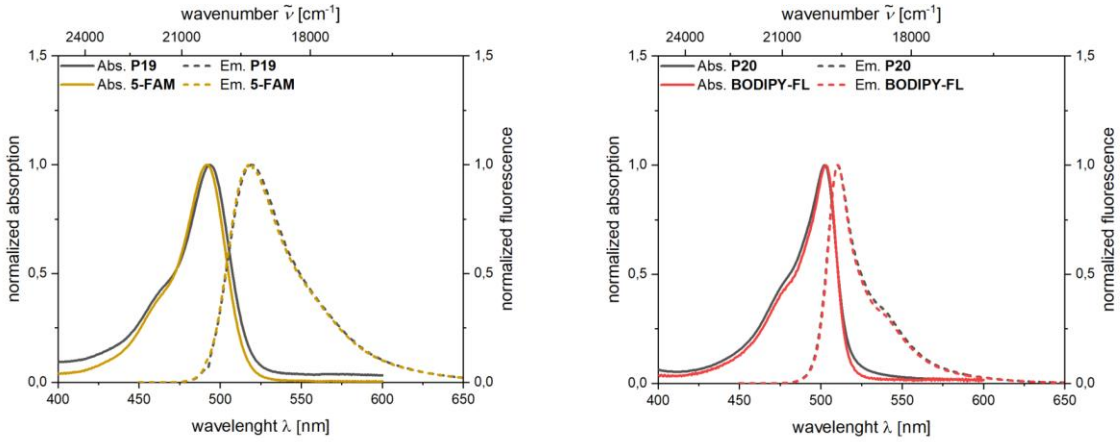

Figure 97: Normalized absorption and emission spectra of fluorescent H_3R ligand **P19** and reference compound 5-FAM in PBS buffer (left) and of fluorescent H_3R ligand **P20** and reference compound BODIPY-FL in PBS buffer (right).

6.4 Summary

This chapter presented the successful development of novel fluorescent H_3R ligands through systematic investigation of two distinct pharmacophore-fluorophore attachment strategies. The rational design strategy explored both direct merging of the **JNJ-5207852**-derived H_3R pharmacophore[595] with fluorescein-based fluorophores (Set A), as well as its connection via **JNJ-5207852**-inspired piperazine linkers to fluorescein-based and BODIPY-based fluorophores (Set B). Pharmacological evaluation revealed distinct differences between these strategies, with the merging approach yielding only moderate to low H_3R affinities (K_i = 608 - 5175 nM), likely due to steric interference and disruption of key binding interactions. In contrast, the linking strategy delivered the highly potent compounds **P19** and **P20**

(K_i = 21.1 - 30.1 nM), presumably because of spatial separation that enables optimal positioning of both pharmacophore and fluorophore components, allowing to preserve the parent pharmacophore's binding mode.[726] Set B compounds furthermore demonstrated excellent selectivity profiles (K_i > 10,000 nM) and favourable cytotoxicity characteristics at relevant concentrations. Following the promising pharmacological results, spectroscopic analysis confirmed the preservation of fluorescent properties, with absorption and emission characteristics matching their parent fluorophores and quantum yields retaining a substantial 67-83% of original values. These findings establish the herein reported linking strategy as the superior approach compared to the merging strategy, successfully delivering new fluorescent molecular tools with excellent pharmacological and spectroscopic properties, expanding the available H_3R research repertoire. Future developments may focus on applying this linking strategy with alternative fluorophores, such as near-infrared dyes, to enable deeper tissue imaging and reduce background autofluorescence, further broadening the applicability of these probes in biological studies.

Part III
Fluorescent ligands for H_4R

7. Development of novel fluorescent H_4R ligands

This chapter describes the design, synthesis and biological evaluation of novel H_4R fluorescent ligands based on three different lead structures exploring systematic variations in pharmacophore-fluorophore attachment composition through varying linker types and lengths, as well as different linker attachment positions and connection chemistries at the respective pharmacophore.

7.1 General rational design

Although several potent H_4R ligands are already known, they consistently lack sufficient selectivity over other histamine receptor subtypes. This highlights the urgent need for highly selective, potent fluorescent H_4R ligands that can reliably identify H_4R in complex biological environments where multiple histamine receptor subtypes are co-expressed. To address this critical research gap, this project aimed to develop novel H_4R-selective fluorescent ligands, designed to function as molecular tools for receptor visualization, localization, and characterization, potentially providing valuable means to investigate the discussed hypothesis of H_4R localization in brain tissues. Given that creating effective fluorescent molecular tools demands a sophisticated balance between maintaining pharmacological activity and incorporating suitable fluorescent properties, this design approach focused on a systematic exploration of multiple structural variables in pharmacophore-fluorophore attachment composition. In this context, to establish a strong pharmacological foundation, three well-characterized H_4R ligands were selected: the selective antagonist **JNJ-7777120 (R31)**,[728] the antagonist **VUF-10558 (R34)**,[353] and the promising in-house developed ligand **ST-2529**. As the fluorescent component, BODIPY-FL was chosen, distinguished by its excellent photophysical properties[571] and potential for structural expansion toward near-infrared derivatives,[729] enabling tissue-preserving visualization assays.[730,731] Following the design concept, multiple linker implementation strategies were supposed to be explored to evaluate their impact on both pharmacological and fluorescent properties. The investigation encompassed variations in linker type and length, ranging from ethyl to hexyl chains and mono- to tri-ethylene glycol units, serving to establish the optimal spatial distance between pharmacophore and fluorophore, as well as different connection types to the pharmacophore including amide, ether, and secondary amine bonds. Additionally, various attachment points on the pharmacophore were evaluated to determine their effect on H_4R affinity. This design strategy (see Figure 98) provided a systematic approach to developing a series of fluorescent ligands, allowing for comprehensive exploration of structure-activity relationships through evaluation of varying linker lengths, properties, and connection types between the structural

components, ultimately optimizing H_4R affinity and selectivity alongside fluorescent properties for their potential application as molecular tools.

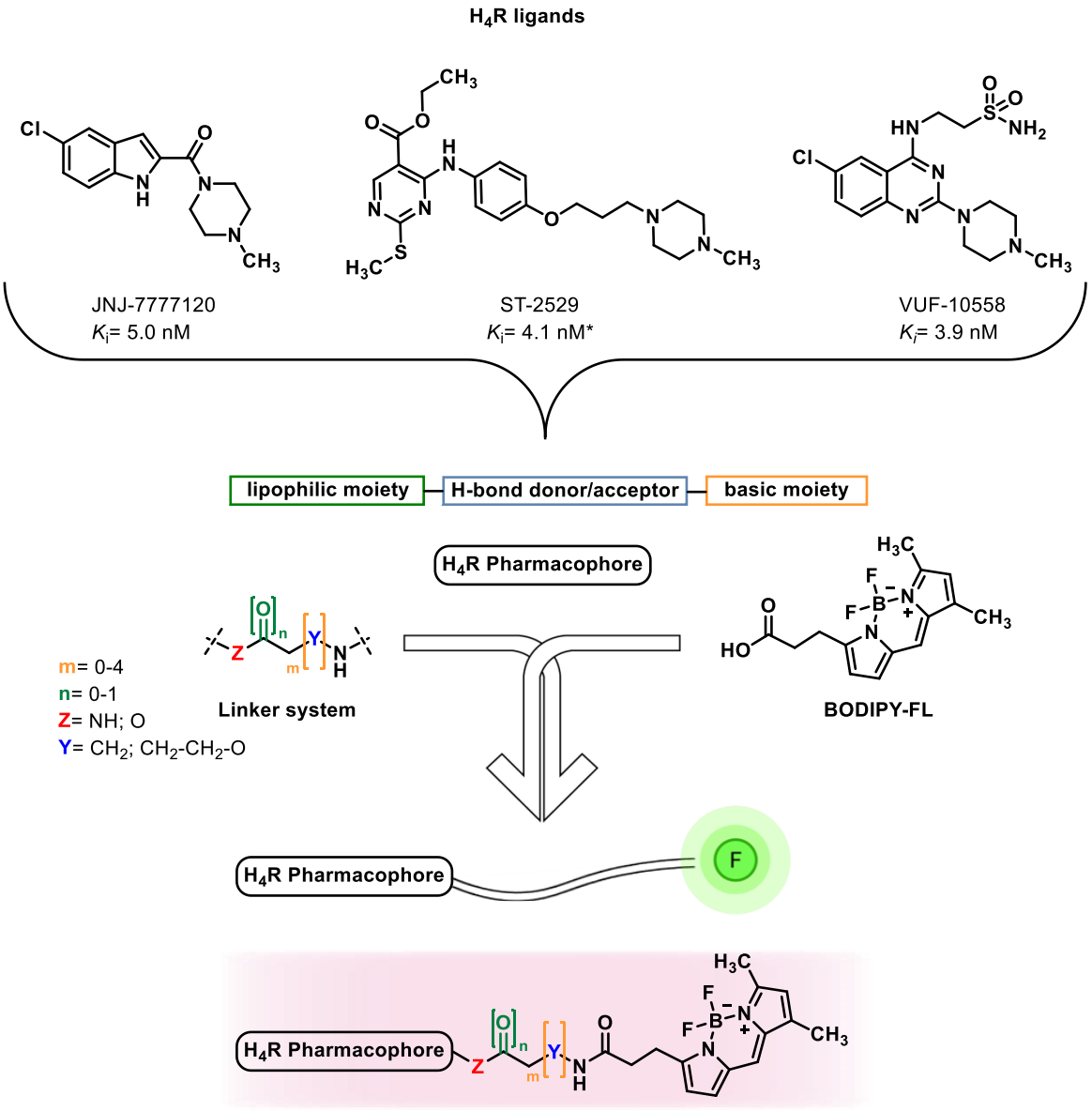

Figure 98: Rational design strategy for novel fluorescent H_4R ligands based on three H_4R lead structures (**JNJ-7777120**, **VUF-10558**, **ST-2529**) exploring systematic variations in pharmacophore-fluorophore attachment composition through different linker types, lengths, and connection points. *in-house value of initial testing result

7.2 Fluorophore synthesis

The planned synthesis of these various H_4R fluorescent ligands required the initial preparation of BODIPY-FL. Given the substantial quantities needed for this project, in-house synthesis proved more economically viable than commercial procurement. Therefore, a synthetic route was designed (see Figure 99), commencing with a Wittig reaction of aldehyde **32**, yielding the α,β-unsaturated compound **33**. Following palladium-catalysed reduction of the double bond, the yielded pyrrole **34** would subsequently undergo a one-pot fluorophore synthesis to

complete the chromophore assembly (**35**). Final cleavage of the ester group would deliver the free carboxylic acid, needed for coupling reactions to the amino-functionalized linker systems.

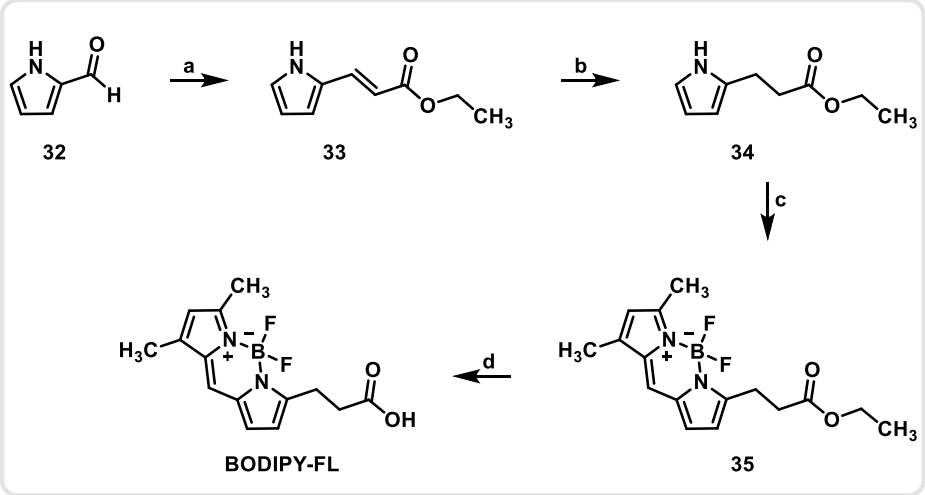

Figure 99: Planned synthetic route for the fluorophore BODIPY-FL, needed for the synthesis of the various H_4R fluorescent ligands. Reaction conditions: a) (ethoxycarbonyl-methyl)triphenylphosphonium bromide, dioxane, 70 °C, 49 h. b) Pd/C, H_2, methanol, room temperature, 20 h. c) phosphorus oxychloride, boron trifluoride etherate, DIPEA, DCM, room temperature, 24 h. d) HCl, THF, room temperature, 24 h.

In the first step of the BODIPY-FL synthesis, a Wittig reaction is employed to attach the side chain that will later serve as the linker coupling site. The reaction was performed between pyrrole **32**, which forms the basis for the later chromophore, and the respective Wittig reagent at 70 °C for 48 hours. This reaction proceeded with excellent efficiency, yielding the desired product in 91% yield.[732] The mechanism[603,733] starts with the nucleophilic attack of the carbon of the ylide at the aldehyde group of pyrrole **32**, establishing the crucial C-C connection and leading to the breaking of the carbonyl C=O double bond (**TS1**). The resulting negatively charged oxygen atom then attacks the positively charged phosphorus atom, forming a four-membered oxaphosphetane ring intermediate (**TS2**). This ring subsequently cleaves to form triphenylphosphine oxide and the desired α,β-unsaturated ester product **33** (see Figure 100), a transformation driven by the formation of the thermodynamically favourable phosphorus-oxygen double bond in the triphenylphosphine oxide byproduct.[643]

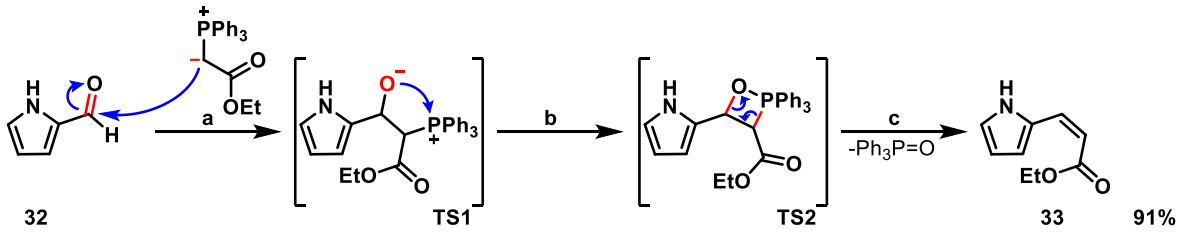

Figure 100: Mechanism of the Wittig reaction to produce the BODIPY-FL building block **33** a) Nucleophilic attack of the ylid b) Formation of oxaphosphetane ring c) Ring cleavage.

In the following step, the α,β-unsaturated side chain of compound **33** was reduced to its saturated form via hydrogenation under palladium catalysis. The reaction was performed in methanol at room temperature for 20 hours, yielding the product in 75% yield after purification.[734] The mechanism,[568] as depicted in Figure 101, begins with the adsorption of the C-C double bond of **33** to the palladium-coated charcoal surface (**TS1**), followed by the adsorption of hydrogen at the surface as well (**TS2**). Subsequently, a hydrogen atom is transferred to the β-position of the double bond, leading to the cleavage of the C-C double bond, with the molecule remaining adsorbed to the palladium surface through the electron pair formerly involved in the double bond formation (**TS3**). Finally, a second hydrogen atom is transferred to the α-position, releasing the reduced saturated product **34** from the charcoal surface (**TS4**).

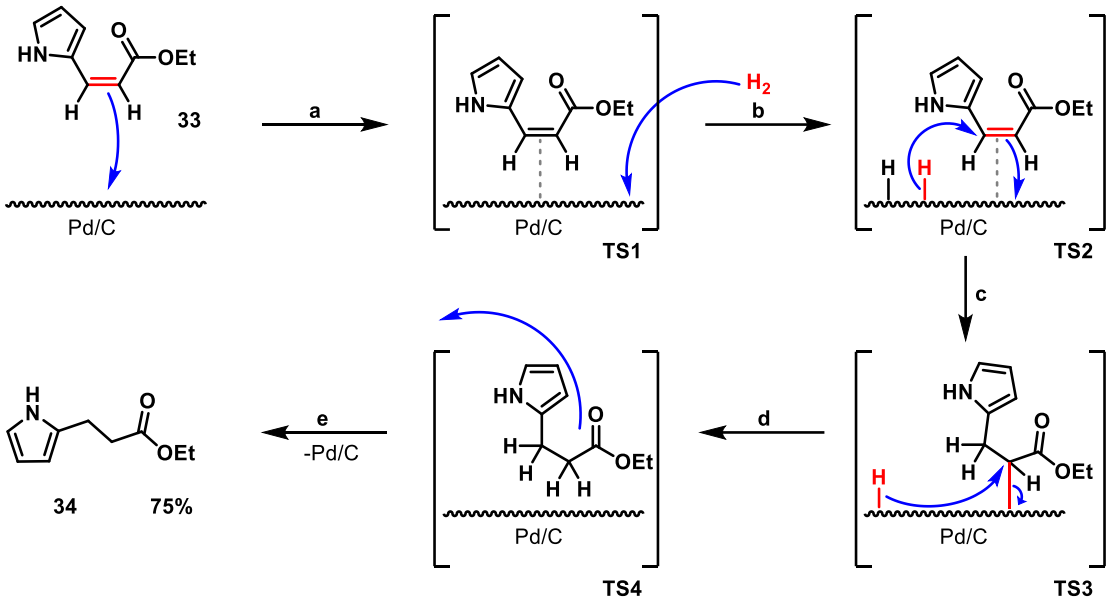

Figure 101: Mechanism of the palladium-catalysed reduction of compound **33**, yielding the α,β-saturated product **34**. a) Adsorption of **33** b) Adsorption of hydrogen c) Hydrogen transfer d) Hydrogen transfer e) Release of product **34**.

Compound **34** was then combined with pyrrole **36** in a one-pot synthesis to construct the chromophore of the desired BODIPY-FL fluorophore. The synthesis was conducted in DCM with phosphoryl oxychloride leading to the condensation intermediate, followed by addition of DIPEA and boron trifluoride etherate as complexation agent. The reaction proceeded at room temperature for 24 hours, yielding the desired fluorescent product **35** in 65% yield.[734] The mechanism,[568] as shown in Figure 102, is initiated by the nucleophilic attack, prepared through intramolecular electron distribution, of the 2-position carbon of the pyrrole ring of **34** at the aldehyde group of **36**, leading to the cleavage of the carbonyl double bond. The resulting negatively charged oxygen atom then attacks the proton at the 2-position, leading to rearomatization of the pyrrole ring (**TS1**). The resulting hydroxyl group of **IM1** then attacks the

phosphoryl oxychloride, which after hydrochloric acid elimination provides a good leaving group (**TS2**). Through intramolecular electron distribution, the phosphor-species is eliminated (**TS3**), establishing a conjugated chromophore system connecting both pyrrole rings (**IM2**). Deprotonation of one pyrrole ring by DIPEA enables the system to coordinate a boron species derived from boron trifluoride etherate (**TS4**), delivering the final fluorescent product **35**.

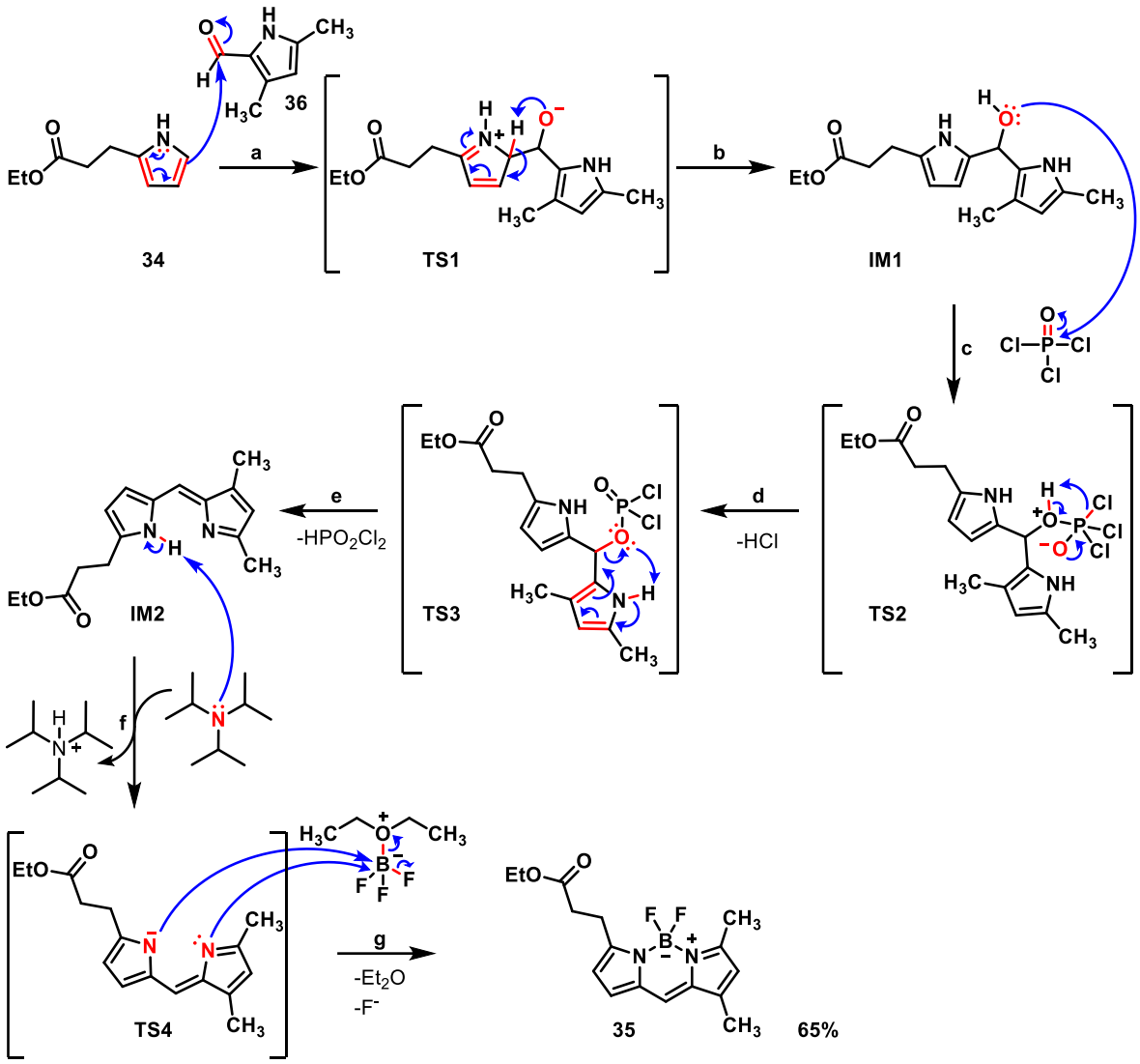

Figure 102: Mechanism of the one-pot fluorophore synthesis of compound **35**. a) Nucleophilic attack of compound **34** b) Rearomatization c) Nucleophilic attack of **IM1** d) Elimination of hydrogen chloride e) Establishment of conjugated system f) Deprotonation of pyrrole g) Coordination of Bor-species.

In the final step of the fluorophore synthesis, the ester of the side chain needed to be cleaved to release the carboxyl group required for linker attachment. Due to the sensitivity of the BODIPY system in basic media,[722] the ester cleavage was performed under acidic conditions. The reaction was carried out in a THF/water mixture with hydrochloric acid at room temperature for 24 hours, yielding the product in 84% yield.[735] The mechanism,[736] as depicted in Figure 103, begins with the protonation of the ester carbonyl group (**TS1**) leading to reduction

of electron density, which enables a nucleophilic attack of water at the carbonyl carbon. After intramolecular proton transfer (**TS2**), ethanol is eliminated (**TS3**), releasing the protonated acid species (**TS4**). Finally, deprotonation by the chloride counterion delivers the final BODIPY-FL product.

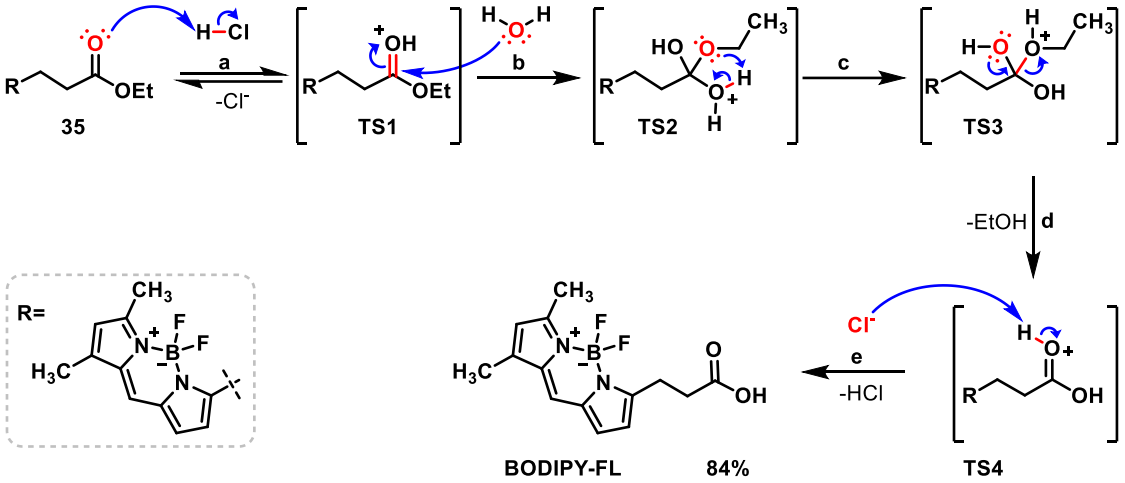

Figure 103: Mechanism of acid-catalysed ester cleavage, yielding BODIPY-FL. a) Protonation b) Nucleophilic attack of water c) Intramolecular proton transfer d) Elimination of ethanol e) Deprotonation.

Next to the fluorophore, the different linker systems envisioned for this project needed to be mono-Boc-protected to prevent side reactions during linker attachment reactions. The different linkers were selectively mono-Boc-protected under basic conditions for five hours using an excess of the linkers to prevent double protection, yielding the respective linkers in 64 to 100%.[737,738] The mechanism,[736] as shown in Figure 104, begins with the nucleophilic attack of the terminal amino group at the carbonyl carbon of the anhydride, leading to the cleavage of the C=O double bond. Through reformation of the carbonyl bond, the anhydride cleaves, decomposing into carbon dioxide and *tert*-butoxide (**TS1**). The latter then deprotonates the carbamate (**TS2**), leading to the final Boc-protected linkers **L1-24**.

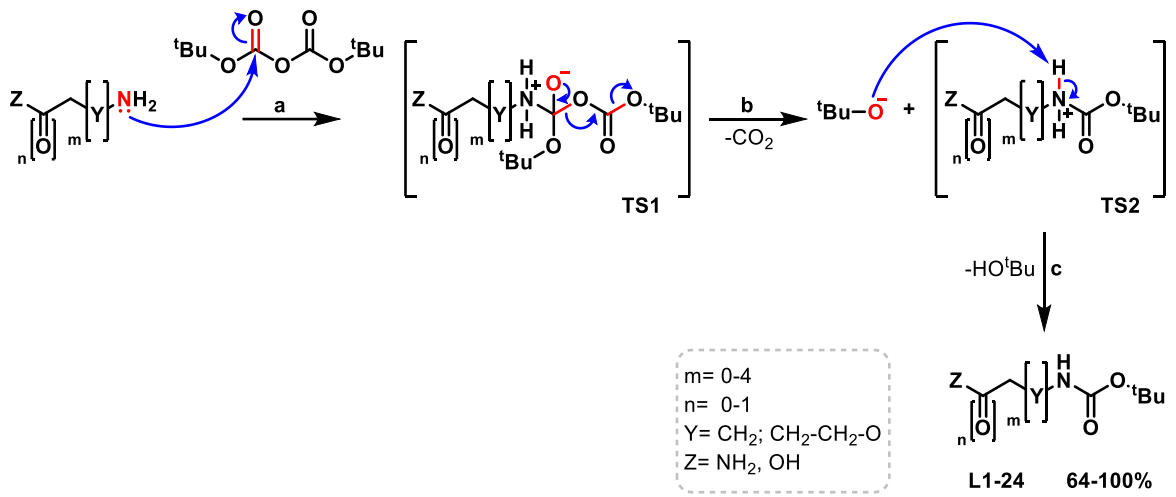

Figure 104: General mechanism of Boc-protection, yielding the linkers **L1-24**. a) Nucleophilic attack of the amine b) Elimination of carbon dioxide and *tert*-butoxide c) Deprotonation.

7.3 JNJ-7777120-based fluorescent H_4R ligands

7.3.1 Rational design

The initial strategy to develop novel fluorescent H_4R ligands employed **JNJ-7777120** as the lead pharmacophore, given its established presence in scientific literature.[325,373,739] This series was designed to attach the linker component at the 3-position of the indole ring of the pharmacophore (see Figure 105), as this position is known to be the most reactive site on the indole scaffold. The selected position can be addressed through electrophilic aromatic substitution to introduce an aromatic amine, which can then be readily connected with the linker motif. This approach allowed for both amide formation and, in one example, implementation of an aliphatic connection as secondary amine to evaluate the different influences of various linker attachment strategies on H_4R affinity. The employed linker systems comprised five different aliphatic alkyl linkers, increasing by one methylene unit, ranging from glycine to 6-aminohexanoic acid, as well as three PEG linkers with increasing ethylene glycol units starting from mono ethylene glycol. All linkers featured either a carboxyl group for coupling with the aromatic amine on the pharmacophore, or an aldehyde group for reductive amination, as shown for the one linker used to achieve the secondary amine connection approach. Additionally, all linkers contained a Boc-protected amine on the opposite end for subsequent BODIPY-FL coupling after deprotection.

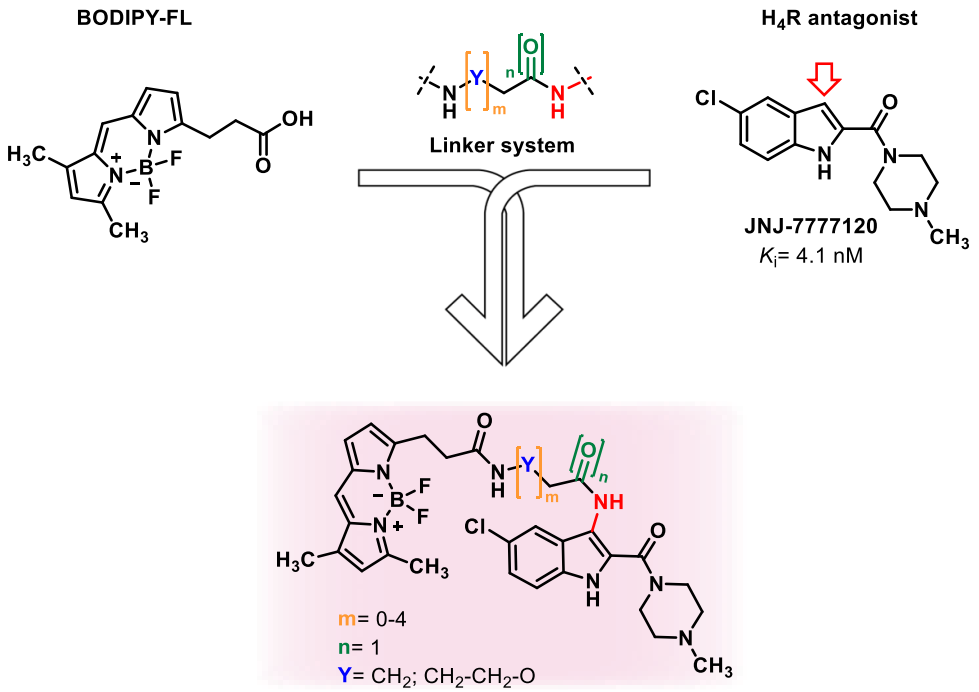

Figure 105: Rational design strategy for novel fluorescent H_4R ligands based on H_4R lead structure **JNJ-7777120**[728] exploring systematic variations in pharmacophore-fluorophore attachment composition through different linker types, lengths, and connection approaches.

7.3.2 Synthesis of pharmacophore building block

The synthetic route (see Figure 106) was designed to begin with the preparation of the lead structure **JNJ-7777120**, which required implementation of an aromatic amine functionality at the 3-position of the indole ring, serving as an anchor point for subsequent linker attachment. To achieve this, a HATU coupling of carboxylic acid **36** with *N*-methylpiperazine (NMP) was performed to introduce the necessary basic moiety for establishing the H_4R pharmacophore structure (**37**). To functionalize the 3-position, the indole aromatic ring was subjected to nitration (**38**). The resulting nitro group was subsequently reduced to the amine, delivering the amino-functionalized lead structure, which served as starting material **SM2** for the subsequent linker attachment.

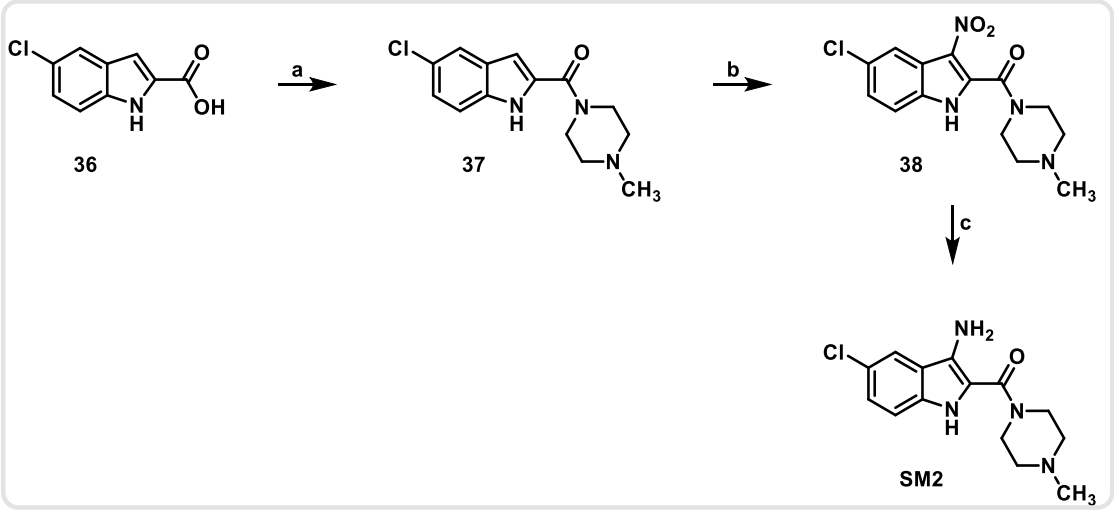

Figure 106: Planned synthetic route for starting material **SM2**, needed for the synthesis of the **JNJ-7777120**-based H_4R fluorescent ligand series. Reaction conditions: a) NMP, HATU, DIPEA, ethyl acetate, room temperature, 20 h. b) acetic anhydride, nitric acid, -70 °C, 24 h. c) Fe, ammonium chloride, isopropanol, 85 °C, 20 h.

The first step involved the synthesis of lead structure **JNJ-7777120** through a coupling reaction of 5-chloro-1*H*-indole-2-carboxylic acid **36** with NMP. The coupling was performed in ethyl acetate with HATU and DIPEA, following the mechanism shown in Figure 57, for 20 hours yielding the desired product **37** in 91% yield (see Figure 107).[728] Ethyl acetate was selected as the reaction solvent instead of previously described DMF due to its easier removal during workup and superior handling properties for large-scale synthesis of this building block, which was possible due to sufficient solubility of the reactants.

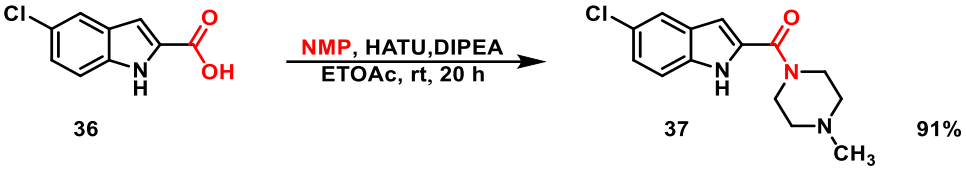

Figure 107: Reaction of the HATU coupling of **36** with NMP, yielding **JNJ-7777120** ligand **37**.

In the following step, the 3-position of the indole ring was addressed electrophilically in a nitration reaction, introducing the precursor of the desired amine functionality needed for a later linker attachment. The reaction was performed in acetic anhydride at -70 °C with concentrated nitric acid, delivering the product in 86% yield after 24 hours (see Figure 108).[740] Mechanistically,[741] the reaction proceeds through initial formation of the nitronium ion via nucleophilic attack of nitric acid on acetic anhydride, resulting in the anhydride's cleavage. The generated nitronium ion (**TS1**) then attacks the electron-rich 3-position of the indole ring of **37**, which gains its nucleophilic character through intramolecular electron delocalization, via electrophilic aromatic substitution. Subsequent deprotonation by the acetate counterion leads to rearomatization (**TS2**), yielding the nitro compound **38**.

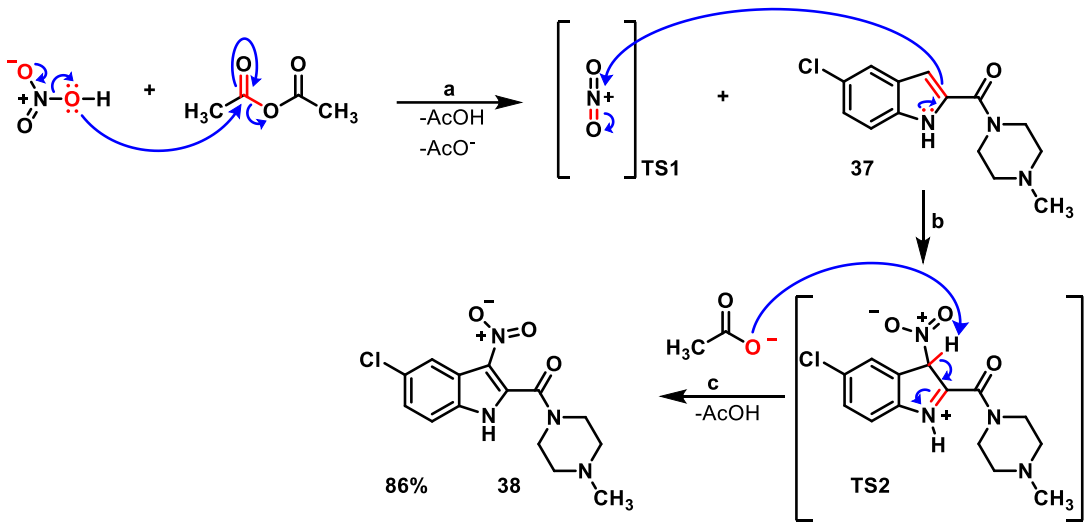

Figure 108: Mechanism of the nitration of compound **37**, yielding compound **38**. a) Formation of nitronium ion b) Electrophilic attack of the nitronium ion at the 3-position of the indole ring c) Rearomatization.

In the final step of the synthetic route toward the amino-functionalized **JNJ-7777120** lead compound, the nitro group was reduced to generate the aromatic amine required for subsequent linker attachment. The reaction was performed using iron under acidic conditions at 85 °C for 20 hours, yielding product **SM2** in 65% yield.[742] The mechanism, as shown in Figure 109, proceeds through a series of acid catalysed electron transfers, as postulated by Béchamp.[743] Initially, the nitro group undergoes a sequence of protonation and single electron transfers (SET, **TS1-4**), with iron serving as the electron donor, leading to the formation of the nitroso intermediate **IM1**. This intermediate then undergoes further protonation and SET steps (**TS5-10**), ultimately delivering the desired amine product **SM2**.

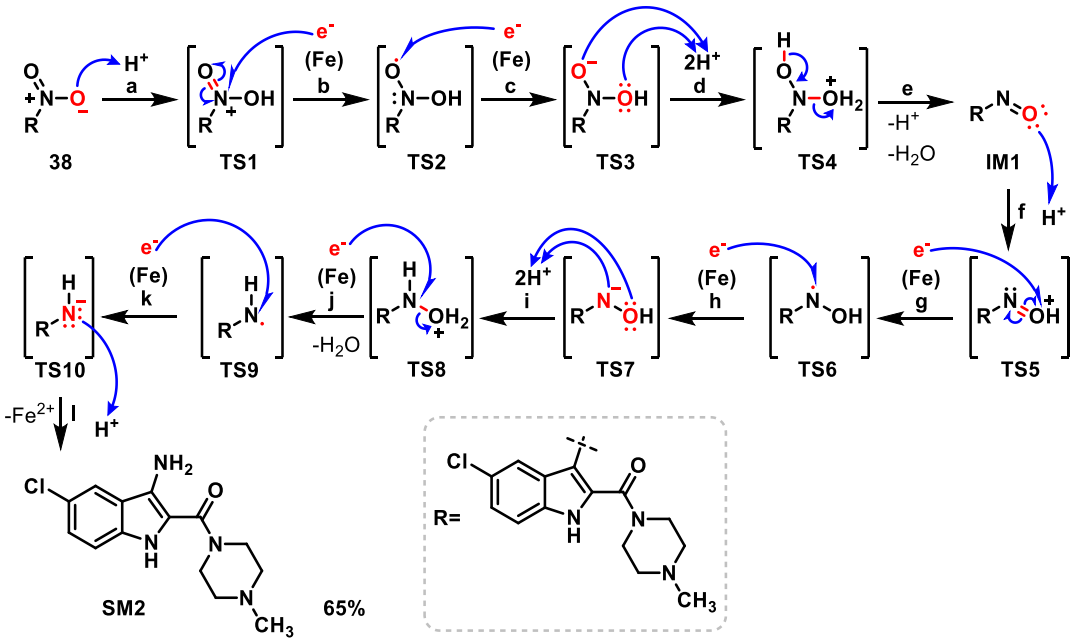

Figure 109: Mechanism of the nitro reduction of compound **38**, yielding compound **SM2**. a) Protonation b) SET c) SET d) Double protonation e) Elimination f) Protonation g) SET h) SET i) Double protonation j) SET k) SET l) Protonation.

7.3.3 Fluorophore attachment through amide linkages

Having the H_4R pharmacophore building block **SM2** in hands, the synthetic route (see Figure 110) for the series of **JNJ-7777120**-based fluorescent H_4R ligands was designed to start with attaching various Boc-protected carboxyl-functionalized linkers through coupling to the pharmacophore at the aromatic amine at the 3-position, implementing an amide bond connection (**P21a-h**). After successful attachment, the Boc protecting groups can be removed to reveal the free amine (**P22a-h**), which then can serve as the connection point for the BODIPY-FL moiety, attachable through another coupling reaction (**P23a-h**).

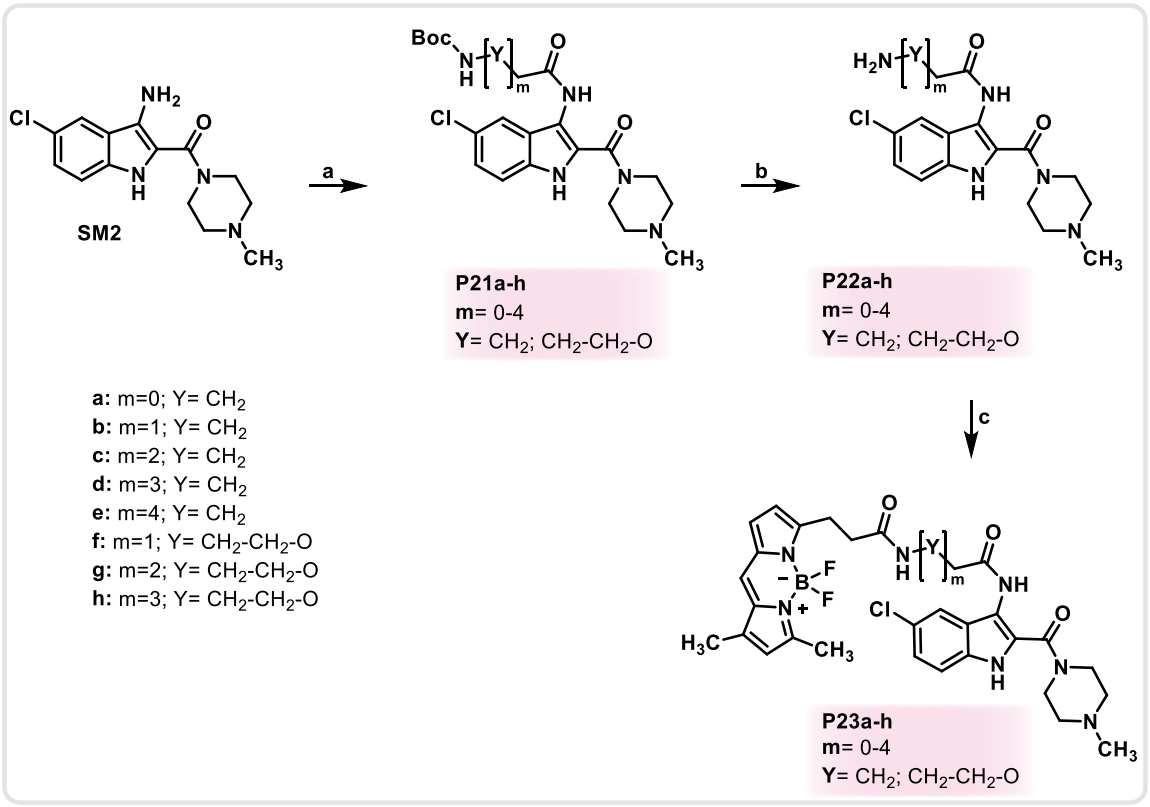

Figure 110: Planned synthetic route for the synthesis of the **JNJ-7777120**-based H_4R fluorescent ligand series. Reaction conditions: a) HATU, DIPEA, linker, DMF, room temperature, 24 h. b) TFA/HCl, DCM/methanol, room temperature, 24 h. c) HATU, DIPEA, BODIPY-FL, DMF, room temperature, 24 h.

The synthesis of the **JNJ-7777120**-based ligand series began with HATU-mediated coupling reactions of the amino-functionalized pharmacophore building block **SM2** with a diverse set of Boc-protected and carboxy-functionalized linker motifs of varying lengths and types (**L1-8**). The employed linker set comprised five alkyl linkers ranging from glycine to 6-aminohexanoic acid, and three PEG-type linkers consisting of mono-, di-, and triethylene glycol linkers. The coupling reactions, following the mechanism shown in Figure 57, were performed in DMF with DIPEA for 20 hours at room temperature, successfully yielding the desired Boc-protected compounds **P21a-h** in moderate to good yields of 42-98% (see Figure 111).[644]

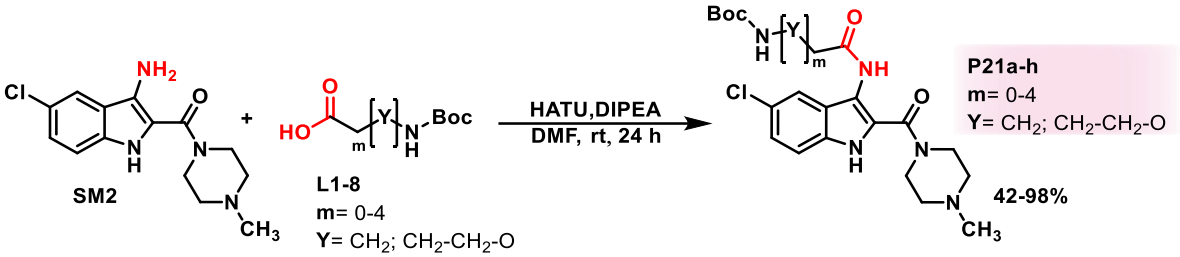

Figure 111: Reaction of the HATU coupling of **SM2** with a diverse Set of different linkers **L1-8**, yielding the Boc-protected compounds **P21a-h**.

Following the successful attachment of the linkers to the pharmacophore, the second step involved deprotection of the linker's terminal end to obtain the free primary amine required for BODIPY-FL conjugation. Following the mechanism shown in Figure 65, the Boc deprotection was accomplished under acidic conditions using trifluoroacetic acid in dichloromethane (**P22a-f**).[744] After 24 hours at room temperature, the reaction yielded the free amines as their corresponding double TFA salts in excellent yields of 83-100% (see Figure 112). For the longer PEG linker derivatives **P22g-h**, where TFA deprotection resulted in degradation, an alternative approach using hydrochloric acid in methanol was implemented.[674] While this method successfully yielded the desired products **P22g-h** as their double hydrochloride salts, only moderate yields (46-55%) were obtained, indicating that degradation processes persisted also under these deprotection conditions.

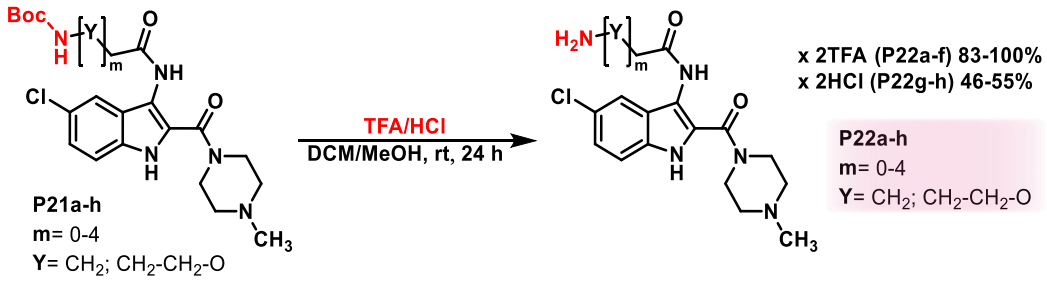

Figure 112: Reaction of the Boc deprotection of compounds **P21a-h**, yielding the deprotected compounds **P22a-h** as their respective salts.

The series was completed by coupling the free primary amine of compounds **P22a-h** with the synthesized BODIPY-FL fluorophore in the final step (see Figure 113). Following the mechanism shown in Figure 57, the reaction was performed in DMF with DIPEA for 20 hours at room temperature, yielding the final fluorescent compounds **P23a-h** in yields ranging from 21-93%.[644] The reduced yields observed for certain compounds can likely be attributed to BODIPY-FL's sensitivity under basic conditions,[722] which are essential for the HATU-mediated coupling mechanism. While the methylpiperazine moiety of the starting material provides sufficient basicity to facilitate coupling, it leads to ammonium salt formation that precipitate

from solution, necessitating additional base to maintain solubility. The risk of potential yield reduction due to BODIPY-FL degradation was justified by the robust and well-established nature of the coupling protocol, which was successfully implemented across the entire H_4R fluorescent ligand project.

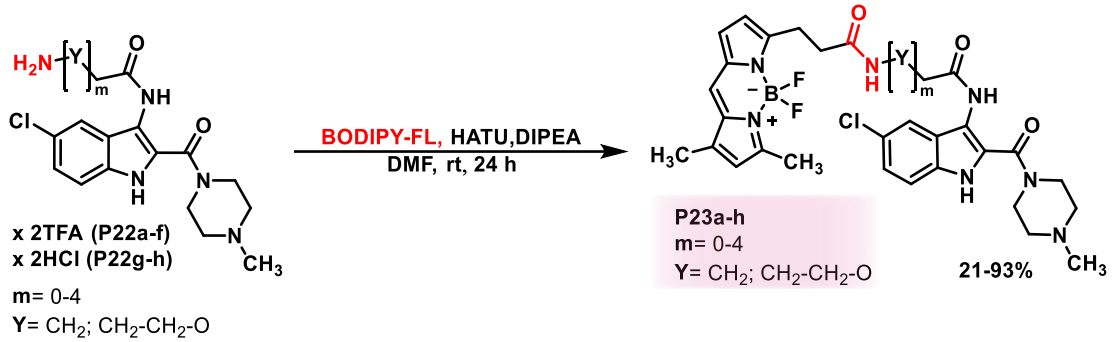

Figure 113: Reaction of the HATU couplings of **P22a-h** with BODIPY-FL, yielding the final fluorescent compounds **P23a-h**.

In addition to the linker-based compounds **P23a-h**, direct conjugation between the fluorophore and the pharmacophore was investigated by exploiting the carboxyl function of BODIPY-FL and the aromatic amine of the pharmacophore building block **SM2**. The coupling was performed via HATU-mediated amide formation mechanism (see Figure 57) in DMF with DIPEA at room temperature for 20 hours, yielding the desired fluorescent compound **P23i** in 56% yield (see Figure 114).[644]

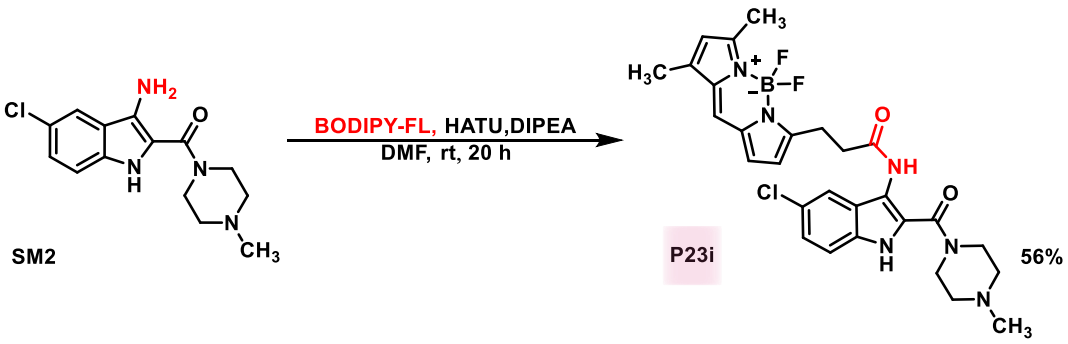

Figure 114: Reaction of the direct HATU coupling of **SM2** with BODIPY-FL, yielding the final fluorescent compound **P23i**.

7.3.4 Fluorophore attachment through secondary amine linkage

In addition to amide-based linker conjugation to the pharmacophore, exploration of secondary amine linkages was pursued, as this modification not only alters flexibility but also affects pharmacokinetic properties including lipophilicity and hydrogen bonding capabilities.[745] This was particularly interesting to investigate since the attachment point's proximity to the pharmacophore structure could potentially influence binding affinity. The formation of the secondary amine linkage required reductive amination between the aromatic amine of the

pharmacophore building block **SM2** and an aldehyde-functionalized linker. This approach was chosen over alkylation due to the lower nucleophilicity of the aromatic amine,[746] necessitating harsh alkylation conditions, which could potentially lead to undesired side reactions at the indole amine or tertiary amine positions.[603] The investigation was limited to a single compound using a commercially available aldehyde linker, as the synthesis of aliphatic aldehydes proved challenging as previously discussed.[617–619] However, this single example would allow comparison of binding affinities between amide and amine linkages, determining whether further exploration of this alternative linker attachment strategy would be beneficial. The synthetic route, as shown in Figure 115, was designed to achieve linker attachment through reductive amination, followed by Boc deprotection to liberate the primary amine of the linker motif. The resulting free amine could then be coupled with BODIPY-FL to furnish the final fluorescent compound **P26** featuring the secondary amine linkage.

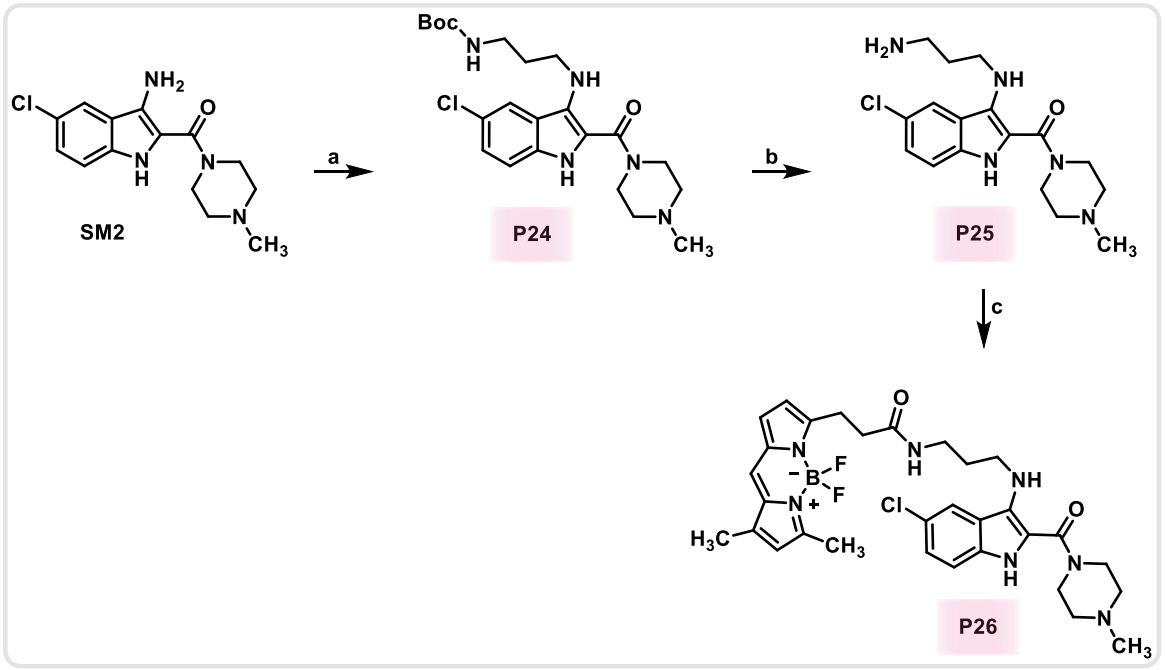

Figure 115: Planned synthetic route for the synthesis of the **JNJ-7777120**-based H_4R fluorescent ligand **P26**, exploring a secondary linkage approach. Reaction conditions: a) HOAc, *tert*-butyl (3-oxopropyl)carbamate, STAB, DCE, room temperature,4 h. b) HCl, methanol, room temperature, 24 h. c) HATU, DIPEA, BODIPY-FL, DMF, room temperature, 24 h.

To initiate the synthetic route, reductive amination between the aromatic primary amine of **SM2** and linker *tert*-butyl (3-oxopropyl)carbamate **39** was performed to establish linker attachment via a secondary amine. Following the mechanism shown in Figure 37, the reaction was conducted in DCE with acetic acid and STAB at room temperature for four hours, yielding the Boc-protected product **P24** in 23% (see Figure 116).[602] The moderate yield can likely be

attributed to competing side reactions at the indole amine position or dialkylation,[747] as well as degradation of the aldehyde under the reaction conditions.[617–619]

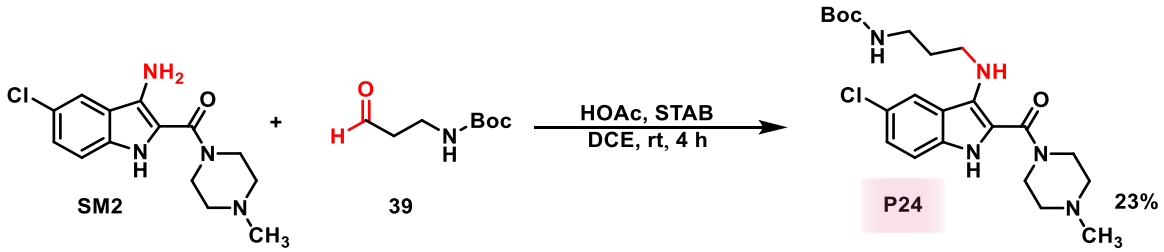

Figure 116: Reaction of the reductive amination of **SM2** with linker **39**, yielding compound **P24**.

The subsequent step involved Boc deprotection of compound **P24** to liberate the free amine required for fluorophore coupling. Following the mechanism shown in Figure 65, the reaction was conducted in MeOH with hydrochloric acid at room temperature for 24 hours, yielding the desired product as its double hydrochloride salt in excellent yield of 95% (see Figure 117).[674]

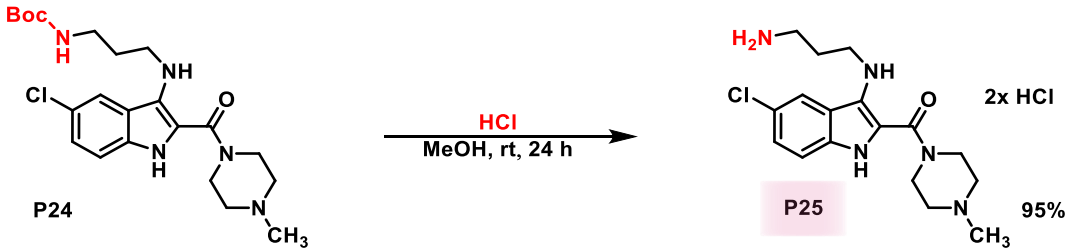

Figure 117: Reaction of the Boc deprotection of compound **P24**, yielding the deprotected compound **P25** as their respective salt.

In the final step, compound **P25** was coupled with BODIPY-FL to furnish the fluorescent ligand **P26** containing the secondary amine linkage at the pharmacophore building block. The HATU-mediated coupling, following the mechanism depicted in Figure 57, was performed in DMF with DIPEA addition for solubility purposes at room temperature for 24 hours, delivering the final target compound **P26** in 58% yield (see Figure 118).[644]

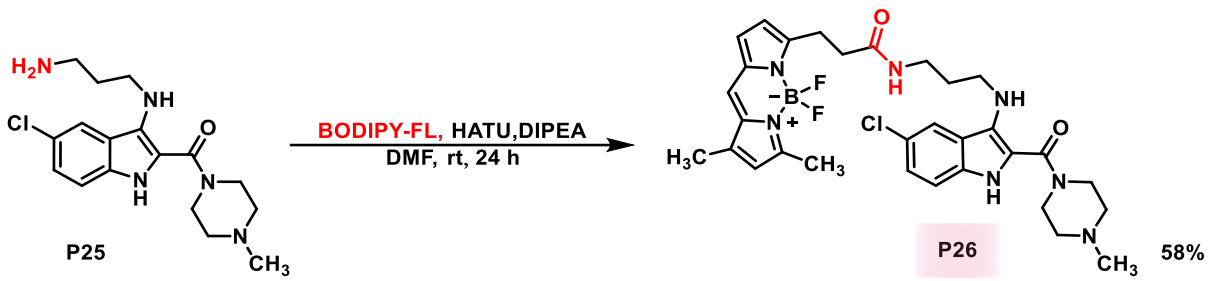

Figure 118: Reaction of the HATU coupling of compound **P25** with BODIPY-FL, yielding the final fluorescent compound **P26**.

7.4.4 Binding profile

To evaluate the rational design, the synthesized compounds were supposed to be tested for their H_4R affinities in a cell-based assay to determine which structural modifications, specifically linkage approach, linker type, and length, best preserved the favourable pharmacological properties of the used pharmacophore building block. Initial assay development challenges led to a period of synthesis without immediate binding data feedback, resulting in the generation of comprehensive compound libraries before affinity screening could commence. Consequently, due to the large number of H_4R compounds and limited testing capacities and resources, a selective subset was chosen as a general initial affinity screening strategy across all H_4R fluorescent ligand series. The designed testing strategy encompassed not only the final fluorescent compounds but also key intermediates along the synthetic route to investigate whether changes in affinity were caused by the different structural modifications of the pharmacophore through the different linker attachment types or positions, or by the fluorophore potentially creating steric hindrance due to its proximity to the binding pocket. Therefore, one representative progression trio or duo was selected for affinity testing for each compound library, consisting of the final fluorescent ligand, its deprotected linker precursor and its Boc-protected linker intermediate when available.For this series, the propyl linker chain derivative **P23b** was selected as a representative example for detailed investigation, as it was the only derivative synthesized using the secondary linkage approach (**P26**) due to commercial availability of the required aldehyde. Having the same propyl linker length, testing both progression trios of **P23b** and **P26** enabled a direct comparison between the two linkage approaches (see Table 14). This initial evaluation focused on establishing the viability of the basic pharmacophore modifications, with the investigation of different linker lengths and types planned as a subsequent step pending favourable affinity results. The results demonstrate that none of the ligands from the respective progression trios maintain the potent affinity of the **JNJ-7777120** pharmacophore building block,[728] indicating that neither the amine nor the amide modifications at position 3 of the indole ring appear to be tolerated. Since both the linker derivatives (**P21-22b** & **P24-P25**) as well as the fluorophore compounds (**P23b** & **P26**) show no affinity, it suggests that the loss of activity is not necessary due to steric hindrance of the bulky fluorophore but rather stems from the fundamental modifications made to the pharmacophore. The observed results may explain the current literature landscape, where despite extensive exploration of the **JNJ-7777120** pharmacophore,[282] only nonpolar substituents such as chloride have been reported at this position,[748,749] suggesting that polar modifications like amides or secondary amines in position 3 might be generally unfavourable for receptor binding. Consequently, the planned evaluation of different linker lengths and types was not conducted, as the fundamental pharmacophore

modifications already proved unsuitable for maintaining receptor affinity. Given the lack of significant binding affinity, also no further investigation of fluorescent properties was pursued.

Table 14: Histamine H_4 receptor affinities of ligands **P21-P23b** from the amid linkage approach and compounds **P24-26** from the secondary amine linkage approach for comparison.

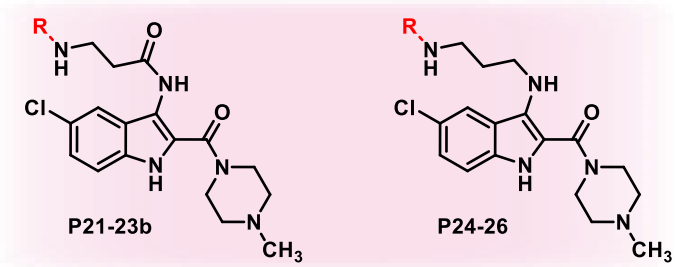

R=	Compound	hH_4R K_i (nM) [95% CI]
-Boc	**P21b**	>10000
-Boc	**P24**	>10000
-H	**P22b (x 2TFA)**	>10000
-H	**P25 (x 2HCl)**	>10000
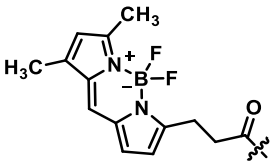	**P23b**	>10000
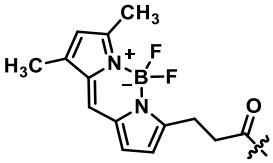	**P26**	>10000
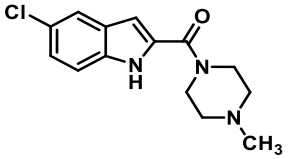	**JNJ-7777120**	**29.4** [24.6; 35.3]

7.4 ST-2529-based fluorescent H_4R ligands

7.4.1 Rational design

The second rational design approach was based on a working group's intern ligand that had demonstrated potent results in initial H_4R affinity assays. Ligand **ST-2529** consists of a central pyrimidine ring, substituted with a thioether motif in 2-position and an ester moiety at 5-position, which when converted to a free carboxylic acid, provides an excellent attachment point for mono-Boc-protected diamine-functionalized linkers through coupling (see Figure 119). These linkers then can be easily coupled with BODIPY-FL fluorophore at their other end after deprotection. Five different alkyl linkers, ranging from ethylenediamine to hexyldiamine, were utilized in this approach. Additionally to the linker series, the oxidation of the thioether sidechain to sulfoxide and sulfone was investigated using one representative compound in a preliminary structure-activity relationship study, serving as a model system before potential expansion to the complete series. This planned modification was inspired by mimicking the properties of the polar methylpiperazine group found in **JNJ-7777120**[728] and at the 2-position of the quinazoline ring in **VUF-10558**.[353] Although Compound **ST-2529** already contains the methylpiperazine moiety at a more distant position from the central heterocycle, the thioether at the 2-position better matches spatially with the methylpiperazine groups of the reference ligands, particularly **VUF-10558**. Due to this spatial match, the thioether was oxidized to better align its physicochemical properties with that of the methylpiperazine group in the reference compounds, allowing evaluation of how those altered properties influences binding affinity for this specific H_4R pharmacophore.

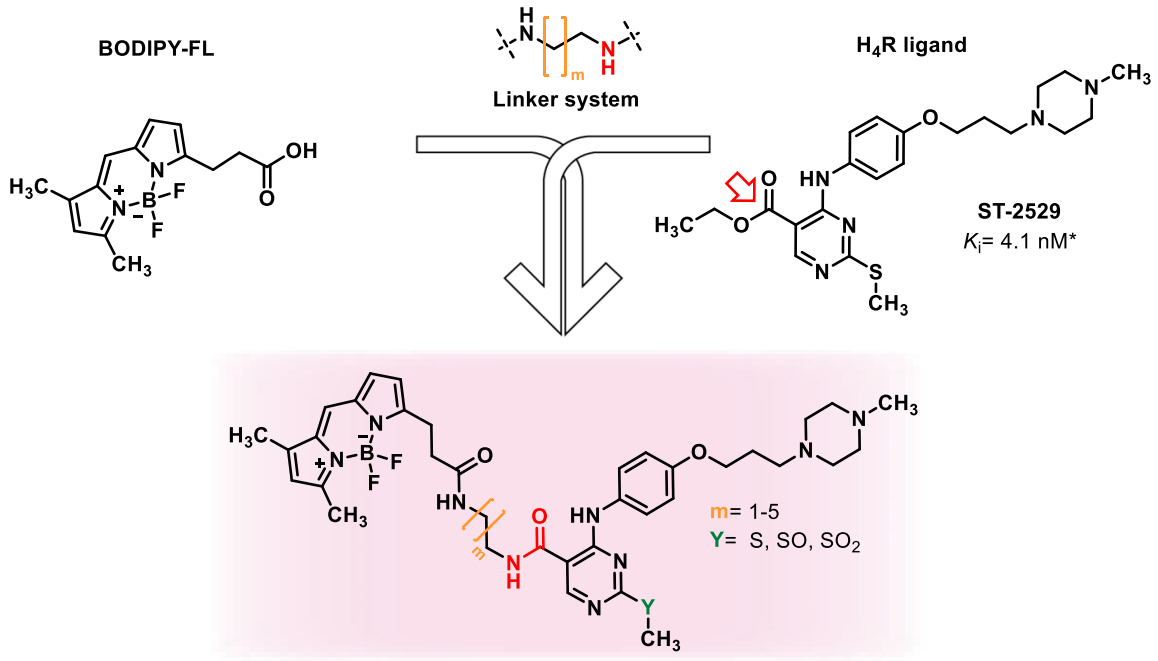

Figure 119: Rational design strategy for novel fluorescent H_4R ligands based on H_4R lead structure **ST-2529**, investigating variable linker lengths and thioether oxidation states. *in-house value of initial testing result

7.4.2 Synthesis of pharmacophore building block

To start synthesis of this H_4R ligand series, lead compound **ST-2529** needed to be synthesized first on a large scale, according to the designed synthetic route shown in Figure 120. From *para*-nitrophenol, a sequential double alkylation can be performed, starting with the phenol alkylation with 1-bromo-3-chloropropane followed by substitution of the chloride with NMP to yield compound **42**. The nitro group can then be reduced to form the aromatic amine (**43**), which serves as a nucleophile in a subsequent nucleophilic aromatic substitution with commercially available pyrimidine derivative **44**, yielding compound **45** (**ST-2529**). Finally, ester cleavage would produce the free carboxylic acid as a lithium salt (**SM3**), functioning as the key pharmacophore building block suitable for linker attachment.

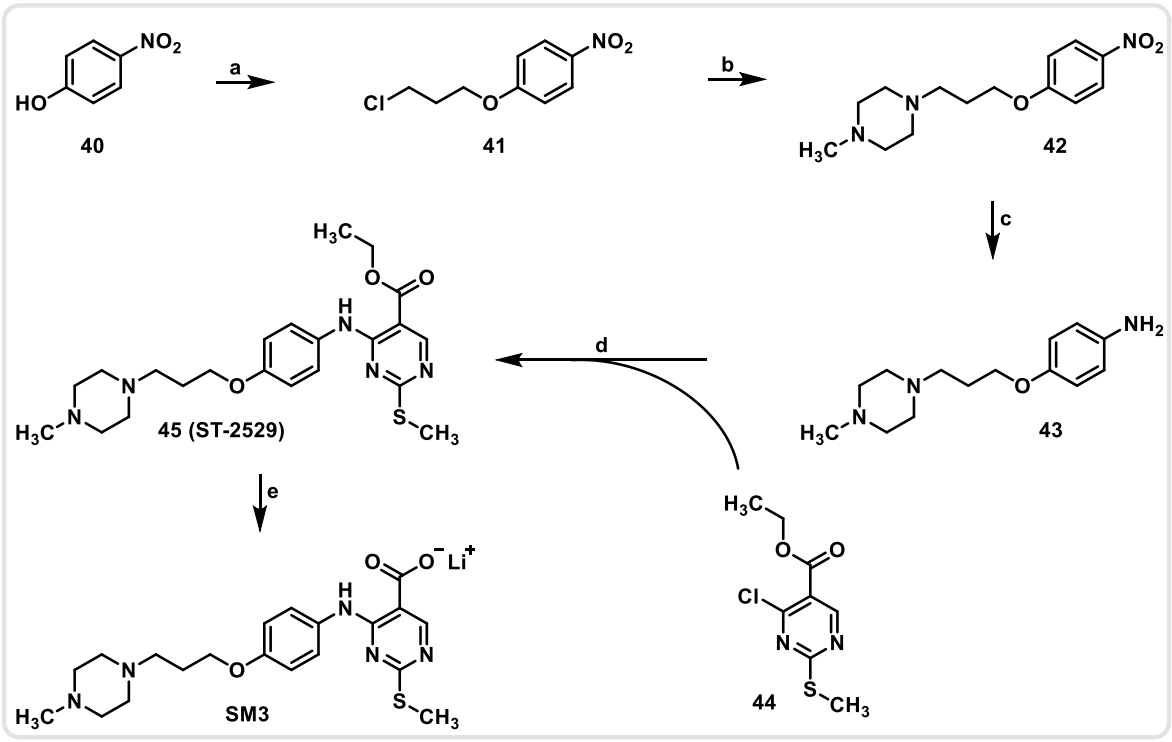

Figure 120: Planned synthetic route for starting material **SM3**, needed for the synthesis of the **ST-2529**-based H_4R fluorescent ligand series. Reaction conditions: a) 1-bromo-3-chloropropane, KI, K_2CO_3, acetone, reflux, 48 h. b) NMP, KI, K_2CO_3, acetone, reflux, 48 h. c) Pd/C, H_2, methanol, room temperature, 24 h. d) DIPEA, isopropanol, 70 °C, 20 h. e) LiOH, THF/water, room temperature, 24 h.

The synthesis of the pharmacophore building block began with a Williamson ether synthesis between *para*-nitrophenol (**40**) and 1-bromo-3-chloropropane. The reaction was performed

under Finkelstein conditions at reflux for 48 hours,[598] providing the desired compound in 56% yield (see Figure 121), following the mechanism shown in Figure 36.

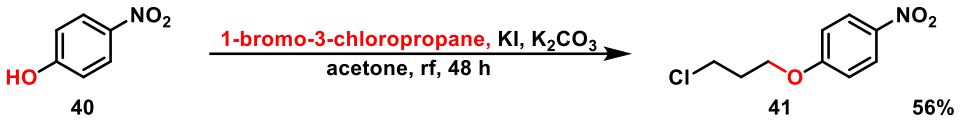

Figure 121: Reaction of the alkylation of compound **40** with 1-bromo-3-chloropropane, yielding compound **41**.

In the next step, compound **41** was reacted with NMP, substituting the chloride and introducing the polar amine moiety common to all lead pharmacophores.[353,728] The reaction, with its mechanism shown in Figure 36, was performed under Finkelstein conditions for 48 hours at reflux,[598] yielding product **42** in 79% yield (see Figure 122).

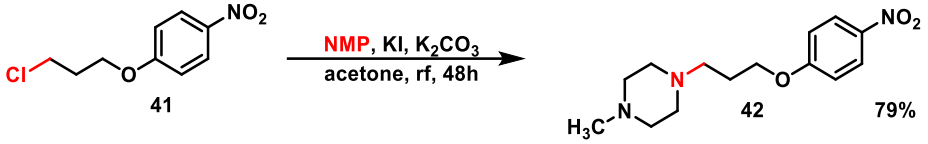

Figure 122: Reaction of the alkylation of compound **41** with NMP, yielding compound **42**.

Following the double alkylation sequence, the nitro group of compound **42** was reduced to the aniline derivative **43** via palladium-catalysed hydrogenation. The reduction was performed in methanol with a palladium on charcoal catalyst under a hydrogen atmosphere at room temperature for 24 hours, yielding the product quantitatively.[750] The mechanism,[603] as shown in Figure 123, begins with the adsorption of both the nitro compound and hydrogen on the catalyst surface. Through a sequence of proton transfers from the surface to the nitro group (**TS1-4**), accompanied by water elimination, the nitro group is converted to the aromatic amine. The reduction mechanism concludes with product **43** desorbing from the catalyst surface (**TS5**).

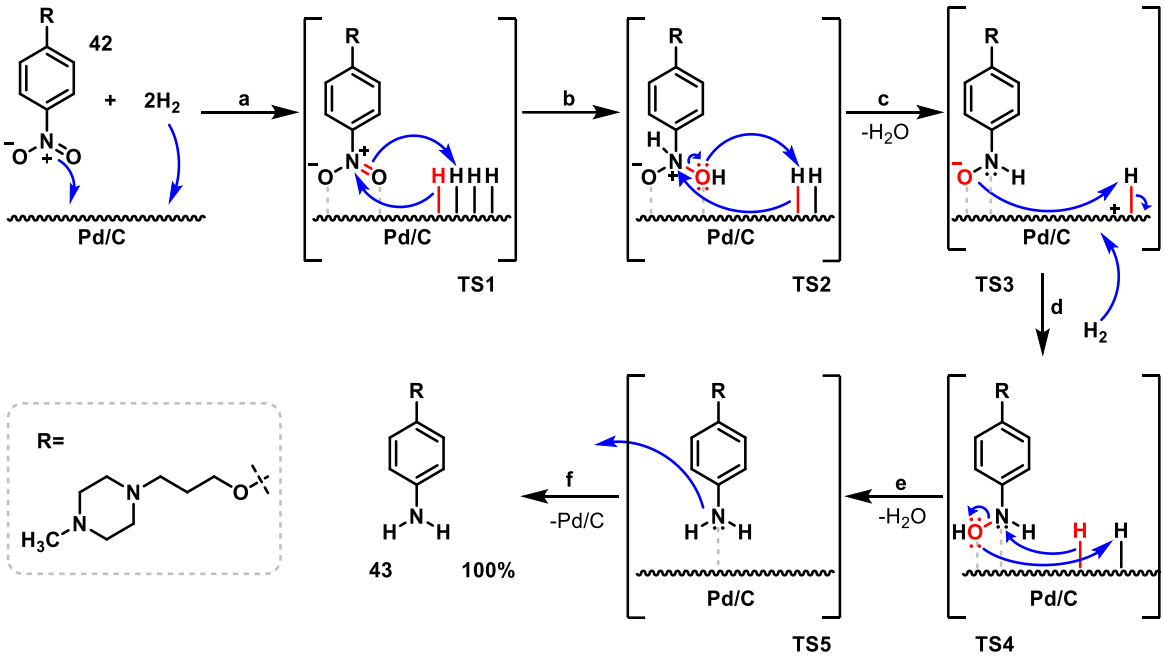

Figure 123: Mechanism of the nitro reduction of compound **42**, yielding compound **43**. a) Adsorption b) Hydrogen transfer c) Water elimination d) Hydrogen transfer e) Water elimination and hydrogen transfer f) Desorption.

In the following step, the synthesized aromatic amine **43** was employed as a nucleophile in a nucleophilic aromatic substitution (S_NAr) with pyrimidine **44**, which readily undergoes such reactions due to its electron-deficient nature resulting from electron-withdrawing substituents and the presence of chloride as a suitable leaving group.[751] The reaction was carried out in isopropanol under basic conditions at 70 °C for 20 hours, yielding product **45** (**ST-2529**) quantitatively.[752] The mechanism,[603] as shown in Figure 124, begins with the nucleophilic attack of the amine's free electron pair at the *ipso*-position to the chloride, forming a resonance-stabilized Meisenheimer complex.[753] In this intermediate, the positive charge is distributed throughout the aromatic system, stabilized by the electron-withdrawing substituents (**TS1**). The elimination of chloride restores aromaticity, followed by deprotonation of the newly formed secondary amine (**TS2**), completing the formation of product **45**.

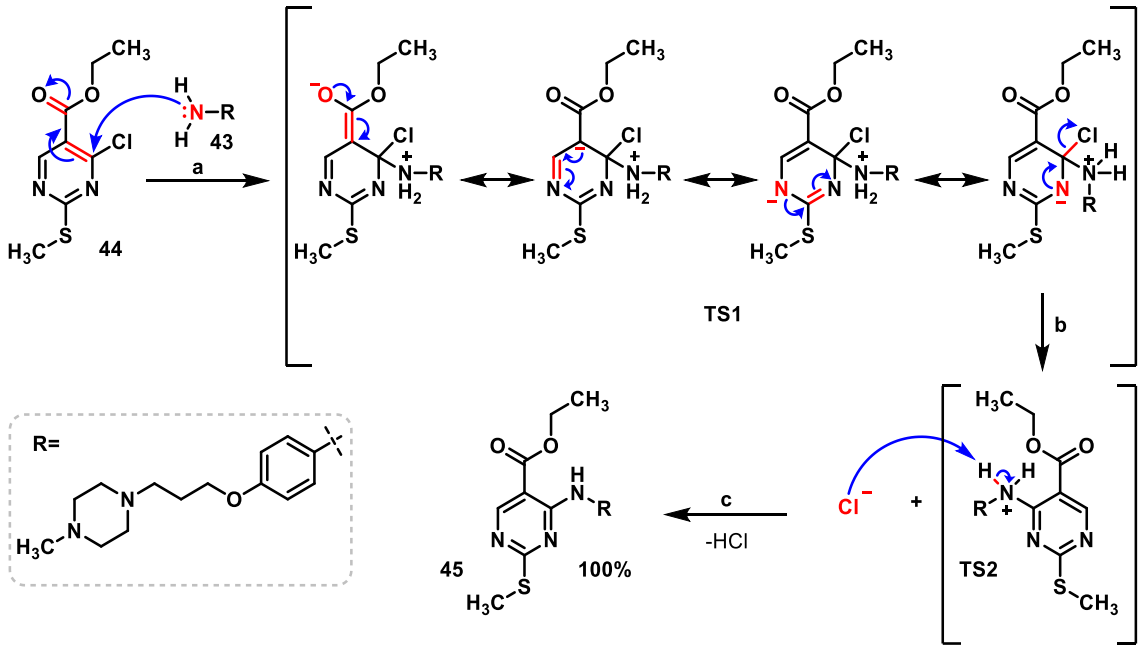

Figure 124: Mechanism of the S_NAr of compound **44**, yielding compound **45**. a) Nucleophilic attack of the amine b) Rearomatization c) Deprotonation.

To finalize the building block needed for this **ST-2529**-based ligand series, the ester group of compound **45** was cleaved to obtain the free acid suitable for subsequent linker coupling. The ester cleavage was performed under basic conditions in a THF/water mixture at room temperature for 24 hours,[641] yielding the lithium salt of the acid **SM3** quantitatively (see Figure 125) following the mechanism depicted in Figure 56.

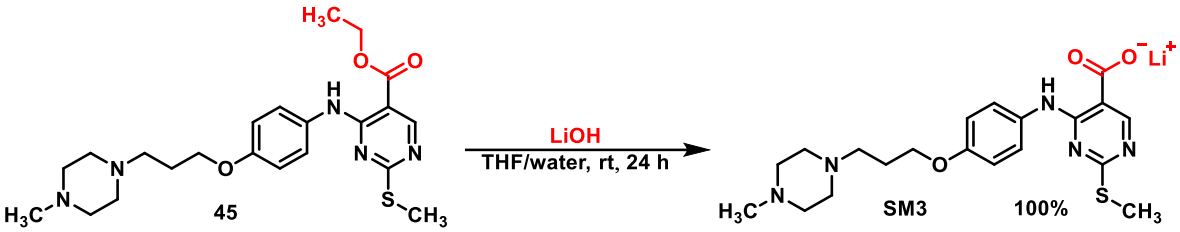

Figure 125: Reaction of the basic ester cleavage of compound **45**, yielding compound **SM3**.

7.4.3 Fluorophore attachment through amide linkage

The synthetic route to achieve the fluorescent **ST-2529**-based H_4R ligands consisted of three steps, as depicted in Figure 126. First, different amino-functionalized linkers needed to be attached at the carboxyl group through coupling (**P27a-e**), followed by Boc deprotection of the other side of the linker, setting the primary amine free (**P28a-e**). Subsequently, the exposed

primary amine can then be used as an attachment point for the BODIPY-FL fluorophore through coupling to yield the final fluorescent compounds **P29a-e**.

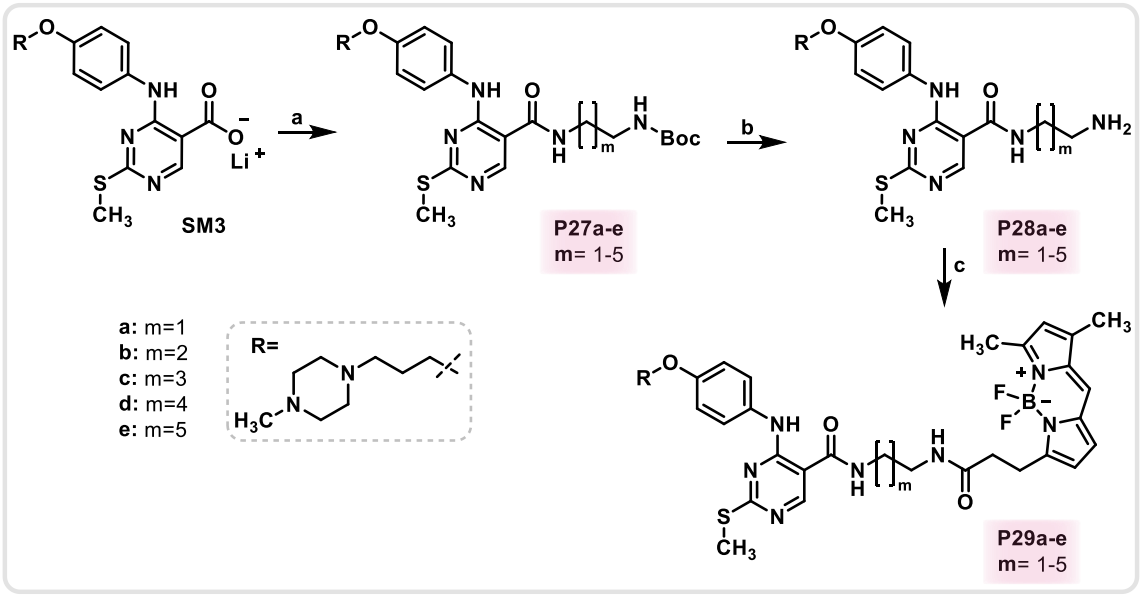

Figure 126: Planned synthetic route for the synthesis of the **ST-2529**-based series of H_4R fluorescent ligands **P29a-e**. Reaction conditions: a) HATU, DIPEA, linker, DMF, room temperature, 24 h. b) HCl, methanol, room temperature, 24 h. c) HATU, DIPEA, BODIPY-FL, DMF, room temperature, 24 h.

The initial step of the **ST-2529**-based series synthesis was the attachment of the different linkers to the H_4R pharmacophore building block (see Figure 127). This was achieved through a HATU-mediated coupling in DMF with DIPEA as the base at room temperature for 20 hours,[644] yielding the Boc-protected compounds **P27a-e** in 36-78% yield, following the mechanism as shown in Figure 57. The moderate yields of some products resulted from the challenging purification process.

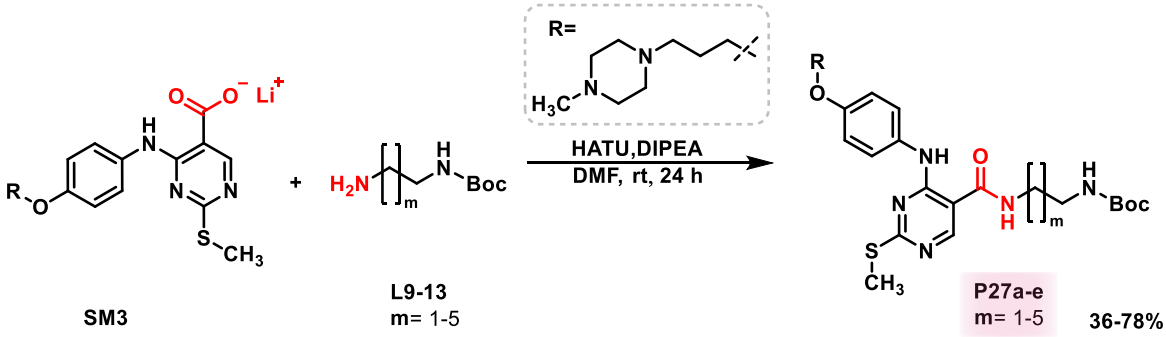

Figure 127: Reaction of the HATU-mediated coupling of compound **SM3** with the different linkers **L9-13**, yielding the compounds **P27a-e**.

Subsequently, compounds **P27a-e** were deprotected to uncover the free amine, needed for the fluorophore attachment. The Boc deprotection, following the mechanism as shown in Figure 65, was performed in methanol with hydrochloric acid as proton source at room

temperature for 24 hours,[674] yielding the products **P28a-e** in 31-90% yield (see Figure 128). Despite converting the dihydrochloride salts to the free base using an ion exchanger to facilitate purification, the challenging separation process still led to only moderate yields for some products.

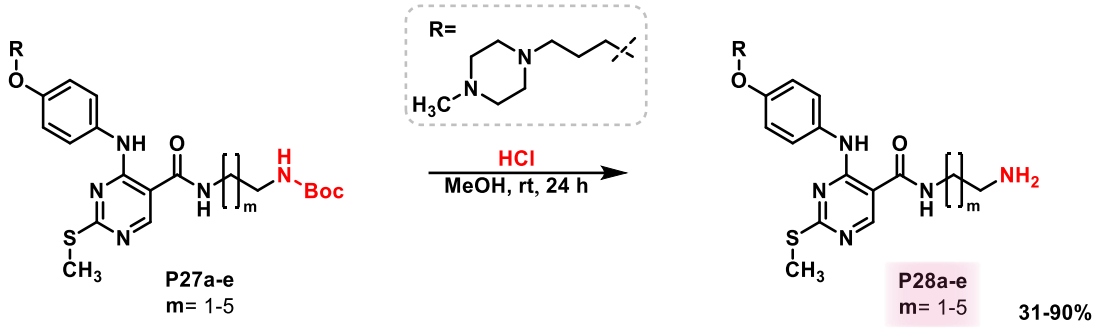

Figure 128: Reaction of the Boc deprotection of compounds **P27a-e**, yielding the compounds **P28a-e**.

In the final step, the fluorophore attachment was conducted to complete the synthesis of the **ST-2529**-based fluorescent ligand series. The HATU-mediated coupling, proceeding via the mechanism shown in Figure 57, was performed in DMF with DIPEA as base for 24 hours at room temperature, yielding the fluorescent ligands **P29a-e** in 26-72% (see Figure 129).[644] While the addition of base was essential to ensure solubility, the moderate yields of some products can likely be attributed to the sensitivity of BODIPY-FL under these basic conditions.[722]

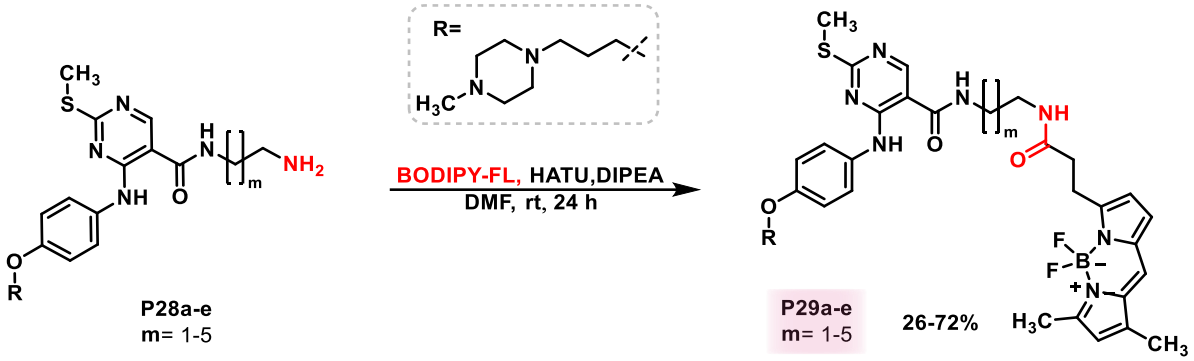

Figure 129: Reaction of the HATU-mediated coupling of compounds **P28a-e** with BODIPY-FL, yielding the fluorescent compounds **P29a-e**.

7.4.4 Synthesis of sulfoxide and sulfone derivatives

To investigate the impact of polarity changes at the 2-position, compound **P27b** was selected for oxidation of its thioether moiety to the corresponding sulfoxide and sulfone derivatives. This modification aimed to mimic the physicochemical properties of the more polar methylpiperazine group found at this position in the pharmacophore of reference ligands **JNJ-7777120**[728] and **VUF-10558**.[353] Oxidation was performed already at the Boc-protected linker stage, allowing for the evaluation of the binding affinities of both the oxidized protected (**P30** and **P31**) and oxidized deprotected linker compounds (**P32** and **P33**), as well as the

oxidized fluorescent derivatives (**P34** and **P35**). This step was essential, as the presence of the BODIPY-FL fluorophore in close proximity to the pharmacophore could potentially influence binding affinity due to steric clashes with the binding pocket. By assessing the oxidized compounds before fluorophore attachment, the specific impact of oxidation on binding affinity could be better distinguished. As depicted in Figure 130, the designed synthetic pathway involves oxidation of **P27b** to its sulfoxide and sulfone forms, followed by Boc deprotection and subsequent coupling with BODIPY-FL to produce the fluorescent compounds **P34** and **P35**.

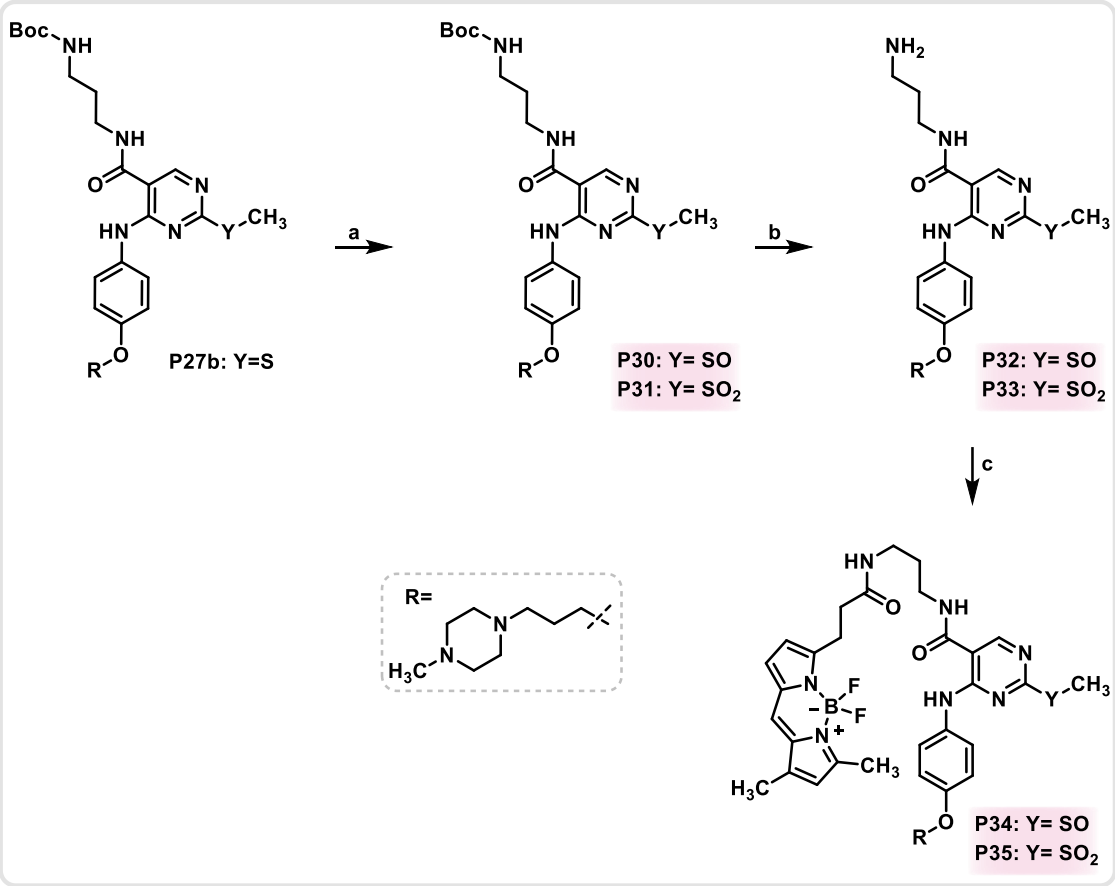

Figure 130: Planned synthetic route for the synthesis of the oxidized derivatives **P34** and **P35** of the **ST-2529**-based series of H_4R fluorescent ligands. Reaction conditions: a) mCPBA, DCM, room temperature, 2 h. b) HCl, methanol, room temperature, 24 h. c) HATU, DIPEA, BODIPY-FL, DMF, room temperature, 24 h.

The first step of this synthetic route involved the oxidation of the thioether moiety of compound **P27b** to the corresponding sulfoxide and sulfone. The reactions were carried out in DCM with *m*-CPBA at room temperature for two hours under argon atmosphere, yielding the sulfoxide **P30** in 25%[754] and the sulfone **P31** in 55%.[755] The different oxidation states were controlled through stoichiometry of *m*-CPBA as the oxidizing agent. The moderate yields can likely be attributed to the fact that the resulting sulfoxide and sulfone moieties can serve as good leaving groups,[756] facilitating nucleophilic aromatic substitution at this position during the reaction or the workup.[751] Another factor potentially affecting yields was the risk of *N*-oxide

formation,[757] due to the presence of tertiary amines within the molecule. Additionally, for the sulfoxide, overoxidation to the sulfone was a problem, as this transformation can occur readily, both during the reaction through excess *m*-CPBA or upon exposure to air.[758] As illustrated in Figure 131, the oxidation mechanism[603] begins with a nucleophilic attack by one of the sulfur's free electron pair on the oxygen of the peroxide, leading to peroxide cleavage and the formation of a sulfenic acid intermediate (**TS1**). This intermediate undergoes deprotonation to yield the sulfoxide **P30**. With an excess of oxidizing agent, a second oxidation step can occur, where the remaining lone electron pair of the sulfur attacks another peroxide molecule, forming a sulfinic acid intermediate (**TS2**), which, after deprotonation, results in the sulfone product **P31**.

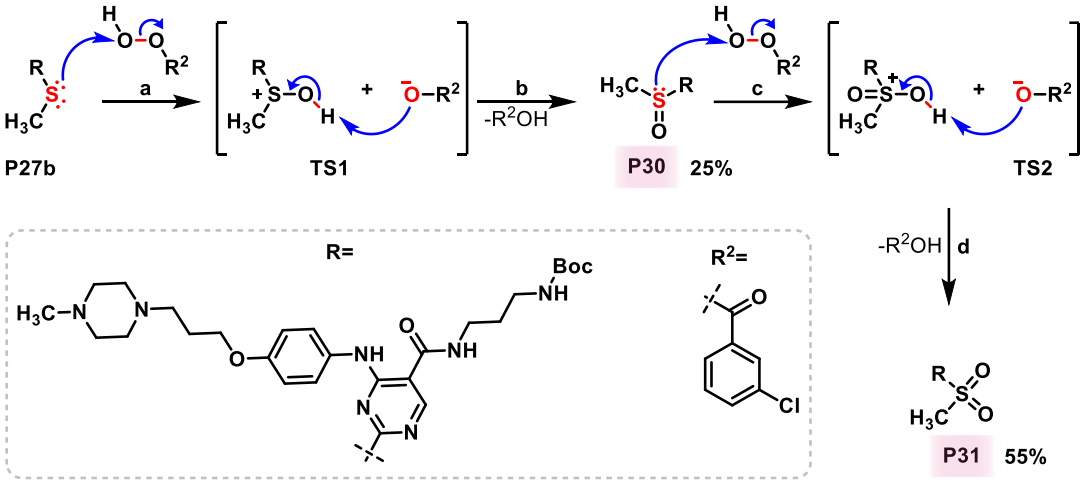

Figure 131: Mechanism of the oxidation of compound **P27b**, yielding the sulfoxide **P30** and the sulfon **P31**. a) Nucleophilic attack of the sulfur b) Deprotonation c) Nucleophilic attack of the sulfur d) Deprotonation.

After successful oxidation, both compounds **P30** and **P31** were subjected to a Boc-deprotection to release the free amine of the linker. The deprotection was performed in methanol with hydrochloric acid at room temperature for 24 hours,[674] following the mechanism shown in Figure 65, delivering the unprotected compounds **P32** and **P33** in 73-87% yield as free bases after ion exchanger treatment (see Figure 132).

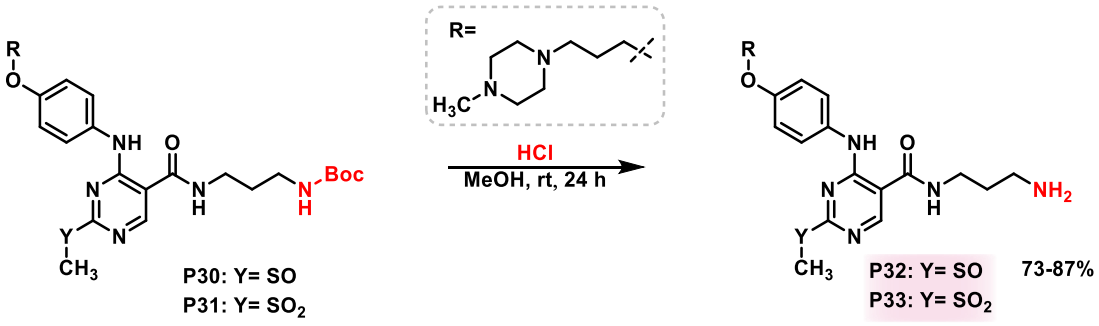

Figure 132: Reaction of the Boc-deprotection of compounds **P30** and **P31**, yielding compounds **P32** and **P33**.

In the final step, the oxidized, unprotected compounds **P32** and **P33** were coupled with BODIPY-FL to attach the fluorophore and complete the synthesis of the oxidized **ST-2529**-based fluorescent H_4R ligands. The reaction was performed with HATU and DIPEA in DMF at room temperature for 24 hours, proceeding via the mechanism shown in Figure 57, yielding the final fluorescent products **P34** and **P35** in 27-34% (see Figure 133).[644] The moderate yields likely resulted from both fluorophore decomposition under basic conditions[722] and competing nucleophilic aromatic substitution reactions at the sulfoxide/sulfone position with the starting materials acting as the nucleophile.[751]

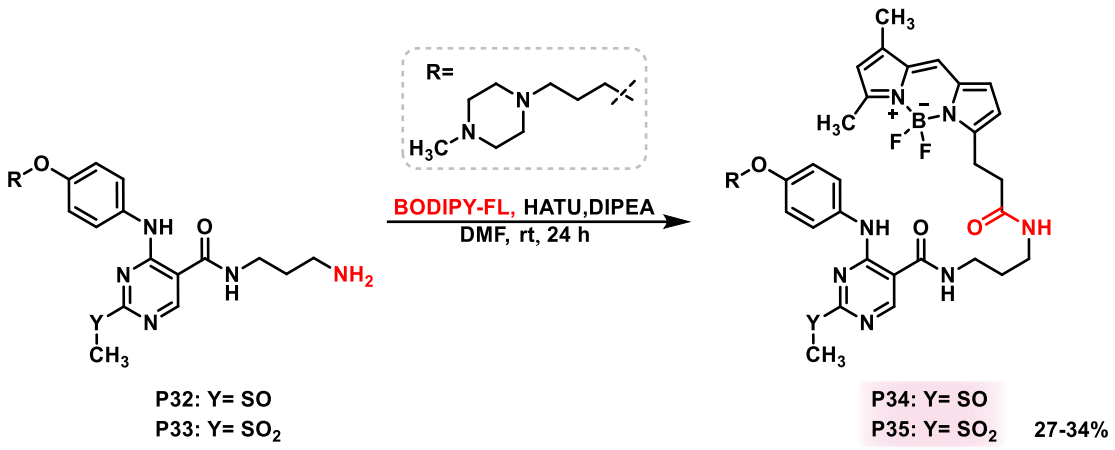

Figure 133: Reaction of the HATU-mediated coupling of compounds **P32** and **P33** with BODIPY-FL, yielding the fluorescent compounds **P34** and **P35**.

7.4.5 Binding profile

For the biological evaluation of this rational design, a progression trio was again selected as a representative set to investigate how linker attachment and pharmacophore modifications affect the high H_4R affinity of the utilized pharmacophore building block **ST-2529**. For consistent comparison, once again the propyl linker derivatives (**P27-29b**) were chosen as the test trio, also because only this derivative was oxidized to form the corresponding sulfoxide and sulfone compounds. Therefore, also both oxidated fluorescent derivatives **P34** and **P35** were subjected to testing to enable a better comparison of how oxidation at the 2-position side chain may affect binding, particularly examining whether adjusting the physicochemical properties to match those of the typically present group at this position influences affinity. The evaluation of different linker lengths was planned as a subsequent step, pending favourable affinity results from this initial pharmacophore modification assessment. The biological evaluation revealed that all tested ligands showed no significant H_4R affinity (see Table 15). This outcome aligns with revised data for the initially promising *in-house* ligand **ST-2529**, which was ultimately found to lack any H_4R affinity in subsequent testing rounds, but the synthetic route had already been designed and executed based on **ST-2529**'s preliminary results.

Unfortunately, neither the modification of the ester to an amide nor the oxidation of the thioether side chain led to enhanced H_4R affinity. With no significant binding observed, further investigation of fluorescent properties and the planned evaluation of different linker lengths were not pursued, allowing resources to be directed toward more promising scaffolds.

Table 15: Histamine H_4 receptor affinities of ligands **P27-29b** and of the oxidated fluorescent ligands **P34** and **P35.**

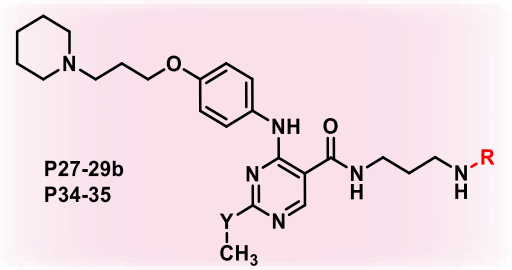

R=	Y=	Compound	hH_4R K_i (nM) [95% CI]
-Boc	S	**P27b**	>10000
-H	S	**P28b**	>10000
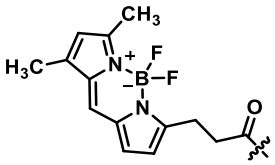	S	**P29b**	>10000
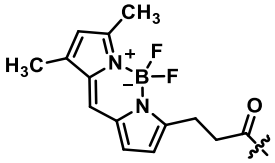	SO	**P34**	>10000
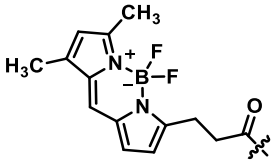	SO_2	**P35**	>10000
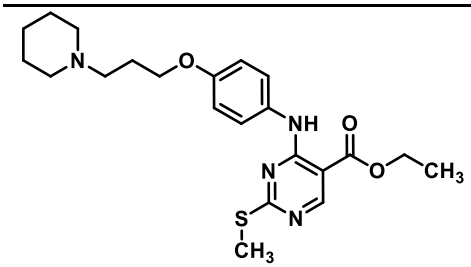		**ST-2529**	4.1/>10000*

**in-house* value of initial testing result/final testing result.

7.5 VUF-10558-based *N*-linked fluorescent H_4R ligands

7.5.1 Rational design

The next rational design approach was based on the H_4R ligand **VUF-10558**,[353] featuring a central quinazoline ring substituted at the 2-position with a methylpiperazine ring, a structural feature common to many H_4R ligands.[351] At the 4-position an ethyl linker is attached to the aromatic core through a secondary amine, bearing a terminal primary sulfonamide. This rational design strategy aimed to maintain the core pharmacophore of **VUF-10558** while modifying only the 4-position linker, preserving the secondary amine as the aromatic connection but replacing the terminal sulfonamide, a substitution already successfully implemented for H_4R ligands,[353,759] with primary Boc-protected amines suitable for BODIPY-FL attachment after deprotection. In this approach, eight different Boc-protected diamine-functionalized linkers were investigated, comprising five alkyl-based linkers ranging from ethylenediamine to hexyldiamine and three PEG-based linkers from mono- to triethylene glycol.

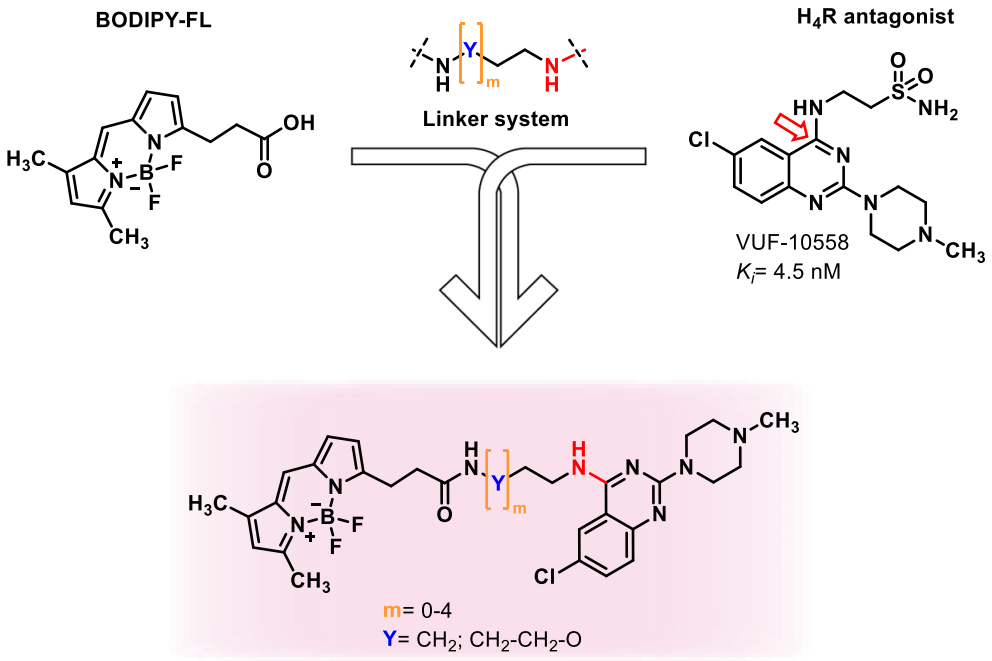

Figure 134: Rational design strategy for novel fluorescent H_4R ligands based on H_4R lead structure **VUF-10558**, investigating an secondary amine linkage approach exploring variable linker lengths and types.

7.5.2 Synthesis of pharmacophore building block

The synthesis of this **VUF-10558**-based series began with the preparation of the 2,4,6-trichloroquinazoline pharmacophore building block **SM4** which allows to address its position 2 and 4 through nucleophilic aromatic substitution. The two-step synthetic route for this building block, shown in Figure 135, is designed to start from 5-chloroanthranilic acid (**46**),

which can undergo a ring closure reaction with urea to form compound **47**. Subsequent chlorination would complete the aromatic system to yield the 2,4,6-trichloroquinazoline **SM4**.

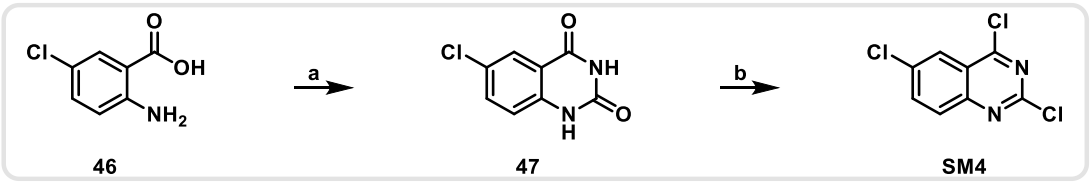

Figure 135: Planned synthetic route for starting material **SM4**, needed for the synthesis of the **VUF-10558**-based H_4R fluorescent ligand series. Reaction conditions: a) urea, 200 °C, 2 h. b) phosphorus oxychloride, *N*,*N*-diethyl anillin, 110 °C, 20 h.

To initiate the building block synthesis, 5-chloroanthranilic acid (**46**) underwent a ring closure reaction with urea. The starting materials were melted together at 200 °C for two hours, delivering the product in 83% yield.[760] The mechanism,[603] as depicted in Figure 136, proceeds through simultaneous nucleophilic attacks, as the urea amide attacks the carbonyl function of **46**, while correspondingly its amine function attacks the carbonyl carbon of urea completing the ring closure (**TS1**). These synchronous reactions result in cleavage of both carbonyl C=O double bonds. Intramolecular proton transfer followed by elimination of water and ammonia (**TS2**) leads to reformation of the carbonyl double bond, thereby stabilizing the newly formed ring and yielding product **47**.

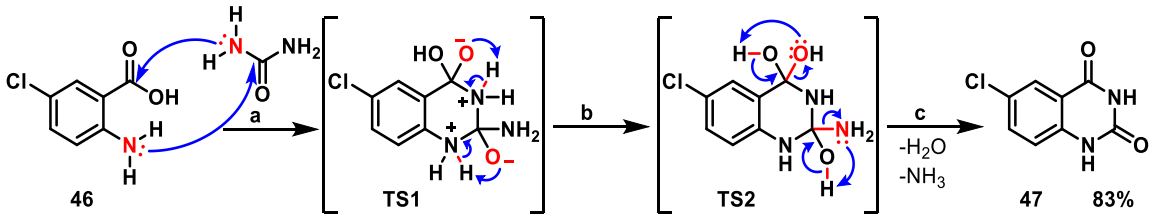

Figure 136: Mechanism of the ring closure reaction of 5-chlorantanilic acid (**46**), yielding product **47**. a) Double nucleophilic attack b) Proton transfer c) Elimination of water and ammonia.

In the second and final step of the 2,4,6-trichloroquinazoline synthesis, chlorination of both carbonyl functions was conducted to aromatize the newly formed ring. The reaction was performed using phosphorus oxychloride as solvent at 110 °C for 20 hours, yielding product **SM4** in 72% yield.[761] The mechanism,[603] as shown in Figure 137, starts with a nucleophilic attack of the hydroxyl group of **47**'s tautomeric form (**47t**) at the phosphorus atom of phosphorus oxychloride, cleaving its P=O double bond. Reformation of this double bond eliminates hydrogen chloride (**TS1**), and the resulting chloride anion then attacks the aromatic ring via nucleophilic aromatic substitution (for mechanism see Figure 124) *ipso* to the phosphinate moiety, which subsequently leaves the molecule (**TS2**). This process is repeated with the hydroxyl group at the other position of the quinazoline ring, proceeding through

phosphinate formation, hydrogen chloride elimination (**TS4**), and nucleophilic aromatic substitution (**TS5**) of the phosphinate to yield the final 2,4,6-trichloroquinazoline product **SM4**.

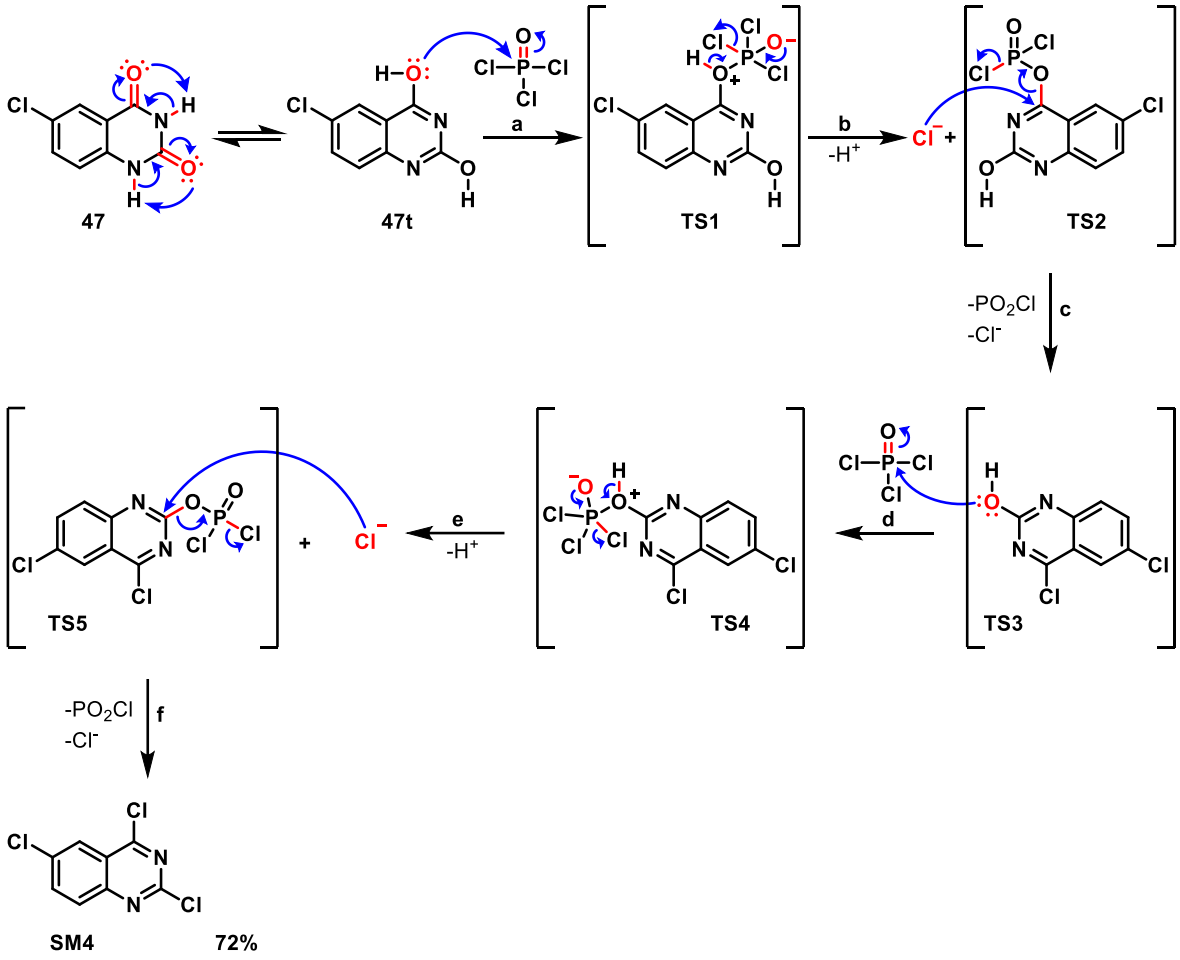

Figure 137: Mechanism of the chlorination compound **47**, yielding product **SM4**. a) Nucleophilic attack b) Elimination of hydrochloride c) Nucleophilic aromatic substitution d) Nucleophilic attack e) Elimination of hydrochloride f) Nucleophilic aromatic substitution.

7.5.3 Fluorophore attachment through secondary amine linkage

The synthetic route of this **VUF-10558**-based H_4R fluorescent ligand series (see Figure 138) was designed to attach the different linkers to the successfully synthesized pharmacophore building block **SM4**, exploring a secondary amine linkage. The 2,4,6-trichloroquinazoline ring allows regioselective nucleophilic aromatic substitution, occurring preferentially at the more reactive 4-position before the 2-position due to a higher LUMO coefficient of the carbon at position 4, resulting in lower activation energy for nucleophilic attack.[762] This reactivity difference enables sequential substitution needed to implement first the different linkers at the 4-position (**48a-h**), matching the secondary amine linkage of the reference ligand **VUF-10558**, followed by methylpiperazine attachment at the 2-position to complete the H_4R pharmacophore (**P36a-h**). A subsequent Boc deprotection would then deliver the free amines

of the linkers (**P37a-h**), enabling coupling with BODIPY-FL to finalize this **VUF-10558**-based H_4R fluorescent ligands **P38a-h**.

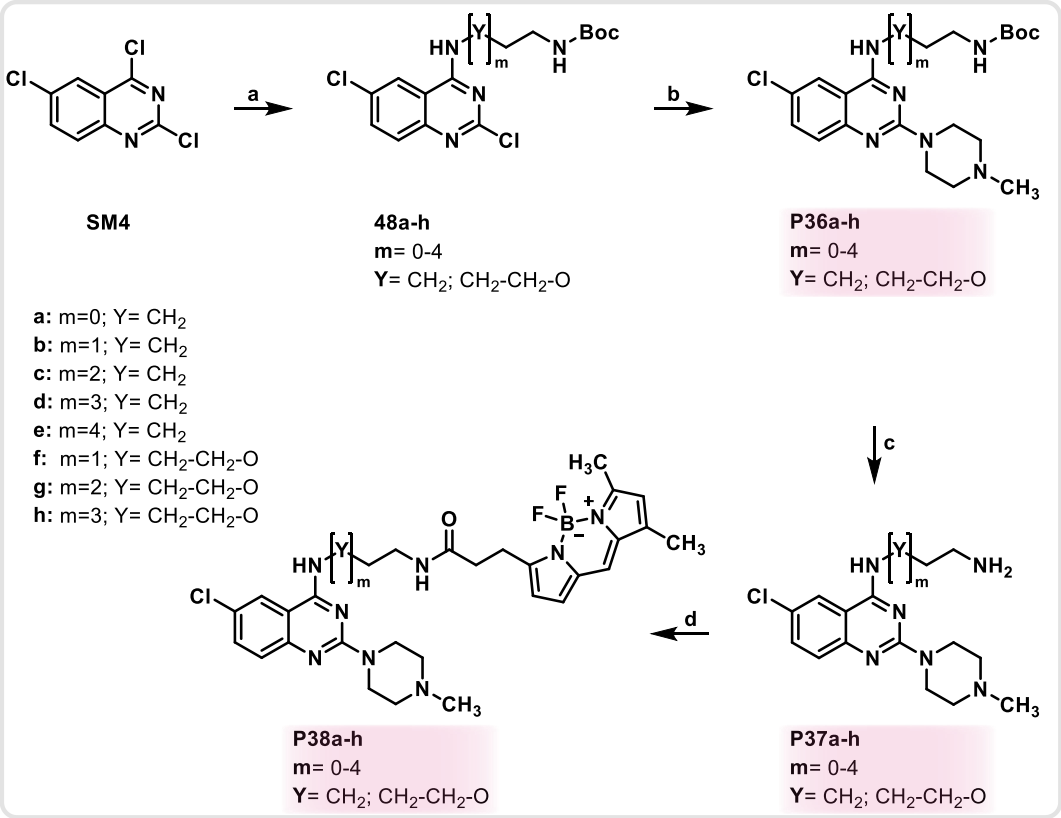

Figure 138: Planned synthetic route for the synthesis of the **VUF-10558**-based series of H_4R fluorescent ligands **P38a-h,** exploring the secondary amine linkage approach. Reaction conditions: a) NEt_3, linker, THF, room temperature, 24 h. b) NMP, DIPEA, isopropanol, 90 °C, 20 h. c) HCl, methanol, room temperature, 24 h. d) HATU, DIPEA, BODIPY-FL, DMF, room temperature, 24 h.

The first step of the synthetic scheme involved the attachment of the various mono-Boc-protected amino-functionalized linkers onto the quinazoline building block **SM4**, achieved through S_NAr at the 4-position. The substitutions, following the mechanism shown in Figure 124, were performed under mild conditions in THF at room temperature with base catalysis for 20 hours, yielding the secondary amines in 35-62% yields (see Figure 139).[761] The moderate yields can likely be attributed to competing nucleophilic attack at the less reactive 2-position,[762] leading to formation of undesired mono- and disubstituted side products.

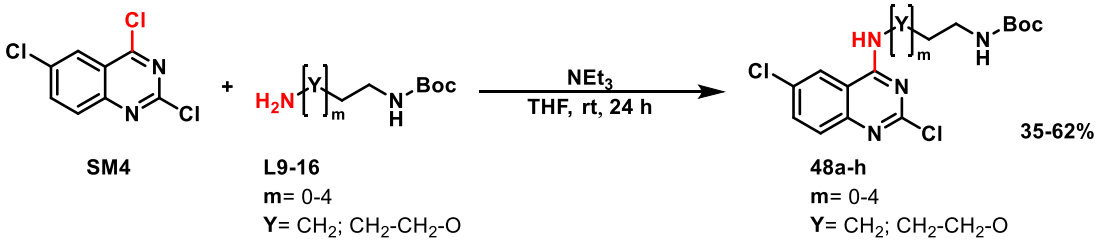

Figure 139: Reaction of the S_NAr of compound **SM4** with linkers **L9-16**, yielding compounds **48a-h**.

In the next step, the H_4R pharmacophore was completed through S_NAr of NMP at the 2-position of the quinazoline ring of compounds **48a-h**. Due to the lower reactivity of the 2-position,[762] the reactions required elevated temperatures and were performed in isopropanol at 90 °C for 20 hours,[761] yielding the products in 20-92% (see Figure 140), following the mechanism depicted in Figure 124. The moderate yields for some products can potentially be linked to partial decomposition of product or starting material under the elevated temperature conditions[763,764] as well as to intermolecular side reactions, where the secondary amine of the attached linker competes with NMP for substitution at the 2-position. Moreover, yield variations may reflect differences in linker properties, such as length, flexibility, or nucleophilicity, particularly between aliphatic and PEG-based linkers, which can impact substitution efficiency at the 2-position.

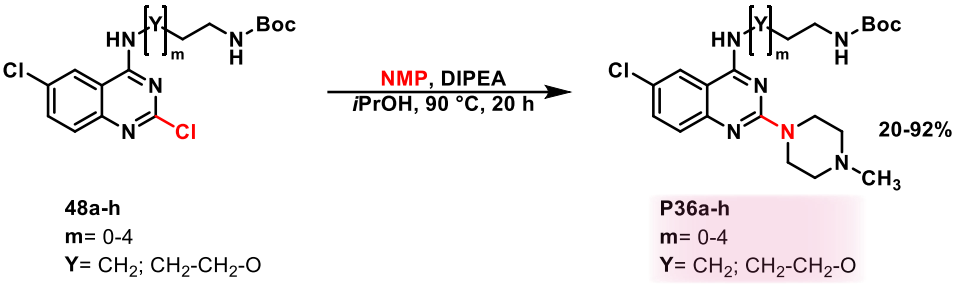

Figure 140: Reaction of the S_NAr of compounds **48a-h** with NMP, yielding compounds **P36a-h**.

After completing the H_4R pharmacophores, the Boc-protecting group of compounds **P36a-h** were removed to obtain the free amines of the linkers, which were required for the later fluorophore attachment. The deprotections, following the mechanism shown in Figure 65, were carried out in methanol with hydrogen chloride at room temperature for 24 hours,[674] yielding the deprotected compounds **P37a-h** in 84-100% (see Figure 141) as their free bases after ion exchanger treatment.

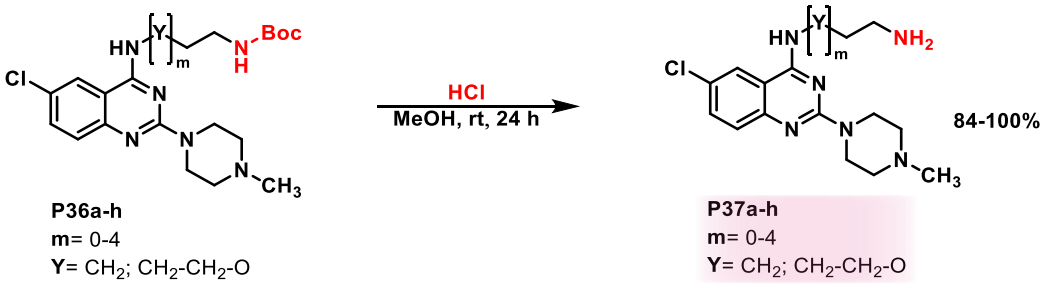

Figure 141: Reaction of the Boc-deprotection of compounds **P36a-h**, yielding compounds **P37a-h**.

In the final step of this **VUF-10558**-based H_4R fluorescent ligand series synthesis, the BODIPY-FL fluorophore was coupled to the free amine of the linkers of compounds **P37a-h** to generate the fluorescent ligands **P37a-h**. The coupling reaction proceeded, following the mechanism shown in Figure 57, with HATU and DIPEA in DMF at room temperature for

24 hours,[644] delivering the final fluorescent compounds **P38a-h** in moderate yields of 16-51% (see Figure 142). The observed yield ranges reflected the stability issues of BODIPY-FL in the basic reaction conditions[722] required for this transformation. Additionally, the observed yield variation may result from differences in linker architecture, as variations in length, flexibility, and steric accessibility of the linker amine can affect coupling efficiency.

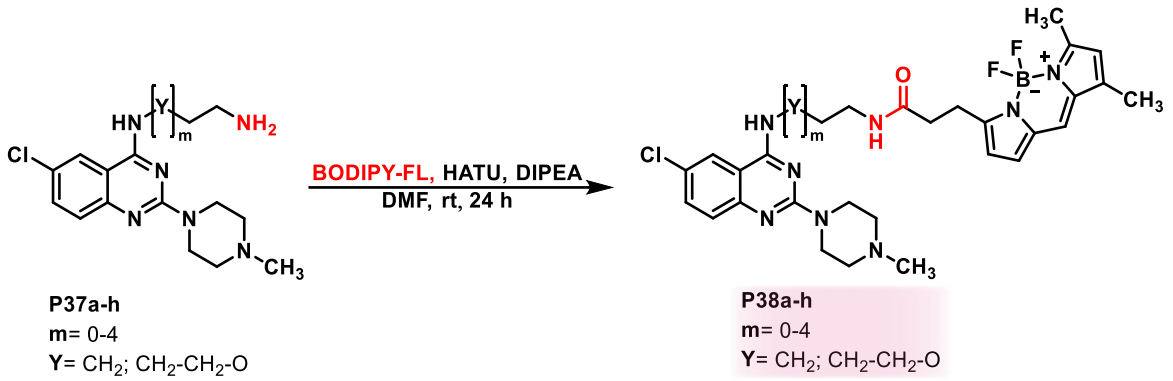

Figure 142: Reaction of the HATU-mediated coupling of compounds **P37a-h** with BODIPY-FL, yielding the fluorescent compounds **P38a-h**.

7.5.4 Binding profile

The initial H_4R affinity assessment for this series was performed using a representative progression trio of the propyl linker derivatives (**P36-38b**), maintaining consistency with previous evaluations. This investigation primarily focused on examining how the removal of the terminal sulfonamide group from the parent pharmacophore **VUF-10588**[353] affects binding affinity and whether its favourable pharmacological properties could be preserved. The evaluation of different linker lengths and types was planned as a subsequent step, following successful preservation of receptor affinity. The binding data revealed that while the Boc-protected and unprotected linker compounds **P36b** and **P37b** maintain some H_4R affinity, their potency is significantly lower compared to the parent ligand **VUF-10558** used as the pharmacophore building block, highlighting the importance of the terminal sulfonamide group for receptor binding (see Table 16). Notably, this unexpectedly low affinity contrasts with literature-reported compounds featuring various secondary amine substitutions at position 4, including both aromatic and aliphatic substituents.[353,759] While these reference compounds typically achieve up to low nanomolar affinities, the highest binding, next to different substituted sulfonamide moieties, was demonstrated by compounds containing aromatic substituents in benzyl position to the secondary amine in 4-position. Even extending the aliphatic chain between the secondary amine and aromatic ring by just one methylene unit leads to reduced affinity,[282] indicating the importance of precise aromatic moiety positioning at this spatial location. This spatial sensitivity is further supported by reported data demonstrating that shortening the ethyl linker between the secondary amine and sulfonamide

group in the parent compound **VUF-10588** by one methylene unit reduces affinity approximately 10-fold.[282] The lower affinity of the compounds of this series compared to these literature examples can therefore likely be attributed to both the lack of an aromatic moiety in benzyl position to the secondary amine and to different electronic effects, particularly for the deprotected compound. Additionally, the results of this series indicate that the specific positioning of such groups is crucial, with the Boc group potentially causing unfavourable interactions in these short-linker compounds. While these data provided valuable insights into position 4 substitution patterns, the complete loss of affinity in the fluorescent ligand **P38b** further suggests that the selected linker length may be insufficient to position the bulky BODIPY-FL fluorophore appropriately, likely resulting in steric interference with the binding pocket.

Therefore, a progressive trio of compound **P36-P38e** with a longer alkyl chain as linker was investigated. The results of the Boc-protected compound **P36e** show a high affinity of 158 nM, although this should be treated with caution due to the high confidence intervals and must be confirmed by the final results of the assay. This significant improvement confirms that the spatial positioning of the Boc group is critical, with the longer linker likely allowing it to extend to a more favourable position relative to the binding pocket. While the results for the unprotect compound **P37e** are still pending, the findings for the fluorescent derivative **P38e** also demonstrated an improvement compared to the short-chain derivative **P38b**, even though the affinity remains in the low micromolar range rather than the low nanomolar range, presumably due to persistent steric hindrance caused by insufficient linker length, which likely still positions the bulky fluorophore too close to the pharmacophore and thereby interferes with optimal receptor binding. Consequently, fluorescence characterization was also not conducted Given the current findings, the longer PEG linker derivatives **P36-P38g/h** need to be examined for their affinity in the future to confirm this observed trend. However, the high affinity of **P36e** already provides a good foundation for further development of fluorescent ligands based on this pharmacophore attachment approach, possibly with the direction of further increasing the linker length between pharmacophore and fluorophore.

Table 16: Histamine H_4 receptor affinities of ligands **P36-38b/e**.

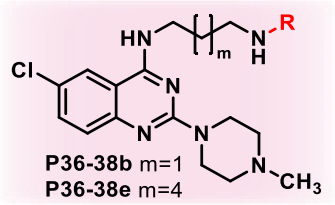

R=	m	Compound	hH_4R K_i (nM) [95% CI]
-Boc	1	**P36b**	**4275** [1375; 13285]
-Boc	4	**P36e**	**158** [11; 2356]
-H	1	**P37b**	**5485** [1350; 22287]
-H	4	**P37e**	**-**
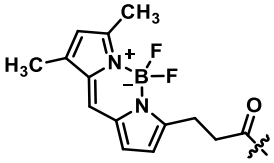	1	**P38b**	>10000
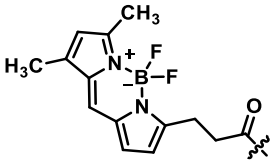	4	**P38e**	**1328** [453; 3888]
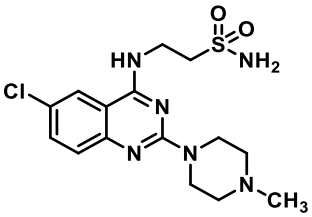		**VUF-10588**	**25.4** [19.9; 32.5]

7.6 VUF-10558-based *O*-linked fluorescent H_4R ligands

7.6.1 Rational design

The rational design approach presented herein (see Figure 143) was also based on the core pharmacophore of the H_4R ligand **VUF-10558**[353], but this time exploring an alternative attachment strategy of the linkers to the pharmacophore through an ether connection. This design replaced the secondary amine present in **VUF-10558** at the 4-position of the quinazoline ring with an oxygen atom, a modification strategy already documented for H_4R ligands although only with aromatic substitutents,[353,759] aiming to investigate how the different physicochemical properties of this aliphatic linking motif would affect receptor affinity. As in the previous series, the primary terminal sulfonamide group of **VUF-10558** was substituted with Boc-protected amines, enabling subsequent BODIPY-FL attachment after deprotection.

This approach investigated a set of eight different linkers with modified terminal groups, featuring a Boc-protected amine on one end and a free hydroxyl group on the other, enabling linker attachment at the pharmacophore through ether formation. The linker series maintained the previously established diversity, comprising five alkyl-based linkers ranging from ethylenediamine to hexyldiamine and three PEG-based linkers spanning from mono- to triethylene glycol.

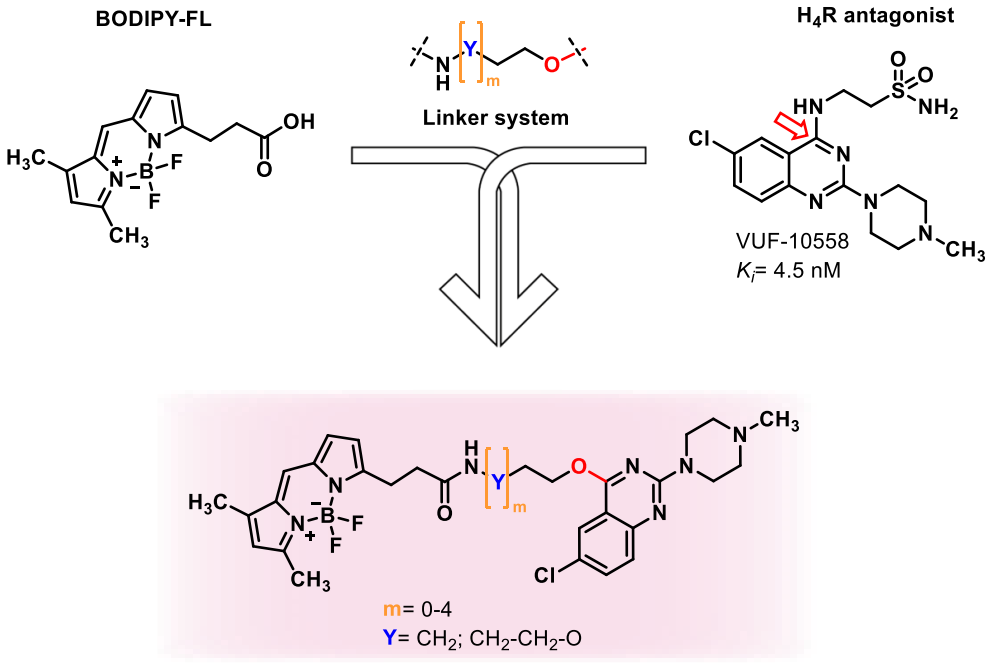

Figure 143: Rational design strategy for novel fluorescent H_4R ligands based on H_4R lead structure **VUF-10558**, applying an ether linkage approach exploring variable linker lengths and types.

7.6.2 Fluorophore attachment through ether linkage

The synthetic route, as shown in Figure 144, proceeded from 2,4,6-trichloroquinazoline **SM4**, similar to the secondary amine linking approach. However, in this sequence, the first S_NAr reaction was performed with the Boc-protected hydroxyl-functionalized linkers at the 4-position to form an ether linkage. The subsequent substitution at the 2-position with NMP completed the H_4R pharmacophore formation (**P39a-h**). Boc deprotection (**P40a-h**) followed by coupling with BODIPY-FL delivered the target **VUF-10558**-based H_4R fluorescent ligands **P41a-h**.

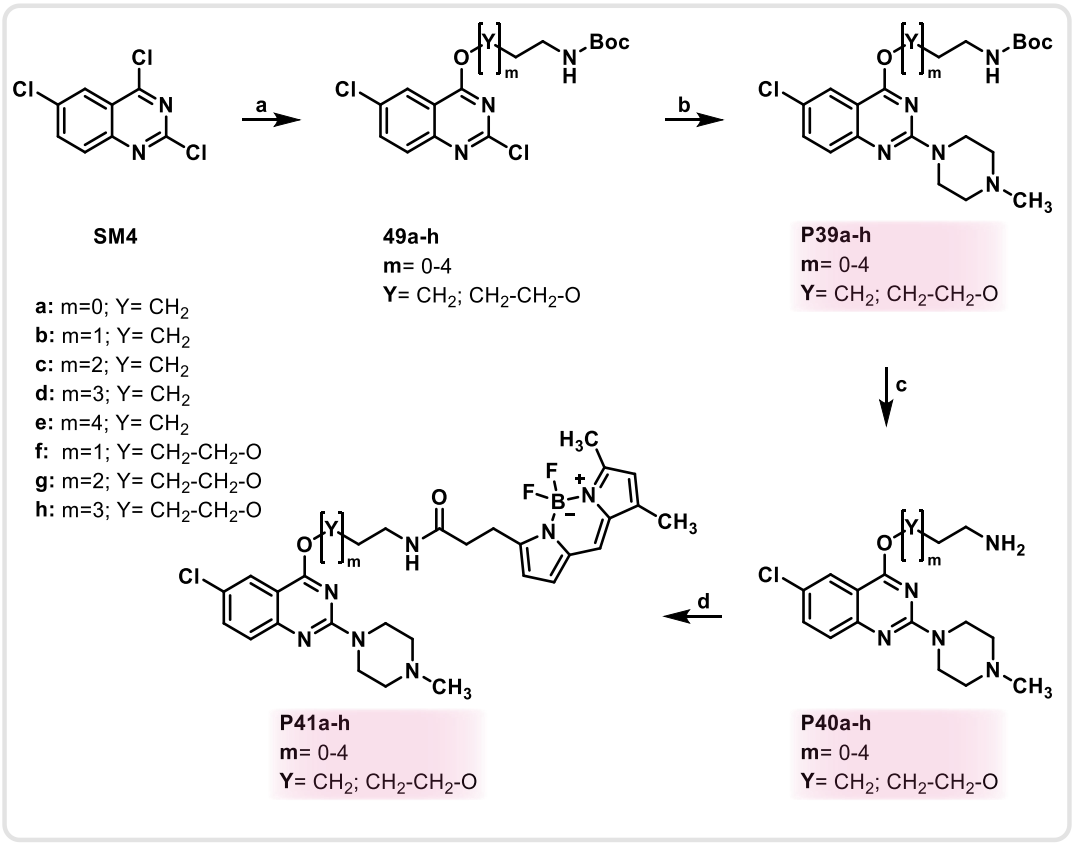

Figure 144: Planned synthetic route for the synthesis of the **VUF-10558**-based series of H_4R fluorescent ligands **P41a-h,** exploring the ether linkage approach. Reaction conditions: a) NAH, THF, room temperature, 24 h. b) NMP, DIPEA, isopropanol, 90 °C, 20 h. c) HCl, methanol, room temperature, 24 h. d) HATU, DIPEA, BODIPY-FL, DMF, room temperature, 24 h.

The first step of the synthetic scheme involved an S_NAr reaction of linkers **L17-24** at the 4-position of the quinazoline ring of **SM4** to establish the ether linkage to the pharmacophore building block. The reactions were performed in THF at room temperature for 20 hours using sodium hydride as base to deprotonate the hydroxyl function of the linkers, generating the alkoxide nucleophile for the S_NAr. This yielded the 4-substituted products **49a-h** in 18-90% (see Figure 145),[765] following the mechanism as depicted in Figure 124. The moderate yields observed for some compounds can likely be attributed to competitive 2-substitution by the

generated alkoxide, which, as a strong nucleophile,[643] can overcome the lower reactivity of the 2-position in S_NAr reactions,[762] leading to undesired mono- and disubstituted products. Additionally, the strong basic conditions could deprotonate the Boc-protected amine,[766–768] forming an additional reactive nucleophile that can potentially participate in S_NAr reactions, resulting in side products.

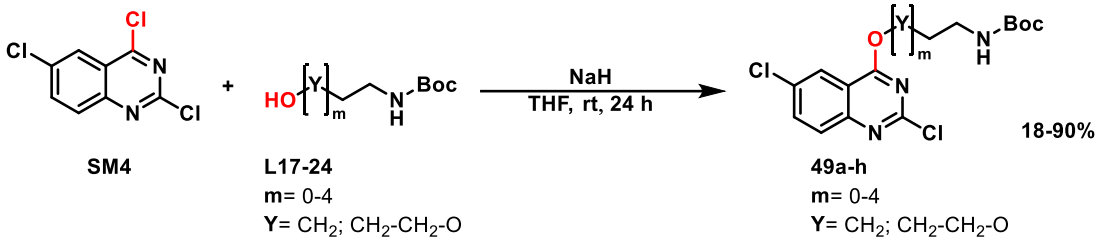

Figure 145: Reaction of the S_NAr of compound **SM4** with linkers **L17-24**, yielding compounds **49a-h**.

In the next step, a second S_NAr reaction was performed with NMP attacking at the 2-position of compounds **49a-h** to complete the H_4R pharmacophore. Since the 2-position exhibits lower reactivity in S_NAr reactions,[762] elevated conditions using isopropanol at 90 °C for 20 hours were employed,[761] delivering the desired products in 33-97% yield (see Figure 146), following the mechanism shown in Figure 124. The moderate yields observed for some products can likely be attributed to the previously discussed thermal decomposition[763,764] and intramolecular side reactions under these conditions, with the observed yield range also reflecting reactivity differences due to linker type and length.

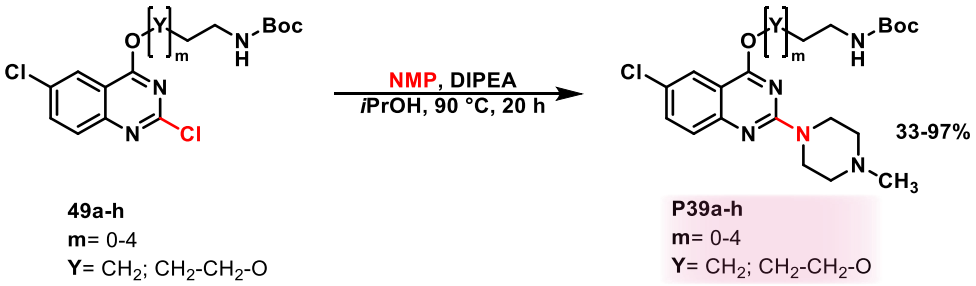

Figure 146: Reaction of the S_NAr of compounds **49a-h** with NMP, yielding compounds **P39a-h**.

Following successful completion of the H_4R pharmacophore, the Boc-protected linker compounds **P39a-h** were deprotected to reveal the primary amine required for subsequent fluorophore coupling. The deprotections, following the mechanism shown in Figure 65, were performed in methanol using hydrochloric acid as proton source at room temperature for 24 hours,[674] delivering the free ligands **P40a-h** in 75-100% yield (see Figure 147). The products were obtained as free bases after ion exchanger treatment.

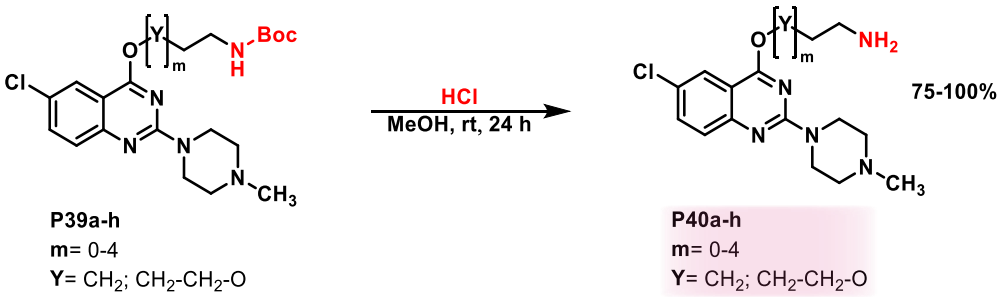

Figure 147: Reaction of the Boc-deprotection of compounds **P39a-h**, yielding compounds **P40a-h**.

Finally, the fluorophore was attached to the free amine of the linkers in compounds **P40a-h**, completing this **VUF-10558**-based ether-linked fluorescent ligand series (see Figure 148). The HATU-mediated couplings, proceeding in the mechanism depicted in Figure 57, were performed under basic conditions required for this transformation in DMF at room temperature for 24 hours,[644] yielding the final fluorescent compounds **P41a-h** in yields of 19-59%. The moderate yields observed for some compounds can likely be attributed to BODIPY-FL's gradual degradation under the basic reaction conditions,[722] with the wide yield range also influenced by differences in linker stability and reactivity.

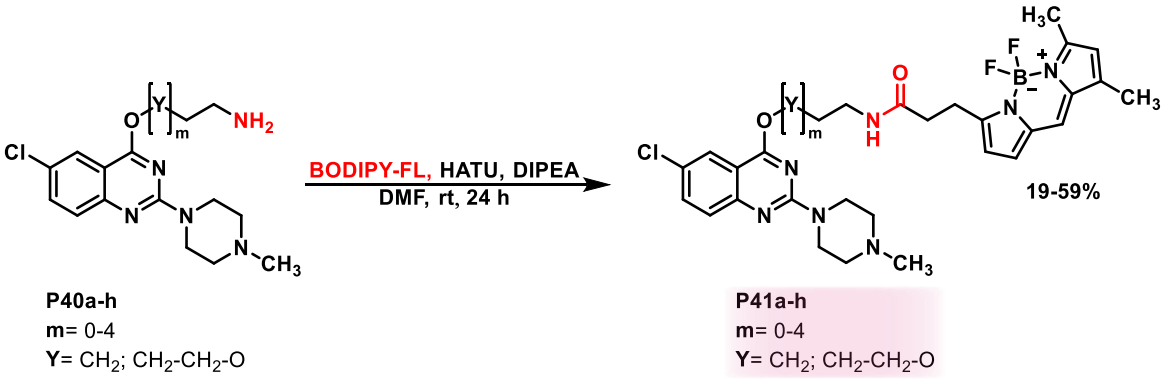

Figure 148: Reaction of the HATU-mediated coupling of compounds **P40a-h** with BODIPY-FL, yielding the fluorescent compounds **P41a-h**.

7.6.3 Binding profile

The initial H_4R affinity assessment was conducted using the propyl linker derivatives **P39b** and **P41b** as the representative progression trio, maintaining consistency with previous evaluations. This first investigation mainly evaluated the impact of replacing the secondary amine of the parent pharmacophore **VUF-10588**[353] with an ether linkage, examining how this modification may influences receptor binding. Systematic exploration of linker variations was designated as the next development phase, building upon demonstrated receptor affinity. The results, shown in Table 17, align with the findings from the previous secondary amine linkage series, reinforcing the importance of the sulfonamide group for receptor interaction. The linker derivatives **P39b** and **P40b** display only low H_4R affinity, while the fluorescent ligand **P41b**

shows no binding, consistent with the previously discussed potential spatial constraints between the BODIPY-FL fluorophore and the binding pocket due to insufficient linker length. However, in contrast to the previous series, the low affinities observed for **P39b** and **P40b** align with the affinities of literature-reported compounds featuring the same ether linkage at the 4-position.[353,759] These findings show that aliphatic substituents connected through an ether linkage at this position unfortunately do not enhance H_4R affinity beyond that of the literature-reported aromatic ether derivatives. Given these low binding data and literature precedent, further evaluation of linker length and type, as well as fluorescence characterization, was not pursued.

Table 17: Histamine H_4 receptor affinities of ligands **P39-41b**.

R=	Compound	hH_4R K_i (nM) [95% CI]
-Boc	**P39b**	**4208** [974; 18177]
-H	**P40b**	**4812** [1644; 14085]
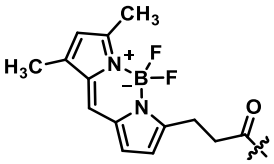	**P41b**	>10000
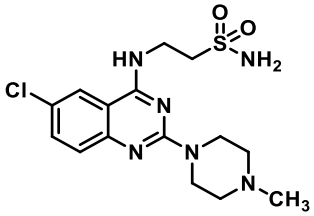	**VUF-10588**	**25.4** [19.9; 32.5]

7.7 VUF-10558-sulfur-bridged fluorescent H_4R ligands

7.7.1 Rational design

This next rational design approach (see Figure 149) was inspired by the promising initial affinity assessment results of **ST-2529** and aimed to merge key structural elements of two H_4R reference ligands, utilizing the quinazoline core from **VUF-10558**[353] while substituting the polar methylpiperazine motif at the 2-position with an **ST-2529**-inspired thioether moiety. This thioether serves as a foundation for potential later oxidation to sulfoxides and sulfones to better match the physicochemical properties of the methylpiperazine typically present at this position.[351] The design maintained the secondary amine linkage at the 4-position for spacer attachment, as found in **VUF-10558**, while replacing the primary terminal sulfonamide group with primary amines to enable subsequent BODIPY-FL attachment.

This approach investigated a set of five different alkyl linkers ranging from ethylenediamine to hexyldiamine, featuring diamino functionalization at both ends, one for pharmacophore attachment via secondary amine linkage and the other for fluorophore coupling. The unprotected forms of the linkers were employed since in this design the second S_NAr at the 2-position were performed with sodium thiomethoxide, a stronger nucleophile than the previously used NMP as well as the free primary amine of the unprotected linkers.[643] This allows the 2-position substitution to proceed effectively, particularly when using excess of sodium thiomethoxide. Moreover, the elimination of a synthetic step justified accepting the risk of potentially lower yields from competitive side reactions.

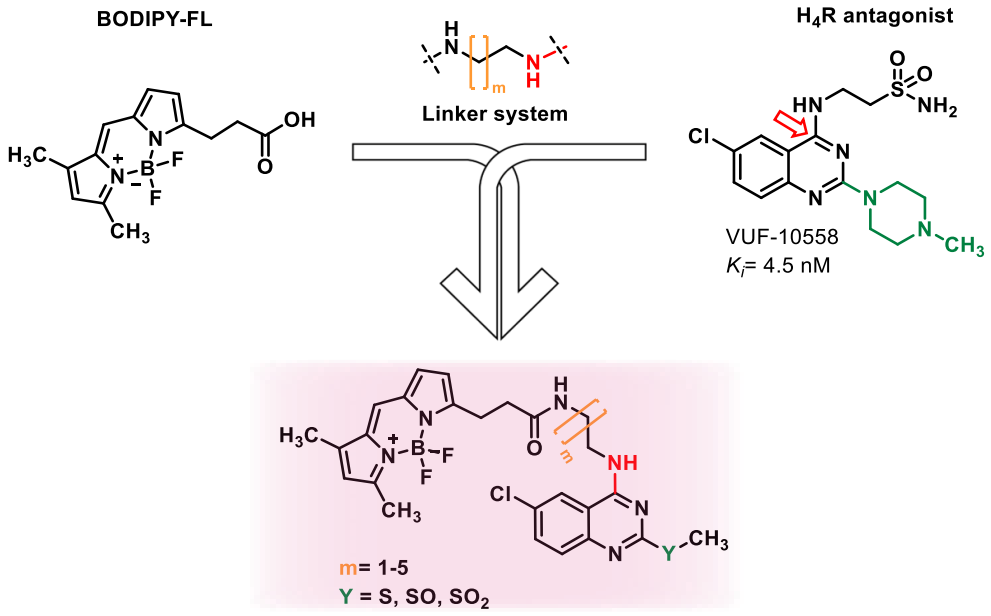

Figure 149: Rational design strategy for novel fluorescent H_4R ligands based on H_4R lead structure **VUF-10558**, incorporating a thioether moiety for subsequent oxidation in place of the methylpiperazine group, inspired by **ST-2529**, while maintaining the secondary amine linkage approach with variable linker length at position 4.

7.7.2 Synthesis of thioether series

The synthetic route of this merged **VUF-10558/ST-2529**-inspired series, as shown in Figure 150, was designed as an efficient two-step sequence starting from 2,4,6-trichloroquinazoline building block **SM4**. The first step comprised a sequential double S_NAr reaction, beginning with 4-position substitution using unprotected diamino functionalized linkers, followed by *in situ* 2-position substitution with sodium thiomethoxide to deliver compounds **P42a-e**. These intermediates contained both the thioether group at 2-position, suitable for possible later oxidation to sulfoxide/sulfone derivatives, and a free primary amine at the linker terminus ready for fluorophore attachment. The final step involved coupling this primary amine with BODIPY-FL to complete the series, yielding the fluorescent compounds **P43a-e**.

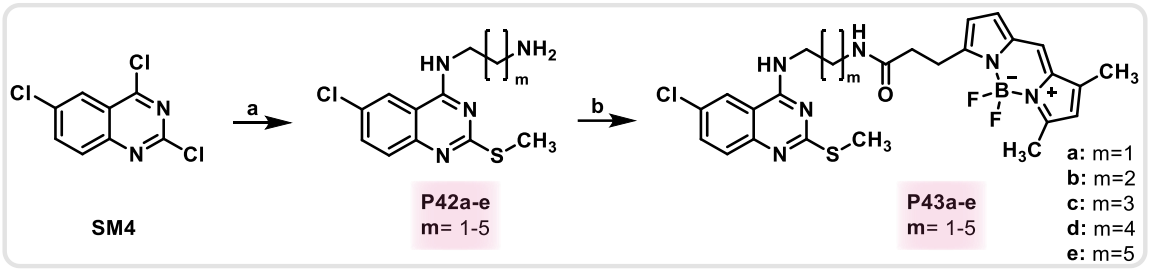

Figure 150: Planned synthetic route for the synthesis of the **VUF-10558**-based series of H_4R fluorescent ligands **P43a-e,** exploring a secondary linkage approach. Reaction conditions: a) i) NEt_3, linker, THF, room temperature, 4 h ii) NaSMe, isopropanol, 90 °C, 20 h. b) HATU, DIPEA, BODIPY-FL, DMF, room temperature, 24 h.

The first step of the designed synthetic route involved a sequential double S_NAr, first substituting the 4-position of **SM4** with the different linkers **L25-29** to establish the amine linkage to the pharmacophore, followed by 2-position substitution with sodium thiomethoxide to introduce the thioether moiety. The initial reactions were conducted at room temperature in THF for four hours,[761] after which the solvent was changed to isopropanol and excess sodium thiomethoxide was added as the nucleophile. The reaction mixtures were then heated to 90 °C for 20 hours[769] to facilitate the more challenging substitution at the 2-position,[762] delivering products **P42a-e** in yields of 17-41% over two steps (see Figure 151), following the mechanism shown in Figure 124. The moderate yields of some products can likely be attributed to

competing substitution reactions from the unprotected amine of the linker motifs, including the risk of dimer formation during 4-substitution, as well as undesired 2-substitutions.

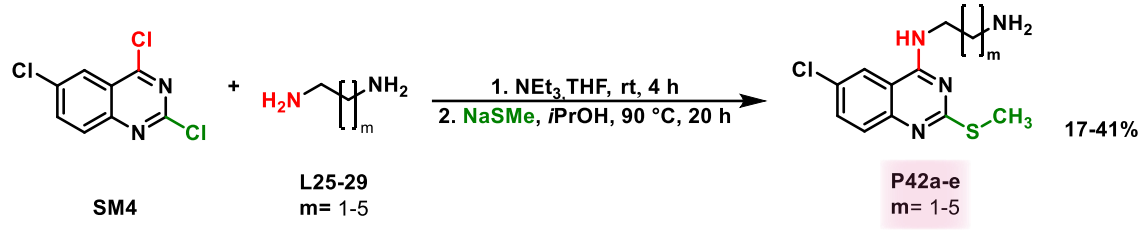

Figure 151: Reaction of the double S_NAr of compound **SM4** with linkers **L25-29** and sodium thiomethoxide, yielding compounds **P42a-e**.

In the final step of the synthetic route of this merged **VUF-10558/ST-2529**-inspired series , the fluorophore was coupled to the amine function of the linker motif in compounds **P42a-e**. The HATU-mediated couplings, following the mechanism depicted in Figure 57, were performed under the required basic conditions in DMF at room temperature for 24 hours,[644] yielding the fluorescent products **P43a-e** in 29-62% yield (see Figure 152). The moderate yields observed for some compounds can likely be attributed to BODIPY-FL's sensitivity to basic conditions.[722]

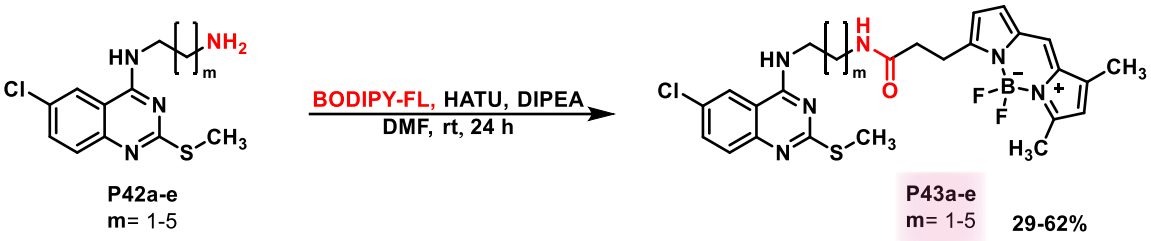

Figure 152: Reaction of the HATU-mediated coupling of compounds **P42a-e** with BODIPY-FL, yielding the fluorescent compounds **P43a-e**.

7.7.3 Synthesis of sulfoxide and sulfone derivatives

As explained in the rational design, the thioether moiety was introduced at the 2-position, inspired by H_4R ligand **ST-2529**, replacing the more polar methylpiperazine typically present in H_4R ligand **VUF-10558**. To better align the physicochemical properties with the methylpiperazine moiety, oxidation to the corresponding sulfoxide and sulfone derivatives was planned. As a preliminary investigation, one representative ligand was initially selected to evaluate the effects of both oxidation states on receptor affinity before extending the modifications to the entire series. The oxidations were intended to be performed on both the final fluorophore-coupled ligand and its free amine precursor to allow affinity evaluation of both compounds, as the fluorophore's proximity to the pharmacophore could influence binding affinity through steric clashes with the binding pocket, potentially masking the specific effects of oxidation.

Since direct oxidation of the unprotected amine was unsuccessful, likely due to *N*-oxide formation,[757] the synthesis had to proceed via the Boc-protected compound, following an oxidation strategy analogous to the **ST-2529**-based ligand series (see Figure 130). Starting from compound **48b**, previously synthesized in the **VUF-10558**-based secondary amine linkage series (see Figure 139), the synthetic route was intended to begin with 2-position substitution using sodium thiomethoxide to yield compound **50**. This intermediate can then be selectively oxidized to the corresponding sulfoxide (**P44**) and sulfone (**P45**) by controlling oxidant equivalents, followed by deprotection (**P46** and **P47**) and final BODIPY-FL coupling to deliver the fluorescent oxidized ligands **P48** and **P49** (see Figure 153).

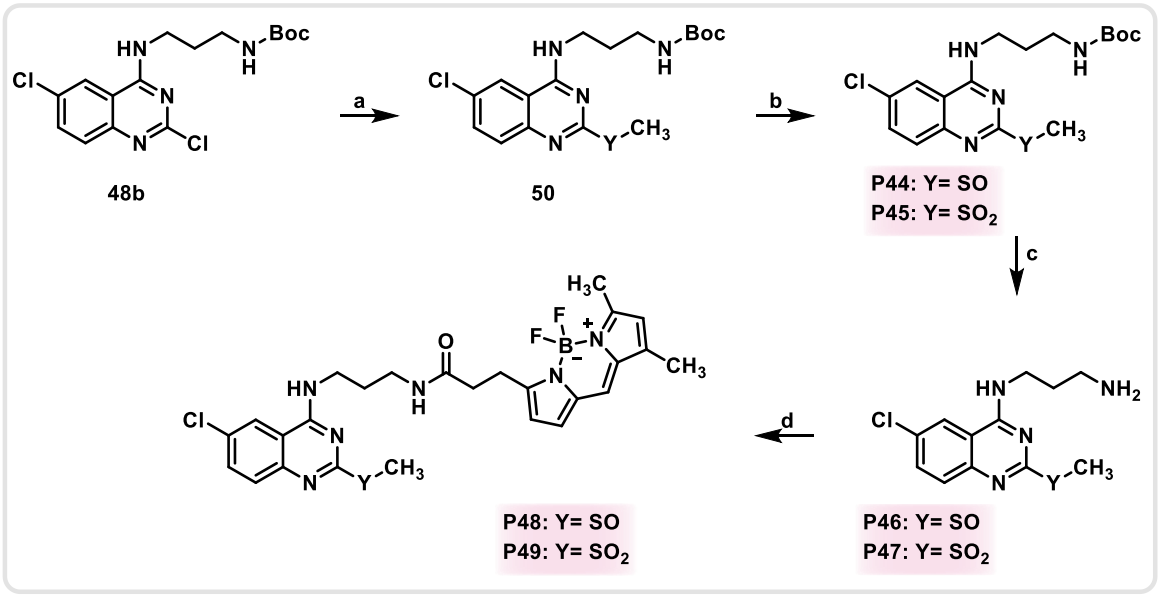

Figure 153: Planned synthetic route for the synthesis of the oxidized derivatives **P48** and **P49** of the **VUF-10558/ST-2529**-inspired series of H_4R fluorescent ligands. Reaction conditions: a) NaSMe, isopropanol, 90 °C, 20 h. b) mCPBA, DCM, room temperature, 2 h. c) HCl, isopropanol, room temperature, 24 h. d) HATU, DIPEA, BODIPY-FL, DMF, room temperature, 24 h.

The initial step of this synthetic route introduced the thioether moiety at the 2-position of compound **48b** through an S_NAr reaction, according to the mechanism depicted in Figure 124. The substitution was performed under basic conditions using sodium thiomethoxide as the nucleophile at 90 °C in isopropanol for 20 hours,[769] delivering the desired product **50** in 77% yield (see Figure 154).

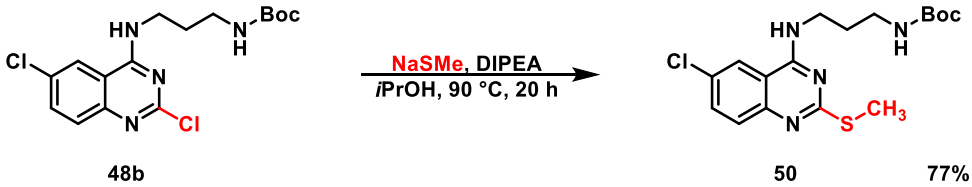

Figure 154: Reaction of the S_NAr of compound **48b** with linkers sodium thiomethoxide, yielding compound **50**.

The second step involved the oxidation of the thioether moiety of compound **50** to the respective sulfoxide and sulfone, following the mechanism shown in Figure 131. Both reactions were carried out in DCM with *m*-CPBA as the oxidant reagent at room temperature for two hours under argon atmosphere, with the different oxidation states achieved through stoichiometric control of *m*-CPBA, delivering sulfoxide **P44** in 36%[754] and sulfone **P45** in 46%[755] yield (see Figure 155). The moderate yields reflect the previously discussed challenges of this oxidation including potential *N*-oxide formation,[757] the tendency of the resulting sulfoxide and sulfone groups to act as leaving groups[756] in S_NAr side reactions,[751] and for sulfoxide synthesis specifically, susceptibility to overoxidation through air exposure or excess of oxidizing agent.[758]

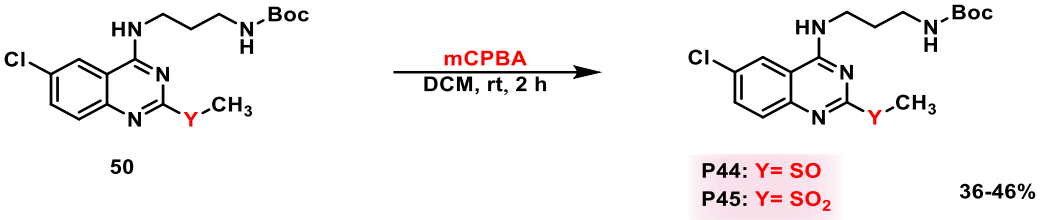

Figure 155: Reaction of the oxidations of compound **50** with *m*-CPBA, yielding compounds **P44** and **P45**.

Following successful oxidation, the Boc group was deprotected to release the amine functionality of the linker of compounds **P44** and **P45** for subsequent fluorophore attachment. The deprotections, following the mechanism depicted in Figure 65, were performed in isopropanol instead of the previously utilized methanol solvent, as preliminary experiments revealed unwanted S_NAr side reactions with methanol acting as a nucleophile. Using hydrochloric acid as proton source, the reaction proceeded at room temperature for 24 hours under argon atmosphere,[674] yielding the sulfoxide derivative **P46** in 42% and the sulfone derivative **P47** in 88% as their respective free bases after ion exchanger treatment (see Figure 156). The moderate yield of the former can likely be attributed to further overoxidation during the reaction or workup.[758]

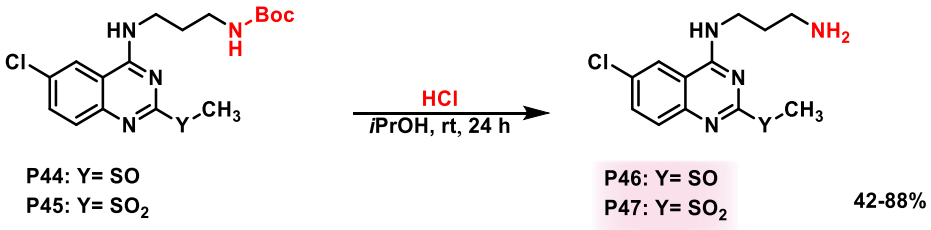

Figure 156: Reaction of the Boc-deprotection of compounds **P44** and **P45**, yielding compounds **P46** and **P47**.

To finish off the synthesis of the oxidized fluorescent ligands of the merged **VUF-10558/ST-2529**-inspired series, the BODIPY-FL fluorophore was coupled to the primary amine function of the linker motif in compounds **P46** and **P47**. The HATU-mediated couplings, following the mechanism depicted in Figure 57, were performed with the addition of required

base in DMF at room temperature for 24 hours,[644] yielding the oxidized fluorescent products **P48** and **P49** in 44% and 76% (see Figure 157). The yield discrepancy between the sulfoxide and sulfone derivatives likely arises again from the inherent tendency of the sulfoxide to undergo further oxidation.[758]

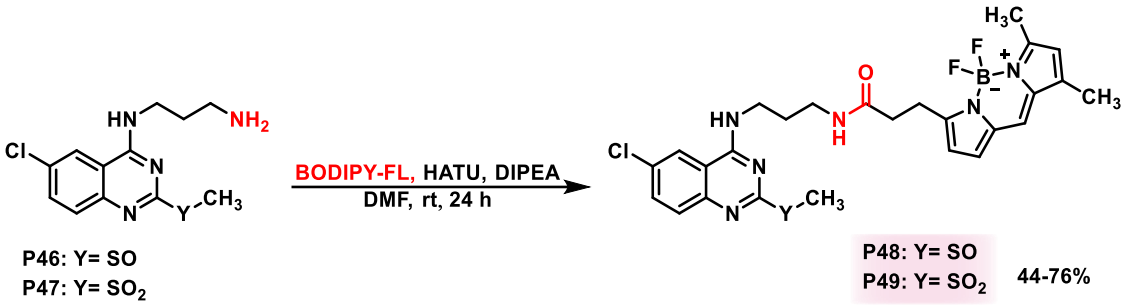

Figure 157: Reaction of the HATU-mediated coupling of compounds **P46** and **P47** with BODIPY-FL, yielding the fluorescent compounds **P48** and **P49**.

7.7.4 Binding profile

The initial H_4R affinity evaluation of this series centred on the propyl linker compounds **P42b** and **P43b** as key representatives. This selection ensured continuity with previous studies and was particularly suitable since only the oxidized sulfoxide and sulfone forms of this derivative was synthesized. The initial screening investigated whether substituting the methylpiperazine group in position 2 with a thiomethylether motif, inspired by **ST-2529**, while returning to the secondary linkage approach in position 4, aligning with the secondary amine present in the parent compound **VUF-10588**,[353] would maintain high affinities comparable to the parent compound. To establish comprehensive structure-activity relationships, the oxidized fluorescent derivatives **P48** and **P49** were included in the testing panel. This enabled analysis of how different oxidation states of the thioether motif in position 2 may influence receptor binding by aligning the physicochemical properties of this moiety more closely with the replaced methylpiperazine motif of the parent compound. The evaluation of different linker lengths was strategically postponed until initial results confirmed that the modified pharmacophore maintained high affinity towards H_4R. The binding data presented in Table 18 reveal complete loss of H_4R affinity across all compounds, indicating that the methylpiperazine moiety at position 2 is essential for receptor binding. While the absence of the terminal sulfonamide might contribute to reduced affinity as shown in the previous **VUF-10558** based series, 4-position amino-linked compounds (**P36b** & **P37b**) retaining the methylpiperazine in position 2 still displayed detectable binding. Therefore, the complete loss of affinity strongly indicates that the thioether substitution is not tolerated by the receptor. This observation aligns with the fact that no H_4R ligands with thioether substitutions at this position have been reported in literature to date. The oxidized thioether derivatives also showed no measurable

affinity, suggesting that merely matching physicochemical parameters of the methylpiperazine motif is insufficient, indicating that the presence of basic centres at this position may be crucial. However, since only the final fluorescent derivatives of the sulfoxide and sulfone compounds were tested due to material constraints, definitive conclusions about the impact of oxidation states on binding cannot be drawn. The lack of affinity might also result from potential steric clashes between the bulky fluorophore and the binding pocket at this linker length, a phenomenon observed in other **VUF-10588**-based series. Given these results, further investigations into linker variations and fluorescence properties were not pursued.

Table 18: Histamine H_4 receptor affinities of ligands **P42-43b** and of the oxidated fluorescent ligands **P48** and **P49.**

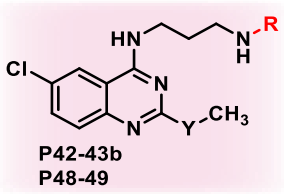

R=	**Y=**	Compound	*h*H_4R K_i (nM) [95% CI]
	S	**P42b**	>10000
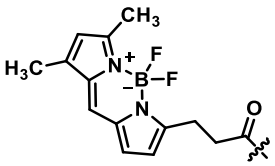	S	**P43b**	>10000
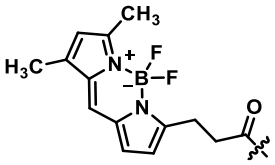	SO	**P48**	>10000
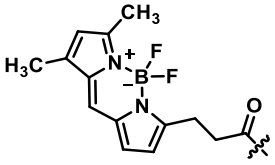	SO_2	**P49**	>10000
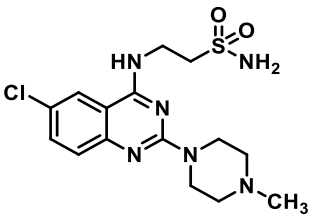		**VUF-10588**	**25.4** [19.9; 32.5]

7.8 VUF-10558-sulfonamide fluorescent H_4R ligands

7.8.1 Rational design

The final rational design strategy in this H_4R fluorescent ligand project (see Figure 158) leveraged again **VUF-10558**[353] as the lead structure while maintaining its complete pharmacophore integrity, strategically attaching the linkers to the terminal primary sulfonamide motif to create secondary sulfonamide derivatives. This modification was particularly promising as similar structural modifications had previously yielded highly potent ligands.[353,770] The study explored a diverse set of linkers, including five different alkyl chains ranging from ethylenediamine to hexyldiamine and PEG-based spacers incorporating one to three ethylene glycol units. These bifunctionalized linkers featured unprotected amino groups at both termini, enabling pharmacophore attachment via secondary sulfonamide formation at one terminus then utilizing the remaining amino group for fluorophore attachment. In contrast to previous designs, in this approach linker attachment occurs at the stage of the fully assembled H_4R pharmacophore, allowing the use of unprotected linkers without having the risk of S_NAr side reactions at positions 2 and 4 of the quinazoline ring. While dimerization represented the only potential side reaction, this could be controlled through use of excess linker. This streamlined synthetic pathway eliminated the need for an additional deprotection step, providing a more direct and efficient route that justified any potential yield reductions due to side reactions.

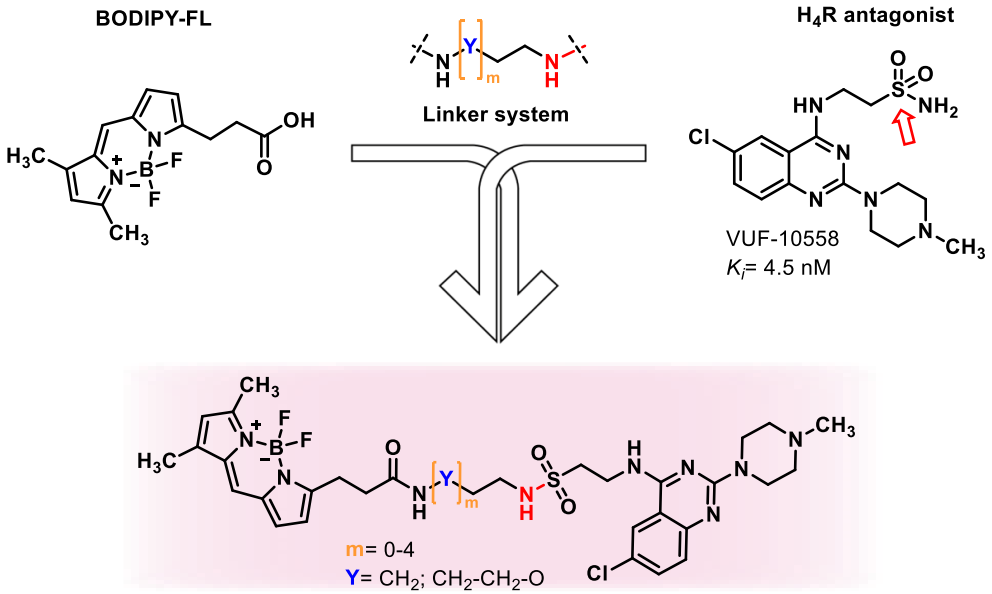

Figure 158: Rational design strategy for novel fluorescent H_4R ligands based on H_4R lead structure **VUF-10558**, preserving the complete pharmacophore through spacer attachment at the sulfonamide motif, exploring different linker lengths and types.

7.8.2 Synthesis of pharmacophore building block

The designed synthetic route of this **VUF-10558**-preserved H_4R fluorescent ligand series (see Figure 159) required initial modification of the parent structure, incorporating a sulfonic acid instead of the primary sulfonamide to create a more accessible spacer attachment point, enabling linker conjugation via sulfonyl chloride formation. For this purpose, building block **SM5** needed to be synthesized in a two-step sequence starting from **SM4**, first introducing the sulfonic acid moiety through 4-position substitution with taurine, followed by NMP substitution at position 2 to complete the pharmacophore.

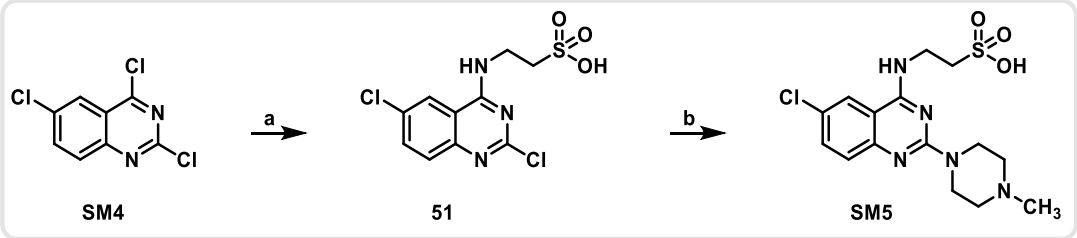

Figure 159: Planned synthetic route for starting material **SM5**, needed for the synthesis of the **VUF-10558**-preserved H_4R fluorescent ligand series. Reaction conditions: a) NEt_3, taurine, THF, 60 °C, 20 h. b) NMP, DIPEA, isopropanol, 90 °C, 20 h.

The first step of the synthesis of building block **SM5** involved 4-position substitution with taurine to establish the sulfonic acid motif, which was required for later linker attachment. The reaction, following the mechanism shown in Figure 124, was performed in THF at 60 °C for 20 hours, yielding product **51** in 100% yield (see Figure 160).[761] The elevated temperature, higher than the previously employed for 4-substitutions of 2,4,6-trichloroquinazoline, was necessary due to taurine's solubility limitations. These constraints arise from taurine's tendency to form zwitterions, due to the presence of both amino and sulfonic acid functionalities in the molecule, leading to precipitation of the formed salt.

Figure 160: Reaction of the S_NAr of compound **SM4** with taurine, yielding compound **51**.

A second S_NAr reaction at position 2 with NMP as the nucleophile completed the synthesis of building block **SM5**, establishing the full pharmacophore. The reaction proceeded via the mechanism shown in Figure 124 and was conducted in isopropanol at 90 °C for 20 hours,[761]

yielding **SM5** in 55% (see Figure 161). The moderate yield can be attributed to purification challenges due to the product's zwitterionic character.

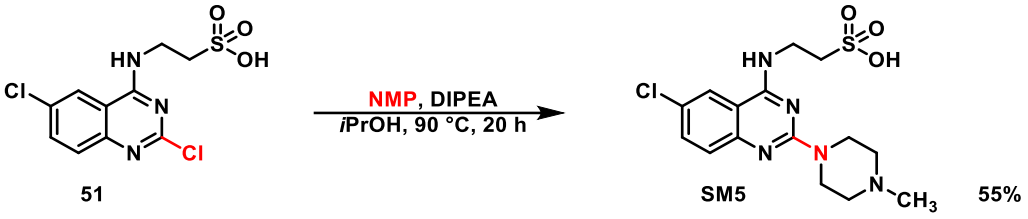

Figure 161: Reaction of the S_NAr of compound **51** with NMP, yielding compound **SM5**.

7.8.3 Fluorophore attachment through sulfonamide linkage

Following successful synthesis of pharmacophore building block **SM5**, the synthetic route (see Figure 162) for the **VUF-10558**-preserved series of H_4R fluorescent ligands was planned to proceed via linker attachment to the pharmacophore through chlorination of the sulfonic acid functionality, and *in situ* substitution of the resulting sulfonyl chloride with the respective unprotected diamino functionalized linkers (**P50a-h**). The remaining free amine can be subsequently coupled to BODIPY-FL to yield the final fluorescent ligands **P51a-h**.

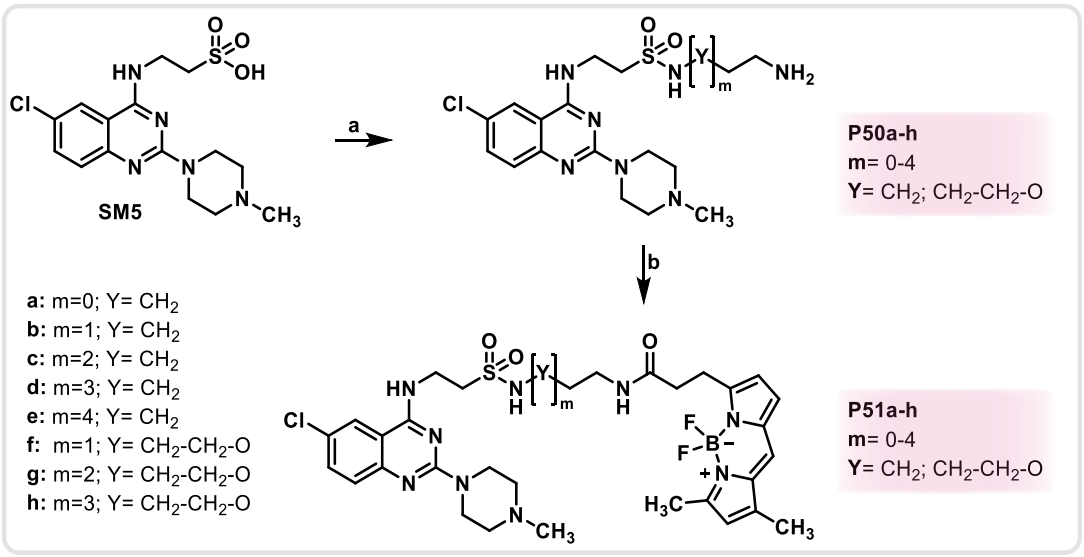

Figure 162: Planned synthetic route for the synthesis of the **VUF-10558**-preserved series of H_4R fluorescent ligands. Reaction conditions: a) oxalyl chloride, DMF, linker, DCM, room temperature, 24 h. b) HATU, DIPEA, BODIPY-FL, DMF, room temperature, 24 h.

The initial step of the synthetic route involves linker attachment at the sulfonic acid motif of compound **SM5** via *in situ* sulfonyl chloride formation, followed by nucleophilic substitution with one of the free primary amines of the unprotected linkers **L25-32**. The reactions were conducted in DCM with catalytic DMF and oxalyl chloride as the chlorinating agent, followed by addition of an excess of linkers **L25-32**, to suppress potential dimerization side reactions. The reactions proceeded at room temperature for 24 hours,[771] yielding the products as triple

hydrochloride salts in 31-76%. The lower yields observed for some compounds in this series can likely be attributed to side reactions of the reactive sulfonyl chloride intermediate generated *in situ*. The mechanism,[603] as shown in Figure 163, begins with the formation of the Vilsmeier reagent[772] from DMF and oxalyl chloride. This process initiates through nucleophilic attack of the carbonyl oxygen of DMF at the oxalyl chloride carbonyl carbon (**TS1**), resulting in chloride elimination. The liberated chloride then attacks the DMF moiety's carbonyl carbon (**TS2**), leading to decomposition of the oxalyl chloride fragment via elimination of carbon monoxide, carbon dioxide, and chloride, forming the needed Vilsmeier reagent (**TS3**). This intermediate then undergoes nucleophilic attack by the sulfonic acid of **SM5**, leading to chloride elimination (**TS4**). The eliminated chloride then attacks the sulphur centre (**TS5**), generating the desired sulfonyl chloride intermediate **IM1** under elimination of DMF. Subsequent nucleophilic attack by the linker amines of **L25-29** on the sulphur centre of **IM1**, followed by chloride elimination (**TS6**) and deprotonation (**TS7**), yields the desired products **P50a-h**. The acidic conditions and hydrogen chloride generation during this reaction mechanism resulted in product precipitations as the triple hydrochloride salts.

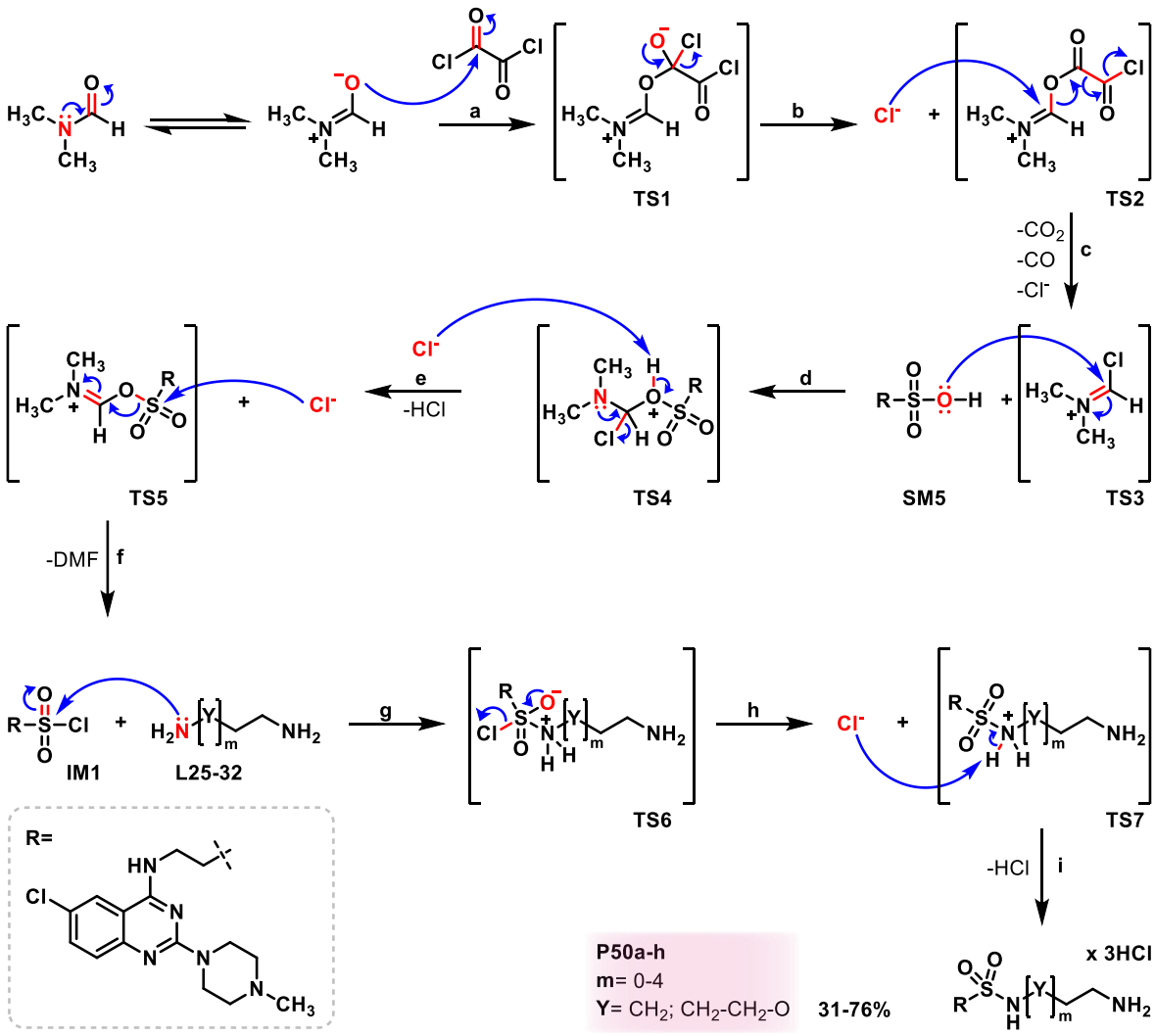

Figure 163: Mechanism of the chlorination and subsequent substitution of compound **SM5** with oxalyl chloride and linkers **L25-32**, yielding products **P50a-h**. a) Nucleophilic attack b) Elimination of chloride c) Elimination of chloride, carbon monoxide and carbon dioxide d) Nucleophilic attack e) Deprotonation and hydrogen chloride elimination f) Nucleophilic attack and DMF elimination g) Nucleophilic attack h) Elimination of chloride i) Deprotonation.

To complete the synthesis of this **VUF-10558**-preserved series of H_4R fluorescent ligands, the linker's free amine of compounds **P50a-h** were coupled to BODIPY-FL to incorporate the fluorophore. The HATU-mediated coupling, following the mechanism shown in Figure 57, was conducted under basic conditions, required to ensure solubility, in DMF at room temperature for 24 hours,[644] yielding the final fluorescent ligands **P51a-h** in 22-52% (see Figure 164). The moderate yields observed for some compounds in the series can likely be attributed to the base sensitivity of the used BODIPY-FL fluorophore.[722] moderate yields observed for some compounds in the series can likely be attributed to the base sensitivity of the used BODIPY-FL fluorophore.[722]

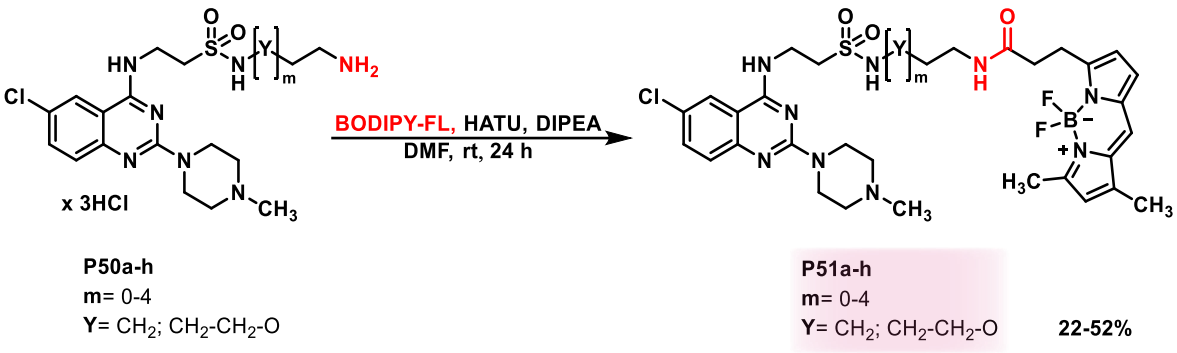

Figure 164: Reaction of the HATU-mediated coupling of compounds **P50a-h** with BODIPY-FL, yielding the fluorescent compounds **P51a-h**.

7.8.4 Binding profile

The initial H_4R affinity evaluation of this final series focused on propyl linker derivatives **P50b** and **P51b** as representative compounds, again to stay consistent with previous studies. This primary screening aimed to assess whether maintaining the complete pharmacophore, including the apparently crucial sulfonamide moiety, would preserve the parent compound's affinity. The conversion of the terminal primary sulfonamide to a secondary sulfonamide through linker attachment performed in this series, while a notable change, follows established literature examples where similar modifications preserved ligand affinity.[353,770] Unlike previous **VUF-10588**-based series, the risk of potential steric clashes of this short linker derivative with the binding pocket was less concerning, as the preservation of the complete pharmacophore naturally provided additional distance through the ethyl linker between the sulfonamide and quinazoline ring. This extended spacing leads to the assumption that the fluorophore would be sufficiently distant from the quinazoline core to avoid steric interference. The systematic evaluation of different linker lengths was planned as a subsequent development phase, contingent upon confirming that the introduced modifications maintained H_4R affinity. The results shown in Table 19 reveal that compounds **P50b** and **P51b** exhibits only low binding affinity (3083 nM and 6640 nM). For both compounds, the favourable affinity of the parent pharmacophore could not be maintained, with the introduced modifications leading to decreased H_4R activity. This finding was particularly surprising since literature-known H_4R ligands featuring the same pharmacophore with various secondary sulfonamide modifications typically retain their affinity.[353] A possible explanation for the reduced affinity of linker compound **P50b** may be the presence of a primary aliphatic amine in its sulfonamide substituent, whereas all literature-known reference compounds with secondary sulfonamides at this position exclusively feature less polar substituents. This structural difference could be significant since the amine can exist in a protonated state under testing buffer conditions, potentially causing unfavourable interactions or ionic repulsion within the binding pocket. The affinity decrease of fluorescent compound **P51b** suggests that

while the potential ionic repulsion issue of **P50b** may be resolved through conversion of the amine to an amide during fluorophore coupling, steric interference from the fluorophore likely still persists due to insufficient linker length.

Table 19: Histamine H_4 receptor affinities of ligands **P50-51b** and **P51g/h**.

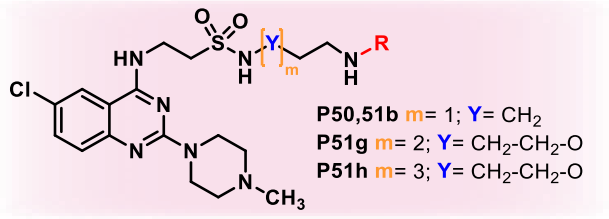

R=	m=	Y=	Compound	hH_4R K_i (nM) [95% CI]
	1	CH_2	**P50b**	**3083** [1068; 8899]
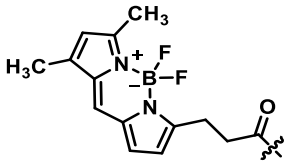	1	CH_2	**P51b**	**6640** [3210; 13732]
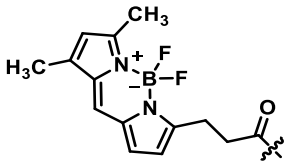	2	CH_2-CH_2-O	**P51g**	**3503** [1319; 9301]
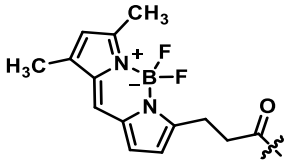	3	CH_2-CH_2-O	**P51h**	**3068** [648; 14524]
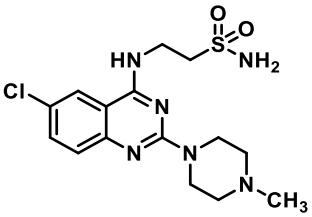			**VUF-10588**	**25.4** [19.9; 32.5]

The investigation of this hypothesis necessitated the evaluation of longer linker lengths, hence fluorescent compounds **P51g** and **P51h** were selected for further affinity testing (see Table 19). Both compounds demonstrated similar affinity than the fluorescent ligand **P51b**, still with an

unsatisfactory affinity of over 3000 nM. These results indicate that the tested linker length remains too short, suggesting that longer linker lengths are likely required to resolve these potential steric problems, as was similarly observed and discussed in the **VUF-10558**-based *N*-linked approach. This insight could guide future fluorescent ligand development based on this **VUF-10558** sulfonamide strategy.

7.9 Summary novel fluorescent H_4R ligands

The histamine H_4 receptor (H_4R) has emerged as a potential therapeutic target, particularly for inflammatory and immune disorders,[345,773] necessitating the better understanding of its precise tissue distribution. The emerging evidence for H_4R's potential presence in brain tissues remains an active field of investigation,[376] highlighting the urgent need for potent and selective fluorescent ligands to advance this research field. To address this research need, in this chapter a systematic approach for developing fluorescent H_4R ligands was presented, with BODIPY-FL selected as the fluorescent label due to its successful track record in GPCR studies.[716–718] The fluorophore offers an optimal combination of compact size, high quantum yield, and excellent photostability,[560,571] while its core structure allows straightforward modification to NIR derivatives, which would enable expanded desired application possibilities.[729] The rational design strategy explored various linker systems, including both alkyl chains ranging from ethylene to hexylene and PEG-based spacers with one to three ethylene glycol units. These different linkers were attached to three distinct pharmacophores (**JNJ-7777120**, **ST-2529**, and **VUF-10558**), utilizing different attachment approaches and positions. Each design strategy aimed to maintain the binding profile of its parent pharmacophore while providing suitable attachment points for the fluorophore. Through subsequent fluorophore coupling, each design approach yielded a series of potential fluorescent ligands for evaluation. Initial screening focused on propyl-linked derivatives as representative examples to assess the viability of each design strategy, conserving testing resources before investing in the evaluation of complete linker series. The first design strategy built upon the established H_4R antagonist **JNJ-7777120**,[728] investigating different linker attachment strategies at the indole's aromatic 3-position through both amide linkage and secondary amine approaches. While a set of compounds featuring the amide linkage and a representative example with a secondary amine were synthesized, initial affinity screening revealed complete loss of affinity compared to parent ligand, suggesting polar substitutions at this position of the pharmacophore are not tolerated, which made further evaluation of the complete series unnecessary. The second approach focused on the promising initial affinity assessment of *in-house* H_4R ligand **ST-2529**, exploring linker attachment through modification of its ester moiety while maintaining the thioether group for potential oxidation to sulfoxide and sulfone derivatives. While a series of compounds, including different oxidation states of the thioether moiety for a representative example, was synthesized, initial affinity screening revealed that the primary promising binding data of **ST-2529** could not be reproduced, making further development of this scaffold unviable. The third design strategy utilized H_4R ligand **VUF-10558**'s pharmacophore,[353] investigating linker attachment through secondary amine formation at the 4-position of its quinazoline core while maintaining the methylpiperazine at

position 2. While a complete series of compounds with varying linker lengths and types was synthesized, initial affinity screening showed significantly reduced binding of a progressive trio of short linker derivatives compared to the parent compound, highlighting the crucial role of the sulfonamide group for receptor interaction and the importance of precise spatial positioning of substituents at this position. However, results with longer alkyl chain linker derivatives showed promising improvements in affinity, suggesting that increased linker length may overcome these spatial limitations that hindered binding with shorter derivatives, providing a foundation for future fluorescent ligand development based on this approach. The fourth approach explored an alternative attachment strategy on the **VUF-10558** scaffold,[353] replacing the secondary amine at position 4 with an ether linkage. Although a series of compounds with different linker lengths and types was successfully synthesized, selective affinity screening revealed only low binding, once again indicating the important role of the sulfonamide group of the parent ligand. These findings combined with literature precedent indicated that this design approach would not yield the desired high-affinity fluorescent tools. The fifth design merged key structural elements from **VUF-10558**[353] and **ST-2529**, replacing the methylpiperazine at position 2 with a thioether moiety while maintaining the secondary amine linkage at position 4. Despite successful synthesis of compounds, also featuring different oxidation states of the thioether group for one representative example, initial screening revealed complete loss of affinity, demonstrating the essential nature of the methylpiperazine moiety in position 2 for receptor binding. The results suggested that alternative design strategies would be more promising for developing fluorescent H_4R ligands. The final approach preserved the complete **VUF-10558** pharmacophore,[353] attaching linkers through modification of the terminal sulfonamide group. While a series of secondary sulfonamide derivatives was synthesized, initial affinity screening showed strongly reduced but detectable binding compared to the parent ligand, suggesting potential for optimization through linker length adjustment. Testing of longer linker derivatives still showed no improvement in affinity, indicating that further extension of linker length may be necessary for successful fluorescent ligand development based on this approach.

Altogether, these findings provide a valuable foundation for future H_4R fluorescent ligand development, establishing critical structure-activity relationships that can guide subsequent optimization efforts. Building upon these insights, further development should focus on extending linker lengths in both the promising **VUF-10558** sulfonamide series and the **VUF-10558**-based *N*-linked strategy, while also exploring alternative pharmacophores that offer strategic attachment points without compromising essential binding interactions in the ongoing pursuit of potent, selective fluorescent H_4R tools.

8. Conclusion and Outlook

The histamine H_3 and H_4 receptors represent promising yet challenging targets in both therapeutic development and fundamental research. This thesis addressed critical gaps in both areas through a multifaceted approach, developing novel ligands with diverse applications ranging from potential therapeutic agents to specialized molecular research tools. Through systematic exploration of different design strategies and synthetic approaches, multiple projects were pursued to advance both the therapeutic potential and fundamental understanding of these important receptor systems.

One such project aimed to address the need for selective fluorescent H_4R ligands to investigate this receptor's controversially discussed presence in brain tissues.[376] The rational design strategy systematically explored the development of fluorescent ligand series based on three H_4R ligands (**JNJ-7777120**, **ST-2529**, and **VUF-10558**), attaching BODIPY-FL fluorophore onto the pharmacophores through various linker systems. The influence of linker attachment position and linkage chemistry on the preservation of parent ligands' binding properties was evaluated through selected screening of representative compounds from each design approach. While most strategies were unsuccessful as linker attachment significantly reduced pharmacophore affinity, the initial screening of short-linked compounds from the **VUF-10558**-based *N*-linked and sulfonamide series showed promising receptor binding, albeit still significantly lower than their parent compound. However, further screening of longer linker compounds of these series demonstrated, that increased linker length improved affinity, especially true for hexyl linker derivative **P36e,** which emerged as a promising compound showing high affinity of 158 nM. The bulky fluorophore attached in **P38e** unfortunately resulted in reduced affinity (1328 nM), likely due to steric clashes with the binding pocket. Nevertheless, these results provide a solid foundation for future development, guiding the synthesis and evaluation of extended linker derivatives of these promising series, particularly building upon **P36/38e** (see Figure 165), while also exploring alternative pharmacophores offering diverse attachment possibilities to develop potent fluorescent H_4R tools.

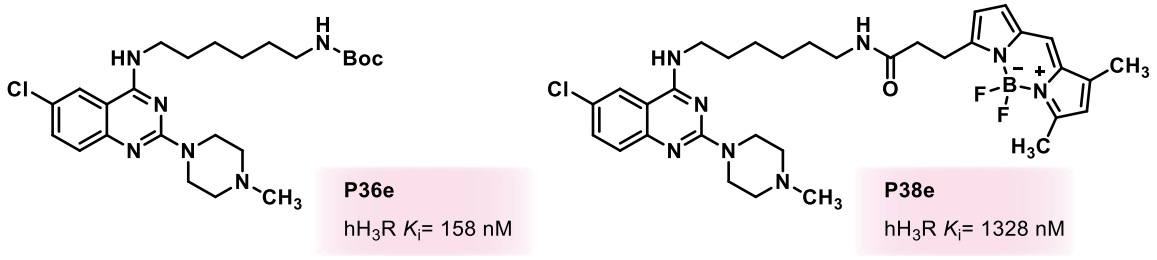

Figure 165: Lead compounds **P36e** and **P38e** with their pharmacological data as the most promising candidates of the H_4R fluorescent ligand project.

Expanding the scope of molecular tool development to H3R, one project focused on first-in-class tetrazine-based H_3R ligands designed for metal-free IEDDA click chemistry applications,[590] expanding the H_3R molecular toolbox with bioorthogonal chemistry-capable ligands that enable precise investigation of receptor dynamics in biological systems.[690] The achieve this, a rational design strategy was employed, incorporating a methyl tetrazine click moiety into the **JNJ-5207852**-derived H_3R pharmacophore through direct attachment as well as through varying alkyl phenol ether linkers. While across the series compounds showed good H_3R affinity, **P15** stood out demonstrating excellent H_3R affinity and outstanding receptor selectivity. Using **P15** as a representative example, the click chemistry capability of the series was successfully validated through a proof-of-concept synthesis of fluorescent derivative **P16a/b**, which maintained strong receptor binding and selectivity while showing excellent fluorescent properties, making it a valuable H_3R research tool in its own right (see Figure 166). Although the accessibility in receptor-bound state still requires confirmation, which is currently ongoing, these compounds, particularly **P15,** demonstrated strong H_3R binding properties and click chemistry capability, making them suitable molecular tools for studying H_3R dynamics through metal-free click chemistry-mediated biorthogonal crosslinking applications.

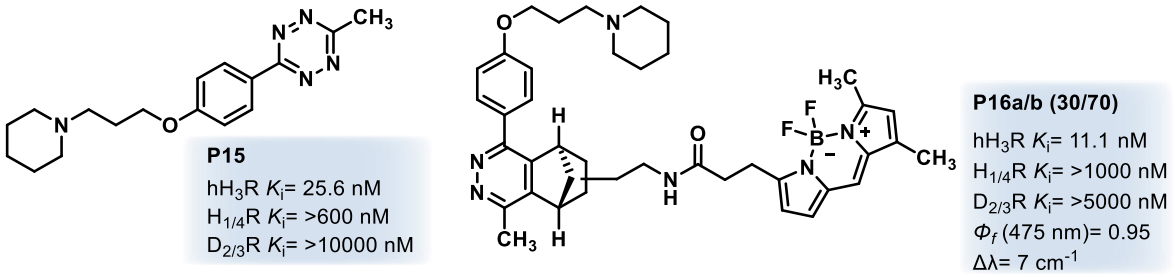

Figure 166: Lead compound **P15** with its pharmacological data from the first H_3R molecular tools approach and the proof-of-concept fluorescent ligand **P16a/b** with its pharmacological data and fluorescent properties.

Complementing the tetrazine-based click-chemistry tools, the second molecular approach increased the diversity of the H_3R toolbox even further by investigating fluorescent H_3R ligands through systematic exploration of different attachment strategies. The rational design explored both direct merging of the **JNJ-5207852**-derived H_3R pharmacophore with fluorescein-based fluorophores and its connection via piperazine linkers to fluorescein- and BODIPY-based fluorophores. Comparative evaluation revealed the linking strategy as clearly superior, with compounds **P19** and **P20** demonstrating high H_3R affinity and excellent selectivity profiles. Spectroscopic analysis confirmed preserved fluorescent properties, establishing these two compounds as valuable additions to the H_3R research toolbox, combining excellent pharmacological and spectroscopic characteristics (see Figure 167), while also laying a solid foundation for applying this pharmacophore-linker system to alternative fluorophores.

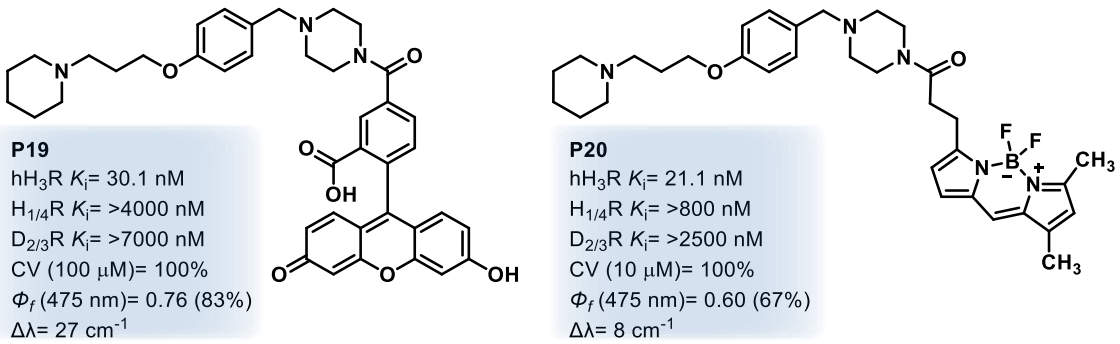

Figure 167: Lead compounds **P19** and **P20** with their pharmacological data and fluorescent properties from the second H_3R molecular tools approach.

In the therapeutic domain, two innovative multi-target directed ligand approaches were investigated combining H_3R antagonism with complementary receptor activities to enable advanced treatment options for neurological disorders, potentially offering improved efficacy while reducing polypharmacy-associated risks.[587] The first project established novel MTDLs for Parkinson's disease, by linking H_3R antagonism with D_2/D_3 receptor agonism in a single molecule, aiming to manage both motor and non-motor symptoms simultaneously. A streamlined synthetic strategy was developed to merge the pharmacophores of H_3R antagonist **JNJ-5207852** and D_2/D_3 agonist **pramipexole**. The resulting lead compound **P1b$_S$** demonstrated excellent H_3R affinity and strong D_2R/D_3R binding with enhanced D_3R selectivity compared to parent ligand **pramipexole**. SAR studies highlighted key structural requirements, demonstrating that at least an ethylene linker between both pharmacophores is necessary for high affinity, while rigid amide linker modification seems to abolished dopamine receptor binding. Notably, deamination of pramipexole's aminothiazole moiety was well tolerated, as demonstrated by **P2$_S$**, which maintained excellent binding profiles, while improving its pharmacokinetic properties. Functional testing of these novel MTDLs at their respective receptors further confirmed their therapeutic potential, showing potent H_3R antagonism/inverse agonism combined with full agonism at D_3R and D_2R for most compounds. Additionally, all developed compounds showed promising safety profiles with 100% cell viability at 100 µM, positioning compounds **P1b$_S$** and **P2$_S$** (see Figure 168) as promising lead candidates for the further exploration of innovative multi-targeting therapeutic agents for PD.

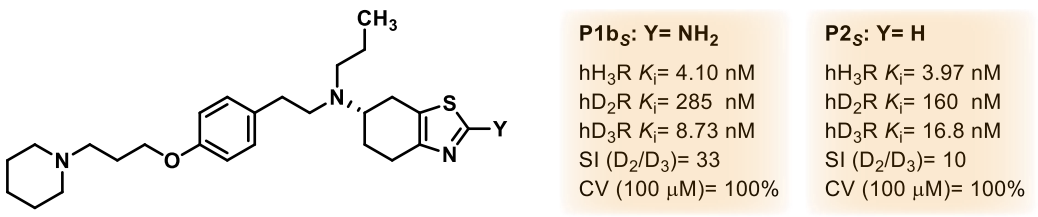

Figure 168: Lead compounds **P1b$_S$** and **P2$_S$** with their pharmacological data from the first MTDL project targeting Parkinson's disease. SI= selectivity index; CV= cell viability.

The second and final therapeutic approach focused on developing dual-targeting compounds for narcolepsy treatment by combining H_3R antagonism with norepinephrine-dopamine reuptake inhibition in a single molecule, enabling engagement of multiple wake-promoting pathways simultaneously. This was achieved through a rational design strategy that merged the pharmacophores of two clinically approved narcolepsy drugs, merging **pitolisant's** H_3R antagonist warhead with **solriamfetol's** NDRI pharmacophore. From the synthesized compound library, which included both enantiomeric series and potential transformation products, the *R*-enantiomerically pure compound **P6**, featuring the unaltered **solriamfetol** eutomer pharmacophore, emerged as the lead compound, demonstrating excellent H_3R affinity and outstanding target selectivity in GPCR screening, while maintaining excellent cell viability at high concentrations of 100 µM. The findings from monoamine transporter assays confirmed that **P6** maintains significant reuptake inhibition activity with an even more balanced profile across DAT, SERT, and NET (see Figure 169) compared to **solriamfetol** itself, establishing a solid foundation for developing innovative single-molecule therapeutics capable of engaging multiple wake-promoting pathways for enhanced narcolepsy treatment.

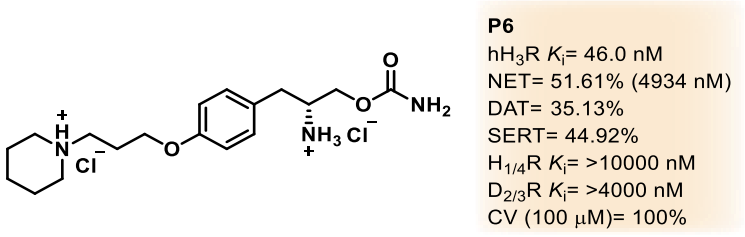

Figure 169: Lead compound **P6** with its pharmacological data from the second MTDL project targeting narcolepsy disease. CV= cell viability.

Collectively, this work has made significant contributions to both therapeutic and basic research aspects of histamine receptor pharmacology. The evaluation of multi-targeting approaches for Parkinson's disease and narcolepsy has established a foundation for developing innovative treatment strategies for these complex neurological disorders. Simultaneously, the creation of novel molecular tools, including click chemistry-capable and fluorescent ligands, has expanded the available methodology for investigating H_3R function, while initial findings in fluorescent H_4R ligand development, provide a clear strategic direction for future molecular tool development. These achievements provide valuable foundations for future drug development and receptor characterization studies in the field of histamine receptor research.

Experimental section

9. Material and methods

9.1 Materials

9.1.1 Chemicals and solvents

All reagents and solvents, with a minimum purity of 90%, were commercially acquired and used without further purification or analysis. Unless otherwise indicated, the solvents were used without prior drying. When dried, molecular sieves of appropriate size were used. For NMR spectroscopy, correspondingly deuterated solvents were utilized.

9.1.2 Reactions under inert gas atmosphere

Unless explicitly noted, syntheses were carried out using non-dried solvents and without exclusion of air. When moisture-free conditions and inert gas atmosphere were required, the glassware was heated under high vacuum and then flushed with argon or nitrogen.

9.1.3 Thin layer chromatography

Reaction monitoring was performed via thin-layer chromatography (TLC) on silica gel 60 F254 plates. The TLC was performed on silica gel-coated aluminum plates type "ALUGRAM® Xtra SIL G/UV254 20x20 cm (Macherey-Nagel, Düren Germany). Mobile phase compositions were specified individually for each chromatographic separation. UV detection was carried out using a UV lamp at wavelengths of 254 nm or 366 nm. The staining of thin layer chromatograms was performed by immersing the TLC plates in the corresponding dipping reagent followed by development using a heat gun. The dipping reagents were prepared independently, and their compositions are listed below:

- 2,4-Dinitrophenylhydrazine reagent: Solution of 1 g 2,4-dinitrophenylhydrazine in 25 mL ethanol, 8 mL water, and 5 mL conc. sulfuric acid.
- Potassium permanganate reagent: Solution of 2 g potassium permanganate and 5 g sodium carbonate in 250 mL water.
- Ninhydrin reagent: Solution of 0.3 g ninhydrin and 5.0 mL glacial acetic acid in 100 mL isopropanol.

9.1.4 Column chromatography

Column chromatography was performed using silica gel 60 with a particle size of 40-63 µM as normal phase. The amount of silica gel used was adjusted according to the specific separation requirements and column size (typically 15-30 cm length, 1.5-2.5 diameter). Mobile phase compositions and elution conditions were specified individually for each chromatographic separation.

9.2 Devices

9.2.1 Flash chromatography

Flash chromatography was carried out with Biotage Isolera™ Spektra Systems with ACI™ and Assist (Biotage, Uppsala, Sweden) using columns of various sizes. For normal phase separations, Biotage® Sfär Silica D columns were used, while C_{18}-Reversed phase silica gel columns, fully end-capped (Sigma Aldrich, Germany), were employed for reversed phase separations.

9.2.2 NMR Spectroscopy

NMR spectra were acquired on a Bruker Avance III spectrometer (Bruker BioSpin GmbH, Rheinstetten, Germany), with proton resonances at 300 or 600 MHz and carbon resonances at 75.5 or 151 MHz. Chemical shifts (δ) are reported in parts per million (ppm) relative to tetramethylsilane (TMS), and coupling constants (J) are expressed in Hertz (Hz). Only ^{3}J coupling constants were considered in the analysis. Signal multiplicities are identified as s (singlet), d (doublet), dd (double of doublets), t (triplet), q (quartet), p (pentet) or m (multiplet). Deuterated solvents used were dimethyl sulfoxide (DMSO-d_6), chloroform ($CDCl_3$), methanol (MeOD-d_4), or deuterium oxide (D_2O). The following solvent signals were used as reference:[774] ^{1}H-NMR (300/600 MHz, DMSO-d_6) δ [ppm] = 2.49 (quint, 6H); ^{1}H-NMR (300/600 MHz, $CDCl_3$) δ [ppm] = 7.26 (s, 1H); ^{1}H-NMR (300/600 MHz, MeOD-d_4) δ [ppm] = 4.87 (s, 1H); ^{1}H-NMR (300/600 MHz, D_2O) δ [ppm] = 4.79 (s, 1H); ^{13}C-NMR (75.5/151 MHz, DMSO-d_6) δ [ppm] = 39.52; ^{13}C-NMR (75.5/151 MHz, $CDCl_3$) δ [ppm] = 77.16; ^{13}C-NMR (75.5/151 MHz, MeOD-d_4) δ [ppm] = 49.00.

9.2.3 Melting point

Melting points were measured on a BÜCHI M-565 device (BÜCHI Labortechnik AG, Flawil, Switzerland) using one-sided open glass capillaries.

9.2.4 Polarimeter

Optical rotation measurements were conducted on a KRÜSS optronic polarimeter P300 (KRÜSS GmbH, Hamburg, Germany) at 20 °C using a wavelength of 589 nm. The solvent and concentration are specified for each measurement.

9.2.5 Lyophilisator

The aqueous fractions were frozen in liquid nitrogen and subsequently lyophilized using a CHRIST ALPHA 2-4 L D plus freeze dryer (Martin Christ Gefriertrocknungsanlagen GmbH, Osterode am Harz, Germany).

9.2.6 Mass spectrometer

Mass spectrometric analysis was performed using an Expression CMS (Advion, Inc., Ithaca, USA) with atmospheric pressure chemical ionization (APCI) in positive mode. The scan range

was set to m/z 100-1000, and results are reported as mass-to-charge ratios (m/z) of the detected ions.

9.2.7 LC-MS

Analytical purity was determined using LC-DAD or LC-MS-DAD measurements. All analyzed compounds showed purity ≥95% (peak area). The chromatographic system consisted of an Elute SP (Bruker Daltonics, Bremen, Germany) equipped with a vacuum degasser, binary pump, autosampler, and column oven. For mass spectrometric detection, either a compact or amaZon speed ETD (Bruker Daltonics, Bremen, Germany) was used. High-resolution mass spectra were recorded on the compact system.Separations were performed on an Intensity Solo 2 C_{18} column (100 mm × 2.1 mm) maintained at 50 °C. The mobile phase consisted of (A) water (LC-MS grade) containing 0.1% formic acid and (B) acetonitrile (LC-MS grade), delivered at 0.2 mL/min. Depending on the separation requirements, one of the following gradient methods was used: Method 1 started with 98% A (0-4 min), followed by a linear gradient to 0% A (4-19 min), and column reconditioning to initial conditions (20-23 min).Method 2 maintained 98% A (0-4 min), followed by a gradient to 95% A (4-5 min), an isocratic hold (5-9 min), a gradient to 0.5% A (9-18 min), and reconditioning to starting conditions (18-22 min).The compact MS utilized electrospray ionization in positive mode (m/z 50-1300) with nitrogen as nebulizer gas (1.8 bar) and dry gas (9 L/min, 220 °C) in UltraScan mode. The amaZon speed ETD operated with electrospray ionization in alternating polarity mode (m/z 80-1200), using nitrogen as nebulizer (15 psi) and dry gas (8 L/min, 200 °C) in UltraScan mode. Mass spectrometric data are reported as mass-to-charge ratios (m/z) of detected ions.

9.2.8 Software

The reaction schemes and mechanisms were created using ChemDraw 23.1.2 64-bit.[775] The illustrations were mainly generated using BioRender[776] as well as Adobe Illustrator 2025[777]. NMR data processing and analysis were performed using MestReNova software version 14.2.0-26256, 64-bit.[778] The cytotoxicity graphs were created with GraphPad Prism version 7.02.[779] The crystal structures were downloaded from the Protein Data Bank,[780] and the images were made with PyMOL 3.1.[781] The fluorescence spectra were illustrated with Origin, version 2024b.[782] Artificial intelligence software such as ChatGPT version 4.0[783] and Cody-AI Coding Assistant[784] were used to correct and refine the text.

9.3 Assays

9.3.1 *In vitro* receptor affinity evaluation

These assays were performed by Tobias Werner, Lamija Momberg and Luisa Leitzbach from the working group of Prof. Dr. Stark, Heinrich-Heine University Düsseldorf. The binding affinities for GPCRs (hH_3R, hH_1R, $hD_{2,short}R$, hD_3R, hH_4R) were evaluated by radioligand displacement assays

on membrane fractions of HEK-293 cells expressing hH_3R, CHO-K1 cells expressing hH_1R, $hD_{2,short}R$, or hD_3R, and HEK-293T-SF-hH_4R-His6-CRE-Luc cells expressing hH_4R as described before.[375,785–788] [^{3}H]*N*$^\alpha$-methylhistamine (2 nM) for hH_3R, [^{3}H]pyrilamine (1 nM) for hH_1R, [^{3}H]spiperone (0.2 nM) for both $hD_{2,short}R$ and hD_3R, and [^{3}H]histamine (10 µM) for hH_4R were used as radiolabelled probes. These were incubated with membrane fractions and test compounds at 25 °C for either 90 minutes (hH_3R, hH_4R) or 120 minutes (hH_1R, $hD_{2,short}R$, hD_3R) in 96-well plates under continuous shaking. Bound ligands were isolated using a cell harvester with GF/B filters pre-treated with 0.3% polyethylenimine solution. Radioactivity quantification was performed via liquid scintillation counting. Specific binding was determined by subtracting non-specific binding, established using reference compounds (pitolisant for hH_3R, chlorpheniramine maleate for hH_1R, haloperidol for $hD_{2,short}R$ and hD_3R, JNJ-7777120 for hH_4R) at 10 µM concentrations. Test compounds were evaluated across concentrations from 30 µM to 0.03 nM. Data analysis for all GPCRs employed nonlinear regression using GraphPad Prism 7.02. K_i values were calculated from IC_{50} values using the Cheng-Prusoff equation, with results expressed as means and 95% confidence intervals and subsequently converted to nanomolar concentrations.

9.3.2 Cytotoxicity evaluation

These assays were performed by Tobias Werner, Lamija Momberg and Luisa Leitzbach from the working group of Prof. Dr. Stark, Heinrich-Heine University Düsseldorf. Cell viability was assessed using the alamar blue assay in neuroblastoma SH-SY5Y cells (8.0 × 103 cells/well) as described before.[789] Cells were seeded in 96-well plates and allowed to attach for 24 hours before treatment with test compounds. Following 24 hour compound exposure, resazurin solution was added, and fluorescence (λ_{Em} = 535 nm, λ_{Ex} = 590 nm) was measured after two hours. Results represent the mean ± SEM from at least three independent experiments performed in triplicate, with cell viability expressed as percentage relative to untreated controls.

9.3.3 Fluorescence characterization

These characterizations were performed by Julius Krenzer from the working group of Prof. Dr. Müller, Heinrich-Heine University Düsseldorf. UV/Vis spectra were recorded on a Perkin Elmer Lambda 19 spectrophotometer. Emission spectra in solution and solid state were measured using an Edinburgh Instruments FS5 spectrofluorometer. Quantum yields were determined using the SC-30 integrating sphere module, and data analysis was performed with FLUORACLE software. All solution spectra were recorded at 298 K using dilutions in 1 cm quartz cuvettes (Hellma GmbH). Solvents of spectroscopic grade (UVASOL®, CHROMASOLV®, or p.a.) were

used after spectroscopic verification of their purity. Data processing and analysis were conducted using Origin 2024b software (OriginLab).

9.3.4 GTPγ[^{35}S] functional assay

The functional assays were performed by Bioprojet Biotech (Illkirch-Graffenstaden, France). CHO cells stably expressing human D_3 receptor were grown in HAM's F12 medium supplemented with 10% fetal bovine serum, zeocine, G418, and hygromycin as selection agents. CHO cells stably expressing human D_2 receptor were maintained in HAM's F12 medium complemented with 10% fetal bovine serum and G418. For human H_3 receptor expression, CHO cells were cultured in MEM alpha medium containing 10% fetal bovine serum and G418. All cell lines were cultivated with Penicillin, Streptomycin and Mycozap. Cells were grown to confluence and harvested by centrifugation at 300 g for 15 minutes at 4 °C. Cell pellets were resuspended in dedicated buffer, gently stirred, and homogenized using a potter homogenizer (ten strokes). The cell lysate was centrifuged at 500 g for five minutes at 4 °C to remove nuclei and cellular debris. The resulting supernatant underwent ultracentrifugation at 48,000 g for 30 minutes at 4 °C, followed by rehomogenization with ten additional potter strokes. The final membrane pellet was resuspended in the same buffer, aliquoted, flash-frozen in liquid nitrogen, and stored at -80 °C until use. Protein concentration was determined using the Bradford method. For the assay, the buffer consisted of 50 mM Tris-HCl, 10 mM $MgCl_2$, 140 mM NaCl, pH 7.4, supplemented with 1 mM phenylmethylsulfonyl fluoride. Membrane preparations were thawed and diluted to a final concentration of 5 µg/180 µL/well in binding buffer (50 mM HEPES, 3 mM $MgCl_2$, 140 mM NaCl, 4 µM GDP, pH 7.4) and distributed in 96-well polystyrene microplates. GTPγ[^{35}S] labeled ligand (0.2-0.3 nM, 1250 Ci/mmol, Revvity) was added, and the mixture was incubated for 30 minutes at room temperature. The reaction mixture was transferred to a Millipore GF/C HTS® microplate, filtered, and washed three times with 250 µL of buffer. Filter-bound radioactivity was measured using a Microbeta liquid scintillation counter (Revvity) with 70 µL of scintillation fluid. For dopamine D_2 and D_3 receptors, the intrinsic activity of test compounds was calculated relative to dopamine stimulation. For histamine H_3 receptor antagonism, the ability of test compounds to reverse the effect of 1 µM *R*-α-methylhistamine was evaluated.

9.3.5 hERG affinity evaluation

The assays were performed by Bioprojet Biotech (Illkirch-Graffenstaden, France). HEK cells overexpressing hERG were cultivated in DMEM F12 supplemented with 10% FBS and G418 and the cell lines were maintained with penicillin, streptomycin, and Mycozap. Membrane preparation followed the same procedure as described for the GTPγ[^{35}S] assay, except that for hERG binding, the dedicated buffer consisted of 50 mM Tris-HCl and 5 mM KCl, pH 7.4. Binding assays were performed using 10 µg of cell membranes from hERG overexpressing HEK cells suspended in 10 mM Na-HEPES pH 7.4, 135 mM NaCl, 60 mM DL-aspartic acid potassium, 1 mM EGTA, 0.8 mM $MgCl_2$, 10 mM (D+) glucose, and 0.01% BSA. In a 96-well plate, approximately 5 nM of [^{3}H]-dofetilide (76 Ci/mmol) was incubated in each well with different doses of test compounds and membranes in a final volume of 200 µL for 60 minutes at room temperature, with the plate under continuous agitation. Non-specific binding was determined in the presence of 1 µM astemizole. The reaction was terminated by filtration through Durapore BV 1.2 µm filters pre-soaked with 230 µL of 0.3% polyethyleneimine for 60 minutes at room temperature. Filters were rinsed twice with 250 µL of ice-cold 25 mM Tris-HCl pH 7.4 buffer. The filter-bound radioactivity was measured in a liquid scintillation counter (Microbeta, Revvity) with 50 µL of scintillation fluid. The hERG binding investigation using [^{3}H]-dofetilide yielded a Bmax of 3.09 pmoles/mg protein and a Kd of 4.24 nM.

9.3.6 *In vitro* transporter affinity evaluation

These assays were performed by the working group of Prof. Dr. Bryan Roth from the University of North Carolina following their NIMH PDSP assay protocol book.[790] Stable HEK293 cells expressing human DAT, NET, or SERT were cultured under G418 selection and plated at 15,000 cells per well in Poly-L-Lysine coated 384-well plates. After incubation, the medium was replaced with assay buffer, and cells were treated with test compounds for 30 minutes at 37 °C. Subsequently, a fluorescent dye was added, and fluorescence intensity was measured after another 30-minute incubation using a FlexStation II (Ex 440 nm, Em 520 nm). Data analysis was performed using Prism 5.0 to determine IC_{50} values, with cocaine, nisoxetine, and fluoxetine serving as positive controls for DAT, NET, and SERT, respectively. Radioligands included [^{3}H]-Win35428 for DAT, [^{3}H]-Nisoxetine for NET, and [^{3}H]-Citalopram for SERT, while reference ligands GBR12909, desipramine, and amitriptyline were used for DAT, NET, and SERT inhibition studies.

10. Chemistry

10.1 H_3R-based MTDLs for Parkinson's disease

4-(3-(Piperidin-1-yl)propoxy)benzaldehyde **(2a)**

The synthesis was based on the procedure previously described.[598] 1-(3-Chloropropyl)piperidine hydrochloride (1013 mg, 5.12 mmol, 1.0 eq.), *para*-hydroxybenzaldehyde (876 mg, 7.17 mmol, 1.4eq.), potassium iodide (1021 mg, 6.15 mmol, 1.2 eq.), and potassium carbonate (1770 mg, 12.81 mmol, 2.5 eq.) were suspended in acetone, and the reaction mixture was refluxed overnight. After 24 hours, the solid was filtered off, and the filtrate was concentrated. The residue was taken up in ethyl acetate and washed three times with 2M sodium hydroxide solution and twice with brine. The organic phase was dried over magnesium sulphate, filtered, and the solvent was removed under reduced pressure. The crude product was used without further purification.

Yield:	1013 mg, (80%)
Chemical formula:	$C_{15}H_{21}NO_2$
Molecular mass:	247.34 g/mol
Appearance:	Yellow oil
Internal code:	MST-005
Synthesis scheme:	Figure 36
^{1}H NMR (300 MHz, $CDCl_3$):	δ 9.79 (s, 1H), 7.74 (d, *J* = 9.8 Hz, 2H), 6.91 (d, *J* = 9.8 Hz, 2H), 4.02 (t, *J* = 6.4 Hz, 2H), 2.58 – 2.26 (m, 6H), 2.06 – 1.82 (m, 2H), 1.63 – 1.51 (m, 4H), 1.47 – 1.28 (m, 2H).

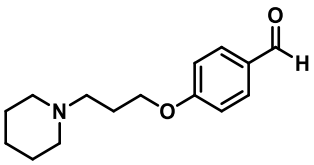

N-Propyl-1,4-dioxaspiro[4.5]decan-8-amine **(4)**

The synthesis was based on the procedure previously described.[602] Cyclohexanedione monoethylene ketal (4193 mg, 26.85 mmol, 1.0 eq.) and propylamine (2204 µL, 26.85 mmol, 1.0 eq.) were dissolved in approximately 200 mL of dichloroethane, and acetic acid (1535 µL, 26.85 mmol, 1.0 eq.) was added. While cooling in an ice bath, sodium triacetoxyborohydride (7966 mg, 37.59 mmol, 1.4 eq.) was added in portions. After the addition was complete, the reaction mixture was allowed to warm to room temperature. After 24 hours, the reaction was quenched with 2M sodium hydroxide solution, the phases were separated, and the organic phase was washed twice with water. The organic phase was dried over magnesium sulphate, filtered, and the solvent was removed under reduced pressure. The crude product was used without further purification.

Yield:	4174 mg, (78%)
Chemical formula:	$C_{11}H_{21}NO_2$
Molecular mass:	199.29 g/mol
Appearance:	Yellow oil
Internal code:	MST-026
Synthesis scheme:	Figure 37
^{1}H NMR (300 MHz, $CDCl_3$):	δ 7.26 (s, 4H), 5.96 – 5.79 (m, 3H), 5.26 – 5.04 (m, 4H), 4.95 – 4.67 (m, 6H), 4.24 (t, *J* = 7.4 Hz, 3H).

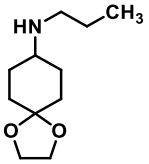

N-(4-(3-(Piperidin-1-yl)propoxy)benzyl)-*N*-propyl-1,4-dioxaspiro[4.5]decan-8-amine **(5a)**

The reductive amination protocol was carried out as described for compound **4**.[602] Compound **2a** (1010 mg, 4.09 mmol, 1.0 eq.), compound **4** (814 mg, 4.09 mmol, 1.0 eq.), acetic acid (467 µL, 8.18 mmol, 2.0 eq.) and sodium triacetoxyborohydride (1733 mg, 8.18 mmol, 2.0 eq.) were subjected to the reaction conditions for 20 hours. The crude product was purified by column chromatography using an isocratic elution of CH_2Cl_2/MeOH (sat. NH_3) 98:2.

Yield:	634 mg, (36%)
Chemical formula:	$C_{26}H_{42}N_2O_3$
Molecular mass:	430.63 g/mol
Appearance:	Yellow oil
Internal code:	MST-035
Synthesis scheme:	Figure 38
^{1}H NMR (300 MHz, $CDCl_3$):	δ 7.22 (d, *J* = 8.7 Hz, 2H), 6.82 (d, *J* = 8.7 Hz, 2H), 3.98 (t, *J* = 6.4 Hz, 2H), 3.92 (s, 4H), 3.53 (s, 2H), 2.52 – 2.34 (m, 9H), 2.02 – 1.91 (m, 2H), 1.83 – 1.69 (m, 4H), 1.62 – 1.34 (m, 12H), 0.81 (t, *J* = 7.3 Hz, 3H).

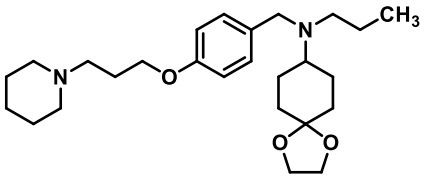

N^6-(4-(3-(Piperidin-1-yl)propoxy)benzyl)-*N*^{6}-propyl-4,5,6,7-tetrahydrobenzo[*d*]thiazole-2,6-diamine **(P1a)**

The synthesis was based on the procedure previously described.[608] Compound **5a** (130 mg, 0.30 mmol, 1.0 eq.) was dissolved in 5 mL of concentrated hydrobromic acid and stirred at room temperature for 45 minutes. Under ice cooling, bromine (16 µL, 0.30 mmol, 1.0 eq.) diluted with hydrobromic acid was then carefully added dropwise with vigorous stirring. After the addition was complete, the reaction mixture was stirred at room temperature for one hour, followed by the addition of thiourea (23 mg, 0.30 mmol, 1.0 eq.). The reaction was then heated under reflux for two hours and stirred at room temperature overnight. The solvent was removed

under reduced pressure, and the residue was purified by column chromatography using an isocratic elution of CH_2Cl_2/MeOH (sat. NH_3) 97:3.

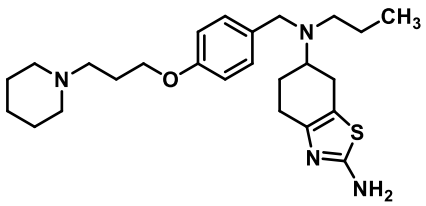

Yield:	21 mg (16%)
Chemical formula:	$C_{25}H_{38}N_4OS$
Molecular mass:	442.67 g/mol
Appearance:	Colourless oil
Internal code:	MST-132, ST-2534
Synthesis scheme:	Figure 39
LC-MS-DAD purity:	95.1%
MS (ESI-(+)):	m/z=443.18 $[M+H^+]^+$ calculated: 443.28
^{1}H NMR (300 MHz, $CDCl_3$):	δ 7.23 (d, *J* = 8.8 Hz, 2H), 6.82 (d, *J* = 8.8 Hz, 2H), 4.76 (s, 2H), 3.98 (t, J = 6.4 Hz, 2H), 3.59 (s, 2H), 3.06 – 2.98 (m, 1H), 2.75 – 2.50 (m, 4H), 2.57 – 2.31 (m, 8H), 2.06 – 1.93 (m, 3H), 1.77 – 1.67 (m, 1H), 1.63 – 1.56 (m, 5H), 1.48 – 1.38 (m, 3H), 0.85 (t, J = 7.4 Hz, 3H).
^{13}C NMR (151 MHz, $CDCl_3$):	δ 165.33, 157.86, 145.21, 132.97, 129.31, 117.72, 114.18, 77.26, 77.05, 76.84, 66.51, 56.32, 56.09, 54.64, 53.99, 51.95, 26.87, 26.62, 25.94, 25.28, 25.09, 24.42, 21.85, 11.83.

2-(4-(3-(Piperidin-1-yl)propoxy)phenyl)ethan-1-ol **(7a)**

The alkylation protocol was carried out as described for compound **2a**.[598] 1-(3-Chloropropyl)piperidine hydrochloride (4700 mg, 23.77 mmol, 1.0 eq.), *para*-hydroxybenzylethanol (3942 mg, 28.53 mmol, 1.2 eq.), potassium iodide (4736 mg, 28.53 mmol, 1.2 eq.), and potassium carbonate (8214 mg, 59.43 mmol, 2.5 eq.) were subjected to the reaction conditions for 48 hours. The residue was purified by flash column chromatography using a gradient elution of hexane/ethyl acetate (0-100%).

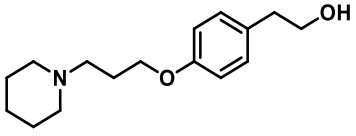

Yield:	4692 mg, (75%)
Chemical formula:	$C_{16}H_{25}NO_2$
Molecular mass:	263.19 g/mol
Appearance:	Yellow oil
Internal code:	MST-013
Synthesis scheme:	Figure 42

^{1}H NMR (300 MHz, $CDCl_3$): δ 7.05 (d, *J* = 8.8 Hz, 2H), 6.76 (d, *J* = 8.8 Hz, 2H), 3.90 (t, *J* = 6.4 Hz, 2H), 3.72 (t, *J* = 6.7 Hz, 2H), 2.72 (t, *J* = 6.7 Hz, 2H), 2.47 – 2.23 (m, 6H), 1.98 – 1.79 (m, 2H), 1.61 – 1.46 (m, 4H), 1.46 – 1.29 (m, 2H).

3-(4-(3-(Piperidin-1-yl)propoxy)phenyl)propan-1-ol **(7b)**

The alkylation protocol was carried out as described for compound **2a**.[598] 1-(3-Chloropropyl)piperidine hydrochloride (1400 mg, 7.08 mmol, 1.0 eq.), 3-(4-hydroxyphenyl)propan-1-ol (1292 mg, 8.50 mmol, 1.2 eq.), potassium iodide (1411 mg, 8.50 mmol, 1.2 eq.), and potassium carbonate (1957 mg, 14.16 mmol, 2.0 eq.) were subjected to the reaction conditions for 48 hours. The residue was purified by flash column chromatography using a gradient elution of hexane/ethyl acetate (0-100%).

Yield:	1296 mg, (66%)
Chemical formula:	$C_{17}H_{27}NO_2$
Molecular mass:	277.41 g/mol
Appearance:	Yellow oil
Internal code:	MST-157
Synthesis scheme:	Figure 42

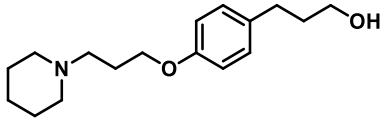

^{1}H NMR (300 MHz, $CDCl_3$): δ 7.09 (d, *J* = 8.9 Hz, 2H), 6.81 (d, *J* = 8.9 Hz, 2H), 3.97 (t, *J* = 6.4 Hz, 2H), 3.65 (t, *J* = 6.4 Hz, 2H), 2.64 (t, *J* = 6.7 Hz, 2H), 2.53 – 2.31 (m, 6H), 2.14 – 1.75 (m, 4H), 1.66 – 1.51 (m, 4H), 1.49 – 1.36 (m, 2H).

1-(3-(4-(2-Chloroethyl)phenoxy)propyl)piperidine hydrochloride **(8a)**

The synthesis was based on the procedure previously described.[621] Compound **7a** (4500 mg, 16.22 mmol, 1.0 eq.) was dissolved in tetrahydrofuran, and under ice-cooling with vigorous stirring, thionyl chloride (1414 µL, 19.47 mmol, 1.2 eq.) was carefully added dropwise. After the addition was complete, the reaction was briefly heated to reflux for 30 minutes and then stirred at room temperature overnight. After 16 hours, the reaction mixture was poured into diethyl ether, and the precipitate was filtered off and washed with diethyl ether. The crude product was used without further purification.

Yield:	5171 mg, (100%)
Chemical formula:	$C_{16}H_{24}ClNO$ x HCl
Molecular mass:	318.83 g/mol
Appearance:	Beige solid
Internal code:	MST-018
Synthesis scheme:	Figure 43
^{1}H NMR (300 MHz, $CDCl_3$):	δ 12.13 (s, 1H), 7.09 (d, *J* = 8.9 Hz, 2H), 6.78 (d, *J* = 8.9 Hz, 2H), 4.02 (t, *J* = 5.5 Hz, 2H), 3.63 (t, *J* = 7.3 Hz, 2H), 3.58 – 3.48 (m, 2H), 3.19 – 3.06 (m, 2H), 2.96 (t, *J* = 7.3 Hz, 2H), 2.75 – 2.57 (m, 2H), 2.49 – 2.38 (m, 2H), 2.33 – 2.16 (m, 2H), 1.94 – 1.76 (m, 3H), 1.50 – 1.33 (m, 1H).

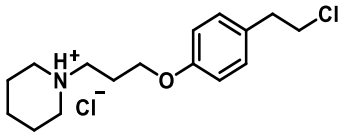

1-(3-(4-(3-Chloropropyl)phenoxy)propyl)piperidine hydrochloride **(8b)**

The chlorination protocol was carried out as described for compound **8a**.[621] Compound **7b** (1291 mg, 4.65 mmol, 1.0 eq.) and thionyl chloride (405 µL, 5.58 mmol, 1.2 eq.) were subjected to the reaction conditions for 16 hours. The crude product was used without further purification.

Yield:	5171 mg, (100%)
Chemical formula:	$C_{17}H_{25}ClNO$ x HCl
Molecular mass:	331.30 g/mol
Appearance:	Beige solid
Internal code:	MST-162
Synthesis scheme:	Figure 43
^{1}H NMR (300 MHz, DMSO-d_6):	δ 10.79 (s, 1H), 7.13 (d, *J* = 8.7 Hz, 2H), 6.86 (d, *J* = 8.7 Hz, 2H), 4.01 (t, *J* = 6.1 Hz, 2H), 3.59 (t, *J* = 6.5 Hz, 2H), 3.46 – 3.36 (m, 2H), 3.18 – 3.05 (m, 2H), 2.95 – 2.78 (m, 2H), 2.63 (t, *J* = 6.5 Hz, 2H), 2.26 – 2.12 (m, 2H), 2.03 – 1.90 (m, 2H), 1.90 – 1.64 (m, 5H), 1.46 – 1.30 (m, 1H).

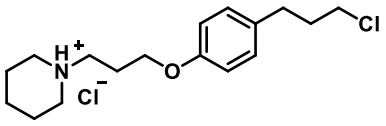

N-(3-(4-(3-(Piperidin-1-yl)propoxy)phenyl)propyl)-*N*-propyl-1,4-dioxaspiro[4.5]decan-8-amine **(5c)**

The alkylation protocol was carried out as described for compound **2a**.[622] Compound **8b** (1187 mg, 4.01 mmol, 1.0 eq.), Compound **4** (800 mg, 4.01 mmol, 1.0 eq.), potassium iodide (799 mg, 4.81 mmol, 1.2 eq.), and potassium carbonate (1110 mg, 8.02 mmol, 2.0 eq.) were subjected to the reaction conditions for 24 hours. The residue was purified by flash column chromatography using a gradient elution of hexane/ethyl acetate (0-100%).

Yield:	754 mg, (41%)
Chemical formula:	$C_{28}H_{46}N_2O_3$
Molecular mass:	458.69 g/mol
Appearance:	Colourless oil
Internal code:	MST-164
Synthesis scheme:	Figure 44
^{1}H NMR (300 MHz, $CDCl_3$):	δ 7.07 (d, *J* = 8.5 Hz, 2H), 6.80 (d, *J* = 8.5 Hz, 2H), 3.97 (t, *J* = 6.4 Hz, 2H), 3.92 (s, 4H), 2.66 – 2.27 (m, 13H), 2.00 – 1.91 (m, 2H), 1.81 – 1.66 (m, 6H), 1.62 – 1.48 (m, 8H), 1.48 – 1.32 (m, 4H), 0.85 (t, *J* = 7.3 Hz, 3H).

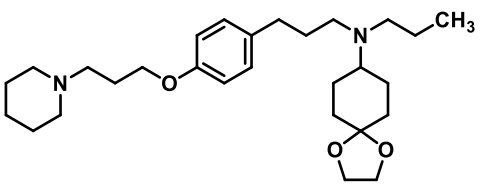

N^6-(3-(4-(3-(Piperidin-1-yl)propoxy)phenyl)propyl)-*N*^{6}-propyl-4,5,6,7-tetrahydrobenzo[*d*]thiazole-2,6-diamine dimalate **(P1c)**

The one-pot synthesis protocol was carried out as described for compound **P1a**.[608] Compound **5c** (230 mg, 0.50 mmol, 1.0 eq.), bromine (26 µL, 0.50 mmol, 1.0 eq.) and thiourea (38 mg, 0.50 mmol, 1.0 eq.) were subjected to the reaction conditions for 24 hours. The crude product was purified by a column chromatography using an isocratic elution of CH_2Cl_2/MeOH (sat. NH_3) 97:3. The product was precipitated as a double malate salt and recrystallized from ethanol.

Yield:	18 mg (5%)
Chemical formula:	$C_{27}H_{42}N_4OS$ x 2 $C_4H_4O_4$
Molecular mass:	702.86 g/mol
Appearance:	Yellow oil
Internal code:	MST-171, ST-2875
Synthesis scheme:	Figure 46
LC-MS-DAD purity:	96.3%
MS (ESI-(+)):	m/z=471.32 $[M+H^+]^+$ calculated: 471.32
^{1}H NMR (300 MHz, $CDCl_3$):	δ 9.04 (s, 1H), 7.17 (d, *J* = 8.6 Hz, 2H), 6.87 (d, *J* = 8.1 Hz, 2H), 6.81 (s, 3H), 6.03 (s, 4H), 4.01 (t, *J* = 6.0 Hz, 2H), 3.75 – 3.39 (m, 2H), 3.26 – 3.10 (m, 2H), 2.98 – 2.70 (m, 5H), 2.60 – 2.51 (m, 5H), 2.20 – 2.03 (m, 4H), 2.00 – 1.56 (m, 13H), 0.91 (t, *J* = 7.3 Hz, 3H).

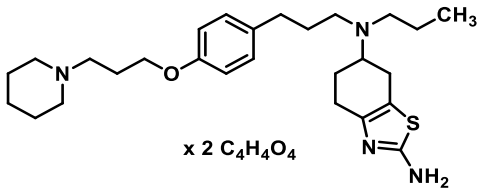

^{13}C NMR (75.5 MHz, $CDCl_3$):	δ 166.09, 165.37, 156.87, 156.77, 144.33, 129.85, 129.79, 114.43, 114.35, 65.15, 58.26, 55.36, 53.55, 53.04, 52.78, 33.92, 29.69, 26.13, 25.28, 25.21, 24.76, 24.15, 22.91, 22.34, 11.76.

4-(2-(Propyl(1,4-dioxaspiro[4.5]decan-8-yl)amino)ethyl)phenol **(10)**

The synthesis was based on the procedure previously described.[627] Tyramine (2301 mg, 16.70 mmol, 1.0 eq.) and cyclohexanedione monoethylene ketal (2620 mg, 16.70 mmol, 1.0 eq.) were dissolved in approximately 100 mL of dichloroethane, and acetic acid (1911 µL, 33.40 mmol, 2.0 eq.) was added. While cooling in an ice bath, sodium triacetoxyborohydride (5332 mg, 25.20 mmol, 1.4 eq.) was added in portions. After the addition was complete, the reaction mixture was allowed to warm to room temperature. After 16 hours, propanal (1197 µL, 16.7 mmol, 1.0 eq) and additional sodium triacetoxyborohydride (5332 mg, 25.20 mmol, 1.4 eq.) were added under ice cooling. After stirring for five hours at room temperature, the reaction was quenched with 2M sodium hydroxide solution, the phases were separated, and the organic phase was washed twice with water. The organic phase was dried over magnesium sulphate, filtered, and the solvent was removed under reduced pressure. The crude product was purified by a column chromatography using a gradient elution of CH_2Cl_2/MeOH (sat. NH_3) (0-20%).

Yield:	1920 mg, (36%)
Chemical formula:	$C_{19}H_{29}NO_3$
Molecular mass:	319.45 g/mol
Appearance:	Yellow oil
Internal code:	MST-193
Synthesis scheme:	Figure 48
^{1}H NMR (300 MHz, $CDCl_3$):	δ 6.90 (d, *J* = 8.4 Hz, 2H), 6.76 (d, *J* = 8.4 Hz, 2H), 5.29 (s, 1H), 4.02 – 3.83 (m, 4H), 3.52 – 3.26 (m, 2H), 3.16 – 3.03 (m, 2H), 2.97 – 2.74 (m, 4H), 2.09 – 2.01 (m, 5H), 1.93 – 1.45 (m, 4H), 0.99 – 0.87 (m, 3H).

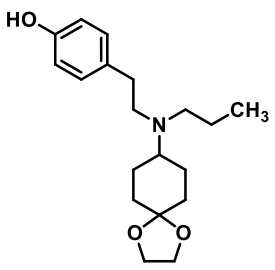

4-(2-(Propyl(1,4-dioxaspiro[4.5]decan-8-yl)amino)ethyl)phenol **(5b)**

The alkylation protocol was carried out as described for compound **2a.**[598] Compound **10** (1936 mg, 6.07 mmol, 1.0 eq.), 1-(3-chloropropyl)piperidine hydrochloride (1200 mg, 6.07 mmol, 1.0 eq.), potassium iodide (1209 mg, 7.28 mmol, 1.2 eq.), and potassium carbonate (1678 mg, 12.14 mmol, 2.0 eq.) were subjected to the reaction conditions for

24 hours. The crude product was purified by a column chromatography using an isocratic elution of CH_2Cl_2/MeOH (sat. NH_3) 97:3.

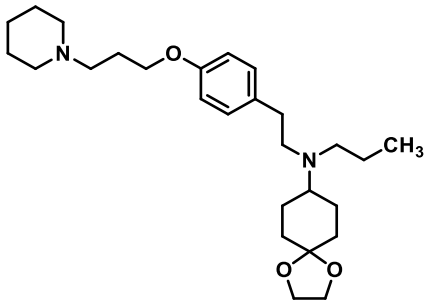

Yield:	1404 mg, (52%)
Chemical formula:	$C_{27}H_{44}N_2O_3$
Molecular mass:	444.66 g/mol
Appearance:	Yellow oil
Internal code:	MST-195
Synthesis scheme:	Figure 49
^{1}H NMR (300 MHz, $CDCl_3$):	δ 7.09 (d, *J* = 8.7 Hz, 2H), 6.77 (d, *J* = 8.7 Hz, 2H), 3.97 (t, *J* = 6.0 Hz, 2H), 3.89 (s, 4H), 2.91 – 2.64 (m, 13H), 2.66 – 2.54 (m, 2H), 2.24 – 2.08 (m, 2H), 1.96 – 1.36 (m, 14H), 0.88 (t, *J* = 7.3 Hz, 3H).

N^6-(4-(3-(Piperidin-1-yl)propoxy)phenethyl)-*N*^{6}-propyl-4,5,6,7-tetrahydrobenzo[*d*]thiazole-2,6-diamine **(P1b)**

The one-pot synthesis protocol was carried out as described for compound **P1a**.[608] Compound **5b** (770 mg, 1.73 mmol, 1.0 eq.), bromine (89 µL, 1.73 mmol, 1.0 eq.) and thiourea (132 mg, 1.73 mmol, 1.0 eq.) were subjected to the reaction conditions for 24 hours. The crude product was purified by a column chromatography using an isocratic elution of CH_2Cl_2/MeOH (sat. NH_3) 97:3.

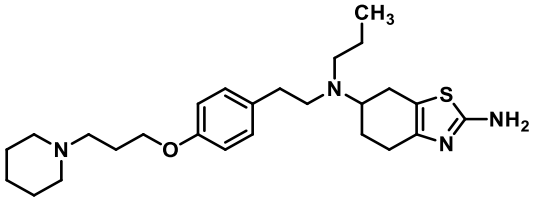

Yield:	32 mg (4%)
Chemical formula:	$C_{26}H_{40}N_4OS$
Molecular mass:	456.69 g/mol
Appearance:	Yellow oil
Internal code:	MST-206, ST-2596
Synthesis scheme:	Figure 50
LC-MS-DAD purity:	97.5%
MS (ESI-(+)):	m/z=457.69 $[M+H^+]^+$ calculated: 457.70
^{1}H NMR (300 MHz, $CDCl_3$):	δ 7.11 (d, *J* = 8.3 Hz, 2H), 6.77 (d, *J* = 8.3 Hz, 2H), 5.52 – 4.98 (m, 2H) 4.01 (t, *J* = 5.6 Hz, 2H), 3.47 – 2.44 (m, 11H), 2.42 – 2.23 (m, 3H), 2.14 – 1.88 (m, 6H), 1.83 – 1.48 (m, 6H), 1.33 – 1.18 (m, 3H), 0.90 (t, *J* = 7.3 Hz, 3H).
^{13}C NMR (75.5 MHz, $CDCl_3$):	δ 165.70, 156.82, 144.82, 132.95, 129.78, 116.93, 114.31, 65.42, 57.90, 55.53, 53.76, 53.20, 52.84, 45.81, 26.45, 25.68, 24.99, 24.70, 23.51, 22.76, 11.83, 8.75.

Methyl 2-(4-(3-(piperidin-1-yl)propoxy)phenyl)acetate **(12)**

The alkylation protocol was carried out as described for compound **2a.**[598] 1-(3-Chloropropyl)piperidine hydrochloride (2957 mg, 15.01 mmol, 1.0 eq.), methyl-4-hydroxyphenylacetate (2500 mg, 15.01 mmol, 1.0 eq.), potassium iodide (4980 mg, 30.02 mmol, 2.0 eq.), and potassium carbonate (8292 mg, 60.04 mmol, 4.0 eq.) were subjected to the reaction conditions for 48 hours. The crude product was purified by a flash column chromatography using a gradient elution of CH_2Cl_2/MeOH (0-20%).

Yield:	1943 mg, (59%)
Chemical formula:	$C_{17}H_{25}NO_3$
Molecular mass:	219.39 g/mol
Appearance:	Yellow oil
Internal code:	MST-581
Synthesis scheme:	Figure 52
^{1}H NMR (300 MHz, $CDCl_3$):	δ 7.17 (d, *J* = 8.6 Hz, 2H), 6.84 (d, *J* = 8.6 Hz, 2H), 3.98 (t, *J* = 6.3 Hz, 2H), 3.67 (s, 3H), 3.55 (s, 2H), 2.57 – 2.38 (m, 6H), 2.07 – 1.93 (m, 2H), 1.69 – 1.56 (m, 4H), 1.51 – 1.35 (m, 2H).

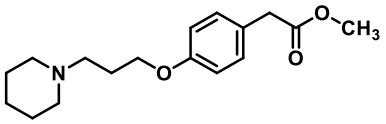

2-(4-(3-(Piperidin-1-yl)propoxy)phenyl)-acetaldehyde **(13)**

The synthesis was based on a procedure previously described.[633] Compound **12** (380 mg, 1.31 mmol, 1.0 eq.) was dissolved in toluene, and the solution was cooled to -78 °C. At this temperature, under a nitrogen atmosphere, DIBAL (1.0 M in THF, 1.95 mmol, 1.5 eq.) was slowly added dropwise. After five hours, the reaction was quenched with Rochelle salt solution and diluted with ethyl acetate. The resulting emulsion was stirred at room temperature for 15 minutes. The phases were separated, and the aqueous phase was extracted twice with ethyl acetate. The combined organic phases were dried over magnesium sulphate, filtered, and the solvent was removed under reduced pressure. The crude product was used without further purification.

Yield:	1943 mg, (100%)
Chemical formula:	$C_{16}H_{23}NO_2$
Molecular mass:	261.37 g/mol
Appearance:	Colourless oil
Internal code:	MST-607
Synthesis scheme:	Figure 53

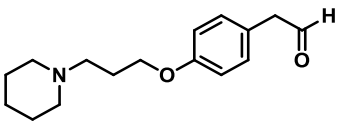

^{1}H NMR (300 MHz, $CDCl_3$):	δ 9.71 (t, *J* = 2.4 Hz, 1H), 7.13 (d, *J* = 8.8 Hz, 2H), 6.86 (d, *J* = 8.8 Hz, 2H), 4.04 – 3.93 (m, 2H), 3.70 – 3.53 (m, 2H), 2.55 – 2.36 (m, 6H), 2.06 – 1.89 (m, 2H), 1.67 – 1.53 (m, 4H), 1.49 – 1.35 (m, 2H).

(*S*)-*N*^{6}-(4-(3-(Piperidin-1-yl)propoxy)phenethyl)-*N*^{6}-propyl-4,5,6,7-tetrahydrobenzo[*d*]thiazole-2,6-diamine **(P1b$_S$)**

The reductive amination protocol was carried out as described for compound **4**.[602] Compound **13** (256 mg, 0.98 mmol, 1.0 eq.), pramipexole hydrochloride **15** (277 mg, 0.98 mmol, 1.0 eq.), acetic acid (67 µL, 1.18 mmol, 1.2 eq.) and sodium triacetoxyborohydride (289 mg, 1.37 mmol, 1.4 eq.) were subjected to the reaction conditions for 20 hours. The crude product was purified by reverse phase flash chromatography using a gradient elution of water/acetonitrile (0-100%).

Yield:	201 mg (45%)
Chemical formula:	$C_{26}H_{40}N_4OS$
Molecular mass:	456.69 g/mol
Appearance:	Colourless oil
Internal code:	MST-631
Synthesis scheme:	Figure 54
α_{589nm}^{20} (10 mg/mL in $CHCl_3$):	-23°
LC-MS-DAD purity:	97.4%
HR-MS (ESI-(+)):	m/z=457.2992 $[M+H^+]^+$ calculated: 457.2996
^{1}H NMR (300 MHz, MeOD):	δ 7.09 (d, *J* = 8.6 Hz, 2H), 6.81 (d, *J* = 8.6Hz, 2H), 3.96 (t, *J* = 6.1 Hz, 2H), 3.11 – 2.95 (m, 1H), 2.86 – 2.25 (m, 16H), 2.04 – 1.88 (m, 3H), 1.75 – 1.41 (m, 9H), 0.90 (t, *J* = 7.3 Hz, 3H).
^{13}C NMR (75.5 MHz, MeOD):	δ 169.70, 158.77, 144.96, 133.95, 130.75, 116.28, 115.50, 67.38, 59.11, 57.25, 55.55, 54.43, 53.97, 35.78, 27.50, 27.24, 26.86, 26.51, 25.84, 25.23, 23.00, 12.23.

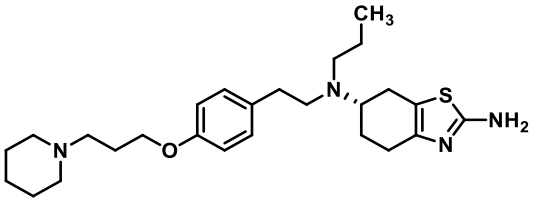

(*S*)-*N*-(4-(3-(Piperidin-1-yl)propoxy)phenethyl)-*N*-propyl-4,5,6,7-tetrahydrobenzo[*d*]thiazol-6-amine **(P2$_S$)**

The synthesis was based on *a* procedure previously described.[636] Compound **P1b$_S$** (50 mg, 0.11 mmol, 1.0 eq.) was dissolved in 20 mL of concentrated hydrochloric acid and the solution was cooled to -30 °C. At this temperature, a 1M aqueous sodium nitrite solution was added dropwise with vigorous stirring. After stirring for one hour at this temperature phosphoric acid (19 µL, 0.33 mmol, 3.0 eq.) was added dropwise. The reaction was allowed to warm to 4 °C and stirred at this temperature overnight. The solution was cooled again to -30 °C, basified by the

addition of 2M NaOH, and subsequently allowed to gradually warm to room temperature. The aqueous solution was extracted three times with ethyl acetate, the combined organic phases were dried over magnesium sulphate, filtered, and the solvent was removed under reduced pressure. The crude product was purified by a column chromatography using a gradient elution of CH_2Cl_2/MeOH (sat. NH_3) (0-20%).

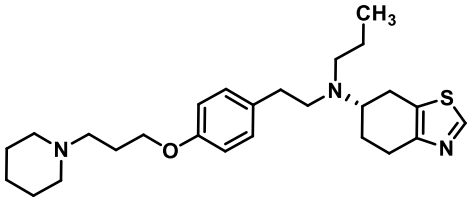

Yield:	26 mg (54%)
Chemical formula:	$C_{26}H_{39}N_3OS$
Molecular mass:	441.68 g/mol
Appearance:	Colourless oil
Internal code:	MST-860, ST-3030
Reaction scheme:	Figure 55
α_{589nm}^{20} (10 mg/mL in $CHCl_3$):	-41°
LC-MS-DAD purity:	100%
HR-MS (ESI-(+)):	m/z=442.2890 $[M+H^+]^+$ calculated: 442.2887
^{1}H NMR (300 MHz, $CDCl_3$):	δ 8.56 (s, 1H), 7.09 (d, *J* = 8.6 Hz, 2H), 6.80 (d, *J* = 8.6 Hz, 2H), 3.98 (t, *J* = 6.3 Hz, 2H), 3.14 – 3.06 (m, 1H), 3.05 – 2.98 (m, 1H), 2.94 – 2.87 (m, 1H), 2.83 – 2.64 (m, 6H), 2.60 – 2.40 (m, 8H), 2.10 – 2.02 (m, 1H), 2.04 – 1.97 (m, 2H), 1.79 – 1.69 (m, 1H), 1.68 – 1.61 (m, 4H), 1.54 – 1.43 (m, 4H), 0. 89 (t, *J* = 7.3 Hz, 3H).
^{13}C NMR (75.5 MHz, $CDCl_3$):	δ 157.26, 150.68, 150.37, 132.75, 129.65, 128.09, 114.38, 66.38, 57.72, 55.96, 54.49, 53.32, 52.87, 35.39, 26.64, 26.51, 25.90, 25.56, 25.46, 24.17, 22.37, 11.88.

2-(4-(3-(Piperidin-1-yl)propoxy)phenyl)acetate lithium salt **(14)**

The synthesis was based on a procedure previously described.[641] Compound **12** (2580 mg, 8.87 mmol, 1.0 eq.) was dissolved in a THF/water mixture (1:1), and lithium hydroxide (1309 mg, 52.40 mmol, 4.0 eq.) was added. The mixture was stirred at room temperature overnight. After 20 hours, the solvent was removed under reduced pressure. The crude product was used without further purification.

Yield:	2513 mg, (100%)
Chemical formula:	$C_{16}H_{22}NO_3Li$
Molecular mass:	283.30 g/mol
Appearance:	Colourless solid
Internal code:	MST-586
Synthesis scheme:	Figure 56
^{1}H NMR (300 MHz, D_2O):	δ 7.26 (d, *J* = 8.7 Hz, 2H), 6.99 (d, *J* = 8.7 Hz, 2H), 4.13 (t, *J* = 5.8 Hz, 2H), 3.65 – 3.46 (m, 4H), 3.31 – 3.20 (m, 2H), 3.01 – 2.87 (m, 2H), 2.24 – 2.15 (m, 2H), 2.03 – 1.65 (m, 5H), 1.58 – 1.41 (m, 1H).

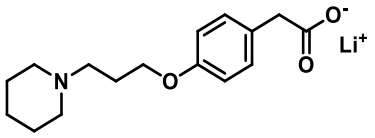

(*S*)-*N*-(2-Amino-4,5,6,7-tetrahydrobenzo[*d*]thiazol-6-yl)-2-(4-(3-(piperidin-1-yl)propoxy)phenyl)-*N*-propylacetamide diacetate **(P3$_S$)**

The synthesis was based on a procedure previously described.[644] Compound **14** (376 mg, 1.36 mmol, 1.0 eq.), pramipexole hydrochloride **15** (385 mg, 1.36 mmol, 1.0 eq.), and DIPEA (200 µL, 1.40 mmol, 1.1 eq.) were dissolved in 10 mL of DMF. HATU (534 mg, 1.40 mmol, 1.1 eq.) was added and the reaction mixture was stirred at room temperature for 24 hours. Subsequently, the solvent was removed under reduced pressure, the residue was taken up in ethyl acetate and washed three times with saturated sodium bicarbonate solution. The organic phase was dried over magnesium sulphate, filtered, and the solvent was removed under reduced pressure. The crude product was purified by reverse phase flash chromatography using a gradient elution of water (0.5% acetic acid)/acetonitrile (0-100%).

Yield:	257 mg (32%)
Chemical formula:	$C_{26}H_{38}N_4O_2S$ x 2 $C_2H_4O_2$
Molecular mass:	590.78 g/mol
Appearance:	Colourless solid
Internal code:	MST-590, ST-3032
Reaction scheme:	Figure 57
α_{589nm}^{20} (10 mg/mL in $CHCl_3$):	-17°
LC-MS-DAD purity:	100%
HR-MS (ESI-(+)):	m/z=471.2964 $[M+H^+]^+$ calculated: 471.2788

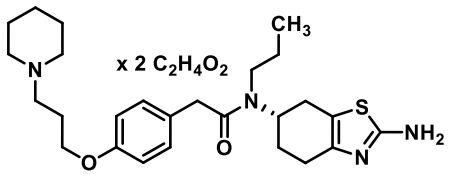

^{1}H NMR (300 MHz, DMSO-d_6):	δ 7.19 (d, *J* = 8.7 Hz, 2H), 6.86 (d, *J* = 8.7 Hz, 2H), 5.20 (s, 3H), 3.95 (t, *J* = 6.4 Hz, 2H), 3.62 (s, 2H), 3.22 – 2.91 (m, 2H), 2.72 – 2.56 (m, 3H), 2.47 – 2.25 (m, 6H), 2.11 – 2.00 (m, 1H), 1.93 – 1.82 (m, 12H), 1.67 (s, 1H), 1.69 – 1.40 (m, 5H), 1.41 – 1.34 (m, 2H), 0.89 (t, *J* = 7.4 Hz, 3H).
^{13}C NMR (75.5 MHz, DMSO-d_6):	δ 172.17, 169.16, 157.52, 155.39, 143.57, 130.12, 126.84, 119.06, 114.34, 65.79, 54.99, 53.92, 53.25, 47.56, 40.80, 27.53, 27.41, 26.06, 25.36, 24.26, 23.94, 21.55, 21.28, 11.56.

10.2 H_3R-based MTDLs for Narcolepsy

Methyl-(*R*)-2-((*tert*-butoxycarbonyl)amino)-3-(4-(3-(piperidin-1-yl)propoxy)phenyl)propanoate **(18)**

The alkylation protocol was carried out as described for compound **2a.**[598] Boc-D-tyrosin-methylester (2900 mg, 9.83 mmol, 1.0 eq.), 1-(3-chloropropyl)piperidine hydrochloride (1927 mg, 9.83 mmol, 1.0 eq.), potassium carbonate (2713 mg, 19.7 mmol, 2.0 eq.), and potassium iodide (3320 mg, 19.7 mmol, 2.0 eq.) were subjected to the reaction conditions for 24 hours. The crude product was used without further purification.

Yield:	2811 mg, (68%)
Chemical formula:	$C_{23}H_{36}N_2O_5$
Molecular mass:	420.55 g/mol
Appearance:	Colourless solid
Internal code:	MST-761
Synthesis scheme:	Figure 62

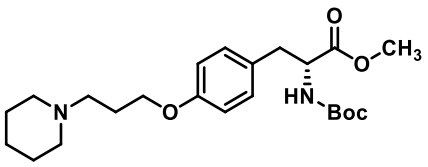

^{1}H NMR (300 MHz, $CDCl_3$):	δ 7.00 (d, *J* = 8.6 Hz, 2H), 6.81 (d, *J* = 8.6 Hz, 2H), 4.95 (d, *J* = 8.3 Hz, 1H), 4.62 – 4.42 (m, 1H), 3.97 (t, *J* = 6.4 Hz, 2H), 3.70 (s, 3H), 3.09 – 2.91 (m, 2H), 2.53 – 2.30 (m, 6H), 2.06 – 1.87 (m, 2H), 1.64 – 1.52 (m, 4H), 1.47 – 1.34 (m, 11H).

tert-Butyl-(*R*)-(1-hydroxy-3-(4-(3-(piperidin-1-yl)propoxy)phenyl)propan-2-yl)carbamate **(P4)**

The synthesis was based on a procedure previously described.[671] Compound **18** (1500 mg, 3.57 mmol, 1.0 eq.) was dissolved in dry tetrahydrofuran and cooled to -78 °C. At this temperature, a 2M solution of lithium aluminium hydride in THF (7.2 mL, 14.3 mmol, 4.0 eq.) was added dropwise with vigorous stirring. The reaction mixture was stirred for two hours at -78 °C, then quenched with a saturated sodium bicarbonate solution. The mixture was

allowed to warm to room temperature, extracted three times with ethyl acetate, dried over magnesium sulphate, filtered, and the solvent was removed under reduced pressure. The crude product was used without further purification.

Yield:	1261 mg, (90%)
Chemical formula:	$C_{22}H_{36}N_2O_4$
Molecular mass:	392.54 g/mol
Appearance:	Colourless solid
Internal code:	MST-767, ST-2945
Synthesis scheme:	Figure 63
α_{589nm}^{20} (10 mg/mL in $CHCl_3$):	+9°
Melting point:	74.2 °C
LC-MS-DAD purity:	100%
HR-MS (ESI-(+)):	m/z=393.2774 $[M+H^+]^+$ calculated: 393.2748
^{1}H NMR (300 MHz, $CDCl_3$):	δ 7.09 (d, *J* = 8.3 Hz, 2H), 6.80 (d, *J* = 8.3 Hz, 2H), 4.81 (d, *J* = 8.1 Hz, 1H), 3.95 (t, *J* = 6.4 Hz, 2H), 3.78 (s, 1H), 3.68 – 3.43 (m, 2H), 2.79 – 2.71 (m, 2H), 2.52 – 2.33 (m, 6H), 2.02 – 1.86 (m, 2H), 1.71 – 1.52 (m, 4H), 1.52 – 1.35 (m, 11H).
^{13}C NMR (75.5 MHz, $CDCl_3$):	δ 157.71, 156.13, 130.23, 129.79, 114.56, 79.57, 77.27, 66.51, 63.86, 56.05, 54.63, 36.56, 28.37, 26.81, 25.91, 24.41.

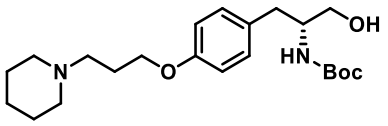

tert-Butyl-(*R*)-(1-(carbamoyloxy)-3-(4-(3-(piperidin-1-yl)propoxy)phenyl)propan-2-yl)carbamate **(P5)**

The synthesis was based on a procedure previously described.[672] Compound **P4** (520 mg, 1.30 mmol, 1.0 eq.) and 1,1'-carbonyldiimidazole (340 mg, 1.95 mmol, 1.5 eq.) were dissolved in THF and stirred at room temperature for four hours. A 25% aqueous ammonia solution was then added, and the mixture was stirred at room temperature for three days. The organic solvent was removed under reduced pressure, and the aqueous phase was extracted three times with ethyl acetate. The combined organic layers were dried over magnesium sulphate, filtered, and the solvent was removed under reduced pressure. The crude product was used without further purification.

Yield:	521 mg, (92%)
Chemical formula:	$C_{23}H_{37}N_3O_5$
Molecular mass:	435.57 g/mol
Appearance:	Colourless solid
Internal code:	MST-782, ST-2951

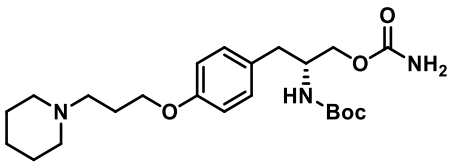

Synthesis scheme:	Figure 64
α_{589nm}^{20} (10 mg/mL in $CHCl_3$):	+3°
Melting point:	122.6 °C
LC-MS-DAD purity:	97.5%
HR-MS (ESI-(+)):	m/z=436.2824 $[M+H^+]^+$ calculated: 436.2806
^{1}H NMR (300 MHz, $CDCl_3$):	δ 7.02 (d, *J* = 8.7 Hz, 2H), 6.74 (d, *J* = 8.7 Hz, 2H), 4.94 – 4.55 (m, 3H), 3.97 – 3.80 (m, 6H), 2.69 – 2.45 (m, 7H), 2.15 – 1.97 (m, 2H), 1.81 – 1.63 (m, 4H), 1.50 – 1.32 (m, 11H).
^{13}C NMR (75.5 MHz, $CDCl_3$):	δ 157.53, 156.72, 155.32, 130.31, 129.43, 114.55, 79.52, 77.26, 65.99, 65.54, 55.81, 54.24, 36.96, 28.37, 25.83, 24.79, 23.66.

tert-Butyl-(*R*)-(1-(carbamoyloxy)-3-(4-(3-(piperidin-1-yl)propoxy)phenyl)propan-2-yl)carbamate) dihydrochloride **(P6)**

The synthesis was based on a procedure previously described.[674] Compound **P5** (280 mg, 0.64 mmol, 1.0 eq.) was dissolved in methanol, and the reaction mixture was cooled to 0 °C in an ice bath. At this temperature, concentrated HCl (ca. 1 mL) was added dropwise. The reaction mixture was allowed to warm to room temperature and stirred for three days. The solvent was removed under reduced pressure. The residue was purified by reverse phase flash chromatography using a gradient elution of water/methanol (0-100%).

Yield:	241 mg, (92%)
Chemical formula:	$C_{18}H_{29}N_3O_5$ x 2HCl
Molecular mass:	409.45 g/mol
Appearance:	Colourless solid
Internal code:	MST-801, ST-2955
Synthesis scheme:	Figure 65
α_{589nm}^{20} (10 mg/mL in $CHCl_3$):	+50°
Melting point:	219.2 °C
LC-MS-DAD purity:	98.7%
HR-MS (ESI-(+)):	m/z=336.2282 $[M+H^+]^+$ calculated: 336.2273
^{1}H NMR (600 MHz, DMSO-d_6):	δ 10.85 (s, 1H), 8.43 (d, *J* = 5.4 Hz, 3H), 7.20 (d, *J* = 9.3 Hz, 2H), 6.91 (d, *J* = 9.3 Hz, 2H), 6.60 (s, 2H), 4.04 (t, *J* = 6.1 Hz, 2H), 4.01 – 3.97 (m, 1H), 3.90 – 3.81 (m, 1H), 3.59 – 3.35 (m, 3H), 3.20 – 3.08 (m, 2H), 3.04 – 2.95 (m, 1H), 2.90 – 2.72 (m, 2H), 2.25 – 2.14 (m, 2H), 1.93 – 1.67 (m, 6H), 1.44 – 1.31 (m, 1H).

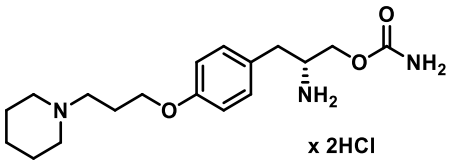

^{13}C NMR (151 MHz, DMSO-d_6):	δ 157.72, 156.53, 130.84, 128.51, 115.12, 65.54, 62.45, 53.82, 52.38, 51.76, 34.48, 23.71, 22.73, 21.90.

tert-Butyl-(*S*)-(1-hydroxy-3-(4-(3-(piperidin-1-yl)propoxy)phenyl)propan-2-yl)carbamate **(P7)**

The alkylation protocol was carried out as described for compound **2a.**[598] Boc-L-tyrosinole (2010 mg, 7.53 mmol, 1.0 eq.), 1-(3-chloropropyl)piperidine hydrochloride (1483 mg, 7.53 mmol, 1.0 eq.), potassium carbonate (2081 mg, 15.06 mmol, 2.0 eq.), and potassium iodide (2500 mg, 15.06 mmol, 2.0 eq.) were subjected to the reaction conditions for 48 hours. The crude product was purified by flash chromatography using a gradient elution of dichloromethane/methanol (0-20%).

Yield:	1005 mg, (34%)
Chemical formula:	$C_{22}H_{36}N_2O_4$
Molecular mass:	392.54 g/mol
Appearance:	Colourless solid
Internal code:	MST-612
Synthesis scheme:	Figure 67
α_{589nm}^{20} (10 mg/mL in $CHCl_3$):	-9°
Melting point:	72.3 °C
LC-MS-DAD purity:	97.2%
HR-MS (ESI-(+)):	m/z=393.2812 $[M+H^+]^+$ calculated: 393.2748
^{1}H NMR (300 MHz, $CDCl_3$):	δ 7.10 (d, *J* = 8.8 Hz, 2H), 6.81 (d, *J* = 8.8 Hz, 2H), 4.78 (d, *J* = 8.0 Hz, 1H), 3.96 (t, *J* = 6.3 Hz, 2H), 3.82 – 3.73 (m, 1H), 3.67 – 3.46 (m, 2H), 3.19 – 3.07 (m, 1H), 2.80 – 2.73 (m, 2H), 2.55 – 2.35 (m, 6H), 2.04 – 1.90 (m, 2H), 1.68 – 1.53 (m, 4H), 1.52 – 1.36 (m, 11H).
^{13}C NMR (75.5 MHz, $CDCl_3$):	δ 157.69, 156.13, 130.23, 129.80, 114.56, 79.59, 66.46, 63.97, 55.97, 54.53, 53.89, 36.54, 28.37, 26.66, 25.76, 24.31.

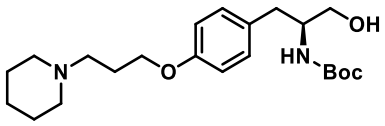

tert-Butyl-(*S*)-(1-(carbamoyloxy)-3-(4-(3-(piperidin-1-yl)propoxy)phenyl)propan-2-yl)carbamate **(P8)**

The carbamate formation protocol was carried out as described for compound **P5**.[672] Compound **P7** (700 mg, 1.79 mmol, 1.0 eq.) and 1,1'-carbonyldiimidazole (340 mg, 2.69 mmol, 1.5 eq.) were subjected to the reaction conditions for three days. The crude product was purified by column chromatography using a gradient elution of dichloromethane/methanol (sat. NH_3) (0-20%).

Yield:	435 mg, (82%)
Chemical formula:	$C_{23}H_{37}N_3O_5$
Molecular mass:	435.57 g/mol
Appearance:	Colourless solid
Internal code:	MST-618
Synthesis scheme:	Figure 68
α_{589nm}^{20} (10 mg/mL in $CHCl_3$):	-2°
Melting point:	116.9 °C
LC-MS-DAD purity:	100%
HR-MS (ESI-(+)):	m/z=436.2850 $[M+H^+]^+$ calculated: 436.2806
^{1}H NMR (300 MHz, $CDCl_3$):	δ 7.06 (d, *J* = 8.6 Hz, 2H), 6.77 (d, *J* = 8.6 Hz, 2H), 5.09 (s, 2H), 4.84 (d, *J* = 7.1 Hz, 1H), 4.01 – 3.86 (m, 5H), 2.80 – 2.44 (m, 8H), 2.10 – 1.95 (m, 2H), 1.73 – 1.60 (m, 4H), 1.50 – 1.33 (m, 11H).
^{13}C NMR (75.5 MHz, $CDCl_3$):	δ 157.57, 157.44, 156.94, 155.37, 130.28, 129.39, 114.54, 79.47, 66.12, 65.46, 55.83, 54.33, 36.91, 28.36, 26.09, 25.11, 23.85.

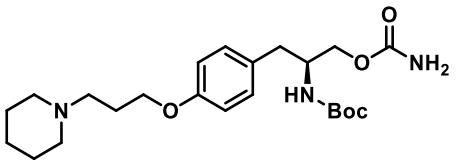

tert-Butyl-(*S*)-(1-(carbamoyloxy)-3-(4-(3-(piperidin-1-yl)propoxy)phenyl)propan-2-yl)carbamate) dihydrochloride **(P9)**

The Boc-deprotection protocol was carried out as described for compound **P6**.[674] Compound **P8** (193 mg, 0.44 mmol, 1.0 eq.) was subjected to the reaction conditions for three days. The residue was purified by reverse phase flash chromatography using a gradient elution of water/acetonitrile (0-100%).

Yield:	212 mg, (76%)
Chemical formula:	$C_{18}H_{29}N_3O_5$ x 2HCl
Molecular mass:	409.45 g/mol
Appearance:	Colourless solid
Internal code:	MST-629, ST-2853
Synthesis scheme:	Figure 69
α_{589nm}^{20} (10 mg/mL in $CHCl_3$):	-49°
Melting point:	221.1 °C
LC-MS-DAD purity:	100%
HR-MS (ESI-(+)):	m/z=336.2287 $[M+H^+]^+$ calculated: 336.2273

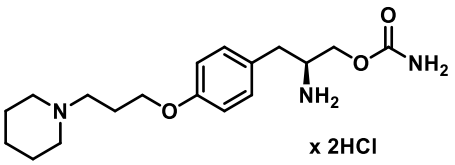

^{1}H NMR (300 MHz, DMSO-d_6):	δ 10.85 (s, 1H), 8.43 (s, 3H), 7.19 (d, *J* = 8.7 Hz, 2H), 6.91 (d, *J* = 8.7 Hz, 2H), 6.59 (s, 2H), 4.13 – 3.77 (m, 4H), 3.56 – 3.39 (m, 1H), 3.20 – 3.06 (m, 2H), 3.04 – 2.69 (m, 5H), 2.28 – 2.09 (m, 2H), 1.95 – 1.62 (m, 6H), 1.46 – 1.28 (m, 1H).
^{13}C NMR (75.5 MHz, DMSO-d_6):	δ 157.21, 156.03, 130.33, 128.01, 114.61, 65.03, 61.92, 53.33, 51.88, 51.26, 33.97, 23.21, 22.23, 21.40.

(*R*)-2-Amino-3-(4-(3-(piperidin-1-yl)propoxy)phenyl)propan-1-ol **(P10)**

The Boc-deprotection protocol was carried out as described for compound **P6**.[674] Compound **P4** (300 mg, 0.76 mmol, 1.0 eq.) was subjected to the reaction conditions for seven days. The crude product was purified by column chromatography using a gradient elution of dichloromethane/methanol (sat. NH_3) (0-20%).

Yield:	198 mg, (89%)
Chemical formula:	$C_{17}H_{28}N_2O_2$
Molecular mass:	292.42 g/mol
Appearance:	Colourless solid
Internal code:	MST-773, ST-2950
Synthesis scheme:	Figure 71
α_{589nm}^{20} (10 mg/mL in $CHCl_3$):	+30°
Melting point:	65.0 °C
LC-MS-DAD purity:	100%
HR-MS (ESI-(+)):	m/z=293.2224 $[M+H^+]^+$ calculated: 293.2224
^{1}H NMR (300 MHz, $CDCl_3$):	δ 7.07 (d, *J* = 8.6 Hz, 2H), 6.82 (d, *J* = 8.6 Hz, 2H), 3.96 (t, *J* = 6.4 Hz, 2H), 3.60 (dd, *J* = 10.6, 3.9 Hz, 1H), 3.41 – 3.29 (m, 1H), 3.12 – 2.98 (m, 1H), 2.71 (dd, *J* = 10.6, 3.2 Hz, 1H), 2.51 – 2.42 (m, 2H), 2.46 – 2.34 (m, 4H), 2.20 – 2.07 (m, 4H), 2.03 – 1.88 (m, 2H), 1.64 – 1.51 (m, 4H), 1.49 – 1.35 (m, 2H).
^{13}C NMR (75.5 MHz, $CDCl_3$):	δ 157.65, 130.56, 130.09, 114.62, 66.53, 66.28, 56.04, 54.63, 54.31, 39.89, 26.82, 25.93, 24.41.

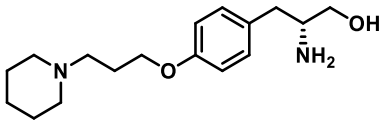

(*S*)-2-Amino-3-(4-(3-(piperidin-1-yl)propoxy)phenyl)propan-1-ol **(P11)**

The Boc-deprotection protocol was carried out as described for compound **P6**.[674] Compound **P7** (200 mg, 0.51 mmol, 1.0 eq.) was subjected to the reaction conditions for seven days. The crude product was purified by column chromatography using a gradient elution of dichloromethane/methanol (sat. NH_3) (0-20%).

Yield:	142 mg, (95%)
Chemical formula:	$C_{17}H_{28}N_2O_2$
Molecular mass:	292.42 g/mol
Appearance:	Colourless solid
Internal code:	MST-722
Synthesis scheme:	Figure 71
α_{589nm}^{20} (10 mg/mL in $CHCl_3$):	-29°
Melting point:	66.4 °C
LC-MS-DAD purity:	100%
HR-MS (ESI-(+)):	m/z=293.2371 $[M+H^+]^+$ calculated: 293.2224
^{1}H NMR (300 MHz, DMSO-d_6):	δ 7.08 (d, *J* = 8.8 Hz, 2H), 6.81 (d, *J* = 8.8 Hz, 2H), 3.93 (t, *J* = 6.4 Hz, 2H), 3.26 (dd, *J* = 10.3, 4.8 Hz, 1H), 3.20 – 3.09 (m, 1H), 2.88 – 2.71 (m, 1H), 2.59 (dd, *J* = 13.3, 5.6 Hz, 1H), 2.43 – 2.20 (m, 8H), 1.93 – 1.74 (m, 2H), 1.58 – 1.27 (m, 8H).
^{13}C NMR (75.5 MHz, DMSO-d_6):	δ 156.83, 131.52, 130.04, 114.07, 65.84, 65.77, 55.19, 54.55, 54.10, 39.29, 26.36, 25.59, 24.14.

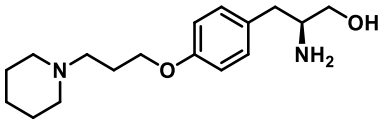

(*R*)-4-(4-(3-(Piperidin-1-yl)propoxy)benzyl)oxazolidin-2-one **(P12)**

The synthesis was based on a procedure previously described.[681] Compound **P4** (300 mg, 0.76 mmol, 1.0 eq.) was dissolved in tetrahydrofuran. The reaction mixture was cooled to 0 °C, and sodium hydride (70 mg, 2.28 mmol, 3.0 eq.) was added in portions. The mixture was then allowed to warm to room temperature and stirred for two days. The reaction was quenched with a saturated ammonium chloride solution. The mixture was extracted three times with ethyl acetate, and the combined organic phases were washed twice with 2M sodium hydroxide solution and once with brine. The organic phase was dried over magnesium sulfate, filtered, and the solvent was removed under reduced pressure. The crude product was purified by column chromatography using a gradient elution of dichloromethane/methanol (sat. NH_3) (0-20%).

Yield:	237 mg, (98%)
Chemical formula:	$C_{18}H_{26}N_2O_3$
Molecular mass:	318.42 g/mol
Appearance:	Colourless solid
Internal code:	MST-774, ST-2949
Synthesis scheme:	Figure 72
α_{589nm}^{20} (10 mg/mL in $CHCl_3$):	+4°
Melting point:	97.1 °C
LC-MS-DAD purity:	96.8%
HR-MS (ESI-(+)):	m/z=319.2031 $[M+H^+]^+$ calculated: 319.2016
^{1}H NMR (300 MHz, DMSO-d_6):	δ 7.75 (s, 1H), 7.13 (d, *J* = 8.6 Hz, 2H), 6.85 (d, *J* = 8.6 Hz, 2H), 4.34 – 4.15 (m, 1H), 4.06 – 3.86 (m, 4H), 2.80 – 2.58 (m, 2H), 2.45 – 2.25 (m, 6H), 1.90 – 1.75 (m, 2H), 1.62 – 1.31 (m, 6H).
^{13}C NMR (75.5 MHz, DMSO-d_6):	δ 158.59, 157.35, 130.37, 128.16, 114.31, 67.90, 65.74, 55.11, 54.04, 52.58, 39.66, 26.24, 25.50, 24.05.

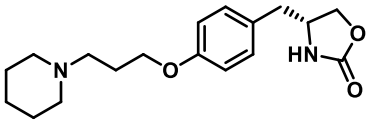

(*S*)-4-(4-(3-(Piperidin-1-yl)propoxy)benzyl)oxazolidin-2-one **(P13)**

The oxazolidine formation protocol was carried out as described for compound **P12**.[681] Compound **P7** (520 mg, 1.33 mmol, 1.0 eq.) was subjected to the reaction conditions for two days. The crude product was purified by column chromatography using a gradient elution of dichloromethane/methanol (sat. NH_3) (0-20%).

Yield:	415 mg, (98%)
Chemical formula:	$C_{18}H_{26}N_2O_3$
Molecular mass:	318.42 g/mol
Appearance:	Colourless solid
Internal code:	MST-723, ST-2950
Synthesis scheme:	Figure 72
α_{589nm}^{20} (10 mg/mL in $CHCl_3$):	-5°
Melting point:	99.1 °C
LC-MS-DAD purity:	97.5%
HR-MS (ESI-(+)):	m/z=319.2032 $[M+H^+]^+$ calculated: 319.2016

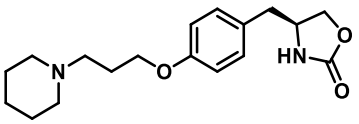

^{1}H NMR (300 MHz, DMSO-d_6):	δ 7.75 (s, 1H), 7.13 (d, *J* = 8.5 Hz, 2H), 6.84 (d, *J* = 8.5 Hz, 2H), 4.30 – 4.18 (m, 1H), 4.07 – 3.89 (m, 4H), 2.83 – 2.59 (m, 2H), 2.43 – 2.26 (m, 6H), 1.93 – 1.74 (m, 2H), 1.57 – 1.44 (m, 4H), 1.44 – 1.30 (m, 2H).
^{13}C NMR (75.5 MHz, DMSO-d_6):	δ 158.58, 157.35, 130.37, 128.16, 114.31, 67.92, 67.90, 65.75, 55.12, 54.05, 52.58, 26.26, 25.52, 24.07.

10.3 H_3R molecular tools for click chemistry

(4-(3-(Piperidin-1-yl)propoxy)phenyl)methanol **(21)**

The alkylation protocol was carried out as described for compound **2a.**[598] 4-Hydroxybenzyl alcohol (1039 mg, 5.26 mmol, 1.0 eq.) 1-(3-chloropropyl)piperidine hydrochloride (1031 mg, 5.26 mmol, 1.0 eq.), potassium carbonate (1454 mg, 10.52 mmol, 2.0 eq.), and potassium iodide (1746 mg, 10.52 mmol, 2.0 eq.) were subjected to the reaction conditions for 48 hours. The residue was purified by flash column chromatography using a gradient elution of hexane/ethyl acetate (0-100%).

Yield:	971 mg, (74%)
Chemical formula:	$C_{15}H_{23}NO_2$
Molecular mass:	249.35 g/mol
Appearance:	Yellow oil
Internal code:	MST-613
Synthesis scheme:	Figure 76
^{1}H NMR (300 MHz, DMSO-d_6):	δ 7.22 (d, *J* = 8.6 Hz, 2H), 6.88 (d, *J* = 8.6 Hz, 2H), 5.04 (t, *J* = 5.6 Hz, 1H), 4.41 (d, *J* = 5.6 Hz, 2H), 3.96 (t, *J* = 6.4 Hz, 2H), 2.42 – 2.27 (m, 6H), 1.91 – 1.76 (m, 2H), 1.56 – 1.31 (m, 6H).

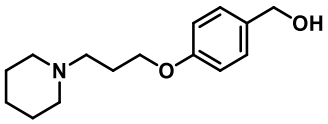

(4-((4-(3-(Piperidin-1-yl)propoxy)benzyl)oxy)benzonitrile **(22a)**

The synthesis was based on a procedure previously described.[694] Compound **21** (515 mg, 2.06 mmol, 1.2 eq.), 4-cyanophenol (205 mg, 1.72 mmol, 1.0 eq.) and triphenylphosphine (540 mg, 2.06 mmol, 1.2 eq.) were dissolved in tetrahydrofuran and the solution was cooled to 0 °C using an ice bath. At this temperature, diethyl azodicarboxylate (323 µL, 2.06 mmol, 1.2 eq.) was added dropwise. The mixture was stirred for 30 minutes at this temperature and then for two days at room temperature. Subsequently, the solvent was evaporated under reduced pressure. The residue was dissolved in ethyl acetate and washed three times with 2M sodium hydroxide solution. The organic phases were combined, dried over magnesium

sulphate, filtered, and concentrated under reduced pressure. The crude product was used without further purification.

Yield:	458 mg, (76%)
Chemical formula:	$C_{22}H_{26}N_2O_2$
Molecular mass:	350.46 g/mol
Appearance:	Colourless solid
Internal code:	MST-614
Synthesis scheme:	Figure 77
^{1}H NMR (300 MHz, $CDCl_3$):	δ 7.57 (d, *J* = 9.0 Hz, 2H), 7.31 (d, *J* = 8.6 Hz, 2H), 7.00 (d, *J* = 9.0 Hz, 2H), 6.90 (d, *J* = 8.6 Hz, 2H), 5.02 (s, 2H), 4.01 (t, *J* = 6.3 Hz, 2H), 2.56 – 2.38 (m, 6H), 2.09 – 1.89 (m, 2H), 1.71 – 1.55 (m, 4H), 1.52 – 1.37 (m, 2H).

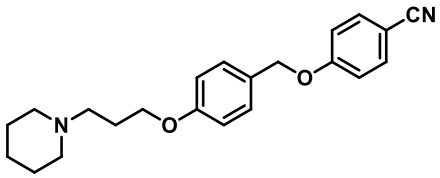

4-(4-(3-(Piperidin-1-yl)propoxy)phenethoxy)benzonitrile **(22b)**

The Mitsunobu protocol was carried out as described for compound **22a**.[694] Compound **7a** (282 mg, 1.07 mmol, 1.2 eq.), 4-cyanophenol (106 mg, 0.89 mmol, 1.0 eq.) and triphenylphosphine (280 mg, 1.07 mmol, 1.2 eq.) and diethyl azodicarboxylate (168 µL, 1.07 mmol, 1.2 eq.) were subjected to the reaction conditions for 48 hours. The residue was purified by flash column chromatography using a gradient elution of dichloromethane/methanol (0-20%).

Yield:	159 mg, (49%)
Chemical formula:	$C_{23}H_{28}N_2O_2$
Molecular mass:	364.49 g/mol
Appearance:	Colourless solid
Internal code:	MST-610
Synthesis scheme:	Figure 77
^{1}H NMR (300 MHz, $CDCl_3$):	δ 7.56 (d, *J* = 8.8 Hz, 2H), 7.16 (d, *J* = 8.5 Hz, 2H), 6.92 (d, *J* = 8.8 Hz, 2H), 6.86 (d, *J* = 8.5 Hz, 2H), 4.16 (t, *J* = 7.0 Hz, 2H), 3.99 (t, *J* = 6.4 Hz, 2H), 3.04 (t, *J* = 7.0 Hz, 2H), 2.54 – 2.36 (m, 6H), 2.07 – 1.87 (m, 2H), 1.69 – 1.55 (m, 4H), 1.50 – 1.39 (m, 2H).

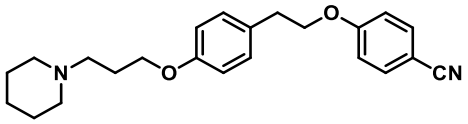

4-(3-(4-(3-(Piperidin-1-yl)propoxy)phenyl)propoxy)benzonitrile **(22c)**

The Mitsunobu protocol was carried out as described for compound **22a**.[694] Compound **7b** (800 mg, 2.12 mmol, 1.2 eq.), 4-cyanophenol (210 mg, 1.77 mmol, 1.0 eq.) and

triphenylphosphine (555 mg, 2.12 mmol, 1.2 eq.) and diethyl azodicarboxylate (332 µL, 2.12 mmol, 1.2 eq.) were subjected to the reaction conditions for 48 hours. The residue was purified by flash column chromatography using a gradient elution of dichloromethane/methanol (0-20%).

Yield:	234 mg, (35%)
Chemical formula:	$C_{24}H_{30}N_2O_2$
Molecular mass:	378.52 g/mol
Appearance:	Colourless solid
Internal code:	MST-626
Synthesis scheme:	Figure 77
^{1}H NMR (300 MHz, $CDCl_3$):	δ 7.55 (d, *J* = 9.2 Hz, 2H), 7.09 (d, *J* = 8.6 Hz, 2H), 6.92 (d, *J* = 9.2 Hz, 2H), 6.83 (d, *J* = 8.6 Hz, 2H), 4.02 – 3.91 (m, 4H), 2.74 (t, *J* = 7.5 Hz, 2H), 2.52 – 2.33 (m, 6H), 2.17 – 1.87 (m, 4H), 1.62 – 1.34 (m, 6H).

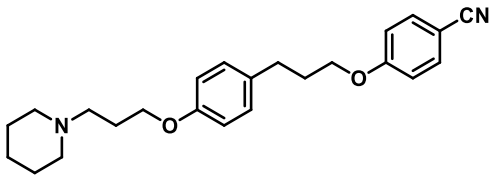

3-Methyl-6-(4-((4-(3-(piperidin-1-yl)propoxy)benzyl)oxy)phenyl)-1,2,4,5-tetrazine **(P14a)**

The synthesis was based on a procedure previously described.[698] Compound **22a** (200 mg, 0.82 mmol, 1.0 eq.) and zinc triflate (149 mg, 0.41 mmol, 0.5 eq.) were dissolved in acetonitrile, and a hydrazine solution (1 mol/L in water, 8.2 mmol, 10 eq.) was added dropwise. The reaction mixture was heated to 60 °C and stirred for two days. Subsequently, a saturated sodium nitrite solution (approximately 5 mL) was carefully added dropwise, followed by the addition of 1 M hydrochloric acid (approximately 5 mL). The aqueous mixture was extracted three times with ethyl acetate. The organic phase was discarded, and the aqueous phase was adjusted to a basic pH of 10. The basic solution was then extracted three more times with ethyl acetate. The organic phases were combined, dried over magnesium sulfate, filtered, and concentrated under reduced pressure. The crude product was purified by flash chromatography using a gradient elution of dichloromethane/methanol (0-20%).

Yield:	17 mg, (5%)
Chemical formula:	$C_{24}H_{29}N_5O_2$
Molecular mass:	419.53 g/mol
Appearance:	Pink solid
Internal code:	MST-617C
Synthesis scheme:	Figure 78
Melting point:	135.4 °C
LC-MS-DAD purity:	96.0%

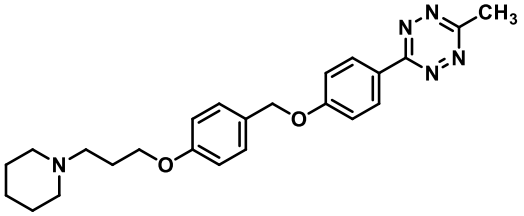

HR-MS (ESI-(+)):	m/z=420.2394 $[M+H^+]^+$ calculated: 420.2394
^{1}H NMR (300 MHz, MeOD):	δ 7.91 (d, *J* = 8.5 Hz, 2H), 7.41 (d, *J* = 8.3 Hz, 2H), 7.12 (d, *J* = 8.5 Hz, 2H), 6.97 (d, *J* = 8.3 Hz, 2H), 5.10 (s, 2H), 4.13 (t, *J* = 5.7 Hz, 2H), 3.63 – 3.57 (m, 2H), 3.36 – 3.28 (m, 4H), 3.02 – 2.96 (m, 2H), 2.48 (s, 3H), 2.29 – 2.18 (m, 2H), 2.10 – 1.48 (m, 6H).
^{13}C NMR (75.5 MHz, MeOD):	δ 160.37, 158.35, 153.93, 129.68, 129.53, 129.07, 121.46, 118.63, 114.68, 114.15, 69.37, 64.59, 54.58, 53.13, 23.86, 22.98, 21.27, 8.46.

3-Methyl-6-(4-((4-(3-(piperidin-1-yl)propoxy)benzyl)oxy)phenyl)-1,4-dihydro-1,2,4,5-tetrazine **(BP14a)**

The title compound was obtained as a byproduct during the reaction procedure described for Compound **P14a**, and isolated during the purification process.

Yield:	59 mg, (15%)
Chemical formula:	$C_{24}H_{31}N_5O_2$
Molecular mass:	421.54 g/mol
Appearance:	Colourless solid
Internal code:	MST-617A, ST-2851
Synthesis scheme:	Figure 78
Melting point:	160.0 °C
LC-MS-DAD purity:	100%
HR-MS (ESI-(+)):	m/z=422.2574 $[M+H^+]^+$ calculated: 422.2551
^{1}H NMR (300 MHz, DMSO-d_6):	δ 7.95 (d, *J* = 9.2 Hz, 2H), 7.42 (d, *J* = 9.0 Hz, 2H), 7.11 (d, *J* = 9.2 Hz, 2H), 6.97 (d, *J* = 9.0 Hz, 2H), 5.98 (s, 2H), 5.10 (s, 2H), 4.07 (t, *J* = 5.9 Hz, 2H), 3.59 – 3.31 (m, 4H), 3.26 – 3.15 (m, 2H), 3.07 – 2.80 (m, 2H), 2.36 (s, 3H), 2.21 – 2.06 (m, 2H), 1.93 – 1.29 (m, 4H).
^{13}C NMR (75.5 MHz, MeOD)	δ 161.78, 160.68, 145.93, 132.31, 131.91, 131.81, 122.74, 121.24, 117.37, 117.14, 71.67, 67.52, 56.16, 54.96, 26.20, 25.38, 23.95, 12.58.

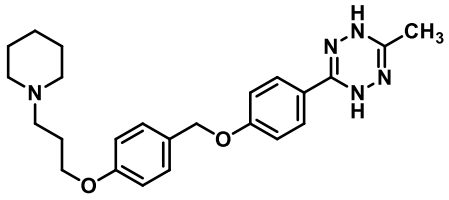

3-Methyl-6-(4-(4-(3-(piperidin-1-yl)propoxy)phenethoxy)phenyl)-1,2,4,5-tetrazine **(P14b)**

The tetrazine formation was carried out as described for compound **P14a**.[698] Compound **22b** (140 mg, 0.38 mmol, 1.0 eq.), zinc triflate (69 mg, 0.19 mmol, 0.5 eq.) and a hydrazine solution (1 mol/L in water, 3.8 mmol, 10 eq.) were subjected to the reaction conditions for 48 hours. The

crude product was purified by flash chromatography using a gradient elution of dichloromethane/methanol (0-20%).

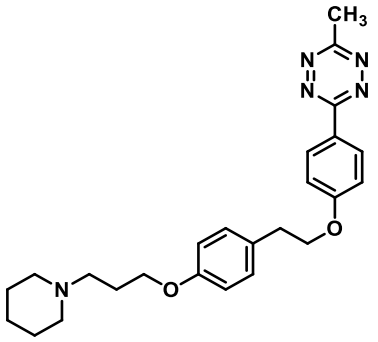

Yield:	10 mg, (6%)
Chemical formula:	$C_{25}H_{31}N_5O_2$
Molecular mass:	433.56 g/mol
Appearance:	Pink solid
Internal code:	MST-613C, ST-2849
Synthesis scheme:	Figure 78
Melting point:	139.2 °C
LC-MS-DAD purity:	96.7%
HR-MS (ESI-(+)):	m/z=434.2542 $[M+H^+]^+$ calculated: 434.2551
^{1}H NMR (300 MHz, $CDCl_3$):	δ 8.52 (d, *J* = 8.7 Hz, 2H), 7.20 (d, *J* = 8.8 Hz, 2H), 7.06 (d, *J* = 8.7 Hz, 2H), 6.87 (d, *J* = 8.8 Hz, 2H), 4.24 (t, *J* = 7.0 Hz, 2H), 3.99 (t, *J* = 6.4 Hz, 2H), 3.18 – 3.00 (m, 5H), 2.51 – 2.37 (m, 6H), 2.04 – 1.90 (m, 2H), 1.64 – 1.54 (m, 4H), 1.49 – 1.38 (m, 2H).
^{13}C NMR (75.5 MHz, $CDCl_3$):	δ 166.57, 163.79, 162.60, 157.89, 129.93, 129.71, 124.11, 123.21, 115.22, 114.65, 69.18, 66.59, 56.03, 54.67, 34.79, 26.87, 26.00, 24.45, 21.05.

3-Methyl-6-(4-(4-(3-(piperidin-1-yl)propoxy)phenethoxy)phenyl)-1,4-dihydro-1,2,4,5-tetrazine **(BP14b)**

The title compound was obtained as a byproduct during the reaction procedure described for Compound **P14b**, and isolated during the purification process.

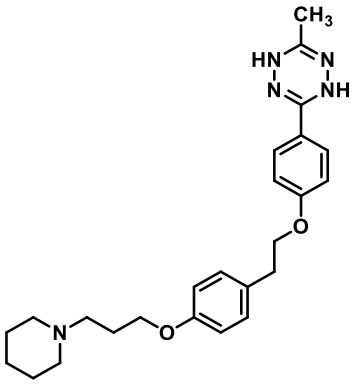

Yield:	45 mg, (27%)
Chemical formula:	$C_{25}H_{33}N_5O_2$
Molecular mass:	435.57 g/mol
Appearance:	Colourless solid
Internal code:	MST-613A
Synthesis scheme:	Figure 78
Melting point:	141.2 °C
LC-MS-DAD purity:	97.5%
HR-MS (ESI-(+)):	m/z=436.2690 $[M+H^+]^+$ calculated: 436.2707

^{1}H NMR (300 MHz, DMSO-d_6):	δ 7.95 (d, *J* = 10.2 Hz, 2H), 7.27 (d, *J* = 9.8 Hz, 2H), 7.04 (d, *J* = 10.2 Hz, 2H), 6.89 (d, *J* = 9.8 Hz, 2H), 6.00 (s, 2H), 4.21 (t, *J* = 8.1 Hz, 2H), 4.03 (t, *J* = 5.9 Hz, 2H), 3.20 (t, *J* = 8.1 Hz, 2H), 3.06 – 2.82 (m, 4H), 2.36 (s, 3H), 2.18 – 2.03 (m, 2H), 1.94 – 1.24 (m, 8H).
^{13}C NMR (75.5 MHz, DMSO-d_6)	δ 159.26, 156.77, 152.94, 151.98, 130.53, 129.98, 129.30, 119.61, 114.36, 114.29, 68.43, 64.73, 53.47, 52.22, 33.93, 23.51, 22.64, 21.21, 9.82.

3-Methyl-6-(4-(3-(4-(3-(piperidin-1-yl)propoxy)phenyl)propoxy)phenyl)-1,2,4,5-tetrazine **(P14c)**

The tetrazine formation protocol was carried out as described for compound **P14a**.[698] Compound **22c** (210 mg, 0.55 mmol, 1.0 eq.), zinc triflate (102 mg, 0.28 mmol, 0.5 eq.) and a hydrazine solution (1 mol/L in water, 5.5 mmol, 10 eq.) were subjected to the reaction conditions for 48 hours. The crude product was purified by flash chromatography using a gradient elution of dichloromethane/methanol (0-20%).

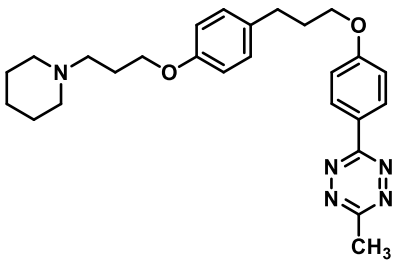

Yield:	12 mg, (5%)
Chemical formula:	$C_{26}H_{33}N_5O_2$
Molecular mass:	447.58 g/mol
Appearance:	Pink solid
Internal code:	MST-636C, ST-2854
Synthesis scheme:	Figure 78
Melting point:	145.1 °C
LC-MS-DAD purity:	97.6%
HR-MS (ESI-(+)):	m/z=448.2739 $[M+H^+]^+$ calculated: 448.2707
^{1}H NMR (300 MHz, $CDCl_3$):	δ 8.51 (d, *J* = 8.9 Hz, 2H), 7.11 (d, *J* = 8.7 Hz, 2H), 7.04 (d, *J* = 8.9 Hz, 2H), 6.79 (d, *J* = 8.7 Hz, 2H), 4.12 – 3.96 (m, 4H), 3.11 – 2.90 (m, 9H), 2.77 (t, *J* = 7.5 Hz, 2H), 2.37 – 2.23 (m, 2H), 2.17 – 2.03 (m, 2H), 2.02 – 1.89 (m, 4H), 1.69 – 1.50 (m, 2H).
^{13}C NMR (75.5 MHz, $CDCl_3$):	δ 159.34, 156.41, 152.84, 152.03, 133.55, 129.33, 129.22, 119.90, 114.38, 114.24, 66.66, 64.71, 53.48, 52.23, 30.48, 23.53, 22.65, 21.22, 9.87, 9.85.

3-Methyl-6-(4-(3-(4-(3-(piperidin-1-yl)propoxy)phenyl)propoxy)phenyl)-1,4-dihydro-1,2,4,5-tetrazine **(BP14c)**

The title compound was obtained as a byproduct during the reaction procedure described for Compound **P14c**, and isolated during the purification process.

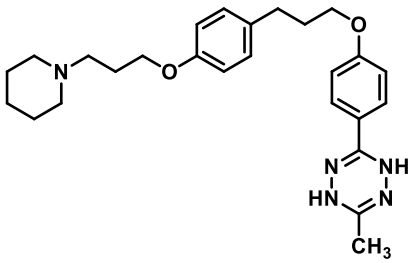

Yield:	35 mg, (14%)
Chemical formula:	$C_{26}H_{35}N_5O_2$
Molecular mass:	449.60 g/mol
Appearance:	Colourless solid
Internal code:	MST-636A, ST-2848
Synthesis scheme:	Figure 78
Melting point:	142.6 °C
LC-MS-DAD purity:	100%
HR-MS (ESI-(+)):	m/z=450.2879 $[M+H^+]^+$ calculated: 450.2864
^{1}H NMR (300 MHz, DMSO-d_6):	δ 7.95 (d, *J* = 9.0 Hz, 2H), 7.17 (d, *J* = 7.8 Hz, 2H), 7.04 (d, *J* = 9.0 Hz, 2H), 6.87 (d, *J* = 7.8 Hz, 2H), 5.98 (s, 2H), 4.08 – 3.91 (m, 4H), 3.58 – 3.44 (m, 2H), 3.19 (t, *J* = 8.3 Hz, 2H), 2.99 – 2.78 (m, 2H), 2.70 (t, *J* = 8.3 Hz, 2H), 2.36 (s, 3H), 2.17 – 1.92 (m, 4H), 1.92 – 1.28 (m, 6H).
^{13}C NMR (75.5 MHz, DMSO-d_6)	δ 159.34, 156.41, 152.84, 152.03, 133.55, 129.33, 129.22, 119.90, 114.38, 114.24, 66.66, 64.71, 53.48, 52.23, 40.33, 30.48, 23.53, 22.65, 21.22, 9.87.

4-(3-(Piperidin-1-yl)propoxy)benzonitrile **(23)**

The alkylation protocol was carried out as described for compound **2a.**[791] 4-Cyanophenol (300 mg, 2.52 mmol, 1.0 eq.), 1 (3 chloropropyl)piperidine hydrochloride (500 mg, 2.52 mmol, 1.0 eq.), potassium iodide (830 mg, 5.04 mmol, 2.0 eq.) and potassium carbonate (1380 mg, 10.1 mmol, 4.0 eq.) were subjected to the reaction conditions for 48 hours. The residue was purified by flash column chromatography using a gradient elution of dichloromethane/methanol (0-20%).

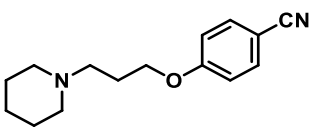

Yield:	443 mg, (72%)
Chemical formula:	$C_{15}H_{20}N_2O$
Molecular mass:	244.34 g/mol
Appearance:	Yellow oil
Internal code:	MST-632
Synthesis scheme:	Figure 80

^{1}H NMR (300 MHz, $CDCl_3$):	7.56 (d, *J* = 9.6 Hz, 2H), 6.93 (d, *J* = 9.6 Hz, 2H), 4.05 (t, *J* = 6.4 Hz, 2H), 2.51 – 2.31 (m, 6H), 2.04 – 1.89 (m, 2H), 1.64 – 1.53 (m, 4H), 1.51 – 1.36 (m, 2H).

3-Methyl-6-(4-(3-(piperidin-1-yl)propoxy)phenyl)-1,2,4,5-tetrazine **(P15)**

The tetrazine formation was carried out as described for compound **P14a**.[698] Compound **23** (200 mg, 0.82 mmol, 1.0 eq.), zinc triflate (149 mg, 0.41 mmol, 0.5 eq.) and a hydrazine solution (1 mol/L in water, 8.2 mmol, 10 eq.) were subjected to the reaction conditions for 48 hours. The crude product was purified by flash chromatography using a gradient elution of dichloromethane/methanol (0-20%).

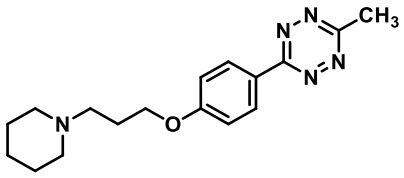

Yield:	44 mg, (17%)
Chemical formula:	$C_{17}H_{23}N_5O$
Molecular mass:	313.401 g/mol
Appearance:	Pink solid
Internal code:	MST-633C
Synthesis scheme:	Figure 81
Melting point:	142.2 °C
LC-MS-DAD purity:	96.1%
HR-MS (ESI-(+)):	m/z=314.1990 $[M+H^+]^+$ calculated: 314.1975
^{1}H NMR (300 MHz, MeOD):	δ 8.54 (d, *J* = 9.0 Hz, 2H), 7.22 (d, *J* = 9.0 Hz, 2H), 4.29 (t, *J* = 5.8 Hz, 2H), 3.51 – 3.29 (m, 6H), 3.05 (s, 3H), 2.46 – 2.25 (m, 2H), 2.06 – 1.62 (m, 6H).
^{13}C NMR (75.5 MHz, MeOD):	δ 168.22, 165.02, 163.53, 130.68, 126.26, 116.28, 66.29, 55.86, 54.59, 25.23, 24.41, 22.69, 20.97.

3-Methyl-6-(4-(3-(piperidin-1-yl)propoxy)phenyl)-1,4-dihydro-1,2,4,5-tetrazine **(BP15)**

The title compound was obtained as a byproduct during the reaction procedure described for Compound **P15**, and isolated during the purification process.

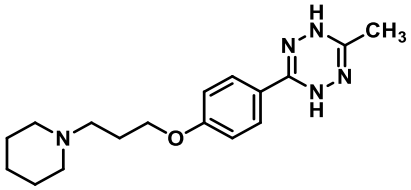

Yield:	49 mg, (19%)
Chemical formula:	$C_{17}H_{25}N_5O$
Molecular mass:	315.42 g/mol
Appearance:	Colourless solid
Internal code:	MST-603A
Synthesis scheme:	Figure 81
Melting point:	156.4 °C

LC-MS-DAD purity:	100%
HR-MS (ESI-(+)):	m/z=316.2193 $[M+H^+]^+$ calculated: 316.2132
^{1}H NMR (300 MHz, DMSO-d_6):	δ 7.97 (d, *J* = 9.0 Hz, 2H), 7.04 (d, *J* = 9.0 Hz, 2H), 6.06 (s, 2H), 4.10 (t, *J* = 6.2 Hz, 2H), 3.12 – 2.81 (m, 6H), 2.36 (s, 3H), 2.24 – 2.11 (m, 2H), 1.85 – 1.65 (m, 4H), 1.59 – 1.41 (m, 2H).
^{13}C NMR (75.5 MHz, DMSO-d_6)	δ 158.98, 152.91, 151.97, 129.18, 120.24, 114.24, 65.36, 53.62, 52.29, 23.68, 22.79, 21.89, 9.94.

2-((5*R*,6*S*,8*S*)-4-Methyl-1(4)-(4-(4(3)-(piperidin-1-yl)propoxy)phenyl)-5,6,7,8-tetrahydro-5,8-methanophthalazin-6-yl)ethan-1-amine **(25a/b)**

The synthesis was based on a procedure previously described.[707] Compound **P15** (25 mg, 0.08 mmol, 1.2 eq.) and 2-((1*R*,2*S*,4*S*)-bicyclo[2.2.1]hept-5-en-2-yl)ethan-1-amine (11 mg, 0.06 mmol, 1.0 eq.) were dissolved in PBS buffer solution. The mixture was heated to 37 °C and stirred for 24 hours. The solvent was then removed under reduced pressure, and the residue was dissolved in ethyl acetate. The organic phase was washed three times with 2M sodium hydroxide solution. The combined organic phases were dried over magnesium sulphate, filtered, and co

Yield:	11 mg, (45%)*
Chemical formula:	$C_{26}H_{36}N_4O$
Molecular mass:	420.60 g/mol
Appearance:	Colourless oil
Internal code:	MST-856
Synthesis scheme:	Figure 83

*LC-MS calculated yield

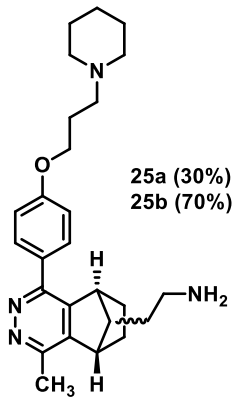

3-(5,5-Difluoro-7,9-dimethyl-5*H*-5λ^4,6λ^4-dipyrrolo[1,2-*c*:2',1'-*f*][1,3,2]diazaborinin-3-yl)-*N*-(2-((5*R*,6*S*,8*S*)-1(4)-methyl-4(1)-(4-(3-(piperidin-1-yl)propoxy)phenyl)-5,6,7,8-tetrahydro-5,8-methanophthalazin-6-yl)ethyl)propanamide **(P16a/b)**

The HATU coupling was carried out as described for compound **P3**.[644] The crude isomer mixture of **25a/b** (11 mg, 0.03 mmol, 1.0 eq.)**,** BODIPY-FL (18 mg, 0.06 mmol, 2.0 eq.), DIPEA (10 µL, 0.06 mmol, 2.0 eq.) and HATU (23 mg, 0.06 mmol, 2.0 eq.) were subjected to the reaction conditions for 20 hours. The crude product was purified by flash chromatography using a gradient elution of dichloromethane/methanol (0-20%), followed by a reverse phase flash chromatography using a gradient elution of water/acetonitrile (0-100%).

Yield:	8 mg, (36%)
Chemical formula:	$C_{40}H_{49}BF_2N_6O_2$
Molecular mass:	694.68 g/mol
Appearance:	Red solid
Internal code:	MST-859, ST-3029
Synthesis scheme:	Figure 85
Melting point:	99.6 °C
LC-MS-DAD purity:	96.4%

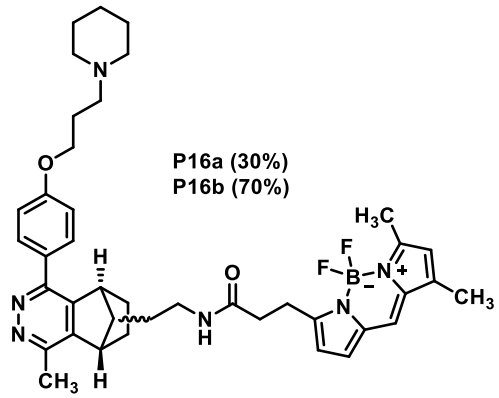

HR-MS (ESI-(+)):	m/z=695.4048 $[M+H^+]^+$ calculated: 695.4051
Quantum yield (475 nm):	0.95
Stoke shift:	7 cm^{-1}
^1H NMR (600 MHz, $CDCl_3$):	δ 7.71 (d, *J* = 9.3 Hz, 2H), 7.07 (s, 1H), 7.00 (d, *J* = 9.3 Hz, 2H), 6.76 (d, *J* = 4.1 Hz, 1H), 6.21 (d, *J* = 4.1 Hz, 1H), 6.12 (s, 1H), 5.47 (t, *J* = 5.2 Hz, 1H), 4.11 – 4.01 (m, 2H), 3.75 – 3.50 (m, 1H), 3.44 – 3.29 (m, 1H), 3.29 – 3.09 (m, 3H), 2.95 – 2.85 (m, 1H), 2.67 (s, 3H), 2.63 – 2.49 (m, 9H), 2.25 (s, 3H), 2.22 – 2.17 (m, 2H), 2.08 – 1.70 (m, 4H), 1.70 – 1.55 (m, 6H), 1.52 – 1.40 (m, 2H), 1.36 – 1.16 (m, 2H), 0.93 – 0.77 (m, 1H), 0.74 – 0.50 (m, 2H).
^{13}C NMR (151 MHz, $CDCl_3$):	δ 171.62, 171.47, 160.38, 159.78, 159.73, 156.98, 156.86, 155.16, 153.24, 152.57, 151.68, 146.62, 144.58, 144.20, 143.74, 141.24, 135.20, 135.17, 133.31, 133.27, 129.97, 129.81, 129.60, 129.27, 128.21, 128.20, 128.12, 123.95, 123.72, 120.53, 117.52, 117.51, 117.46, 117.43, 114.70, 114.65, 76.82, 66.59, 66.55, 55.89, 55.87, 54.54, 54.52, 50.26, 49.33, 45.56, 45.42, 42.49, 41.18, 38.18, 38.16, 37.91, 36.40, 36.24, 35.97, 35.89, 35.87, 34.00, 33.96, 32.45, 32.15, 29.71, 26.63, 26.61, 25.76, 24.96, 24.31, 19.42, 19.37, 14.99, 11.39, 11.34.

10.4 Fluorescent H_3R ligands

2-(3-Oxo-6-(3-(piperidin-1-yl)propoxy)-3*H*-xanthen-9-yl)benzoic acid acetate **(P17)**

The synthesis was based on a procedure previously described.[720] 2-(6-Hydroxy-3-oxo-3*H*-xanthen-9-yl)benzoic acid (326 mg, 0.91 mmol, 1.0 eq.), potassium carbonate (251 mg, 1.82 mmol, 2.0 eq.) and 1-(3-chloropropyl)piperidine hydrochloride (178 mg, 0.91 mmol, 1.0 eq.) were suspended in DMF. The reaction mixture was heated in a microwave at 80 °C for

30 minutes. After completion, the solvent was removed under reduced pressure, and the crude product was purified by reverse phase flash chromatography using a gradient elution of water (0.5% acetic acid)/acetonitrile (0-100%).

Yield:	329 mg, (70%)
Chemical formula:	$C_{28}H_{27}NO_5$ x $C_2H_4O_2$
Molecular mass:	517.58 g/mol
Appearance:	Yellow solid
Internal code:	MST-616
Synthesis scheme:	Figure 88
Melting point:	205.0 °C
LC-MS-DAD purity:	100%
HR-MS (ESI-(+)):	m/z=458.2021 $[M+H^+]^+$ calculated: 458.1962
^{1}H NMR (300 MHz, DMSO-d_6):	δ 8.15 – 8.06 (m, 1H), 7.87 – 7.65 (m, 2H), 7.46 – 7.37 (m, 1H), 6.61 (d, *J* = 9.1 Hz, 2H), 6.41 – 6.23 (m, 4H), 3.91 (t, *J* = 6.3 Hz, 2H), 2.15 – 2.05 (m, 4H), 1.92 (t, *J* = 7.0 Hz, 2H), 1.84 (s, 3H), 1.45 – 1.25 (m, 8H).
^{13}C NMR (75.5 MHz, DMSO-d_6):	δ 189.90, 177.98, 172.98, 165.59, 159.35, 159.23, 156.92, 150.68, 134.16, 132.54, 130.57, 130.40, 130.34, 129.42, 129.39, 129.30, 129.24, 122.86, 122.77, 110.77, 103.10, 63.50, 54.45, 53.69, 25.45, 25.04, 24.01, 22.15

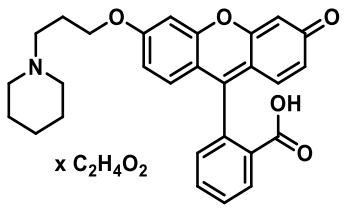

4-(3-Oxo-6-(3-(piperidin-1-yl)propoxy)-3*H*-xanthen-9-yl)isophthalic acid **(P18)**

The alkylation protocol was carried out as described for compound **P17.**[720] 4-(6-Hydroxy-3-oxo-3H-xanthen-9-yl)isophthalic acid (30 mg, 0.08 mmol, 1.0 eq.), potassium carbonate (22 mg, 0.16 mmol, 2.0 eq.) and 1 (3 chloropropyl)piperidine hydrochloride (16 mg, 0.08 mmol, 1.0 eq.) were subjected to the reaction conditions for 30 minutes. The crude product was purified by flash chromatography using a gradient elution of dichloromethane/methanol (0-20%).

Yield:	18 mg, (45%)
Chemical formula:	$C_{29}H_{27}NO_7$
Molecular mass:	501.54 g/mol
Appearance:	Yellow solid
Internal code:	MST-594
Synthesis scheme:	Figure 89

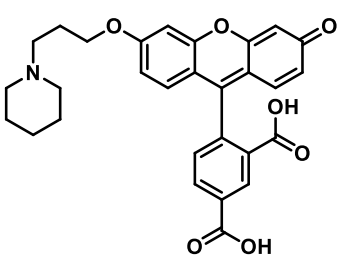

Melting point:	290.1 °C
LC-MS-DAD purity:	97.5%
HR-MS (ESI-(+)):	m/z=502.1881 $[M+H^+]^+$ calculated: 502.1860
^{1}H NMR (300 MHz, MeOD):	δ 8.84 – 8.76 (m, 1H), 8.37 – 8.21 (m, 1H), 7.43 (d, *J* = 7.9 Hz, 1H), 7.00 – 6.89 (m, 2H), 6.63 – 6.54 (m, 4H), 4.07 (t, *J* = 6.0 Hz, 2H), 2.96 – 2.77 (m, 4H), 2.72 – 2.61 (m, 2H), 1.86 – 1.58 (m, 8H).
^{13}C NMR (75.5 MHz, MeOD):	δ 180.63, 180.51, 172.80, 166.95, 166.83, 165.83, 159.68, 157.02, 140.98, 137.20, 135.02, 134.32, 134.29, 132.86, 131.77, 131.53, 131.30, 123.95, 114.13, 113.99, 104.63, 55.55, 54.59, 24.97, 24.93, 24.76, 23.19.

1-(3-(4-(3-Chloropropyl)phenoxy)propyl)piperidine hydrochloride **(28)**

The chlorination protocol was carried out as described for compound **8a**.[621] Compound **21** (1380 mg, 5.53 mmol, 1.0 eq.) and thionyl chloride (1009 µL, 13.8 mmol, 2.5 eq.) were subjected to the reaction conditions for two hours. The crude product was used without further purification.

Yield:	1683 mg, (100%)
Chemical formula:	$C_{15}H_{23}ClNO$ x HCl
Molecular mass:	304.25 g/mol
Appearance:	Beige solid
Internal code:	MST-158
Synthesis scheme:	Figure 91
^{1}H NMR (300 MHz, $CDCl_3$):	δ 12.15 (s, 1H), 7.30 (d, *J* = 8.6 Hz, 2H), 6.83 (d, *J* = 8.6 Hz, 2H), 4.55 (s, 2H), 4.07 (t, *J* = 5.5 Hz, 2H), 3.65 – 3.50 (m, 2H), 3.22 – 3.05 (m, 2H), 2.77 – 2.56 (m, 2H), 2.54 – 2.39 (m, 2H), 2.39 – 2.18 (m, 2H), 2.00 – 1.26 (m, 4H).

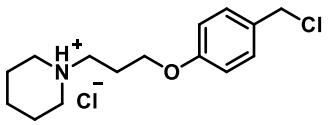

tert-Butyl 4-(4-(3-(piperidin-1-yl)propoxy)benzyl)piperazine-1-carboxylate **(29)**

The alkylation protocol was carried out as described for compound **2a**.[598] 1-Boc-piperazine (334 mg, 1.83 mmol, 1.1 eq.), compound **28** (503 mg, 1.66 mmol, 1.0 eq.), potassium iodide (551 mg, 3.32 mmol, 2.0 eq.) and potassium carbonate (903 mg, 6.64 mmol, 4.0 eq.) were subjected to the reaction conditions for 48 hours. The crude product was used without further purification.

Yield:	548 mg, (79%)
Chemical formula:	$C_{24}H_{39}N_3O_3$
Molecular mass:	417.59 g/mol
Appearance:	Colourless solid
Internal code:	MST-729
Synthesis scheme:	Figure 92
^{1}H NMR (300 MHz, $CDCl_3$):	δ 7.19 (d, *J* = 9.0 Hz, 2H), 6.84 (d, *J* = 9.0 Hz, 2H), 3.98 (t, *J* = 6.4 Hz, 2H), 3.47 – 3.33 (m, 6H), 2.48 – 2.28 (m, 10H), 2.01 – 1.89 (m, 2H), 1.68 – 1.50 (m, 4H), 1.49 – 1.41 (m, 11H)

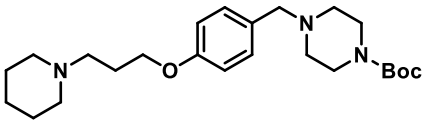

1-(4-(3-(Piperidin-1-yl)propoxy)benzyl)piperazine **(30)**

The Boc-deprotection protocol was carried out as described for compound **P6**.[674] Compound **29** (500 mg, 1.20 mmol, 1.0 eq.) was subjected to the reaction conditions for 20 hours. The crude product was purified by column chromatography using a gradient elution of dichloromethane/methanol (sat. NH_3) (0-20%).

Yield:	380 mg, (100%)
Chemical formula:	$C_{19}H_{31}N_3O$
Molecular mass:	317.48 g/mol
Appearance:	Colourless solid
Internal code:	MST-730
Synthesis scheme:	Figure 93
^{1}H NMR (300 MHz, $CDCl_3$):	δ 7.19 (d, *J* = 8.4 Hz, 2H), 6.83 (d, *J* = 8.4 Hz, 2H), 3.98 (t, *J* = 6.4 Hz, 2H), 3.41 (s, 2H), 2.92 – 2.82 (m, 4H), 2.52 – 2.31 (m, 10H), 2.03 – 1.88 (m, 2H), 1.80 – 1.49 (m, 4H), 1.50 – 1.36 (m, 2H).

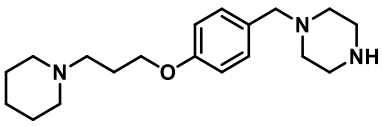

2-(6-Hydroxy-3-oxo-3*H*-xanthen-9-yl)-5-(4-(4-(3-(piperidin-1-yl)propoxy)benzyl)piperazine-1-carbonyl)benzoic acid **(P19)**

The HATU coupling was carried out as described for compound **P3**.[644] Compound **30** (95 mg, 0.30 mmol, 1.1 eq.), DIPEA (53 µL, 0.30 mmol, 1.1 eq.), 4-(6-hydroxy-3-oxo-3*H*-xanthen-9-yl)isophthalic acid (102 mg, 0.27 mmol, 1.0 eq.) and HATU (114 mg, 0.30 mmol, 1.1 eq.) were subjected to the reaction conditions for 20 hours. The crude product was purified by reverse phase flash chromatography using a gradient elution of water/methanol (0-100%).

Yield:	46 mg, (25%)
Chemical formula:	$C_{40}H_{41}N_3O_7$
Molecular mass:	675.78 g/mol
Appearance:	Yellow solid
Internal code:	MST-733, ST-2944
Synthesis scheme:	Figure 94
Melting point:	>350 °C
LC-MS-DAD purity:	100%
HR-MS (ESI-(+)):	m/z=676.2999 $[M+H^+]^+$ calculated: 676.3017
Quantum yield (475 nm):	0.76
Stoke shift:	27 cm^{-1}
^1H NMR (600 MHz, DMSO-d_6):	δ 11.65 – 11.31 (m, 1H), 10.45 (s, 1H), 9.98 (s, 1H), 7.84 – 5.92 (m, 12H), 4.00 – 3.58 (m, 4H), 2.85 – 2.75 (m, 2H), 2.15 (s, 2H), 2.01 – 1.24 (m, 5H), 1.12 – 0.66 (m, 8H), 0.58 – 0.33 (m, 5H).
^{13}C NMR (151 MHz, DMSO-d_6):	δ 168.55, 168.55, 168.25, 167.45, 160.24, 160.21, 153.63, 152.53, 152.36, 134.70, 134.67, 132.20, 132.17, 132.17, 132.07, 129.63, 129.13, 127.02, 125.01, 123.61, 115.13, 115.08, 113.13, 109.57, 102.78, 68.27, 52.41, 36.85, 33.45, 32.02, 31.08, 26.23, 23.66, 22.74, 22.50, 19.78, 14.66, 14.34.

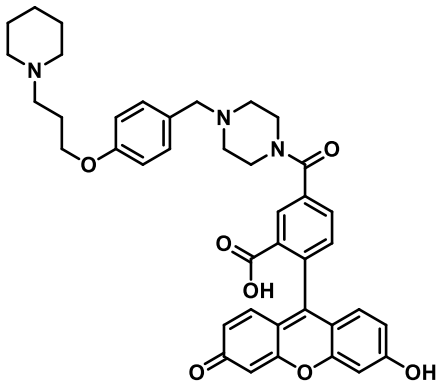

3-(5,5-Difluoro-7,9-dimethyl-5*H*-5λ⁴,6λ⁴-dipyrrolo[1,2-*c*:2',1'-*f*][1,3,2]diazaborinin-3-yl)-1-(4-(4-(3-(piperidin-1-yl)propoxy)benzyl)piperazin-1-yl)propan-1-one **(P20)**

The HATU coupling was carried out as described for compound **P3**.[644] Compound **30** (60 mg, 0.19 mmol, 1.1 eq.), DIPEA (45 µL, 0.19 mmol, 1.1 eq.), BODIPY FL (50 mg, 0.17 mmol, 1.0 eq.) and HATU (72 mg, 0.19 mmol, 1.1 eq.) were subjected to the reaction conditions for 20 hours. The crude product was purified by column chromatography using a gradient elution of dichloromethane/methanol (sat. NH3) (0-20%).

Yield:	45 mg, (45%)
Chemical formula:	$C_{33}H_{44}BF_2N_5O_2$
Molecular mass:	591.55 g/mol
Appearance:	Red solid
Internal code:	MST-734, ST-2940
Synthesis scheme:	Figure 95
Melting point:	312.1 °C
LC-MS-DAD purity:	98.9%
HR-MS (ESI-(+)):	m/z=592.3629 $[M+H^+]^+$ calculated: 592.3629
Quantum yield (475 nm):	0.60
Stoke shift:	8 cm^{-1}
^1H NMR (600 MHz, DMSO-d_6):	δ 7.70 (s, 1H), 7.48 (d, *J* = 7.5 Hz, 2H), 7.09 (d, *J* = 4.0 Hz, 1H), 6.96 (d, *J* = 7.5 Hz, 2H), 6.41 (d, *J* = 4.0 Hz, 1H), 6.30 (s, 1H), 4.06 (t, *J* = 6.1 Hz, 2H), 3.59 – 3.25 (m, 8H), 3.16 – 3.10 (m, 2H), 3.09 – 3.04 (m, 2H), 2.94 – 2.66 (m, 6H), 2.46 (s, 3H), 2.26 (s, 3H), 2.24 – 2.08 (m, 2H), 1.94 – 1.20 (m, 8H).
^{13}C NMR (151 MHz, DMSO-d_6):	δ 170.01, 159.59, 158.23, 147.91, 144.56, 134.90, 133.49, 129.36, 128.39, 127.87, 125.82, 120.74, 117.55, 114.92, 65.60, 53.81, 52.43, 40.53, 31.46, 24.16, 23.71, 22.78, 21.89, 14.98, 11.48.

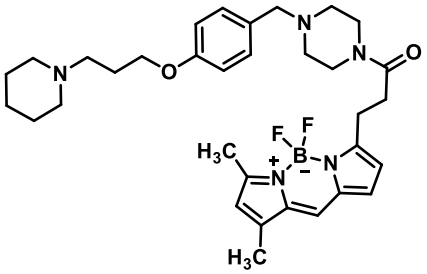

10.5 Fluorescent H_4R ligands

10.5.1 Fluorophore and linkers

Ethyl (*Z*)-3-(1*H*-pyrrol-2-yl)acrylate **(33)**

The synthesis was based on a previously described procedure.[732] 1*H*-Pyrrole-2-carbaldehyde (2000 mg, 21.1 mmol, 1.0 eq.) and potassium carbonate (4368 mg, 31.7 mmol, 1.5 eq.) were dissolved in a dioxane/water mixture (50:50). Then (ethoxycarbonyl-methyl)triphenylphosphonium bromide (9052 mg, 21.1 mmol, 1.0 eq.) was added to the reaction mixture and heated to 70 °C for 48 hours. The solvent was removed under reduced pressure and the residue was taken up in ethyl acetate and washed three times with 2N sodium hydroxide solution and three times with brine. The organic phase was dried over magnesium sulphate, filtered, and the solvent was removed under reduced pressure. The crude product was used without further purification.

Yield:	3150 mg, (91%)
Chemical formula:	$C_9H_{11}NO_2$
Molecular mass:	165.19 g/mol
Appearance:	Colourless oil
Internal code:	MST-545
Synthesis scheme:	Figure 100
^{1}H NMR (300 MHz, $CDCl_3$):	δ 9.40 (s, 1H), 7.62 (d, *J* = 15.9 Hz, 1H), 6.97 – 6.90 (m, 1H), 6.67 – 6.51 (m, 1H), 6.33 – 6.25 (m, 1H), 6.12 (d, *J* = 15.9 Hz, 1H), 4.27 (q, *J* = 7.1 Hz, 2H), 1.34 (t, *J* = 7.1 Hz, 3H).

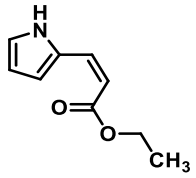

Ethyl 3-(1*H*-pyrrol-2-yl)propanoate **(34)**

The synthesis was based on a previously described procedure.[734] Compound **33** (3125 mg, 18.9 mmol, 1.0 eq.) was dissolved in methanol, and a catalytic amount of 10% palladium on charcoal was added. The reaction mixture was exposed to a hydrogen atmosphere and stirred at room temperature for 20 hours. The suspension was filtered through a Celite pad, and the solvent was removed under reduced pressure. The residue was purified by flash chromatography using a gradient elution of hexane/ethyl acetate (0-100%).

Yield:	2370 mg, (75%)
Chemical formula:	$C_9H_{13}NO_2$
Molecular mass:	167.21 g/mol
Appearance:	Colourless oil
Internal code:	MST-548
Synthesis scheme:	Figure 101
^{1}H NMR (300 MHz, $CDCl_3$):	δ 8.57 (s, 1H), 6.72 – 6.62 (m, 1H), 6.17 – 6.05 (m, 1H), 5.98 – 5.89 (m, 1H), 4.16 (q, *J* = 7.1 Hz, 2H), 2.92 (t, *J* = 6.3 Hz, 2H), 2.64 (t, *J* = 6.3 Hz, 2H), 1.27 (t, *J* = 7.1 Hz, 3H).

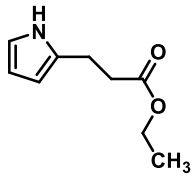

Ethyl 3-(5,5-difluoro-7,9-dimethyl-5*H*-5λ^4,6λ^4-dipyrrolo[1,2-*c*:2',1'-*f*][1,3,2]diazaborinin-3-yl)propanoate **(35)**

The synthesis was based on a previously described procedure.[734] Compound **34** (1165 mg, 6.98 mmol, 1.0 eq.) and 3,5-dimethyl-1*H*-pyrrole-2-carbaldehyde (953 mg, 7.75 mmol, 1.1 eq.) were dissolved in DCM and the solution was cooled to 0 °C. Then phosphorus oxychloride (719 µL, 7.75 mmol, 1.1 eq.) was added at this temperature and after stirring for 30 minutes, the mixture was stirred for six hours at room temperature. The reaction mixture was cooled back to 0 °C and boron trifluoride etherate (3452 µL, 27.9 mmol, 4.0 eq.) was added, followed by DIPEA (4013 µL, 27.9 mmol, 4.0 eq.). The mixture was stirred overnight at room temperature.

The suspension was filtered through Celite and then extracted three times with water. The organic phase was dried over magnesium sulphate, filtered, and the solvent was removed under reduced pressure. The crude product was purified by flash chromatography using a gradient elution of hexane/ethyl acetate (0-100%).

Yield:	1445 mg, (65%)
Chemical formula:	$C_{16}H_{19}BF_2N_2O_2$
Molecular mass:	320.15 g/mol
Appearance:	Red Solid
Internal code:	MST-553
Synthesis scheme:	Figure 102
^{1}H NMR (300 MHz, $CDCl_3$):	δ 7.08 (s, 1H), 6.88 (d, *J* = 4.1 Hz, 1H), 6.27 (d, *J* = 4.1 Hz, 1H), 6.11 (s, 1H), 4.15 (q, *J* = 7.1 Hz, 2H), 3.29 (t, *J* = 6.9 Hz, 2H), 2.75 (t, *J* = 6.9 Hz, 2H), 2.56 (s, 3H), 2.25 (s, 3H), 1.25 (t, *J* = 7.1 Hz, 3H).

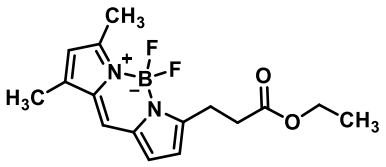

3-(5,5-Difluoro-7,9-dimethyl-5*H*-5λ^4,6λ^4-dipyrrolo[1,2-*c*:2',1'-*f*][1,3,2]diazaborinin-3-yl)propanoic acid **(36)**

The synthesis was based on a previously described procedure.[735] Compound **35** (1302 mg, 4.07 mmol, 1.0 eq.) was dissolved in a mixture of THF/water (70:30), and concentrated hydrochloric acid (approx. 1 mL) was added. The reaction mixture was stirred at room temperature for 24 hours, then diluted with dichloromethane and washed three times with water. The organic phase was dried over magnesium sulphate, filtered, and the solvent was removed under reduced pressure. The crude product was purified by flash chromatography using a gradient elution of hexane/ethyl acetate (0-100%).

Yield:	998 mg, (84%)
Chemical formula:	$C_{14}H_{15}BF_2N_2O_2$
Molecular mass:	292.09 g/mol
Appearance:	Red Solid
Internal code:	MST-568
Synthesis scheme:	Figure 103
^{1}H NMR (300 MHz, $CDCl_3$):	δ 7.09 (s, 1H), 6.89 (d, *J* = 4.1 Hz, 1H), 6.29 (d, *J* = 4.1 Hz, 1H), 6.12 (s, 1H), 3.30 (t, *J* = 7.5 Hz, 2H), 2.83 (t, *J* = 7.5 Hz, 2H), 2.57 (s, 3H), 2.25 (s, 3H).

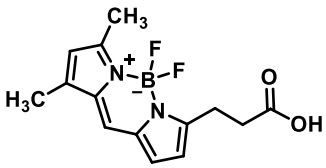

4-((*tert*-Butoxycarbonyl)amino)butanoic acid **(L3)**

The synthesis was based on a previously described procedure.[737] GABA (612 mg, 5.93 mmol, 1.0 eq.) and sodium hydrogen carbonate (996 mg, 11.9 mmol, 2.0 eq.) were dissolved in water. Under ice cooling, a solution of Boc anhydride (721 mg, 7.12 mmol, 1.2 eq.) in dioxane was added dropwise. The mixture was stirred at room temperature for four hours, then acidified through addition of 2N HCl solution and extracted with ethyl acetate. The organic phase was dried over magnesium sulphate, filtered, and the solvent was removed under reduced pressure. The crude product was used without further purification.

Yield:	1205 mg, (100%)
Chemical formula:	$C_9H_{17}NO_4$
Molecular mass:	203.24 g/mol
Appearance:	Colourless oil
Internal code:	MST-349
Synthesis scheme:	Figure 104
^{1}H NMR (300 MHz, $CDCl_3$):	δ 3.18 – 3.05 (m, 2H), 2.32 (t, *J* = 7.2 Hz, 2H), 1.84 – 1.67 (m, 2H), 1.37 (s, 9H).

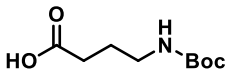

5-((*tert*-Butoxycarbonyl)amino)pentanoic acid **(L4)**

The Boc protection was carried out as described for compound **L3.**[737] 5-Aminovaleric acid (197 mg, 1.68 mmol, 1.0 eq.), sodium hydrogen carbonate (283 mg, 3.36 mmol, 2.0 eq.) and Boc anhydride (551 mg, 2.52 mmol, 1.5 eq.) were subjected to the reaction conditions for five hours. The crude product was used without further purification.

Yield:	365 mg, (100%)
Chemical formula:	$C_{10}H_{19}NO_4$
Molecular mass:	217.27 g/mol
Appearance:	Colourless oil
Internal code:	MST-226
Synthesis scheme:	Figure 104
^{1}H NMR (300 MHz, $CDCl_3$):	δ 3.14 – 2.97 (m, 2H), 2.30 (t, *J* = 7.3 Hz, 2H), 1.66 – 1.51 (m, 2H), 1.50 – 1.42 (m, 11H).

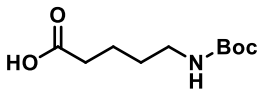

6-((*tert*-Butoxycarbonyl)amino)hexanoic acid **(L5)**

The Boc protection was carried out as described for compound **L3.**[737] 6-Aminohexanoic acid (267 mg, 2.04 mmol, 1.0 eq.), sodium hydrogen carbonate (342 mg, 4.08 mmol, 2.0 eq.) and

Boc anhydride (612 mg, 3.06 mmol, 1.5 eq.) were subjected to the reaction conditions for five hours. The crude product was used without further purification.

Yield:	472 mg, (100%)
Chemical formula:	$C_{11}H_{21}NO_4$
Molecular mass:	231.29 g/mol
Appearance:	Colourless oil
Internal code:	MST-238
Synthesis scheme:	Figure 104
^{1}H NMR (300 MHz, $CDCl_3$):	δ 3.15 – 3.01 (m, 2H), 2.33 (t, *J* = 7.4 Hz, 2H), 1.73 – 1.57 (m, 2H), 1.55 – 1.28 (m, 13H).

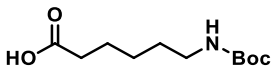

tert-Butyl (2-aminoethyl)carbamate **(L9)**

The synthesis was based on a previously described procedure.[738] Ethane-1,2-diamine (888 µL, 16.5 mmol, 1.0 eq.) and triethylamine (2275 µL, 16.5 mmol, 1.0 eq.) were dissolved in dichloromethane. Under ice cooling, a solution of Boc anhydride (717 mg, 3.29 mmol, 0.2 eq.) in dichloromethane was added dropwise. The mixture was stirred at room temperature for four hours, and then the solvent was removed under reduced pressure. The crude product was purified by flash chromatography using a gradient elution of dichloromethane/methanol (0-20%).

Yield:	432 mg, (82%)
Chemical formula:	$C_7H_{16}N_2O_2$
Molecular mass:	160.22 g/mol
Appearance:	Colourless oil
Internal code:	MST-363
Synthesis scheme:	Figure 104
^{1}H NMR (300 MHz, $CDCl_3$):	δ 4.95 – 4.76 (m, 1H), 3.24 – 3.10 (m, 2H), 2.79 (t, *J* = 5.9 Hz, 2H), 1.44 (s, 9H), 1.30 – 1.21 (m, 2H).

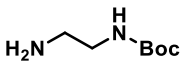

tert-Butyl (3-aminopropyl)carbamate **(L10)**

The Boc protection was carried out as described for compound **L9.**[738] Propane-1,3-diamine (1395 mg, 18.9 mmol, 1.0 eq.), triethylamine (2609 µL, 18.9 mmol, 1.0 eq.) and Boc anhydride (822 mg, 3.77 mmol, 0.2 eq.) were subjected to the reaction conditions for five hours. The crude product was purified by flash chromatography using a gradient elution of dichloromethane/methanol (0-20%).

Yield:	512 mg, (78%)
Chemical formula:	$C_8H_{18}N_2O_2$
Molecular mass:	174.24 g/mol
Appearance:	Colourless oil
Internal code:	MST-366
Synthesis scheme:	Figure 104
^{1}H NMR (300 MHz, $CDCl_3$):	δ 5.10 – 4.83 (m, 1H), 3.23 – 3.06 (m, 2H), 2.73 (t, *J* = 6.9 Hz, 2H), 1.90 – 1.62 (m, 2H), 1.65 – 1.50 (m, 2H), 1.41 (s, 9H).

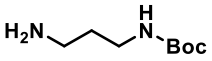

tert-Butyl (4-aminobutyl)carbamate **(L11)**

The Boc protection was carried out as described for compound **L9.**[738] Butane-1,4-diamine (1450 mg, 16.7 mmol, 1.0 eq.), triethylamine (2305 µL, 16.7 mmol, 1.0 eq.) and Boc anhydride (726 mg, 3.33 mmol, 0.2 eq.) were subjected to the reaction conditions for five hours. The crude product was purified by flash chromatography using a gradient elution of dichloromethane/methanol (0-20%).

Yield:	439 mg, (70%)
Chemical formula:	$C_9H_{20}N_2O_2$
Molecular mass:	188.27 g/mol
Appearance:	Colourless oil
Internal code:	MST-367
Synthesis scheme:	Figure 104
^{1}H NMR (300 MHz, $CDCl_3$):	δ 4.72 – 4.53 (m, 1H), 3.17 – 3.04 (m, 2H), 2.70 (t, *J* = 6.6 Hz, 2H), 1.58 – 1.38 (m, 13H), 1.35 – 1.22 (m, 2H).

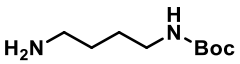

tert-Butyl (5-aminopentyl)carbamate **(L12)**

The Boc protection was carried out as described for compound **L9.**[738] Pentane-1,5-diamine (1391 mg, 13.6 mmol, 1.0 eq.), triethylamine (1881 µL, 13.6 mmol, 1.0 eq.) and Boc anhydride (594 mg, 2.70 mmol, 0.2 eq.) were subjected to the reaction conditions for five hours. The crude product was purified by flash chromatography using a gradient elution of dichloromethane/methanol (0-20%).

Yield:	464 mg, (85%)
Chemical formula:	$C_{10}H_{22}N_2O_2$
Molecular mass:	202.30 g/mol
Appearance:	Colourless oil

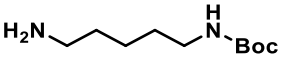

Internal code:	MST-368
Synthesis scheme:	Figure 104
^{1}H NMR (300 MHz, $CDCl_3$):	δ 4.62 – 4.49 (m, 1H), 3.17 – 3.02 (m, 2H), 2.67 (t, *J* = 6.8 Hz, 2H), 1.54 – 1.25 (m, 17H).

tert-Butyl (6-aminohexyl)carbamate **(L13)**

The Boc protection was carried out as described for compound **L9.**[738] Hexane-1,6-diamine (1208 mg, 10.4 mmol, 1.0 eq.), triethylamine (1438 µL, 10.4 mmol, 1.0 eq.) and Boc anhydride (454 mg, 2.08 mmol, 0.2 eq.) were subjected to the reaction conditions for five hours. The crude product was purified by flash chromatography using a gradient elution of dichloromethane/methanol (0-20%).

Yield:	364 mg, (81%)
Chemical formula:	$C_{11}H_{24}N_2O_2$
Molecular mass:	216.33 g/mol
Appearance:	Colourless oil
Internal code:	MST-369
Synthesis scheme:	Figure 104
^{1}H NMR (300 MHz, $CDCl_3$):	δ 4.55 – 4.40 (m, 1H), 3.09 – 2.98 (m, 2H), 2.61 (t, *J* = 6.8 Hz, 2H), 1.47 – 1.20 (m, 19H).

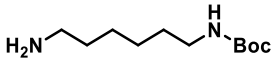

tert-Butyl (2-(2-aminoethoxy)ethyl)carbamate **(L14)**

The Boc protection was carried out as described for compound **L9.**[738] 2,2'-Oxybis(ethan-1-amine) (3754 mg, 16.3 mmol, 1.0 eq.), triethylamine (2255 µL, 16.3 mmol, 1.0 eq.) and Boc anhydride (652 mg, 3.26 mmol, 0.2 eq.) were subjected to the reaction conditions for five hours. The crude product was purified by flash chromatography using a gradient elution of dichloromethane/methanol (0-20%).

Yield:	572 mg, (86%)
Chemical formula:	$C_9H_{20}N_2O_3$
Molecular mass:	204.27 g/mol
Appearance:	Colourless oil
Internal code:	MST-242
Synthesis scheme:	Figure 104
^{1}H NMR (300 MHz, $CDCl_3$):	δ 5.17 – 4.92 (m, 1H), 3.59 – 3.41 (m, 4H), 3.32 – 3.22 (m, 2H), 2.87 – 2.73 (m, 2H), 1.62 – 1.53 (m, 2H), 1.42 (s, 9H).

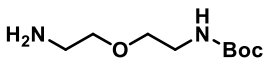

tert-Butyl (2-(2-(2-aminoethoxy)ethoxy)ethyl)carbamate **(L15)**

The Boc protection was carried out as described for compound **L9.**[738] 2,2'-(Ethane-1,2-diylbis(oxy))bis(ethan-1-amine) (1000 mg, 6.76 mmol, 1.0 eq.), triethylamine (940 µL, 6.76 mmol, 1.0 eq.) and Boc anhydride (441 mg, 2.02 mmol, 0.2 eq.) were subjected to the reaction conditions for five hours. The crude product was purified by flash chromatography using a gradient elution of dichloromethane/methanol (0-20%).

Yield:	416 mg, (83%)
Chemical formula:	$C_{11}H_{24}N_2O_4$
Molecular mass:	248.32 g/mol
Appearance:	Colourless oil
Internal code:	MST-374
Synthesis scheme:	Figure 104
^{1}H NMR (300 MHz, $CDCl_3$):	δ 5.10 – 4.96 (m, 1H), 3.65 – 3.58 (m, 4H), 3.56 – 3.49 (m, 4H), 3.35 – 3.26 (m, 4H), 1.50 – 1.40 (m, 11H).

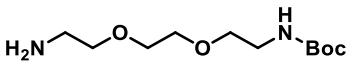

tert-Butyl (2-(2-(2-(2-aminoethoxy)ethoxy)ethoxy)ethyl)carbamate **(L16)**

The Boc protection was carried out as described for compound **L9.**[738] 2, 2,2'-((Oxybis(ethane-2,1-diyl))bis(oxy))bis(ethan-1-amine) (1000 mg, 5.21 mmol, 1.0 eq.), triethylamine (719 µL, 5.21 mmol, 1.0 eq.) and Boc anhydride (340 mg, 1.56 mmol, 0.3 eq.) were subjected to the reaction conditions for five hours. The crude product was purified by flash chromatography using a gradient elution of dichloromethane/methanol (0-20%).

Yield:	291 mg, (64%)
Chemical formula:	$C_{13}H_{28}N_2O_5$
Molecular mass:	292.38 g/mol
Appearance:	Colourless oil
Internal code:	MST-375
Synthesis scheme:	Figure 104
^{1}H NMR (300 MHz, $CDCl_3$):	δ 5.43 – 4.90 (m, 1H), 3.67 – 3.57 (m, 8H), 3.57 – 3.45 (m, 4H), 3.34 – 3.25 (m, 2H), 2.86 (t, *J* = 5.2 Hz, 2H), 1.92 – 1.78 (m, 2H), 1.43 (s, 9H).

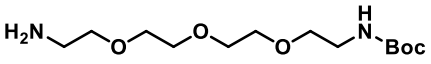

tert-Butyl (2-hydroxyethyl)carbamate **(L17)**

The Boc protection was carried out as described for compound **L9.**[738] 2-Aminoethan-1-ol (550 mg, 9.02 mmol, 1.0 eq.), triethylamine (1248 µL, 9.02 mmol, 1.0 eq.) and Boc anhydride (590 mg, 2.71 mmol, 0.3 eq.) were subjected to the reaction conditions for five hours. The

crude product was purified by flash chromatography using a gradient elution of dichloromethane/methanol (0-20%).

Yield:	436 mg, (100%)
Chemical formula:	$C_7H_{15}NO_3$
Molecular mass:	161.20 g/mol
Appearance:	Colourless oil
Internal code:	MST-298
Synthesis scheme:	Figure 104
^{1}H NMR (300 MHz, $CDCl_3$):	δ 5.31 – 4.74 (m, 1H), 3.73 – 3.64 (m, 2H), 3.28 (t, *J* = 5.1 Hz, 2H), 2.93 – 2.56 (m, 1H), 1.45 (s, 9H).

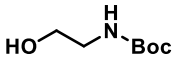

tert-Butyl (3-hydroxypropyl)carbamate **(L18)**

The Boc protection was carried out as described for compound **L9.**[738] 3-Aminopropan-1-ol (505 mg, 6.73 mmol, 1.0 eq.), triethylamine (931 µL, 6.73 mmol, 1.0 eq.) and Boc anhydride (440 mg, 2.02 mmol, 0.3 eq.) were subjected to the reaction conditions for five hours. The crude product was purified by flash chromatography using a gradient elution of dichloromethane/methanol (0-20%).

Yield:	354 mg, (100%)
Chemical formula:	$C_8H_{17}NO_3$
Molecular mass:	175.23 g/mol
Appearance:	Colourless oil
Internal code:	MST-247
Synthesis scheme:	Figure 104
^{1}H NMR (300 MHz, $CDCl_3$):	δ 5.29 – 4.81 (m, 1H), 3.60 (t, *J* = 5.8 Hz, 2H), 3.49 – 3.28 (m, 1H), 3.21 (t, *J* = 6.3 Hz, 2H), 1.67 – 1.56 (m, 2H), 1.39 (s, 9H).

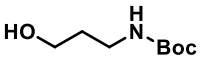

tert-Butyl (4-hydroxybutyl)carbamate **(L19)**

The Boc protection was carried out as described for compound **L9.**[738] 4-Aminobutan-1-ol (564 mg, 6.33 mmol, 1.0 eq.), triethylamine (876 µL, 6.33 mmol, 1.0 eq.) and Boc anhydride (414 mg, 1.90 mmol, 0.3 eq.) were subjected to the reaction conditions for five hours. The crude product was purified by flash chromatography using a gradient elution of dichloromethane/methanol (0-20%).

Yield:	352 mg, (98%)
Chemical formula:	$C_9H_{19}NO_3$
Molecular mass:	189.26 g/mol
Appearance:	Colourless oil
Internal code:	MST-253
Synthesis scheme:	Figure 104
^{1}H NMR (300 MHz, $CDCl_3$):	δ 4.79 – 4.23 (m, 1H), 3.57 (t, *J* = 6.4 Hz, 2H), 3.05 (t, *J* = 6.9 Hz, 2H), 2.16 – 1.73 (m, 1H), 1.57 – 1.47 (m, 2H), 1.43 – 1.27 (m, 11H).

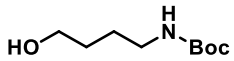

tert-Butyl (5-hydroxypentyl)carbamate **(L20)**

The Boc protection was carried out as described for compound **L9.**[738] 5-aminopentan-1-ol (575 mg, 5.58 mmol, 1.0 eq.), triethylamine (772 µL, 5.58 mmol, 1.0 eq.) and Boc anhydride (365 mg, 1.67 mmol, 0.3 eq.) were subjected to the reaction conditions for five hours. The crude product was purified by flash chromatography using a gradient elution of dichloromethane/methanol (0-20%).

Yield:	339 mg, (100%)
Chemical formula:	$C_{10}H_{21}NO_3$
Molecular mass:	203.28 g/mol
Appearance:	Colourless oil
Internal code:	MST-254
Synthesis scheme:	Figure 104
^{1}H NMR (300 MHz, $CDCl_3$):	δ 4.66 – 4.27 (m, 1H), 3.57 (t, *J* = 6.4 Hz, 2H), 3.05 (t, *J* = 6.9 Hz, 2H), 1.87 (s, 1H), 1.57 – 1.47 (m, 2H), 1.44 – 1.28 (m, 13H).

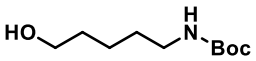

tert-Butyl (6-hydroxyhexyl)carbamate **(L21)**

The Boc protection was carried out as described for compound **L9.**[738] 6-Aminohexan-1-ol (1122 mg, 9.59 mmol, 1.0 eq.), triethylamine (1327 µL, 9.59 mmol, 1.0 eq.) and Boc anhydride (627 mg, 2.88 mmol, 0.3 eq.) were subjected to the reaction conditions for five hours. The crude product was purified by flash chromatography using a gradient elution of dichloromethane/methanol (0-20%).

Yield:	625 mg, (100%)
Chemical formula:	$C_{11}H_{23}NO_3$
Molecular mass:	217.31 g/mol

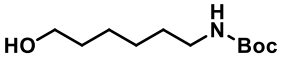

Appearance:	Colourless oil
Internal code:	MST-308
Synthesis scheme:	Figure 104
^{1}H NMR (300 MHz, $CDCl_3$):	δ 4.65 – 4.47 (m, 1H), 3.67 – 3.53 (m, 2H), 3.15 – 2.98 (m, 2H), 1.97 – 1.86 (m, 1H), 1.62 – 1.50 (m, 2H), 1.46 – 1.26 (m, 15H).

tert-Butyl (2-(2-hydroxyethoxy)ethyl)carbamate **(L22)**

The Boc protection was carried out as described for compound **L9.**[738] 2-(2-Aminoethoxy)ethan-1-ol (4507 mg, 42.9 mmol, 1.0 eq.), triethylamine (5935 µL, 42.9 mmol, 1.0 eq.) and Boc anhydride (2806 mg, 12.9 mmol, 0.3 eq.) were subjected to the reaction conditions for five hours. The crude product was purified by flash chromatography using a gradient elution of dichloromethane/methanol (0-20%).

Yield:	2644 mg, (100%)
Chemical formula:	$C_9H_{19}NO_4$
Molecular mass:	205.25 g/mol
Appearance:	Colourless oil
Internal code:	MST-227
Synthesis scheme:	Figure 104
^{1}H NMR (300 MHz, $CDCl_3$):	δ 5.13 – 5.07 (m, 1H), 3.78 – 3.69 (m, 2H), 3.62 – 3.50 (m, 4H), 3.33 (t, *J* = 5.1 Hz, 2H), 2.62 – 2.56 (m, 1H), 1.44 (s, 9H).

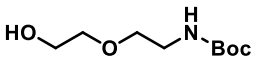

tert-Butyl (2-(2-(2-hydroxyethoxy)ethoxy)ethyl)carbamate **(L23)**

The Boc protection was carried out as described for compound **L9.**[738] 2-(2-(2-Aminoethoxy)ethoxy)ethan-1-ol (720 mg, 4.83 mmol, 1.0 eq.), triethylamine (668 µL, 4.83 mmol, 1.0 eq.) and Boc anhydride (316 mg, 1.45 mmol, 0.3 eq.) were subjected to the reaction conditions for five hours. The crude product was purified by flash chromatography using a gradient elution of dichloromethane/methanol (0-20%).

Yield:	303 mg, (84%)
Chemical formula:	$C_{11}H_{23}NO_5$
Molecular mass:	249.31 g/mol
Appearance:	Colourless oil
Internal code:	MST-257
Synthesis scheme:	Figure 104

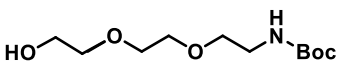

^{1}H NMR (300 MHz, $CDCl_3$):	δ 5.26 – 4.70 (m, 1H), 3.71 – 3.63 (m, 2H), 3.62 – 3.46 (m, 8H), 3.43 – 3.36 (m, 2H), 3.25 (t, *J* = 5.2 Hz, 1H), 1.38 (s, 9H).

tert-Butyl (2-(2-(2-(2-hydroxyethoxy)ethoxy)ethoxy)ethyl)carbamate **(L24)**

The Boc protection was carried out as described for compound **L9.**[738] 2-(2-(2-(2-Aminoethoxy)ethoxy)ethoxy)ethan-1-ol (1667 mg, 8.64 mmol, 1.0 eq.), triethylamine (1195 µL, 8.64 mmol, 1.0 eq.) and Boc anhydride (565 mg, 2.59 mmol, 0.3 eq.) were subjected to the reaction conditions for five hours. The crude product was purified by flash chromatography using a gradient elution of dichloromethane/methanol (0-20%).

Yield:	759 mg, (100%)
Chemical formula:	$C_{13}H_{27}NO_6$
Molecular mass:	293.36 g/mol
Appearance:	Colourless oil
Internal code:	MST-295
Synthesis scheme:	Figure 104
^{1}H NMR (300 MHz, $CDCl_3$):	δ 4.28 – 4.15 (m, 1H), 3.75 – 3.48 (m, 12H), 3.47 – 3.36 (m, 2H), 3.34 – 3.25 (m, 2H), 3.13 – 3.02 (m, 1H), 1.43 (s, 9H).

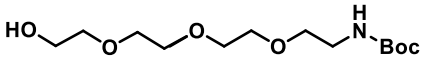

10.5.2 JNJ-7777120-based ligands

(5-Chloro-1*H*-indol-2-yl)(4-methylpiperazin-1-yl)methanone (37)

The HATU coupling was carried out as described for compound **P3**.[728] 5-Chloro-1*H*-indole-2-carboxylic acid (1080 mg, 5.52 mmol, 1.1 eq.), DIPEA (1033 µL, 6.07 mmol, 1.1 eq.), *N*-methylpiperazine (553 mg, 5.52 mmol, 1.0 eq.) and HATU (2306 mg, 6.07 mmol, 1.1 eq.) were subjected to the reaction conditions for 20 hours. The crude product was purified by column chromatography using a gradient elution of dichloromethane/methanol (sat. NH_3) (0-20%).

Yield:	1391 mg, (91%)
Chemical formula:	$C_{14}H_{16}ClN_3O$
Molecular mass:	277.75 g/mol
Appearance:	Yellow solid
Internal code:	MST-040
Synthesis scheme:	Figure 107

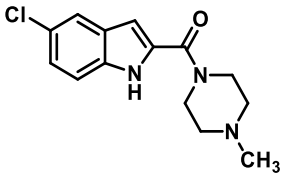

^{1}H NMR (300 MHz, $CDCl_3$):	δ 10.14 (s, 1H), 7.54 – 7.49 (m, 1H), 7.31 – 7.25 (m, 1H), 7.15 – 7.10 (m, 1H), 6.64 – 6.59 (m, 1H), 3.95 – 3.83 (m, 4H), 2.47 – 2.40 (m, 4H), 2.28 (s, 3H).

(5-Chloro-3-nitro-1*H*-indol-2-yl)(4-methylpiperazin-1-yl)methanone **(38)**

The synthesis was based on a previously described procedure.[740] Compound **37** (1300 mg, 4.69 mmol, 1.0 eq.) was dissolved in acetic anhydride and cooled down to -70 °C. At this temperature, concentrated nitric acid (429 µL, 9.39 mmol, 2.0 eq.) was added dropwise under vigorous stirring. The reaction mixture was allowed to warm up to 0 °C and stirred overnight at this temperature. After 24 hours, the mixture was poured onto ice and the resulting aqueous solution was basified with 4N sodium hydroxide solution, then extracted three times with ethyl acetate. The combined organic phases were dried over magnesium sulphate and the solvent was removed under reduced pressure. The crude product was purified by column chromatography using gradient elution with dichloromethane/methanol (sat. NH_3) (0-20%).

Yield:	1299 mg, (86%)
Chemical formula:	$C_{14}H_{15}ClN_4O_3$
Molecular mass:	322.75 g/mol
Appearance:	Yellow solid
Internal code:	MST-113
Synthesis scheme:	Figure 108
^{1}H NMR (300 MHz, DMSO-d_6):	δ 8.10 – 8.03 (m, 1H), 7.64 – 7.56 (m, 1H), 7.46 – 7.36 (m, 1H), 3.78 – 3.69 (m, 2H), 3.31 – 3.21 (m, 2H), 2.55 – 2.49 (m, 2H), 2.39 – 2.32 (m, 2H), 2.28 (s, 3H).

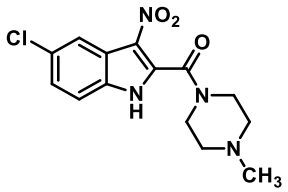

(3-Amino-5-chloro-1*H*-indol-2-yl)(4-methylpiperazin-1-yl)methanone **(39)**

The synthesis was based on a previously described procedure.[742] Compound **38** (1250 mg, 3.88 mmol, 1.0 eq.) and iron powder (2173 mg, 38.8 mmol, 10 eq.) were dissolved in isopropanol and a saturated ammonium chloride solution was added (approx. 20 mL). The mixture was heated to 85 °C for 20 hours. Then the mixture was filtered over Celite and the aqueous solution was extracted three times with dichloromethane. The combined organic phases were dried over magnesium sulphate and the solvent was removed under reduced pressure. The crude product was purified by column chromatography using gradient elution with dichloromethane/methanol (sat. NH_3) (0-20%).

Yield:	736 mg, (65%)
Chemical formula:	$C_{14}H_{17}ClN_4O$
Molecular mass:	292.77 g/mol
Appearance:	Yellow solid
Internal code:	MST-212
Synthesis scheme:	Figure 109
^{1}H NMR (300 MHz, DMSO-d_6):	δ 10.53 (s, 1H), 7.89 – 7.82 (m, 1H), 7.34 – 7.21 (m, 1H), 7.24 – 7.11 (m, 1H), 6.06 (s, 2H), 3.80 – 3.74 (m, 4H), 3.30 – 3.18 (m, 4H), 2.81 (s, 3H).

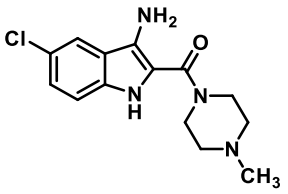

tert-Butyl-(2-((5-chloro-2-(4-methylpiperazine-1-carbonyl)-1*H*-indol-3-yl)amino)-2-oxoethyl)carbamate **(P21a)**

The HATU coupling was carried out as described for compound **P3**.[644] Compound **39** (128 mg, 0.44 mmol, 1.0 eq.), DIPEA (69 µL, 0.48 mmol, 1.1 eq.), Boc-glycine **L1** (92 mg, 0.53 mmol, 1.2 eq.) and HATU (211 mg, 0.66 mmol, 1.5 eq.) were subjected to the reaction conditions for 20 hours. The crude product was purified by column chromatography using a gradient elution of dichloromethane/methanol (sat. NH_3) (0-20%).

Yield:	188 mg, (95%)
Chemical formula:	$C_{21}H_{28}ClN_5O_4$
Molecular mass:	449.94 g/mol
Appearance:	Colourless solid
Internal code:	MST-283, ST-2568
Synthesis scheme:	Figure 111
Melting point:	257.9 °C
LC-MS purity:	100%
MS (ESI-(+)):	m/z=450.23 $[M+H^+]^+$ calculated: 450.1903
^{1}H NMR (300 MHz, DMSO-d_6):	δ 11.62 (s, 1H), 9.67 (s, 1H), 7.52 – 7.49 (m, 1H), 7.38 – 7.32 (m, 1H), 7.19 – 7.14 (m, 1H), 7.14 – 7.09 (m, 1H), 3.78 (d, *J* = 6.1 Hz, 2H), 3.58 – 3.42 (m, 4H), 2.36 – 2.24 (m, 4H), 2.19 (s, 3H), 1.42 (s, 9H).
^{13}C NMR (75.5 MHz, DMSO-d_6):	δ 168.57, 161.38, 155.90, 132.65, 125.09, 123.78, 123.62, 123.10, 119.12, 113.49, 112.18, 78.09, 54.53, 54.46, 45.57, 43.38, 28.19.

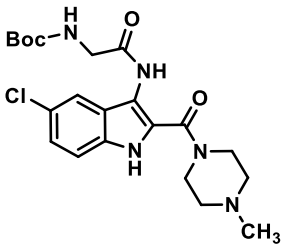

tert-Butyl-(3-((5-chloro-2-(4-methylpiperazine-1-carbonyl)-1*H*-indol-3-yl)amino)-3-oxopropyl)carbamate **(P21b)**

The HATU coupling was carried out as described for compound **P3**.[644] Compound **39** (113 mg, 0.39 mmol, 1.0 eq.), DIPEA (101 µL, 0.58 mmol, 1.5 eq.), 3-((*tert*-butoxycarbonyl)-amino)propanoic acid **L2** (81 mg, 0.43 mmol, 1.1 eq.) and HATU (186 mg, 0.58 mmol, 1.5 eq.) were subjected to the reaction conditions for 20 hours. The crude product was purified by column chromatography using a gradient elution of dichloromethane/methanol (sat. NH_3) (0-20%).

Yield:	147 mg, (81%)
Chemical formula:	$C_{22}H_{30}ClN_5O_4$
Molecular mass:	463.96 g/mol
Appearance:	Colourless solid
Internal code:	MST-255, ST-2576
Synthesis scheme:	Figure 111
Melting point:	252.2 °C
LC-MS purity:	100%
MS (ESI-(+)):	m/z=464.26 $[M+H^+]^+$ calculated: 464.2059
^{1}H NMR (300 MHz, DMSO-d_6):	δ 11.61 (s, 1H), 9.70 (s, 1H), 7.54 – 7.47 (m, 1H), 7.40 – 7.31 (m, 1H), 7.22 – 7.12 (m, 1H), 6.84 (t, *J* = 6.3 Hz, 1H), 3.52 – 3.46 (m, 4H), 3.32 – 3.20 (m, 2H), 2.59 – 2.51 (m, 2H), 2.34 – 2.28 (m, 4H), 2.20 (s, 3H), 1.41 (s, 9H).
^{13}C NMR (75.5 MHz, DMSO-d_6):	δ 169.40, 161.54, 155.51, 132.60, 125.05, 123.72, 123.62, 123.04, 118.98, 113.42, 112.19, 77.61, 54.59, 54.51, 45.62, 36.67, 35.63, 28.20.

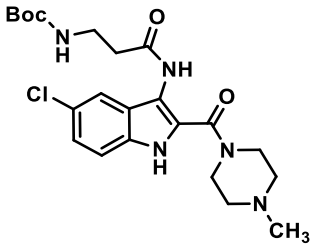

tert-Butyl-(4-((5-chloro-2-(4-methylpiperazine-1-carbonyl)-1*H*-indol-3-yl)amino)-4-oxobutyl)carbamate **(P21c)**

The HATU coupling was carried out as described for compound **P3**.[644] Compound **39** (169 mg, 0.58 mmol, 1.0 eq.), DIPEA (128 µL, 0.69 mmol, 1.2 eq.), 4-((*tert*-butoxycarbonyl)-amino)butanoic acid **L3** (141 mg, 0.69 mmol, 1.2 eq.) and HATU (264 mg, 0.69 mmol, 1.2 eq.) were subjected to the reaction conditions for 20 hours. The crude product was purified by column chromatography using a gradient elution of dichloromethane/methanol (sat. NH_3) (0-20%).

Yield:	144 mg, (52%)
Chemical formula:	$C_{23}H_{32}ClN_5O_4$
Molecular mass:	477.99 g/mol
Appearance:	Colourless solid
Internal code:	MST-353, ST-2606
Synthesis scheme:	Figure 111
Melting point:	273.2 °C
LC-DAD purity:	100%
MS (ESI-(+)):	m/z=478.27 $[M+H^+]^+$ calculated: 478.2216
^{1}H NMR (300 MHz, $CDCl_3$):	δ 10.00 (s, 1H), 9.48 (s, 1H), 7.20 – 6.93 (m, 3H), 4.95 (t, *J* = 6.6 Hz, 1H), 3.67 – 3.61 (m, 4H), 3.40 – 3.32 (m, 2H), 2.56 – 2.46 (m, 2H), 2.42 – 2.33 (m, 4H), 2.30 (s, 3H), 2.05 – 1.91 (m, 2H), 1.46 (s, 9H).
^{13}C NMR (75.5 MHz, $CDCl_3$):	δ 171.24, 163.14, 156.93, 133.23, 126.32, 125.61, 124.60, 123.10, 122.28, 119.74, 112.89, 79.85, 77.24, 76.89, 55.00, 45.96, 39.78, 33.47, 28.51.

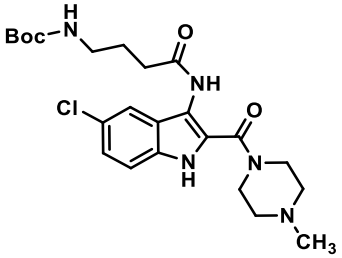

tert-butyl-(5-((5-chloro-2-(4-methylpiperazine-1-carbonyl)-1*H*-indol-3-yl)amino)-5-oxopentyl)carbamate **(P21d)**

The HATU coupling was carried out as described for compound **P3**.[644] Compound **39** (110 mg, 0.38 mmol, 1.0 eq.), DIPEA (65 µL, 0.46 mmol, 1.2 eq.), compound **L4** (82 mg, 0.38 mmol, 1.0 eq.) and HATU (217 mg, 0.57 mmol, 1.5 eq.) were subjected to the reaction conditions for 20 hours. The crude product was purified by column chromatography using a gradient elution of dichloromethane/methanol (sat. NH_3) (0-20%).

Yield:	78 mg, (42%)
Chemical formula:	$C_{24}H_{34}ClN_5O_4$
Molecular mass:	492.02 g/mol
Appearance:	Colourless solid
Internal code:	MST-336
Synthesis scheme:	Figure 111
Melting point:	263.5 °C
LC-DAD purity:	97.5%
MS (ESI-(+)):	m/z=492.52 $[M+H^+]^+$ calculated: 492.2372
^{1}H NMR (300 MHz, MeOD):	δ 7.55 – 7.49 (m, 1H), 7.41 – 7.32 (m, 1H), 7.25 – 7.16 (m, 1H), 3.71 – 3.63 (m, 4H), 3.13 (t, *J* = 6.8 Hz, 2H), 2.56 – 2.44 (m, 6H),

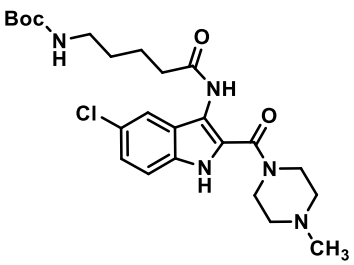

	2.36 (s, 3H), 1.86 – 1.70 (m, 2H), 1.68 – 1.53 (m, 2H), 1.46 (s, 9H).
^{13}C NMR (75.5 MHz, MeOD):	δ 174.73, 164.71, 134.39, 126.70, 125.91, 125.20, 125.08, 119.60, 115.04, 114.33, 114.09, 79.90, 55.68, 46.01, 40.95, 36.62, 36.57, 30.63, 28.83, 24.28.

tert-Butyl-(6-((5-chloro-2-(4-methylpiperazine-1-carbonyl)-1*H*-indol-3-yl)amino)-6-oxohexyl)carbamate **(P21e)**

The HATU coupling was carried out as described for compound **P3**.[644] Compound **39** (118 mg, 0.40 mmol, 1.0 eq.), DIPEA (69 µL, 0.48 mmol, 1.2 eq.), compound **L5** (92 mg, 0.40 mmol, 1.0 eq.) and HATU (342 mg, 0.60 mmol, 1.5 eq.) were subjected to the reaction conditions for 20 hours. The crude product was purified by column chromatography using a gradient elution of dichloromethane/methanol (sat. NH_3) (0-20%).

Yield:	198 mg, (98%)
Chemical formula:	$C_{25}H_{36}ClN_5O_4$
Molecular mass:	506.04 g/mol
Appearance:	Colourless solid
Internal code:	MST-337, ST-2604
Synthesis scheme:	Figure 111
Melting point:	249.5 °C
LC-DAD purity:	100%
MS (ESI-(+)):	m/z=506.54 $[M+H^+]^+$ calculated: 506.2529
^{1}H NMR (300 MHz, DMSO-d_6):	δ 11.60 (s, 1H), 9.62 (s, 1H), 7.48 – 7.42 (m, 1H), 7.40 – 7.31 (m, 1H), 7.22 – 7.13 (m, 1H), 6.79 (t, *J* = 5.6 Hz, 1H), 3.52 – 3.46 (m, 4H), 3.00 – 2.87 (m, 2H), 2.41 – 2.27 (m, 6H), 2.20 (s, 3H), 1.70 – 1.54 (m, 2H), 1.49 – 1.16 (m, 13H).
^{13}C NMR (75.5 MHz, DMSO-d_6):	δ 171.13, 161.65, 155.55, 132.60, 125.08, 123.77, 123.58, 122.98, 118.80, 113.48, 112.36, 77.27, 54.47, 54.45, 45.57, 35.75, 35.16, 29.28, 28.24, 26.08, 24.96.

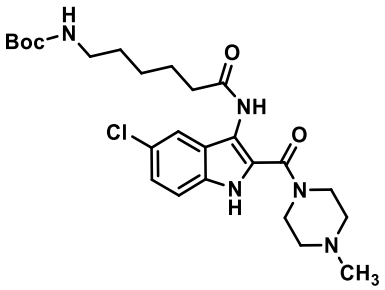

tert-Butyl-(2-(2-((5-chloro-2-(4-methylpiperazine-1-carbonyl)-1*H*-indol-3-yl)amino)-2-oxoethoxy)ethyl)carbamate **(P21f)**

The HATU coupling was carried out as described for compound **P3**.[644] Compound **39** (130 mg, 0.50 mmol, 1.0 eq.), DIPEA (130 µL, 0.75 mmol, 1.5 eq.), compound **L6** (120 mg, 0.55 mmol, 1.1 eq.) and HATU (239 mg, 0.75 mmol, 1.5 eq.) were subjected to the reaction conditions for

20 hours. The crude product was purified by column chromatography using a gradient elution of dichloromethane/methanol (sat. NH_3) (0-20%).

Yield:	173 mg, (70%)
Chemical formula:	$C_{23}H_{32}ClN_5O_5$
Molecular mass:	493.99 g/mol
Appearance:	Colourless solid
Internal code:	MST-279, ST-2567
Synthesis scheme:	Figure 111
Melting point:	275.4 °C
LC-MS purity:	95.9%
MS (ESI-(+)):	m/z=494.28 $[M+H^+]^+$ calculated: 494.2165
^{1}H NMR (300 MHz, DMSO-d_6):	δ 11.70 (s, 1H), 9.61 (s, 1H), 7.54 – 7.47 (m, 1H), 7.47 – 7.32 (m, 1H), 7.29 – 7.15 (m, 1H), 7.04 (t, *J* = 5.7 Hz, 1H), 4.13 (s, 2H), 3.59 – 3.43 (m, 6H), 3.28 – 3.17 (m, 2H), 2.41 – 2.35 (m, 4H), 2.23 (s, 3H), 1.38 (s, 9H).
^{13}C NMR (75.5 MHz, DMSO-d_6):	δ 168.26, 161.47, 155.58, 132.72, 125.35, 123.81, 123.77, 123.25, 119.13, 113.62, 111.96, 77.71, 70.12, 69.83, 69.81, 54.31, 54.25, 45.42, 28.19.

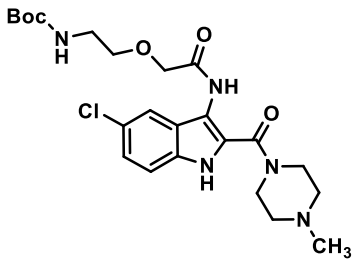

tert-Butyl-(2-(2-(2-((5-chloro-2-(4-methylpiperazine-1-carbonyl)-1*H*-indol-3-yl)amino)-2-oxoethoxy)ethoxy)ethyl)carbamate **(P21g)**

The HATU coupling was carried out as described for compound **P3**.[644] Compound **39** (128 mg, 0.44 mmol, 1.0 eq.), DIPEA (100 µL, 0.53 mmol, 1.2 eq.), compound **L7** (137 mg, 0.53 mmol, 1.2 eq.) and HATU (201 mg, 0.53 mmol, 1.2 eq.) were subjected to the reaction conditions for 20 hours. The crude product was purified by column chromatography using a gradient elution of dichloromethane/methanol (sat. NH_3) (0-20%).

Yield:	104 mg, (44%)
Chemical formula:	$C_{25}H_{36}ClN_5O_6$
Molecular mass:	538.04 g/mol
Appearance:	Colourless solid
Internal code:	MST-358, ST-2601
Synthesis scheme:	Figure 111
Melting point:	279.4 °C
LC-DAD purity:	100%
MS (ESI-(+)):	m/z=538.55 $[M+H^+]^+$ calculated: 538.2427

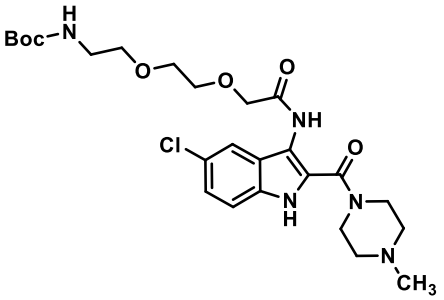

^{1}H NMR (300 MHz, $CDCl_3$):	δ 9.67 (s, 1H), 8.92 (s, 1H), 7.48 – 7.42 (m, 1H), 7.19 – 7.04 (m, 2H), 5.25 – 5.19 (m, 1H), 4.15 (s, 2H), 3.79 – 3.63 (m, 4H), 3.63 – 3.48 (m, 6H), 3.23 – 3.11 (m, 2H), 2.37 – 2.25 (m, 4H), 2.20 (s, 3H), 1.32 (s, 9H).
^{13}C NMR (75.5 MHz, $CDCl_3$):	δ 168.46, 162.61, 156.08, 133.22, 126.08, 125.96, 125.00, 123.56, 119.96, 113.32, 113.07, 79.27, 71.14, 70.75, 70.53, 70.10, 54.85, 45.90, 40.32, 28.48, 28.39.

tert-Butyl-(2-(2-(2-(2-((5-chloro-2-(4-methylpiperazine-1-carbonyl)-1*H*-indol-3-yl)amino)-2-oxoethoxy)ethoxy)ethoxy)ethyl)carbamate **(P21h)**

The HATU coupling was carried out as described for compound **P3**.[644] Compound **39** (205 mg, 0.70 mmol, 1.0 eq.), DIPEA (121 µL, 0.84 mmol, 1.2 eq.), compound **L8** (258 mg, 0.84 mmol, 1.2 eq.) and HATU (319 mg, 0.84 mmol, 1.2 eq.) were subjected to the reaction conditions for 20 hours. The crude product was purified by column chromatography using a gradient elution of dichloromethane/methanol (sat. NH_3) (0-20%).

Yield:	293 mg, (72%)
Chemical formula:	$C_{27}H_{40}ClN_5O_7$
Molecular mass:	582.10 g/mol
Appearance:	Colourless solid
Internal code:	MST-385, ST-2607
Synthesis scheme:	Figure 111
Melting point:	281.6 °C
LC-DAD purity:	100%
MS (ESI-(+)):	m/z=582.63 $[M+H^+]^+$ calculated: 582.2689
^{1}H NMR (300 MHz, MeOD):	δ 7.64 – 7.54 (m, 1H), 7.43 – 7.29 (m, 1H), 7.25 – 7.14 (m, 1H), 4.24 (s, 2H), 3.89 – 3.61 (m, 10H), 3.61 – 3.51 (m, 2H), 3.42 – 3.28 (m, 2H), 3.16 – 3.05 (m, 2H), 2.57 – 2.44 (m, 4H), 2.31 (s, 3H), 1.39 (s, 9H).
^{13}C NMR (75.5 MHz, MeOD):	δ 171.52, 164.48, 158.34, 134.48, 126.74, 126.02, 125.41, 125.05, 120.14, 114.51, 113.69, 80.08, 72.27, 71.60, 71.58, 71.51, 71.25, 71.18, 71.05, 55.67, 46.07, 41.20, 28.85.

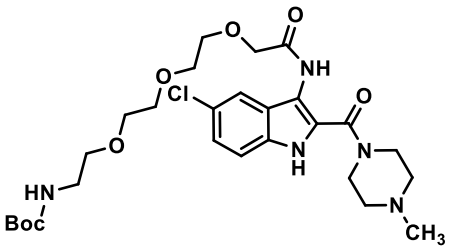

2-Amino-*N*-(5-chloro-2-(4-methylpiperazine-1-carbonyl)-1*H*-indol-3-yl)acetamide ditriofluoroacetate **(P22a)**

The synthesis was based on a procedure previously described.[744] Compound **P21a** (146 mg, 0.32 mmol, 1.0 eq.) was dissolved in dichloromethane, and the reaction mixture was cooled to

0 °C in an ice bath. At this temperature, trifluoroacetic acid (ca. 1 mL) was added dropwise. The reaction mixture was allowed to warm to room temperature and stirred for 24 hours. The solvent was removed under reduced pressure. The residue was purified by reverse phase flash chromatography using a gradient elution of water/methanol (0-100%).

Yield:	185 mg, (100%)
Chemical formula:	$C_{16}H_{20}ClN_5O_2$ x 2 $C_2HF_3O_2$
Molecular mass:	577.84 g/mol
Appearance:	Colourless solid
Internal code:	MST-293, ST-2570
Synthesis scheme:	Figure 112
Melting point:	80.4 °C
LC-MS purity:	100%
MS (ESI-(+)):	m/z=350.18 $[M+H^+]^+$ calculated: 350.1378
^{1}H NMR (300 MHz, DMSO-d_6):	δ 11.88 (s, 1H), 10.75 (s, 1H), 10.40 (s, 1H), 8.28 (s, 3H), 7.68 – 7.62 (m, 1H), 7.48 – 7.39 (m, 1H), 7.28 – 7.19 (m, 1H), 3.91 (s, 2H), 3.77 – 2.98 (m, 8H), 2.85 (s, 3H).
^{13}C NMR (75.5 MHz, DMSO-d_6):	δ 164.94, 161.82, 158.81, 132.50, 124.04, 124.01, 123.55, 123.13, 119.06, 118.69, 113.83, 111.87, 52.18, 52.07, 42.45. 39.87.

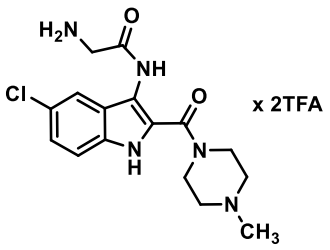

3-Amino-*N*-(5-chloro-2-(4-methylpiperazine-1-carbonyl)-1*H*-indol-3-yl)propanamide ditriofluoroacetate **(P22b)**

The Boc deprotection was carried out as described for compound **P22a**.[744] Compound **P21b** (115 mg, 0.25 mmol, 1.0 eq.) was subjected to the reaction conditions for 24 hours. The crude product was purified by reverse phase flash chromatography using a gradient elution of water/methanol (0-100%).

Yield:	148 mg, (100%)
Chemical formula:	$C_{17}H_{22}ClN_5O_2$ x 2 $C_2HF_3O_2$
Molecular mass:	591.87 g/mol
Appearance:	Colourless solid
Internal code:	MST-287, ST-2569
Synthesis scheme:	Figure 112
Melting point:	81.4 °C
LC-MS purity:	100%
MS (ESI-(+)):	m/z=364.20 $[M+H^+]^+$ calculated: 364.1535

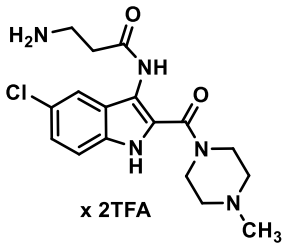

^{1}H NMR (300 MHz, DMSO-d_6):	δ 11.78 (s, 1H), 10.74 (s, 1H), 10.12 (s, 1H), 7.95 (s, 3H), 7.70 – 7.63 (m, 1H), 7.45 – 7.36 (m, 1H), 7.26 – 7.17 (m, 1H), 4.24 – 3.23 (m, 8H), 3.19 – 3.07 (m, 2H), 2.85 (s, 3H), 2.85 – 2.74 (m, 2H).
^{13}C NMR (75.5 MHz, DMSO-d_6):	δ 168.20, 162.08, 158.78, 158.36, 132.51, 123.84, 123.58, 123.47, 123.15, 118.89, 113.67, 112.66, 52.31, 52.25, 42.38, 35.06, 32.17.

4-Amino-*N*-(5-chloro-2-(4-methylpiperazine-1-carbonyl)-1*H*-indol-3-yl)butanamide ditriofluoroacetate **(P22c)**

The Boc deprotection was carried out as described for compound **P22a**.[744] Compound **P21c** (40 mg, 0.08 mmol, 1.0 eq.) was subjected to the reaction conditions for 24 hours. The crude product was purified by reverse phase flash chromatography using a gradient elution of water/methanol (0-100%).

Yield:	48 mg, (100%)
Chemical formula:	$C_{18}H_{24}ClN_5O_2$ x 2 $C_2HF_3O_2$
Molecular mass:	605.87 g/mol
Appearance:	Colourless solid
Internal code:	MST-240, ST-2564
Synthesis scheme:	Figure 112
Melting point:	86.4 °C
LC-MS purity:	97.1%
MS (ESI-(+)):	m/z=378.21 $[M+H^+]^+$ calculated: 378.1691
^{1}H NMR (300 MHz, DMSO-d_6):	δ 11.76 (s, 1H), 10.82 (s, 1H), 9.97 (s, 1H), 7.95 (s, 3H), 7.64 – 7.57 (m, 1H), 7.45 – 7.36 (m, 1H), 7.26 – 7.16 (m, 1H), 3.79 – 3.04 (m, 10H), 2.94 – 2.86 (m, 2H), 2.83 (s, 3H), 1.98 – 1.82 (m, 2H).
^{13}C NMR (75.5 MHz, DMSO-d_6):	δ 170.04, 162.21, 158.54, 132.45, 123.80, 123.60, 123.38, 123.17, 121.15, 118.56, 113.68, 112.95, 52.27, 42.44, 39.32, 38.46, 31.85, 23.17.

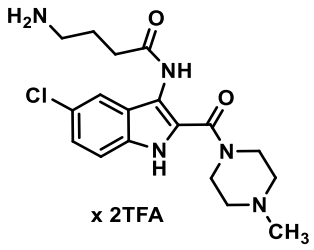

5-Amino-*N*-(5-chloro-2-(4-methylpiperazine-1-carbonyl)-1*H*-indol-3-yl)pentanamide ditriofluoroacetate **(P22d)**

The Boc deprotection was carried out as described for compound **P22a**.[744] Compound **P21d** (64 mg, 0.13 mmol, 1.0 eq.) was subjected to the reaction conditions for 24 hours. The crude

product was purified by reverse phase flash chromatography using a gradient elution of water/methanol (0-100%).

Yield:	67 mg, (83%)
Chemical formula:	$C_{19}H_{26}ClN_5O_2$ x 2 $C_2HF_3O_2$
Molecular mass:	619.95 g/mol
Appearance:	Colourless solid
Internal code:	MST-251, ST-2566
Synthesis scheme:	Figure 112
Melting point:	74.9 °C
LC-MS purity:	96.4%
MS (ESI-(+)):	m/z=392.22 $[M+H^+]^+$ calculated: 392.1848
^{1}H NMR (300 MHz, DMSO-d_6):	δ 11.76 (s, 1H), 11.19 (s, 1H), 9.92 (s, 1H), 7.93 (s, 3H), 7.64 – 7.57 (m, 1H), 7.45 – 7.36 (m, 1H), 7.26 – 7.16 (m, 1H), 4.32 – 3.91 (m, 8H), 3.65 – 2.74 (m, 5H), 2.47 – 2.37 (m, 2H), 1.76 – 1.57 (m, 4H).
^{13}C NMR (75.5 MHz, DMSO-d_6):	δ 170.57, 162.18, 158.56, 132.50, 123.74, 123.44, 123.35, 123.18, 118.65, 114.92, 113.64, 113.06, 52.20, 42.34, 40.26, 39.04, 34.49, 26.67, 22.09.

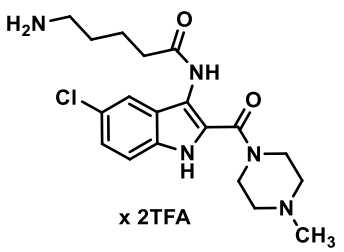

6-Amino-*N*-(5-chloro-2-(4-methylpiperazine-1-carbonyl)-1*H*-indol-3-yl)hexanamide ditriofluoroacetate **(P22e)**

The Boc deprotection was carried out as described for compound **P22a**.[744] Compound **P21e** (180 mg, 0.35 mmol, 1.0 eq.) was subjected to the reaction conditions for 24 hours. The crude product was purified by reverse phase flash chromatography using a gradient elution of water/methanol (0-100%).

Yield:	222 mg, (100%)
Chemical formula:	$C_{20}H_{28}ClN_5O_2$ x 2 $C_2HF_3O_2$
Molecular mass:	633.93 g/mol
Appearance:	Colourless solid
Internal code:	MST-249, ST-2565
Synthesis scheme:	Figure 112
Melting point:	71.4 °C
LC-MS purity:	96.0%
MS (ESI-(+)):	m/z=406.24 $[M+H^+]^+$ calculated: 406.2004

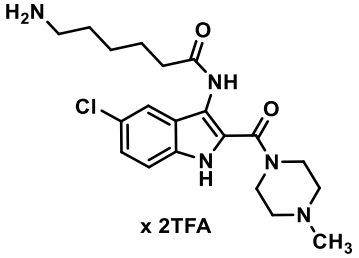

^{1}H NMR (300 MHz, DMSO-d_6):	δ 11.76 (s, 1H), 10.91 (s, 1H), 9.89 (s, 1H), 7.93 (s, 3H), 7.63 – 7.57 (m, 1H), 7.45 – 7.36 (m, 1H), 7.27 – 7.16 (m, 1H), 3.92 – 3.01 (m, 8H), 2.83 (s, 3H), 2.39 (t, *J* = 7.4 Hz, 2H), 1.78 – 1.13 (m, 8H).
^{13}C NMR (75.5 MHz, DMSO-d_6):	δ 170.83, 162.21, 159.03, 132.49, 123.73, 123.47, 123.32, 123.21, 118.93, 118.62, 113.63, 113.12, 52.20, 42.34, 38.67, 34.91, 26.75, 25.49, 24.69, 17.91.

2-(2-Aminoethoxy)-*N*-(5-chloro-2-(4-methylpiperazine-1-carbonyl)-1*H*-indol-3-yl)acetamide ditriofluoroacetate **(P22f)**

The Boc deprotection was carried out as described for compound **P22a**.[744] Compound **P21f** (71 mg, 0.14 mmol, 1.0 eq.) was subjected to the reaction conditions for 24 hours. The crude product was purified by reverse phase flash chromatography using a gradient elution of water/methanol (0-100%).

Yield:	87 mg, (83%)
Chemical formula:	$C_{18}H_{24}ClN_5O_3$ x 2 $C_2HF_3O_2$
Molecular mass:	621.87 g/mol
Appearance:	Colourless solid
Internal code:	MST-302, ST-2572
Synthesis scheme:	Figure 112
Melting point:	73.7 °C
LC-MS purity:	100%
MS (ESI-(+)):	m/z=394.19 $[M+H^+]^+$ calculated: 394.1640
^{1}H NMR (300 MHz, DMSO-d_6):	δ 11.85 (s, 1H), 10.63 (s, 1H), 9.73 (s, 1H), 8.01 (s, 3H), 7.62 – 7.55 (m, 1H), 7.48 – 7.39 (m, 1H), 7.29 – 7.19 (m, 1H), 4.22 (s, 2H), 3.77 (t, *J* = 5.0 Hz, 2H), 3.54 – 3.28 (m, 8H), 3.16 – 3.10 (m, 2H), 2.82 (s, 3H).
^{13}C NMR (75.5 MHz, DMSO-d_6):	δ 167.88, 161.94, 158.69, 132.62, 124.39, 124.01, 123.61, 123.48, 120.98, 118.80, 113.84, 112.30, 67.10, 62.52, 52.45, 52.40, 42.54, 42.46.

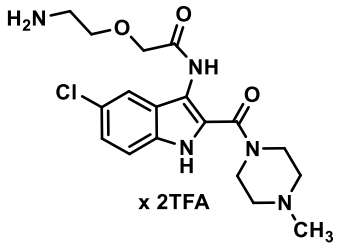

2-(2-(2-Aminoethoxy)ethoxy)-*N*-(5-chloro-2-(4-methylpiperazine-1-carbonyl)-1*H*-indol-3-yl)acetamide dihydrochloride **(P22g)**

The Boc-deprotection protocol was carried out as described for compound **P6**.[674] Compound **P21g** (200 mg, 0.37 mmol, 1.0 eq.) was subjected to the reaction conditions for 24 hours. The

crude product was purified by reverse phase flash chromatography using a gradient elution of water/methanol (0-100%).

Yield:	87 mg, (46%)
Chemical formula:	$C_{20}H_{28}ClN_5O_4$ x 2 HCl
Molecular mass:	509.93 g/mol
Appearance:	Colourless solid
Internal code:	MST-714, ST-2939
Synthesis scheme:	Figure 112
Melting point:	74.6 °C
LC-MS-DAD purity:	100%
HR-MS (ESI-(+)):	m/z=438.1908 $[M+H^+]^+$ calculated: 438.1903
^{1}H NMR (300 MHz, DMSO-d_6):	δ 12.45 (s, 1H), 11.94 (s, 1H), 11.68 (s, 1H), 8.10 (s, 3H), 8.01 – 7.55 (m, 1H), 7.53 – 7.36 (m, 1H), 7.33 – 7.11 (m, 1H), 4.30 – 4.10 (m, 4H), 4.04 (s, 2H), 3.83 – 3.29 (m, 10H), 3.18 – 2.87 (m, 2H), 2.77 (s, 3H).
^{13}C NMR (75.5 MHz, MeOD):	δ 170.14, 163.12, 133.11, 129.36, 125.36, 123.97, 123.59, 118.63, 113.05, 112.41, 72.42, 72.15, 70.87, 70.17, 69.92, 69.82, 44.63, 40.69.

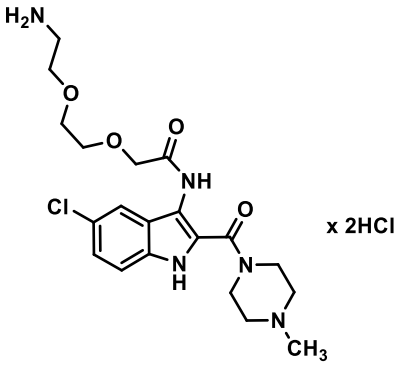

2-(2-(2-(2-Aminoethoxy)ethoxy)ethoxy)-*N*-(5-chloro-2-(4-methylpiperazine-1-carbonyl)-1*H*-indol-3-yl)acetamide dihydrochloride **(P22h)**

The Boc-deprotection protocol was carried out as described for compound **P6**.[674] Compound **P21h** (200 mg, 0.34 mmol, 1.0 eq.) was subjected to the reaction conditions for 24 hours. The crude product was purified by reverse phase flash chromatography using a gradient elution of water/methanol (0-100%).

Yield:	104 mg, (55%)
Chemical formula:	$C_{22}H_{32}ClN_5O_5$ x 2 HCl
Molecular mass:	554.22 g/mol
Appearance:	Colourless solid
Internal code:	MST-713, ST-2938
Synthesis scheme:	Figure 112
Melting point:	77.8 °C
LC-MS-DAD purity:	96.3%
HR-MS (ESI-(+)):	m/z=482.2172 $[M+H^+]^+$ calculated: 482.2165

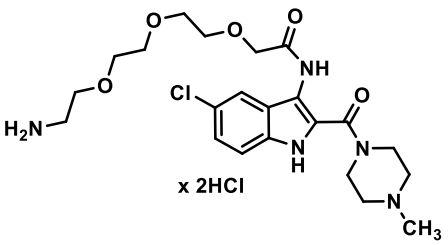

^{1}H NMR (300 MHz, DMSO-d_6):	δ 11.95 (s, 1H), 11.72 (s, 1H), 9.88 (s, 1H), 8.11 (s, 3H), 8.02 – 7.60 (m, 1H), 7.55 – 7.37 (m, 1H), 7.33 – 7.15 (m, 1H), 4.26 – 4.10 (m, 4H), 4.02 (s, 2H), 3.77 – 3.31 (m, 14H), 3.00 – 2.86 (m, 2H), 2.78 (s, 3H).
^{13}C NMR (75.5 MHz, MeOD):	δ 170.21, 163.14, 133.14, 125.31, 124.79, 123.90, 123.68, 118.60, 113.07, 112.19, 72.16, 70.90, 70.23, 70.12, 70.08, 69.93, 69.79, 54.27, 44.64, 40.62.

N-(2-((5-Chloro-2-(4-methylpiperazine-1-carbonyl)-1*H*-indol-3-yl)amino)-2-oxoethyl)-3-(5,5-difluoro-7,9-dimethyl-5*H*-5λ^4,6λ^4-dipyrrolo[1,2-*c*:2',1'-*f*][1,3,2]diazaborinin-3-yl)propanamide (**P23a**)

The HATU coupling was carried out as described for compound **P3**.[644] Compound **P22a** (52 mg, 0.09 mmol, 1.0 eq.), DIPEA (17 µL, 0.10 mmol, 1.1 eq.), BODIPY-FL (26 mg, 0.09 mmol, 1.0 eq.) and HATU (38 mg, 0.10 mmol, 1.1 eq.) were subjected to the reaction conditions for 20 hours. The crude product was purified by column chromatography using a gradient elution of dichloromethane/methanol (sat. NH_3) (0-20%).

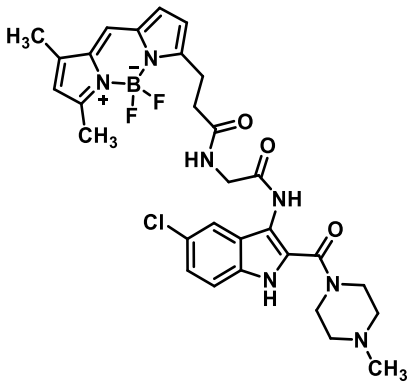

Yield:	188 mg, (66%)
Chemical formula:	$C_{30}H_{33}BClF_2N_7O_3$
Molecular mass:	623.90 g/mol
Appearance:	Orange solid
Internal code:	MST-658
Synthesis scheme:	Figure 113
Melting point:	109.4 °C
LC-MS-DAD purity:	100%
HR-MS (ESI-(+)):	m/z=624.2460 $[M+H^+]^+$ calculated: 624.2467
^{1}H NMR (300 MHz, DMSO-d_6):	δ 11.73 (s, 1H), 9.86 (s, 1H), 8.47 (t, *J* = 5.8 Hz, 1H), 7.69 (s, 1H), 7.55 (d, *J* = 4.0 Hz, 1H), 7.43 – 7.34 (m, 1H), 7.23 – 7.13 (m, 1H), 7.12 – 7.04 (m, 1H), 6.43 (d, *J* = 4.0 Hz, 1H), 6.29 (s, 1H), 4.00 (d, *J* = 5.8 Hz, 2H), 3.45 – 3.34 (m, 8H), 3.13 (t, *J* = 7.7 Hz, 2H), 2.69 – 2.58 (m, 2H), 2.46 (s, 3H), 2.39 (s, 3H), 2.25 (s, 3H).
^{13}C NMR (75.5 MHz, DMSO-d_6):	δ 172.05, 168.68, 162.20, 159.58, 158.30, 144.54, 134.90, 133.46, 133.14, 129.44, 125.83, 125.30, 124.23, 124.13, 123.71, 120.72, 119.45, 117.14, 114.10, 112.72, 72.78, 70.23, 60.64, 42.68, 33.90, 24.32, 14.97, 11.47.

N-(5-Chloro-2-(4-methylpiperazine-1-carbonyl)-1*H*-indol-3-yl)-3-(3-(5,5-difluoro-7,9-dimethyl-5*H*-5λ^4,6λ^4-dipyrrolo[1,2-c:2',1'-*f*][1,3,2]diazaborinin-3-yl)propanamido)propanamide **(P23b)**

The HATU coupling was carried out as described for compound **P3**.[644] Compound **P22b** (42 mg, 0.10 mmol, 1.0 eq.), DIPEA (19 µL, 0.11 mmol, 1.1 eq.), BODIPY-FL (30 mg, 0.10 mmol, 1.0 eq.) and HATU (42 mg, 0.11 mmol, 1.1 eq.) were subjected to the reaction conditions for 20 hours. The crude product was purified by column chromatography using a gradient elution of dichloromethane/methanol (sat. NH_3) (0-20%).

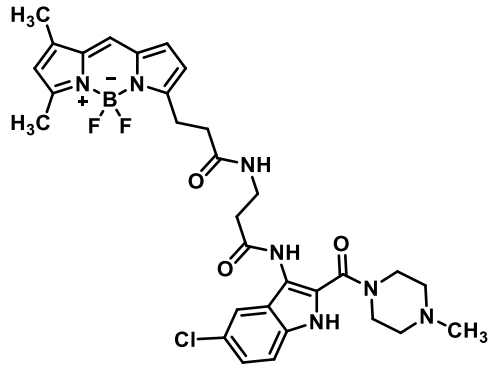

Yield:	26 mg, (41%)
Chemical formula:	$C_{31}H_{35}BClF_2N_7O_3$
Molecular mass:	637.92 g/mol
Appearance:	Orange solid
Internal code:	MST-799,ST-2962
Synthesis scheme:	Figure 113
Melting point:	105.5 °C
LC-MS-DAD purity:	95.2%
HR-MS (ESI-(+)):	m/z=638.2612 $[M+H^+]^+$ calculated: 638.2624
^{1}H NMR (600 MHz, DMSO-d_6):	δ 11.61 (s, 1H), 9.72 (s, 1H), 8.09 (t, *J* = 7.8 Hz, 1H), 7.68 (s, 1H), 7.51 (d, *J* = 4.0 Hz, 1H), 7.40 – 7.28 (m, 1H), 7.24 – 7.12 (m, 1H), 7.09 – 7.04 (m, 1H), 6.36 (d, *J* = 4.0 Hz, 1H), 6.30 (s, 1H), 3.57 – 3.43 (m, 4H), 3.41 – 3.37 (m, 2H), 3.10 (t, *J* = 7.8 Hz, 2H), 2.59 – 2.51 (m, 4H), 2.47 (s, 3H), 2.34 – 2.27 (m, 4H), 2.26 (s, 3H), 2.17 (s, 3H).
^{13}C NMR (151 MHz, DMSO-d_6):	δ 171.39, 169.90, 162.08, 159.58, 158.35, 144.53, 134.91, 133.46, 133.10, 129.40, 125.81, 125.50, 124.20, 124.14, 123.56, 120.72, 119.50, 117.03, 113.94, 112.77, 70.25, 46.09, 40.53, 35.82, 35.78, 34.14, 24.44, 14.98, 11.47.

N-(5-Chloro-2-(4-methylpiperazine-1-carbonyl)-1*H*-indol-3-yl)-3-(3-(5,5-difluoro-7,9-dimethyl-5*H*-5λ^4,6λ^4-dipyrrolo[1,2-*c*:2',1'-*f*][1,3,2]diazaborinin-3-yl)propanamido)-butanamide **(P23c)**

The HATU coupling was carried out as described for compound **P3**.[644] Compound **P22c** (20 mg, 0.03 mmol, 1.0 eq.), DIPEA (6 µL, 0.04 mmol, 1.1 eq.), BODIPY-FL (10 mg, 0.03 mmol, 1.0 eq.) and HATU (14 mg, 0.04 mmol, 1.1 eq.) were subjected to the reaction conditions for 20 hours. The crude product was purified by column chromatography using a gradient elution of dichloromethane/methanol (sat. NH_3) (0-20%).

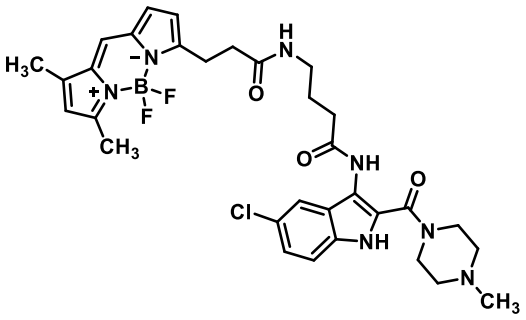

Yield:	18 mg, (93%)
Chemical formula:	$C_{32}H_{37}BClF_2N_7O_3$
Molecular mass:	651.95 g/mol
Appearance:	Orange solid
Internal code:	MST-660
Synthesis scheme:	Figure 113
Melting point:	100.3 °C
LC-MS-DAD purity:	97.9%
HR-MS (ESI-(+)):	m/z=652.2758 $[M+H^+]^+$ calculated: 652.2780
^{1}H NMR (600 MHz, $CDCl_3$):	δ 9.82 (s, 1H), 9.19 (s, 1H), 7.16 (s, 1H), 7.11 – 7.06 (m, 2H), 7.06 – 7.01 (m, 1H), 6.92 – 6.88 (m, 1H), 6.34 – 6.26 (m, 2H), 6.11 (s, 1H), 3.65 – 3.62 (m, 4H), 3.38 – 3.32 (m, 2H), 3.30 (t, *J* = 7.4 Hz, 2H), 2.72 (t, *J* = 7.4 Hz, 2H), 2.55 (s, 3H), 2.39 – 2.31 (m, 6H), 2.26 (s, 3H), 2.23 (s, 3H), 1.91 – 1.83 (m, 2H).
^{13}C NMR (151 MHz, $CDCl_3$):	δ 172.86, 171.34, 163.06, 160.66, 156.71, 144.31, 135.29, 133.35, 133.19, 128.26, 125.67, 124.67, 123.93, 123.44, 122.82, 120.65, 119.69, 117.42, 114.26, 112.94, 54.93, 45.90, 38.81, 35.92, 33.49, 29.71, 26.29, 24.95, 15.00, 11.32.

N-(5-Chloro-2-(4-methylpiperazine-1-carbonyl)-1*H*-indol-3-yl)-3-(3-(5,5-difluoro-7,9-dimethyl-5*H*-5λ^4,6λ^4-dipyrrolo[1,2-c:2',1'-*f*][1,3,2]diazaborinin-3-yl)propanamido)pentanamide **(P23d)**

The HATU coupling was carried out as described for compound **P3**.[644] Compound **P22d** (30 mg, 0.08 mmol, 1.0 eq.), DIPEA (13 µL, 0.09 mmol, 1.1 eq.), BODIPY-FL (23 mg, 0.08 mmol, 1.0 eq.) and HATU (38 mg, 0.09 mmol, 1.1 eq.) were subjected to the reaction conditions for 20 hours. The crude product was purified by column chromatography using a gradient elution of dichloromethane/methanol (sat. NH_3) (0-20%).

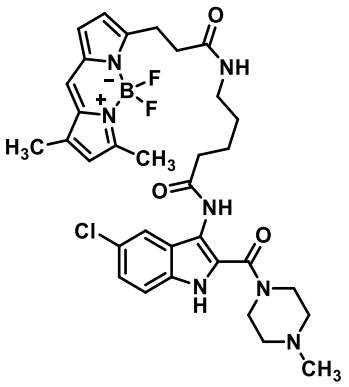

Yield:	24 mg, (45%)
Chemical formula:	$C_{33}H_{39}BClF_2N_7O_3$
Molecular mass:	665.98 g/mol
Appearance:	Orange solid
Internal code:	MST-800, ST-2965
Synthesis scheme:	Figure 113
Melting point:	98.0 °C
LC-MS-DAD purity:	95.3%
HR-MS (ESI-(+)):	m/z=666.2939 $[M+H^+]^+$ calculated: 666.2937
^{1}H NMR (600 MHz, DMSO-d_6):	δ 11.61 (s, 1H), 9.64 (s, 1H), 7.97 (t, *J* = 5.6 Hz, 1H), 7.67 (s, 1H), 7.47 (d, *J* = 4.0 Hz, 1H), 7.43 – 7.31 (m, 1H), 7.20 – 7.12 (m, 1H), 7.12 – 7.00 (m, 1H), 6.36 (d, *J* = 4.0 Hz, 1H), 6.30 (s, 1H), 3.56 – 3.38 (m, 6H), 3.15 – 3.06 (m, 4H), 2.54 – 2.49 (m, 2H), 2.47 (s, 3H), 2.39 (t, *J* = 7.5 Hz, 2H), 2.35 – 2.29 (m, 2H), 2.26 (s, 3H), 2.19 (s, 3H), 1.68 – 1.57 (m, 2H), 1.53 – 1.45 (m, 2H).
^{13}C NMR (151 MHz, DMSO-d_6):	δ 171.55, 171.11, 162.14, 159.55, 158.42, 144.50, 134.88, 133.44, 133.10, 129.41, 125.78, 125.57, 124.25, 124.10, 123.49, 120.70, 119.32, 117.08, 113.98, 112.84, 70.25, 49.07, 46.05, 38.81, 35.32, 34.26, 29.33, 24.50, 23.21, 14.97, 11.45.

N-(5-Chloro-2-(4-methylpiperazine-1-carbonyl)-1*H*-indol-3-yl)-3-(3-(5,5-difluoro-7,9-dimethyl-5*H*-5λ^4,6λ^4-dipyrrolo[1,2-*c*:2',1'-*f*][1,3,2]diazaborinin-3-yl)propanamido)-hexanamide **(P23e)**

The HATU coupling was carried out as described for compound **P3**.[644] Compound **P22e** (67 mg, 0.11 mmol, 1.0 eq.), DIPEA (16 µL, 0.12 mmol, 1.1 eq.), BODIPY-FL (31 mg, 0.11 mmol, 1.0 eq.) and HATU (44 mg, 0.12 mmol, 1.1 eq.) were subjected to the reaction conditions for 20 hours. The crude product was purified by column chromatography using a gradient elution of dichloromethane/methanol (sat. NH_3) (0-20%).

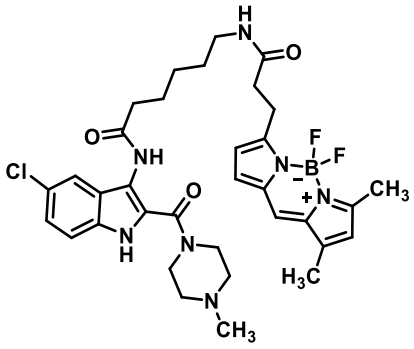

Yield:	16 mg, (21%)
Chemical formula:	$C_{34}H_{41}BClF_2N_7O_3$
Molecular mass:	680.00 g/mol
Appearance:	Orange solid
Internal code:	MST-662, ST-2937
Synthesis scheme:	Figure 113
Melting point:	109.5 °C
LC-MS-DAD purity:	100%
HR-MS (ESI-(+)):	m/z=680.3091 $[M+H^+]^+$ calculated: 680.3093
^{1}H NMR (600 MHz, DMSO-d_6):	δ 11.61 (s, 1H), 9.65 (s, 1H), 7.94 (t, *J* = 5.6 Hz, 1H), 7.67 (s, 1H), 7.46 (d, *J* = 4.0 Hz, 1H), 7.37 – 7.32 (m, 1H), 7.22 – 7.13 (m, 1H), 7.11 – 7.05 (m, 1H), 6.34 (d, *J* = 4.0 Hz, 1H), 6.29 (s, 1H), 3.59 – 3.40 (m, 4H), 3.14 – 3.00 (m, 4H), 2.49 – 2.47 (m, 2H), 2.46 (s, 3H), 2.36 (t, *J* = 7.5 Hz, 2H), 2.34 – 2.28 (m, 4H), 2.25 (s, 3H), 2.19 (s, 3H), 1.73 – 1.56 (m, 2H), 1.52 – 1.41 (m, 2H), 1.40 – 1.28 (m, 2H).
^{13}C NMR (151 MHz, DMSO-d_6):	δ 171.66, 171.09, 162.16, 159.56, 158.40, 144.52, 134.89, 133.44, 133.09, 129.41, 125.78, 125.59, 124.26, 124.10, 123.49, 120.72, 119.29, 117.07, 114.00, 112.86, 54.92, 46.03, 40.50, 38.98, 35.64, 34.23, 29.41, 26.70, 25.48, 24.51, 14.97, 11.45.

N-(2-(2-((5-Cchloro-2-(4-methylpiperazine-1-carbonyl)-1*H*-indol-3-yl)amino)-2-oxoethoxy)ethyl)-3-(5,5-difluoro-7,9-dimethyl-5*H*-5λ⁴,6λ⁴-dipyrrolo[1,2-c:2',1'-*f*][1,3,2]diazaborinin-3-yl)propanamide **(P23f)**

The HATU coupling was carried out as described for compound **P3**.[644] Compound **P22f** (41 mg, 0.07 mmol, 1.0 eq.), DIPEA (11 µL, 0.08 mmol, 1.1 eq.), BODIPY-FL (19 mg, 0.07 mmol, 1.0 eq.) and HATU (28 mg, 0.08 mmol, 1.1 eq.) were subjected to the reaction conditions for 20 hours. The crude product was purified by column chromatography using a gradient elution of dichloromethane/methanol (sat. NH_3) (0-20%).

Yield:	21 mg, (45%)
Chemical formula:	$C_{32}H_{37}BClF_2N_7O_4$
Molecular mass:	667.95 g/mol
Appearance:	Orange solid
Internal code:	MST-663
Synthesis scheme:	Figure 113
Melting point:	93.5 °C
LC-MS-DAD purity:	100%
HR-MS (ESI-(+)):	m/z=668.2734 $[M+H^+]^+$ calculated: 668.2735
^{1}H NMR (300 MHz, DMSO-d_6):	δ 11.73 (s, 1H), 9.66 (s, 1H), 8.17 (t, *J* = 5.6 Hz, 1H), 7.68 (s, 1H), 7.54 (d, *J* = 4.0 Hz, 1H), 7.44 – 7.35 (m, 1H), 7.24 – 7.15 (m, 1H), 7.12 – 7.04 (m, 1H), 6.36 (d, *J* = 4.0 Hz, 1H), 6.30 (s, 1H), 4.17 (s, 2H), 3.61 (t, *J* = 5.6 Hz, 2H), 3.44 – 3.32 (m, 6H), 3.11 (t, *J* = 7.7 Hz, 2H), 2.60 – 2.52 (m, 2H), 2.47 (s, 3H), 2.39 – 2.30 (m, 4H), 2.26 (s, 3H), 2.20 (s, 3H).
^{13}C NMR (151 MHz, DMSO-d_6):	δ 171.42, 168.76, 162.08, 159.59, 158.27, 144.54, 134.91, 133.44, 133.18, 129.38, 125.80, 125.63, 124.27, 124.18, 123.74, 120.72, 119.69, 117.06, 114.13, 112.73, 70.42, 70.32, 54.74, 45.84, 40.51, 38.98, 34.23, 24.42, 14.97, 11.46.

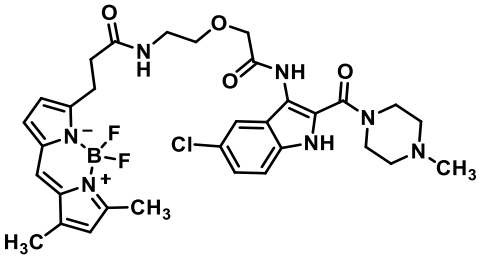

N-(2-(2-(2-((5-Chloro-2-(4-methylpiperazine-1-carbonyl)-1*H*-indol-3-yl)amino)-2-oxoethoxy)ethoxy)ethyl)-3-(5,5-difluoro-7,9-dimethyl-5*H*-5λ^4,6λ^4-dipyrrolo[1,2-*c*:2',1'-*f*][1,3,2]diazaborinin-3-yl)propanamide **(P23g)**

The HATU coupling was carried out as described for compound **P3**.[644] Compound **P22g** (20 mg, 0.04 mmol, 1.0 eq.), DIPEA (9 µL, 0.05 mmol, 1.1 eq.), BODIPY-FL (13 mg, 0.05 mmol, 1.0 eq.) and HATU (19 mg, 0.05 mmol, 1.1 eq.) were subjected to the reaction conditions for 20 hours. The crude product was purified by column chromatography using a gradient elution of dichloromethane/methanol (sat. NH_3) (0-20%).

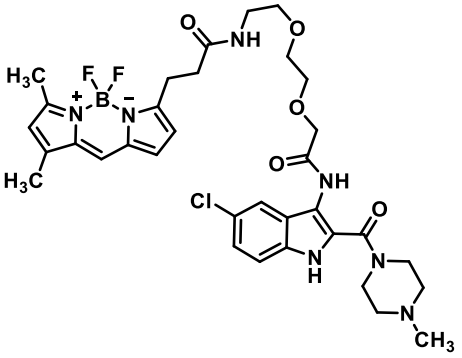

Yield:	13 mg, (46%)
Chemical formula:	$C_{34}H_{41}BClF_2N_7O_5$
Molecular mass:	712.00 g/mol
Appearance:	Orange solid
Internal code:	MST-763, ST-2970
Synthesis scheme:	Figure 113
Melting point:	98.3 °C
LC-MS-DAD purity:	100%
HR-MS (ESI-(+)):	m/z=712.2995 $[M+H^+]^+$ calculated: 712.2992
^{1}H NMR (600 MHz, DMSO-d_6):	δ 11.67 (s, 1H), 9.58 (s, 1H), 8.00 (t, *J* = 5.6 Hz, 1H), 7.68 (s, 1H), 7.53 (d, *J* = 4.0 Hz, 1H), 7.43 – 7.32 (m, 1H), 7.25 – 7.13 (m, 1H), 7.10 – 7.03 (m, 1H), 6.33 (d, *J* = 4.0 Hz, 1H), 6.30 (s, 1H), 4.17 (s, 2H), 3.77 – 3.70 (m, 2H), 3.69 – 3.62 (m, 2H), 3.56 – 3.50 (m, 4H), 3.48 (t, *J* = 5.6 Hz, 2H), 3.27 – 3.22 (m, 2H), 3.06 (t, *J* = 7.7 Hz, 2H), 2.49 – 2.46 (m, 5H), 2.38 – 2.31 (m, 4H), 2.26 (s, 3H), 2.21 (s, 3H).
^{13}C NMR (151 MHz, DMSO-d_6):	δ 171.39, 168.85, 162.10, 144.50, 134.89, 133.44, 133.15, 129.40, 129.38, 125.79, 125.47, 124.23, 124.10, 123.74, 120.71, 119.73, 117.06, 116.78, 114.09, 112.87, 70.88, 70.49, 70.25, 69.92, 69.67, 49.07, 45.94, 39.05, 34.07, 24.42, 14.97, 11.46.

N-(2-(2-(2-(2-((5-Chloro-2-(4-methylpiperazine-1-carbonyl)-1*H*-indol-3-yl)amino)-2-oxoethoxy)ethoxy)ethoxy)ethyl)-3-(5,5-difluoro-7,9-dimethyl-5*H*-5λ^4,6λ^4-dipyrrolo[1,2-*c*:2',1'-*f*][1,3,2]diazaborinin-3-yl)propanamide **(P23h)**

The HATU coupling was carried out as described for compound **P3**.[644] Compound **P22h** (20 mg, 0.04 mmol, 1.0 eq.), DIPEA (8 µL, 0.05 mmol, 1.1 eq.), BODIPY-FL (12 mg, 0.04 mmol, 1.0 eq.) and HATU (19 mg, 0.05 mmol, 1.1 eq.) were subjected to the reaction conditions for 20 hours. The crude product was purified by column chromatography using a gradient elution of dichloromethane/methanol (sat. NH_3) (0-20%).

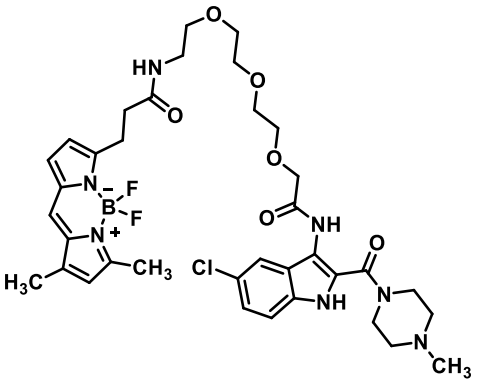

Yield:	8 mg, (27%)
Chemical formula:	$C_{36}H_{45}BClF_2N_7O_6$
Molecular mass:	756.06 g/mol
Appearance:	Orange solid
Internal code:	MST-762, ST-2977
Synthesis scheme:	Figure 113
Melting point:	101.1 °C
LC-MS-DAD purity:	100%
HR-MS (ESI-(+)):	m/z=756.3247 $[M+H^+]^+$ calculated: 756.3254
^{1}H NMR (600 MHz, DMSO-d_6):	δ 11.67 (s, 1H), 9.56 (s, 1H), 7.98 (t, *J* = 5.7 Hz, 1H), 7.68 (s, 1H), 7.52 (d, *J* = 4.0 Hz, 1H), 7.41 – 7.33 (m, 1H), 7.23 – 7.16 (m, 1H), 7.11 – 7.03 (m, 1H), 6.34 (d, *J* = 4.0 Hz, 1H), 6.29 (s, 1H), 4.16 (s, 2H), 3.76 – 3.69 (m, 2H), 3.67 – 3.63 (m, 2H), 3.61 – 3.54 (m, 2H), 3.53 – 3.49 (m, 8H), 3.37 (t, *J* = 5.7 Hz, 2H), 3.21 – 3.13 (m, 2H), 3.06 (t, *J* = 7.7 Hz, 2H), 2.47 (s, 3H), 2.37 – 2.32 (m, 4H), 2.25 (s, 3H), 2.21 (s, 3H).
^{13}C NMR (151 MHz, DMSO-d_6):	δ 171.36, 168.90, 162.10, 159.57, 158.35, 134.91, 133.44, 133.16, 129.44, 129.40, 125.80, 124.24, 124.11, 123.75, 120.72, 119.69, 117.07, 117.01, 114.10, 112.81, 70.94, 70.47, 70.25, 70.16, 70.02, 69.58, 55.38, 54.85, 40.53, 39.02, 34.08, 24.43, 14.96, 11.45.

7-(3-((5-Chloro-2-(4-methylpiperazine-1-carbonyl)-1*H*-indol-3-yl)amino)-3-oxopropyl)-5,5-difluoro-1,3-dimethyl-5*H*-4λ^4-dipyrrolo[1,2-*c*:2',1'-*f*][1,3,2]diazaborinin-5-uide **(P23i)**

The HATU coupling was carried out as described for compound **P3**.[644] Compound **SM2** (20 mg, 0.07 mmol, 1.0 eq.), DIPEA (11 µL, 0.08 mmol, 1.1 eq.), BODIPY-FL (20 mg, 0.07 mmol, 1.0 eq.) and HATU (30 mg, 0.08 mmol, 1.1 eq.) were subjected to the reaction conditions for 20 hours. The crude product was purified by column chromatography using a gradient elution of dichloromethane/methanol (sat. NH_3) (0-20%).

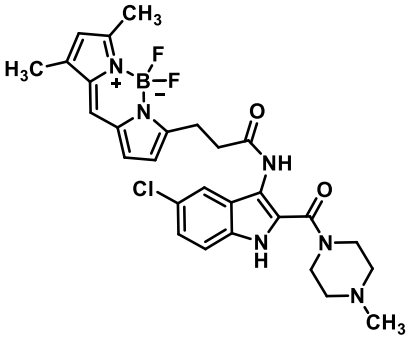

Yield:	22 mg, (56%)
Chemical formula:	$C_{28}H_{30}BClF_2N_6O_2$
Molecular mass:	566.85 g/mol
Appearance:	Orange solid
Internal code:	MST-792, ST-2967
Synthesis scheme:	Figure 114
Melting point:	153.5 °C
LC-MS-DAD purity:	96.8%
HR-MS (ESI-(+)):	m/z=567.2251 $[M+H^+]^+$ calculated: 567.2258
^{1}H NMR (600 MHz, DMSO-d_6):	δ 11.63 (s, 1H), 9.77 (s, 1H), 7.73 (s, 1H), 7.46 (d, *J* = 4.0 Hz, 1H), 7.40 – 7.30 (m, 1H), 7.23 – 7.16 (m, 1H), 7.14 – 7.11 (m, 1H), 6.47 (d, *J* = 4.0 Hz, 1H), 6.32 (s, 1H), 3.59 – 3.39 (m, 4H), 3.21 (t, *J* = 8.4 Hz, 2H), 2.83 (d, *J* = 8.4 Hz, 2H), 2.49 (s, 3H), 2.36 – 2.28 (m, 4H), 2.27 (s, 3H), 2.18 (s, 3H).
^{13}C NMR (151 MHz, DMSO-d_6):	δ 170.45, 162.07, 159.77, 158.00, 144.66, 135.02, 133.51, 133.12, 129.29, 125.92, 125.68, 124.27, 124.14, 123.52, 120.79, 119.42, 117.32, 114.00, 112.68, 54.84, 45.97, 34.27, 25.96, 24.34, 14.99, 11.47.

tert-Butyl-(3-((5-chloro-2-(4-methylpiperazine-1-carbonyl)-1*H*-indol-3-yl)amino)propyl)carbamate **(P24)**

The reductive amination protocol was carried out as described for compound **4**.[602] Compound **SM2** (202 mg, 0.69 mmol, 1.0 eq.), *tert*-butyl (3-oxopropyl)carbamate (119 mg, 0.69 mmol, 1.0 eq.), acetic acid (43 µL, 0.76 mmol, 1.1 eq.) and sodium triacetoxyborohydride (204 mg, 0.97 mmol, 1.4 eq.) were subjected to the reaction conditions for 20 hours. The crude product was purified by column chromatography using a gradient elution of dichloromethane/methanol (sat. NH_3) (0-20%).

Yield:	71 mg, (23%)
Chemical formula:	$C_{22}H_{32}ClN_5O_3$
Molecular mass:	449.98 g/mol
Appearance:	Colourless solid
Internal code:	MST-819, ST-2974
Synthesis scheme:	Figure 116
Melting point:	89.4 °C
LC-MS-DAD purity:	100%
HR-MS (ESI-(+)):	m/z=450.2291 $[M+H^+]^+$ calculated: 450.2266
^{1}H NMR (300 MHz, $CDCl_3$):	δ 8.45 (s, 1H), 7.68 (s, 1H), 7.23 – 7.11 (m, 2H), 4.72 (t, *J* = 5.9 Hz, 1H), 4.53 – 4.49 (m, 1H), 3.77 – 3.64 (m, 4H), 3.37 – 3.12 (m, 4H), 2.55 – 2.37 (m, 4H), 2.31 (s, 3H), 1.73 – 1.60 (m, 2H), 1.45 (s, 9H).
^{13}C NMR (75.5 MHz, $CDCl_3$):	δ 164.87, 156.40, 133.94, 129.78, 129.74, 125.16, 124.54, 122.31, 119.56, 116.04, 112.95, 79.39, 55.17, 46.08, 45.22, 44.95, 30.77, 28.43.

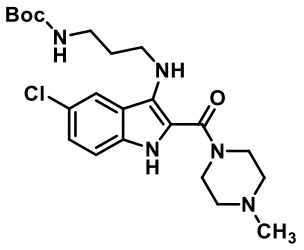

(3-((3-Aminopropyl)amino)-5-chloro-1*H*-indol-2-yl)(4-methylpiperazin-1-yl)methanone dihydrochloride **(P25)**

The Boc deprotection was carried out as described for compound **P6**.[674] Compound **P24** (35 mg, 0.10 mmol, 1.0 eq.) was subjected to the reaction conditions for 24 hours. The crude product was purified by reverse phase flash chromatography using a gradient elution of water/methanol (0-100%).

Yield:	33 mg, (95%)
Chemical formula:	$C_{17}H_{24}ClN_5O$ x 2 HCl
Molecular mass:	349.86 g/mol
Appearance:	Colourless solid
Internal code:	MST-825, ST-2987
Synthesis scheme:	Figure 117
Melting point:	68.0 °C
LC-MS purity:	95.2%
MS (ESI-(+)):	m/z=350.1738 $[M+H^+]^+$ calculated: 350.1742
^{1}H NMR (600 MHz, MeOD):	δ 7.92 – 7.87 (m, 1H), 7.53 – 7.48 (m, 1H), 7.36 – 7.33 (m, 1H), 4.56 – 4.40 (m, 2H), 3.71 – 3.42 (m, 8H), 3.21 – 3.11 (m, 2H), 2.99 (s, 3H), 2.24 – 2.12 (m, 2H).

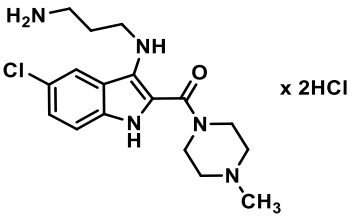

^{13}C NMR (151 MHz, MeOD):	δ 162.75, 133.37, 126.59, 126.53, 125.60, 121.49, 121.44, 117.73, 114.01, 52.59, 47.99, 42.32, 41.89, 36.90, 25.17.

N-(3-((5-Chloro-2-(4-methylpiperazine-1-carbonyl)-1*H*-indol-3-yl)amino)propyl)-3-(5,5-difluoro-7,9-dimethyl-5*H*-5λ^4,6λ^4-dipyrrolo[1,2-*c*:2',1'-*f*][1,3,2]diazaborinin-3-yl)propanamide **(P26)**

The HATU coupling was carried out as described for compound **P3**.[644] Compound **P25** (30 mg, 0.09 mmol, 1.0 eq.), DIPEA (15 µL, 0.10 mmol, 1.1 eq.), BODIPY-FL (25 mg, 0.09 mmol, 1.0 eq.) and HATU (36 mg, 0.10 mmol, 1.1 eq.) were subjected to the reaction conditions for 20 hours. The crude product was purified by column chromatography using a gradient elution of dichloromethane/methanol (sat. NH_3) (0-20%).

Yield:	33 mg, (58%)
Chemical formula:	$C_{31}H_{37}BClF_2N_7O_2$
Molecular mass:	623.94 g/mol
Appearance:	Orange solid
Internal code:	MST-838, ST-3005
Synthesis scheme:	Figure 118
Melting point:	74.5 °C
LC-MS-DAD purity:	100%
HR-MS (ESI-(+)):	m/z=624.2808 $[M+H^+]^+$ calculated: 624.2831
^{1}H NMR (600 MHz, $CDCl_3$):	δ 8.25 (s, 1H), 7.60 (s, 1H), 7.14 – 7.05 (m, 2H), 6.95 (s, 1H), 6.75 (d, *J* = 4.0 Hz, 1H), 6.20 (d, *J* = 4.0 Hz, 1H), 6.08 – 5.97 (m, 2H), 4.64 – 4.46 (m, 1H), 3.69 – 3.59 (m, 4H), 3.23 – 3.13 (m, 4H), 3.09 (t, *J* = 7.4 Hz, 2H), 2.57 (t, *J* = 7.4 Hz, 2H), 2.48 (s, 3H), 2.42 – 2.32 (m, 4H), 2.24 (s, 3H), 2.15 (s, 3H), 1.57 – 1.46 (m, 2H).
^{13}C NMR (151 MHz, $CDCl_3$):	δ 172.11, 164.86, 160.21, 157.29, 143.96, 135.10, 133.95, 133.36, 130.14, 128.32, 125.23, 124.56, 123.83, 122.36, 120.45, 119.66, 117.52, 115.59, 112.94, 55.16, 46.07, 45.12, 44.63, 36.70, 35.83, 30.04, 24.87, 14.97, 11.31.

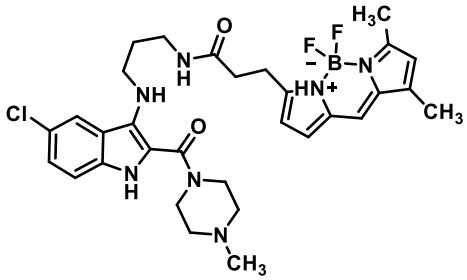

10.5.3 ST-2529-based ligands

1-(3-Chloropropoxy)-4-nitrobenzene **(41)**

The alkylation protocol was carried out as described for compound **2a**.[598] 4-Nitrophenol (5315 mg, 38.2 mmol, 1.0 eq.), 1-bromo-3-chloropropane (4149 µL mg, 42.0 mmol, 1.1 eq.), potassium iodide (12682 mg, 76.4 mmol, 2.0 eq.) and potassium carbonate (10543 mg, 76.4 mmol, 2.0 eq.) were subjected to the reaction conditions for 48 hours. The crude product was used without further purification.

Yield:	4599 mg, (56%)
Chemical formula:	$C_9H_{10}ClNO_3$
Molecular mass:	215.63 g/mol
Appearance:	Yellow oil
Internal code:	MST-728
Synthesis scheme:	Figure 121
^{1}H NMR (300 MHz, $CDCl_3$):	δ 8.19 (d, *J* = 9.3 Hz, 2H), 6.96 (d, *J* = 9.3 Hz, 2H), 4.22 (t, *J* = 5.9 Hz, 2H), 3.75 (t, *J* = 6.2 Hz, 2H), 2.33 – 2.23 (m, 2H).

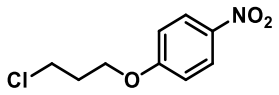

1-Methyl-4-(3-(4-nitrophenoxy)propyl)piperazine **(42)**

The alkylation protocol was carried out as described for compound **2a**.[598] Compound **41** (4500 mg, 20.9 mmol, 1.0 eq.), 1-methylpiperazine (2814 µL mg, 23.0 mmol, 1.1 eq.), potassium iodide (6939 mg, 41.8 mmol, 2.0 eq.) and potassium carbonate (5768 mg, 41.8 mmol, 2.0 eq.) were subjected to the reaction conditions for 48 hours. The crude product was purified by column chromatography using a gradient elution of dichloromethane/methanol (sat. NH_3) (0-20%).

Yield:	4607 mg, (79%)
Chemical formula:	$C_{14}H_{21}N_3O_3$
Molecular mass:	279.34 g/mol
Appearance:	Yellow solid
Internal code:	MST-731
Synthesis scheme:	Figure 122
^{1}H NMR (300 MHz, $CDCl_3$):	δ 8.11 (t, *J* = 9.6 Hz, 2H), 6.88 (d, *J* = 9.6 Hz, 2H), 4.05 (t, *J* = 6.3 Hz, 2H), 2.53 – 2.31 (m, 10H), 2.22 (s, 3H), 2.00 – 1.85 (m, 2H).

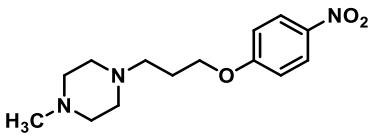

4-(3-(4-Methylpiperazin-1-yl)propoxy)aniline **(43)**

The synthesis was based on a procedure previously described.[750] Compound **P42** (4550 mg, 16.3 mmol, 1.0 eq.) was dissolved in methanol, and a catalytic amount of 10% palladium on charcoal was added. The reaction mixture was exposed to a hydrogen atmosphere and stirred at room temperature for 24 hours. The suspension was filtered through a celite pad, and the solvent was removed under reduced pressure. The crude product was used without further purification.

Yield:	4059 mg, (100%)
Chemical formula:	$C_{14}H_{23}N_3O$
Molecular mass:	249.36 g/mol
Appearance:	Yellow solid
Internal code:	MST-732
Synthesis scheme:	Figure 123
^{1}H NMR (300 MHz, $CDCl_3$):	δ 6.71 (d, *J* = 9.8 Hz, 2H), 6.60 (d, *J* = 9.8 Hz, 2H), 3.90 (t, *J* = 6.4 Hz, 2H), 3.28 (s, 2H), 2.56 – 2.32 (m, 10H), 2.26 (s, 3H), 1.98 – 1.82 (m, 2H).

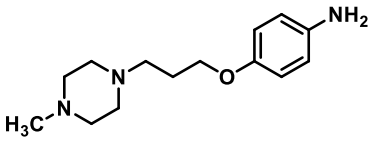

Ethyl-4-((4-(3-(4-methylpiperazin-1-yl)propoxy)phenyl)amino)-2-(methylthio)pyrimidine-5-carboxylate **(45)**

The synthesis was based on a procedure previously described.[752] Ethyl-4-chloro-2-(methylthio)pyrimidine-5-carboxylate **44** (2200 mg, 9.48 mmol, 1.0 eq.), compound **43** (2361 mg, 9.48 mmol, 1.0 eq.) and DIPEA (1359 µL, 9.48 mmol, 1.0 eq.) were dissolved in isopropanol and the reaction mixture was heated to 70 °C and stirred at this temperature for 20 hours. The solvent was removed under reduced pressure and the crude product was purified by column chromatography using a gradient elution of dichloromethane/methanol (sat. NH_3) (0-20%).

Yield:	4219 mg, (100%)
Chemical formula:	$C_{22}H_{31}N_5O_3S$
Molecular mass:	445.58 g/mol
Appearance:	Colourless solid
Internal code:	MST-518
Synthesis scheme:	Figure 124

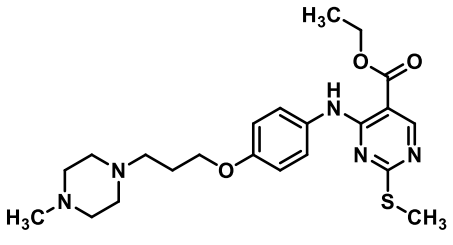

^{1}H NMR (300 MHz, $CDCl_3$):	δ 10.17 (s, 1H), 8.71 (s, 1H), 7.51 (d, *J* = 9.6 Hz, 2H), 6.86 (d, *J* = 9.6 Hz, 2H), 4.43 – 4.26 (m, 2H), 4.07 – 3.95 (m, 4H), 2.77 – 2.55 (m, 8H), 2.47 (s, 3H), 2.41 (s, 3H), 2.05 – 1.92 (m, 2H), 1.38 (t, *J* = 7.1 Hz, 3H).

4-((4-(3-(4-Methylpiperazin-1-yl)propoxy)phenyl)amino)-2-(methylthio)pyrimidine-5-carboxylate lithium salt **(SM3)**

The ester cleavage protocol was carried out as described for compound **14**.[641] Compound **45** (4000 mg, 8.97 mmol, 1.0 eq.) and lithium hydroxide (862 mg, 35.9 mmol, 4.0 eq.) were subjected to the reaction conditions for 24 hours. The crude product was used without further purification.

Yield:	4219 mg, (100%)
Chemical formula:	$C_{22}H_{26}N_5O_3S$ x Li
Molecular mass:	423.46 g/mol
Appearance:	Colourless solid
Internal code:	MST-520
Synthesis scheme:	Figure 125
^{1}H NMR (300 MHz, DMSO-d_6):	δ 13.15 (s, 1H), 8.51 (s, 1H), 7.58 (d, *J* = 8.6 Hz, 2H), 6.91 (d, *J* = 8.6 Hz, 2H), 3.97 (d, *J* = 6.3 Hz, 2H), 2.49 – 2.36 (m, 13H), 2.20 (s, 3H), 1.91 – 1.81 (m, 2H).

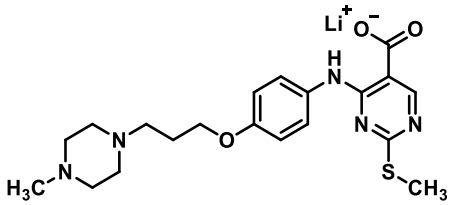

tert-Butyl-(2-(4-((4-(3-(4-methylpiperazin-1-yl)propoxy)phenyl)amino)-2-(methylthio)pyrimidine-5-carboxamido)ethyl)carbamate **(P27a)**

The HATU coupling was carried out as described for compound **P3**.[644] Compound **SM3** (50 mg, 0.12 mmol, 1.0 eq.), DIPEA (20 µL, 0.14 mmol, 1.2 eq.), compound **L9** (19 mg, 0.12 mmol, 1.0 eq.) and HATU (53 mg, 0.14 mmol, 1.2 eq.) were subjected to the reaction conditions for 20 hours. The crude product was purified by column chromatography using a gradient elution of dichloromethane/methanol (sat. NH_3) (0-20%).

Yield:	52 mg, (78%)
Chemical formula:	$C_{27}H_{41}N_7O_4S$
Molecular mass:	559.73 g/mol
Appearance:	Yellow solid
Internal code:	MST-572, ST-2773
Synthesis scheme:	Figure 127
Melting point:	160.3 °C

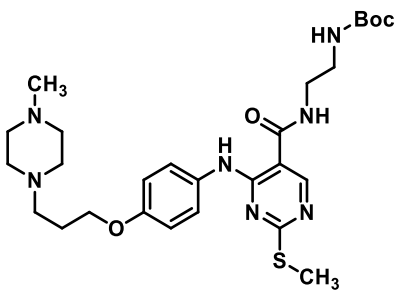

LC-MS-DAD purity:	96.9%
HR-MS (ESI-(+)):	m/z=560.3499 $[M+H^+]^+$ calculated: 560.3014
^{1}H NMR (300 MHz, MeOD):	δ 8.31 (s, 1H), 7.40 (d, *J* = 8.5 Hz, 2H), 6.76 (d, *J* = 8.5 Hz, 2H), 3.88 (t, *J* = 6.1 Hz, 2H), 3.37 – 3.22 (m, 2H), 3.22 – 3.12 (m, 2H), 2.50 – 2.39 (m, 10H), 2.36 (s, 3H), 2.18 (s, 3H), 1.92 – 1.77 (m, 2H), 1.31 (s, 9H).
^{13}C NMR (75.5 MHz, MeOD):	δ 175.57, 168.77, 159.22, 158.78, 157.14, 155.50, 132.46, 124.19, 115.58, 105.44, 80.21, 67.38, 56.25, 55.62, 53.72, 46.00, 41.16, 40.80, 28.83, 27.61, 14.54.

tert-Butyl-(3-(4-((4-(3-(4-methylpiperazin-1-yl)propoxy)phenyl)amino)-2-(methylthio)pyrimidine-5-carboxamido)propyl)carbamate **(P27b)**

The HATU coupling was carried out as described for compound **P3**.[644] Compound **SM3** (49 mg, 0.12 mmol, 1.0 eq.), DIPEA (20 µL, 0.14 mmol, 1.2 eq.), compound **L10** (21 mg, 0.12 mmol, 1.0 eq.) and HATU (53 mg, 0.14 mmol, 1.2 eq.) were subjected to the reaction conditions for 20 hours. The crude product was purified by column chromatography using a gradient elution of dichloromethane/methanol (sat. NH_3) (0-20%).

Yield:	25 mg, (36%)
Chemical formula:	$C_{28}H_{43}N_7O_4S$
Molecular mass:	573.76 g/mol
Appearance:	Colourless solid
Internal code:	MST-571, ST-2780
Synthesis scheme:	Figure 127
Melting point:	162.3 °C
LC-MS-DAD purity:	95.1%
HR-MS (ESI-(+)):	m/z=574.3644 $[M+H^+]^+$ calculated: 574.3170
^{1}H NMR (300 MHz, MeOD):	δ 8.33 (s, 1H), 7.41 (d, *J* = 8.6 Hz, 2H), 6.77 (d, *J* = 8.6 Hz, 2H), 3.89 (t, *J* = 6.1 Hz, 2H), 3.34 – 3.24 (m, 2H), 3.09 – 2.98 (m, 2H), 2.61 – 2.41 (m, 10H), 2.36 (s, 3H), 2.22 (s, 3H), 1.96 – 1.79 (m, 2H), 1.71 – 1.62 (m, 2H), 1.33 (s, 9H).
^{13}C NMR (75.5 MHz, MeOD):	δ 175.55, 168.52, 159.26, 158.64, 157.15, 155.37, 132.47, 124.25, 115.58, 105.48, 80.08, 67.35, 56.19, 55.55, 53.60, 45.87, 38.91, 38.07, 30.73, 28.84, 27.58, 14.53.

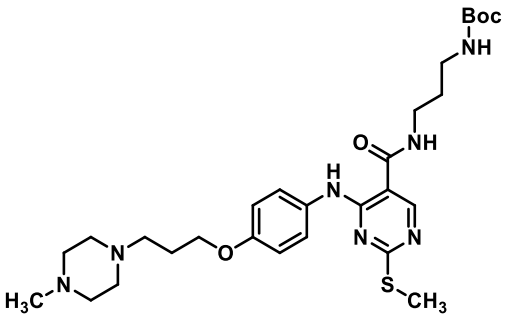

tert-Butyl-(4-(4-((4-(3-(4-methylpiperazin-1-yl)propoxy)phenyl)amino)-2-(methylthio)pyrimidine-5-carboxamido)butyl)carbamate **(P27c)**

The HATU coupling was carried out as described for compound **P3**.[644] Compound **SM3** (53 mg, 0.13 mmol, 1.0 eq.), DIPEA (22 µL, 0.15 mmol, 1.2 eq.), compound **L11** (24 mg, 0.13 mmol, 1.0 eq.) and HATU (57 mg, 0.15 mmol, 1.2 eq.) were subjected to the reaction conditions for 20 hours. The crude product was purified by column chromatography using a gradient elution of dichloromethane/methanol (sat. NH_3) (0-20%).

Yield:	25 mg, (38%)
Chemical formula:	$C_{29}H_{45}N_7O_4S$
Molecular mass:	587.78 g/mol
Appearance:	Colourless solid
Internal code:	MST-565, ST-2781
Synthesis scheme:	Figure 127
Melting point:	163.6 °C
LC-MS-DAD purity:	95.1%
HR-MS (ESI-(+)):	m/z=588.3870 $[M+H^+]^+$ calculated: 588.3327
^{1}H NMR (300 MHz, MeOD):	δ 8.32 (s, 1H), 7.42 (d, *J* = 8.7 Hz, 2H), 6.78 (d, *J* = 8.7 Hz, 2H), 3.90 (t, *J* = 6.1 Hz, 2H), 3.30 – 3.23 (m, 2H), 3.03 – 2.90 (m, 2H), 2.59 – 2.33 (m, 13H), 2.18 (s, 3H), 1.92 – 1.77 (m, 2H), 1.58 – 1.36 (m, 4H), 1.32 (s, 9H).
^{13}C NMR (75.5 MHz, MeOD):	δ 175.52, 168.49, 159.30, 158.59, 157.18, 155.34, 132.45, 124.26, 115.59, 105.55, 79.90, 67.38, 56.24, 55.59, 53.69, 45.95, 41.03, 40.40, 28.83, 28.53, 27.69, 27.59, 14.49.

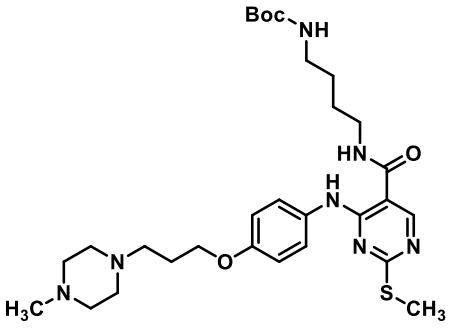

tert-Butyl-(5-(4-((4-(3-(4-methylpiperazin-1-yl)propoxy)phenyl)amino)-2-(methylthio)pyrimidine-5-carboxamido)pentyl)carbamate **(P27d)**

The HATU coupling was carried out as described for compound **P3**.[644] Compound **SM3** (49 mg, 0.12 mmol, 1.0 eq.), DIPEA (20 µL, 0.14 mmol, 1.2 eq.), compound **L12** (24 mg, 0.12 mmol, 1.0 eq.) and HATU (53 mg, 0.14 mmol, 1.2 eq.) were subjected to the reaction conditions for 20 hours. The crude product was purified by column chromatography using a gradient elution of dichloromethane/methanol (sat. NH_3) (0-20%).

Yield:	35 mg, (49%)
Chemical formula:	$C_{30}H_{47}N_7O_4S$
Molecular mass:	601.81 g/mol
Appearance:	Colourless solid
Internal code:	MST-564, ST-2774
Synthesis scheme:	Figure 127
Melting point:	165.1 °C
LC-MS-DAD purity:	95.2%
HR-MS (ESI-(+)):	m/z=602.3968 $[M+H^+]^+$ calculated: 602.3483

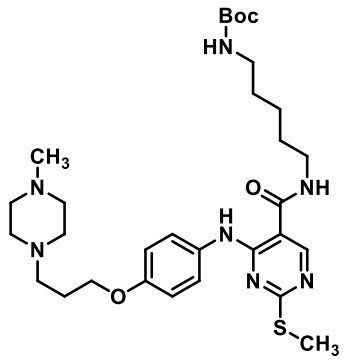

^{1}H NMR (300 MHz, MeOD):	δ 8.45 (s, 1H), 7.55 (d, *J* = 8.7 Hz, 2H), 6.94 (d, *J* = 8.7 Hz, 2H), 4.08 (t, *J* = 6.0 Hz, 2H), 3.37 (t, *J* = 7.1 Hz, 2H), 3.28 – 3.15 (m, 4H), 3.12 – 2.84 (m, 8H), 2.81 (s, 3H), 2.51 (s, 3H), 2.12 – 2.00 (m, 2H), 1.78 – 1.48 (m, 4H), 1.43 (s, 11H).
^{13}C NMR (75.5 MHz, MeOD):	δ 174.82, 168.16, 159.22, 158.60, 157.23, 154.24, 132.32, 124.45, 115.69, 105.67, 79.86, 66.72, 55.26, 54.23, 51.55, 43.95, 40.67, 30.71, 30.04, 28.82, 26.92, 25.26, 24.24, 14.48.

tert-Butyl-(6-(4-((4-(3-(4-methylpiperazin-1-yl)propoxy)phenyl)amino)-2-(methylthio)pyrimidine-5-carboxamido)hexyl)carbamate **(P27e)**

The HATU coupling was carried out as described for compound **P3**.[644] Compound **SM3** (70 mg, 0.17 mmol, 1.0 eq.), DIPEA (29 µL, 0.20 mmol, 1.2 eq.), compound **L13** (36 mg, 0.17 mmol, 1.0 eq.) and HATU (76 mg, 0.20 mmol, 1.2 eq.) were subjected to the reaction conditions for 20 hours. The crude product was purified by column chromatography using a gradient elution of dichloromethane/methanol (sat. NH_3) (0-20%).

Yield:	66 mg, (63%)
Chemical formula:	$C_{31}H_{49}N_7O_4S$
Molecular mass:	615.84 g/mol
Appearance:	Colourless solid
Internal code:	MST-552, ST-2753
Synthesis scheme:	Figure 127
Melting point:	159.5 °C
LC- DAD purity:	100%
MS (ESI-(+)):	m/z=616.38 $[M+H^+]^+$ calculated: 616.3640

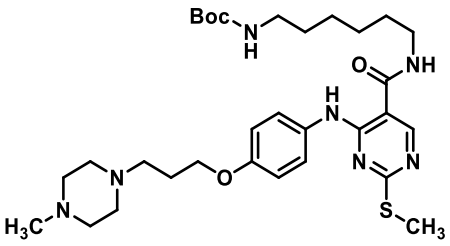

^{1}H NMR (300 MHz, $CDCl_3$):	δ 10.85 (s, 1H), 8.35 (s, 1H), 7.47 (d, *J* = 8.9 Hz, 2H), 6.98 (s, 1H), 6.79 (d, *J* = 8.9 Hz, 2H), 4.61 (t, *J* = 5.8 Hz, 1H), 3.93 (t, *J* = 6.3 Hz, 2H), 3.40 – 3.26 (m, 2H), 3.17 – 2.86 (m, 4H), 2.52 – 2.39 (m, 9H), 2.23 (s, 3H), 1.97 – 1.82 (m, 2H), 1.62 – 1.48 (m, 2H), 1.47 – 1.20 (m, 17H).
^{13}C NMR (75.5 MHz, $CDCl_3$):	δ 174.43, 166.99, 158.10, 156.27, 155.60, 153.99, 131.18, 123.20, 114.46, 104.22, 79.14, 66.49, 55.11, 53.13, 45.98, 39.92, 39.81, 39.18, 30.08, 29.14, 28.43, 26.79, 25.84, 25.54, 14.33.

N-(2-Aminoethyl)-4-((4-(3-(4-methylpiperazin-1-yl)propoxy)phenyl)amino)-2-(methylthio)pyrimidine-5-carboxamide **(P28a)**

The Boc-deprotection protocol was carried out as described for compound **P6**.[674] Compound **P27a** (50 mg, 0.09 mmol, 1.0 eq.) was subjected to the reaction conditions for 24 hours. The crude product was converted to its free base using a strong basic anion exchanger and subsequently purified by reverse phase flash chromatography using a gradient elution of water/methanol (0-100%).

Yield:	18 mg, (44%)
Chemical formula:	$C_{22}H_{33}N_7O_2S$
Molecular mass:	459.61 g/mol
Appearance:	Colourless solid
Internal code:	MST-582, ST-2776
Synthesis scheme:	Figure 128
Melting point:	149.2 °C
LC-MS-DAD purity:	97.9%
HR-MS (ESI-(+)):	m/z=460.2832 $[M+H^+]^+$ calculated: 460.2489
^{1}H NMR (300 MHz, MeOD):	δ 8.51 (s, 1H), 7.53 (d, *J* = 8.9 Hz, 2H), 6.92 (d, *J* = 8.9 Hz, 2H), 4.03 (t, *J* = 6.1 Hz, 2H), 3.70 – 3.60 (m, 2H), 3.16 (t, *J* = 5.6 Hz, 2H), 2.81 – 2.53 (m, 10H), 2.48 (s, 3H), 2.40 (s, 3H), 2.05 – 1.94 (m, 2H).
^{13}C NMR (75.5 MHz, MeOD):	δ 174.52, 168.20, 157.96, 155.95, 154.38, 130.89, 123.12, 114.21, 103.61, 65.96, 54.77, 54.12, 52.18, 44.42, 39.84, 38.11, 26.13, 13.01.

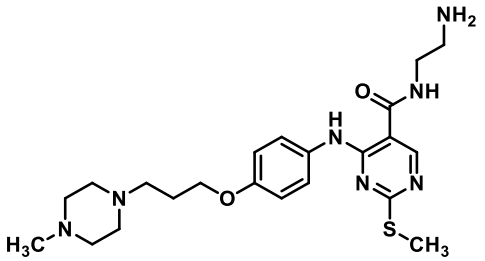

N-(3-Aminopropyl)-4-((4-(3-(4-methylpiperazin-1-yl)propoxy)phenyl)amino)-2-(methylthio)pyrimidine-5-carboxamide **(P28b)**

The Boc-deprotection protocol was carried out as described for compound **P6**.[674] Compound **P27b** (20 mg, 0.03 mmol, 1.0 eq.) was subjected to the reaction conditions for 24 hours. The crude product was converted to its free base using a strong basic anion exchanger and subsequently purified by reverse phase flash chromatography using a gradient elution of water/methanol (0-100%).

Yield:	12 mg, (73%)
Chemical formula:	$C_{23}H_{35}N_7O_2S$
Molecular mass:	473.64 g/mol
Appearance:	Colourless solid
Internal code:	MST-587
Synthesis scheme:	Figure 128
Melting point:	153.1 °C
LC-MS-DAD purity:	95.2%
HR-MS (ESI-(+)):	m/z=474.2662 $[M+H^+]^+$ calculated: 474.2646
^{1}H NMR (300 MHz, MeOD):	δ 8.37 (s, 1H), 7.43 (d, *J* = 9.0 Hz, 2H), 6.81 (d, *J* = 9.0 Hz, 2H), 3.93 (t, *J* = 6.1 Hz, 2H), 3.69 – 3.54 (m, 2H), 3.42 – 3.27 (m, 2H), 2.91 (t, *J* = 7.1 Hz, 2H), 2.72 – 2.41 (m, 10H), 2.38 (s, 3H), 2.30 (s, 3H), 1.95 – 1.84 (m, 2H).
^{13}C NMR (75.5 MHz, MeOD):	δ 174.50, 167.89, 157.96, 155.93, 154.24, 130.91, 123.10, 114.21, 103.65, 65.89, 54.64, 53.95, 51.90, 44.17, 36.98, 35.82, 27.57, 26.08, 13.02.

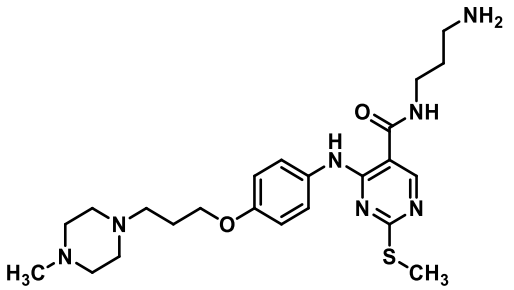

N-(4-Aminobutyl)-4-((4-(3-(4-methylpiperazin-1-yl)propoxy)phenyl)amino)-2-(methylthio)pyrimidine-5-carboxamide **(P28c)**

The Boc-deprotection protocol was carried out as described for compound **P6**.[674] Compound **P27c** (20 mg, 0.03 mmol, 1.0 eq.) was subjected to the reaction conditions for 24 hours. The crude product was converted to its free base using a strong basic anion exchanger and subsequently purified by reverse phase flash chromatography using a gradient elution of water/methanol (0-100%).

Yield:	8 mg, (51%)
Chemical formula:	$C_{24}H_{37}N_7O_2S$
Molecular mass:	487.67 g/mol
Appearance:	Colourless solid
Internal code:	MST-588, ST-2775
Synthesis scheme:	Figure 128
Melting point:	151.1 °C
LC-MS-DAD purity:	96.7%
HR-MS (ESI-(+)):	m/z=488.2991 $[M+H^+]^+$ calculated: 488.2802

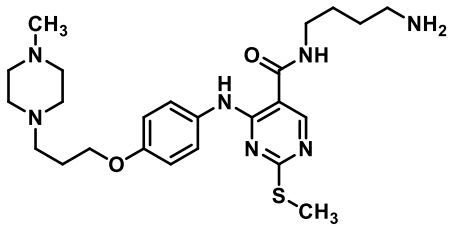

^{1}H NMR (300 MHz, MeOD):	δ 8.35 (s, 1H), 7.43 (d, *J* = 9.0 Hz, 2H), 6.82 (d, *J* = 9.0 Hz, 2H), 3.93 (t, *J* = 6.1 Hz, 2H), 3.34 – 3.29 (m, 2H), 2.89 – 2.82 (m, 2H), 2.50 – 2.45 (m, 12H), 2.39 (s, 3H), 2.20 (s, 3H), 1.93 – 1.84 (m, 2H), 1.62 – 1.59 (m, 2H).
^{13}C NMR (75.5 MHz, MeOD):	δ 174.33, 167.30, 158.00, 155.93, 154.00, 130.93, 123.01, 114.23, 104.01, 65.99, 54.82, 54.18, 52.28, 44.52, 39.20, 38.43, 26.15, 26.12, 25.24, 13.00.

N-(5-Aminopentyl)-4-((4-(3-(4-methylpiperazin-1-yl)propoxy)phenyl)amino)-2-(methylthio)pyrimidine-5-carboxamide **(P28d)**

The Boc-deprotection protocol was carried out as described for compound **P6**.[674] Compound **P27d** (30 mg, 0.05 mmol, 1.0 eq.) was subjected to the reaction conditions for 24 hours. The crude product was converted to its free base using a strong basic anion exchanger and subsequently purified by reverse phase flash chromatography using a gradient elution of water/methanol (0-100%).

Yield:	8 mg, (31%)
Chemical formula:	$C_{25}H_{39}N_7O_2S$
Molecular mass:	501.69 g/mol
Appearance:	Colourless solid
Internal code:	MST-583
Synthesis scheme:	Figure 128
Melting point:	155.8 °C
LC-MS-DAD purity:	97.4%
HR-MS (ESI-(+)):	m/z=502.2954 $[M+H^+]^+$ calculated: 502.2959

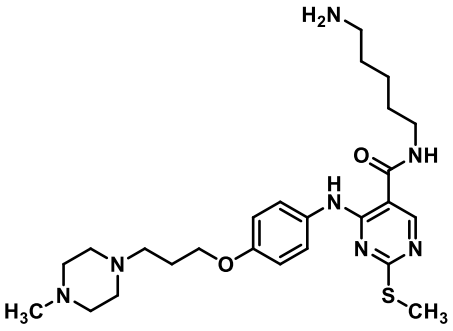

^{1}H NMR (300 MHz, MeOD):	δ 8.35 (s, 1H), 7.44 (d, *J* = 8.6 Hz, 2H), 6.83 (d, *J* = 8.6 Hz, 2H), 3.95 (t, *J* = 6.1 Hz, 2H), 3.29 (t, *J* = 7.0 Hz, 2H), 2.91 – 2.80 (m, 2H), 2.74 – 2.50 (m, 10H), 2.39 (s, 3H), 2.36 (s, 3H), 2.00 – 1.85 (m, 2H), 1.69 – 1.51 (m, 4H), 1.44 – 1.30 (m, 2H).
^{13}C NMR (75.5 MHz, MeOD):	δ 175.68, 168.63, 159.42, 157.34, 155.39, 132.35, 124.43, 115.64, 105.51, 67.40, 56.24, 55.58, 53.69, 45.93, 40.27, 36.76, 29.98, 29.98, 27.56, 24.89, 14.40.

N-(6-Aminohexyl)-4-((4-(3-(4-methylpiperazin-1-yl)propoxy)phenyl)amino)-2-(methylthio)pyrimidine-5-carboxamide **(P28e)**

The Boc-deprotection protocol was carried out as described for compound **P6**.[674] Compound **P27d** (50 mg, 0.08 mmol, 1.0 eq.) was subjected to the reaction conditions for 24 hours. The crude product was converted to its free base using a strong basic anion exchanger and subsequently purified by reverse phase flash chromatography using a gradient elution of water/methanol (0-100%).

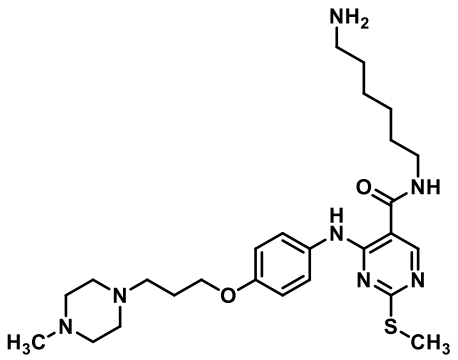

Yield:	38 mg, (90%)
Chemical formula:	$C_{26}H_{41}N_7O_2S$
Molecular mass:	515.72 g/mol
Appearance:	Colourless solid
Internal code:	MST-557, ST-2757
Synthesis scheme:	Figure 128
Melting point:	155.9 °C
LC-DAD purity:	97.1%
MS (ESI-(+)):	m/z=516.38 $[M+H^+]^+$ calculated: 516.3115
^{1}H NMR (300 MHz, MeOD):	δ 8.46 (s, 1H), 7.54 (d, *J* = 9.5 Hz, 2H), 6.91 (d, *J* = 9.5 Hz, 2H), 4.03 (t, *J* = 6.0 Hz, 2H), 3.78 – 3.58 (m, 2H), 3.40 – 3.34 (m, 2H), 2.99 – 2.64 (m, 12H), 2.53 (s, 3H), 2.49 (s, 3H), 2.06 – 1.96 (m, 2H), 1.74 – 1.62 (m, 2H), 1.50 – 1.41 (m, 4H).
^{13}C NMR (75.5 MHz, MeOD):	δ 175.54, 168.49, 159.32, 157.15, 155.39, 132.49, 124.26, 115.63, 105.56, 67.12, 55.72, 54.85, 52.54, 44.88, 40.62, 30.23, 28.60, 27.61, 27.35, 27.22, 23.44, 14.49.

N-(2-(3-(5,5-Difluoro-7,9-dimethyl-5*H*-5λ⁴,6λ⁴-dipyrrolo[1,2-*c*:2',1'-*f*][1,3,2]diazaborinin-3-yl)propanamido)ethyl)-4-((4-(3-(4-methylpiperazin-1-yl)propoxy)phenyl)amino)-2-(methylthio)pyrimidine-5-carboxamide **(P29a)**

The HATU coupling was carried out as described for compound **P3**.[644] Compound **P28a** (10 mg, 0.02 mmol, 1.0 eq.), DIPEA (3 µL, 0.02 mmol, 1.1 eq.), BODIPY-FL (6 mg, 0.02 mmol, 1.0 eq.) and HATU (9 mg, 0.02 mmol, 1.1 eq.) were subjected to the reaction conditions for 20 hours. The crude product was purified by column chromatography using a gradient elution of dichloromethane/methanol (sat. NH_3) (0-20%).

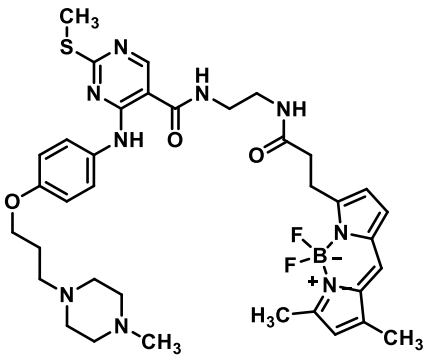

Yield:	4 mg, (26%)
Chemical formula:	$C_{36}H_{46}BF_2N_9O_3S$
Molecular mass:	733.69 g/mol
Appearance:	Red solid
Internal code:	MST-772, ST-2952
Synthesis scheme:	Figure 129
Melting point:	96.5 °C
LC-MS-DAD purity:	97.2%
HR-MS (ESI-(+)):	m/z=734.3569 $[M+H^+]^+$ calculated: 734.3578
^{1}H NMR (300 MHz, MeOD):	δ 8.34 (s, 1H), 7.48 (d, *J* = 9.1 Hz, 2H), 7.21 (s, 1H), 6.92 – 6.80 (m, 3H), 6.25 (d, *J* = 4.0 Hz, 1H), 6.11 (s, 1H), 3.99 (t, *J* = 6.1 Hz, 2H), 3.46 – 3.41 (m, 4H), 3.21 (t, *J* = 7.3 Hz, 2H), 2.71 – 2.48 (m, 15H), 2.46 (s, 3H), 2.30 (s, 3H), 2.18 (s, 3H), 2.01 – 1.93 (m, 2H).
^{13}C NMR (151 MHz, MeOD):	δ 174.08, 173.85, 167.47, 159.89, 157.77, 156.75, 155.68, 154.09, 144.32, 135.07, 133.38, 131.10, 128.00, 124.15, 122.77, 119.94, 116.15, 114.13, 103.88, 65.95, 54.80, 54.16, 52.24, 44.49, 39.20, 38.69, 34.56, 34.50, 26.17, 24.18, 13.07, 9.88.

N-(3-(3-(5,5-Difluoro-7,9-dimethyl-5*H*-5λ⁴,6λ⁴-dipyrrolo[1,2-*c*:2',1'-*f*][1,3,2]diazaborinin-3-yl)propanamido)propyl)-4-((4-(3-(4-methylpiperazin-1-yl)propoxy)phenyl)amino)-2-(methylthio)pyrimidine-5-carboxamide **(P29b)**

The HATU coupling was carried out as described for compound **P3**.[644] Compound **P28b** (10 mg, 0.02 mmol, 1.0 eq.), DIPEA (3 µL, 0.02 mmol, 1.1 eq.), BODIPY-FL (6 mg, 0.02 mmol, 1.0 eq.) and HATU (8 mg, 0.02 mmol, 1.1 eq.) were subjected to the reaction conditions for 20 hours. The crude product was purified by column chromatography using a gradient elution of dichloromethane/methanol (sat. NH_3) (0-20%).

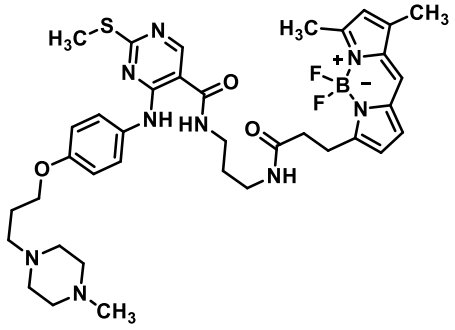

Yield:	4 mg, (28%)
Chemical formula:	$C_{37}H_{48}BF_2N_9O_3S$
Molecular mass:	747.72 g/mol
Appearance:	Red solid
Internal code:	MST-771, ST-2963
Synthesis scheme:	Figure 129
Melting point:	98.8 °C
LC-MS-DAD purity:	99.0%
HR-MS (ESI-(+)):	m/z=748.3745 $[M+H^+]^+$ calculated: 748.3735
^{1}H NMR (600 MHz, DMSO-d_6):	δ 11.10 (s, 1H), 8.72 (t, *J* = 5.6 Hz, 1H), 8.64 (s, 1H), 7.99 (t, *J* = 5.7 Hz, 1H), 7.66 (s, 1H), 7.54 (d, *J* = 6.2 Hz, 2H), 7.08 (d, *J* = 4.0 Hz, 1H), 6.91 (d, *J* = 6.2 Hz, 2H), 6.36 (d, *J* = 4.0 Hz, 1H), 6.28 (s, 1H), 3.97 (t, *J* = 6.4 Hz, 2H), 3.37 – 3.20 (m, 2H), 3.19 – 3.06 (m, 4H), 2.55 – 2.28 (m, 18H), 2.25 (s, 3H), 2.20 (s, 3H), 1.89 – 1.80 (m, 2H), 1.75 – 1.64 (m, 2H).
^{13}C NMR (151 MHz, DMSO-d_6):	δ 173.62, 171.35, 166.78, 159.59, 158.27, 158.01, 155.49, 155.44, 144.51, 134.92, 133.45, 131.42, 129.36, 125.76, 123.21, 120.71, 117.04, 114.96, 104.60, 66.40, 54.96, 54.75, 52.85, 45.83, 37.39, 36.93, 34.31, 29.45, 26.66, 24.51, 14.96, 14.16, 11.44.

N-(4-(3-(5,5-Difluoro-7,9-dimethyl-5*H*-5λ⁴,6λ⁴-dipyrrolo[1,2-*c*:2',1'-*f*][1,3,2]diazaborinin-3-yl)propanamido)butyl)-4-((4-(3-(4-methylpiperazin-1-yl)propoxy)phenyl)amino)-2-(methylthio)pyrimidine-5-carboxamide **(P29c)**

The HATU coupling was carried out as described for compound **P3**.[644] Compound **P28c** (8 mg, 0.02 mmol, 1.0 eq.), DIPEA (3 µL, 0.02 mmol, 1.1 eq.), BODIPY-FL (5 mg, 0.02 mmol, 1.0 eq.) and HATU (6 mg, 0.02 mmol, 1.1 eq.) were subjected to the reaction conditions for 20 hours. The crude product was purified by column chromatography using a gradient elution of dichloromethane/methanol (sat. NH_3) (0-20%).

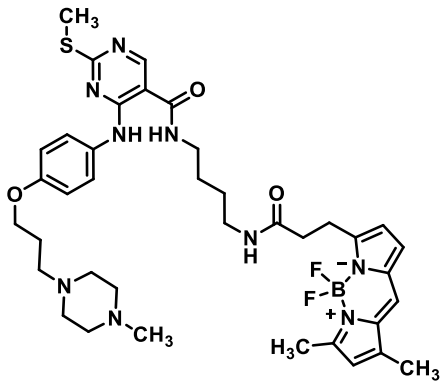

Yield:	7 mg, (58%)
Chemical formula:	$C_{38}H_{50}BF_2N_9O_3S$
Molecular mass:	761.75 g/mol
Appearance:	Red solid
Internal code:	MST-770,ST-2953
Synthesis scheme:	Figure 129
Melting point:	101.0 °C
LC-MS-DAD purity:	100%
HR-MS (ESI-(+)):	m/z=762.3872 $[M+H^+]^+$ calculated: 762.3891
^{1}H NMR (600 MHz, DMSO-d_6):	δ 11.14 (s, 1H), 8.71 (t, *J* = 5.5 Hz, 1H), 8.64 (s, 1H), 7.90 (t, *J* = 5.4 Hz, 1H), 7.66 (s, 1H), 7.54 (d, *J* = 7.4 Hz, 2H), 7.08 (d, *J* = 4.1 Hz, 1H), 6.91 (d, *J* = 7.4 Hz, 2H), 6.34 (d, *J* = 4.1 Hz, 1H), 6.28 (s, 1H), 3.97 (t, *J* = 6.4 Hz, 2H), 3.31 – 3.22 (m, 2H), 3.10 – 3.04 (m, 4H), 2.52 – 2.41(m, 16H), 2.25 (s, 3H), 2.23 (s, 3H), 1.89 – 1.79 (m, 2H), 1.58 – 1.51 (m, 2H), 1.49 – 1.40 (m, 2H), 1.37 – 1.29 (m, 2H).
^{13}C NMR (151 MHz, DMSO-d_6):	δ 173.57, 171.08, 166.72, 159.55, 158.38, 158.04, 155.48, 155.45, 144.48, 134.89, 133.44, 131.43, 129.34, 125.75, 123.20, 120.69, 117.03, 114.97, 104.58, 66.39, 54.86, 54.71, 52.73, 45.71, 38.93, 34.25, 29.31, 29.03, 26.63, 24.52, 24.37, 14.96, 14.15, 11.44.

N-(5-(3-(5,5-Difluoro-7,9-dimethyl-5*H*-5λ⁴,6λ⁴-dipyrrolo[1,2-*c*:2',1'-*f*][1,3,2]diazaborinin-3-yl)propanamido)pentyl)-4-((4-(3-(4-methylpiperazin-1-yl)propoxy)phenyl)amino)-2-(methylthio)pyrimidine-5-carboxamide **(P29d)**

The HATU coupling was carried out as described for compound **P3**.[644] Compound **P28d** (8 mg, 0.02 mmol, 1.0 eq.), DIPEA (3 µL, 0.02 mmol, 1.1 eq.), BODIPY-FL (5 mg, 0.02 mmol, 1.0 eq.) and HATU (7 mg, 0.02 mmol, 1.1 eq.) were subjected to the reaction conditions for 20 hours. The crude product was purified by column chromatography using a gradient elution of dichloromethane/methanol (sat. NH_3) (0-20%).

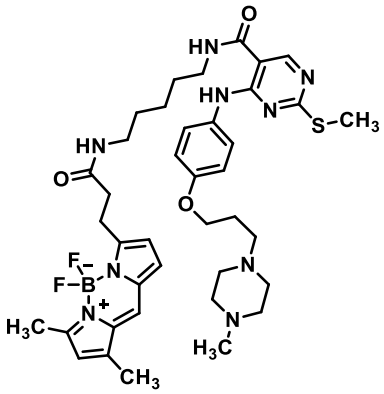

Yield:	5 mg, (44%)
Chemical formula:	$C_{39}H_{52}BF_2N_9O_3S$
Molecular mass:	775.77 g/mol
Appearance:	Red solid
Internal code:	MST-769,ST-2954
Synthesis scheme:	Figure 129
Melting point:	105.2 °C
LC-MS-DAD purity:	100%
HR-MS (ESI-(+)):	m/z=776.4115 $[M+H^+]^+$ calculated: 776.4048
^{1}H NMR (600 MHz, MeOD):	δ 8.42 (s, 1H), 7.53 (d, *J* = 9.1 Hz, 2H), 7.33 (s, 1H), 6.95 (d, *J* = 4.0 Hz, 1H), 6.89 (d, *J* = 9.1 Hz, 2H), 6.31 (d, *J* = 4.0 Hz, 1H), 6.16 (s, 1H),4.01 (t, *J* = 6.2 Hz, 2H), 3.38 – 3.33 (m, 4H), 3.27 – 3.21 (m, 6H), 2.71 – 2.52 (m, 10H), 2.51 – 2.44 (m, 6H), 2.32 (s, 3H), 2.23 (s, 3H), 2.01 – 1.94 (m, 2H), 1.64 – 1.53 (m, 4H).
^{13}C NMR (151 MHz, MeOD):	δ 174.11, 173.24, 167.06, 159.92, 157.88, 157.00, 155.76, 153.93, 135.09, 133.46, 131.04, 128.12, 124.24, 122.85, 122.85, 119.94, 116.29, 114.18, 104.11, 65.95, 54.81, 54.16, 52.25, 47.18, 44.50, 38.88, 38.61, 34.65, 26.42, 26.31, 26.16, 24.33, 13.50, 13.04, 9.83.

N-(6-(3-(5,5-Difluoro-7,9-dimethyl-5*H*-5λ⁴,6λ⁴-dipyrrolo[1,2-*c*:2',1'-*f*][1,3,2]diazaborinin-3-yl)propanamido)hexyl)-4-((4-(3-(4-methylpiperazin-1-yl)propoxy)phenyl)amino)-2-(methylthio)pyrimidine-5-carboxamide **(P29e)**

The HATU coupling was carried out as described for compound **P3**.[644] Compound **P28e** (30 mg, 0.06 mmol, 1.0 eq.), DIPEA (9 µL, 0.06 mmol, 1.1 eq.), BODIPY-FL (17 mg, 0.06 mmol, 1.0 eq.) and HATU (24 mg, 0.06 mmol, 1.1 eq.) were subjected to the reaction conditions for 20 hours. The crude product was purified by column chromatography using a gradient elution of dichloromethane/methanol (sat. NH_3) (0-20%).

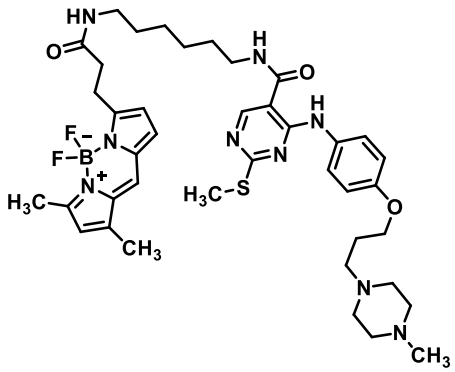

Yield:	34 mg, (72%)
Chemical formula:	$C_{40}H_{54}BF_2N_9O_3S$
Molecular mass:	789.80 g/mol
Appearance:	Red solid
Internal code:	MST-669
Synthesis scheme:	Figure 129
Melting point:	104.1 °C
LC-MS-DAD purity:	98.0%
HR-MS (ESI-(+)):	m/z=790.4204 $[M+H^+]^+$ calculated: 790.4204
^{1}H NMR (600 MHz, DMSO-d_6):	δ 11.15 (s, 1H), 8.84 (t, *J* = 5.6 Hz, 1H), 8.69 (s, 1H), 7.96 (t, *J* = 5.6 Hz, 1H), 7.68 (s, 1H), 7.54 (d, *J* = 8.9 Hz, 2H), 7.09 (d, *J* = 4.1 Hz, 1H), 6.92 (d, *J* = 8.9 Hz, 2H), 6.35 (d, *J* = 4.1 Hz, 1H), 6.29 (s, 1H), 3.98 (t, *J* = 6.4 Hz, 2H), 3.51 – 3.22 (m, 4H), 3.12 – 2.99 (m, 4H), 2.49 – 2.38 (m, 16H), 2.25 (s, 3H), 2.20 (s, 3H), 1.89 – 1.81 (m, 2H), 1.58 – 1.49 (m, 2H), 1.46 – 1.36 (m, 2H), 1.36 – 1.23 (m, 4H).
^{13}C NMR (151 MHz, MeOD):	δ 174.11, 173.24, 167.06, 159.92, 157.88, 157.00, 155.76, 153.93, 135.09, 133.46, 131.04, 128.12, 124.24, 122.85, 122.85, 119.94, 116.29, 114.18, 104.11, 65.95, 54.81, 54.16, 52.25, 47.18, 44.50, 40.41, 38.88, 38.61, 34.65, 26.42, 26.31, 26.16, 24.33, 13.50, 13.04, 9.83.

tert-Butyl(3-(4-((4-(3-(4-methylpiperazin-1-yl)propoxy)phenyl)amino)-2-(methylsulfinyl)pyrimidine-5-carboxamido)propyl)carbamate **(P30)**

The synthesis was based on a procedure previously described.[754] Compound **P27b** (270 mg, 0.47 mmol, 1.0 eq.) was dissolved in dichloromethane and the mixture was cooled in an ice bath. At this temperature, 3-chloroperoxybenzoic acid (81 mg, 0.47 mmol, 1.0 eq.) was added portion-wise and then the mixture was allowed to warm to room temperature and stirred for 2 hours. The solvent was removed under reduced pressure and the crude product was purified by column chromatography using a gradient elution of dichloromethane/methanol (sat. NH_3) (0-20%).

Yield:	55 mg, (20%)
Chemical formula:	$C_{28}H_{43}N_7O_5S$
Molecular mass:	589.76 g/mol
Appearance:	Colourless solid
Internal code:	MST-815,ST-2976
Synthesis scheme:	Figure 131
Melting point:	162.9 °C
LC-MS-DAD purity:	100%
HR-MS (ESI-(+)):	m/z=590.3122 $[M+H^+]^+$ calculated: 590.3119
^{1}H NMR (300 MHz, MeOD):	δ 8.46 (s, 1H), 7.54 (d, *J* = 9.1 Hz, 2H), 6.91 (d, *J* = 9.1 Hz, 2H), 4.05 (t, *J* = 6.2 Hz, 2H), 3.55 – 3.37 (m, 4H), 3.21 (s, 3H), 3.20 – 3.10 (m, 4H), 2.98 – 2.61 (m, 6H), 2.49 (s, 3H), 2.15 – 1.92 (m, 2H), 1.87 – 1.72 (m, 2H), 1.45 (s, 9H).
^{13}C NMR (75.5 MHz, MeOD):	δ 175.57, 168.56, 159.32, 158.65, 157.25, 155.40, 132.43, 124.35, 115.60, 105.53, 80.08, 67.12, 66.61, 66.58, 55.15, 38.94, 38.89, 38.05, 30.71, 28.82, 27.78, 14.47.

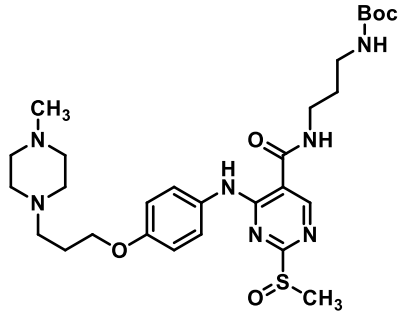

tert-Butyl-(3-(4-((4-(3-(4-methylpiperazin-1-yl)propoxy)phenyl)amino)-2-(methylsulfonyl)pyrimidine-5-carboxamido)propyl)carbamate **(P31)**

The Oxidation protocol was carried out as described for compound **P30**.[755] Compound **P27b** (128 mg, 0.22 mmol, 1.0 eq.) and 3-chloroperoxybenzoic acid (77 mg, 0.44 mmol, 2.0 eq.) were subjected to the reaction conditions for 2 hours. The crude product was purified by column chromatography using a gradient elution of dichloromethane/methanol (sat. NH_3) (0-20%).

Yield:	79 mg, (59%)
Chemical formula:	$C_{28}H_{43}N_7O_6S$
Molecular mass:	605.76 g/mol
Appearance:	Colourless solid
Internal code:	MST-808, ST-2966
Synthesis scheme:	Figure 131
Melting point:	171.8 °C
LC-MS-DAD purity:	100%
HR-MS (ESI-(+)):	m/z=606.3051 $[M+H^+]^+$ calculated: 606.3068
^{1}H NMR (600 MHz, DMSO-d_6):	δ 11.09 (s, 1H), 8.80 (t, *J* = 5.6 Hz, 1H), 8.66 (s, 1H), 7.54 (d, *J* = 8.4 Hz, 2H), 7.07 – 6.80 (m, 3H), 4.12 – 4.02 (m, 4H), 4.01 – 3.90 (m, 2H), 3.41 – 3.35 (m, 4H), 3.31 – 3.23 (m, 2H), 3.16 (s, 3H), 3.03 – 2.88 (m, 4H), 2.46 (s, 3H), 2.33 – 2.23 (m, 2H), 1.68 – 1.61 (m, 2H), 1.37 (s, 9H).
^{13}C NMR (151 MHz, DMSO-d_6):	δ 173.59, 166.75, 158.02, 156.09, 155.51, 155.32, 131.55, 123.26, 115.08, 104.63, 77.98, 67.51, 66.41, 60.94, 60.03, 59.55, 38.19, 37.35, 29.72, 28.73, 22.53, 14.16.

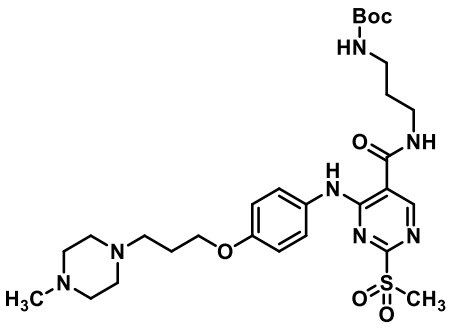

N-(3-Aminopropyl)-4-((4-(3-(4-methylpiperazin-1-yl)propoxy)phenyl)amino)-2-(methylsulfinyl)pyrimidine-5-carboxamide **(P32)**

The Boc-deprotection protocol was carried out as described for compound **P6**.[674] Compound **P30** (40 mg, 0.07 mmol, 1.0 eq.) was subjected to the reaction conditions for 24 hours. The crude product was converted to its free base using a strong basic anion exchanger and subsequently purified by reverse phase flash chromatography using a gradient elution of water/methanol (0-100%).

Yield:	25 mg, (73%)
Chemical formula:	$C_{23}H_{35}N_7O_3S$
Molecular mass:	489.64 g/mol
Appearance:	Colourless solid
Internal code:	MST-824, ST-2988
Synthesis scheme:	Figure 132
Melting point:	152.5 °C
LC-MS-DAD purity:	100%
HR-MS (ESI-(+)):	m/z=490.2608 $[M+H^+]^+$ calculated: 490.2595

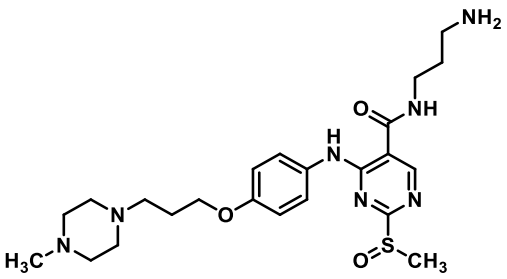

^{1}H NMR (600 MHz, MeOD):	δ 8.51 (s, 1H), 7.54 (d, *J* = 9.0 Hz, 2H), 6.94 (d, *J* = 9.0 Hz, 2H), 4.06 (t, *J* = 6.1 Hz, 2H), 3.58 – 3.46 (m, 4H), 3.27 – 3.20 (m, 5H), 3.05 (t, *J* = 7.4 Hz, 2H), 2.94 – 2.78 (m, 4H), 2.68 (t, *J* = 7.4 Hz, 2H), 2.50 (s, 3H), 2.19 – 1.93 (m, 4H).
^{13}C NMR (151 MHz, MeOD):	δ 174.53, 167.93, 157.96, 155.99, 154.27, 130.86, 123.13, 114.22, 103.61, 65.72, 65.08, 65.07, 53.70, 46.99, 37.01, 35.76, 27.46, 26.34, 13.02.

N-(3-Aminopropyl)-4-((4-(3-(4-methylpiperazin-1-yl)propoxy)phenyl)amino)-2-(methylsulfonyl)pyrimidine-5-carboxamide **(P33)**

The Boc-deprotection protocol was carried out as described for compound **P6**.[674] Compound **P31** (50 mg, 0.08 mmol, 1.0 eq.) was subjected to the reaction conditions for 24 hours. The crude product was converted to its free base using a strong basic anion exchanger and subsequently purified by reverse phase flash chromatography using a gradient elution of water/methanol (0-100%).

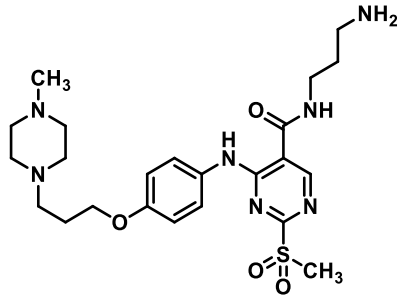

Yield:	35 mg, (87%)
Chemical formula:	$C_{23}H_{35}N_7O_4S$
Molecular mass:	505.64 g/mol
Appearance:	Colourless solid
Internal code:	MST-821, ST-2989
Synthesis scheme:	Figure 132
Melting point:	153.8 °C
LC-MS-DAD purity:	100%
HR-MS (ESI-(+)):	m/z=506.2539 $[M+H^+]^+$ calculated: 506.2544
^{1}H NMR (300 MHz, MeOD):	δ 8.50 (s, 1H), 7.54 (d, *J* = 8.8 Hz, 2H), 6.95 (d, *J* = 8.8 Hz, 2H), 4.25 – 4.04 (m, 6H), 3.69 – 3.58 (m, 2H), 3.49 (t, *J* = 6.5 Hz, 2H), 3.35 (s, 3H), 3.31 – 3.23 (m, 4H), 3.03 (t, *J* = 7.3 Hz, 2H), 2.47 (s, 3H), 2.46 – 2.34 (m, 2H), 2.05 – 1.92 (m, 2H).
^{13}C NMR (75.5 MHz, MeOD):	δ 175.92, 169.31, 159.35, 156.95, 155.69, 132.65, 124.49, 115.69, 105.03, 69.28, 66.57, 61.50, 60.11, 60.04, 38.43, 37.17, 28.87, 23.56, 14.44.

N-(3-(3-(5,5-Difluoro-7,9-dimethyl-5*H*-5λ⁴,6λ⁴-dipyrrolo[1,2-*c*:2',1'-*f*][1,3,2]diazaborinin-3-yl)propanamido)propyl)-4-((4-(3-(4-methylpiperazin-1-yl)propoxy)phenyl)amino)-2-(methylsulfinyl)pyrimidine-5-carboxamide **(P34)**

The HATU coupling was carried out as described for compound **P3**.[644] Compound **P32** (15 mg, 0.03 mmol, 1.0 eq.), DIPEA (5 µL, 0.03 mmol, 1.1 eq.), BODIPY-FL (9 mg, 0.03 mmol, 1.0 eq.) and HATU (13 mg, 0.03 mmol, 1.1 eq.) were subjected to the reaction conditions for 24 hours. The crude product was purified by column chromatography using a gradient elution of dichloromethane/methanol (sat. NH_3) (0-20%).

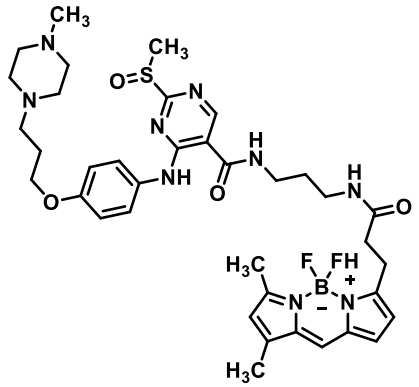

Yield:	8 mg, (34%)
Chemical formula:	$C_{37}H_{48}BF_2N_9O_4S$
Molecular mass:	763.72 g/mol
Appearance:	Red solid
Internal code:	MST-832
Synthesis scheme:	Figure 133
Melting point:	145.2 °C
LC-MS-DAD purity:	96.8%
HR-MS (ESI-(+)):	m/z=764.3663 $[M+H^+]^+$ calculated: 764.3684
^{1}H NMR (600 MHz,$CDCl_3$):	δ 10.94 (s, 1H), 8.53 (s, 1H), 7.98 (t, *J* = 6.1 Hz, 1H), 7.49 (d, *J* = 9.9 Hz, 2H), 7.01 (s, 1H), 6.81 (d, *J* = 4.0 Hz, 1H), 6.77 (d, *J* = 9.9 Hz, 2H), 6.33 (t, *J* = 6.7 Hz, 1H), 6.22 (d, *J* = 4.0 Hz, 1H), 6.05 (s, 1H), 4.32 – 4.24 (m, 2H), 4.23 – 4.15 (m, 2H), 4.03 (t, *J* = 5.7 Hz, 2H), 3.53 – 3.43 (m, 2H), 3.28 (s, 3H), 3.26 – 3.14 (m, 6H), 3.13 – 3.06 (m, 4H), 2.64 (t, *J* = 7.3 Hz, 2H), 2.49 (s, 3H), 2.43 (s, 3H), 2.41 – 2.35 (m, 2H), 2.17 (s, 3H), 1.62 – 1.51 (m, 2H).
^{13}C NMR (151 MHz, $CDCl_3$):	δ 174.52, 173.03, 166.98, 160.65, 158.12, 156.74, 154.78, 154.56, 135.24, 133.29, 131.96, 131.55, 128.22, 123.87, 123.11, 120.67, 117.43, 114.38, 104.22, 68.75, 65.53, 61.11, 60.31, 59.62, 36.13, 35.88, 35.35, 29.22, 24.80, 22.63, 15.00, 14.33, 11.35.

N-(3-(3-(5,5-Difluoro-7,9-dimethyl-5*H*-5λ⁴,6λ⁴-dipyrrolo[1,2-*c*:2',1'-*f*][1,3,2]diazaborinin-3-yl)propanamido)propyl)-4-((4-(3-(4-methylpiperazin-1-yl)propoxy)phenyl)amino)-2-(methylsulfonyl)pyrimidine-5-carboxamide **(P35)**

The HATU coupling was carried out as described for compound **P3**.[644] Compound **P33** (30 mg, 0.06 mmol, 1.0 eq.), DIPEA (10 µL, 0.07 mmol, 1.1 eq.), BODIPY-FL (18 mg, 0.06 mmol, 1.0 eq.) and HATU (27 mg, 0.07 mmol, 1.1 eq.) were subjected to the reaction conditions for 24 hours. The crude product was purified by column chromatography using a gradient elution of dichloromethane/methanol (sat. NH_3) (0-20%).

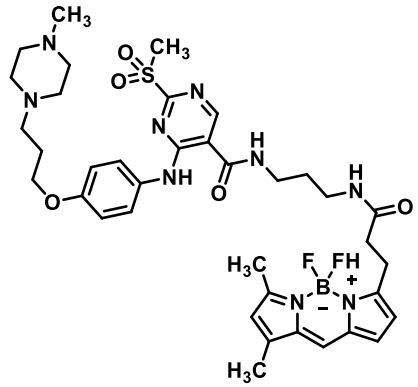

Yield:	13 mg, (27%)
Chemical formula:	$C_{37}H_{48}BF_2N_9O_5S$
Molecular mass:	779.72 g/mol
Appearance:	Red solid
Internal code:	MST-833
Synthesis scheme:	Figure 133
Melting point:	153.7 °C
LC-MS-DAD purity:	100%
HR-MS (ESI-(+)):	m/z=780.3657 $[M+H^+]^+$ calculated: 780.3633
^{1}H NMR (600 MHz,$CDCl_3$):	δ 11.27 (s, 1H), 8.91 (s, 1H), 8.62 – 8.39 (m, 1H), 7.64 – 7.52 (m, 2H), 7.09 (s, 1H), 6.92 – 6.82 (m, 3H), 6.29 (d, *J* = 4.0 Hz, 1H), 6.24 (t, *J* = 6.8 Hz, 1H), 6.13 (s, 1H), 4.41 – 4.21 (m, 4H), 4.17 – 4.06 (m, 2H), 3.67 – 3.52 (m, 2H), 3.35 (s, 3H), 3.34 – 3.26 (m, 6H), 3.26 (s, 3H), 3.20 – 3.15 (m, 4H), 2.78 – 2.70 (m, 2H), 2.56 (s, 3H), 2.50 – 2.43 (m, 2H), 2.25 (s, 3H), 1.70 – 1.61 (m, 2H).
^{13}C NMR (151 MHz, MeOD):	δ 174.17, 173.36, 167.13, 163.45, 157.94, 155.45, 154.10, 144.41, 135.12, 133.50, 131.40, 131.06, 128.24, 124.39, 123.00, 120.01, 116.32, 114.29, 104.18, 67.88, 65.20, 60.11, 58.72, 58.64, 39.08, 36.49, 35.56, 30.27, 28.71, 22.16, 13.53, 13.03, 9.84.

10.5.4 VUF-10558-based *N*-linked ligands

6-Chloroquinazoline-2,4(1*H*,3*H*)-dione **(47)**

The synthesis was based on a procedure previously described.[760] 2-Amino-5-chlorobenzoic acid (15525 mg, 90.5 mmol, 1.0 eq.) and urea (27185 mg, 452.5 mmol, 5.0 eq.) were combined and melted at 200 °C without solvent for two hours. The molten mixture was suspended in water at 50 °C for one hour, filtered while warm, and the residue was lyophilized. The crude product was used without further purification.

Yield:	14722 mg, (83%)
Chemical formula:	$C_8H_5ClN_2O_2$
Molecular mass:	196.59 g/mol
Appearance:	Yellow solid
Internal code:	MST-039
Synthesis scheme:	Figure 136
^{1}H NMR (300 MHz, DMSO-d_6):	δ 11.44 (s, 1H), 11.27 (s, 1H), 7.91 – 7.74 (m, 1H), 7.74 – 7.58 (m, 1H), 7.25 – 6.95 (m, 1H).

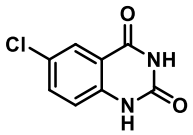

2,4,6-Trichloroquinazoline **(SM4)**

The synthesis was based on a procedure previously described.[761] Compound **47** (14000 mg, 71.4 mmol, 1.0 eq.) was dissolved in phosphoryl chloride. Triethylamine (9879 µL, 71.4 mmol, 1.0 eq.) and *N*,*N*-diethyl aniline (11439 µL, 71.4 mmol, 1.0 eq.) were added dropwise, and the mixture was heated to 110 °C for 20 hours. The reaction mixture was poured onto ice, and the aqueous phase was extracted three times with diethyl ether. The combined organic phases were dried over magnesium sulphate, filtered, and concentrated under reduced pressure. The crude product was purified by flash column chromatography using a gradient elution of ethyl acetate/hexane (0-100%).

Yield:	12003 mg, (72%)
Chemical formula:	$C_8H_3Cl_3N_2$
Molecular mass:	233.48 g/mol
Appearance:	Yellow solid
Internal code:	MST-046
Synthesis scheme:	Figure 137
^{1}H NMR (300 MHz, $CDCl_3$):	δ 8.19 – 8.13 (m, 1H), 7.94 – 7.80 (m, 2H).

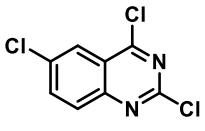

tert-Butyl (2-((2,6-dichloroquinazolin-4-yl)amino)ethyl)carbamate **(48a)**

The synthesis was based on a procedure previously described.[761] **SM4** (270 mg, 1.16 mmol, 1.0 eq.) and triethylamine (179 µL, 1.27 mmol, 1.1 eq.) were dissolved in tetrahydrofuran, and a solution of compound **L9** (204 mg, 1.27 mmol, 1.1 eq.) in tetrahydrofuran was added. The reaction mixture was stirred at room temperature for 20 hours. The solvent was removed under reduced pressure and the crude product was purified by flash chromatography using a gradient elution of ethyl acetate/hexane (0-100%).

Yield:	207 mg, (50%)
Chemical formula:	$C_{15}H_{18}Cl_2N_4O_2$
Molecular mass:	357.24 g/mol
Appearance:	Yellow solid
Internal code:	MST-378
Synthesis scheme:	Figure 139
^{1}H NMR (300 MHz, $CDCl_3$):	δ 8.05 – 7.98 (m, 1H), 7.86 – 7.83 (m, 1H), 7.70 – 7.59 (m, 2H), 5.26 – 5.14 (m, 1H), 3.76 – 3.63 (m, 2H), 3.59 – 3.49 (m, 2H), 1.46 (s, 9H).

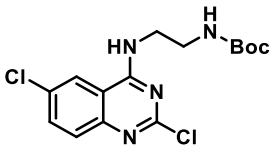

tert-Butyl (3-((2,6-dichloroquinazolin-4-yl)amino)propyl)carbamate **(48b)**

The nucleophilic aromatic substitution was carried out as described for compound **48a**.[761] Compound **SM4** (297 mg, 1.27 mmol, 1.0 eq.), triethylamine (194 µL, 1.40 mmol, 1.1 eq.) and compound **L10** (244 mg, 1.40 mmol, 1.1 eq.) were subjected to the reaction conditions for 20 hours. The crude product was purified by flash chromatography using a gradient elution of ethyl acetate/hexane (0-100%).

Yield:	212 mg, (45%)
Chemical formula:	$C_{16}H_{20}Cl_2N_4O_2$
Molecular mass:	371.26 g/mol
Appearance:	Yellow solid
Internal code:	MST-379
Synthesis scheme:	Figure 139
^{1}H NMR (300 MHz, $CDCl_3$):	δ 8.13 – 8.05 (m, 1H), 7.93 – 7.89 (m, 1H), 7.67 – 7.57 (m, 2H), 5.12 – 4.86 (m, 1H), 3.83 – 3.60 (m, 2H), 3.58 – 3.50 (m, 2H), 2.10 – 1.78 (m, 2H), 1.42 (s, 9H).

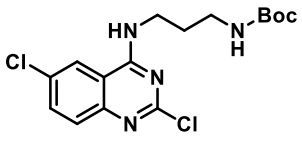

tert-Butyl (4-((2,6-dichloroquinazolin-4-yl)amino)butyl)carbamate **(48c)**

The nucleophilic aromatic substitution was carried out as described for compound **48a**.[761] Compound **SM4** (300 mg, 1.29 mmol, 1.0 eq.), triethylamine (196 µL, 1.42 mmol, 1.1 eq.) and compound **L11** (266 mg, 1.42 mmol, 1.1 eq.) were subjected to the reaction conditions for 20 hours. The crude product was purified by flash chromatography using a gradient elution of ethyl acetate/hexane (0-100%).

Yield:	174 mg, (35%)
Chemical formula:	$C_{17}H_{22}Cl_2N_4O_2$
Molecular mass:	385.29 g/mol
Appearance:	Yellow solid
Internal code:	MST-395
Synthesis scheme:	Figure 139
^{1}H NMR (300 MHz, $CDCl_3$):	δ 8.23 – 8.10 (m, 1H), 7.82 – 7.71 (m, 1H), 7.72 – 7.53 (m, 2H), 4.96 – 4.85 (m, 1H), 3.79 – 3.62 (m, 2H), 3.29 – 3.15 (m, 2H), 1.88 – 1.55 (m, 4H), 1.49 (s, 9H).

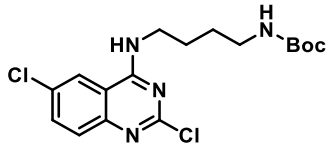

tert-Butyl (5-((2,6-dichloroquinazolin-4-yl)amino)pentyl)carbamate **(48d)**

The nucleophilic aromatic substitution was carried out as described for compound **48a**.[761] Compound **SM4** (300 mg, 1.29 mmol, 1.0 eq.), triethylamine (196 µL, 1.42 mmol, 1.1 eq.) and compound **L12** (286 mg, 1.42 mmol, 1.1 eq.) were subjected to the reaction conditions for 20 hours. The crude product was purified by flash chromatography using a gradient elution of ethyl acetate/hexane (0-100%).

Yield:	216 mg, (42%)
Chemical formula:	$C_{18}H_{24}Cl_2N_4O_2$
Molecular mass:	399.32 g/mol
Appearance:	Yellow solid
Internal code:	MST-396
Synthesis scheme:	Figure 139
^{1}H NMR (300 MHz, $CDCl_3$):	δ 7.90 – 7.84 (m, 1H), 7.63 – 7.49 (m, 2H), 7.01 – 6.95 (m, 1H), 4.78 – 4.61 (m, 1H), 3.62 – 3.49 (m, 2H), 3.11 – 2.97 (m, 2H), 1.73 – 1.59 (m, 2H), 1.53 – 1.41 (m, 4H), 1.36 (s, 9H).

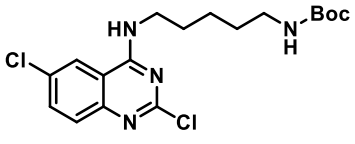

tert-Butyl (6-((2,6-dichloroquinazolin-4-yl)amino)hexyl)carbamate **(48e)**

The nucleophilic aromatic substitution was carried out as described for compound **48a**.[761] Compound **SM4** (300 mg, 1.29 mmol, 1.0 eq.), triethylamine (196 µL, 1.42 mmol, 1.1 eq.) and compound **L13** (306 mg, 1.42 mmol, 1.1 eq.) were subjected to the reaction conditions for 20 hours. The crude product was purified by flash chromatography using a gradient elution of ethyl acetate/hexane (0-100%).

Yield:	330 mg, (62%)
Chemical formula:	$C_{19}H_{26}Cl_2N_4O_2$
Molecular mass:	413.34 g/mol
Appearance:	Yellow solid
Internal code:	MST-399
Synthesis scheme:	Figure 139
^{1}H NMR (300 MHz, $CDCl_3$):	δ 8.03 – 7.98 (m, 1H), 7.59 – 7.49 (m, 2H), 7.35 (t, *J* = 5.8 Hz, 1H), 4.72 (t, *J* = 6.2 Hz, 1H), 3.61 – 3.47 (m, 2H), 3.16 – 2.92 (m, 2H), 1.71 – 1.52 (m, 2H), 1.49 – 1.12 (m, 15H).

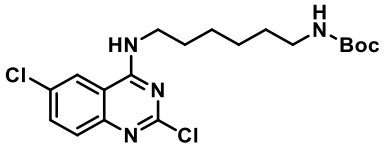

tert-Butyl (2-(2-((2,6-dichloroquinazolin-4-yl)amino)ethoxy)ethyl)carbamate **(48f)**

The nucleophilic aromatic substitution was carried out as described for compound **48a**.[761] Compound **SM4** (223 mg, 0.96 mmol, 1.0 eq.), triethylamine (145 µL, 1.05 mmol, 1.1 eq.) and compound **L14** (231 mg, 1.05 mmol, 1.1 eq.) were subjected to the reaction conditions for 20 hours. The crude product was purified by flash chromatography using a gradient elution of ethyl acetate/hexane (0-100%).

Yield:	150 mg, (39%)
Chemical formula:	$C_{17}H_{22}Cl_2N_4O_3$
Molecular mass:	401.29 g/mol
Appearance:	Yellow solid
Internal code:	MST-401
Synthesis scheme:	Figure 139
^{1}H NMR (300 MHz, $CDCl_3$):	δ 7.94 – 7.86 (m, 1H), 7.62 – 7.44 (m, 2H), 7.32 – 7.26 (m, 1H), 5.12 – 5.01 (m, 1H), 3.84 – 3.71 (m, 2H), 3.74 – 3.62 (m, 2H), 3.56 – 3.41 (m, 2H), 3.34 – 3.17 (m, 2H), 1.34 (s, 9H).

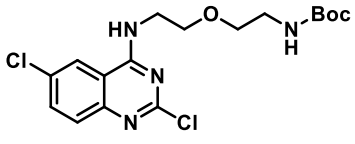

tert-Butyl-(2-(2-(2-((2,6-dichloroquinazolin-4-yl)amino)ethoxy)ethoxy)ethyl)carbamate **(48g)**

The nucleophilic aromatic substitution was carried out as described for compound **48a**.[761] Compound **SM4** (600 mg, 2.57 mmol, 1.0 eq.), triethylamine (391 µL, 2.83 mmol, 1.1 eq.) and compound **L15** (701 mg, 2.83 mmol, 1.1 eq.) were subjected to the reaction conditions for 20 hours. The crude product was purified by flash chromatography using a gradient elution of ethyl acetate/hexane (0-100%).

Yield:	400 mg, (35%)
Chemical formula:	$C_{19}H_{26}Cl_2N_4O_4$
Molecular mass:	445.34 g/mol
Appearance:	Yellow solid
Internal code:	MST-433
Synthesis scheme:	Figure 139
^{1}H NMR (300 MHz, $CDCl_3$):	δ 8.11 – 8.05 (m, 1H), 7.65 – 7.48 (m, 2H), 7.40 – 7.31 (m, 1H), 5.19 – 5.03 (m, 1H), 3.84 – 3.76 (m, 2H), 3.75 – 3.65 (m, 4H), 3.52 – 3.41 (m, 4H), 3.35 – 3.18 (m, 2H), 1.37 (s, 9H).

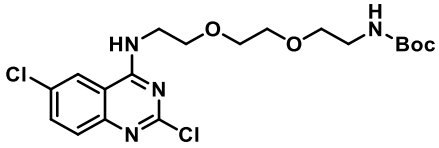

tert-Butyl-(2-(2-(2-(2-((2,6-dichloroquinazolin-4-yl)amino)ethoxy)ethoxy)ethoxy)ethyl)carbamate **(48h)**

The nucleophilic aromatic substitution was carried out as described for compound **48a**.[761] Compound **SM4** (300 mg, 1.29 mmol, 1.0 eq.), triethylamine (196 µL, 1.42 mmol, 1.1 eq.) and compound **L16** (414 mg, 1.42 mmol, 1.1 eq.) were subjected to the reaction conditions for 20 hours. The crude product was purified by flash chromatography using a gradient elution of ethyl acetate/hexane (0-100%).

Yield:	303 mg, (48%)
Chemical formula:	$C_{21}H_{30}Cl_2N_4O_5$
Molecular mass:	489.39 g/mol
Appearance:	Yellow solid
Internal code:	MST-403
Synthesis scheme:	Figure 139
^{1}H NMR (300 MHz, $CDCl_3$):	δ 7.99 – 7.78 (m, 1H), 7.70 – 7.43 (m, 2H), 7.42 – 7.22 (m, 1H), 5.13 – 5.07 (m, 1H), 3.92 – 3.69 (m, 2H), 3.71 – 3.39 (m, 10H), 3.34 – 3.15 (m, 2H), 3.03 – 2.70 (m, 2H), 1.35 (s, 9H).

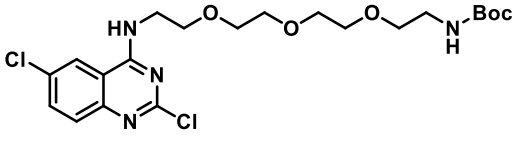

tert-Butyl-(2-((6-chloro-2-(4-methylpiperazin-1-yl)quinazolin-4-yl)amino)ethyl)carbamate **(P36a)**

The synthesis was based on a procedure previously described.[761] Compound **48a** (136 mg, 0.38 mmol, 1.0 eq.) and DIPEA (80 µL, 0.46 mmol, 1.2 eq.) were dissolved in isopropanol, and *N*-methylpiperazine (51 µL, 0.46 mmol, 1.1 eq.) was added. The reaction mixture was heated to 90 °C and stirred at this temperature for 20 hours. The solvent was removed under reduced pressure and the crude product was purified by column chromatography using a gradient elution of dichloromethane/methanol (sat. NH_3) (0-20%).

Yield:	57 mg, (36%)
Chemical formula:	$C_{20}H_{29}ClN_6O_2$
Molecular mass:	420.94 g/mol
Appearance:	Colourless solid
Internal code:	MST-392, ST-2599
Synthesis scheme:	Figure 140
Melting point:	137.2 °C
LC-DAD purity:	100%
MS (ESI-(+)):	m/z=421.29 $[M+H^+]^+$ calculated: 421.2113
^{1}H NMR (300 MHz, $CDCl_3$):	δ 7.54 – 7.47 (m, 1H), 7.39 – 7.24 (m, 2H), 6.77 (t, *J* = 6.5 Hz, 1H), 5.18 (t, *J* = 4.9 Hz, 1H), 3.88 – 3.79 (m, 4H), 3.61 – 3.54 (m, 2H), 3.48 – 3.38 (m, 2H), 2.43 – 2.29 (m, 4H), 2.26 (s, 3H), 1.38 (s, 9H).
^{13}C NMR (75.5 MHz, $CDCl_3$):	δ 159.49, 159.00, 157.95, 150.63, 132.91, 127.18, 125.75, 120.93, 111.25, 80.31, 55.19, 46.28, 43.80, 43.63, 39.92, 28.40.

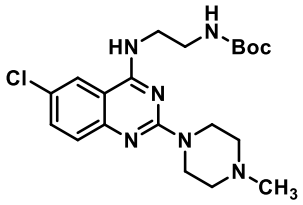

tert-Butyl-(3-((6-chloro-2-(4-methylpiperazin-1-yl)quinazolin-4-yl)amino)propyl)carbamate **(P36b)**

The nucleophilic aromatic substitution was carried out as described for compound **P36a**.[761] Compound **48b** (214 mg, 0.58 mmol, 1.0 eq.), DIPEA (108 µL, 0.64 mmol, 1.1 eq.) and *N*-methylpiperazine (71 µL, 0.64 mmol, 1.1 eq.) were subjected to the reaction conditions for 20 hours. The crude product was purified by column chromatography using a gradient elution of dichloromethane/methanol (sat. NH_3) (0-20%).

Yield:	96 mg, (38%)
Chemical formula:	$C_{21}H_{31}ClN_6O_2$
Molecular mass:	434.97 g/mol
Appearance:	Colourless solid
Internal code:	MST-398, ST-2603
Synthesis scheme:	Figure 140
Melting point:	134.3 °C
LC-DAD purity:	98.6%
MS (ESI-(+)):	m/z=435.29 $[M+H^+]^+$ calculated: 435.2270
^{1}H NMR (300 MHz, $CDCl_3$):	δ 7.68 – 7.61 (m, 1H), 7.37 – 7.24 (m, 2H), 6.94 – 6.88 (m, 1H), 5.10 – 4.99 (m, 1H), 3.91 – 3.80 (m, 4H), 3.61 – 3.45 (m, 2H), 3.21 – 3.09 (m, 2H), 2.45 – 2.36 (m, 4H), 2.26 (s, 3H), 1.78 – 1.63 (m, 2H), 1.39 (s, 9H).
^{13}C NMR (75.5 MHz, $CDCl_3$):	δ 159.30, 158.91, 157.01, 150.42, 132.83, 126.95, 125.70, 121.12, 111.49, 79.72, 55.32, 55.13, 46.21, 43.80, 37.45, 29.49, 28.44.

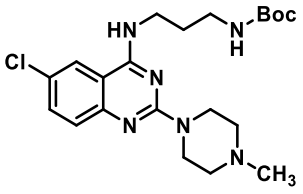

tert-Butyl-(4-((6-chloro-2-(4-methylpiperazin-1-yl)quinazolin-4-yl)amino)butyl)carbamate **(P36c)**

The nucleophilic aromatic substitution was carried out as described for compound **P36a**.[761] Compound **48c** (190 mg, 0.49 mmol, 1.0 eq.), DIPEA (101 µL, 0.54 mmol, 1.1 eq.) and *N*-methylpiperazine (60 µL, 0.54 mmol, 1.1 eq.) were subjected to the reaction conditions for 20 hours. The crude product was purified by column chromatography using a gradient elution of dichloromethane/methanol (sat. NH_3) (0-20%).

Yield:	62 mg, (28%)
Chemical formula:	$C_{22}H_{33}ClN_6O_2$
Molecular mass:	449.00 g/mol
Appearance:	Colourless solid
Internal code:	MST-405, ST-2600
Synthesis scheme:	Figure 140
Melting point:	131.7 °C
LC-DAD purity:	100%
MS (ESI-(+)):	m/z=449.29 $[M+H^+]^+$ calculated: 449.2426

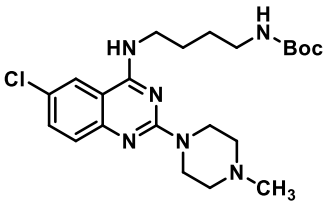

^{1}H NMR (300 MHz, $CDCl_3$):	δ 7.66 – 7.60 (m, 1H), 7.39 – 7.25 (m, 2H), 6.26 (t, *J* = 5.6 Hz, 1H), 4.72 (t, *J* = 6.9 Hz, 1H), 3.89 – 3.79 (m, 4H), 3.59 – 3.47 (m, 2H), 3.17 – 3.04 (m, 2H), 2.45 – 2.38 (m, 4H), 2.26 (s, 3H), 1.72 – 1.47 (m, 4H), 1.39 (s, 9H).
^{13}C NMR (75.5 MHz, $CDCl_3$):	δ 159.25, 159.02, 156.47, 150.70, 132.80, 127.19, 125.58, 120.89, 111.35, 79.50, 55.18, 54.20, 46.27, 43.80, 41.07, 39.94, 28.46, 25.49.

tert-Butyl-(5-((6-chloro-2-(4-methylpiperazin-1-yl)quinazolin-4-yl)amino)pentyl)carbamate **(P36d)**

The nucleophilic aromatic substitution was carried out as described for compound **P36a**.[761] Compound **48d** (120 mg, 0.29 mmol, 1.0 eq.), DIPEA (54 µL, 0.32 mmol, 1.1 eq.) and *N*-methylpiperazine (36 µL, 0.32 mmol, 1.1 eq.) were subjected to the reaction conditions for 20 hours. The crude product was purified by column chromatography using a gradient elution of dichloromethane/methanol (sat. NH_3) (0-20%).

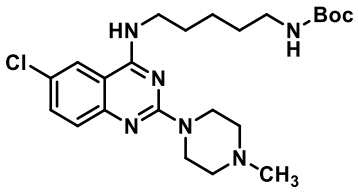

Yield:	124 mg, (92%)
Chemical formula:	$C_{23}H_{35}ClN_6O_2$
Molecular mass:	463.02 g/mol
Appearance:	Colourless solid
Internal code:	MST-411, ST-2605
Synthesis scheme:	Figure 140
Melting point:	128.1 °C
LC-DAD purity:	100%
MS (ESI-(+)):	m/z=463.29 $[M+H^+]^+$ calculated: 463.2583
^{1}H NMR (300 MHz, $CDCl_3$):	δ 7.52 – 7.45 (m, 1H), 7.38 – 7.24 (m, 2H), 5.83 – 5.77 (m, 1H), 4.67 – 4.61 (m, 1H), 3.88 – 3.79 (m, 4H), 3.54 – 3.40 (m, 2H), 3.11 – 2.98 (m, 2H), 2.50 – 2.36 (m, 4H), 2.26 (s, 3H), 1.68 – 1.53 (m, 2H), 1.52 – 1.18 (m, 13H).
^{13}C NMR (75.5 MHz, $CDCl_3$):	δ 159.15, 159.04, 156.16, 150.76, 132.81, 127.30, 125.50, 120.52, 111.20, 79.18, 55.16, 46.26, 43.79, 41.09, 40.37, 29.98, 28.76, 28.44, 24.27.

tert-Butyl-(6-((6-chloro-2-(4-methylpiperazin-1-yl)quinazolin-4-yl)amino)hexyl)carbamate **(P36e)**

The nucleophilic aromatic substitution was carried out as described for compound **P36a**.[761] Compound **48e** (140 mg, 0.34 mmol, 1.0 eq.), DIPEA (63 µL, 0.37 mmol, 1.1 eq.) and

N-methylpiperazine (42 µL, 0.37 mmol, 1.1 eq.) were subjected to the reaction conditions for 20 hours. The crude product was purified by column chromatography using a gradient elution of dichloromethane/methanol (sat. NH_3) (0-20%).

Yield:	117 mg, (72%)
Chemical formula:	$C_{24}H_{37}ClN_6O_2$
Molecular mass:	477.05 g/mol
Appearance:	Colourless solid
Internal code:	MST-412, ST-2608
Synthesis scheme:	Figure 140
Melting point:	125.2 °C
LC-DAD purity:	100%
MS (ESI-(+)):	m/z=477.31 $[M+H^+]^+$ calculated: 477.2739
^{1}H NMR (300 MHz, $CDCl_3$):	δ 7.60 – 7.54 (m, 1H), 7.38 – 7.24 (m, 2H), 6.09 – 6.03 (m, 1H), 4.68 – 4.62 (m, 1H), 3.88 – 3.79 (m, 4H), 3.54 – 3.40 (m, 2H), 3.11 – 2.99 (m, 2H), 2.44 – 2.29 (m, 4H), 2.25 (s, 3H), 1.66 – 1.50 (m, 2H), 1.43 – 1.20 (m, 15H).
^{13}C NMR (75.5 MHz, $CDCl_3$):	δ 159.17, 159.11, 156.26, 150.76, 132.75, 127.23, 125.49, 120.71, 111.36, 79.15, 55.17, 46.26, 43.79, 40.63, 39.94, 30.14, 28.79, 28.45, 26.11, 25.83.

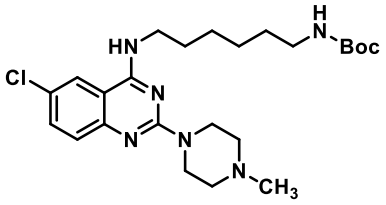

tert-Butyl-(2-(2-((6-chloro-2-(4-methylpiperazin-1-yl)quinazolin-4-yl)amino)ethoxy)ethyl)carbamate **(P36f)**

The nucleophilic aromatic substitution was carried out as described for compound **P36a**.[760] Compound **48f** (170 mg, 0.43 mmol, 1.0 eq.), DIPEA (80 µL, 0.47 mmol, 1.1 eq.) and *N*-methylpiperazine (53 µL, 0.47 mmol, 1.1 eq.) were subjected to the reaction conditions for 20 hours. The crude product was purified by column chromatography using a gradient elution of dichloromethane/methanol (sat. NH_3) (0-20%).

Yield:	100 mg, (50%)
Chemical formula:	$C_{22}H_{33}ClN_6O_3$
Molecular mass:	465.00 g/mol
Appearance:	Colourless solid
Internal code:	MST-414, ST-2609
Synthesis scheme:	Figure 140
Melting point:	138.1 °C
LC-DAD purity:	100%

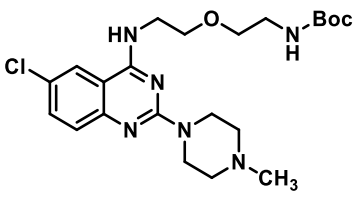

MS (ESI-(+)):	m/z=465.26 $[M+H^+]^+$ calculated: 465.2375
^{1}H NMR (300 MHz, $CDCl_3$):	δ 7.51 – 7.45 (m, 1H), 7.41 – 7.26 (m, 2H), 5.90 (t, *J* = 5.3 Hz, 1H), 4.82 (t, *J* = 6.4 Hz, 1H), 3.88 – 3.79 (m, 4H), 3.77 – 3.59 (m, 4H), 3.50 (t, *J* = 5.3 Hz, 2H), 3.34 – 3.23 (m, 2H), 2.45 – 2.36 (m, 4H), 2.27 (s, 3H), 1.37 (s, 9H).
^{13}C NMR (75.5 MHz, $CDCl_3$):	δ 159.09, 158.94, 156.08, 150.92, 133.00, 127.44, 125.66, 120.50, 111.14, 79.56, 70.29, 69.26, 55.18, 53.43, 46.30, 43.81, 40.94, 28.40.

tert-Butyl-(2-(2-(2-((6-chloro-2-(4-methylpiperazin-1-yl)quinazolin-4-yl)amino)ethoxy)ethoxy)ethyl)carbamate **(P36g)**

The nucleophilic aromatic substitution was carried out as described for compound **P36a**.[761] Compound **48g** (234 mg, 0.53 mmol, 1.0 eq.), DIPEA (98 µL, 0.58 mmol, 1.1 eq.) and *N*-methylpiperazine (65 µL, 0.58 mmol, 1.1 eq.) were subjected to the reaction conditions for 20 hours. The crude product was purified by column chromatography using a gradient elution of dichloromethane/methanol (sat. NH_3) (0-20%).

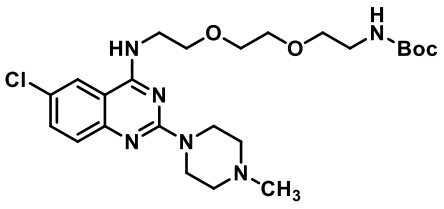

Yield:	170 mg, (63%)
Chemical formula:	$C_{24}H_{37}ClN_6O_4$
Molecular mass:	509.05 g/mol
Appearance:	Colourless solid
Internal code:	MST-436
Synthesis scheme:	Figure 140
Melting point:	139.8 °C
LC-DAD purity:	97.1%
MS (ESI-(+)):	m/z=509.31 $[M+H^+]^+$ calculated: 509.2638
^{1}H NMR (300 MHz, MeOD):	δ 7.86 – 7.79 (m, 1H), 7.41 – 7.32 (m, 1H), 7.28 – 7.19 (m, 1H), 3.83 – 3.73 (m, 4H), 3.69 – 3.63 (m, 4H), 3.61 – 3.47 (m, 4H), 3.47 – 3.35 (m, 2H), 3.10 (t, *J* = 5.6 Hz, 2H), 2.45 – 2.36 (m, 4H), 2.23 (s, 3H), 1.31 (s, 9H).
^{13}C NMR (75.5 MHz, MeOD):	δ 161.04, 160.49, 158.41, 151.67, 133.98, 127.52, 127.16, 122.90, 112.93, 80.10, 71.40, 71.29, 71.13, 70.23, 55.99, 46.24, 44.70, 41.93, 41.21, 28.77.

tert-Butyl-(2-(2-(2-(2-((6-chloro-2-(4-methylpiperazin-1-yl)quinazolin-4-yl)amino)ethoxy)ethoxy)ethoxy)ethyl)carbamate **(P36h)**

The nucleophilic aromatic substitution was carried out as described for compound **P36a**.[761] Compound **48h** (300 mg, 0.61 mmol, 1.0 eq.), DIPEA (114 µL, 0.67 mmol, 1.1 eq.) and *N*-methylpiperazine (75 µL, 0.67 mmol, 1.1 eq.) were subjected to the reaction conditions for 20 hours. The crude product was purified by column chromatography using a gradient elution of dichloromethane/methanol (sat. NH_3) (0-20%).

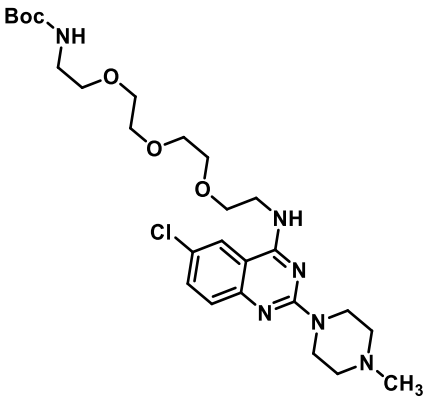

Yield:	152 mg, (45%)
Chemical formula:	$C_{26}H_{41}ClN_6O_5$
Molecular mass:	553.10 g/mol
Appearance:	Colourless solid
Internal code:	MST-419, ST-2610
Synthesis scheme:	Figure 140
Melting point:	142.5 °C
LC-DAD purity:	98.7%
MS (ESI-(+)):	m/z=553.35 $[M+H^+]^+$ calculated: 553.2900
^{1}H NMR (300 MHz, $CDCl_3$):	δ 7.55 – 7.49 (m, 1H), 7.40 – 7.24 (m, 2H), 6.27 – 6.21 (m, 1H), 5.02 – 4.96 (m, 1H), 3.88 – 3.79 (m, 4H), 3.75 – 3.67 (m, 4H), 3.65 – 3.53 (m, 6H), 3.46 (t, *J* = 5.1 Hz, 2H), 3.27 – 3.15 (m, 2H), 2.45 – 2.31 (m, 4H), 2.30 – 2.19 (m, 5H), 1.35 (s, 9H).
^{13}C NMR (75.5 MHz, $CDCl_3$):	δ 159.18, 159.02, 156.01, 150.87, 132.86, 127.32, 125.49, 120.77, 111.32, 79.20, 70.55, 70.46, 70.32, 70.23, 69.34, 55.19, 46.29, 43.80, 41.04, 40.96, 40.36, 28.42.

N^1-(6-Chloro-2-(4-methylpiperazin-1-yl)quinazolin-4-yl)ethane-1,2-diamine **(P37a)**

The Boc-deprotection protocol was carried out as described for compound **P6**.[674] Compound **P36a** (55 mg, 0.13 mmol, 1.0 eq.) was subjected to the reaction conditions for 24 hours. The crude product was converted to its free base using a strong basic anion exchanger and subsequently purified by reverse phase flash chromatography using a gradient elution of water/methanol (0-100%).

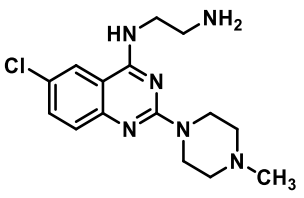

Yield:	42 mg, (100%)
Chemical formula:	$C_{15}H_{21}ClN_6$
Molecular mass:	320.83 g/mol
Appearance:	Colourless solid
Internal code:	MST-560

Synthesis scheme:	Figure 141
Melting point:	211.7 °C
LC-MS-DAD purity:	100%
HR-MS (ESI-(+)):	m/z=321.1643 $[M+H^+]^+$ calculated: 321.1589
^{1}H NMR (300 MHz, MeOD):	δ 7.95 – 7.87 (m, 1H), 7.52 – 7.25 (m, 2H), 3.93 – 3.84 (m, 4H), 3.68 – 3.59 (m, 2H), 3.00 – 2.91 (m, 2H), 2.55 – 2.43 (m, 4H), 2.33 (s, 3H).
^{13}C NMR (75.5 MHz, MeOD):	δ 161.26, 160.53, 151.69, 133.92, 127.54, 127.10, 122.89, 112.93, 56.01, 46.27, 44.73, 44.55, 41.55.

N^1-(6-Chloro-2-(4-methylpiperazin-1-yl)quinazolin-4-yl)propane-1,3-diamine **(P37b)**

The Boc-deprotection protocol was carried out as described for compound **P6**.[674] Compound **P36b** (80 mg, 0.18 mmol, 1.0 eq.) was subjected to the reaction conditions for 24 hours. The crude product was converted to its free base using a strong basic anion exchanger and subsequently purified by reverse phase flash chromatography using a gradient elution of water/methanol (0-100%).

Yield:	60 mg, (100%)
Chemical formula:	$C_{16}H_{23}ClN_6$
Molecular mass:	334.85 g/mol
Appearance:	Colourless solid
Internal code:	MST-456
Synthesis scheme:	Figure 141
Melting point:	207.2 °C
LC-MS-DAD purity:	96.2%
HR-MS (ESI-(+)):	m/z=335.1789 $[M+H^+]^+$ calculated: 335.1745
^{1}H NMR (300 MHz, MeOD):	δ 7.97 – 7.93 (m, 1H), 7.55 – 7.49 (m, 1H), 7.41 – 7.35 (m, 1H), 4.07 – 3.92 (m, 4H), 3.69 (t, *J* = 6.6 Hz, 2H), 3.08 – 2.96 (m, 2H), 2.84 – 2.75 (m, 4H), 2.54 (s, 3H), 2.15 – 2.00 (m, 2H).
^{13}C NMR (75.5 MHz, $CDCl_3$):	δ 163.77, 162.39, 153.56, 136.82, 130.29, 130.02, 125.41, 115.42, 57.84, 46.50, 41.56, 41.30, 30.87, 25.22.

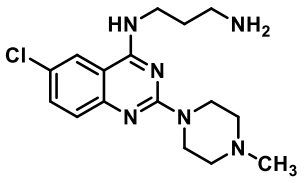

N^1-(6-Chloro-2-(4-methylpiperazin-1-yl)quinazolin-4-yl)butane-1,4-diamine **(P37c)**

The Boc-deprotection protocol was carried out as described for compound **P6**.[674] Compound **P36c** (51 mg, 0.11 mmol, 1.0 eq.) was subjected to the reaction conditions for 24 hours. The crude product was converted to its free base using a strong basic anion exchanger and

subsequently purified by reverse phase flash chromatography using a gradient elution of water/methanol (0-100%).

Yield:	38 mg, (100%)
Chemical formula:	$C_{17}H_{25}ClN_6$
Molecular mass:	348.88 g/mol
Appearance:	Colourless solid
Internal code:	MST-457, ST-2758
Synthesis scheme:	Figure 141
Melting point:	214.1 °C
LC-DAD purity:	96.3%
MS (ESI-(+)):	m/z=349.24 $[M+H^+]^+$ calculated: 349.1902
^{1}H NMR (300 MHz, D_2O):	δ 7.86 – 7.78 (m, 1H), 7.67 – 7.57 (m, 1H), 7.41 – 7.33 (m, 1H), 3.77 – 3.18 (m, 10H), 3.03 – 2.91 (m, 5H), 1.79 – 1.63 (m, 4H).
^{13}C NMR (75.5 MHz, D_2O):	δ 158.73, 151.70, 137.31, 135.12, 130.10, 122.64, 119.09, 110.69, 52.50, 43.01, 41.94, 41.17, 39.21, 24.85, 24.42.

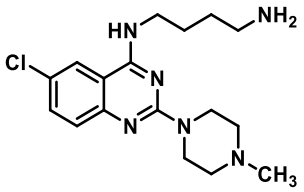

N^1-(6-Chloro-2-(4-methylpiperazin-1-yl)quinazolin-4-yl)pentane-1,5-diamine **(P37d)**

The Boc-deprotection protocol was carried out as described for compound **P6**.[674] Compound **P36d** (136 mg, 0.29 mmol, 1.0 eq.) was subjected to the reaction conditions for 24 hours. The crude product was converted to its free base using a strong basic anion exchanger and subsequently purified by reverse phase flash chromatography using a gradient elution of water/methanol (0-100%).

Yield:	105 mg, (100%)
Chemical formula:	$C_{18}H_{27}ClN_6$
Molecular mass:	362.91 g/mol
Appearance:	Colourless solid
Internal code:	MST-458, ST-2755
Synthesis scheme:	Figure 141
Melting point:	222.2 °C
LC-DAD purity:	100%
MS (ESI-(+)):	m/z=363.36 $[M+H^+]^+$ calculated: 363.2058
^{1}H NMR (300 MHz, D_2O):	δ 7.80 – 7.72 (m, 1H), 7.63 – 7.50 (m, 1H), 7.45 – 7.27 (m, 1H), 3.99 – 3.16 (m, 10H), 3.02 – 2.91 (m, 5H), 1.77 – 1.54 (m, 4H), 1.50 – 1.34 (m, 2H).

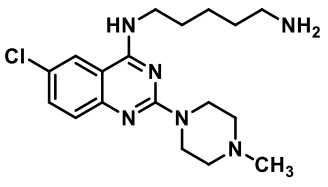

^{13}C NMR (75.5 MHz, D_2O):	δ 158.34, 151.49, 137.06, 135.02, 130.04, 122.57, 118.98, 110.51, 52.49, 43.03, 41.96, 41.73, 39.40, 27.24, 26.57, 23.35.

N^1-(6-Chloro-2-(4-methylpiperazin-1-yl)quinazolin-4-yl)hexane-1,5-diamine **(P37e)**

The Boc-deprotection protocol was carried out as described for compound **P6**.[674] Compound **P36e** (93 mg, 0.20 mmol, 1.0 eq.) was subjected to the reaction conditions for 24 hours. The crude product was converted to its free base using a strong basic anion exchanger and subsequently purified by reverse phase flash chromatography using a gradient elution of water/methanol (0-100%).

Yield:	75 mg, (100%)
Chemical formula:	$C_{19}H_{29}ClN_6$
Molecular mass:	376.93 g/mol
Appearance:	Colourless solid
Internal code:	MST-459, ST-2759
Synthesis scheme:	Figure 141
Melting point:	218.2 °C
LC-DAD purity:	99.4%
MS (ESI-(+)):	m/z=377.24 $[M+H^+]^+$ calculated: 377.2215
^{1}H NMR (300 MHz, MeOD):	δ 8.00 – 7.97 (m, 1H), 7.53 – 7.47 (m, 1H), 7.42 – 7.26 (m, 1H), 4.07 – 3.97 (m, 4H), 3.58 (t, *J* = 7.0 Hz, 2H), 2.97 – 2.86 (m, 6H), 2.61 (s, 3H), 1.79 – 1.64 (m, 4H), 1.52 – 1.43 (m, 4H).
^{13}C NMR (75.5 MHz, MeOD):	δ 160.99, 159.41, 150.08, 134.19, 127.93, 126.89, 123.06, 113.07, 54.97, 44.84, 43.70, 42.12, 40.60, 28.66, 27.81, 27.39, 23.20.

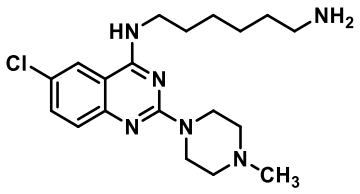

N-(2-(2-aminoethoxy)ethyl)-6-chloro-2-(4-methylpiperazin-1-yl)quinazolin-4-amine **(P37f)**

The Boc-deprotection protocol was carried out as described for compound **P6**.[674] Compound **P36f** (85 mg, 0.18 mmol, 1.0 eq.) was subjected to the reaction conditions for 24 hours. The crude product was converted to its free base using a strong basic anion exchanger and subsequently purified by reverse phase flash chromatography using a gradient elution of water/methanol (0-100%).

Yield:	55 mg, (84%)
Chemical formula:	$C_{17}H_{25}ClN_6O$
Molecular mass:	364.88 g/mol
Appearance:	Colourless solid

Internal code:	MST-551
Synthesis scheme:	Figure 141
Melting point:	228.4 °C
LC-MS-DAD purity:	100%

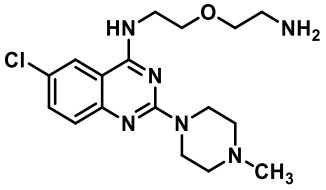

HR-MS (ESI-(+)):	m/z=365.1900 $[M+H^+]^+$ calculated: 365.1851
^{1}H NMR (300 MHz, MeOD):	δ 8.04 – 7.98 (m, 1H), 7.54 – 7.48 (m, 1H), 7.42 – 7.33 (m, 1H), 4.10 – 4.00 (m, 4H), 3.90 – 3.70 (m, 4H), 3.78 – 3.71 (m, 2H), 3.19 – 3.11 (m, 2H), 3.02 – 2.93 (m, 4H), 2.66 (s, 3H).
^{13}C NMR (75.5 MHz, MeOD):	δ 161.13, 159.36, 150.39, 134.30, 127.92, 127.15, 123.18, 113.03, 70.16, 67.84, 54.82, 44.62, 43.47, 40.55, 23.21.

N-(2-(2-(2-Aminoethoxy)ethoxy)ethyl)-6-chloro-2-(4-methylpiperazin-1-yl)quinazolin-4-amine **(P37g)**

The Boc-deprotection protocol was carried out as described for compound **P6**.[674] Compound **P36g** (18 mg, 0.04 mmol, 1.0 eq.) was subjected to the reaction conditions for 24 hours. The crude product was converted to its free base using a strong basic anion exchanger and subsequently purified by reverse phase flash chromatography using a gradient elution of water/methanol (0-100%).

Yield:	16 mg, (100%)
Chemical formula:	$C_{19}H_{29}ClN_6O_2$
Molecular mass:	408.93 g/mol
Appearance:	Colourless solid
Internal code:	MST-462, ST-2760
Synthesis scheme:	Figure 141
Melting point:	232.1 °C
LC-DAD purity:	100%

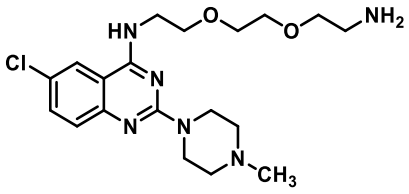

MS (ESI-(+)):	m/z= 409.25 $[M+H^+]^+$ calculated: 409.2113
^{1}H NMR (300 MHz, MeOD):	δ 8.26 – 8.13 (m, 1H), 7.89 – 7.69 (m, 1H), 7.66 – 7.53 (m, 1H), 4.27 – 4.00 (m, 2H), 3.91 – 3.86 (m, 2H), 3.85 – 3.81 (m, 2H), 3.76 – 3.69 (m, 8H), 3.43 – 3.34 (m, 4H), 3.14 – 3.09 (m, 2H), 2.93 (s, 3H).
^{13}C NMR (151 MHz, MeOD):	δ 159.81, 142.41, 142.26, 142.12, 134.24, 128.51, 122.39, 111.53, 70.03, 68.46, 66.52, 52.87, 48.15, 42.57, 41.93, 41.23, 39.30.

N-(2-(2-(2-(2-Aminoethoxy)ethoxy)ethoxy)ethyl)-6-chloro-2-(4-methylpiperazin-1-yl)quinazolin-4-amine **(P37h)**

The Boc-deprotection protocol was carried out as described for compound **P6**.[674] Compound **P36h** (145 mg, 0.26 mmol, 1.0 eq.) was subjected to the reaction conditions for 24 hours. The crude product was converted to its free base using a strong basic anion exchanger and subsequently purified by reverse phase flash chromatography using a gradient elution of water/methanol (0-100%).

Yield:	118 mg, (100%)
Chemical formula:	$C_{21}H_{33}ClN_6O_3$
Molecular mass:	452.98 g/mol
Appearance:	Colourless solid
Internal code:	MST-464, ST-2761
Synthesis scheme:	Figure 141
Melting point:	239.1 °C
LC-DAD purity:	96.4%
MS (ESI-(+)):	m/z= 453.28 $[M+H^+]^+$ calculated: 453.2375
^{1}H NMR (300 MHz, MeOD):	δ 8.26 – 8.13 (m, 1H), 7.89 – 7.69 (m, 1H), 7.66 – 7.53 (m, 1H), 4.27 – 4.00 (m, 2H), 3.91 – 3.86 (m, 2H), 3.85 – 3.81 (m, 2H), 3.76 – 3.69 (m, 8H), 3.43 – 3.34 (m, 4H), 3.14 – 3.09 (m, 2H), 2.93 (s, 3H).
^{13}C NMR (75.5 MHz, MeOD):	δ 160.73, 153.22, 139.31, 136.60, 132.00, 124.70, 120.76, 112.64, 71.51, 71.49, 71.33, 71.24, 69.44, 67.84, 53.65, 43.70, 43.26, 40.78, 40.67.

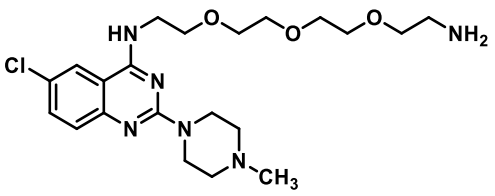

N-(2-((6-Chloro-2-(4-methylpiperazin-1-yl)quinazolin-4-yl)amino)ethyl)-3-(5,5-difluoro-7,9-dimethyl-5*H*-5λ^4,6λ^4-dipyrrolo[1,2-*c*:2',1'-*f*][1,3,2]diazaborinin-3-yl)propanamide **(P38a)**

The HATU coupling was carried out as described for compound **P3**.[644] Compound **P37a** (36 mg, 0.12 mmol, 1.0 eq.), DIPEA (23 µL, 0.13 mmol, 1.1 eq.), BODIPY-FL (35 mg, 0.12 mmol, 1.0 eq.) and HATU (50 mg, 0.13 mmol, 1.1 eq.) were subjected to the reaction conditions for 24 hours. The crude product was purified by column chromatography using a gradient elution of dichloromethane/methanol (sat. NH_3) (0-20%).

Yield:	16 mg, (22%)
Chemical formula:	$C_{29}H_{34}BClF_2N_8O$
Molecular mass:	594.90 g/mol

Appearance:	Red solid
Internal code:	MST-577, ST-2779
Synthesis scheme:	Figure 142
Melting point:	147.8 °C
LC-MS-DAD purity:	100%

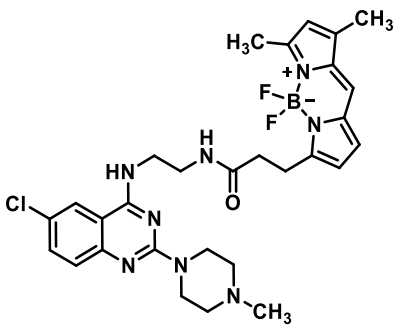

HR-MS (ESI-(+)):	m/z= 595.3123 $[M+H^+]^+$ calculated: 595.2678
^{1}H NMR (300 MHz, MeOD):	δ 7.73 – 7.67 (m, 1H), 7.41 – 7.31 (m, 1H), 7.27 – 7.18 (m, 1H), 7.09 (s, 1H), 6.68 (d, *J* = 4.1 Hz, 1H), 6.13 (d, *J* = 4.1 Hz, 1H), 6.05 (s, 1H), 3.82 – 3.72 (m, 4H), 3.58 – 3.45 (m, 2H), 3.43 – 3.33 (m, 2H), 3.09 (t, *J* = 7.4 Hz, 2H), 2.50 (t, *J* = 7.4 Hz, 2H), 2.46 – 2.31 (m, 7H), 2.22 (s, 3H), 2.13 (s, 3H).
^{13}C NMR (151 MHz, MeOD):	δ 175.16, 161.21, 160.37, 158.06, 151.54, 145.78, 136.46, 134.76, 133.98, 129.37, 127.45, 127.17, 125.60, 122.92, 121.33, 117.62, 117.57, 112.90, 55.96, 46.15, 44.66, 41.83, 39.81, 36.12, 25.61, 25.54, 11.27.

N-(3-((6-Chloro-2-(4-methylpiperazin-1-yl)quinazolin-4-yl)amino)propyl)-3-(5,5-difluoro-7,9-dimethyl-5*H*-5λ^4,6λ^4-dipyrrolo[1,2-*c*:2',1'-*f*][1,3,2]diazaborinin-3-yl)propanamide **(P38b)**

The HATU coupling was carried out as described for compound **P3**.[644] Compound **P37b** (40 mg, 0.14 mmol, 1.0 eq.), DIPEA (25 µL, 0.15 mmol, 1.1 eq.), BODIPY-FL (41 mg, 0.14 mmol, 1.0 eq.) and HATU (59 mg, 0.15 mmol, 1.1 eq.) were subjected to the reaction conditions for 24 hours. The crude product was purified by column chromatography using a gradient elution of dichloromethane/methanol (sat. NH_3) (0-20%).

Yield:	14 mg, (16%)
Chemical formula:	$C_{30}H_{36}BClF_2N_8O$
Molecular mass:	608.93 g/mol
Appearance:	Red solid
Internal code:	MST-580
Synthesis scheme:	Figure 142
Melting point:	144.3 °C
LC-MS-DAD purity:	95.3%
HR-MS (ESI-(+)):	m/z= 609.3302 $[M+H^+]^+$ calculated: 609.2834

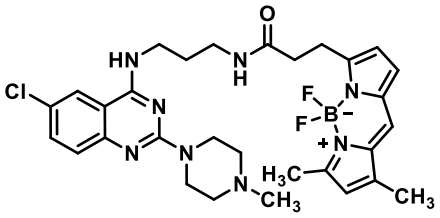

^{1}H NMR (300 MHz, MeOD):	δ 7.84 – 7.79 (m, 1H), 7.40 – 7.35 (m, 1H), 7.28 – 7.21 (m, 2H), 6.84 (d, *J* = 4.0 Hz, 1H), 6.21 (d, *J* = 4.0 Hz, 1H), 6.06 (s, 1H), 3.80 – 3.77 (m, 4H), 3.43 (t, *J* = 7.0 Hz, 2H), 3.19 (t, *J* = 6.8 Hz, 2H), 3.15 – 3.09 (m, 2H), 2.54 – 2.45 (m, 6H), 2.36 (s, 3H), 2.27 (s, 3H), 2.13 (s, 3H), 1.80 – 1.73 (m, 2H).
^{13}C NMR (151 MHz, MeOD):	δ 173.26, 159.80, 159.46, 157.28, 156.84, 144.39, 135.02, 133.34, 132.94, 128.07, 126.86, 124.89, 124.26, 121.63, 119.88, 116.12, 116.05, 111.51, 53.60, 43.41, 42.34, 38.35, 36.70, 34.51, 29.25, 28.18, 24.14, 9.69.

N-(4-((6-Chloro-2-(4-methylpiperazin-1-yl)quinazolin-4-yl)amino)butyl)-3-(5,5-difluoro-7,9-dimethyl-5*H*-5λ^{4},6λ^{4}-dipyrrolo[1,2-*c*:2',1'-*f*][1,3,2]diazaborinin-3-yl)propanamide **(P38c)**

The HATU coupling was carried out as described for compound **P3**.[644] Compound **P37c** (24 mg, 0.08 mmol, 1.0 eq.), DIPEA (15 µL, 0.09 mmol, 1.1 eq.), BODIPY-FL (23 mg, 0.08 mmol, 1.0 eq.) and HATU (33 mg, 0.09 mmol, 1.1 eq.) were subjected to the reaction conditions for 24 hours. The crude product was purified by column chromatography using a gradient elution of dichloromethane/methanol (sat. NH_3) (0-20%).

Yield:	18 mg, (35%)
Chemical formula:	$C_{31}H_{38}BClF_2N_8O$
Molecular mass:	622.96 g/mol
Appearance:	Red solid
Internal code:	MST-615
Synthesis scheme:	Figure 142
Melting point:	135.8 °C
LC-MS-DAD purity:	99.2%
HR-MS (ESI-(+)):	m/z= 623.3053 $[M+H^+]^+$ calculated: 623.2991
^{1}H NMR (300 MHz, MeOD):	δ 7.85 – 7.78 (m, 1H), 7.42 – 7.30 (m, 1H), 7.29 – 7.18 (m, 2H), 6.79 (d, *J* = 4.1 Hz, 1H), 6.19 (d, *J* = 4.1 Hz, 1H), 6.07 (s, 1H), 3.82 – 3.72 (m, 4H), 3.49 – 3.39 (m, 2H), 3.19 – 3.06 (m, 4H), 2.52 – 2.46 (m, 2H), 2.49 – 2.34 (m, 7H), 2.21 (s, 3H), 2.14 (s, 3H), 1.66 – 1.38 (m, 4H).
^{13}C NMR (151 MHz, MeOD):	δ 178.45, 173.21, 168.91, 159.89, 159.55, 159.09, 157.02, 150.06, 144.43, 135.10, 133.45, 132.51, 128.11, 125.98,

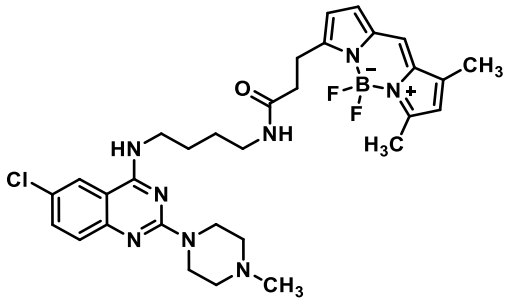

124.30, 121.47, 119.94, 116.31, 63.03, 58.97, 56.71, 54.50, 44.70, 43.22, 40.25, 38.75, 26.62, 25.92, 9.80.

N-(5-((6-Chloro-2-(4-methylpiperazin-1-yl)quinazolin-4-yl)amino)pentyl)-3-(5,5-difluoro-7,9-dimethyl-5*H*-5λ^4,6λ^4-dipyrrolo[1,2-*c*:2',1'-*f*][1,3,2]diazaborinin-3-yl)propanamide **(P38d)**

The HATU coupling was carried out as described for compound **P3**.[644] Compound **P37d** (35 mg, 0.10 mmol, 1.0 eq.), DIPEA (19 µL, 0.11 mmol, 1.1 eq.), BODIPY-FL (29 mg, 0.10 mmol, 1.0 eq.) and HATU (42 mg, 0.11 mmol, 1.1 eq.) were subjected to the reaction conditions for 24 hours. The crude product was purified by column chromatography using a gradient elution of dichloromethane/methanol (sat. NH_3) (0-20%).

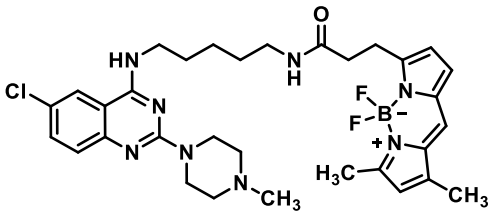

Yield:	29 mg, (45%)
Chemical formula:	$C_{32}H_{40}BClF_2N_8O$
Molecular mass:	636.98 g/mol
Appearance:	Red solid
Internal code:	MST-601
Synthesis scheme:	Figure 142
Melting point:	137.5 °C
LC-MS-DAD purity:	97.8%
HR-MS (ESI-(+)):	m/z= 637.3216 $[M+H^+]^+$ calculated: 637.3147
^{1}H NMR (300 MHz, MeOD):	δ 8.27 – 7.98 (m, 1H), 7.79 – 7.52 (m, 1H), 7.52 – 7.45 (m, 1H), 7.41 (s, 1H), 6.98 (d, *J* = 4.1 Hz, 1H), 6.27 (d, *J* = 4.1 Hz, 1H), 6.20 (s, 1H), 4.27 – 4.03 (m, 4H), 3.63 (t, *J* = 8.0 Hz, 2H), 3.37 – 3.32 (m, 4H), 3.26 – 3.08 (m, 4H), 2.88 (s, 3H), 2.56 – 2.47 (m, 5H), 2.27 (s, 3H), 1.78 – 1.69 (m, 2H), 1.62 – 1.51 (m, 2H), 1.49 – 1.36 (m, 2H).
^{13}C NMR (151 MHz, MeOD):	δ 173.57, 161.36, 160.28, 160.22, 159.84, 152.03, 144.83, 142.60, 135.45, 133.85, 128.53, 124.68, 122.35, 120.32, 120.30, 116.49, 116.41, 111.94, 58.94, 55.38, 53.49, 53.35, 42.40, 41.29, 39.00, 29.00, 26.60, 23.27, 21.57, 10.09.

N-(6-((6-Chloro-2-(4-methylpiperazin-1-yl)quinazolin-4-yl)amino)hexyl)-3-(5,5-difluoro-7,9-dimethyl-5*H*-5λ^4,6λ^4-dipyrrolo[1,2-*c*:2',1'-*f*][1,3,2]diazaborinin-3-yl)propanamide **(P38e)**

The HATU coupling was carried out as described for compound **P3**.[644] Compound **P37e** (64 mg, 0.17 mmol, 1.0 eq.), DIPEA (32 µL, 0.19 mmol, 1.1 eq.), BODIPY-FL (50 mg, 0.17 mmol, 1.0 eq.)

and HATU (71 mg, 0.19 mmol, 1.1 eq.) were subjected to the reaction conditions for 24 hours. The crude product was purified by column chromatography using a gradient elution of dichloromethane/methanol (sat. NH_3) (0-20%).

Yield:	30 mg, (27%)
Chemical formula:	$C_{33}H_{42}BClF_2N_8O$
Molecular mass:	651.01 g/mol
Appearance:	Red solid
Internal code:	MST-598
Synthesis scheme:	Figure 142
Melting point:	107.0 °C
LC-MS-DAD purity:	97.8%
HR-MS (ESI-(+)):	m/z= 651.3314 $[M+H^+]^+$ calculated: 651.3304
^{1}H NMR (300 MHz, MeOD):	δ 7.97 – 7.91 (m, 1H), 7.53 – 7.44 (m, 1H), 7.39 – 7.28 (m, 2H), 6.95 (d, *J* = 4.1 Hz, 1H), 6.30 (d, *J* = 4.1 Hz, 1H), 6.14 (s, 1H), 3.95 – 3.83 (m, 4H), 3.51 (t, *J* = 7.1 Hz, 2H), 3.26 – 3.12 (m, 4H), 2.63 – 2.53 (m, 6H), 2.48 (s, 3H), 2.38 (s, 3H), 2.23 (s, 3H), 1.76 – 1.62 (m, 2H), 1.56 – 1.23 (m, 6H).
^{13}C NMR (75.5 MHz, MeOD):	δ 174.55, 161.28, 160.91, 160.12, 158.48, 150.88, 145.79, 136.52, 134.87, 134.00, 129.55, 127.45, 127.09, 125.72, 122.95, 121.37, 117.63, 113.05, 55.75, 45.90, 44.50, 42.07, 40.27, 35.95, 35.91, 30.35, 29.84, 27.84, 27.61, 25.72, 11.20.

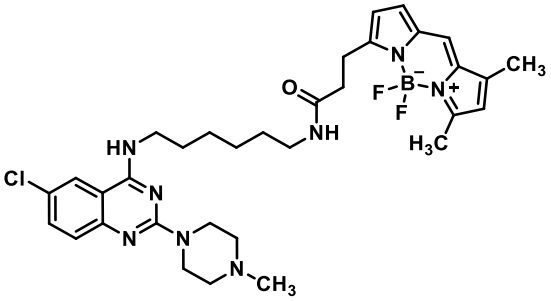

N-(2-(2-((6-Chloro-2-(4-methylpiperazin-1-yl)quinazolin-4-yl)amino)ethoxy)ethyl)-3-(5,5-difluoro-7,9-dimethyl-5*H*-5λ^4,6λ^4-dipyrrolo[1,2-*c*:2',1'-*f*][1,3,2]diazaborinin-3-yl)propanamide **(P38f)**

The HATU coupling was carried out as described for compound **P3**.[644] Compound **P37f** (28 mg, 0.06 mmol, 1.0 eq.), DIPEA (12 µL, 0.07 mmol, 1.1 eq.), BODIPY-FL (18 mg, 0.17 mmol, 1.0 eq.) and HATU (27 mg, 0.07 mmol, 1.1 eq.) were subjected to the reaction conditions for 24 hours. The crude product was purified by column chromatography using a gradient elution of dichloromethane/methanol (sat. NH_3) (0-20%).

Yield:	20 mg, (51%)
Chemical formula:	$C_{31}H_{38}BClF_2N_8O_2$
Molecular mass:	638.96 g/mol
Appearance:	Red solid
Internal code:	MST-609

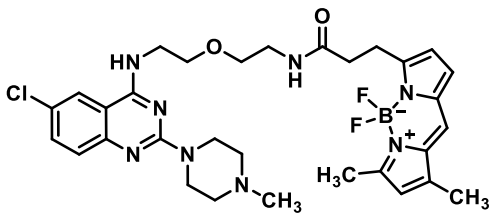

Synthesis scheme:	Figure 142
Melting point:	122.3 °C
LC-MS-DAD purity:	100%
HR-MS (ESI-(+)):	m/z= 639.3012 $[M+H^+]^+$ calculated: 639.2940
^{1}H NMR (300 MHz, MeOD):	δ 7.99 – 7.88 (m, 1H), 7.52 – 7.43 (m, 1H), 7.38 – 7.29 (m, 2H), 6.93 (d, *J* = 4.1 Hz, 1H), 6.27 (d, *J* = 4.1 Hz, 1H), 6.14 (s, 1H), 4.00 – 3.88 (m, 4H), 3.78 – 3.66 (m, 4H), 3.55 (t, *J* = 5.4 Hz, 2H), 3.42 – 3.35 (m, 2H), 3.19 (t, *J* = 7.6 Hz, 2H), 2.81 – 2.67 (m, 4H), 2.60 – 2.52 (m, 2H), 2.50 (s, 3H), 2.46 (s, 3H), 2.23 (s, 3H).
^{13}C NMR (75.5 MHz, MeOD):	δ 174.83, 161.22, 161.04, 159.49, 158.39, 150.34, 145.78, 136.49, 134.88, 134.28, 129.56, 127.87, 126.91, 125.71, 123.06, 121.34, 117.68, 112.95, 70.56, 69.81, 55.46, 45.44, 44.16, 42.01, 40.36, 35.91, 25.66, 11.22, 11.21.

N-(2-(2-(2-((6-Chloro-2-(4-methylpiperazin-1-yl)quinazolin-4-yl)amino)ethoxy)ethoxy)-ethyl)-3-(5,5-difluoro-7,9-dimethyl-5*H*-5λ^4,6λ^4-dipyrrolo[1,2-*c*:2',1'-*f*][1,3,2]diazaborinin-3-yl)propanamide **(P38g)**

The HATU coupling was carried out as described for compound **P3**.[644] Compound **P37g** (30 mg, 0.07 mmol, 1.0 eq.), DIPEA (14 µL, 0.08 mmol, 1.1 eq.), BODIPY-FL (20 mg, 0.17 mmol, 1.0 eq.) and HATU (30 mg, 0.08 mmol, 1.1 eq.) were subjected to the reaction conditions for 24 hours. The crude product was purified by column chromatography using a gradient elution of dichloromethane/methanol (sat. NH_3) (0-20%).

Yield:	8 mg, (17%)
Chemical formula:	$C_{33}H_{42}BClF_2N_8O_3$
Molecular mass:	683.01 g/mol
Appearance:	Red solid
Internal code:	MST-625
Synthesis scheme:	Figure 142
Melting point:	126.4 °C
LC-MS-DAD purity:	97.4%
HR-MS (ESI-(+)):	m/z= 683.3227 $[M+H^+]^+$ calculated: 683.3202
^{1}H NMR (600 MHz, DMSO-d_6):	δ 8.18 – 8.13 (m, 2H), 8.01 (t, *J* = 6.2 Hz, 1H), 7.67 (s, 1H), 7.52 – 7.47 (m, 1H), 7.29 – 7.24 (m, 1H), 7.07 (d, *J* = 4.0 Hz, 1H), 6.35 (d, *J* = 4.0 Hz, 1H), 6.30 (s, 1H), 3.80 – 3.77 (m, 4H), 3.68 – 3.60

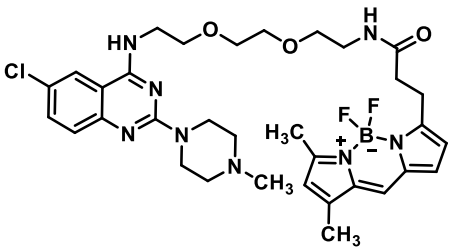

(m, 6H), 3.59 – 3.48 (m, 6H), 3.41 (t, *J* = 5.9 Hz, 2H), 3.24 – 3.16 (m, 2H), 2.60 – 2.41 (m, 10H), 2.27 (s, 3H).

^{13}C NMR (151 MHz, DMSO-d_6): δ 171.39, 159.66, 159.00, 158.30, 150.93, 144.52, 134.90, 133.44, 133.05, 129.37, 127.48, 125.80, 124.63, 122.61, 120.71, 117.07, 117.06, 111.79, 70.08, 70.01, 69.57, 68.69, 54.72, 40.91, 40.53, 39.04, 34.10, 29.47, 24.44, 22.56, 14.96.

N-(2-(2-(2-(2-((6-Chloro-2-(4-methylpiperazin-1-yl)quinazolin-4-yl)amino)ethoxy)ethoxy)-ethoxy)ethyl)-3-(5,5-difluoro-7,9-dimethyl-5*H*-5λ^4,6λ^4-dipyrrolo[1,2-*c*:2',1'-*f*][1,3,2]diazaborinin-3-yl)propanamide **(P38h)**

The HATU coupling was carried out as described for compound **P3**.[644] Compound **P37h** (37 mg, 0.08 mmol, 1.0 eq.), DIPEA (16 µL, 0.09 mmol, 1.1 eq.), BODIPY-FL (23 mg, 0.17 mmol, 1.0 eq.) and HATU (33 mg, 0.09 mmol, 1.1 eq.) were subjected to the reaction conditions for 24 hours. The crude product was purified by column chromatography using a gradient elution of dichloromethane/methanol (sat. NH_3) (0-20%).

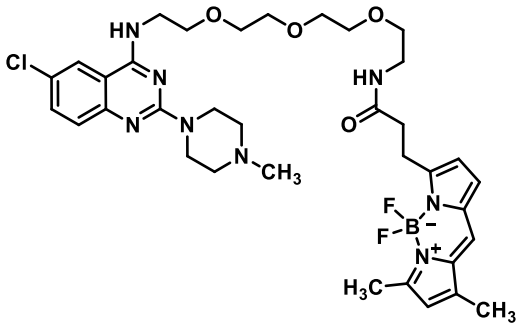

Yield:	13 mg, (22%)
Chemical formula:	$C_{35}H_{46}BClF_2N_8O_4$
Molecular mass:	727.06 g/mol
Appearance:	Red solid
Internal code:	MST-620
Synthesis scheme:	Figure 142
Melting point:	135.2 °C
LC-MS-DAD purity:	100%
HR-MS (ESI-(+)):	m/z= 727.3490 $[M+H^+]^+$ calculated: 727.3464
^{1}H NMR (300 MHz, MeOD):	δ 7.85 – 7.64 (m, 1H), 7.45 – 7.28 (m, 1H), 7.28 – 7.09 (m, 2H), 6.83 (d, *J* = 4.1 Hz, 1H), 6.18 (d, *J* = 4.1 Hz, 1H), 6.02 (s, 1H), 3.84 – 3.65 (m, 4H), 3.64 – 3.58 (m, 4H), 3.56 – 3.48 (m, 6H), 3.48 – 3.41 (m, 2H), 3.42 – 3.35 (m, 2H), 3.28 – 3.22 (m, 2H), 3.10 (t, *J* = 7.7 Hz, 2H), 2.57 – 2.45 (m, 2H), 2.44 – 2.31 (m, 7H), 2.22 (s, 3H), 2.12 (s, 3H).
^{13}C NMR (75.5 MHz, MeOD):	δ 174.66, 160.95, 160.20, 151.31, 145.73, 137.36, 136.45, 134.86, 134.04, 129.62, 129.57, 127.34, 127.28, 125.70, 122.98, 117.70, 117.67, 112.94, 71.57, 71.33, 71.20, 70.53, 70.11, 69.73, 55.84, 46.05, 44.54, 42.02, 41.98, 40.45, 35.90, 35.86, 11.25.

10.5.5 VUF-10558-based *O*-linked ligands

tert-Butyl (2-((2,6-dichloroquinazolin-4-yl)oxy)ethyl)carbamate **(49a)**

The synthesis was based on a procedure previously described.[765] Compound **L17** (170 mg, 1.06 mmol, 1.1 eq.) was dissolved in tetrahydrofuran and under ice cooling sodium hydride (25 mg, 1.06 mmol, 1.1 eq.) was added. Then a solution of **SM4** (223 mg, 0.96 mmol, 1.0 eq.) in tetrahydrofuran was added. The reaction mixture was stirred at room temperature for 20 hours. The solvent was removed under reduced pressure and the crude product was purified by flash chromatography using a gradient elution of ethyl acetate/hexane (0-100%).

Yield:	309 mg, (90%)
Chemical formula:	$C_{15}H_{17}Cl_2N_3O_3$
Molecular mass:	358.22 g/mol
Appearance:	Colourless solid
Internal code:	MST-284
Synthesis scheme:	Figure 145
^{1}H NMR (300 MHz, $CDCl_3$):	δ 8.11 – 8.09 (m, 1H), 7.83 – 7.74 (m, 2H), 4.93 (t, *J* = 6.6 Hz, 1H), 4.66 (t, *J* = 5.3 Hz, 2H), 3.71 – 3.62 (m, 2H), 1.44 (s, 9H).

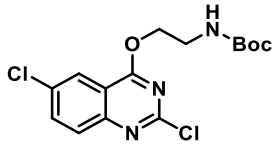

tert-Butyl (3-((2,6-dichloroquinazolin-4-yl)oxy)propyl)carbamate **(49b)**

The nucleophilic aromatic substitution was carried out as described for compound **49a**.[765] Compound **SM4** (197 mg, 0.84 mmol, 1.0 eq.), sodium hydride (22 mg, 0.92 mmol, 1.1 eq.) and compound **L18** (161 mg, 0.92 mmol, 1.1 eq.) were subjected to the reaction conditions for 20 hours. The crude product was purified by flash chromatography using a gradient elution of ethyl acetate/hexane (0-100%).

Yield:	156 mg, (50%)
Chemical formula:	$C_{16}H_{19}Cl_2N_3O_3$
Molecular mass:	372.25 g/mol
Appearance:	Colourless solid
Internal code:	MST-300
Synthesis scheme:	Figure 145
^{1}H NMR (300 MHz, $CDCl_3$):	δ 8.11 – 8.07 (m, 1H), 7.84 – 7.75 (m, 2H), 4.86 – 4.73 (m, 1H), 4.68 (t, *J* = 6.1 Hz, 2H), 3.41 – 3.29 (m, 2H), 2.18 – 2.03 (m, 2H), 1.44 (s, 9H).

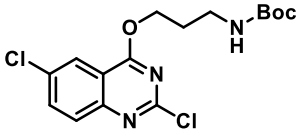

tert-Butyl (4-((2,6-dichloroquinazolin-4-yl)oxy)butyl)carbamate **(49c)**

The nucleophilic aromatic substitution was carried out as described for compound **49a**.[765] Compound **SM4** (410 mg, 1.76 mmol, 1.0 eq.), sodium hydride (46 mg, 1.94 mmol, 1.1 eq.) and compound **L12** (367 mg, 1.94 mmol, 1.1 eq.) were subjected to the reaction conditions for 20 hours. The crude product was purified by flash chromatography using a gradient elution of ethyl acetate/hexane (0-100%).

Yield:	217 mg, (32%)
Chemical formula:	$C_{17}H_{21}Cl_2N_3O_3$
Molecular mass:	386.27 g/mol
Appearance:	Colourless solid
Internal code:	MST-324
Synthesis scheme:	Figure 145
^{1}H NMR (300 MHz, $CDCl_3$):	δ 8.03 – 7.98 (m, 1H), 7.66 – 7.62 (m, 2H), 4.65 – 4.53 (m, 3H), 3.28 – 3.15 (m, 2H), 1.98 – 1.84 (m, 2H), 1.76 – 1.62 (m, 2H), 1.44 (s, 9H).

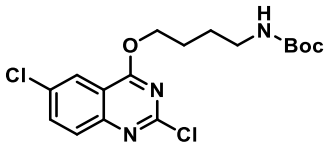

tert-Butyl (5-((2,6-dichloroquinazolin-4-yl)oxy)pentyl)carbamate **(49d)**

The nucleophilic aromatic substitution was carried out as described for compound **49a**.[765] Compound **SM4** (235 mg, 1.01 mmol, 1.0 eq.), sodium hydride (27 mg, 1.11 mmol, 1.1 eq.) and compound **L13** (226 mg, 1.11 mmol, 1.1 eq.) were subjected to the reaction conditions for 20 hours. The crude product was purified by flash chromatography using a gradient elution of ethyl acetate/hexane (0-100%).

Yield:	218 mg, (54%)
Chemical formula:	$C_{18}H_{23}Cl_2N_3O_3$
Molecular mass:	400.30 g/mol
Appearance:	Colourless solid
Internal code:	MST-307
Synthesis scheme:	Figure 145
^{1}H NMR (300 MHz, $CDCl_3$):	δ 8.08 – 8.05 (m, 1H), 7.82 – 7.72 (m, 2H), 4.65 – 4.53 (m, 3H), 3.20 – 3.09 (m, 2H), 1.98 – 1.87 (m, 2H), 1.62 – 1.49 (m, 4H), 1.43 (s, 9H).

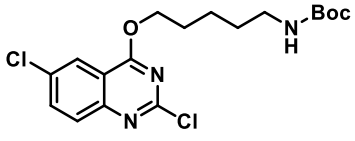

tert-Butyl (6-((2,6-dichloroquinazolin-4-yl)oxy)hexyl)carbamate **(49e)**

The nucleophilic aromatic substitution was carried out as described for compound **49a**.[765] Compound **SM4** (217 mg, 0.93 mmol, 1.0 eq.), sodium hydride (24 mg, 1.02 mmol, 1.1 eq.) and

compound **L14** (222 mg, 1.02 mmol, 1.1 eq.) were subjected to the reaction conditions for 20 hours. The crude product was purified by flash chromatography using a gradient elution of ethyl acetate/hexane (0-100%).

Yield:	69 mg, (18%)
Chemical formula:	$C_{19}H_{25}Cl_2N_3O_3$
Molecular mass:	414.33 g/mol
Appearance:	Colourless solid
Internal code:	MST-319
Synthesis scheme:	Figure 145
^{1}H NMR (300 MHz, $CDCl_3$):	δ 8.08 – 8.05 (m, 1H), 7.81 – 7.72 (m, 2H), 4.62 – 4.49 (m, 3H), 3.18 – 3.06 (m, 2H), 1.95 – 1.84 (m, 2H), 1.58 – 1.39 (m, 16H).

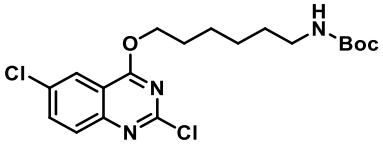

tert-Butyl (2-(2-((2,6-dichloroquinazolin-4-yl)oxy)ethoxy)ethyl)carbamate **(49f)**

The nucleophilic aromatic substitution was carried out as described for compound **49a**.[765] Compound **SM4** (152 mg, 0.65 mmol, 1.0 eq.), sodium hydride (17 mg 0.72 mmol, 1.1 eq.) and compound **L15** (147 mg, 0.72 mmol, 1.1 eq.) were subjected to the reaction conditions for 20 hours. The crude product was purified by flash chromatography using a gradient elution of ethyl acetate/hexane (0-100%).

Yield:	175 mg, (67%)
Chemical formula:	$C_{17}H_{21}Cl_2N_3O_4$
Molecular mass:	402.27 g/mol
Appearance:	Colourless solid
Internal code:	MST-335
Synthesis scheme:	Figure 145
^{1}H NMR (300 MHz, $CDCl_3$):	δ 8.16 – 8.03 (m, 1H), 7.81 – 7.60 (m, 2H), 4.82 (t, *J* = 7.1 Hz, 1H), 4.74 – 4.65 (m, 2H), 3.90 – 3.81 (m, 2H), 3.64 – 3.42 (m, 2H), 3.34 – 3.21 (m, 2H), 1.39 (s, 9H).

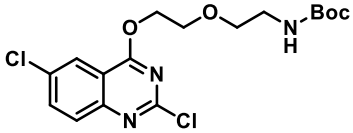

tert-Butyl-(2-(2-(2-((2,6-dichloroquinazolin-4-yl)oxy)ethoxy)ethoxy)ethyl)carbamate **(49g)**

The nucleophilic aromatic substitution was carried out as described for compound **49a**.[765] Compound **SM4** (139 mg, 0.60 mmol, 1.0 eq.), sodium hydride (16 mg, 0.66 mmol, 1.1 eq.) and compound **L16** (164 mg, 0.66 mmol, 1.1 eq.) were subjected to the reaction conditions for 20 hours. The crude product was purified by flash chromatography using a gradient elution of ethyl acetate/hexane (0-100%).

Yield:	91 mg, (34%)
Chemical formula:	$C_{19}H_{25}Cl_2N_3O_5$
Molecular mass:	446.33 g/mol
Appearance:	Colourless solid
Internal code:	MST-339
Synthesis scheme:	Figure 145
^{1}H NMR (300 MHz, $CDCl_3$):	δ 8.10 – 8.03 (m, 1H), 7.78 – 7.65 (m, 2H), 4.95 (t, *J* = 6.7 Hz, 2H), 4.75 – 4.64 (m, 2H), 4.19 – 4.08 (m, 2H), 3.94 – 3.85 (m, 2H), 3.73 – 3.42 (m, 4H), 3.30 – 3.18 (m, 2H), 1.36 (s, 9H).

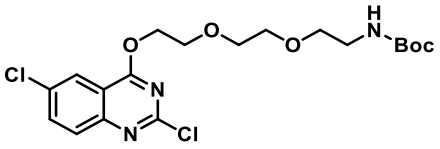

tert-Butyl-(2-(2-(2-(2-((2,6-dichloroquinazolin-4-yl)oxy)ethoxy)ethoxy)ethoxy)ethyl)carbamate **(49h)**

The nucleophilic aromatic substitution was carried out as described for compound **49a**.[765] Compound **SM4** (300 mg, 1.29 mmol, 1.0 eq.), sodium hydride (196 µL, 1.42 mmol, 1.1 eq.) and compound **L17** (416 mg, 1.42 mmol, 1.1 eq.) were subjected to the reaction conditions for 20 hours. The crude product was purified by flash chromatography using a gradient elution of ethyl acetate/hexane (0-100%).

Yield:	142 mg, (29%)
Chemical formula:	$C_{21}H_{29}Cl_2N_3O_6$
Molecular mass:	490.38 g/mol
Appearance:	Colourless solid
Internal code:	MST-404
Synthesis scheme:	Figure 145
^{1}H NMR (300 MHz, $CDCl_3$):	δ 8.12 – 8.03 (m, 1H), 7.83 – 7.68 (m, 2H), 4.99 (t, *J* = 6.3 Hz, 2H), 4.78 – 4.65 (m, 2H), 4.25 – 4.18 (m, 2H), 3.99 – 3.85 (m, 2H), 3.75 – 3.38 (m, 6H), 3.33 – 3.12 (m, 4H), 1.39 (s, 9H).

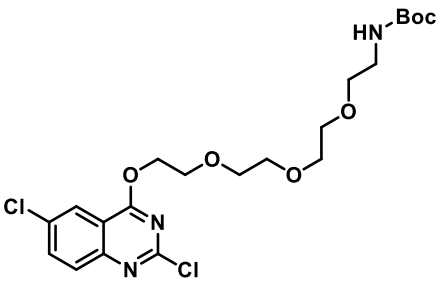

tert-Butyl-(2-((6-chloro-2-(4-methylpiperazin-1-yl)quinazolin-4-yl)oxy)ethyl)carbamate **(P39a)**

The nucleophilic aromatic substitution was carried out as described for compound **P36a**.[761] Compound **49a** (242 mg, 0.68 mmol, 1.0 eq.), DIPEA (127 µL, 0.75 mmol, 1.1 eq.) and *N*-methylpiperazine (83 µL, 0.75 mmol, 1.1 eq.) were subjected to the reaction conditions for 20 hours. The crude product was purified by column chromatography using a gradient elution of dichloromethane/methanol (sat. NH_3) (0-20%).

Yield:	178 mg, (62%)
Chemical formula:	$C_{20}H_{28}ClN_5O_3$
Molecular mass:	421.93 g/mol
Appearance:	Colourless solid
Internal code:	MST-294, ST-2571
Synthesis scheme:	Figure 146
Melting point:	136.1 °C
LC-MS purity:	100%
MS (ESI-(+)):	m/z=422.25 $[M+H^+]^+$ calculated: 422.1953
^{1}H NMR (300 MHz, $CDCl_3$):	δ 7.80 – 7.77 (m, 1H), 7.47 – 7.41 (m, 1H), 7.37 – 7.33 (m, 1H), 4.92 (t, *J* = 5.7 Hz, 1H), 4.47 (t, *J* = 5.1 Hz, 2H), 3.89 – 3.77 (m, 4H), 3.63 – 3.50 (m, 2H), 2.47 – 2.36 (m, 4H), 2.29 (s, 3H), 1.39 (s, 9H).
^{13}C NMR (75.5 MHz, $CDCl_3$):	δ 165.98, 158.25, 155.88, 152.13, 134.26, 129.99, 126.64, 122.72, 111.78, 79.75, 66.18, 55.01, 46.22, 43.93, 39.78, 28.40.

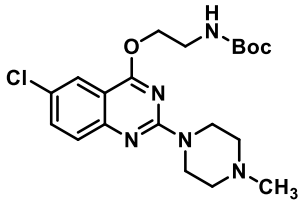

tert-Butyl-(3-((6-chloro-2-(4-methylpiperazin-1-yl)quinazolin-4-yl)oxy)propyl)carbamate **(P39b)**

The nucleophilic aromatic substitution was carried out as described for compound **P36a**.[761] Compound **49b** (160 mg, 0.43 mmol, 1.0 eq.), DIPEA (80 µL, 0.47 mmol, 1.1 eq.) and *N*-methylpiperazine (53 µL, 0.47 mmol, 1.1 eq.) were subjected to the reaction conditions for 20 hours. The crude product was purified by column chromatography using a gradient elution of dichloromethane/methanol (sat. NH_3) (0-20%).

Yield:	120 mg, (64%)
Chemical formula:	$C_{21}H_{30}ClN_5O_3$
Molecular mass:	435.95 g/mol
Appearance:	Colourless solid
Internal code:	MST-305, ST-2573
Synthesis scheme:	Figure 146
Melting point:	139.1 °C
LC-MS purity:	100%
MS (ESI-(+)):	m/z=436.24 $[M+H^+]^+$ calculated: 436.2110

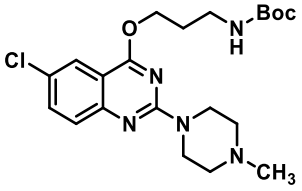

^{1}H NMR (300 MHz, $CDCl_3$):	δ 7.85 – 7.81 (m, 1H), 7.52 – 7.47 (m, 1H), 7.43 – 7.38 (m, 1H), 4.78 (t, *J* = 4.9 Hz, 1H), 4.54 (t, *J* = 6.1 Hz, 2H), 4.00 – 3.82 (m, 4H), 3.41 – 3.23 (m, 2H), 2.53 – 2.42 (m, 4H), 2.35 (s, 3H), 2.14 – 1.99 (m, 2H), 1.43 (s, 9H).
^{13}C NMR (75.5 MHz, $CDCl_3$):	δ 166.04, 158.36, 155.96, 152.44, 152.06, 134.15, 126.61, 122.69, 111.93, 79.37, 64.51, 55.04, 46.25, 43.96, 37.86, 29.23, 28.41.

tert-Butyl-(4-((6-chloro-2-(4-methylpiperazin-1-yl)quinazolin-4-yl)oxy)butyl)carbamate **(P39c)**

The nucleophilic aromatic substitution was carried out as described for compound **P36a**.[761] Compound **49c** (117 mg, 0.30 mmol, 1.0 eq.), DIPEA (56 µL, 0.33 mmol, 1.1 eq.) and *N*-methylpiperazine (37 µL, 0.33 mmol, 1.1 eq.) were subjected to the reaction conditions for 20 hours. The crude product was purified by column chromatography using a gradient elution of dichloromethane/methanol (sat. NH_3) (0-20%).

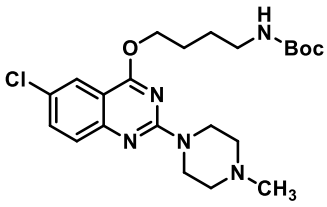

Yield:	126 mg, (93%)
Chemical formula:	$C_{22}H_{32}ClN_5O_3$
Molecular mass:	449.98 g/mol
Appearance:	Colourless solid
Internal code:	MST-350, ST-2595
Synthesis scheme:	Figure 146
Melting point:	127.1 °C
LC-MS purity:	98.8%
MS (ESI-(+)):	m/z=450.25 $[M+H^+]^+$ calculated: 450.2266
^{1}H NMR (300 MHz, $CDCl_3$):	δ 7.80 – 7.74 (m, 1H), 7.47 – 7.38 (m, 1H), 7.36 – 7.30 (m, 1H), 4.54 (d, *J* = 6.7 Hz, 1H), 4.41 (t, *J* = 6.3 Hz, 2H), 4.03 – 3.72 (m, 4H), 3.26 – 3.02 (m, 2H), 2.58 – 2.36 (m, 4H), 2.28 (s, 3H), 1.96 – 1.73 (m, 2H), 1.73 – 1.57 (m, 2H), 1.38 (s, 9H).
^{13}C NMR (75.5 MHz, $CDCl_3$):	δ 166.11, 158.45, 156.00, 152.02, 134.06, 126.57, 126.52, 122.75, 112.04, 79.27, 66.22, 55.05, 46.27, 43.95, 40.28, 28.43, 26.93, 26.07.

tert-Butyl-(5-((6-chloro-2-(4-methylpiperazin-1-yl)quinazolin-4-yl)oxy)pentyl)carbamate **(P39d)**

The nucleophilic aromatic substitution was carried out as described for compound **P36a**.[761] Compound **49d** (175 mg, 0.44 mmol, 1.0 eq.), DIPEA (82 µL, 0.48 mmol, 1.1 eq.) and

N-methylpiperazine (54 µL, 0.48 mmol, 1.1 eq.) were subjected to the reaction conditions for 20 hours. The crude product was purified by column chromatography using a gradient elution of dichloromethane/methanol (sat. NH_3) (0-20%).

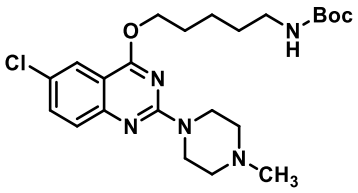

Yield:	190 mg, (93%)
Chemical formula:	$C_{23}H_{34}ClN_5O_3$
Molecular mass:	464.01 g/mol
Appearance:	Colourless solid
Internal code:	MST-311, ST-2575
Synthesis scheme:	Figure 146
Melting point:	121.2 °C
LC-MS purity:	100%
MS (ESI-(+)):	m/z=464.30 $[M+H^+]^+$ calculated: 464.2423
^{1}H NMR (300 MHz, $CDCl_3$):	δ 7.86 – 7.83 (m, 1H), 7.52 – 7.47 (m, 1H), 7.42 – 7.38 (m, 1H), 4.56 (t, *J* = 5.8 Hz, 1H), 4.45 (t, *J* = 6.5 Hz, 2H), 3.97 – 3.88 (m, 4H), 3.22 – 3.11 (m, 2H), 2.54 – 2.44 (m, 4H), 2.35 (s, 3H), 1.94 – 1.80 (m, 2H), 1.65 – 1.47 (m, 4H), 1.43 (s, 9H).
^{13}C NMR (75.5 MHz, $CDCl_3$):	δ 166.18, 158.48, 156.01, 151.98, 134.04, 126.55, 126.51, 122.80, 112.10, 79.17, 77.25, 66.54, 55.05, 46.26, 43.93, 40.46, 29.93, 28.42, 23.43.

tert-Butyl-(6-((6-chloro-2-(4-methylpiperazin-1-yl)quinazolin-4-yl)oxy)hexyl)carbamate **(P39e)**

The nucleophilic aromatic substitution was carried out as described for compound **P36a**.[761] Compound **49e** (30 mg, 0.07 mmol, 1.0 eq.), DIPEA (13 µL, 0.08 mmol, 1.1 eq.) and *N*-methylpiperazine (9 µL, 0.08 mmol, 1.1 eq.) were subjected to the reaction conditions for 20 hours. The crude product was purified by column chromatography using a gradient elution of dichloromethane/methanol (sat. NH_3) (0-20%).

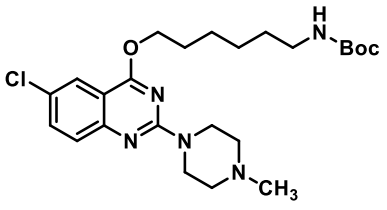

Yield:	30 mg, (90%)
Chemical formula:	$C_{24}H_{36}ClN_5O_3$
Molecular mass:	478.03 g/mol
Appearance:	Colourless solid
Internal code:	MST-321, ST-2575
Synthesis scheme:	Figure 146
Melting point:	124.6 °C
LC-MS purity:	100%

MS (ESI-(+)):	m/z=478.31 $[M+H^+]^+$ calculated: 478.2579
^{1}H NMR (300 MHz, $CDCl_3$):	δ 7.80 – 7.76 (m, 1H), 7.45 – 7.29 (m, 2H), 4.50 (t, *J* = 6.5 Hz, 1H), 4.38 (t, *J* = 6.5 Hz, 2H), 3.90 – 3.80 (m, 4H), 3.13 – 2.99 (m, 2H), 2.45 – 2.36 (m, 4H), 2.28 (s, 3H), 1.85 – 1.71 (m, 2H), 1.50 – 1.30 (m, 15H).
^{13}C NMR (75.5 MHz, $CDCl_3$):	δ 166.20, 158.51, 156.00, 151.98, 133.99, 126.54, 126.46, 122.81, 112.13, 79.07, 66.65, 55.06, 46.27, 43.95, 40.53, 30.09, 28.63, 28.43, 26.57, 25.89.

tert-Butyl-(2-(2-((6-chloro-2-(4-methylpiperazin-1-yl)quinazolin-4-yl)oxy)ethoxy)ethyl)carbamate **(P39f)**

The nucleophilic aromatic substitution was carried out as described for compound **P36a**.[761] Compound **49f** (120 mg, 0.30 mmol, 1.0 eq.), DIPEA (56 µL, 0.33 mmol, 1.1 eq.) and *N*-methylpiperazine (37 µL, 0.47 mmol, 1.1 eq.) were subjected to the reaction conditions for 20 hours. The crude product was purified by column chromatography using a gradient elution of dichloromethane/methanol (sat. NH_3) (0-20%).

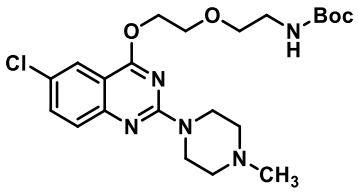

Yield:	136 mg, (97%)
Chemical formula:	$C_{22}H_{32}ClN_5O_4$
Molecular mass:	465.98 g/mol
Appearance:	Colourless solid
Internal code:	MST-351, ST-2597
Synthesis scheme:	Figure 146
Melting point:	145.4 °C
LC-DAD purity:	100%
MS (ESI-(+)):	m/z=466.26 $[M+H^+]^+$ calculated: 466.2216
^{1}H NMR (300 MHz, $CDCl_3$):	δ 7.93 – 7.87 (m, 1H), 7.57 – 7.47 (m, 1H), 7.47 – 7.38 (m, 1H), 4.94 (t, *J* = 6.6 Hz, 1H), 4.68 – 4.59 (m, 2H), 3.98 – 3.86 (m, 6H), 3.64 (t, *J* = 5.2 Hz, 2H), 3.45 – 3.31 (m, 2H), 2.55 – 2.46 (m, 4H), 2.37 (s, 3H), 1.44 (s, 9H).
^{13}C NMR (75.5 MHz, $CDCl_3$):	δ 166.00, 158.27, 155.98, 152.08, 134.22, 126.66, 126.56, 122.84, 111.90, 79.37, 70.39, 68.86, 65.77, 55.02, 50.77, 46.24, 43.94, 28.38.

tert-Butyl-(2-(2-(2-((6-chloro-2-(4-methylpiperazin-1-yl)quinazolin-4-yl)oxy)ethoxy)ethoxy)ethyl)carbamate **(P39g)**

The nucleophilic aromatic substitution was carried out as described for compound **P36a**.[761] Compound **49g** (90 mg, 0.20 mmol, 1.0 eq.), DIPEA (37 µL, 0.22 mmol, 1.1 eq.) and *N*-methylpiperazine (25 µL, 0.22 mmol, 1.1 eq.) were subjected to the reaction conditions for 20 hours. The crude product was purified by column chromatography using a gradient elution of dichloromethane/methanol (sat. NH_3) (0-20%).

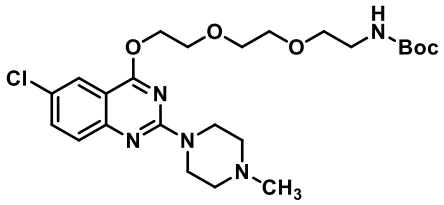

Yield:	34 mg, (33%)
Chemical formula:	$C_{24}H_{36}ClN_5O_5$
Molecular mass:	510.03 g/mol
Appearance:	Colourless solid
Internal code:	MST-354, ST-2598
Synthesis scheme:	Figure 146
Melting point:	137.2 °C
LC-DAD purity:	96.8%
MS (ESI-(+)):	m/z=510.28 $[M+H^+]^+$ calculated: 510.2478
^{1}H NMR (300 MHz, $CDCl_3$):	δ 7.85 – 7.79 (m, 1H), 7.48 – 7.40 (m, 1H), 7.39 – 7.30 (m, 1H), 4.93 (t, *J* = 6.4 Hz, 1H), 4.62 – 4.53 (m, 2H), 3.91 – 3.81 (m, 6H), 3.71 – 3.62 (m, 2H), 3.62 – 3.54 (m, 2H), 3.54 – 3.44 (m, 2H), 3.33 – 3.19 (m, 2H), 2.47 – 2.37 (m, 4H), 2.28 (s, 3H), 1.35 (s, 9H).
^{13}C NMR (75.5 MHz, $CDCl_3$):	δ 166.02, 158.30, 155.95, 152.07, 134.18, 126.60, 126.55, 122.90, 111.94, 79.20, 77.24, 70.76, 70.34, 69.18, 65.85, 55.02, 46.23, 43.93, 40.38, 28.40.

tert-Butyl-(2-(2-(2-(2-((6-chloro-2-(4-methylpiperazin-1-yl)quinazolin-4-yl)oxy)ethoxy)ethoxy)ethoxy)ethyl)carbamate **(P39h)**

The nucleophilic aromatic substitution was carried out as described for compound **P36a**.[761] Compound **49h** (190 mg, 0.39 mmol, 1.0 eq.), DIPEA (73 µL, 0.43 mmol, 1.1 eq.) and *N*-methylpiperazine (48 µL, 0.43 mmol, 1.1 eq.) were subjected to the reaction conditions for 20 hours. The crude product was purified by column chromatography using a gradient elution of dichloromethane/methanol (sat. NH_3) (0-20%).

Yield:	166 mg, (77%)
Chemical formula:	$C_{26}H_{40}ClN_5O_6$
Molecular mass:	554.09 g/mol
Appearance:	Colourless solid
Internal code:	MST-406, ST-2602
Synthesis scheme:	Figure 146
Melting point:	135.4 °C
LC-DAD purity:	96.3%
MS (ESI-(+)):	m/z=554.29 $[M+H^+]^+$ calculated: 554.2740
^{1}H NMR (300 MHz, $CDCl_3$):	δ 7.84 – 7.77 (m, 1H), 7.45 – 7.39 (m, 1H), 7.37 – 7.29 (m, 1H), 5.05 (t, *J* = 5.3 Hz, 1H), 4.61 – 4.51 (m, 2H), 3.91 – 3.79 (m, 6H), 3.73 – 3.40 (m, 10H), 3.32 – 3.16 (m, 2H), 2.45 – 2.36 (m, 4H), 2.27 (s, 3H), 1.35 (s, 9H).
^{13}C NMR (75.5 MHz, $CDCl_3$):	δ 165.98, 158.27, 155.97, 152.04, 134.10, 126.52, 126.49, 122.85, 111.91, 79.09, 77.31, 70.83, 70.58, 70.25, 70.21, 69.12, 65.83, 54.99, 46.22, 43.92, 40.33, 28.41.

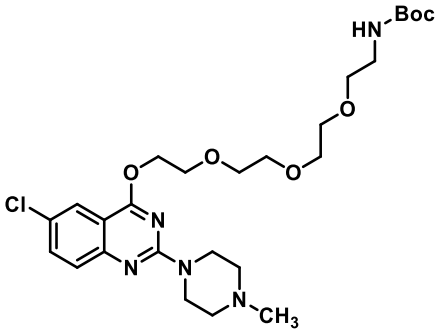

2-((6-Chloro-2-(4-methylpiperazin-1-yl)quinazolin-4-yl)oxy)ethan-1-amine **(P40a)**

The Boc-deprotection protocol was carried out as described for compound **P6**.[674] Compound **P39a** (178 mg, 0.43 mmol, 1.0 eq.) was subjected to the reaction conditions for 24 hours. The crude product was converted to its free base using a strong basic anion exchanger and subsequently purified by reverse phase flash chromatography using a gradient elution of water/methanol (0-100%).

Yield:	107 mg, (77%)
Chemical formula:	$C_{15}H_{20}ClN_5O$
Molecular mass:	321.81 g/mol
Appearance:	Colourless solid
Internal code:	MST-330, ST-2611
Synthesis scheme:	Figure 147
Melting point:	269.1 °C
LC-DAD purity:	97.0%
MS (ESI-(+)):	m/z=322.16 $[M+H^+]^+$ calculated: 322.1429

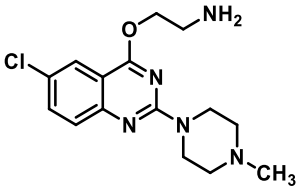

^{1}H NMR (300 MHz, $CDCl_3$):	δ 8.19 – 8.11 (m, 1H), 8.03 (t, *J* = 5.6 Hz, 2H), 7.53 – 7.43 (m, 1H), 7.34 – 7.08 (m, 1H), 3.81 – 3.72 (m, 4H), 3.63 (t, *J* = 5.6 Hz, 2H), 3.58 – 3.47 (m, 2H), 2.42 – 2.33 (m, 4H), 2.23 (s, 3H).
^{13}C NMR (75.5 MHz, $CDCl_3$):	δ 164.46, 163.85, 155.68, 137.68, 132.17, 129.23, 127.40, 116.61, 64.17, 59.69, 50.87, 48.65, 48.37.

3-((6-Chloro-2-(4-methylpiperazin-1-yl)quinazolin-4-yl)oxy)propan-1-amine **(P40b)**

The Boc-deprotection protocol was carried out as described for compound **P6**.[674] Compound **P39b** (120 mg, 0.28 mmol, 1.0 eq.) was subjected to the reaction conditions for 24 hours. The crude product was converted to its free base using a strong basic anion exchanger and subsequently purified by reverse phase flash chromatography using a gradient elution of water/methanol (0-100%).

Yield:	83 mg, (88%)
Chemical formula:	$C_{16}H_{22}ClN_5O$
Molecular mass:	335.84 g/mol
Appearance:	Colourless solid
Internal code:	MST-331, ST-2650
Synthesis scheme:	Figure 147
Melting point:	266.2 °C
LC-DAD purity:	96.1%
MS (ESI-(+)):	m/z=336.18 $[M+H^+]^+$ calculated: 336.1586
^{1}H NMR (300 MHz, D_2O):	δ 7.83 – 7.79 (m, 1H), 7.66 – 7.55 (m, 1H), 7.42 – 7.31 (m, 1H), 4.60 – 4.12 (m, 2H), 3.49 – 3.11 (m, 10H), 2.88 (s, 3H), 2.29 – 2.12 (m, 2H).
^{13}C NMR (151 MHz, D_2O):	δ 165.87, 156.41, 148.04, 134.78, 127.91, 124.09, 122.61, 111.36, 64.81, 53.06, 43.04, 41.42, 37.02, 26.14.

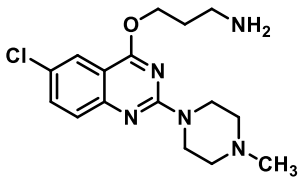

4-((6-Chloro-2-(4-methylpiperazin-1-yl)quinazolin-4-yl)oxy)butan-1-amine **(P40c)**

The Boc-deprotection protocol was carried out as described for compound **P6**.[674] Compound **P39c** (102 mg, 0.23 mmol, 1.0 eq.) was subjected to the reaction conditions for 24 hours. The crude product was converted to its free base using a strong basic anion exchanger and subsequently purified by reverse phase flash chromatography using a gradient elution of water/methanol (0-100%).

Yield:	80 mg, (100%)
Chemical formula:	$C_{17}H_{24}ClN_5O$
Molecular mass:	349.86 g/mol
Appearance:	Colourless solid
Internal code:	MST-426, ST-2612
Synthesis scheme:	Figure 147
Melting point:	257.5 °C
LC-DAD purity:	95.3%
MS (ESI-(+)):	m/z=350.19 $[M+H^+]^+$ calculated: 350.1742
^{1}H NMR (300 MHz, DMSO-d_6):	δ 8.01 – 7.95 (m, 2H), 7.84 – 7.72 (m, 1H), 7.70 – 7.65 (m, 1H), 7.64 – 7.56 (m, 1H), 4.38 – 4.28 (m, 4H), 3.39 (t, *J* = 12.8 Hz, 2H), 2.97 – 2.84 (m, 2H), 2.63 – 2.48 (m, 7H), 1.69 – 1.56 (m, 2H), 1.59 – 1.43 (m, 2H).
^{13}C NMR (75.5 MHz, DMSO-d_6):	δ 166.31, 154.43, 135.74, 128.41, 128.31, 122.98, 122.76, 111.46, 66.32, 51.43, 42.12, 41.85, 38.28, 25.02, 23.64.

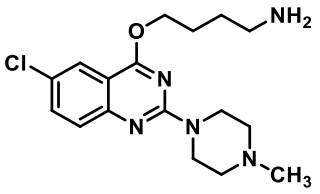

5-((6-Chloro-2-(4-methylpiperazin-1-yl)quinazolin-4-yl)oxy)pentan-1-amine **(P40d)**

The Boc-deprotection protocol was carried out as described for compound **P6**.[674] Compound **P39d** (155 mg, 0.33 mmol, 1.0 eq.) was subjected to the reaction conditions for 24 hours. The crude product was converted to its free base using a strong basic anion exchanger and subsequently purified by reverse phase flash chromatography using a gradient elution of water/methanol (0-100%).

Yield:	90 mg, (75%)
Chemical formula:	$C_{18}H_{26}ClN_5O$
Molecular mass:	363.89 g/mol
Appearance:	Colourless solid
Internal code:	MST-332, ST-2651
Synthesis scheme:	Figure 147
Melting point:	222.2 °C
LC-DAD purity:	99.6%
MS (ESI-(+)):	m/z=364.21 $[M+H^+]^+$ calculated: 364.1899

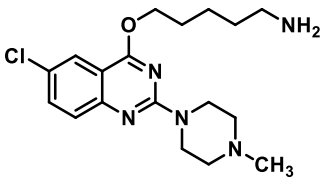

^{1}H NMR (300 MHz, D_2O):	δ 7.76 – 7.72 (m, 1H), 7.58 – 7.52 (m, 1H), 7.32 – 7.27 (m, 1H), 4.41 (t, *J* = 6.3 Hz, 2H), 3.66 – 3.08 (m, 8H), 3.02 – 2.93 (m, 2H), 2.88 (s, 3H), 1.92 – 1.79 (m, 2H), 1.77 – 1.64 (m, 2H), 1.62 – 1.44 (m, 2H).
^{13}C NMR (151 MHz, D_2O):	δ 166.74, 157.95, 150.26, 134.63, 127.57, 125.34, 122.88, 112.23, 67.28, 53.27, 43.12, 41.50, 39.51, 27.50, 26.63, 22.51.

6-((6-Chloro-2-(4-methylpiperazin-1-yl)quinazolin-4-yl)oxy)hexan-1-amine **(P40e)**

The Boc-deprotection protocol was carried out as described for compound **P6**.[674] Compound **P39e** (24 mg, 0.05 mmol, 1.0 eq.) was subjected to the reaction conditions for 24 hours. The crude product was converted to its free base using a strong basic anion exchanger and subsequently purified by reverse phase flash chromatography using a gradient elution of water/methanol (0-100%).

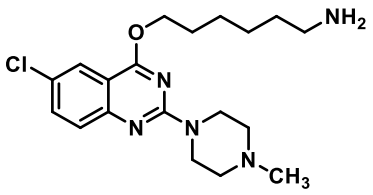

Yield:	16 mg, (84%)
Chemical formula:	$C_{19}H_{28}ClN_5O$
Molecular mass:	377.92 g/mol
Appearance:	Colourless solid
Internal code:	MST-333, ST-2652
Synthesis scheme:	Figure 147
Melting point:	261.8 °C
LC-DAD purity:	96.4%
MS (ESI-(+)):	m/z=378.23 $[M+H^+]^+$ calculated: 378.2055
^{1}H NMR (300 MHz, D_2O):	δ 7.79 – 7.75 (m, 1H), 7.63 – 7.55 (m, 1H), 7.36 – 7.31 (m, 1H), 4.44 (t, *J* = 6.0 Hz, 2H), 3.73 – 3.04 (m, 8H), 3.00 – 2.89 (m, 5H), 1.90 – 1.77 (m, 2H), 1.74 – 1.58 (m, 2H), 1.56 – 1.37 (m, 4H).
^{13}C NMR (151 MHz, D_2O):	δ 179.29, 167.45, 156.70, 147.66, 135.49, 123.70, 123.48, 112.41, 68.11, 53.00, 52.72, 43.04, 41.70, 39.48, 27.43, 26.59, 22.48.

2-(2-((6-Chloro-2-(4-methylpiperazin-1-yl)quinazolin-4-yl)oxy)ethoxy)ethan-1-amine **(P40f)**

The Boc-deprotection protocol was carried out as described for compound **P6**.[674] Compound **P40f** (150 mg, 0.32 mmol, 1.0 eq.) was subjected to the reaction conditions for 24 hours. The crude product was converted to its free base using a strong basic anion exchanger and subsequently purified by reverse phase flash chromatography using a gradient elution of water/methanol (0-100%).

Yield:	117 mg, (100%)
Chemical formula:	$C_{17}H_{24}ClN_5O_2$
Molecular mass:	365.86 g/mol
Appearance:	Colourless solid
Internal code:	MST-432, ST-2614
Synthesis scheme:	Figure 147
Melting point:	269.1 °C
LC-DAD purity:	100%
MS (ESI-(+)):	m/z=366.19 $[M+H^+]^+$ calculated: 366.1691
^{1}H NMR (300 MHz, DMSO-d_6):	δ 8.29 – 8.23 (m, 2H), 8.03 – 7.95 (m, 2H), 7.94 – 7.85 (m, 1H), 4.81 – 4.72 (m, 2H), 3.98 – 3.89 (m, 2H), 3.80 – 3.69 (m, 2H), 3.70 – 3.48 (m, 6H), 3.30 – 2.92 (m, 4H), 2.80 (s, 3H).
^{13}C NMR (75.5 MHz, DMSO-d_6):	δ 166.28, 154.83, 154.63, 135.63, 128.08, 128.04, 123.04, 111.48, 79.27, 67.87, 67.52, 66.61, 66.32, 51.45, 41.84.

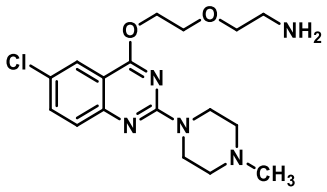

2-(2-(2-((6-Chloro-2-(4-methylpiperazin-1-yl)quinazolin-4-yl)oxy)ethoxy)ethoxy)ethan-1-amine **(P40g)**

The Boc-deprotection protocol was carried out as described for compound **P6**.[674] Compound **P39g** (30 mg, 0.06 mmol, 1.0 eq.) was subjected to the reaction conditions for 24 hours. The crude product was converted to its free base using a strong basic anion exchanger and subsequently purified by reverse phase flash chromatography using a gradient elution of water/methanol (0-100%).

Yield:	25 mg, (100%)
Chemical formula:	$C_{19}H_{28}ClN_5O_3$
Molecular mass:	409.92 g/mol
Appearance:	Colourless solid
Internal code:	MST-439, ST-2617
Synthesis scheme:	Figure 147
Melting point:	270.1 °C
LC-DAD purity:	100%
MS (ESI-(+)):	m/z= 410.21 $[M+H^+]^+$ calculated: 410.1953

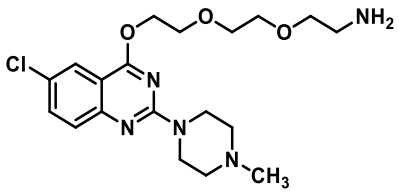

^{1}H NMR (300 MHz, MeOD):	δ 8.09 – 8.03 (m, 1H), 7.92 – 7.78 (m, 2H), 3.99 – 3.90 (m, 2H), 3.77 – 3.50 (m, 12H), 3.39 – 3.33 (m, 4H), 3.08 – 2.99 (m, 2H), 2.93 (s, 3H).
^{13}C NMR (75.5 MHz, MeOD):	δ 169.25, 154.56, 142.39, 138.23, 132.49, 125.37, 121.40, 113.35, 71.72, 71.41, 70.61, 69.69, 67.96, 53.58, 44.04, 43.70, 40.73.

2-(2-(2-(2-((6-Chloro-2-(4-methylpiperazin-1-yl)quinazolin-4-yl)oxy)ethoxy)ethoxy)ethoxy)ethan-1-amine **(P40h)**

The Boc-deprotection protocol was carried out as described for compound **P6**.[674] Compound **P39h** (137 mg, 0.25 mmol, 1.0 eq.) was subjected to the reaction conditions for 24 hours. The crude product was converted to its free base using a strong basic anion exchanger and subsequently purified by reverse phase flash chromatography using a gradient elution of water/methanol (0-100%).

Yield:	114 mg, (100%)
Chemical formula:	$C_{21}H_{32}ClN_5O_4$
Molecular mass:	453.97 g/mol
Appearance:	Colourless solid
Internal code:	MST-435, ST-2616
Synthesis scheme:	Figure 147
Melting point:	269.1 °C
LC-DAD purity:	100%
MS (ESI-(+)):	m/z=454.25 $[M+H^+]^+$ calculated: 454.2216
^{1}H NMR (300 MHz, DMSO-d_6):	δ 8.20 – 8.14 (m, 2H), 8.01 – 7.84 (m, 3H), 4.77 – 4.68 (m, 2H), 3.95 – 3.86 (m, 2H), 3.73 – 3.44 (m, 14H), 3.35 – 3.09 (m, 4H), 3.00 – 2.84 (m, 2H), 2.79 (s, 3H).
^{13}C NMR (75.5 MHz, DMSO-d_6):	δ 166.23, 147.67, 135.50, 127.86, 123.72, 122.78, 115.41, 111.47, 69.85, 69.70, 69.60, 69.60, 67.98, 67.59, 66.54, 66.32, 51.49, 41.85, 38.33.

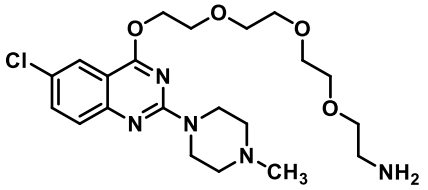

N-(2-((6-Chloro-2-(4-methylpiperazin-1-yl)quinazolin-4-yl)oxy)ethyl)-3-(5,5-difluoro-7,9-dimethyl-5*H*-5λ^4,6λ^4-dipyrrolo[1,2-*c*:2',1'-*f*][1,3,2]diazaborinin-3-yl)propanamide **(P41a)**

The HATU coupling was carried out as described for compound **P3**.[644] Compound **P40a** (30 mg, 0.09 mmol, 1.0 eq.), DIPEA (17 µL, 0.10 mmol, 1.1 eq.), BODIPY-FL (26 mg, 0.12 mmol, 1.0 eq.) and HATU (38 mg, 0.10 mmol, 1.1 eq.) were subjected to the reaction conditions for 24 hours.

The crude product was purified by column chromatography using a gradient elution of dichloromethane/methanol (sat. NH_3) (0-20%).

Yield:	10 mg, (19%)
Chemical formula:	$C_{29}H_{33}BClF_2N_7O_2$
Molecular mass:	595.89 g/mol
Appearance:	Red solid
Internal code:	MST-584, ST-2777
Synthesis scheme:	Figure 148
Melting point:	145.2 °C
LC-MS-DAD purity:	95.6%
HR-MS (ESI-(+)):	m/z= 596.2989 $[M+H^+]^+$ calculated: 596.2518
^{1}H NMR (300 MHz, MeOD):	δ 7.78 – 7.70 (m, 1H), 7.39 – 7.29 (m, 1H), 7.29 – 7.19 (m, 1H), 7.15 (s, 1H), 6.69 (d, *J* = 4.1 Hz, 1H), 6.10 (d, *J* = 4.1 Hz, 1H), 6.07 (s, 1H), 4.27 (t, *J* = 5.6 Hz, 2H), 3.82 – 3.73 (m, 4H), 3.68 (t, *J* = 5.6 Hz, 2H), 3.09 (t, *J* = 7.3 Hz, 2H), 2.65 (t, *J* = 7.4 Hz, 2H), 2.48 – 2.30 (m, 7H), 2.23 (s, 3H), 2.15 (s, 3H).
^{13}C NMR (151 MHz, MeOD):	δ 172.86, 160.01, 159.71, 158.86, 156.44, 150.12, 144.47, 135.13, 133.37, 132.63, 127.91, 126.01, 125.85, 124.28, 121.53, 119.99, 115.83, 111.46, 62.23, 54.47, 44.66, 43.20, 39.65, 32.67, 32.62, 23.51, 9.83.

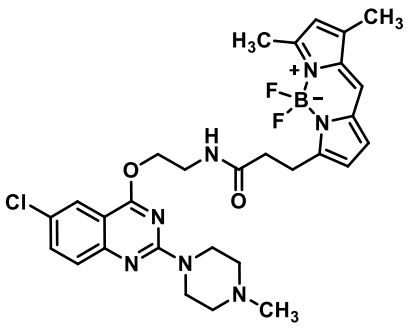

N-(3-((6-Chloro-2-(4-methylpiperazin-1-yl)quinazolin-4-yl)oxy)propyl)-3-(5,5-difluoro-7,9-dimethyl-5*H*-5λ^4,6λ^4-dipyrrolo[1,2-*c*:2',1'-*f*][1,3,2]diazaborinin-3-yl)propanamide **(P41b)**

The HATU coupling was carried out as described for compound **P3**.[644] Compound **P40b** (30 mg, 0.09 mmol, 1.0 eq.), DIPEA (17 µL, 0.10 mmol, 1.1 eq.), BODIPY-FL (26 mg, 0.14 mmol, 1.0 eq.) and HATU (38 mg, 0.10 mmol, 1.1 eq.) were subjected to the reaction conditions for 24 hours. The crude product was purified by column chromatography using a gradient elution of dichloromethane/methanol (sat. NH_3) (0-20%).

Yield:	23 mg, (42%)
Chemical formula:	$C_{30}H_{35}BClF_2N_7O_2$
Molecular mass:	609.91 g/mol
Appearance:	Red solid
Internal code:	MST-652
Synthesis scheme:	Figure 148
Melting point:	139.6 °C

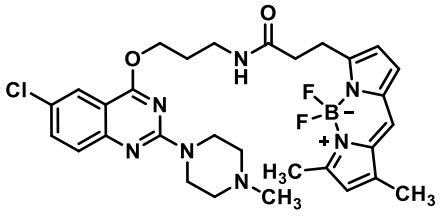

LC-MS-DAD purity:	100%
HR-MS (ESI-(+)):	m/z= 610.2691 $[M+H^+]^+$ calculated: 610.2675
^{1}H NMR (300 MHz, MeOD):	δ 7.85 – 7.79 (m, 1H), 7.57 – 7.49 (m, 1H), 7.44 – 7.34 (m, 1H), 7.23 (s, 1H), 6.88 (d, *J* = 4.1 Hz, 1H), 6.29 (d, *J* = 4.1 Hz, 1H), 6.12 (s, 1H), 4.42 (t, *J* = 6.4 Hz, 2H), 3.95 – 3.84 (m, 4H), 3.40 (t, *J* = 6.6 Hz, 2H), 3.21 (t, *J* = 7.4 Hz, 2H), 2.61 (t, *J* = 7.5 Hz, 2H), 2.56 – 2.51 (m, 4H), 2.45 (s, 3H), 2.34 (s, 3H), 2.21 (s, 3H), 2.12 – 1.98 (m, 2H).
^{13}C NMR (75.5 MHz, MeOD):	δ 174.72, 167.47, 161.32, 159.65, 158.20, 153.06, 145.81, 136.46, 135.25, 134.76, 129.44, 128.01, 127.54, 125.61, 123.78, 121.34, 117.60, 113.20, 65.83, 55.74, 46.06, 44.61, 37.33, 36.04, 29.50, 25.64, 11.26, 11.24.

N-(4-((6-Chloro-2-(4-methylpiperazin-1-yl)quinazolin-4-yl)oxy)butyl)-3-(5,5-difluoro-7,9-dimethyl-5*H*-5λ^4,6λ^4-dipyrrolo[1,2-c:2',1'-*f*][1,3,2]diazaborinin-3-yl)propanamide **(P41c)**

The HATU coupling was carried out as described for compound **P3**.[644] Compound **P40c** (35 mg, 0.08 mmol, 1.0 eq.), DIPEA (15 µL, 0.09 mmol, 1.1 eq.), BODIPY-FL (23 mg, 0.08 mmol, 1.0 eq.) and HATU (33 mg, 0.09 mmol, 1.1 eq.) were subjected to the reaction conditions for 24 hours. The crude product was purified by column chromatography using a gradient elution of dichloromethane/methanol (sat. NH_3) (0-20%).

Yield:	29 mg, (58%)
Chemical formula:	$C_{31}H_{37}BClF_2N_7O_2$
Molecular mass:	623.94 g/mol
Appearance:	Red solid
Internal code:	MST-653
Synthesis scheme:	Figure 148
Melting point:	150.2 °C
LC-MS-DAD purity:	95.2%
HR-MS (ESI-(+)):	m/z= 624.2851 $[M+H^+]^+$ calculated: 624.2831
^{1}H NMR (300 MHz, MeOD):	δ 7.73 – 7.65 (m, 1H), 7.50 – 7.40 (m, 1H), 7.37 – 7.27 (m, 1H), 7.17 (s, 1H), 6.81 (d, *J* = 4.0 Hz, 1H), 6.21 (d, *J* = 4.0 Hz, 1H), 6.01 (s, 1H), 4.34 (t, *J* = 6.4 Hz, 2H), 3.89 – 3.75 (m, 4H), 3.20 – 3.07 (m, 4H), 2.60 – 2.44 (m, 6H), 2.34 (s, 3H), 2.29 (s, 3H), 2.08 (s, 3H), 1.80 – 1.66 (m, 2H), 1.65 – 1.51 (m, 2H).

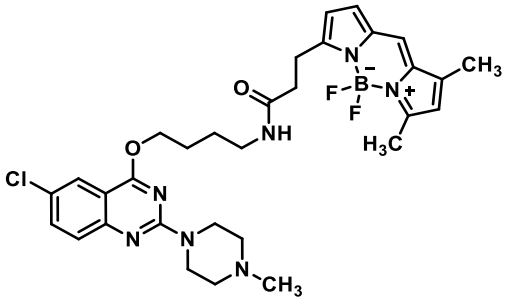

^{13}C NMR (75.5 MHz, MeOD): δ 174.64, 167.59, 159.67, 158.31, 153.07, 145.76, 136.48, 135.28, 134.84, 129.44, 128.06, 127.59, 125.63, 123.75, 121.33, 117.70, 117.37, 113.26, 67.86, 55.65, 45.89, 44.47, 40.00, 36.03, 27.10, 27.01, 25.75, 25.71, 11.21.

N-(5-((6-Chloro-2-(4-methylpiperazin-1-yl)quinazolin-4-yl)oxy)pentyl)-3-(5,5-difluoro-7,9-dimethyl-5*H*-5λ^4,6λ^4-dipyrrolo[1,2-*c*:2',1'-*f*][1,3,2]diazaborinin-3-yl)propanamide **(P41d)**

The HATU coupling was carried out as described for compound **P3**.[644] Compound **P40d** (30 mg, 0.11 mmol, 1.0 eq.), DIPEA (20 µL, 0.12 mmol, 1.1 eq.), BODIPY-FL (32 mg, 0.11 mmol, 1.0 eq.) and HATU (46 mg, 0.11 mmol, 1.1 eq.) were subjected to the reaction conditions for 24 hours. The crude product was purified by column chromatography using a gradient elution of dichloromethane/methanol (sat. NH_3) (0-20%).

Yield:	17 mg, (24%)
Chemical formula:	$C_{32}H_{39}BClF_2N_7O_2$
Molecular mass:	637.97 g/mol
Appearance:	Red solid
Internal code:	MST-566, ST-2762
Synthesis scheme:	Figure 148
Melting point	141.2 °C
LC-DAD purity:	95.1%
MS (ESI-(+)):	m/z= 638.32 $[M+H^+]^+$ calculated: 638.2988
^{1}H NMR (600 MHz, MeOD):	δ 7.93 – 7.87 (m, 1H), 7.66 – 7.61 (m, 1H), 7.53 – 7.49 (m, 1H), 7.43 (s, 1H), 7.04 (d, *J* = 4.1 Hz, 1H), 6.39 (d, *J* = 4.1 Hz, 1H), 6.24 (s, 1H), 4.57 (t, *J* = 6.5 Hz, 2H), 4.03 – 3.91 (m, 4H), 3.44 – 3.36 (m, 4H), 2.72 – 2.64 (m, 2H), 2.65 – 2.51 (m, 7H), 2.43 (s, 3H), 2.32 (s, 3H), 2.01 – 1.91 (m, 2H), 1.71 – 1.63 (m, 2H), 1.63 – 1.55 (m, 2H).
^{13}C NMR (151 MHz, MeOD):	δ 173.17, 166.28, 159.93, 158.49, 157.18, 151.80, 144.35, 135.14, 133.79, 128.12, 126.62, 126.15, 124.20, 122.29, 122.28, 119.93, 116.32, 111.90, 66.75, 66.73, 54.45, 44.75, 43.42, 38.81, 34.72, 28.66, 27.97, 24.36, 23.03, 9.71.

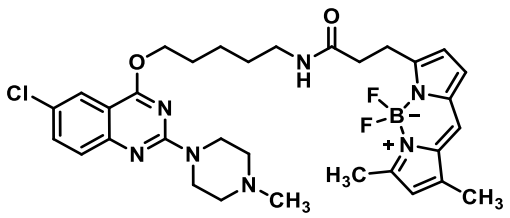

N-(6-((6-Chloro-2-(4-methylpiperazin-1-yl)quinazolin-4-yl)oxy)hexyl)-3-(5,5-difluoro-7,9-dimethyl-5*H*-5λ^4,6λ^4-dipyrrolo[1,2-c:2',1'-*f*][1,3,2]diazaborinin-3-yl)propanamide **(P41e)**

The HATU coupling was carried out as described for compound **P3**.[644] Compound **P40e** (36 mg, 0.08 mmol, 1.0 eq.), DIPEA (15 µL, 0.09 mmol, 1.1 eq.), BODIPY-FL (23 mg, 0.08 mmol, 1.0 eq.) and HATU (34 mg, 0.19 mmol, 1.1 eq.) were subjected to the reaction conditions for 24 hours. The crude product was purified by column chromatography using a gradient elution of dichloromethane/methanol (sat. NH_3) (0-20%).

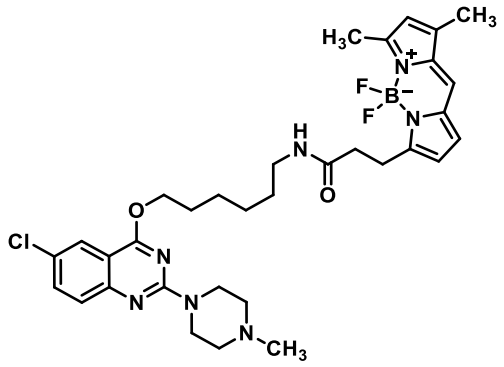

Yield:	18 mg, (35%)
Chemical formula:	$C_{33}H_{41}BClF_2N_7O_2$
Molecular mass:	651.99 g/mol
Appearance:	Red solid
Internal code:	MST-654
Synthesis scheme:	Figure 148
Melting point:	139.3 °C
LC-MS-DAD purity:	97.6%
HR-MS (ESI-(+)):	m/z= 652.3155 $[M+H^+]^+$ calculated: 652.3144
^{1}H NMR (300 MHz, MeOD):	δ 7.83 – 7.75 (m, 1H), 7.59 – 7.51 (m, 1H), 7.46 – 7.38 (m, 1H), 7.34 (s, 1H), 6.96 (d, *J* = 4.1 Hz, 1H), 6.31 (d, *J* = 4.1 Hz, 1H), 6.13 (s, 1H), 4.46 (t, *J* = 6.6 Hz, 2H), 4.00 – 3.80 (m, 4H), 3.27 – 3.15 (m, 4H), 2.65 – 2.53 (m, 6H), 2.45 (s, 3H), 2.38 (s, 3H), 2.22 (s, 3H), 1.92 – 1.77 (m, 2H), 1.62 – 1.34 (m, 6H).
^{13}C NMR (75.5 MHz, MeOD):	δ 174.56, 167.64, 159.72, 153.06, 136.49, 135.25, 134.87, 129.57, 129.53, 128.04, 127.60, 125.71, 123.69, 121.35, 117.70, 117.65, 117.60, 113.29, 68.24, 55.68, 45.94, 44.52, 40.29, 36.00, 30.28, 29.63, 27.62, 26.85, 25.73, 11.22, 11.20.

N-(2-(2-((6-Chloro-2-(4-methylpiperazin-1-yl)quinazolin-4-yl)oxy)ethoxy)ethyl)-3-(5,5-difluoro-7,9-dimethyl-5*H*-5λ^4,6λ^4-dipyrrolo[1,2-*c*:2',1'-*f*][1,3,2]diazaborinin-3-yl)propanamide **(P41f)**

The HATU coupling was carried out as described for compound **P3**.[644] Compound **P40f** (55 mg, 0.12 mmol, 1.0 eq.), DIPEA (22 µL, 0.13 mmol, 1.1 eq.), BODIPY-FL (35 mg, 0.12 mmol, 1.0 eq.) and HATU (50 mg, 0.13 mmol, 1.1 eq.) were subjected to the reaction conditions for 24 hours. The crude product was purified by column chromatography using a gradient elution of dichloromethane/methanol (sat. NH_3) (0-20%).

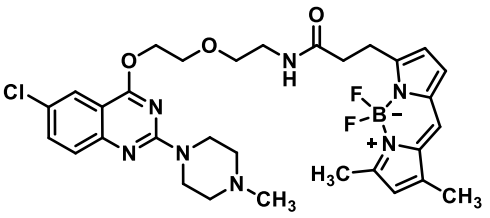

Yield:	45 mg, (59%)
Chemical formula:	$C_{31}H_{37}BClF_2N_7O_3$
Molecular mass:	639.94 g/mol
Appearance:	Red solid
Internal code:	MST-655
Synthesis scheme:	Figure 148
Melting point:	136.7 °C
LC-MS-DAD purity:	97.5%
HR-MS (ESI-(+)):	m/z= 640.2804 $[M+H^+]^+$ calculated: 640.2780
^{1}H NMR (600 MHz, DMSO-d_6):	δ 8.04 (t, *J* = 5.7 Hz, 1H), 7.86 – 7.77 (m, 1H), 7.65 (s, 1H), 7.64 – 7.62 (m, 1H), 7.44 – 7.34 (m, 1H), 7.06 (d, *J* = 4.0 Hz, 1H), 6.34 (d, *J* = 4.0 Hz, 1H), 6.28 (s, 1H), 4.65 – 4.56 (m, 2H), 3.86 – 3.84 (m, 2H), 3.83 – 3.79 (m, 4H), 3.54 (t, *J* = 5.7 Hz, 2H), 3.29 – 3.22 (m, 2H), 3.08 (t, *J* = 7.7 Hz, 2H), 2.51 – 2.46 (m, 2H), 2.46 (s, 3H), 2.42 – 2.37 (m, 4H), 2.25 (s, 3H), 2.23 (s, 3H).
^{13}C NMR (151 MHz, DMSO-d_6):	δ 171.41, 166.03, 159.54, 158.28, 158.28, 152.11, 144.48, 134.88, 134.66, 133.43, 129.31, 127.28, 125.92, 125.73, 122.73, 120.69, 117.01, 111.74, 69.63, 68.43, 66.46, 54.69, 45.97, 43.78, 39.03, 34.11, 24.46, 14.95, 11.44.

N-(2-(2-(2-((6-Chloro-2-(4-methylpiperazin-1-yl)quinazolin-4-yl)oxy)ethoxy)ethoxy)ethyl)-3-(5,5-difluoro-7,9-dimethyl-5*H*-5λ^4,6λ^4-dipyrrolo[1,2-c:2',1'-*f*][1,3,2]diazaborinin-3-yl)propanamide **(P41g)**

The HATU coupling was carried out as described for compound **P3**.[644] Compound **P40g** (20 mg, 0.05 mmol, 1.0 eq.), DIPEA (9 µL, 0.06 mmol, 1.1 eq.), BODIPY-FL (15 mg, 0.05 mmol, 1.0 eq.) and HATU (23 mg, 0.06 mmol, 1.1 eq.) were subjected to the reaction conditions for 24 hours. The crude product was purified by column chromatography using a gradient elution of dichloromethane/methanol (sat. NH_3) (0-20%).

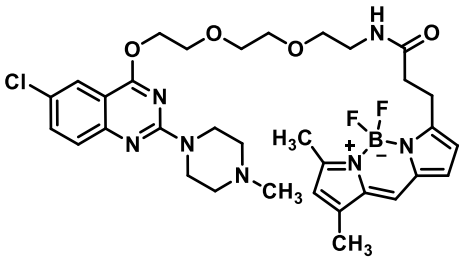

Yield:	10 mg, (28%)
Chemical formula:	$C_{33}H_{41}BClF_2N_7O_4$
Molecular mass:	683.99 g/mol
Appearance:	Red solid
Internal code:	MST-656, ST-2933
Synthesis scheme:	Figure 148
Melting point:	152.2 °C
LC-MS-DAD purity:	100%
HR-MS (ESI-(+)):	m/z= 684.3049 $[M+H^+]^+$ calculated: 684.3042
^{1}H NMR (300 MHz, MeOD):	δ 7.96 – 7.89 (m, 1H), 7.50 – 7.43 (m, 1H), 7.37 – 7.34 (m, 1H), 7.32 (s, 1H), 6.95 (d, *J* = 4.1 Hz, 1H), 6.28 (d, *J* = 4.1 Hz, 1H), 6.15 (s, 1H), 3.97 – 3.82 (m, 4H), 3.80 – 3.69 (m, 6H), 3.69 – 3.57 (m, 4H), 3.53 (t, *J* = 5.4 Hz, 2H), 3.39 – 3.33 (m, 2H), 3.18 (t, *J* = 7.2 Hz, 2H), 2.67 – 2.50 (m, 7H), 2.40 (s, 3H), 2.25 (s, 3H).
^{13}C NMR (151 MHz, MeOD):	δ 173.34, 159.65, 158.57, 158.54, 157.04, 149.53, 144.35, 135.10, 133.47, 132.74, 128.21, 126.15, 125.77, 124.32, 121.60, 119.90, 116.25, 111.55, 70.01, 69.89, 69.19, 68.76, 54.29, 48.46, 44.39, 42.99, 40.57, 38.94, 34.49, 29.37, 9.81.

N-(2-(2-(2-(2-((6-Chloro-2-(4-methylpiperazin-1-yl)quinazolin-4-yl)oxy)ethoxy)ethoxy)-ethoxy)ethyl)-3-(5,5-difluoro-7,9-dimethyl-5*H*-5λ^4,6λ^4-dipyrrolo[1,2-*c*:2',1'-*f*][1,3,2]diazaborinin-3-yl)propanamide **(P41h)**

The HATU coupling was carried out as described for compound **P3**.[644] Compound **P40h** (56 mg, 0.11 mmol, 1.0 eq.), DIPEA (20 µL, 0.12 mmol, 1.1 eq.), BODIPY-FL (32 mg, 0.11 mmol, 1.0 eq.) and HATU (46 mg, 0.12 mmol, 1.1 eq.) were subjected to the reaction conditions for 24 hours. The crude product was purified by column chromatography using a gradient elution of dichloromethane/methanol (sat. NH_3) (0-20%).

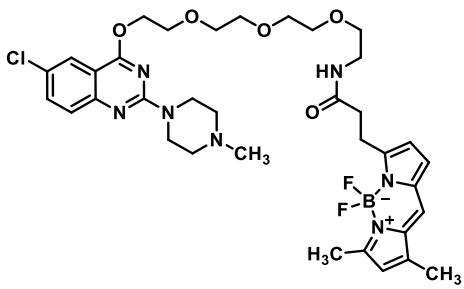

Yield:	16 mg, (20%)
Chemical formula:	$C_{35}H_{45}BClF_2N_7O_5$
Molecular mass:	728.05 g/mol
Appearance:	Red solid
Internal code:	MST-657
Synthesis scheme:	Figure 148
Melting point:	138.4 °C
LC-MS-DAD purity:	95.0%
HR-MS (ESI-(+)):	m/z= 728.3294 $[M+H^+]^+$ calculated: 728.3305
^{1}H NMR (600 MHz, DMSO-d_6):	δ 7.99 (t, *J* = 5.6 Hz, 1H), 7.82 – 7.77 (m, 1H), 7.70 – 7.63 (m, 2H), 7.48 – 7.39 (m, 1H), 7.07 (d, *J* = 4.0 Hz, 1H), 6.35 (d, *J* = 4.0 Hz, 1H), 6.28 (s, 1H), 4.65 – 4.59 (m, 2H), 3.90 – 3.79 (m, 6H), 3.65 – 3.61 (m, 2H), 3.57 – 3.47 (m, 6H), 3.40 (t, *J* = 5.9 Hz, 2H), 3.23 – 3.19 (m, 2H), 3.07 (t, *J* = 7.7 Hz, 2H), 2.50 – 2.44 (m, 9H), 2.27 (s, 3H), 2.25 (s, 3H).
^{13}C NMR (151 MHz, DMSO-d_6):	δ 171.35, 166.06, 159.54, 158.30, 158.28, 152.12, 144.49, 134.88, 134.69, 133.42, 129.36, 127.34, 125.94, 125.76, 122.68, 120.69, 117.04, 111.77, 70.40, 70.25, 70.21, 70.05, 69.56, 68.69, 66.52, 54.62, 45.85, 43.70, 39.06, 34.11, 24.44, 14.95, 11.45.

10.5.6 VUF-10558-based thioether ligands

N[1]-(6-Chloro-2-(methylthio)quinazolin-4-yl)ethane-1,2-diamine **(P42a)**

The synthesis was based on a procedure previously described.[761,769] Compound **SM4** (180 mg, 0.77 mmol, 1.0 eq.) and triethylamine (120 µL, 0.85 mmol, 1.1 eq.) were dissolved in tetrahydrofuran, and a solution of ethane-1,2-diamine **L25** (57 µL, 0.85 mmol, 1.1 eq.) in tetrahydrofuran was added. The reaction mixture was stirred at room temperature for four hours and the solvent was then evaporated. The residue was dissolved in isopropanol and DIPEA (144 µL, 0.85 mmol, 1.1 eq.) and sodium thiomethoxide (60 mg, 0.85 mmol, 1.1 eq.) were added. The mixture was heated to 90 °C and stirred at this temperature for 20 hours. The solvent was removed under reduced pressure and the crude product was purified by column chromatography using a gradient elution of dichloromethane/methanol (sat. NH_3) (0-20%).

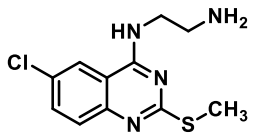

Yield:	85 mg, (41%)
Chemical formula:	$C_{11}H_{13}ClN_4S$
Molecular mass:	268.76 g/mol
Appearance:	Yellow solid
Internal code:	MST-496/498, ST-2718
Synthesis scheme:	Figure 151
Melting point:	178.1 °C
LC-MS-DAD purity:	95.3%
HR-MS (ESI-(+)):	m/z=269.0482 $[M+H^+]^+$ calculated: 269.0622
^{1}H NMR (300 MHz, DMSO-d_6):	δ 8.41 – 8.32 (m, 1H), 7.78 – 7.65 (m, 1H), 7.61 – 7.40 (m, 2H), 3.50 (t, *J* = 6.4 Hz, 2H), 3.30 – 3.14 (m, 2H), 2.81 (t, *J* = 6.4 Hz, 2H), 2.50 (s, 3H).
^{13}C NMR (75.5 MHz, DMSO-d_6):	δ 167.64, 157.97, 148.31, 133.03, 128.09, 127.96, 122.46, 113.82, 44.41, 40.38, 13.39.

N[1]-(6-Chloro-2-(methylthio)quinazolin-4-yl)propane-1,3-diamine **(P42b)**

The nucleophilic aromatic substitution was carried out as described for compound **P42a**.[761,769] Compound **SM4** (400 mg, 1.72 mmol, 1.0 eq.), triethylamine (261 µL, 1.89 mmol, 1.1 eq.), propane-1,3-diamine **L26** (159 µL, 1.89 mmol, 1.0 eq.), DIPEA (321 µL, 1.89 mmol, 1.1 eq.) and sodium thiomethoxide (134 mg, 1.89 mmol, 1.1 eq.) were subjected to the reaction conditions for 24 hours. The crude product was purified by column chromatography using a gradient elution of dichloromethane/methanol (sat. NH_3) (0-20%).

Yield:	107 mg, (22%)
Chemical formula:	$C_{12}H_{15}ClN_4S$
Molecular mass:	282.79 g/mol
Appearance:	Yellow solid
Internal code:	MST-500/502, ST-2716
Synthesis scheme:	Figure 151
Melting point:	172.7 °C
LC-MS-DAD purity:	95.8%
HR-MS (ESI-(+)):	m/z=283.0610 $[M+H^+]^+$ calculated: 283.0779
^{1}H NMR (300 MHz, MeOD):	δ 7.93 – 7.86 (m, 1H), 7.53 – 7.43 (m, 1H), 7.39 – 7.30 (m, 1H), 3.57 (t, *J* = 6.8 Hz, 2H), 2.67 (t, *J* = 7.0 Hz, 2H), 2.45 (s, 3H), 1.95 – 1.71 (m, 2H).
^{13}C NMR (75.5 MHz, MeOD):	δ 170.14, 159.75, 149.63, 134.48, 130.60, 128.37, 123.02, 114.85, 39.74, 39.46, 32.26, 14.15.

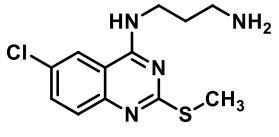

N^1-(6-Chloro-2-(methylthio)quinazolin-4-yl)butane-1,4-diamine **(P42c)**

The nucleophilic aromatic substitution was carried out as described for compound **P42a**.[761,769] Compound **SM4** (200 mg, 0.86 mmol, 1.0 eq.), triethylamine (130 µL, 0.94 mmol, 1.1 eq.), butane-1,4-diamine **L27** (83 mg, 0.94 mmol, 1.0 eq.), DIPEA (160 µL, 0.94 mmol, 1.1 eq.) and sodium thiomethoxide (68 mg, 0.94 mmol, 1.1 eq.) were subjected to the reaction conditions for 24 hours. The crude product was purified by column chromatography using a gradient elution of dichloromethane/methanol (sat. NH_3) (0-20%).

Yield:	43 mg, (17%)
Chemical formula:	$C_{13}H_{17}ClN_4S$
Molecular mass:	296.82 g/mol
Appearance:	Yellow solid
Internal code:	MST-501/503, ST-2739
Synthesis scheme:	Figure 151
Melting point:	162.1 °C
LC-DAD purity:	98.0%
MS (ESI-(+)):	m/z=297.12 $[M+H^+]^+$ calculated: 297.0935
^{1}H NMR (300 MHz, MeOD):	δ 8.06 – 8.01 (m, 1H), 7.61 – 7.55 (m, 1H), 7.48 – 7.40 (m, 1H), 3.62 (t, *J* = 6.9 Hz, 2H), 2.80 (t, *J* = 7.2 Hz, 2H), 2.56 (s, 3H), 1.84 – 1.55 (m, 4H).

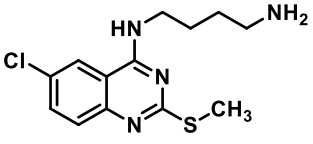

^{13}C NMR (75.5 MHz, MeOD):	δ 168.68, 158.10, 148.06, 132.89, 128.97, 126.68, 121.54, 113.31, 40.27, 40.22, 28.04, 25.71, 12.67.

N^1-(6-Chloro-2-(methylthio)quinazolin-4-yl)pentane-1,5-diamine **(P42d)**

The nucleophilic aromatic substitution was carried out as described for compound **P42a**.[761,769] Compound **SM4** (250 mg, 1.07 mmol, 1.0 eq.), triethylamine (163 µL, 1.18 mmol, 1.1 eq.), pentane-1,5-diamine **L28** (120 mg, 1.18 mmol, 1.0 eq.), DIPEA (200 µL, 1.18 mmol, 1.1 eq.) and sodium thiomethoxide (86 mg, 1.18 mmol, 1.1 eq.) were subjected to the reaction conditions for 24 hours. The crude product was purified by column chromatography using a gradient elution of dichloromethane/methanol (sat. NH_3) (0-20%).

Yield:	77 mg, (23%)
Chemical formula:	$C_{14}H_{19}ClN_4S$
Molecular mass:	310.84 g/mol
Appearance:	Yellow solid
Internal code:	MST-514/517, ST-2747
Synthesis scheme:	Figure 151
Melting point:	171.1 °C
LC-DAD purity:	96.8%
MS (ESI-(+)):	m/z=311.14 $[M+H^+]^+$ calculated: 311.1092
^{1}H NMR (300 MHz, MeOD):	δ 8.05 – 7.98 (m, 1H), 7.60 – 7.53 (m, 1H), 7.45 – 7.37 (m, 1H), 3.57 (t, *J* = 7.2 Hz, 2H), 2.68 (t, *J* = 7.1 Hz, 2H), 2.54 (s, 3H), 1.80 – 1.66 (m, 2H), 1.59 – 1.50 (m, 2H), 1.50 – 1.36 (m, 2H).
^{13}C NMR (75.5 MHz, MeOD):	δ 168.72, 158.08, 148.08, 132.87, 128.94, 126.67, 121.55, 113.35, 40.69, 31.22, 28.16, 23.94, 21.09, 12.68.

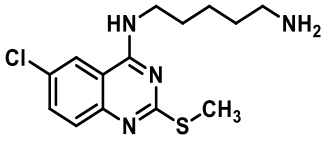

N^1-(6-Chloro-2-(methylthio)quinazolin-4-yl)hexane-1,6-diamine **(P42e)**

The nucleophilic aromatic substitution was carried out as described for compound **P42a**.[761,769] Compound **SM4** (600 mg, 2.58 mmol, 1.0 eq.), triethylamine (388 µL, 2.83 mmol, 1.1 eq.), hexane-1,6-diamine **L29** (328 mg, 2.83 mmol, 1.0 eq.), DIPEA (481 µL, 2.83 mmol, 1.1 eq.) and sodium thiomethoxide (207 mg, 2.83 mmol, 1.1 eq.) were subjected to the reaction conditions for 24 hours. The crude product was purified by column chromatography using a gradient elution of dichloromethane/methanol (sat. NH_3) (0-20%).

Yield:	285 mg, (34%)
Chemical formula:	$C_{15}H_{21}ClN_4S$
Molecular mass:	324.87 g/mol

Appearance:	Yellow solid
Internal code:	MST-511/513, ST-2745
Synthesis scheme:	Figure 151
Melting point:	175.9 °C
LC-DAD purity:	96.1%
MS (ESI-(+)):	m/z=325.15 $[M+H^+]^+$ calculated: 325.1248
^{1}H NMR (300 MHz, MeOD):	δ 8.06 – 7.96 (m, 1H), 7.59 – 7.51 (m, 1H), 7.46 – 7.36 (m, 1H), 3.56 (t, *J* = 6.8 Hz, 2H), 2.75 (t, *J* = 7.3 Hz, 2H), 2.54 (s, 3H), 1.77 – 1.64 (m, 2H), 1.63 – 1.49 (m, 2H), 1.47 – 1.34 (m, 4H).
^{13}C NMR (75.5 MHz, MeOD):	δ 168.67, 158.04, 148.04, 132.85, 128.92, 126.62, 121.57, 113.33, 40.63, 40.15, 29.85, 28.26, 26.35, 26.02, 12.68.

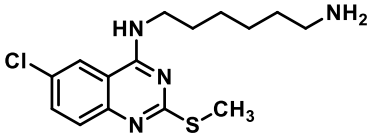

N-(2-((6-Chloro-2-(methylthio)quinazolin-4-yl)amino)ethyl)-3-(5,5-difluoro-7,9-dimethyl-5*H*-5λ^4,6 λ^4-dipyrrolo[1,2-*c*:2',1'-*f*][1,3,2]diazaborinin-3-yl)propanamide **(P43a)**

The HATU coupling was carried out as described for compound **P3**.[644] Compound **P42a** (20 mg, 0.07 mmol, 1.0 eq.), DIPEA (14 µL, 0.08 mmol, 1.1 eq.), BODIPY-FL (20 mg, 0.07 mmol, 1.0 eq.) and HATU (30 mg, 0.08 mmol, 1.1 eq.) were subjected to the reaction conditions for 24 hours. The crude product was purified by column chromatography using a gradient elution of dichloromethane/methanol (sat. NH_3) (0-20%).

Yield:	24 mg, (62%)
Chemical formula:	$C_{25}H_{26}BClF_2N_6OS$
Molecular mass:	542.84 g/mol
Appearance:	Red solid
Internal code:	MST-668
Synthesis scheme:	Figure 152
Melting point:	128.3 °C
LC-MS-DAD purity:	98.0%
HR-MS (ESI-(+)):	m/z= 543.1739 $[M+H^+]^+$ calculated: 543.1711
^{1}H NMR (300 MHz, DMSO-d_6):	δ 8.48 (t, *J* = 5.4 Hz, 1H), 8.31 – 8.26 (m, 1H), 8.12 (t, *J* = 5.8 Hz, 1H), 7.77 – 7.68 (m, 1H), 7.66 (s, 1H), 7.62 – 7.50 (m, 1H), 7.04 (d, *J* = 4.0 Hz, 1H), 6.33 (d, *J* = 4.0 Hz, 1H), 6.29 (s, 1H), 3.63 – 3.53 (m, 2H), 3.46 – 3.37 (m, 2H), 3.10 (t, *J* = 7.7 Hz, 2H), 2.61 – 2.41 (m, 8H), 2.26 (s, 3H).

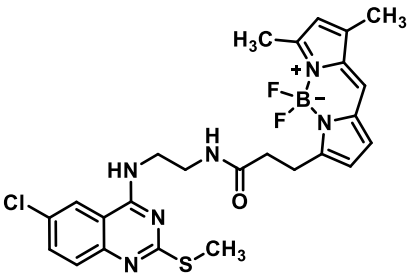

^{13}C NMR (151 MHz, DMSO-d_6):	δ 171.69, 168.13, 159.60, 158.45, 158.22, 148.82, 144.54, 134.91, 133.59, 133.41, 129.31, 128.61, 128.52, 125.76, 122.91, 120.72, 117.02, 114.29, 40.88, 38.03, 34.27, 24.38, 14.96, 13.92, 11.45.

N-(3-((6-Chloro-2-(methylthio)quinazolin-4-yl)amino)propyl)-3-(5,5-difluoro-7,9-dimethyl-5*H*-5λ^4,6 λ^4-dipyrrolo[1,2-*c*:2',1'-*f*][1,3,2]diazaborinin-3-yl)propanamide **(P43b)**

The HATU coupling was carried out as described for compound **P3**.[644] Compound **P42b** (30 mg, 0.11 mmol, 1.0 eq.), DIPEA (20 µL, 0.12 mmol, 1.1 eq.), BODIPY-FL (31 mg, 0.11 mmol, 1.0 eq.) and HATU (46 mg, 0.12 mmol, 1.1 eq.) were subjected to the reaction conditions for 24 hours. The crude product was purified by column chromatography using a gradient elution of dichloromethane/methanol (sat. NH_3) (0-20%).

Yield:	20 mg, (33%)
Chemical formula:	$C_{26}H_{28}BClF_2N_6OS$
Molecular mass:	556.87 g/mol
Appearance:	Red solid
Internal code:	MST-667
Synthesis scheme:	Figure 152
Melting point:	155.7 °C
LC-MS-DAD purity:	100%
HR-MS (ESI-(+)):	m/z= 557.1875 $[M+H^+]^+$ calculated: 557.1868
^{1}H NMR (300 MHz, DMSO-d_6):	δ 8.39 (t, *J* = 5.4 Hz, 1H), 8.35 – 8.27 (m, 1H), 8.00 (t, *J* = 5.6 Hz, 1H), 7.75 – 7.63 (m, 2H), 7.63 – 7.47 (m, 1H), 7.08 (d, *J* = 4.0 Hz, 1H), 6.36 (d, *J* = 4.0 Hz, 1H), 6.29 (s, 1H), 3.56 – 3.46 (m, 2H), 3.27 – 3.05 (m, 4H), 2.59 – 2.43 (m, 8H), 2.26 (s, 3H), 1.87 – 1.73 (m, 2H).
^{13}C NMR (151 MHz, DMSO-d_6):	δ 171.28, 168.15, 159.60, 158.26, 148.81, 144.54, 134.91, 133.57, 133.57, 133.43, 129.37, 128.64, 128.54, 125.79, 122.80, 120.71, 117.05, 114.25, 39.06, 37.03, 34.30, 28.86, 24.48, 14.97, 13.89, 11.45.

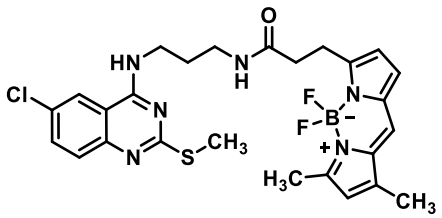

N-(4-((6-Chloro-2-(methylthio)quinazolin-4-yl)amino)butyl)-3-(5,5-difluoro-7,9-dimethyl-5*H*-5λ^4,6 λ^4-dipyrrolo[1,2-*c*:2',1'-*f*][1,3,2]diazaborinin-3-yl)propanamide **(P43c)**

The HATU coupling was carried out as described for compound **P3**.[644] Compound **P42c** (35 mg, 0.12 mmol, 1.0 eq.), DIPEA (22 µL, 0.13 mmol, 1.1 eq.), BODIPY-FL (35 mg, 0.12 mmol, 1.0 eq.) and HATU (49 mg, 0.13 mmol, 1.1 eq.) were subjected to the reaction conditions for 24 hours. The crude product was purified by column chromatography using a gradient elution of dichloromethane/methanol (sat. NH_3) (0-20%).

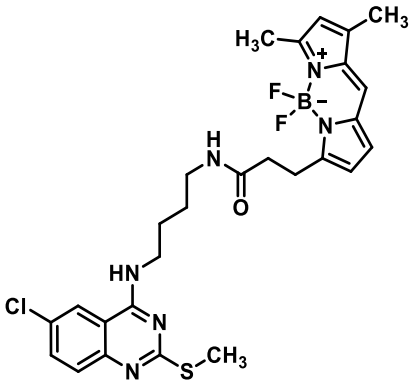

Yield:	23 mg, (33%)
Chemical formula:	$C_{27}H_{30}BClF_2N_6OS$
Molecular mass:	570.89 g/mol
Appearance:	Red solid
Internal code:	MST-666
Synthesis scheme:	Figure 152
Melting point:	167.3 °C
LC-MS-DAD purity:	100%
HR-MS (ESI-(+)):	m/z= 571.2047 $[M+H^+]^+$ calculated: 571.2024
^{1}H NMR (300 MHz, DMSO-d_6):	δ 8.40 (t, *J* = 5.4 Hz, 1H), 8.38 – 8.29 (m, 1H), 7.94 (t, *J* = 5.6 Hz, 1H), 7.76 – 7.59 (m, 2H), 7.59 – 7.48 (m, 1H), 7.06 (d, *J* = 4.0 Hz, 1H), 6.35 (d, *J* = 4.0 Hz, 1H), 6.28 (s, 1H), 3.58 – 3.44 (m, 2H), 3.20 – 3.03 (m, 4H), 2.58 – 2.41 (m, 8H), 2.25 (s, 3H), 1.73 – 1.42 (m, 4H).
^{13}C NMR (151 MHz, DMSO-d_6):	δ 169.02, 166.06, 157.45, 156.24, 156.14, 146.72, 142.37, 132.77, 131.39, 127.21, 126.48, 126.38, 123.59, 120.70, 118.58, 116.40, 114.93, 112.12, 38.72, 36.66, 32.16, 25.14, 24.10, 22.40, 12.84, 11.76, 9.31.

N-(5-((6-Chloro-2-(methylthio)quinazolin-4-yl)amino)pentyl)-3-(5,5-difluoro-7,9-dimethyl-5*H*-5λ^4,6 λ^4-dipyrrolo[1,2-*c*:2',1'-*f*][1,3,2]diazaborinin-3-yl)propanamide **(P43d)**

The HATU coupling was carried out as described for compound **P3**.[644] Compound **P42d** (40 mg, 0.13 mmol, 1.0 eq.), DIPEA (24 µL, 0.14 mmol, 1.1 eq.), BODIPY-FL (38 mg, 0.13 mmol, 1.0 eq.) and HATU (53 mg, 0.14 mmol, 1.1 eq.) were subjected to the reaction conditions for 24 hours. The crude product was purified by column chromatography using a gradient elution of dichloromethane/methanol (sat. NH_3) (0-20%).

Yield:	22 mg, (29%)
Chemical formula:	$C_{28}H_{32}BClF_2N_6OS$
Molecular mass:	584.92 g/mol
Appearance:	Red solid
Internal code:	MST-665
Synthesis scheme:	Figure 152
Melting point:	171.1 °C
LC-MS-DAD purity:	97.4%
HR-MS (ESI-(+)):	m/z= 585.2169 $[M+H^+]^+$ calculated: 585.2181
^{1}H NMR (300 MHz, DMSO-d_6):	δ 8.48 – 8.26 (m, 2H), 7.91 (t, *J* = 5.5 Hz, 1H), 7.75 – 7.64 (m, 2H), 7.59 – 7.45 (m, 1H), 7.09 (d, *J* = 4.1 Hz, 1H), 6.35 (d, *J* = 4.1 Hz, 1H), 6.30 (s, 1H), 3.55 – 3.43 (m, 2H), 3.17 – 2.99 (m, 4H), 2.59 – 2.39 (m, 8H), 2.26 (s, 3H), 1.74 – 1.55 (m, 2H), 1.53 – 1.27 (m, 4H).
^{13}C NMR (151 MHz, DMSO-d_6):	δ 171.09, 168.17, 159.56, 158.38, 158.24, 148.83, 144.52, 134.89, 133.54, 133.43, 129.36, 128.61, 128.49, 125.77, 122.83, 120.71, 117.05, 114.25, 41.12, 38.93, 34.24, 29.35, 28.38, 24.52, 24.42, 14.97, 13.86, 11.45.

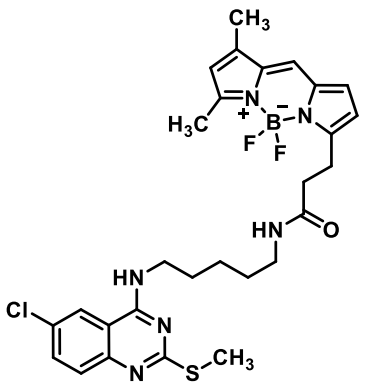

N-(6-((6-Chloro-2-(methylthio)quinazolin-4-yl)amino)hexyl)-3-(5,5-difluoro-7,9-dimethyl-5*H*-5λ^4,6 λ^4-dipyrrolo[1,2-*c*:2',1'-*f*][1,3,2]diazaborinin-3-yl)propanamide **(P43e)**

The HATU coupling was carried out as described for compound **P3**.[644] Compound **P42e** (41 mg, 0.13 mmol, 1.0 eq.), DIPEA (24 µL, 0.14 mmol, 1.1 eq.), BODIPY-FL (38 mg, 0.13 mmol, 1.0 eq.) and HATU (53 mg, 0.14 mmol, 1.1 eq.) were subjected to the reaction conditions for 24 hours. The crude product was purified by column chromatography using a gradient elution of dichloromethane/methanol (sat. NH_3) (0-20%).

Yield:	27 mg, (35%)
Chemical formula:	$C_{29}H_{34}BClF_2N_6OS$
Molecular mass:	598.95 g/mol
Appearance:	Red solid
Internal code:	MST-664
Synthesis scheme:	Figure 152
Melting point:	166.1 °C
LC-MS-DAD purity:	100%
HR-MS (ESI-(+)):	m/z= 599.2366 $[M+H^+]^+$ calculated: 599.2337

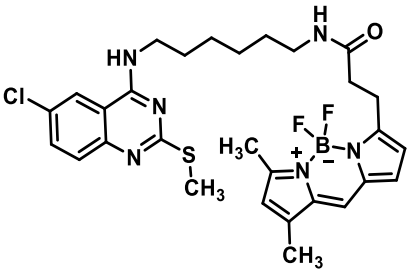

^{1}H NMR (300 MHz, DMSO-d_6):	δ 8.38 (t, *J* = 5.4 Hz, 1H), 8.35 – 8.32 (m, 1H), 7.90 (t, *J* = 5.6 Hz, 1H), 7.74 – 7.63 (m, 2H), 7.59 – 7.47 (m, 1H), 7.07 (d, *J* = 4.1 Hz, 1H), 6.35 (d, *J* = 4.1 Hz, 1H), 6.28 (s, 1H), 3.56 – 3.42 (m, 2H), 3.18 – 3.01 (m, 4H), 2.53 – 2.44 (m, 8H), 2.25 (s, 3H), 1.70 – 1.56 (m, 2H), 1.49 – 1.26 (m, 6H).
^{13}C NMR (151 MHz, DMSO-d_6):	δ 171.06, 168.17, 159.56, 158.39, 158.22, 148.82, 144.48, 134.88, 133.51, 133.43, 129.32, 128.60, 128.48, 125.72, 122.81, 120.69, 117.03, 114.24, 41.10, 38.96, 34.23, 29.57, 28.68, 26.75, 26.66, 24.53, 14.95, 13.86, 11.44.

tert-Butyl (3-((6-chloro-2-(methylthio)quinazolin-4-yl)amino)propyl)carbamate **(50)**

The synthesis was based on a procedure previously described.[769] Compound **48b** (1120 mg, 3.03 mmol, 1.0 eq.) and DIPEA (565 µL, 3.33 mmol, 1.1 eq.) were dissolved in isopropanol and sodium thiomethoxide (243 mg, 3.33 mmol, 1.1 eq.) was added. The mixture was heated to 90 °C and stirred at this temperature for 20 hours. The solvent was removed under reduced pressure and the crude product was purified by column chromatography using a gradient elution of dichloromethane/methanol (sat. NH_3) (0-20%).

Yield:	894 mg, (77%)
Chemical formula:	$C_{17}H_{23}ClN_4O_2S$
Molecular mass:	382.91 g/mol
Appearance:	Yellow oil
Internal code:	MST-758
Synthesis scheme:	Figure 154

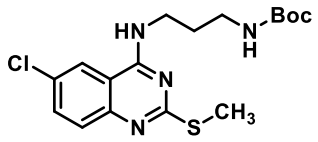

^{1}H NMR (300 MHz, MeOD):	δ 7.96 – 7.86 (m, 1H), 7.55 – 7.47 (m, 1H), 7.44 – 7.39 (m, 1H), 3.58 (t, *J* = 6.5 Hz, 2H), 2.69 (t, *J* = 7.0 Hz, 2H), 2.43 (s, 3H), 1.97 – 1.75 (m, 2H), 1.39 (s, 9H).

tert-Butyl (3-((6-chloro-2-(methylsulfinyl)quinazolin-4-yl)amino)propyl)carbamate **(P44)**

The Oxidation protocol was carried out as described for compound **P30**.[754] Compound **50** (171 mg, 0.45 mmol, 1.0 eq.) and 3-chloroperoxybenzoic acid (77 mg, 0.45 mmol, 1.0 eq.) were subjected to the reaction conditions for two hours. The crude product was purified by column chromatography using a gradient elution of dichloromethane/isopropanol (0-40%).

Yield:	65 mg, (36%)
Chemical formula:	$C_{17}H_{23}ClN_4O_3S$
Molecular mass:	398.91 g/mol

Appearance:	Colourless oil
Internal code:	MST-809, ST-2973
Synthesis scheme:	Figure 155
LC-MS-DAD purity:	98.4%
HR-MS (ESI-(+)):	m/z= 399.1265 $[M+H^+]^+$ calculated: 399.1252
^{1}H NMR (300 MHz, $CDCl_3$):	δ 8.38 (t, *J* = 6.5 Hz, 1H), 8.23 – 8.16 (m, 1H), 7.81 – 7.72 (m, 1H), 7.66 – 7.57 (m, 1H), 5.40 (t, *J* = 7.0 Hz, 1H), 3.76 – 3.66 (m, 2H), 3.31 – 3.18 (m, 2H), 2.96 (s, 3H), 1.85 – 1.71 (m, 2H), 1.43 (s, 9H).
^{13}C NMR (75.5 MHz, $CDCl_3$):	δ 169.10, 159.75, 157.36, 147.98, 133.84, 132.45, 129.86, 122.18, 116.10, 79.86, 39.68, 37.83, 37.24, 29.20, 28.41.

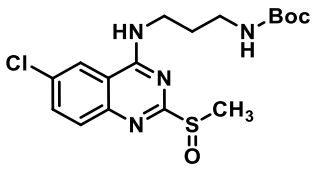

tert-Butyl (3-((6-chloro-2-(methylsulfonyl)quinazolin-4-yl)amino)propyl)carbamate **(P45)**

The Oxidation protocol was carried out as described for compound **P30**.[755] Compound **50** (297 mg, 0.78 mmol, 1.0 eq.) and 3-chloroperoxybenzoic acid (269 mg, 1.56 mmol, 2.0 eq.) were subjected to the reaction conditions for two hours. The crude product was purified by column chromatography using a gradient elution of dichloromethane/isopropanol (0-40%).

Yield:	149 mg, (46%)
Chemical formula:	$C_{17}H_{23}ClN_4O_4S$
Molecular mass:	414.91 g/mol
Appearance:	Colourless oil
Internal code:	MST-816, ST-2975
Synthesis scheme:	Figure 155
LC-MS-DAD purity:	95.1%
HR-MS (ESI-(+)):	m/z= 415.1224 $[M+H^+]^+$ calculated: 415.1201
^{1}H NMR (300 MHz, $CDCl_3$):	δ 8.24 (t, *J* = 6.5 Hz, 1H), 8.09 – 8.02 (m, 1H), 7.78 – 7.71 (m, 1H), 7.65 – 7.58 (m, 1H), 5.13 (t, *J* = 6.8 Hz, 1H), 3.75 – 3.58 (m, 2H), 3.29 (s, 3H), 3.25 – 3.10 (m, 2H), 1.84 – 1.66 (m, 2H), 1.41 (s, 9H).
^{13}C NMR (75.5 MHz, $CDCl_3$):	δ 162.20, 160.33, 157.63, 147.11, 134.22, 133.63, 130.53, 121.87, 116.45, 80.23, 38.94, 38.00, 37.28, 29.26, 28.42.

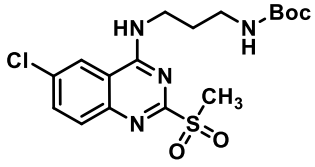

N^1-(6-Chloro-2-(methylsulfinyl)quinazolin-4-yl)propane-1,3-diamine **(P46)**

The Boc-deprotection protocol was carried out as described for compound **P6**.[674] Compound **P44** (62 mg, 0.16 mmol, 1.0 eq.) was subjected to the reaction conditions for 24 hours using

isopropanol as solvent. The crude product was converted to its free base using a strong basic anion exchanger and subsequently purified by column chromatography using a gradient elution of dichloromethane/isopropanol (0-60%).

Yield:	20 mg, (42%)
Chemical formula:	$C_{12}H_{15}ClN_4OS$
Molecular mass:	298.79 g/mol
Appearance:	Colourless solid
Internal code:	MST-830, ST-2994
Synthesis scheme:	Figure 156
Melting point:	242.1 °C
LC-MS-DAD purity:	100%
HR-MS (ESI-(+)):	m/z= 299.0721 $[M+H^+]^+$ calculated: 299.0728
^{1}H NMR (300 MHz, DMSO-d_6):	δ 8.49 – 8.43 (m, 1H), 7.93 – 7.85 (m, 1H), 7.84 – 7.76 (m, 1H), 3.73 – 3.58 (m, 2H), 2.96 – 2.85 (m, 5H), 2.02 – 1.88 (m, 2H).
^{13}C NMR (75.5 MHz, DMSO-d_6):	δ 169.38, 159.85, 147.48, 133.99, 131.04, 129.62, 122.72, 115.54, 38.75, 37.60, 36.44, 26.98.

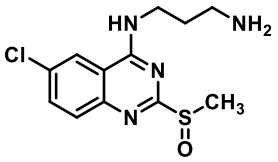

N^1-(6-Chloro-2-(methylsulfonyl)quinazolin-4-yl)propane-1,3-diamin **(P47)**

The Boc-deprotection protocol was carried out as described for compound **P6**.[674] Compound **P44** (35 mg, 0.08 mmol, 1.0 eq.) was subjected to the reaction conditions for 24 hours using isopropanol as solvent.. The crude product was converted to its free base using a strong basic anion exchanger and subsequently purified by column chromatography using a gradient elution of dichloromethane/isopropanol (0-60%).

Yield:	22 mg, (88%)
Chemical formula:	$C_{12}H_{15}ClN_4O_2S$
Molecular mass:	314.79 g/mol
Appearance:	Colourless solid
Internal code:	MST-826, ST-2991
Synthesis scheme:	Figure 156
Melting point:	236.7 °C
LC-MS-DAD purity:	95.1%
HR-MS (ESI-(+)):	m/z= 315.0681 $[M+H^+]^+$ calculated: 315.0677

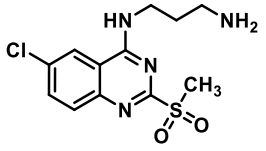

^{1}H NMR (600 MHz, DMSO-d_6):	δ 9.17 (t, *J* = 5.6 Hz, 1H), 8.54 – 8.46 (m, 1H), 7.95 – 7.92 (m, 1H), 7.88 – 7.82 (m, 3H), 3.67 – 3.62 (m, 2H), 3.36 (s, 3H), 2.97 – 2.88 (m, 2H), 2.00 – 1.92 (m, 2H).
^{13}C NMR (151 MHz, DMSO-d_6):	δ 162.79, 160.54, 147.32, 134.84, 132.59, 130.76, 123.28, 116.59, 39.31, 38.73, 37.32, 26.96.

N-(3-((6-Chloro-2-(methylsulfinyl)quinazolin-4-yl)amino)propyl)-3-(5,5-difluoro-7,9-dimethyl-5*H*-5λ^4,6 λ^4-dipyrrolo[1,2-*c*:2',1'-*f*][1,3,2]diazaborinin-3-yl)propanamide **(P48)**

The HATU coupling was carried out as described for compound **P3**.[644] Compound **P46** (15 mg, 0.05 mmol, 1.0 eq.), DIPEA (10 µL, 0.06 mmol, 1.1 eq.), BODIPY-FL (15 mg, 0.05 mmol, 1.0 eq.) and HATU (23 mg, 0.06 mmol, 1.1 eq.) were subjected to the reaction conditions for 24 hours. The crude product was purified by column chromatography using a gradient elution dichloromethane/isopropanol (0-40%).

Yield:	13 mg, (44%)
Chemical formula:	$C_{26}H_{28}BClF_2N_6O_2S$
Molecular mass:	572.87 g/mol
Appearance:	Red solid
Internal code:	MST-836
Synthesis scheme:	Figure 157
Melting point:	130.2 °C
LC-MS-DAD purity:	100%
HR-MS (ESI-(+)):	m/z= 573.1827 $[M+H^+]^+$ calculated: 573.1817
^{1}H NMR (300 MHz, $CDCl_3$):	δ 8.05 – 7.93 (m, 2H), 7.90 – 7.72 (m, 1H), 7.64 – 7.54 (m, 1H), 7.00 (s, 1H), 6.81 – 6.73 (m, 2H), 6.25 (d, *J* = 4.1 Hz, 1H), 6.04 (s, 1H), 3.57 – 3.45 (m, 2H), 3.35 – 3.17 (m, 4H), 2.86 (s, 3H), 2.75 (t, *J* = 7.4 Hz, 2H), 2.47 (s, 3H), 2.17 (s, 3H), 1.70 – 1.55 (m, 2H).
^{13}C NMR (151 MHz, $CDCl_3$):	δ 173.78, 169.05, 159.91, 147.94, 144.20, 134.41, 134.05, 133.29, 132.95, 132.66, 129.91, 129.61, 128.18, 123.85, 121.80, 120.60, 117.18, 115.95, 39.66, 37.18, 36.20, 35.50, 29.05, 24.85, 14.97, 11.35.

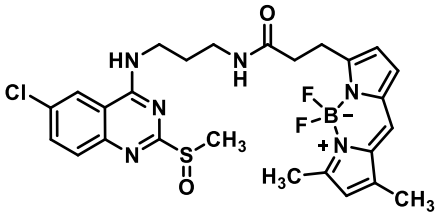

N-(3-((6-Chloro-2-(methylsulfonyl)quinazolin-4-yl)amino)propyl)-3-(5,5-difluoro-7,9-dimethyl-5*H*-5λ^4,6 λ^4-dipyrrolo[1,2-*c*:2',1'-*f*][1,3,2]diazaborinin-3-yl)propanamide **(P49)**

The HATU coupling was carried out as described for compound **P3**.[644] Compound **P47** (15 mg, 0.05 mmol, 1.0 eq.), DIPEA (10 µL, 0.06 mmol, 1.1 eq.), BODIPY-FL (15 mg, 0.05 mmol, 1.0 eq.)

and HATU (23 mg, 0.06 mmol, 1.1 eq.) were subjected to the reaction conditions for 24 hours. The crude product was purified by column chromatography using a gradient elution of dichloromethane/isopropanol (0-40%).

Yield:	22 mg, (76%)
Chemical formula:	$C_{26}H_{28}BClF_2N_6O_3S$
Molecular mass:	588.87 g/mol
Appearance:	Red solid
Internal code:	MST-835
Synthesis scheme:	Figure 157
Melting point:	138.8 °C
LC-MS-DAD purity:	95.5%
HR-MS (ESI-(+)):	m/z= 589.1774 $[M+H^+]^+$ calculated: 589.1766
^{1}H NMR (600 MHz, $CDCl_3$):	δ 8.11 (t, *J* = 6.1 Hz, 1H), 8.05 – 8.00 (m, 1H), 7.81 – 7.76 (m, 1H), 7.69 – 7.64 (m, 1H), 7.04 (s, 1H), 6.78 (d, *J* = 4.0 Hz, 1H), 6.28 – 6.23 (m, 1H), 6.22 (d, *J* = 4.0 Hz, 1H), 6.07 (s, 1H), 3.50 – 3.45 (m, 2H), 3.30 – 3.23 (m, 7H), 2.78 – 2.71 (m, 2H), 2.50 (s, 3H), 2.20 (s, 3H), 1.67 – 1.57 (m, 2H).
^{13}C NMR (151 MHz, $CDCl_3$):	δ 173.78, 162.34, 160.91, 160.24, 156.20, 147.22, 144.54, 134.29, 133.75, 133.26, 130.66, 128.15, 124.03, 121.70, 120.78, 120.77, 117.16, 116.53, 38.84, 36.93, 36.00, 35.73, 28.78, 24.76, 15.02, 11.38.

10.5.7 VUF-10558-sulfonamide ligands

2-((2,6-Dichloroquinazolin-4-yl)amino)ethane-1-sulfonic acid **(51)**

The synthesis was based on a procedure previously described.[761] Compound **SM4** (1230 mg, 5.28 mmol, 1.0 eq.), triethylamine (804 µL, 5.81 mmol, 1.1 eq.) and 2-aminoethanesulfonic acid (726 mg, 5.81 mmol, 1.1 eq.) were dissolved in tetrahydrofuran. The reaction mixture was heated up to 60 °C and was stirred at this temperature for 20 hours. The solvent was removed under reduced pressure and the crude product was used without further purification.

Yield:	1700 mg, (100%)
Chemical formula:	$C_{10}H_9Cl_2N_3O_3S$
Molecular mass:	322.16 g/mol
Appearance:	Yellow solid
Internal code:	MST-640
Synthesis scheme:	Figure 160

^{1}H NMR (300 MHz, DMSO-d_6):	δ 8.34 (t, *J* = 5.3 Hz, 1H), 8.04 – 8.01 (m, 1H), 7.56 – 7.51 (m, 1H), 7.35 – 7.24 (m, 1H), 3.83 – 3.64 (m, 2H), 2.90 – 2.79 (m, 2H).

2-((6-Chloro-2-(4-methylpiperazin-1-yl)quinazolin-4-yl)amino)ethane-1-sulfonicacid **(SM5)**

The nucleophilic aromatic substitution was carried out as described for compound **P36a**.[761] Compound **50** (1700 mg, 5.28 mmol, 1.0 eq.), DIPEA (764 µL, 5.81 mmol, 1.1 eq.) and *N*-methylpiperazine (652 µL, 5.81 mmol, 1.1 eq.) were subjected to the reaction conditions for 20 hours. The crude product was purified by column chromatography using a gradient elution of dichloromethane/methanol (0-20%).

Yield:	1121 mg, (55%)
Chemical formula:	$C_{15}H_{20}ClN_5O_3S$
Molecular mass:	385.87 g/mol
Appearance:	Colourless solid
Internal code:	MST-641
Synthesis scheme:	Figure 161
^{1}H NMR (300 MHz, DMSO-d_6):	δ 8.34 (t, *J* = 5.3 Hz, 1H), 8.07 – 7.93 (m, 1H), 7.59 – 7.50 (m, 1H), 7.40 – 7.24 (m, 1H), 4.24 – 3.87 (m, 4H), 3.78 – 3.66 (m, 2H), 3.28 – 3.03 (m, 4H), 2.93 – 2.79 (m, 2H), 2.75 (s, 3H).

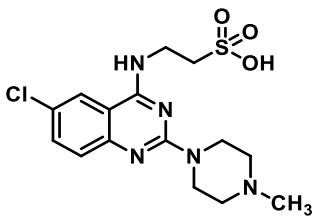

N-(2-Aminoethyl)-2-((6-chloro-2-(4-methylpiperazin-1-yl)quinazolin-4-yl)amino)ethane-1-sulfonamide trihydrochloride **(P50a)**

The synthesis was based on a procedure previously described.[771] Compound **SM5** (52 mg, 0.14 mmol, 1.0 eq.) was dissolved in DCM with a few drops of DMF. Oxalyl chloride (36 µL, 0.42 mmol, 3.0 eq.) was added dropwise and the reaction mixture was stirred at room temperature for 20 hours. After removing the solvent under reduced pressure, the residue was dissolved in DCM and this solution was added to a DCM solution of ethane-1,2-diamine (28 µL, 0.42 mmol, 3.0 eq.). The reaction mixture was stirred at room temperature for four hours. The solvent was removed under reduced pressure and the crude product was purified by reverse phase flash column chromatography using a gradient elution of water/methanol (0-100%).

Yield:	39 mg, (52%)
Chemical formula:	$C_{17}H_{26}ClN_7O_2S$ x 3 HCl
Molecular mass:	537.33 g/mol
Appearance:	Colourless solid
Internal code:	MST-679, ST-2936
Synthesis scheme:	Figure 163
Melting point:	252.1 °C
LC-MS-DAD purity:	96.6%
HR-MS (ESI-(+)):	m/z=428.1637 $[M+H^+]^+$ calculated: 428.1630
^{1}H NMR (600 MHz, DMSO-d_6):	δ 13.58 (s, 1H), 11.70 (s, 1H), 10.55 (t, *J* = 5.6 Hz, 1H), 8.76 – 8.72 (m, 1H), 8.34 – 8.28 (m, 3H), 8.28 – 8.24 (m, 1H), 7.94 – 7.86 (m, 2H), 4.00 – 3.91 (m, 2H), 3.79 – 3.65 (m, 2H), 3.58 – 3.39 (m, 6H), 3.32 – 3.20 (m, 4H), 2.94 – 2.88 (m, 2H), 2.81 (s, 3H).
^{13}C NMR (151 MHz, DMSO-d_6):	δ 158.89, 152.07, 139.01, 135.52, 129.49, 124.31, 120.24, 111.52, 70.23, 60.64, 51.86, 49.18, 42.31, 39.35, 36.58.

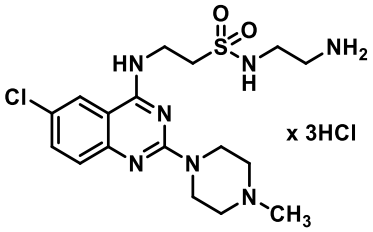

N-(3-Aminopropyl)-2-((6-chloro-2-(4-methylpiperazin-1-yl)quinazolin-4-yl)amino)ethane-1-sulfonamide trihydrochloride **(P50b)**

The reaction protocol was carried out as described for compound **P50a**.[771] Compound **SM5** (65 mg, 0.17 mmol, 1.0 eq.), oxalyl chloride (43 µL, 0.51 mmol, 3.0 eq.) and propane-1,3-diamine (42 µL, 0.51 mmol, 3.0 eq.) were subjected to the reaction conditions for 24 hours. The crude product was purified by reverse phase flash column chromatography using a gradient elution of water/methanol (0-100%).

Yield:	71 mg, (76%)
Chemical formula:	$C_{18}H_{28}ClN_7O_2S$ x 3 HCl
Molecular mass:	551.36 g/mol
Appearance:	Colourless solid
Internal code:	MST-682, ST-2942
Synthesis scheme:	Figure 163
Melting point:	256.9 °C
LC-MS-DAD purity:	100%
HR-MS (ESI-(+)):	m/z=442.1802 $[M+H^+]^+$ calculated: 442.1786

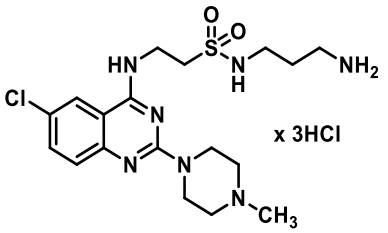

^{1}H NMR (300 MHz, DMSO-d_6):	δ 13.54 (s, 1H), 11.68 (s, 1H), 10.51 (t, *J* = 7.0 Hz, 1H), 8.79 – 8.60 (m, 1H), 8.28 – 8.08 (m, 4H), 7.94 – 7.83 (m, 1H), 7.67 (t, *J* = 5.9 Hz, 1H), 4.08 – 3.83 (m, 2H), 3.78 – 3.16 (m, 12H), 3.09 – 2.93 (m, 2H), 2.81 (s, 3H), 1.90 – 1.70 (m, 2H).
^{13}C NMR (151 MHz, DMSO-d_6):	δ 158.88, 135.47, 135.46, 127.84, 124.29, 124.28, 111.54, 111.54, 70.24, 63.50, 60.64, 51.86, 49.27, 42.31, 36.89, 28.25.

N-(4-Aminobutyl)-2-((6-chloro-2-(4-methylpiperazin-1-yl)quinazolin-4-yl)amino)ethane-1-sulfonamide trihydrochloride **(P50c)**

The reaction protocol was carried out as described for compound **P50a**.[771] Compound **SM5** (53 mg, 0.14 mmol, 1.0 eq.), oxalyl chloride (36 µL, 0.42 mmol, 3.0 eq.) and butane-1,4-diamine (37 mg, 0.42 mmol, 3.0 eq.) were subjected to the reaction conditions for 24 hours. The crude product was purified by reverse phase flash column chromatography using a gradient elution of water/methanol (0-100%).

Yield:	39 mg, (49%)
Chemical formula:	$C_{19}H_{30}ClN_7O_2S$ x 3 HCl
Molecular mass:	565.39 g/mol
Appearance:	Colourless solid
Internal code:	MST-684
Synthesis scheme:	Figure 163
Melting point:	260.1 °C
LC-MS-DAD purity:	100%
HR-MS (ESI-(+)):	m/z=456.2034 $[M+H^+]^+$ calculated: 456.1943
^{1}H NMR (300 MHz, DMSO-d_6):	δ 13.51 (s, 1H), 11.66 (s, 1H), 10.48 (t, *J* = 7.1 Hz, 1H), 8.75 – 8.68 (m, 1H), 8.26 – 8.01 (m, 4H), 7.96 – 7.84 (m, 1H), 7.47 (t, *J* = 5.7 Hz, 1H), 3.99 – 3.87 (m, 2H), 3.80 – 3.22 (m, 12H), 2.97 – 2.66 (m, 5H), 1.64 – 1.48 (m, 2H), 1.52 – 1.20 (m, 2H).
^{13}C NMR (151 MHz, DMSO-d_6):	δ 158.86, 135.48, 135.47, 135.46, 135.44, 127.84, 124.26, 111.53, 70.24, 63.51, 51.88, 49.06, 42.56, 42.33, 29.36, 26.90, 23.43.

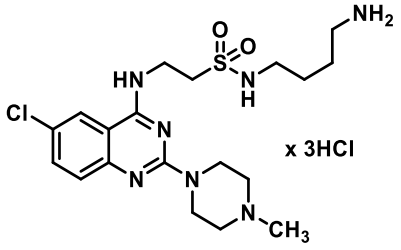

N-(5-Aminopentyl)-2-((6-chloro-2-(4-methylpiperazin-1-yl)quinazolin-4-yl)amino)ethane-1-sulfonamide trihydrochloride **(P50d)**

The reaction protocol was carried out as described for compound **P50a**.[771] Compound **SM5** (53 mg, 0.14 mmol, 1.0 eq.), oxalyl chloride (36 µL, 0.42 mmol, 3.0 eq.) and propane-1,5-

diamine (43 mg, 0.42 mmol, 3.0 eq.) were subjected to the reaction conditions for 24 hours. The crude product was purified by reverse phase flash column chromatography using a gradient elution of water/methanol (0-100%).

Yield:	41 mg, (51%)
Chemical formula:	$C_{20}H_{32}ClN_7O_2S$ x 3 HCl
Molecular mass:	578.03 g/mol
Appearance:	Colourless solid
Internal code:	MST-685, ST-2935
Synthesis scheme:	Figure 163
Melting point:	257.5 °C
LC-MS-DAD purity:	100%
HR-MS (ESI-(+)):	m/z=470.2115 $[M+H^+]^+$ calculated: 470.2099
^{1}H NMR (300 MHz, DMSO-d_6):	δ 13.59 (s, 1H), 11.73 (s, 1H), 10.62 (t, *J* = 5.6 Hz, 1H), 8.92 – 8.63 (m, 1H), 8.38 – 8.19 (m, 1H), 8.21 – 8.10 (m, 3H), 7.98 – 7.79 (m, 1H), 7.64 – 7.42 (m, 1H), 3.97 – 3.87 (m, 2H), 3.80 – 3.38 (m, 8H), 3.34 – 3.17 (m, 2H), 3.03 – 2.89 (m, 2H), 2.89 – 2.67 (m, 5H), 1.66 – 1.41 (m, 6H).
^{13}C NMR (151 MHz, DMSO-d_6):	δ 158.81, 152.05, 138.97, 135.49, 129.46, 124.36, 120.20, 111.52, 70.23, 60.63, 51.84, 49.14, 42.29, 42.26, 38.77, 36.63, 27.03, 24.69.

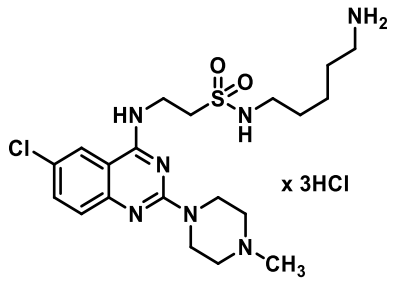

N-(6-Aminohexyl)-2-((6-chloro-2-(4-methylpiperazin-1-yl)quinazolin-4-yl)amino)ethane-1-sulfonamide trihydrochloride **(P50e)**

The reaction protocol was carried out as described for compound **P50a**.[771] Compound **SM5** (63 mg, 0.16 mmol, 1.0 eq.), oxalyl chloride (41 µL, 0.48 mmol, 3.0 eq.) and hexane-1,6-diamine (56 mg, 0.48 mmol, 3.0 eq.) were subjected to the reaction conditions for 24 hours. The crude product was purified by reverse phase flash column chromatography using a gradient elution of water/methanol (0-100%).

Yield:	60 mg, (63%)
Chemical formula:	$C_{21}H_{34}ClN_7O_2S$ x 3 HCl
Molecular mass:	592.06 g/mol
Appearance:	Colourless solid
Internal code:	MST-702, ST-2941
Synthesis scheme:	Figure 163
Melting point:	249.1 °C

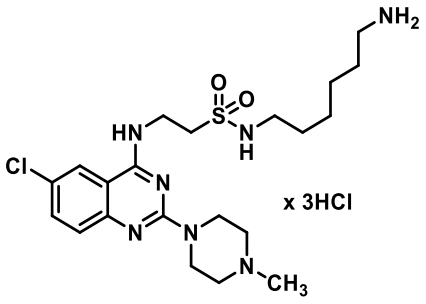

LC-MS-DAD purity:	100%
HR-MS (ESI-(+)):	m/z=484.2279 $[M+H^+]^+$ calculated: 484.2256
^{1}H NMR (300 MHz, DMSO-d_6):	δ 13.50 (s, 1H), 11.64 (s, 1H), 10.46 (t, *J* = 7.7 Hz, 1H), 8.76 – 8.62 (m, 1H), 8.24 – 8.13 (m, 1H), 8.11 – 7.94 (m, 3H), 7.92 – 7.83 (m, 1H), 7.43 (t, *J* = 5.8 Hz, 1H), 4.00 – 3.87 (m, 2H), 3.78 – 3.17 (m, 10H), 2.98 – 2.63 (m, 7H), 1.64 – 1.37 (m, 4H), 1.34 – 1.12 (m, 4H).
^{13}C NMR (151 MHz, MeOD):	δ 159.39, 158.91, 150.41, 132.80, 126.34, 125.89, 121.32, 111.33, 69.88, 54.61, 49.56, 44.85, 43.33, 42.58, 41.07, 35.74, 32.40, 29.91, 26.15.

N-(2-(2-Aminoethoxy)ethyl)-2-((6-chloro-2-(4-methylpiperazin-1-yl)quinazolin-4-yl)amino)ethane-1-sulfonamide trihydrochloride **(P50f)**

The reaction protocol was carried out as described for compound **P50a**.[771] Compound **SM5** (66 mg, 0.17 mmol, 1.0 eq.), oxalyl chloride (44 µL, 0.51 mmol, 3.0 eq.) and 2,2'-oxybis(ethan-1-amine) (53 mg, 0.51 mmol, 3.0 eq.) were subjected to the reaction conditions for 24 hours. The crude product was purified by reverse phase flash column chromatography using a gradient elution of water/methanol (0-100%).

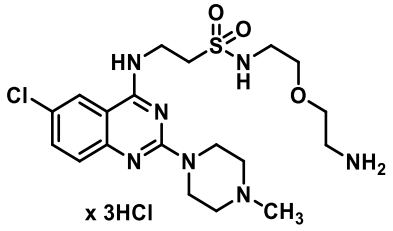

Yield:	39 mg, (40%)
Chemical formula:	$C_{19}H_{30}ClN_7O_3S$ x 3 HCl
Molecular mass:	580.01 g/mol
Appearance:	Colourless solid
Internal code:	MST-703, ST-2934
Synthesis scheme:	Figure 163
Melting point:	265.1 °C
LC-MS-DAD purity:	100%
HR-MS (ESI-(+)):	m/z=472.1895 $[M+H^+]^+$ calculated: 472.1892
^{1}H NMR (300 MHz, DMSO-d_6):	δ 13.50 (s, 1H), 11.65 (s, 1H), 10.47 (t, *J* = 5.6 Hz, 1H), 8.88 – 8.68 (m, 1H), 8.40 – 8.08 (m, 4H), 8.03 – 7.80 (m, 1H), 7.58 (t, *J* = 5.7 Hz, 1H), 4.00 – 3.90 (m, 2H), 3.90 – 3.36 (m, 14H), 3.35 – 3.10 (m, 2H), 3.06 – 2.94 (m, 2H), 2.80 (s, 3H).
^{13}C NMR (151 MHz, DMSO-d_6):	δ 158.84, 152.11, 139.04, 135.52, 129.44, 124.30, 120.30, 111.51, 72.80, 70.24, 69.85, 66.73, 60.65, 51.88, 42.58, 42.33, 39.01.

N-(2-(2-(2-Aminoethoxy)ethoxy)ethyl)-2-((6-chloro-2-(4-methylpiperazin-1-yl)quinazolin-4-yl)amino)ethane-1-sulfonamide trihydrochloride **(P50g)**

The reaction protocol was carried out as described for compound **P50a**.[771] Compound **SM5** (65 mg, 0.17 mmol, 1.0 eq.), oxalyl chloride (44 µL, 0.51 mmol, 3.0 eq.) and 2,2'-(ethane-1,2-diylbis(oxy))bis(ethan-1-amine) (75 mg, 0.51 mmol, 3.0 eq.) were subjected to the reaction conditions for 24 hours. The crude product was purified by reverse phase flash column chromatography using a gradient elution of water/methanol (0-100%).

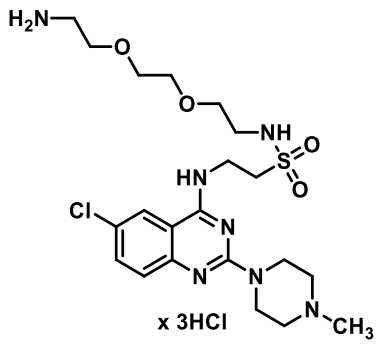

Yield:	33 mg, (31%)
Chemical formula:	$C_{21}H_{34}ClN_7O_4S$ x 3 HCl
Molecular mass:	624.06 g/mol
Appearance:	Colourless solid
Internal code:	MST-704, ST-2931
Synthesis scheme:	Figure 163
Melting point:	271.1 °C
LC-MS-DAD purity:	95.7%
HR-MS (ESI-(+)):	m/z=258.6188 $[M+2H^+]^+$ calculated: 258.6114
^{1}H NMR (300 MHz, DMSO-d_6):	δ 13.48 (s, 1H), 11.71 (s, 1H), 10.54 (t, *J* = 5.5 Hz, 1H), 8.81 – 8.59 (m, 1H), 8.28 – 8.03 (m, 4H), 7.94 – 7.79 (m, 1H), 7.58 (t, *J* = 5.8 Hz, 1H), 4.11 – 3.85 (m, 2H), 3.80 – 3.39 (m, 16H), 3.35 – 3.19 (m, 2H), 3.17 – 3.05 (m, 2H), 3.00 – 2.89 (m, 2H), 2.81 (s, 3H).
^{13}C NMR (151 MHz, DMSO-d_6):	δ 158.77, 152.00, 138.94, 135.47, 129.46, 124.31, 120.18, 111.46, 70.23, 70.07, 70.05, 69.90, 67.01, 51.85, 49.48, 42.56, 42.31, 38.90, 36.70.

N-(2-(2-(2-(2-aminoethoxy)ethoxy)ethoxy)ethyl)-2-((6-chloro-2-(4-methylpiperazin-1-yl)quinazolin-4-yl)amino)ethane-1-sulfonamide trihydrochloride **(P50h)**

The reaction protocol was carried out as described for compound **P50a**.[771] Compound **SM5** (67 mg, 0.17 mmol, 1.0 eq.), oxalyl chloride (44 µL, 0.51 mmol, 3.0 eq.) and 2,2'-((oxybis(ethane-2,1-diyl))bis(oxy))bis(ethan-1-amine) (98 mg, 0.51 mmol, 3.0 eq.) were subjected to the reaction conditions for 24 hours. The crude product was purified by reverse phase flash column chromatography using a gradient elution of water/methanol (0-100%).

Yield:	37 mg, (40%)
Chemical formula:	$C_{23}H_{38}ClN_7O_5S$ x 3 HCl
Molecular mass:	668.11 g/mol
Appearance:	Colourless solid
Internal code:	MST-705, ST-2943
Synthesis scheme:	Figure 163
Melting point:	271.0 °C
LC-MS-DAD purity:	100%
HR-MS (ESI-(+)):	m/z=560.2547 $[M+2H^+]^+$ calculated: 560.2416
^{1}H NMR (300 MHz, DMSO-d_6):	δ 13.61 (s, 1H), 11.81 (s, 1H), 10.64 (t, *J* = 5.6 Hz, 1H), 8.81 – 8.71 (m, 1H), 8.35 – 8.23 (m, 1H), 8.23 – 8.08 (m, 3H), 7.93 – 7.79 (m, 1H), 7.69 – 7.52 (m, 1H), 4.01 – 3.84 (m, 2H), 3.78 – 3.36 (m, 20H), 3.34 – 3.19 (m, 2H), 3.12 – 3.02 (m, 2H), 2.97 – 2.85 (m, 2H), 2.79 (s, 3H).
^{13}C NMR (151 MHz, MeOD):	δ 159.34, 159.01, 150.38, 132.70, 126.26, 125.78, 121.40, 111.42, 72.15, 70.86, 70.06, 70.00, 69.75, 69.74, 60.57, 54.62, 49.64, 44.86, 43.34, 40.68, 36.13.

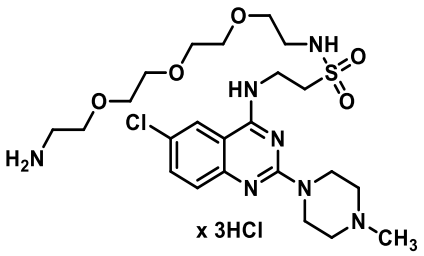

N-(2-((2-((6-Chloro-2-(4-methylpiperazin-1-yl)quinazolin-4-yl)amino)ethyl)sulfonamido)-ethyl)-3-(5,5-difluoro-7,9-dimethyl-5*H*-5λ^4,6λ^4-dipyrrolo[1,2-*c*:2',1'-*f*][1,3,2]diazaborinin-3-yl)propanamide **(P51a)**

The HATU coupling was carried out as described for compound **P3**.[644] Compound **P50a** (25 mg, 0.06 mmol, 1.0 eq.), DIPEA (12 µL, 0.07 mmol, 1.1 eq.), BODIPY-FL (18 mg, 0.06 mmol, 1.0 eq.) and HATU (27 mg, 0.07 mmol, 1.1 eq.) were subjected to the reaction conditions for 24 hours. The crude product was purified by column chromatography using a gradient elution of dichloromethane/methanol (sat. NH_3) (0-20%).

Yield:	20 mg, (48%)
Chemical formula:	$C_{31}H_{39}BClF_2N_9O_3S$
Molecular mass:	702.03 g/mol
Appearance:	Red solid
Internal code:	MST-783, ST-2972
Synthesis scheme:	Figure 164
Melting point:	101.5 °C
LC-MS-DAD purity:	100%
HR-MS (ESI-(+)):	m/z=702.2722 $[M+H^+]^+$ calculated: 702.2719

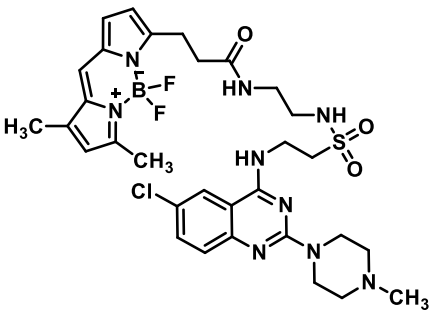

^{1}H NMR (600 MHz, DMSO-d_6):	δ 8.24 (t, *J* = 5.6 Hz, 1H), 8.07 – 8.02 (m, 2H), 7.68 (s, 1H), 7.55 – 7.50 (m, 1H), 7.34 (t, *J* = 6.0 Hz, 1H), 7.31 – 7.24 (m, 1H), 7.07 (d, *J* = 4.0 Hz, 1H), 6.33 (d, *J* = 4.0 Hz, 1H), 6.30 (s, 1H), 3.84 – 3.76 (m, 6H), 3.53 – 3.50 (m, 4H), 3.24 – 3.15 (m, 2H), 3.08 (t, *J* = 7.8 Hz, 2H), 3.05 – 2.98 (m, 2H), 2.49 – 2.45 (m, 3H), 2.35 (t, *J* = 5.0 Hz, 4H), 2.26 (s, 3H), 2.20 (s, 3H).
^{13}C NMR (151 MHz, DMSO-d_6):	δ 171.55, 159.97, 159.65, 159.64, 159.34, 158.96, 158.95, 158.93, 150.97, 133.44, 133.19, 127.53, 125.81, 125.80, 124.63, 122.43, 111.65, 111.63, 70.25, 54.99, 49.89, 46.22, 43.74, 42.33, 36.03, 34.21, 24.35, 14.97, 11.46.

N-(3-((2-((6-Chloro-2-(4-methylpiperazin-1-yl)quinazolin-4-yl)amino)ethyl)sulfonamido)-propyl)-3-(5,5-difluoro-7,9-dimethyl-5*H*-5λ^4,6λ^4-dipyrrolo[1,2-*c*:2',1'-*f*][1,3,2]diazaborinin-3-yl)propanamide **(P51b)**

The HATU coupling was carried out as described for compound **P3**.[644] Compound **P50b** (32 mg, 0.07 mmol, 1.0 eq.), DIPEA (14 µL, 0.08 mmol, 1.1 eq.), BODIPY-FL (20 mg, 0.07 mmol, 1.0 eq.) and HATU (30 mg, 0.08 mmol, 1.1 eq.) were subjected to the reaction conditions for 24 hours. The crude product was purified by column chromatography using a gradient elution of dichloromethane/methanol (sat. NH_3) (0-20%).

Yield:	26 mg, (52%)
Chemical formula:	$C_{32}H_{41}BClF_2N_9O_3S$
Molecular mass:	716.06 g/mol
Appearance:	Red solid
Internal code:	MST-802, ST-2964
Synthesis scheme:	Figure 164
Melting point:	99.1 °C
LC-MS-DAD purity:	95.3%
HR-MS (ESI-(+)):	m/z=716.2888 $[M+H^+]^+$ calculated: 716.2875
^{1}H NMR (600 MHz, DMSO-d_6):	δ 8.26 (t, *J* = 5.6 Hz, 1H), 8.10 – 8.04 (m, 1H), 7.95 (t, *J* = 5.6 Hz, 1H), 7.67 (s, 1H), 7.54 – 7.47 (m, 1H), 7.32 – 7.25 (m, 1H), 7.21 (t, *J* = 5.9 Hz, 1H), 7.07 (d, *J* = 4.0 Hz, 1H), 6.34 (d, *J* = 4.0 Hz, 1H), 6.29 (s, 1H), 3.86 – 3.72 (m, 4H), 3.41 – 3.35 (m, 4H), 3.14 – 3.02 (m, 4H), 2.98 – 2.92 (m, 2H), 2.49 – 2.36 (m, 9H), 2.32 – 2.17 (m, 6H), 1.65 – 1.54 (m, 2H).

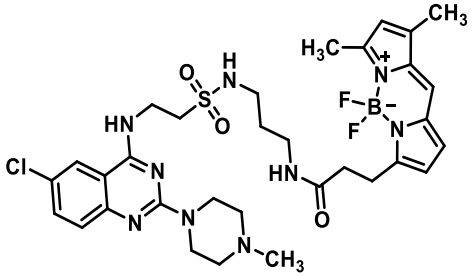

^{13}C NMR (151 MHz, DMSO-d_6):	δ 171.32, 159.61, 159.35, 158.92, 158.27, 150.95, 144.55, 134.92, 133.43, 133.20, 129.38, 127.54, 125.79, 124.67, 122.45, 120.73, 117.03, 111.65, 54.90, 49.64, 46.08, 43.63, 40.76, 36.65, 36.04, 34.21, 30.28, 24.45, 14.97, 11.46.

N-(4-((2-((6-Chloro-2-(4-methylpiperazin-1-yl)quinazolin-4-yl)amino)ethyl)sulfonamido)-butyl)-3-(5,5-difluoro-7,9-dimethyl-5*H*-5λ^4,6λ^4-dipyrrolo[1,2-c:2',1'-*f*][1,3,2]diazaborinin-3-yl)propanamide **(P51c)**

The HATU coupling was carried out as described for compound **P3**.[644] Compound **P50c** (30 mg, 0.07 mmol, 1.0 eq.), DIPEA (14 µL, 0.08 mmol, 1.1 eq.), BODIPY-FL (20 mg, 0.07 mmol, 1.0 eq.) and HATU (30 mg, 0.08 mmol, 1.1 eq.) were subjected to the reaction conditions for 24 hours. The crude product was purified by column chromatography using a gradient elution of dichloromethane/methanol (sat. NH_3) (0-20%).

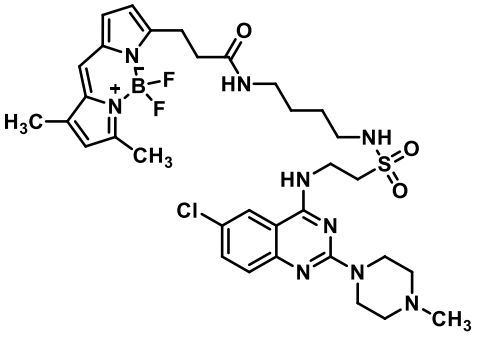

Yield:	21 mg, (42%)
Chemical formula:	$C_{33}H_{43}BClF_2N_9O_3S$
Molecular mass:	730.08 g/mol
Appearance:	Red solid
Internal code:	MST-780, ST-2992
Synthesis scheme:	Figure 164
Melting point:	107.1 °C
LC-MS-DAD purity:	96.6%
HR-MS (ESI-(+)):	m/z=730.3045 $[M+H^+]^+$ calculated: 730.3032
^{1}H NMR (600 MHz, DMSO-d_6):	δ 8.29 (t, *J* = 5.6 Hz, 1H), 8.13 – 8.03 (m, 1H), 7.93 (t, *J* = 5.6 Hz, 1H), 7.67 (s, 1H), 7.56 – 7.47 (m, 1H), 7.31 – 7.26 (m, 1H), 7.20 (t, *J* = 5.9 Hz, 1H), 7.07 (d, *J* = 4.1 Hz, 1H), 6.33 (d, *J* = 4.1 Hz, 1H), 6.29 (s, 1H), 3.88 – 3.77 (m, 6H), 3.42 – 3.33 (m, 2H), 3.10 – 3.00 (m, 4H), 2.96 – 2.89 (m, 2H), 2.49 – 2.44 (m, 9H), 2.29 (s, 3H), 2.25 (s, 3H), 1.46 – 1.38 (m, 4H).
^{13}C NMR (151 MHz, DMSO-d_6):	δ 171.12, 159.57, 159.38, 158.85, 158.35, 150.90, 144.52, 134.89, 133.43, 133.23, 129.39, 127.54, 125.79, 124.79, 122.48, 120.71, 117.05, 111.70, 54.63, 49.56, 43.33, 42.59, 38.57, 37.47, 36.06, 34.24, 27.56, 26.85, 24.49, 14.97, 11.46.

N-(5-((2-((6-Chloro-2-(4-methylpiperazin-1-yl)quinazolin-4-yl)amino)ethyl)sulfonamido)-pentyl)-3-(5,5-difluoro-7,9-dimethyl-5*H*-5λ^4,6λ^4-dipyrrolo[1,2-c:2',1'-*f*][1,3,2]diazaborinin-3-yl)propanamide **(P51d)**

The HATU coupling was carried out as described for compound **P3**.[644] Compound **P50d** (22 mg, 0.05 mmol, 1.0 eq.), DIPEA (10 µL, 0.06 mmol, 1.1 eq.), BODIPY-FL (15 mg, 0.05 mmol, 1.0 eq.) and HATU (23 mg, 0.06 mmol, 1.1 eq.) were subjected to the reaction conditions for 24 hours. The crude product was purified by column chromatography using a gradient elution of dichloromethane/methanol (sat. NH_3) (0-20%).

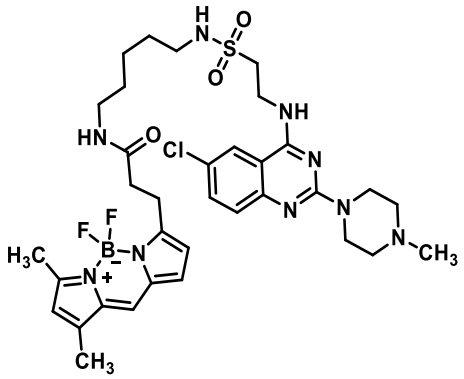

Yield:	12 mg, (31%)
Chemical formula:	$C_{34}H_{45}BClF_2N_9O_3S$
Molecular mass:	744.11 g/mol
Appearance:	Red solid
Internal code:	MST-781
Synthesis scheme:	Figure 164
Melting point:	104.2 °C
LC-MS-DAD purity:	96.4%
HR-MS (ESI-(+)):	m/z=744.3191 $[M+H^+]^+$ calculated: 744.3188
^{1}H NMR (600 MHz, $CDCl_3$):	δ 7.65 – 7.61 (m, 1H), 7.35 – 7.30 (m, 1H), 7.30 – 7.24 (m, 1H), 7.13 (t, *J* = 5.8 Hz, 1H), 6.98 (s, 1H), 6.77 (d, *J* = 4.0 Hz, 1H), 6.20 (d, *J* = 4.0 Hz, 1H), 6.08 (t, *J* = 5.1 Hz, 1H), 6.01 (s, 1H), 5.57 (t, *J* = 5.8 Hz, 1H), 3.97 – 3.92 (m, 2H), 3.85 – 3.80 (m, 4H), 3.36 – 3.31 (m, 2H), 3.19 (t, *J* = 7.5 Hz, 2H), 3.13 – 3.06 (m, 2H), 2.90 – 2.80 (m, 2H), 2.63 (t, *J* = 7.5 Hz, 2H), 2.45 (s, 3H), 2.42 – 2.38 (m, 4H), 2.26 (s, 3H), 2.15 (s, 3H), 1.37 – 1.30 (m, 2H), 1.30 – 1.22 (m, 2H), 1.13 – 1.05 (m, 2H).
^{13}C NMR (151 MHz, $CDCl_3$):	δ 172.74, 160.45, 159.01, 158.81, 156.66, 150.91, 144.23, 135.20, 133.31, 133.10, 128.33, 127.30, 125.70, 123.90, 121.08, 120.56, 117.21, 111.20, 55.16, 49.97, 46.27, 43.81, 42.84, 39.04, 36.25, 35.85, 28.99, 28.74, 24.88, 23.16, 14.96, 11.33.

N-(6-((2-((6-Chloro-2-(4-methylpiperazin-1-yl)quinazolin-4-yl)amino)ethyl)sulfonamido)-hexyl)-3-(5,5-difluoro-7,9-dimethyl-5*H*-5λ^4,6λ^4-dipyrrolo[1,2-*c*:2',1'-*f*][1,3,2]diazaborinin-3-yl)propanamide **(P51e)**

The HATU coupling was carried out as described for compound **P3**.[644] Compound **P50e** (45 mg, 0.09 mmol, 1.0 eq.), DIPEA (17 µL, 0.10 mmol, 1.1 eq.), BODIPY-FL (26 mg, 0.09 mmol, 1.0 eq.) and HATU (38 mg, 0.10 mmol, 1.1 eq.) were subjected to the reaction conditions for 24 hours. The crude product was purified by column chromatography using a gradient elution of dichloromethane/methanol (sat. NH_3) (0-20%).

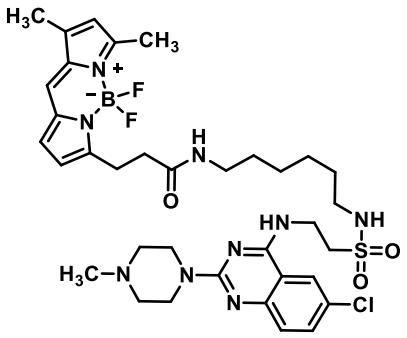

Yield:	45 mg, (31%)
Chemical formula:	$C_{35}H_{47}BClF_2N_9O_3S$
Molecular mass:	758.14 g/mol
Appearance:	Red solid
Internal code:	MST-776, ST-2993
Synthesis scheme:	Figure 164
Melting point:	102.4 °C
LC-MS-DAD purity:	96.0%
HR-MS (ESI-(+)):	m/z=758.3359 $[M+H^+]^+$ calculated: 758.3345
^{1}H NMR (600 MHz, DMSO-d_6):	δ 8.31 (t, *J* = 5.6 Hz, 1H), 8.13 – 8.08 (m, 1H), 7.91 (t, *J* = 5.9 Hz, 1H), 7.70 (s, 1H), 7.58 – 7.53 (m, 1H), 7.35 – 7.31 (m, 1H), 7.17 (t, *J* = 5.1 Hz, 1H), 7.11 (d, *J* = 4.1 Hz, 1H), 6.37 (d, *J* = 4.1 Hz, 1H), 6.32 (s, 1H), 3.90 – 3.87 (m, 4H), 3.87 – 3.81 (m, 2H), 3.41 – 3.36 (m, 2H), 3.13 – 3.03 (m, 4H), 2.96 – 2.89 (m, 2H), 2.65 – 2.62 (m, 4H), 2.53 – 2.44 (m, 5H), 2.41 (s, 3H), 2.28 (s, 3H), 1.49 – 1.42 (m, 2H), 1.44 – 1.35 (m, 2H), 1.30 – 1.22 (m, 4H).
^{13}C NMR (151 MHz, DMSO-d_6):	δ 171.05, 159.57, 159.40, 158.77, 158.36, 150.84, 144.53, 134.90, 133.44, 133.27, 129.36, 127.57, 125.77, 124.92, 122.46, 120.71, 117.04, 111.72, 54.41, 49.54, 43.07, 42.86, 38.92, 36.10, 34.24, 30.06, 29.53, 29.17, 26.49, 26.35, 24.52, 14.96, 11.45.

N-(2-(2-((2-((6-Chloro-2-(4-methylpiperazin-1-yl)quinazolin-4-yl)amino)ethyl)-sulfonamido)ethoxy)ethyl)-3-(5,5-difluoro-7,9-dimethyl-5*H*-5λ^4,6λ^4-dipyrrolo[1,2-*c*:2',1'-*f*][1,3,2]diazaborinin-3-yl)propanamide **(P51f)**

The HATU coupling was carried out as described for compound **P3**.[644] Compound **P50f** (30 mg, 0.05 mmol, 1.0 eq.), DIPEA (10 µL, 0.06 mmol, 1.1 eq.), BODIPY-FL (15 mg, 0.05 mmol, 1.0 eq.) and HATU (23 mg, 0.06 mmol, 1.1 eq.) were subjected to the reaction conditions for 24 hours. The crude product was purified by column chromatography using a gradient elution of dichloromethane/methanol (sat. NH_3) (0-20%).

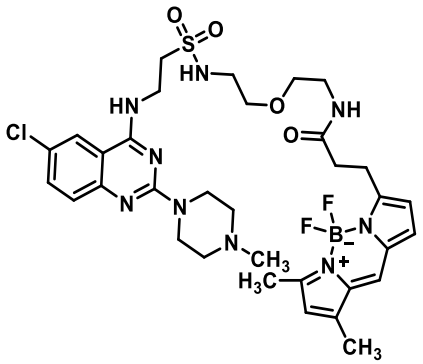

Yield:	32 mg, (47%)
Chemical formula:	$C_{33}H_{43}BClF_2N_9O_4S$
Molecular mass:	746.08 g/mol
Appearance:	Red solid
Internal code:	MST-778, ST-2969
Synthesis scheme:	Figure 164
Melting point:	108.2 °C
LC-MS-DAD purity:	100%
HR-MS (ESI-(+)):	m/z=746.2995 $[M+H^+]^+$ calculated: 746.2981
^{1}H NMR (600 MHz, DMSO-d_6):	δ 8.31 (t, *J* = 5.7 Hz, 1H), 8.10 – 8.03 (m, 1H), 7.98 (t, *J* = 5.6 Hz, 1H), 7.67 (s, 1H), 7.56 – 7.52 (m, 1H), 7.32 – 7.30 (m, 1H), 7.27 (t, *J* = 5.9 Hz, 1H), 7.07 (d, *J* = 4.0 Hz, 1H), 6.33 (d, *J* = 4.0 Hz, 1H), 6.29 (s, 1H), 4.00 – 3.70 (m, 2H), 3.54 – 3.49 (m, 4H), 3.48 – 3.37 (m, 8H), 3.27 – 3.20 (m, 2H), 3.16 – 3.03 (m, 4H), 2.91 – 2.64 (m, 4H), 2.49 (s, 3H), 2.46 (s, 3H), 2.26 (s, 3H).
^{13}C NMR (151 MHz, DMSO-d_6):	δ 171.45, 159.64, 159.46, 158.65, 158.19, 158.17, 144.57, 134.91, 134.66, 133.41, 133.33, 129.34, 127.58, 125.79, 122.49, 120.74, 117.00, 111.81, 70.25, 69.87, 69.43, 50.02, 42.61, 40.52, 38.95, 36.11, 34.14, 28.71, 24.42, 14.97, 11.46.

N-(2-(2-(2-((2-((6-Chloro-2-(4-methylpiperazin-1-yl)quinazolin-4-yl)amino)ethyl)-sulfonamido)ethoxy)ethoxy)ethyl)-3-(5,5-difluoro-7,9-dimethyl-5*H*-5λ^4,6 λ^4-dipyrrolo[1,2-*c*:2',1'-*f*][1,3,2]diazaborinin-3-yl)propanamide **(P51g)**

The HATU coupling was carried out as described for compound **P3**.[644] Compound **P50g** (30 mg, 0.05 mmol, 1.0 eq.), DIPEA (10 µL, 0.06 mmol, 1.1 eq.), BODIPY-FL (14 mg, 0.05 mmol, 1.0 eq.) and HATU (23 mg, 0.06 mmol, 1.1 eq.) were subjected to the reaction conditions for 24 hours. The crude product was purified by column chromatography using a gradient elution of dichloromethane/methanol (sat. NH_3) (0-20%).

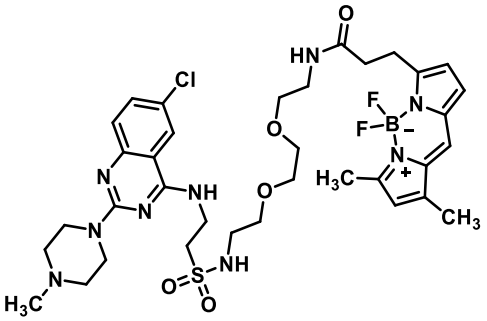

Yield:	16 mg, (22%)
Chemical formula:	$C_{35}H_{47}BClF_2N_9O_5S$
Molecular mass:	790.14 g/mol
Appearance:	Red solid
Internal code:	MST-779, ST-2956
Synthesis scheme:	Figure 164
Melting point:	110.2 °C
LC-MS-DAD purity:	100%
HR-MS (ESI-(+)):	m/z=790.3271 $[M+H^+]^+$ calculated: 790.3243
^{1}H NMR (600 MHz, DMSO-d_6):	δ 8.21 (t, *J* = 5.6 Hz, 1H), 8.06 – 8.01 (m, 1H), 7.98 (t, *J* = 5.7 Hz, 1H), 7.67 (s, 1H), 7.58 – 7.47 (m, 1H), 7.29 – 7.25 (m, 2H), 7.08 (d, *J* = 4.0 Hz, 1H), 6.35 (d, *J* = 4.0 Hz, 1H), 6.29 (s, 1H), 3.85 – 3.74 (m, 6H), 3.54 – 3.29 (m, 10H), 3.23 – 3.18 (m, 2H), 3.14 – 3.02 (m, 4H), 2.52 – 2.47 (m, 2H), 2.46 (s, 3H), 2.40 – 2.33 (m, 4H), 2.25 (s, 3H), 2.22 (s, 3H).
^{13}C NMR (151 MHz, DMSO-d_6):	δ 171.39, 159.57, 159.33, 158.94, 158.30, 150.97, 144.51, 134.89, 133.43, 133.17, 129.36, 127.53, 125.77, 124.62, 122.43, 120.70, 117.05, 111.64, 70.21, 70.03, 69.92, 69.56, 55.00, 50.04, 46.23, 43.72, 42.65, 39.02, 36.09, 34.11, 24.44, 14.96, 11.45.

N-(2-(2-(2-(2-((2-((6-Chloro-2-(4-methylpiperazin-1-yl)quinazolin-4-yl)amino)ethyl)-sulfonamido)ethoxy)ethoxy)ethoxy)ethyl)-3-(5,5-difluoro-7,9-dimethyl-5*H*-5λ^4,6λ^4-dipyrrolo[1,2-*c*:2',1'-*f*][1,3,2]diazaborinin-3-yl)propanamide **(P51h)**

The HATU coupling was carried out as described for compound **P3**.[644] Compound **P50h** (15 mg, 0.03 mmol, 1.0 eq.), DIPEA (7 µL, 0.04 mmol, 1.1 eq.), BODIPY-FL (9 mg, 0.03 mmol, 1.0 eq.) and HATU (15 mg, 0.04 mmol, 1.1 eq.) were subjected to the reaction conditions for 24 hours. The crude product was purified by column chromatography using a gradient elution of dichloromethane/methanol (sat. NH_3) (0-20%).

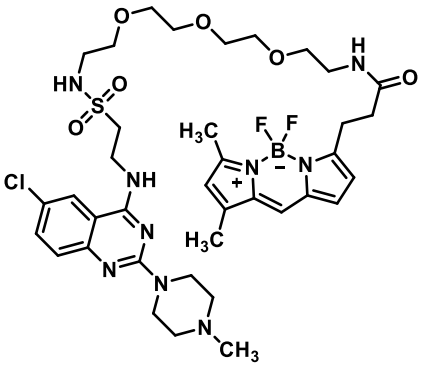

Yield:	10 mg, (40%)
Chemical formula:	$C_{37}H_{51}BClF_2N_9O_6S$
Molecular mass:	834.19 g/mol
Appearance:	Red solid
Internal code:	MST-775, ST-2978
Synthesis scheme:	Figure 164
Melting point:	114.1 °C
LC-MS-DAD purity:	100%
HR-MS (ESI-(+)):	m/z=834.3528 $[M+H^+]^+$ calculated: 834.3505
^{1}H NMR (600 MHz, DMSO-d_6):	δ 8.56 – 8.36 (m, 1H), 8.36 – 8.19 (m, 1H), 8.02 (t, *J* = 5.7 Hz, 1H), 7.91 – 7.76 (m, 1H), 7.69 – 7.64 (m, 2H), 7.40 (t, *J* = 5.3 Hz, 1H), 7.08 (d, *J* = 4.0 Hz, 1H), 6.35 (d, *J* = 4.0 Hz, 1H), 6.29 (s, 1H), 3.98 – 3.86 (m, 2H), 3.57 – 3.38 (m, 20H), 3.24 – 3.18 (m, 2H), 3.13 – 3.04 (m, 4H), 2.82 – 2.78 (m, 4H), 2.49 (s, 3H), 2.46 (s, 3H), 2.26 (s, 3H).
^{13}C NMR (151 MHz, DMSO-d_6):	δ 171.42, 159.58, 158.28, 158.28, 144.55, 134.90, 134.90, 133.57, 133.47, 133.44, 129.38, 125.79, 120.73, 117.04, 117.03, 113.98, 111.65, 111.63, 70.29, 70.25, 70.18, 70.15, 70.07, 70.00, 69.54, 52.10, 49.80, 42.65, 42.46, 40.55, 39.04, 34.11, 24.45, 14.96, 11.47.

11. References

1. Dale, H. H. & Laidlaw, P. P. The physiological action of beta-iminazolylethylamine. *J. Physiol.* **41**, 318–344 (1910).
2. Haas, H. L., Sergeeva, O. A. & Selbach, O. Histamine in the nervous system. *Physiol. Rev.* **88**, 1183–1241 (2008).
3. Branco, A. C. C. C., Yoshikawa, F. S. Y., Pietrobon, A. J. & Sato, M. N. Role of histamine in modulating the immune response and inflammation. *Mediators Inflamm.* **2018**, 9524075 (2018).
4. Smolinska, S., Jutel, M., Crameri, R. & O'Mahony, L. Histamine and gut mucosal immune regulation. *Allergy Eur. J. Allergy Clin. Immunol.* **69**, 273–281 (2014).
5. Reite, O. B. Comparative physiology of histamine. *Physiol Rev.* **52**, 778–819 (1972).
6. Sanes, J. R. & Zipursky, S. L. Design Principles of Insect and Vertebrate Visual Systems. *Neuron* **66**, 15–36 (2010).
7. Volonté, C., Liguori, F. & Amadio, S. A Closer Look at Histamine in Drosophila. *Int. J. Mol. Sci.* **25**, 4449 (2024).
8. Mulero, I. N., Sepulcre, M. P., Meseguer, J., García-Ayala, A. & Mulero, V. Histamine Is Stored in Mast Cells of Most Evolutionarily Advanced Fish and Regulates the Fish Inflammatory Response. *Proc. Natl. Acad. Sci. U.S.A.* **104 (49)**, 19434-19439 (2007).
9. Bergqvist, E. & Obrink, K. J. Gastrin-Histamine as a Normal Sequence in Gastric Acid Stimulation in the Rabbit. *Upsala J Med. Sci.* **84(2)**, 145-154 (1979).
10. Huang, H., Li, Y., Liang, J. & Finkelman, F. D. Molecular Regulation of Histamine Synthesis. *Front. Immunol.* **9**, 1392 (2018).
11. Komori, H., Nitta, Y., Ueno, H. & Higuchi, Y. Structural study reveals that Ser-354 determines substrate specificity on human histidine decarboxylase *J. Biol. Chem*. **287**, 29175–29183 (2012).
12. Moya-Garcia, A. A., Medina, M. Á. & Sánchez-Jiménez, F. Mammalian histidine decarboxylase: From structure to function. *BioEssays* **27**, 57–63 (2005).
13. Hirasawa, N., Torigoe, M., Kano, K. & Ohuchi, K. Involvement of Sp1 in lipopolysaccharide-induced expression of HDC mRNA in RAW 264 cells. *Biochem. Biophys. Res. Commun.* **349**, 833–837 (2006).
14. Kuramasu, A., Saito, H., Suzuki, S., Watanabe, T. & Ohtsu, H. Mast Cell-/Basophil-specific Transcriptional Regulation of Human Histidine Decarboxylase Gene by CpG Methylation in the Promoter Region. *J. Biol. Chem.* **273**, 31607–31614 (1998).
15. Moriguchi, T. & Takai, J. Histamine and histidine decarboxylase: Immunomodulatory functions and regulatory mechanisms. *Genes to Cells* **25**, 443–449 (2020).
16. Ai, W., Takaishi, S., Wang, T. C. & Fleming, J. V. Regulation of l-Histidine Decarboxylase and Its Role in Carcinogenesis. *Prog. Nucleic Acid Res. Mol. Biol.* **81**, 231–270 (2006).
17. Maintz, L. & Novak, N. Histamine and histamine intolerance. *Am J Clin Nutr* **85**, 1185–1196 (2007).
18. Neumann, J. *et al.* Histamine can be Formed and Degraded in the Human and Mouse Heart. *Front Pharmacol* **12**, 582916 (2021).
19. Yoshikawa, T., Nakamura, T. & Yanai, K. Histamine N-methyltransferase in the brain. *Int. J. Mol. Sci.* **20**, 737 (2019).
20. Thangam, E. B. *et al.* The role of histamine and histamine receptors in mast cell-mediated allergy and inflammation: The hunt for new therapeutic targets. *Front. Immunol.* **9**,1873 (2018).
21. Wernersson, S. & Pejler, G. Mast cell secretory granules: Armed for battle. *Nat. Rev. Immunol.* **14**, 478–494 (2014).
22. Haas, H. & Panula, P. The role of histamine and the tuberomamillary nucleus in the nervous system. *Nat. Rev. Neurosci.* **4**, 121–130 (2003).
23. Parsons, M. E. & Ganellin, C. R. Histamine and its receptors. *Br. J. Pharmacol.* **147(S1)**, 127-135 (2006).

24. Graham, H. T., Lowry, O. H., Wheelwright, F., Lenz, M. A. & Parish Jr, H. H. Distribution of histamine among leukocytes and platelets. *Blood* **10**, 467–481 (1955).
25. Brown, R. E., Stevens, D. R. & Haas, H. L. The physiology of brain histamine. *Prog. Neurobiol.* **63**, 637–672 (2001).
26. Fernández-Novoa, L. & Cacabelos, R. Histamine function in brain disorders. *Behav. Brain Res.* **124**, 213–233 (2001).
27. Zhou, Z., An, Q., Zhang, W., Li, Y., Zhang, Q. & Yan, H. Histamine and receptors in neuroinflammation: Their roles on neurodegenerative diseases. *Behav. Brain Res.* **465**, 114964 (2024).
28. Jutel, M., Akdis, M. & Akdis, C. A. Histamine, histamine receptors and their role in immune pathology. *Clin. Exp. Allergy* **39**, 1786–1800 (2009).
29. White, M. V. The role of histamine in allergic diseases. *J. Allergy Clin. Immunol.* **86**, 599–605 (1990).
30. Akdis, C. A. & Blaser, K. Histamine in the immune regulation of allergic inflammation. *J. Allergy Clin. Immunol.* **112**, 15–22 (2003).
31. Schubert, M. L. Gastric acid secretion. *Curr. Opin. Gastroenterol.* **32**, 452–460 (2016).
32. Hansen, M. B. Neurohumoral Control of Gastrointestinal Motility. *Physiol. Res* **52**, 1–30 (2003).
33. Ashina, K. *et al.* Histamine induces vascular hyperpermeability by increasing blood flow and endothelial barrier disruption in vivo. *PLoS One* **10**, e0132367 (2015).
34. Izumi, H. *et al.* Comparison of nitric oxide and prostacyclin in endothelium-dependent vasorelaxation of human umbilical artery at midgestation. *Am. J. Obstet. Gynecol.* **175**, 375–381 (1996).
35. Clejan, S. *et al.* Blood histamine is associated with coronary artery disease, cardiac events and severity of inflammation and atherosclerosis. *J. Cell. Mol. Med.* **6**, 583–592 (2002).
36. Levick, S. P. Histamine receptors in heart failure. *Heart Fail. Rev.* **27**, 1355–1372 (2022).
37. Monczor, F. & Fernandez, N. Current knowledge and perspectives on histamine H1 and H2 receptor pharmacology: functional selectivity, receptor crosstalk, and repositioning of classic histaminergic ligands. *Mol. Pharmacol.* **90**, 640–648 (2016).
38. Threlfell, S. *et al.* Histamine H3 receptors inhibit serotonin release in substantia nigra pars reticulata. *J. Neurosci.* **24**, 8704–8710 (2004).
39. González-Sepúlveda, M. *et al.* Cellular distribution of the histamine H3 receptor in the basal ganglia: Functional modulation of dopamine and glutamate neurotransmission. *Basal Ganglia* **3**, 109–121 (2013).
40. Zocco, D., McMorrow, J. P. & Murphy, E. P. Histamine modulation of peripheral CRH receptor type 1α expression is dependent on Ca2+ signalling and NF-κB/p65 transcriptional activity. *Mol. Immunol.* **47**, 1426–1437 (2010).
41. Fan, R. *et al.* The role of heterodimers formed by histamine H3 receptors and dopamine D1 receptors on the methamphetamine-induced conditioned place preference. *Eur. J. Pharmacol.* **981**, (2024).
42. Panula, P. *et al.* International union of basic and clinical pharmacology. XCVIII. histamine receptors. *Pharmacol. Rev.* **67**, 601–655 (2015).
43. Kawakami, Y., Kasakura, K. & Kawakami, T. Histamine-releasing factor, a new therapeutic target in allergic diseases. *Cells* **8**, 1515 (2019).
44. Sarasola, M. de la P., Taquez Delgado, M. A., Nicoud, M. B. & Medina, V. A. Histamine in cancer immunology and immunotherapy. Current status and new perspectives. *Pharmacol. Res. Perspect.* **9**, e00778 (2021).
45. Sun, Z. & Qu, C. Research progress of histamine and its receptors in heart diseases. *Adv. Precision Med.* **9**, 20–25 (2024).
46. Tiligada, E., Kyriakidis, K., Chazot, P. L. & Passani, M. B. Histamine pharmacology and new CNS drug targets. *CNS Neurosci. Ther.* **17**, 620–628 (2011).

47. Kooistra, A. J., Kuhne, S., de Esch, I. J. P., Leurs, R. & de Graaf, C. A structural chemogenomics analysis of aminergic GPCRs: lessons for histamine receptor ligand design. *Br. J. Pharmacol.* **170**, 101–126 (2013).
48. Rosenbaum, D. M., Rasmussen, S. G. F. & Kobilka, B. K. The structure and function of G-protein-coupled receptors. *Nature* **459**, 356–363 (2009).
49. Lefkowitz, R. J. A brief history of G-protein coupled receptors (Nobel Lecture). *Angew. Chem. Int. Ed.* **52**, 6366–6378 (2013).
50. Hilger, D., Masureel, M. & Kobilka, B. K. Structure and dynamics of GPCR signaling complexes. *Nat. Struct. Mol. Biol.* **25**, 4–12 (2018).
51. Hauser, A. S., Attwood, M. M., Rask-Andersen, M., Schiöth, H. B. & Gloriam, D. E. Trends in GPCR drug discovery: new agents, targets and indications. *Nat. Rev. Drug. Discov.* **16**, 829–842 (2017).
52. Oldham, W. M. & Hamm, H. E. Heterotrimeric G protein activation by G-protein-coupled receptors. *Nat. Rev. Mol. Cell. Biol.* **9**, 60–71 (2008).
53. Smrcka, A. V. G protein βγ subunits: Central mediators of G protein-coupled receptor signaling. *Cell. Mol. Life Sci.* **65**, 2191–2214 (2008).
54. McCudden, C. R., Hains, M. D., Kimple, R. J., Siderovski, D. P. & Willard, F. S. G-protein signaling: back to the future. *Cell. Mol. Life Sci.* **62**, 551–577 (2005).
55. Ross, E. M. & Gilman, A. G. Resolution of some components of adenylate cyclase necessary for catalytic activity. *J. Biol. Chem.* **252**, 6966–6969 (1977).
56. Hildebrandt, J. D. *et al.* Stimulation and inhibition of adenylyl cyclases mediated by distinct regulatory proteins. *Nature* **302**, 706–709 (1983).
57. Rhee, S. G. Regulation of phosphoinositide-specific phospholipase C. *Annu. Rev. Biochem.* **70**, 281–312 (2001).
58. Wolfe, J. T., Wang, H., Howard, J., Garrison, J. C. & Barrett, P. Q. T-type calcium channel regulation by specific G-protein βγ subunits. *Nature* **424**, 209–213 (2003).
59. García, D. E. *et al.* G-protein β-subunit specificity in the fast membrane-delimited inhibition of Ca^{2+} channels. *J. Neurosci.* **18**, 9163 (1998).
60. Coso, O. A., Teramoto, H., Simonds, W. F. & Gutkind, J. S. Signaling from G protein-coupled receptors to c-Jun kinase involves βγ subunits of heterotrimeric G proteins acting on a Ras and Rac1-dependent pathway. *J. Biol. Chem.* **271**, 3963–3966 (1996).
61. Yamauchi, J., Nagao, M., Kaziro, Y. & Itoh, H. Activation of p38 mitogen-activated protein kinase by signaling through G protein-coupled receptors: involvement of Gβγ and Gαq/11 subunits. *J. Biol. Chem.* **272**, 27771–27777 (1997).
62. Crespo, P., Xu, N., Simonds, W. F. & Gutkind, J. S. Ras-dependent activation of MAP kinase pathway mediated by G-protein βγ subunits. *Nature* **369**, 418–420 (1994).
63. Ravhe, I. S., Krishnan, A. & Manoj, N. Evolutionary history of histamine receptors: Early vertebrate origin and expansion of the H3-H4 subtypes. *Mol. Phylogenet. Evol.* **154**, 106989 (2021).
64. Lim, H. D. *et al.* Evaluation of histamine H1-, H2-, and H3-receptor ligands at the human histamine H4 receptor: identification of 4-methylhistamine as the first potent and selective H4 receptor agonist. *J. Pharmacol. Exp. Ther.* **314**, 1310–1321 (2005).
65. Sadek, B. & Stark, H. Cherry-picked ligands at histamine receptor subtypes. *Neuropharmacology* **106**, 56–73 (2016).
66. Rovati, G. E., Capra, V. & Neubig, R. R. The highly conserved DRY motif of class AG protein-coupled receptors: beyond the ground state. *Mol. Pharmacol.* **71**, 959–964 (2007).
67. Bovet, D. Action protectrice des ethers phenoliques au cours de intoxication histaminiques. *CR. Soc. Biol.* 547–549 (1937).
68. Shimamura, T. *et al.* Structure of the human histamine H1 receptor complex with doxepin. *Nature* **475**, 65–70 (2011).

69. Ohta, K. *et al*. Site-Directed Mutagenesis of the Histamine H1 Receptor: Roles of Aspartic Acid107, Asparagine198 and Threonine194. *Biochem. Biophys. Res. Commun*. **203**, 1096–1101 (1994).
70. Xia, R. *et al*. Cryo-EM structure of the human histamine H1 receptor/Gq complex. *Nat. Commun*. **12**, 2086 (2021).
71. Jongejan, A. *et al*. Linking agonist binding to histamine H1 receptor activation. *Nat. Chem. Biol*. **1**, 98–103 (2005).
72. Kiss, R., Kovári, Z. & Keserű, G. M. Homology modelling and binding site mapping of the human histamine H1 receptor. *Eur. J. Med. Chem*. **39**, 959–967 (2004).
73. Wieland, K. *et al*. Mutational analysis of the antagonist-binding site of the histamine H1 receptor. *J. Biol. Chem*. **274**, 29994–30000 (1999).
74. Nonaka, H. *et al*. Unique binding pocket for KW-4679 in the histamine H1 receptor. *Eur. J. Pharmacol*. **345**, 111–117 (1998).
75. Bakker, R. A. *et al*. Constitutively Active Mutants of the Histamine H1 Receptor Suggest a Conserved Hydrophobic Asparagine-Cage That Constrains the Activation of Class A G Protein-Coupled Receptors. *Mol. Pharmacol*. **73**, 94–103 (2008).
76. Zhang, X., Liu, G., Li, X., & Gong, W. Cryo-EM structure of histamine H1 receptor in complex with histamine and miniGq. *PDB* **8YN2**, (2024).
77. Rocha, S. M. *et al*. Histamine induces microglia activation and dopaminergic neuronal toxicity via H1 receptor activation. *J. Neuroinflammation* **13**, 137 (2016).
78. Giustizieri, M. L. *et al*. H1 histamine receptor mediates inflammatory responses in human keratinocytes. *J. Allergy Clin. Immunol*. **114**, 1176–1182 (2004).
79. Hide, M., Fukui, H., Watanabe, T., Wada, H. & Yamamoto, S. Histamine H1-receptor in endothelial and smooth muscle cells of guinea-pig aorta. *Eur. J. Pharmacol*. **148**, 161–169 (1988).
80. Nuutinen, S. & Panula, P. Histamine in neurotransmission and brain diseases. *Adv. Exp. Med. Biol*. **709**, 95–107 (2010).
81. Thurmond, R. L., Gelfand, E. W. & Dunford, P. J. The role of histamine H1 and H4 receptors in allergic inflammation: the search for new antihistamines. *Nat. Rev. Drug. Discov*. **7**, 41–53 (2008).
82. Michinaga, S., Nagata, A., Ogami, R., Ogawa, Y. & Hishinuma, S. Histamine H1 receptor-mediated JNK phosphorylation is regulated by Gq protein-dependent but arrestin-independent pathways. *Int. J. Mol. Sci*. **25(6)**, 3395 (2024).
83. Mitsuhashi, M. & Payan, D. G. Molecular and cellular analysis of histamine H1 receptors on cultured smooth muscle cells. *J. Cell. Biochem*. **40**, 183–192 (1989).
84. Barnes, P. J. Histamine receptors in the lung. *Agents. Actions. Suppl*. **33**, 103–122 (1991).
85. Li, H. *et al*. Histamine Upregulates Gene Expression of Endothelial Nitric Oxide Synthase in Human Vascular Endothelial Cells. *Circulation* **107**, 2348–2354 (2003).
86. Shasby, D. M., Ries, D. R., Shasby, S. S. & Winter, M. C. Histamine stimulates phosphorylation of adherens junction proteins and alters their link to vimentin. *Am. J. Physiol.-Lung Cell. Mol. Physiol*. **282(6)**, 1330–1338 (2002).
87. Bhuiyan, M. E. et al. Histamine receptor H1 in the nucleus tractus solitarii regulates arterial pressure and heart rate in rats. *Am. J. Physiol.-Heart Circ. Physiol*. **301**, 523–529 (2011).
88. Lassen, L. H., Thomsen, L. L. & Olesen, J. Histamine induces migraine via the H1-receptor. Support for the NO hypothesis of migraine. *Neuroreport* **6**, 1475–1479 (1995).
89. Yamauchi, K. & Ogasawara, M. The role of histamine in the pathophysiology of asthma and the clinical efficacy of antihistamines in asthma therapy. *Int. J. Mol. Sci*. **20(7)**, 1733 (2019).
90. Tabarean, I. V. Functional pharmacology of H1 histamine receptors expressed in mouse preoptic/anterior hypothalamic neurons. *Br. J. Pharmacol*. **170**, 415–425 (2013).

91. Zhou, F.-W., Xu, J.-J., Zhao, Y., LeDoux, M. S. & Zhou, F.-M. Opposite functions of histamine H1 and H2 receptors and H3 receptor in substantia nigra pars reticulata. *J. Neurophysiol.* **96**, 1581–1591 (2006).
92. Korotkova, T. M., Sergeeva, O. A., Ponomarenko, A. A. & Haas, H. L. Histamine excites noradrenergic neurons in locus coeruleus in rats. *Neuropharmacology* **49**, 129–134 (2005).
93. Manahan-Vaughan, D., Reymann, K. G. & Brown, R. E. In vivo electrophysiological investigations into the role of histamine in the dentate gyrus of the rat. *Neuroscience* **84**, 783–790 (1998).
94. Reiner, P. B. & Kamondi, A. Mechanisms of antihistamine-induced sedation in the human brain: H1 receptor activation reduces a background leakage potassium current. *Neuroscience* **59**, 579–588 (1994).
95. Breunig, E. et al. Histamine excites neurones in the human submucous plexus through activation of H1, H2, H3 and H4 receptors. *J. Physiol.* **583**, 731–742 (2007).
96. Masaki, T. *et al.* Involvement of hypothalamic histamine H1 receptor in the regulation of feeding rhythm and obesity. *Diabetes* **53**, 2250–2260 (2004).
97. Tashiro, M. *et al.* Roles of histamine in regulation of arousal and cognition: functional neuroimaging of histamine H1 receptors in human brain. *Life Sci.* **72**, 409–414 (2002).
98. Li–gui, H., En–tong, W., Wei, C. & Wei–xi, G. Role of histamine H1 receptors in vestibular nucleus in motion sickness. *J. Otol.* **6**, 20–25 (2011).
99. Griend, J. P. Vande & Anderson, S. L. Histamine-1 receptor antagonism for treatment of insomnia. *J. Am. Pharm. Assoc.* **52**, 210–219 (2012).
100. Hon, K. L., Leung, A. K. C., Ng, W. G. G. & Loo, S. K. Chronic urticaria: an overview of treatment and recent patents. *Recent Pat. Inflamm. Allergy Drug Discov.* **13**, 27–37 (2019).
101. Ohsawa, Y. & Hirasawa, N. The role of histamine H1 and H4 receptors in atopic dermatitis: from basic research to clinical study. *Allergol. Int.* **63**, 533–542 (2014).
102. Iriyoshi, N., Takeuchi, K., Yuta, A., Ukai, K. & Sakakura, Y. Increased expression of histamine H1 receptor mRNA in allergic rhinitis. *Clin. Exp. Allergy* **26**, 379–385 (1996).
103. Nielsen, H. J. & Hammer, J. H. Possible role of histamine in pathogenesis of autoimmune diseases: implications for immunotherapy with histamine-2 receptor antagonists. *Med. Hypotheses* **39(4)**, 349–355 (1992).
104. Simon, F. E. R. & Simons, K. J. H1 antihistamines: current status and future directions. *World Allergy Organ. J.* **1**, 145–155 (2008).
105. Church, M. K. *et al.* Risk of first-generation H1-antihistamines: a GA2LEN position paper. *Allergy* **65(4)**, 459–466 (2010).
106. Slater, J. W., Zechnich, A. D. & Haxby, D. G. Second-generation antihistamines. *Drugs* **57(1)**, 31–47 (1999).
107. Mittal, P., Godse, K. & Patil, S. Second-generation antihistamines. *Indian J. Drugs Dermatol.* **2**, 3 (2016).
108. Handley, D. A., Magnetti, A. & Higgins, A. J. Therapeutic advantages of third generation antihistamines. *Expert. Opin. Investig. Drugs.* **7**, 1045–1054 (1998).
109. Abraham, O., Schleiden, L. & Albert, S. M. Over-the-counter medications containing diphenhydramine and doxylamine used by older adults to improve sleep. *Int. J. Clin. Pharm.* **39**, 808–817 (2017).
110. Wood, C. D. Medications for vertigo and motion sickness. *Am. J. Nurs.* 1764–1767 (1966).
111. Holtmann, S., Clarke, A. H., Scherer, H. & Höhn, M. The anti-motion sickness mechanism of ginger: a comparative study with placebo and dimenhydrinate. *Acta Otolaryngol.* **108**, 168–174 (1989).
112. Anthes, J. C. *et al.* Biochemical characterization of desloratadine, a potent antagonist of the human histamine H1 receptor. *Eur. J. Pharmacol.* **449**, 229–237 (2002).

113. Perona, A., Ros, M. P., Mills, A., Morreale, A. & Gago, F. Distinct binding of cetirizine enantiomers to human serum albumin and the human histamine receptor H1. *J. Comput. Aided Mol. Des.* **34**, 1045–1062 (2020).
114. Gillard, M., Van Der Perren, C., Moguilevsky, N., Massingham, R. & Chatelain, P. Binding Characteristics of Cetirizine and Levocetirizine to Human H1 Histamine Receptors: Contribution of Lys191 and Thr194. *Mol. Pharmacol.* **61**, 391–399 (2002).
115. Ghoneim, O. M., Legere, J. A., Golbraikh, A., Tropsha, A. & Booth, R. G. Novel ligands for the human histamine H1 receptor: Synthesis, pharmacology, and comparative molecular field analysis studies of 2-dimethylamino-5-(6)-phenyl-1,2,3,4-tetrahydronaphthalenes. *Bioorg. Med. Chem.* **14**, 6640–6658 (2006).
116. Moguilevsky, N. *et al.* Stable Expression of Human H1-histamine-receptor cDNA in Chinese Hamster Ovary Cells. *Eur. J. Biochem.* **224**, 489–496 (1994).
117. Bosma, R., van den Bor, J., Vischer, H. F., Labeaga, L. & Leurs, R. The long duration of action of the second generation antihistamine bilastine coincides with its long residence time at the histamine H1 receptor. *Eur. J. Pharmacol.* **838**, 107–111 (2018).
118. Black, J. W., Duncan, W. A. M., DURANT, C. J., Ganellin, C. R. & Parsons, E. M. Definition and antagonism of histamine H 2-receptors. *Nature* **236**, (1972).
119. Traiffort, E. *et al.* The Guinea Pig Histamine H2 Receptor: Gene Cloning, Tissue Expression and Chromosomal Localization of Its Human Counterpart. *Biochem. Biophys. Res. Commun.* **211**, 570–577 (1995).
120. Nederkoorn, P. H. J., van Gelder, E. M., Donné-Op den Kelder, G. M. & Timmerman, H. The agonistic binding site at the histamine H2 receptor. II. Theoretical investigations of histamine binding to receptor models of the seven α-helical transmembrane domain. *J. Comput. Aided. Mol. Des.* **10**, 479–489 (1996).
121. Zhang, X. *et al.* Structural basis of ligand recognition and activation of the histamine receptor family. *Nat. Commun.* **15**, 8296 (2024).
122. Gantz, I. *et al.* Molecular basis for the interaction of histamine with the histamine H2 receptor. *J. Biol. Chem.* **267**, 20840–20843 (1992).
123. Zhang, J., Qi, T. & Wei, J. Homology modeling and antagonist binding site study of the human histamine H2 receptor. *Med. Chem.* **8(6)**, 1084–1092 (2012).
124. Alewijnse, A. E. *et al.* The Effect of Mutations in the DRY Motif on the Constitutive Activity and Structural Instability of the Histamine H2 Receptor. *Mol. Pharmacol.* **57**, 890–898 (2000).
125. Smit, M. J. *et al.* Inverse agonism of histamine H2 antagonist accounts for upregulation of spontaneously active histamine H2 receptors. *Proc. Natl. Acad. Sci.* **93**, 6802–6807 (1996).
126. Wang, L.-D., Hoeltzel, M., Gantz, I., Hunter, R. & Del Valle, J. Characterization of the Histamine H2 Receptor Structural Components Involved in Dual Signaling. *J. Pharmacol. Exp. Ther.* **285**, 573–578 (1998).
127. Sheng, M., Thompson, M. A. & Greenberg, M. E. CREB: a Ca^{2+}-regulated transcription factor phosphorylated by calmodulin-dependent kinases. *Science* **252**, 1427–1430 (1991).
128. Zhang, X., Liu, G., Li, X., & Gong, W. Cryo-EM structure of histamine H2 receptor in complex with histamine and miniGs. *PDB* **8YN3** (2024).
129. Fukushima, Y. *et al.* Localization of the Histamine H2 Receptor, a Target for Antiulcer Drugs, in Gastric Parietal Cells. *Digestion* **60**, 522–527 (1999).
130. Singh, V., Gohil, N. & Ramírez-García, R. New insight into the control of peptic ulcer by targeting the histamine H2 receptor. *J. Cell. Biochem.* **119**, 2003–2011 (2018).
131. Kobayashi, T. *et al.* Abnormal functional and morphological regulation of the gastric mucosa in histamine H2 receptor-deficient mice. *J. Clin. Invest.* **105**, 1741–1749 (2000).
132. Zeng, Z. *et al.* Disruption of histamine H2 receptor slows heart failure progression through reducing myocardial apoptosis and fibrosis. *Clin. Sci.* **127**, 435–448 (2014).

133. Luo, T. *et al*. Histamine H2 receptor activation exacerbates myocardial ischemia/reperfusion injury by disturbing mitochondrial and endothelial function. *Basic Res. Cardiol*. **108**, 1–14 (2013).
134. Xu, L. *et al*. An H2R-dependent medial septum histaminergic circuit mediates feeding behavior. *Curr. Biol*. **32**, 1937–1948 (2022).
135. Ma, Q. *et al*. Histamine H2 receptor deficit in glutamatergic neurons contributes to the pathogenesis of schizophrenia. *Proc. Natl. Acad. Sci.* **120(9)**, e2207003120 (2023).
136. Panula, P. & Nuutinen, S. The histaminergic network in the brain: basic organization and role in disease. *Nat. Rev. Neurosci.* **14(7)**, 472–487 (2013).
137. Lee, S. E. *et al*. H2 receptor-mediated relaxation of circular smooth muscle in human gastric corpus: The role of nitric oxide (NO). *Korean J. Physiol. Pharmacol*. **18**, 425–430 (2014).
138. Jafarzadeh, A., Nemati, M., Khorramdelazad, H. & Hassan, Z. M. Immunomodulatory properties of cimetidine: Its therapeutic potentials for treatment of immune-related diseases. *Int. Immunopharmacol*. **70**, 156–166 (2019).
139. Smolinska, S. *et al*. Histamine Receptor 2 is Required to Suppress Innate Immune Responses to Bacterial Ligands in Patients with Inflammatory Bowel Disease. *Inflamm. Bowel Dis.* **22**, 1575–1586 (2016).
140. von Rahden, B. H. A. *et al*. Allergic predisposition, histamine and histamine receptor expression (H1R, H2R) are associated with complicated courses of sigmoid diverticulitis. *J. Gastrointest. Surg.* **16**, 173–182 (2012).
141. Freston, J. W. Cimetidine in the treatment of gastric ulcer: Review and commentary. *Gastroenterology* **74**, 426–430 (1978).
142. Winship, D. H. Cimetidine in the treatment of duodenal ulcer: review and commentary. *Gastroenterology* **74**, 402–406 (1978).
143. Mark, F. & E, B. M. Histamine2-Receptor Antagonists. *N. Engl. J. Med*. **323**, 1672–1680 (1990).
144. Cole, A. T. *et al*. Ranitidine: differential effects on gastric bleeding and mucosal damage induced by aspirin. *Aliment Pharmacol. Ther.* **6**, 707–715 (1992).
145. Taha, A. S. *et al*. Famotidine for the prevention of gastric and duodenal ulcers caused by nonsteroidal antiinflammatory drugs. *N. Engl. J. Med*. **334**, 1435–1439 (1996).
146. Kumar, Ashir. Cimetidine: An Immunomodulator. *DICP* **24**, 289–295 (1990).
147. Kou, E., Zhang, X., Dong, B., Wang, B. & Zhu, Y. Combination of H1 and H2 Histamine Receptor Antagonists: Current Knowledge and Perspectives of a Classic Treatment Strategy. *Life* **14(2)**, 164 (2024).
148. Arrang, J.-M., Garbarg, M. & Schwartz, J.-C. Auto-inhibition of brain histamine release mediated by a novel class (H3) of histamine receptor. *Nature* **302**, 832–837 (1983).
149. Arrang, J. M., Drutel, G. & Schwartz, J.-C. Characterization of histamine H3 receptors regulating acetylcholine release in rat entorhinal cortex. *Br. J. Pharmacol.* **114**, 1518–1522 (1995).
150. Varaschin, R. K. *et al*. Histamine H3 receptors decrease dopamine release in the ventral striatum by reducing the activity of striatal cholinergic interneurons. *Neuroscience* **376**, 188–203 (2018).
151. Blandizzi, C., Tognetti, M., Colucci, R. & Tacca, M. Del. Histamine H3 receptors mediate inhibition of noradrenaline release from intestinal sympathetic nerves. *Br. J. Pharmacol.* **129**, 1387–1396 (2000).
152. Ellenbroek, B. A. & Ghiabi, B. The other side of the histamine H3 receptor. *Trends Neurosci*. **37**, 191–199 (2014).
153. Leurs, R., Bakker, R. A., Timmerman, H. & De Esch, I. J. The histamine H3 receptor: from gene cloning to H3 receptor drugs. *Nat. Rev. Drug Discov.* **4(2)**, 107–120 (2005).
154. Lovenberg, T. W. *et al*. Cloning and functional expression of the human histamine H3 receptor. *Mol. Pharmacol.* **55**, 1101–1107 (1999).

155. Tardivel-Lacombe, J., Morisset, S., Gbahou, F., Schwartz, J.-C. & Arrang, J.-M. Chromosomal mapping and organization of the human histamine H3 receptor gene. *Neuroreport* **12**, (2001).
156. Coge, F. *et al*. Genomic organization and characterization of splice variants of the human histamine H3 receptor. *Biochem. J.* **355(2)**, 279–288 (2001).
157. Wiedemann, P., Bönisch, H., Oerters, F. & Brüss, M. Structure of the human histamine H_3 receptor gene (HRH3) and identification of naturally occurring variations. *J. Neural Transm.* **109**, 443–453 (2002).
158. Bakker, R. A. *et al*. Discovery of naturally occurring splice variants of the rat histamine H3 receptor that act as dominant-negative isoforms. *Mol. Pharmacol.* **69**, 1194–1206 (2006).
159. Gao, M., Ooms, J. F., Leurs, R. & Vischer, H. F. Histamine H3 receptor isoforms: insights from alternative splicing to functional complexity. *Biomolecules* **14(7)**, 761 (2024).
160. Uveges, A. J. *et al*. The Role of Transmembrane Helix 5 in Agonist Binding to the Human H3 Receptor. *J. Pharmacol. Exp. Ther.* **301**, 451–458 (2002).
161. Yao, B. B. *et al*. Molecular modeling and pharmacological analysis of species-related histamine H_3 receptor heterogeneity. *Neuropharmacology* **44**, 773–786 (2003).
162. Schlegel, B. *et al*. Generation of a homology model of the human histamine H3 receptor for ligand docking and pharmacophore-based screening. *J. Comput. Aided Mol. Des.* **21**, 437–453 (2007).
163. Peng, X., Yang, L., Liu, Z., Lou, S., Mei, S., Li, M. *et al*. Structural basis for recognition of antihistamine drug by human histamine receptor. *Nat. Commun.* **13**, 6105 (2022).
164. Zhang, X., Liu, G., Li, X., & Gong, W. Cryo-EM structure of histamine H3 receptor in complex with histamine and Gi. *PDB* **8YN5**, (2024).
165. Rouleau, A. *et al*. Histamine H3-receptor-mediated [35S] GTPγ [S] binding: evidence for constitutive activity of the recombinant and native rat and human H3 receptors. *Br. J. Pharmacol.* **135**, 383–392 (2002).
166. Arrang, J.-M., Morisset, S. & Gbahou, F. Constitutive activity of the histamine H_3 receptor. *Trends Pharmacol. Sci.* **28**, 350–357 (2007).
167. Ferrada, C. *et al*. Interactions between histamine H3 and dopamine D2 receptors and the implications for striatal function. *Neuropharmacology* **55**, 190–197 (2008).
168. Ferrada, C. *et al*. Marked changes in signal transduction upon heteromerization of dopamine D 1 and histamine H 3 receptors. *Br. J. Pharmacol.* **157**, 64–75 (2009).
169. Kononoff Vanhanen, J., Nuutinen, S., Tuominen, M. & Panula, P. Histamine H3 Receptor Regulates Sensorimotor Gating and Dopaminergic Signaling in the Striatum. *J. Pharmacol. Exp. Ther.* **357**, 264–272 (2016).
170. Schlicker, E. & Kathmann, M. Role of the histamine H_3 receptor in the central nervous system. In: Hattori, Y. & Seifert, R. Histamine and histamine receptors in health and disease. *Handb. Exp. Pharmacol.* **241**, 237–261 (Cham: Springer, 2016).
171. Obuchowicz, R., Pawlik, M. W., Brzozowski, T., Konturek, S. J. & Pawlik, W. W. Involvement of central and peripheral histamine H_3. *J. Physiol. Pharmacol.* **55**, 255–267 (2004).
172. Pillot, C., Heron, A., Cochois, V., Tardivel-Lacombe, J., Ligneau, X., Schwartz, J. C. & Arrang, J. M. A detailed mapping of the histamine H_3 receptor and its gene transcripts in rat brain. *Neuroscience* **114(1)**, 173–193 (2002).
173. Jin, C. Y. & Panula, P. The laminar histamine receptor system in human prefrontal cortex suggests multiple levels of histaminergic regulation. *Neuroscience* **132**, 137–149 (2005).
174. Panula, P. Histamine receptors, agonists, and antagonists in health and disease. *Handb. Clin. Neurol.* **180**, 377–387 (2021).
175. Passani, M. B., Blandina, P. & Torrealba, F. The histamine H_3 receptor and eating behavior. *J. Pharmacol. Exp. Ther.* **336**, 24–29 (2011).

176. Parmentier, R. *et al*. Anatomical, physiological, and pharmacological characteristics of histidine decarboxylase knock-out mice: evidence for the role of brain histamine in behavioral and sleep–wake control. *J. Neurosci.* **22(17)**, 7695–7711 (2002).
177. Medhurst, A. D. *et al*. GSK189254, a novel H3 receptor antagonist that binds to histamine H3 receptors in Alzheimer's disease brain and improves cognitive performance in preclinical models. *J. Pharmacol. Exp. Ther.* **321**, 1032–1045 (2007).
178. Cannon, K. E. *et al*. Immunohistochemical localization of histamine H3 receptors in rodent skin, dorsal root ganglia, superior cervical ganglia, and spinal cord: potential antinociceptive targets. *Pain* **129**, 76–92 (2007).
179. Molderings, G. J., Weißenborn, G., Schlicker, E., Likungu, J. & Göthert, M. Inhibition of noradrenaline release from the sympathetic nerves of the human saphenous vein by presynaptic histamine H_3 receptors. *Naunyn Schmiedebergs Arch. Pharmacol.* **346**, 46–50 (1992).
180. Imamura, M., Seyedi, N., Lander, H. M. & Levi, R. Functional Identification of Histamine H3-Receptors in the Human Heart. *Circ. Res.* **77**, 206–210 (1995).
181. Cardell, L. O. & Edvinsson, L. Characterization of the histamine receptors in the guinea-pig lung: evidence for relaxant histamine H3 receptors in the trachea. *Br. J. Pharmacol.* **111**, 445–454 (1994).
182. Gomez-Ramirez, J., Ortiz, J. & Blanco, I. Presynaptic H_3 autoreceptors modulate histamine synthesis through cAMP pathway. *Mol. Pharmacol.* **61(1)**, 239–245 (2002).
183. Moreno-Delgado, D. *et al*. Constitutive activity of H_3 autoreceptors modulates histamine synthesis in rat brain through the cAMP/PKA pathway. *Neuropharmacology* **51**, 517–523 (2006).
184. Seyedi, N. *et al*. Histamine H3-receptor-induced attenuation of norepinephrine exocytosis: a decreased protein kinase a activity mediates a reduction in intracellular calcium. *J. Pharmacol. Exp. Ther.* **312**, 272–280 (2005).
185. Bongers, G., Bakker, R. A. & Leurs, R. Molecular aspects of the histamine H3 receptor. *Biochem. Pharmacol.* **73**, 1195–1204 (2007).
186. Farooqui, A. A. & Horrocks, L. A. Phospholipase A_2-generated lipid mediators in the brain: the good, the bad, and the ugly. *Neuroscientist* **12**, 245–260 (2006).
187. Krueger, K. M. *et al*. G protein-dependent pharmacology of histamine H3 receptor ligands: evidence for heterogeneous active state receptor conformations. *J. Pharmacol. Exp. Ther.* **314**, 271–281 (2005).
188. Thiels, E. & Klann, E. Extracellular signal-regulated kinase, synaptic plasticity, and memory. *Rev. Neurosci.* **12**, 327–346 (2001).
189. Gutkind, J. S. Regulation of mitogen-activated protein kinase signaling networks by G protein-coupled receptors. *Sci. STKE* **2000(40)**, re1–re1 (2000).
190. Brazil, D. P., Yang, Z. Z. & Hemmings, B. A. Advances in protein kinase B signalling: AKTion on multiple fronts. *Trends Biochem. Sci.* **29(5)**, 233–242 (2004).
191. Drutel, G. *et al*. Identification of rat H3 receptor isoforms with different brain expression and signaling properties. *Mol. Pharmacol.* **59**, 1–8 (2001).
192. Anichtchik, O. V, Peitsaro, N., Rinne, J. O., Kalimo, H. & Panula, P. Distribution and modulation of histamine H3 receptors in basal ganglia and frontal cortex of healthy controls and patients with Parkinson's disease. *Neurobiol. Dis.* **8**, 707–716 (2001).
193. Pérez-García, C., Morales, L., Cano, M. V., Sancho, I. & Alguacil, L. F. Effects of histamine H_3 receptor ligands in experimental models of anxiety and depression. *Psychopharmacology (Berl.)* **142**, 215–220 (1999).
194. Lin, J.-S., Sergeeva, O. A. & Haas, H. L. Histamine H3 receptors and sleep-wake regulation. *J. Pharmacol. Exp. Ther.* **336**, 17–23 (2011).
195. Jadidi-Niaragh, F. & Mirshafiey, A. Histamine and histamine receptors in pathogenesis and treatment of multiple sclerosis. *Neuropharmacology* **59**, 180–189 (2010).

196. Vohora, D., Pal, S. N. & Pillai, K. K. Histamine and selective H3-receptor ligands: a possible role in the mechanism and management of epilepsy. *Pharmacol. Biochem. Behav.* **68**, 735–741 (2001).
197. Lai, Y. Y., Hsieh, K. C., Cheng, Y. H., Chew, K. T., Nguyen, D., Ramanathan, L. & Siegel, J. M. Striatal histamine mechanism in the pathogenesis of restless legs syndrome. *Sleep* **43(2)**, zsz223 (2020).
198. Pullen, L. C., Picone, M., Tan, L., Johnston, C. & Stark, H. 0771 Pitolisant Is a Safe and Effective Treatment for Children with Prader-willi Syndrome (pws). *Sleep* **42**, 309–310 (2019).
199. Vohora, D. & Bhowmik, M. Histamine H_3 receptor antagonists/inverse agonists on cognitive and motor processes: relevance to Alzheimer's disease, ADHD, schizophrenia, and drug abuse. *Front. Syst. Neurosci.* **6**, 72 (2012).
200. Bitner, R. S., Markosyan, S., Nikkel, A. L. & Brioni, J. D. In-vivo histamine H3 receptor antagonism activates cellular signaling suggestive of symptomatic and disease modifying efficacy in Alzheimer's disease. *Neuropharmacology* **60**, 460–466 (2011).
201. Jin, C. Y., Anichtchik, O. & Panula, P. Altered histamine H3 receptor radioligand binding in post-mortem brain samples from subjects with psychiatric diseases. *Br. J. Pharmacol.* **157**, 118–129 (2009).
202. Nuutinen, S., Karlstedt, K., Aitta-Aho, T., Korpi, E. R. & Panula, P. Histamine and H_3 receptor-dependent mechanisms regulate ethanol stimulation and conditioned place preference in mice. *Psychopharmacology (Berl.)* **208**, 75–86 (2010).
203. Femenía, T., Magara, S., DuPont, C. M. & Lindskog, M. Hippocampal-dependent antidepressant action of the H_3 receptor antagonist clobenpropit in a rat model of depression. *Int. J. Neuropsychopharmacol.* **18**, 1–11 (2015).
204. Rizk, A., Curley, J., Robertson, J. & Raber, J. Anxiety and cognition in histamine H_3 receptor-/- mice. *Eur. J. Neurosci.* **19**, 1992–1996 (2004).
205. Bañuelos-Cabrera, I. *et al.* Pharmacoresistant temporal lobe epilepsy modifies histamine turnover and H3 receptor function in the human hippocampus and temporal neocortex. *Epilepsia* **57**, 76–80 (2016).
206. Díaz, N. F., Flores-Herrera, H., García-López, G. & Molina-Hernández, A. Central histamine, the H_3-receptor and obesity therapy. *CNS Neurol. Disord. Drug Targets* **18(7)**, 516–522 (2019).
207. Arrang, J.-M. *et al.* Highly potent and selective ligands for histamine H3-receptors. *Nature* **327**, 117–123 (1987).
208. Malmberg-Aiello, P., Lamberti, C., Ghelardini, C., Giotti, A. & Bartolini, A. Role of histamine in rodent antinociception. *Br. J. Pharmacol.* **111**, 1269–1279 (1994).
209. Nakamura, T. *et al.* The role of histamine H_3 receptor in pancreatic β-cells. *Nano-Biomedical Engineering* **2012**, 291–297 (2012).
210. Rubio, S., Begega, A., Santín, L. J., Miranda, R. & Arias, J. L. Effects of histamine precursor and (R)-α-methylhistamine on the avoidance response in rats. *Behav. Brain Res.* **124**, 177–181 (2001).
211. Vollinga, R. C., de Koning, J. P., Jansen, F. P., Leurs, R., Menge, W. M. & Timmerman, H. A new potent and selective histamine H_3 receptor agonist, 4-(1H-imidazol-4-ylmethyl) piperidine. *J. Med. Chem.* **37(3)**, 332–333 (1994).
212. Howson, W., Parsons, M. E., Raval, P., & Swayner, G. T. Novel, potent, and selective histamine H_3 receptor agonists. *Bioorg. Med. Chem. Lett.* **2**(**1**), 71–78 (1992).
213. Kitbunnadaj, R. *et al.* Identification of 4-(1H-Imidazol-4(5)-ylmethyl)pyridine (Immethridine) as a Novel, Potent, and Highly Selective Histamine H3 Receptor Agonist. *J. Med. Chem.* **47**, 2414–2417 (2004).
214. Kitbunnadaj, R. *et al.* N-Substituted Piperidinyl Alkyl Imidazoles: Discovery of Methimepip as a Potent and Selective Histamine H3 Receptor Agonist. *J. Med. Chem.* **48**, 2100–2107 (2005).

215. Sander, K., Kottke, T., & Stark, H. Histamine H3 receptor antagonists go to clinics. *Biol. Pharm. Bull.* **31**(**12**), 2163–2181 (2008).
216. Gbahou, F. *et al*. Protean agonism at histamine H3 receptors in vitro and in vivo. *Proc. Natl. Acad. Sci. U.S.A.* **100**(**1**), 11086–11091 (2003).
217. Ito, S. *et al*. Detailed pharmacological characterization of GT-2331 for the rat histamine H3 receptor. *Eur. J. Pharmacol.* **529**, 40–46 (2006).
218. Monti, J. M. *et al*. Effects of selective activation or blockade of the histamine H3 receptor on sleep and wakefulness. *Eur. J. Pharmacol.* **205**, 283–287 (1991).
219. Thakkar, M. M. Histamine in the regulation of wakefulness. *Sleep Med. Rev.* **15**(**1**), 65–74 (2011).
220. Burgaud, J. L. & Oudart, N. Effect of an histaminergic H3 agonist on the non-adrenergic non-cholinergic contraction in guinea-pig perfused bronchioles. *J. Pharm. Pharmacol.* **45**(**1**), 955–958 (1993).
221. Ichinose, M. & Barnes, P. J. Histamine H3-receptors modulate nonadrenergic noncholinergic neural bronchoconstriction in guinea-pig in vivo. *Eur. J. Pharmacol.* **174**, 49–55 (1989).
222. Toshio, M., Moskowitz, M. A. & Zhihong, H. UK-14,304, R (−)-α-methyl-histamine and SMS 201-995 block plasma protein leakage within dura mater by prejunctional mechanisms. *Eur. J. Pharmacol.* **224**, 145–150 (1992).
223. Rouleau, A. *et al*. Bioavailability, Antinociceptive and Antiinflammatory Properties of BP 2-94, a Histamine H3 Receptor Agonist Prodrug1. *J. Pharmacol. Exp. Ther.* **281**, 1085–1094 (1997).
224. Millán-Guerrero, R. O., Isais-Millán, R., Benjamín, T.-H. & Tene, C. E. Nα-Methyl histamine safety and efficacy in migraine prophylaxis: phase III study. *Can. J. Neurol. Sci.* **33**(**1**), 195–199 (2006).
225. Millán-Guerrero, R. O., Pineda-Lucatero, A. G., Hernández-Benjamín, T., Tene, C. E. & Pacheco, M. F. Nα-Methylhistamine safety and efficacy in migraine prophylaxis: phase I and phase II studies. *Headache* **43**(**1**), 389–394 (2003).
226. Levi, R. & Smith, N. C. E. Histamine H3-receptors: a new frontier in myocardial ischemia. *J. Pharmacol. Exp. Ther.* **292**, 825–830 (2000).
227. Krause, M., Stark, H., & Schunack, W. Azomethine prodrugs of (R)-alpha-methylhistamine, a highly potent and selective histamine H3-receptor agonist. *Curr. Med. Chem.* **8**(**11**), 1329–1340 (2001).
228. Wulff, B. S., Hastrup, S. & Rimvall, K. Characteristics of recombinantly expressed rat and human histamine H3 receptors. *Eur. J. Pharmacol.* **453**, 33–41 (2002).
229. Ligneau, X. *et al*. Neurochemical and Behavioral Effects of Ciproxifan, A Potent Histamine H3-Receptor Antagonist. *J. Pharmacol. Exp. Ther.* **287**, 658–666 (1998).
230. van der Goot, H., Schepers, M. J. P., Sterk, G. J. & Timmerman, H. Isothiourea analogues of histamine as potent agonists or antagonists of the histamine H3-receptor. *Eur. J. Med. Chem.* **27**, 511–517 (1992).
231. Lim, H. D. *et al*. Clobenpropit analogs as dual activity ligands for the histamine H3 and H4 receptors: Synthesis, pharmacological evaluation, and cross-target QSAR studies. *Bioorg. Med. Chem.* **17**, 3987–3994 (2009).
232. Esbenshade, T. A. *et al*. Two Novel and Selective Nonimidazole Histamine H3 Receptor Antagonists A-304121 and A-317920: I. In Vitro Pharmacological Effects. *J. Pharmacol. Exp. Ther.* **305**, 887–896 (2003).
233. Levoin, N. *et al*. Refined docking as a valuable tool for lead optimization: application to histamine H3 receptor antagonists. *Arch. Pharm. (Weinheim)* **341**, 610–623 (2008).
234. Sadek, B., Saad, A., Sadeq, A., Jalal, F. & Stark, H. Histamine H3 receptor as a potential target for cognitive symptoms in neuropsychiatric diseases. *Behav. Brain Res.* **312**(**1**), 415–430 (2016).

235. Letavic, M. A. *et al.* Novel Benzamide-Based Histamine H3 Receptor Antagonists: The Identification of Two Candidates for Clinical Development. *ACS Med. Chem. Lett.* **6**, 450–454 (2015).
236. Berlin, M., Boyce, C. W. & de Lera Ruiz, M. Histamine H3 Receptor as a Drug Discovery Target. *J. Med. Chem.* **54**, 26–53 (2011).
237. Ligneau, X. *et al.* BF2.649 [1-{3-[3-(4-Chlorophenyl)propoxy]propyl}piperidine, Hydrochloride], a Nonimidazole Inverse Agonist/Antagonist at the Human Histamine H3 Receptor: Preclinical Pharmacology. *J. Pharmacol. Exp. Ther.* **320**, 365–375 (2007).
238. Fox, G. B. *et al.* Pharmacological Properties of ABT-239 [4-(2-{2-[(2 R)-2-Methylpyrrolidinyl]ethyl}-benzofuran-5-yl)benzonitrile]: II. Neurophysiological Characterization and Broad Preclinical Efficacy in Cognition and Schizophrenia of a Potent and Selective Histamine H3 Receptor Antagonist. *J. Pharmacol. Exp. Ther.* **313**, 176–190 (2005).
239. Celanire, S., Wijtmans, M., Talaga, P., Leurs, R. & de Esch, I. J. P. Keynote review: Histamine H3 receptor antagonists reach out for the clinic. *Drug Discov. Today* **10**, 1613–1627 (2005).
240. Łażewska, D. *et al.* Ether derivatives of 3-piperidinopropan-1-ol as non-imidazole histamine H3 receptor antagonists. *Bioorg. Med. Chem.* **14**, 3522–3529 (2006).
241. Komater, V. A. *et al.* H3 receptor blockade by thioperamide enhances cognition in rats without inducing locomotor sensitization. *Psychopharmacology (Berl)* **167**(**1**), 363–372 (2003).
242. Miyazaki, S., Imaizumi, M., & Onodera, K. Effects of thioperamide on the cholinergic system and the step-through passive avoidance test in mice. *Methods Find. Exp. Clin. Pharmacol.* **17**(**10**), 653–658 (1995).
243. Yehorenko, O., Pervak, M., Poshyvak, O., Liashenko, A. & Godlevsky, L. Enhancement of the anticonvulsant effect of the H3 histamine receptor blocker thioperamide against the use of pioglitazone. *J. Educ. Health Sport* **12**(**1**), 293–302 (2022).
244. Itoh, E., Fujimiya, M. & Inui, A. Thioperamide, a histamine H3 receptor antagonist, powerfully suppresses peptide YY-induced food intake in rats. *Biol. Psychiatry* **45**, 475–481 (1999).
245. Bardgett, M. E., Davis, N. N., Schultheis, P. J. & Griffith, M. S. Ciproxifan, an H3 receptor antagonist, alleviates hyperactivity and cognitive deficits in the APPTg2576 mouse model of Alzheimer's disease. *Neurobiol. Learn Mem.* **95**, 64–72 (2011).
246. Yokoyama, H. *et al.* Clobenpropit (VUF-9153), a new histamine H3 receptor antagonist, inhibits electrically induced convulsions in mice. *Eur. J. Pharmacol.* **260**, 23–28 (1994).
247. J Nathan, P. *et al.* The safety, tolerability, pharmacokinetics and cognitive effects of GSK239512, a selective histamine H3 receptor antagonist in patients with mild to moderate Alzheimer's disease: a preliminary investigation. *Curr. Alzheimer Res.* **10**, 240–251 (2013).
248. Brioni, J. D., Esbenshade, T. A., Garrison, T. R., Bitner, S. R. & Cowart, M. D. Discovery of Histamine H3 Antagonists for the Treatment of Cognitive Disorders and Alzheimer's Disease. *J. Pharmacol. Exp. Ther.* **336**, 38–46 (2011).
249. Haig, G. M. *et al.* A randomized trial of the efficacy and safety of the H3 antagonist ABT-288 in cognitive impairment associated with schizophrenia. *Schizophr. Bull.* **40**, 1433–1442 (2014).
250. Haig, G. M. *et al.* A randomized study of H3 antagonist ABT-288 in mild-to-moderate Alzheimer's dementia. *J. Alzheimer's Dis.* **42**(**1**), 959–971 (2014).
251. Borgonetti, V. & Galeotti, N. The Histamine H4 Receptor Participates in the Neuropathic Pain-Relieving Activity of the Histamine H3 Receptor Antagonist GSK189254. *Int. J. Mol. Sci.* **23**, 14314 (2022).
252. McGaraughty, S., Chu, K. L., Cowart, M. D. & Brioni, J. D. Antagonism of Supraspinal Histamine H3 Receptors Modulates Spinal Neuronal Activity in Neuropathic Rats. *J. Pharmacol. Exp. Ther.* **343**, 13–20 (2012).

253. Galici, R. *et al*. JNJ-39220675, a novel selective histamine H3 receptor antagonist, reduces the abuse-related effects of alcohol in rats. *Psychopharmacology (Berl.)* **214**, 829–841 (2011).
254. Bahi, A., Sadek, B., Nurulain, S. M., Łażewska, D. & Kieć-Kononowicz, K. The novel non-imidazole histamine H3 receptor antagonist DL77 reduces voluntary alcohol intake and ethanol-induced conditioned place preference in mice. *Physiol. Behav.* **151**, 189–197 (2015).
255. Sadek, B. *et al*. Anticonvulsant and procognitive properties of the non-imidazole histamine H3 receptor antagonist DL77 in male adult rats. *Neuropharmacology* **106**, 46–55 (2016).
256. Weisler, R. H., Pandina, G. J., Daly, E. J., Cooper, K. & Gassmann-Mayer, C. Randomized clinical study of a histamine H 3 receptor antagonist for the treatment of adults with attention-deficit hyperactivity disorder. *CNS Drugs* **26**, 421–434 (2012).
257. Kuhne, S., Wijtmans, M., Lim, H. D., Leurs, R. & de Esch, I. J. P. Several down, a few to go: histamine H3 receptor ligands making the final push towards the market? *Expert. Opin. Investig. Drugs* **20**, 1629–1648 (2011).
258. Syed, Y. Y. Pitolisant: First Global Approval. *Drugs* **76**, 1313–1318 (2016).
259. Szakacs, Z. *et al*. Safety and efficacy of pitolisant on cataplexy in patients with narcolepsy: a randomised, double-blind, placebo-controlled trial. *Lancet Neurol.* **16**, 200–207 (2017).
260. Dauvilliers, Y. *et al*. Pitolisant versus placebo or modafinil in patients with narcolepsy: a double-blind, randomised trial. *Lancet Neurol.* **12**, 1068–1075 (2013).
261. Kollb-Sielecka, M. *et al*. The European Medicines Agency review of pitolisant for treatment of narcolepsy: summary of the scientific assessment by the Committee for Medicinal Products for Human Use. *Sleep Med.* **33**, 125–129 (2017).
262. Łażewska, D. & Kieć-Kononowicz, K. Progress in the development of histamine H3 receptor antagonists/inverse agonists: a patent review (2013-2017). *Expert Opin. Ther. Pat.* **28**, 175–196 (2018).
263. Mocking, T. A. M., Verweij, E. W. E., Vischer, H. F. & Leurs, R. Homogeneous, real-time NanoBRET binding assays for the histamine H3 and H4 receptors on living cells. *Mol. Pharmacol.* **94**, 1371–1381 (2018).
264. Middleton, R. J. & Kellam, B. Fluorophore-tagged GPCR ligands. *Curr. Opin. Chem. Biol.* **9**, 517–525 (2005).
265. Stoddart, L. A., White, C. W., Nguyen, K., Hill, S. J. & Pfleger, K. D. G. Fluorescence-and bioluminescence-based approaches to study GPCR ligand binding. *Br. J. Pharmacol.* **173**, 3028–3037 (2016).
266. Bartole, E. *et al*. UR-DEBa242: a Py-5-labeled fluorescent multipurpose probe for investigations on the histamine H3 and H4 receptors. *J. Med. Chem.* **63**, 5297–5311 (2020).
267. Stark, H. *et al*. [125I] iodoproxyfan and related compounds: a reversible radioligand and novel classes of antagonists with high affinity and selectivity for the histamine H3 receptor. *J. Med. Chem.* **39**, 1220–1226 (1996).
268. Tomasch, M., Schwed, J. S., Paulke, A. & Stark, H. Bodilisant—A Novel Fluorescent, Highly Affine Histamine H3 Receptor Ligand. *ACS Med. Chem. Lett.* **4**, 269–273 (2013).
269. Tomasch, M., Schwed, J. S., Weizel, L. & Stark, H. Novel chalcone-based fluorescent human histamine H3 receptor ligands as pharmacological tools. *Front. Syst. Neurosci.* **6**, 14 (2012).
270. Amon, M. *et al*. Highly Potent Fluorescence-Tagged Nonimidazole Histamine H3 Receptor Ligands. *ChemMedChem* **2**, 708–716 (2007).
271. Rosier, N. *et al*. A Versatile Sub-Nanomolar Fluorescent Ligand Enables NanoBRET Binding Studies and Single-Molecule Microscopy at the Histamine H3Receptor. *J. Med. Chem.* **64**, 11695–11708 (2021).

272. Nguyen, T. *et al*. Discovery of a novel member of the histamine receptor family. *Mol. Pharmacol*. **59**, 427–433 (2001).
273. Zhu, Y. *et al*. Cloning, expression, and pharmacological characterization of a novel human histamine receptor. *Mol. Pharmacol*. **59**, 434–441 (2001).
274. Oda, T., Morikawa, N., Saito, Y., Masuho, Y. & Matsumoto, S. Molecular cloning and characterization of a novel type of histamine receptor preferentially expressed in leukocytes. *J. Biol. Chem*. **275**(**1**), 36781–36786 (2000).
275. Zampeli, E. & Tiligada, E. The role of histamine H4 receptor in immune and inflammatory disorders. *Br. J. Pharmacol*. **157**, 24–33 (2009).
276. Leurs, R., Chazot, P. L., Shenton, F. C., Lim, H. D. & De Esch, I. J. P. Molecular and biochemical pharmacology of the histamine H4 receptor. *Br. J. Pharmacol*. **157**, 14–23 (2009).
277. Cogé, F., Guénin, S. P., Rique, H., Boutin, J. A. & Galizzi, J. P. Structure and expression of the human histamine H4-receptor gene. *Biochem. Biophys. Res. Commun*. **284**, 301–309 (2001).
278. van Rijn, R. M. *et al*. Cloning and characterization of dominant negative splice variants of the human histamine H4 receptor. *Biochem. J*. **414**(**1**), 121–131 (2008).
279. Shin, N. *et al*. Molecular modeling and site-specific mutagenesis of the histamine-binding site of the histamine H4 receptor. *Mol. Pharmacol*. **62**, 38–47 (2002).
280. Jongejan, A. *et al*. Delineation of agonist binding to the human histamine H4 receptor using mutational analysis, homology modeling, and ab initio calculations. *J. Chem. Inf. Model*. **48**, 1455–1463 (2008).
281. Lim, H. D. *et al*. Phenylalanine 169 in the second extracellular loop of the human histamine H4 receptor is responsible for the difference in agonist binding between human and mouse H4 receptors. *J. Pharmacol. Exp. Ther*. **327**, 88–96 (2008).
282. Istyastono, P. E., de Graaf, C., de Esch, J. P., & Leurs, R. Molecular determinants of selective agonist and antagonist binding to the histamine H4 receptor. *Curr. Top. Med. Chem*. **11**(**6**), 661–679 (2011).
283. Schultes, S. *et al*. Combining quantum mechanical ligand conformation analysis and protein modeling to elucidate GPCR-ligand binding modes. *ChemMedChem* **8**, 49–53 (2012).
284. Im, D., Iwata, S., Asada, H. Cryo-EM structure of the histamine-bound histamine H4 receptor and Gq complex. *PDB* **7YFC**, (2024).
285. Smit, M. J. *et al*. Pharmacogenomic and structural analysis of constitutive G protein–coupled receptor activity. *Annu. Rev. Pharmacol. Toxicol*. **47**, 53–87 (2007).
286. Schneider, E. H., Schnell, D., Strasser, A., Dove, S. & Seifert, R. Impact of the DRY motif and the missing “ionic lock” on constitutive activity and G-protein coupling of the human histamine H4 receptor. *J. Pharmacol. Exp. Ther*. **333**, 382–392 (2010).
287. Nijmeijer, S., Leurs, R., Smit, M. J. & Vischer, H. F. The Epstein-Barr virus-encoded G protein-coupled receptor BILF1 hetero-oligomerizes with human CXCR4, scavenges Gαi proteins, and constitutively impairs CXCR4 functioning. *J. Biol. Chem*. **285**(**1**), 29632–29641 (2010).
288. van Rijn, R. M. *et al*. Oligomerization of recombinant and endogenously expressed human histamine H4 receptors. *Mol. Pharmacol*. **70**, 604–615 (2006).
289. O’Reilly, M. *et al*. Identification of a histamine H4 receptor on human eosinophils—role in eosinophil chemotaxis. *J. Recept. Signal Transduct*. **22**(**1**), 431–448 (2002).
290. Bäumer, W. *et al*. Histamine H4 receptors modulate dendritic cell migration through skin–immunomodulatory role of histamine. *Allergy* **63**, 1387–1394 (2008).
291. Jemima, E. A., Prema, A. & Thangam, E. B. Functional characterization of histamine H4 receptor on human mast cells. *Mol. Immunol*. **62**, 19–28 (2014).
292. Mommert, S. *et al*. Human basophil chemotaxis and activation are regulated via the histamine H4 receptor. *Allergy* **71**, 1264–1273 (2016).

293. Dib, K. *et al*. The histamine H4 receptor is a potent inhibitor of adhesion-dependent degranulation in human neutrophils. *J. Leukoc. Biol.* **96**, 411–418 (2014).
294. Gutzmer, R. *et al*. The histamine H4 receptor is functionally expressed on TH2 cells. *J. Allergy Clin. Immunol.* **123**(**1**), 619–625 (2009).
295. Damaj, B. B., Becerra, C. B., Esber, H. J., Wen, Y. & Maghazachi, A. A. Functional expression of H4 histamine receptor in human natural killer cells, monocytes, and dendritic cells. *J. Immunol.* **179**(**1**), 7907–7915 (2007).
296. Boer, K. *et al*. Decreased expression of histamine H1 and H4 receptors suggests disturbance of local regulation in human colorectal tumours by histamine. *Eur. J. Cell. Biol.* **87**, 227–236 (2008).
297. Gschwandtner, M. *et al*. Murine and human Langerhans cells express a functional histamine H4 receptor: modulation of cell migration and function. *Allergy* **65**, 840–849 (2010).
298. Dijkstra, D. *et al*. Histamine downregulates monocyte CCL2 production through the histamine H4 receptor. *J. Allergy Clin. Immunol.* **120**(**1**), 300–307 (2007).
299. Yu, B. *et al*. Copy number variations of the human histamine H4 receptor gene are associated with systemic lupus erythematosus. *Br. J. Dermatol.* **163**(**1**), 935–940 (2010).
300. Yu, B. *et al*. Polymorphisms in human histamine receptor H4 gene are associated with atopic dermatitis. *Br. J. Dermatol.* **162**(**1**), 1038–1043 (2010).
301. Simon, T. *et al*. Asthma endophenotypes and polymorphisms in the histamine receptor HRH4 gene. *Int. Arch. Allergy Immunol.* **159**, 109–120 (2012).
302. Strakhova, M. I. *et al*. Localization of histamine H4 receptors in the central nervous system of human and rat. *Brain Res.* **1250**, 41–48 (2009).
303. Connelly, W. M. *et al*. The histamine H4 receptor is functionally expressed on neurons in the mammalian CNS. *Br. J. Pharmacol.* **157**, 55–63 (2009).
304. Desmadryl, G. *et al*. Histamine H4 receptor antagonists as potent modulators of mammalian vestibular primary neuron excitability. *Br. J. Pharmacol.* **167**, 905–916 (2012).
305. Beermann, S., Seifert, R. & Neumann, D. Commercially available antibodies against human and murine histamine H 4-receptor lack specificity. *Naunyn Schmiedebergs Arch. Pharmacol.* **385**, 125–135 (2012).
306. De Esch, I. J., Thurmond, R. L., Jongejan, A., & Leurs, R. The histamine H4 receptor as a new therapeutic target for inflammation. *Trends Pharmacol. Sci.* **26**(**9**), 462–469 (2005).
307. Mayr, B. & Montminy, M. Transcriptional regulation by the phosphorylation-dependent factor CREB. *Nat. Rev. Mol. Cell. Biol.* **2**, 599–609 (2001).
308. Hofstra, C. L., Desai, P. J., Thurmond, R. L. & Fung-Leung, W.-P. Histamine H4 receptor mediates chemotaxis and calcium mobilization of mast cells. *J. Pharmacol. Exp. Ther.* **305**, 1212–1221 (2003).
309. Raible, D. G., Lenahan, T., Fayvilevich, Y., Kosinski, R. & Schulman, E. S. Pharmacologic characterization of a novel histamine receptor on human eosinophils. *Am. J. Respir. Crit. Care Med.* **149**, 1506–1511 (1994).
310. Buckland, K. F., Williams, T. J. & Conroy, D. M. Histamine induces cytoskeletal changes in human eosinophils via the H4 receptor. *Br. J. Pharmacol.* **140**, 1117–1127 (2003).
311. Barnard, R., Barnard, A., Salmon, G., Liu, W. & Sreckovic, S. Histamine-induced actin polymerization in human eosinophils: an imaging approach for histamine H4 receptor. *Cytometry A* **73**(**1**), 299–304 (2008).
312. Desai, P. & Thurmond, R. L. Histamine H4 receptor activation enhances LPS-induced IL-6 production in mast cells via ERK and PI3K activation. *Eur. J. Immunol.* **41**, 1764–1773 (2011).
313. Ferreira, R. *et al*. Histamine modulates microglia function. *J. Neuroinflammation* **9**, 90 (2012).

314. Gutzmer, R. *et al*. Histamine H4 receptor stimulation suppresses IL-12p70 production and mediates chemotaxis in human monocyte-derived dendritic cells. *J. Immunol.* **174**(**1**), 5224–5232 (2005).
315. Horr, B., Borck, H., Thurmond, R., Grösch, S. & Diel, F. STAT1 phosphorylation and cleavage is regulated by the histamine (H4) receptor in human atopic and non-atopic lymphocytes. *Int. Immunopharmacol.* **6**, 1577–1585 (2006).
316. Rosethorne, E. M. & Charlton, S. J. Agonist-Biased Signaling at the Histamine H4 Receptor: JNJ7777120 Recruits β-Arrestin without Activating G Proteins. *Mol. Pharmacol.* **79**, 749–757 (2011).
317. Ling, P. *et al*. Histamine H4 receptor mediates eosinophil chemotaxis with cell shape change and adhesion molecule upregulation. *Br. J. Pharmacol.* **142**, 161–171 (2004).
318. Takahashi, Y. *et al*. Effect of histamine H4 receptor antagonist on allergic rhinitis in mice. *Int. Immunopharmacol.* **9**, 734–738 (2009).
319. Shiraishi, Y. *et al*. Sequential engagement of FcεRI on mast cells and basophil histamine H4 receptor and FcεRI in allergic rhinitis. *J. Immunol.* **190**(**1**), 539–548 (2013).
320. Dunford, P. J. *et al*. The histamine H4 receptor mediates allergic airway inflammation by regulating the activation of CD4+ T cells. *J. Immunol.* **176**(**1**), 7062–7070 (2006).
321. Ikawa, Y. *et al*. Histamine H4 receptor expression in human synovial cells obtained from patients suffering from rheumatoid arthritis. *Biol. Pharm. Bull.* **28**, 2016–2018 (2005).
322. Ohki, E. *et al*. Expression of histamine H4 receptor in synovial cells from rheumatoid arthritic patients. *Biol. Pharm. Bull.* **30**, 2217–2220 (2007).
323. Grzybowska-Kowalczyk, A., Wojtecka-Lukasik, E., Maslinska, D., Gujski, M. & Maslinski, S. Human and clinical aspects of histamine: Distribution pattern of histamine H4 receptor in human synovial tissue from patients with rheumatoid arthritis. *Inflamm. Res.* **56**, S59–S60 (2007).
324. Del Rio, R. *et al*. Histamine H4 receptor optimizes T regulatory cell frequency and facilitates anti-inflammatory responses within the central nervous system. *J. Immunol.* **188**(**1**), 541–547 (2012).
325. Thurmond, R. L. *et al*. A potent and selective histamine H4 receptor antagonist with anti-inflammatory properties. *J. Pharmacol. Exp. Ther.* **309**, 404–413 (2004).
326. Gantner, F. *et al*. Histamine H4 and H2 receptors control histamine-induced interleukin-16 release from human CD8+ T cells. *J. Pharmacol. Exp. Ther.* **303**, 300–307 (2002).
327. Ikawa, Y. *et al*. Comparative study of histamine H4 receptor expression in human dermal fibroblasts. *J. Toxicol. Sci.* **33**, 503–508 (2008).
328. Dijkstra, D. *et al*. Human inflammatory dendritic epidermal cells express a functional histamine H4 receptor. *J. Investig. Dermatol.* **128**(**1**), 1696–1703 (2008).
329. Lippert, U. *et al*. Human skin mast cells express H2 and H4, but not H3 receptors. *J. Investig. Dermatol.* **123**(**1**), 116–123 (2004).
330. Glatzer, F. *et al*. Histamine induces proliferation in keratinocytes from patients with atopic dermatitis through the histamine 4 receptor. *J. Allergy Clin. Immunol.* **132**(**1**), 1358–1367 (2013).
331. Varga, C. *et al*. Inhibitory effects of histamine H4 receptor antagonists on experimental colitis in the rat. *Eur. J. Pharmacol.* **522**, 130–138 (2005).
332. Sanna, M. D. & Galeotti, N. Central neuronal functions of histamine H4 receptors. *Oncotarget* **8**(**1**), 12556 (2017).
333. Coruzzi, G., Adami, M., Guaita, E., de Esch, I. J. P. & Leurs, R. Antiinflammatory and antinociceptive effects of the selective histamine H4-receptor antagonists JNJ7777120 and VUF6002 in a rat model of carrageenan-induced acute inflammation. *Eur. J. Pharmacol.* **563**, 240–244 (2007).
334. Hashimoto, T. *et al*. A selective human H4-receptor agonist:(−)-2-Cyano-1-methyl-3-{(2 R, 5 R)-5-[1 H-imidazol-4 (5)-yl] tetrahydrofuran-2-yl} methylguanidine. *J. Med. Chem.* **46**, 3162–3165 (2003).

335. Smits, R. A. *et al*. Characterization of the histamine H4 receptor binding site. Part 1. Synthesis and pharmacological evaluation of dibenzodiazepine derivatives. *J. Med. Chem*. **49**, 4512–4516 (2006).
336. Ghorai, P. *et al*. Acylguanidines as bioisosteres of guanidines: N G-acylated imidazolylpropylguanidines, a new class of histamine H2 receptor agonists. *J. Med. Chem*. **51**, 7193–7204 (2008).
337. Igel, P. *et al*. Synthesis and structure− activity relationships of cyanoguanidine-type and structurally related histamine H4 receptor agonists. *J. Med. Chem*. **52**, 6297–6313 (2009).
338. Nijmeijer, S., de Graaf, C., Leurs, R. & Vischer, H. F. Molecular pharmacology of histamine H4 receptors. *Front. Biosci*. **17**, 2089–2106 (2012).
339. Savall, B. M. *et al*. Agonist/antagonist modulation in a series of 2-aryl benzimidazole H4 receptor ligands. *Bioorg. Med. Chem. Lett* **20**, 3367–3371 (2010).
340. Sander, K. *et al*. 2, 4-Diaminopyrimidines as histamine H4 receptor ligands—Scaffold optimization and pharmacological characterization. *Bioorg. Med. Chem*. **17**, 7186–7196 (2009).
341. Gschwandtner, M., Koether, B., Werfel, T., Stark, H. & Gutzmer, R. Profiling of histamine H 4 receptor agonists in native human monocytes. *Br. J. Pharmacol*. **170**, 136–143 (2013).
342. Morgan, R. K. *et al*. Histamine 4 receptor activation induces recruitment of FoxP3$^+$ T cells and inhibits allergic asthma in a murine model. *J. Immunol*. **178**(**1**), 8081–8089 (2007).
343. Saligrama, N., Case, L. K., Del Rio, R., Noubade, R. & Teuscher, C. Systemic lack of canonical histamine receptor signaling results in increased resistance to autoimmune encephalomyelitis. *J. Immunol*. **191**(**1**), 614–622 (2013).
344. Gee, K., Guzzo, C., Che Mat, N. F., Ma, W. & Kumar, A. The IL-12 family of cytokines in infection, inflammation and autoimmune disorders. *Inflamm. Allergy Drug Targets* **8**(**1**), 40–52 (2009).
345. Zhang, M., Thurmond, R. L. & Dunford, P. J. The histamine H4 receptor: A novel modulator of inflammatory and immune disorders. *Pharmacol. Ther*. **113**, 594–606 (2007).
346. Venable, J. D. *et al*. Preparation and Biological Evaluation of Indole, Benzimidazole, and Thienopyrrole Piperazine Carboxamides: Potent Human Histamine H4 Antagonists. *J. Med. Chem*. **48**, 8289–8298 (2005).
347. Terzioglu, N., van Rijn, R. M., Bakker, R. A., De Esch, I. J. P. & Leurs, R. Synthesis and structure–activity relationships of indole and benzimidazole piperazines as histamine H4 receptor antagonists. *Bioorg. Med. Chem. Lett*. **14**, 5251–5256 (2004).
348. Lee-Dutra, A. *et al*. Identification of 2-arylbenzimidazoles as potent human histamine H4 receptor ligands. *Bioorg. Med. Chem. Lett*. **16**, 6043–6048 (2006).
349. Edwards, J. P., Kindrachuk, D. E. & Venable, J. D. Benzoimidazol-2-yl pyrimidines and pyrazines as modulators of the histamine H4 receptor. **WO 2007/117399 A2** (Janssen Pharmaceutica NV. 2007)
350. Edwards, J. P., Kindrachuk, D. E. & Venable, J. D. Benzoimidazol-2-yl pyrimidines and pyrazines as modulators of the histamine H4 receptor. **WO 2007/117400 A2** (Janssen Pharmaceutica NV, 2007).
351. Kiss, R. & Keseru, G. M. Novel histamine H4 receptor ligands and their potential therapeutic applications: an update. *Expert Opin. Ther. Patents* **24**(**11**), 1185–1197 (2014).
352. Smits, R. A. *et al*. Fragment Based Design of New H4 Receptor−Ligands with Anti-inflammatory Properties in Vivo. *J. Med. Chem*. **51**, 2457–2467 (2008).
353. Smits, R. A. *et al*. Synthesis and QSAR of Quinazoline Sulfonamides As Highly Potent Human Histamine H4 Receptor Inverse Agonists. *J. Med. Chem*. **53**, 2390–2400 (2010).

354. Sato, H. *et al*. 2-Aminopyrimidine derivatives. **WO 2005/014556 A1** (Bayer Healthcare AG, 2005).
355. Sato, H. *et al*. 2-Aminopyrimidine derivatives. **WO 2005/054239 A1** (Bayer Healthcare AG, 2005).
356. Carceller Gonzalez, E. *et al*. 2-Aminopyrimidine derivatives as modulators of the histamine H4 receptor activity. **WO 2007/031529 A1** (Palau Pharma SA, 2007).
357. Bell, A. S. *et al*. Pyrimidine derivatives. **WO 2007/072163 A2** (Pfizer Ltd, 2007).
358. Raphy, G. *et al*. Novel 2-amino-pyrimidine derivatives, processes for preparing them, pharmaceutical compositions thereof. **WO 2008/031556 A2** (UCB Pharma SA, 2008).
359. Cai, H. *et al*. 2-Aminopyrimidine modulators of the histamine H4 receptor. **WO 2008/100565 A1** (Janssen Pharmaceutica NV, 2008).
360. Reid, A. *et al*. Enantiomers of amino pyrimidine compounds for the treatment of inflammatory disorders. **WO 2007/090853 A1** (Cellzome UK Ltd, 2007).
361. Harris, N. *et al*. Pyrimidine compounds as histamine modulators. **WO 2006/050965 A1** (Argenta Discovery Ltd, 2006).
362. Reid, A. *et al*. Azetidine amino pyrimidine compounds for the treatment of inflammatory disorders. **WO 2007/090854 A1** (Cellzome UK Ltd, 2007).
363. Reid, A. *et al*. Amino pyrimidine compounds for the treatment of inflammatory disorders. **WO 2007/090852 A1** (Cellzome UK Ltd, 2007).
364. Dyke, H., Price, S. & Cramp, S. Pyrimidine compounds for the treatment of inflammatory disorders. **WO 2007/039467 A1** (Cellzome UK Ltd, 2007).
365. Chavez F. *et al*. Benzofuro- and benzothienopyrimidine modulators of the histamine H4 receptor. **WO2008008359A2** (Janssen Pharmaceutica NV, 2008).
366. Kiss, R. & and Keseru˝, G. M. Histamine H4 receptor ligands and their potential therapeutic applications. *Expert Opin. Ther. Pat.* **19**, 119–135 (2009).
367. Smits, R. A., Leurs, R., & de Esch, I. J. Major advances in the development of histamine H4 receptor ligands. *Drug Discov. Today* **14**(**15–16**), 745–753 (2009).
368. Stark, H. Histamine H4 receptor. *De Gruyter Open Poland*, Warsaw, Poland (2014).
369. Yamaura, K. *et al*. Expression of histamine H4 receptor in human epidermal tissues and attenuation of experimental pruritus using H4 receptor antagonist. *J. Toxicol. Sci.* **34**, 427–431 (2009).
370. Dunford, P. J. *et al*. Histamine H4 receptor antagonists are superior to traditional antihistamines in the attenuation of experimental pruritus. *J. Allergy Clin. Immunol.* **119**(**1**), 176–183 (2007).
371. Roßbach, K. *et al*. Histamine H4 receptor antagonism reduces hapten-induced scratching behaviour but not inflammation. *Exp. Dermatol.* **18**, 57–63 (2009).
372. Ohsawa, Y. & Hirasawa, N. The antagonism of histamine H1 and H4 receptors ameliorates chronic allergic dermatitis via anti-pruritic and anti-inflammatory effects in NC/Nga mice. *Allergy* **67**, 1014–1022 (2012).
373. Neumann, D. *et al*. The dual H3/4R antagonist thioperamide does not fully mimic the effects of the 'standard' H4R antagonist JNJ 7777120 in experimental murine asthma. *Naunyn Schmiedebergs Arch. Pharmacol.* **386**, 983–990 (2013).
374. Cowart, M. D. *et al*. Rotationally Constrained 2,4-Diamino-5,6-disubstituted Pyrimidines: A New Class of Histamine H4 Receptor Antagonists with Improved Druglikeness and in Vivo Efficacy in Pain and Inflammation Models. *J. Med. Chem.* **51**, 6547–6557 (2008).
375. Bartole, E. *et al*. [3H]UR-DEBa176: A 2,4-Diaminopyrimidine-Type Radioligand Enabling Binding Studies at the Human, Mouse, and Rat Histamine H4 Receptors. *J. Med. Chem.* **62**, 8338–8356 (2019).
376. Schneider, E. H., Neumann, D. & Seifert, R. Histamine H4-receptor expression in the brain? *Naunyn-Schmiedeberg's Arch. Pharmacol.* **388**, 5–9 (2015).

377. Lethbridge, N. L. & Chazot, P. Immunological identification of the mouse H_4 histamine receptor on spinal cord motor neurons using a novel anti-mouse H_4R antibody. *Inflamm. Res.* **59**, 197–198 (2010).
378. Geyer, R. *Hetarylalkyl (aryl) cyanoguanidines as histamine H4 receptor ligands: Synthesis, chiral separation, pharmacological characterization, structure-activity and-selectivity relationships*. Doctoral dissertation, (Univ. Regensburg, 2011).
379. Mirzahosseini, A., Kovács, M., Kánai, K., Csutora, P. & Dalmadi, B. BODIPY® FL histamine as a new modality for quantitative detection of histamine receptor upregulation upon I g E sensitization in murine bone marrow-derived mast cells. *Cytometry Part A* **87**, 23–31 (2015).
380. Beaulieu, J.-M. & Gainetdinov, R. R. The Physiology, Signaling, and Pharmacology of Dopamine Receptors. *Pharmacol. Rev.* **63**, 182–217 (2011).
381. Klein, M. O. *et al.* Dopamine: Functions, Signaling, and Association with Neurological Diseases. *Cell. Mol. Neurobiol.* **39**, 31–59 (2019).
382. Nagatsu, T., Levitt, M., & Udenfriend, S. Tyrosine hydroxylase: the initial step in norepinephrine biosynthesis. *J. Biol. Chem.* **239**, 2910–2917 (1964).
383. Hadjiconstantinou, M. & Neff, N. H. Enhancing Aromatic L-amino Acid Decarboxylase Activity: Implications for L-DOPA Treatment in Parkinson's Disease. *CNS Neurosci. Ther.* **14**, 340–351 (2008).
384. Eisenhofer, G., Kopin, I. J. & Goldstein, D. S. Catecholamine Metabolism: A Contemporary View with Implications for Physiology and Medicine. *Pharmacol. Rev.* **56**, 331–349 (2004).
385. Eiden, L. E. & Weihe, E. VMAT2: a dynamic regulator of brain monoaminergic neuronal function interacting with drugs of abuse. *Ann. N. Y. Acad. Sci.* **1216**, 86–98 (2011).
386. Llinás, R., Steinberg, I. Z. & Walton, K. Relationship between presynaptic calcium current and postsynaptic potential in squid giant synapse. *Biophys. J.* **33**, 323–351 (1981).
387. Schultz, W. Predictive Reward Signal of Dopamine Neurons. *J. Neurophysiol.* **80**, 1–27 (1998).
388. Floresco, S. B., West, A. R., Ash, B., Moore, H. & Grace, A. A. Afferent modulation of dopamine neuron firing differentially regulates tonic and phasic dopamine transmission. *Nat. Neurosci.* **6**, 968–973 (2003).
389. Kristensen, A. S. *et al.* SLC6 Neurotransmitter Transporters: Structure, Function, and Regulation. *Pharmacol. Rev.* **63**, 585–640 (2011).
390. Sibley, D. R. & Monsma, F. J. Molecular biology of dopamine receptors. *Trends Pharmacol. Sci.* **13**, 61–69 (1992).
391. Missale, C., Nash, S. R., Robinson, S. W., Jaber, M. & Caron, M. G. Dopamine receptors: From structure to function. *Physiol. Rev.* **78**, 189–225 (1998).
392. Fuxe, K., Marcellino, D., Genedani, S. & Agnati, L. Adenosine A2A receptors, dopamine D2 receptors and their interactions in Parkinson's disease. *Mov. Disord.* **22**, 1990–2017 (2007).
393. Seeman, P. Targeting the dopamine D2 receptor in schizophrenia. *Expert Opin. Ther. Targets.* **10**, 515–531 (2006).
394. Juza, R., Musilek, K., Mezeiova, E., Soukup, O. & Korabecny, J. Recent advances in dopamine D2 receptor ligands in the treatment of neuropsychiatric disorders. *Med. Res. Rev.* **43**, 55–211 (2023).
395. Schneier, F. R. et al. Dopamine transporters, D2 receptors, and dopamine release in generalized social anxiety disorder. *Depress. Anxiety* **26**, 411–418 (2009).
396. Jaber, M., Robinson, S. W., Missale, C. & Caron, M. G. Dopamine receptors and brain function. *Neuropharmacology* **35**, 1503–1519 (1996).
397. Santambrogio, L., Lipartiti, M., Bruni, A. & Toso, R. D. Dopamine receptors on human T- and B-lymphocytes. *J. Neuroimmunol.* **45**, 113–119 (1993).

398. Cote, T. E. et al. Biochemical and Physiological Studies of the Beta-Adrenoceptor and the D-2 Dopamine Receptor in the Intermediate Lobe of the Rat Pituitary Gland: A Review. *Neuroendocrinology* **35**, 217–224 (2008).
399. Del'Guidice, T., Lemasson, M. & Beaulieu, J.-M. Role of Beta-Arrestin 2 Downstream of Dopamine Receptors in the Basal Ganglia. *Front. Neuroanat.* **5**, (2011).
400. Sun, W. L., Quizon, P. M., & Zhu, J. (2016). Molecular mechanism: ERK signaling, drug addiction, and behavioral effects. *Prog. Mol. Biol. Transl. Sci.* **137**, 1-40.
401. Beaulieu, J.-M. *et al.* An Akt/β-Arrestin 2/PP2A Signaling Complex Mediates Dopaminergic Neurotransmission and Behavior. *Cell* **122**, 261–273 (2005).
402. Beaulieu, J.-M. et al. (2004). Lithium antagonizes dopamine-dependent behaviors mediated by an AKT/glycogen synthase kinase 3 signaling cascade. *Proc. Natl. Acad. Sci.* **101**, 5099–5104.
403. Scarselli, M. et al. (2001). D2/D3 dopamine receptor heterodimers exhibit unique functional properties. *J. Biol. Chem.* **276**, 30308–30314.
404. Borroto-Escuela, D. O. *et al.* Dopamine D2 and D4 receptor heteromerization and its allosteric receptor–receptor interactions. *Biochem. Biophys. Res. Commun.* **404**, 928–934 (2011).
405. Borroto-Escuela, D. O. *et al.* Dopamine D2 and 5-hydroxytryptamine 5-HT2A receptors assemble into functionally interacting heteromers. *Biochem. Biophys. Res. Commun.* **401**, 605–610 (2010).
406. Gerfen, C. R. & Surmeier, D. J. Modulation of Striatal Projection Systems by Dopamine. *Annu. Rev. Neurosci.* **34**, 441–466 (2011).
407. Ikemoto, S., Glazier, B. S., Murphy, J. M., & McBride, W. J. (1997). Role of dopamine D1 and D2 receptors in the nucleus accumbens in mediating reward. *J. Neurosci.* **17**, 8580–8587.
408. Hranilovic, D., Bucan, M., & Wang, Y. (2008). Emotional response in dopamine D2L receptor-deficient mice. *Behav. Brain Res.* **195**, 246–250.
409. Salamone, J. D. & Correa, M. The Mysterious Motivational Functions of Mesolimbic Dopamine. *Neuron* **76**, 470–485 (2012).
410. van Holstein, M. *et al.* Human cognitive flexibility depends on dopamine D2 receptor signaling. *Psychopharmacol. (Berl.)* **218**, 567–578 (2011).
411. Volkow, N. D. et al. (1998). Association between decline in brain dopamine activity with age and cognitive and motor impairment in healthy individuals. *Am. J. Psychiatry* **155**(3), 344–349.
412. Seeman, P. All Roads to Schizophrenia Lead to Dopamine Supersensitivity and Elevated Dopamine D2High Receptors. *CNS Neurosci. Ther.* **17**, 118–132 (2011).
413. Seeman, P. *et al.* Psychosis pathways converge via D2High dopamine receptors. *Synapse* **60**, 319–346 (2006).
414. Seeman, P., Lee, T., Chau-Wong, M., & Wong, K. (1976). Antipsychotic drug doses and neuroleptic/dopamine receptors. *Nature* **261**(5562), 717–719.
415. Wang, M. *et al.* Schizophrenia, amphetamine-induced sensitized state and acute amphetamine exposure all show a common alteration: increased dopamine D2 receptor dimerization. *Mol. Brain* **3**, 25 (2010).
416. Rinne, J. O. et al. (1993). PET study on striatal dopamine D2 receptor changes during the progression of early Parkinson's disease. *Mov. Disord.* **8**, 134–138.
417. Tinsley, R. B. *et al.* Dopamine D2 receptor knockout mice develop features of Parkinson disease. *Ann. Neurol.* **66**, 472–484 (2009).
418. Antonini, A., Schwarz, J., Oertel, W. H., Pogarell, O. & Leenders, K. L. Long-term changes of striatal dopamine D2 Receptors in patients with Parkinson's disease: A study with positron emission tomography and [11C]Raclopride. *Mov. Disord.* **12**, 33–38 (1997).
419. Kaasinen, V. *et al.* Extrastriatal dopamine D2 receptors in Parkinson's disease: a longitudinal study. *J. Neural. Transm.* **110**, 591–601 (2003).

420. Sokoloff, P., Giros, B., Martres, M.-P., Bouthenet, M.-L. & Schwartz, J.-C. Molecular cloning and characterization of a novel dopamine receptor (D3) as a target for neuroleptics. *Nature* **347**, 146–151 (1990).
421. Joyce, J. N. & Millan, M. J. Dopamine D3 receptor antagonists as therapeutic agents. *Drug Discov. Today* **10**, 917–925 (2005).
422. Heidbreder, C. A. & Newman, A. H. Current perspectives on selective dopamine D3 receptor antagonists as pharmacotherapeutics for addictions and related disorders. *Ann. N. Y. Acad. Sci.* **1187**, 4–34 (2010).
423. Eryilmaz, I. E. *et al.* Contribution of functional dopamine D2 and D3 receptor variants to motor and non-motor symptoms of early onset Parkinson's disease. *Clin. Neurol. Neurosurg.* **199**, 106257 (2020).
424. Gurevich, E. V. & Joyce, J. N. Distribution of dopamine D3 receptor expressing neurons in the human forebrain: comparison with D2 receptor expressing neurons. *Neuropsychopharmacology* **20**, 60–80 (1999).
425. Cardinal, R. N., Parkinson, J. A., Hall, J. & Everitt, B. J. Emotion and motivation: the role of the amygdala, ventral striatum, and prefrontal cortex. *Neurosci. Biobehav. Rev.* **26**, 321–352 (2002).
426. Jose, P. A., Eisner, G. M. & Felder, R. A. Renal Dopamine Receptors in Health and Hypertension. *Pharmacol. Ther.* **80**, 149–182 (1998).
427. Prieto, G Aleph. Abnormalities of Dopamine D3 Receptor Signaling in the Diseased Brain. *J. Cent. Nerv. Syst. Dis.* **9**, 1179573517726335 (2017).
428. Kim, K.-M. et al. Differential regulation of the dopamine D2 and D3 receptors by G protein-coupled receptor kinases and β-arrestins. *J. Biol. Chem.* **276**, 37409–37414 (2001).
429. Pillai, G., Brown, N. A., McAllister, G., Milligan, G. & Seabrook, G. R. Human D2 and D4 dopamine receptors couple through βγ G-protein subunits to inwardly rectifying K+ channels (GIRK1) in a Xenopus oocyte expression system: selective antagonism by L-741,626 and L-745,870 respectively. *Neuropharmacology* **37**, 983–987 (1998).
430. Kuzhikandathil, E. V. & Oxford, G. S. Activation of human D3 dopamine receptor inhibits P/Q-type calcium channels and secretory activity in AtT-20 cells. *J. Neurosci.* **19**, 1698 (1999).
431. Stanwood, G. D., Artymyshyn, R. P., Kung, M. P., Kung, H. F., Lucki, I. & McGonigle, P. Quantitative autoradiographic mapping of rat brain dopamine D3 binding with [^{125}I] 7-OH-PIPAT: evidence for the presence of D3 receptors on dopaminergic and nondopaminergic cell bodies and terminals. *J. Pharmacol. Exp. Ther.* **295**, 1223–1231 (2000).
432. Le Foll, B., Goldberg, S. R. & Sokoloff, P. The dopamine D3 receptor and drug dependence: Effects on reward or beyond? *Neuropharmacology* **49**, 525–541 (2005).
433. Heidbreder, C. A. *et al.* The role of central dopamine D3 receptors in drug addiction: a review of pharmacological evidence. *Brain Res. Rev.* **49**, 77–105 (2005).
434. Pritchard, L. M. *et al.* The dopamine D3 receptor antagonist NGB 2904 increases spontaneous and amphetamine-stimulated locomotion. *Pharmacol. Biochem. Behav.* **86**, 718–726 (2007).
435. Gross, G. & Drescher, K. The role of dopamine D_3 receptors in antipsychotic activity and cognitive functions. *Nov. Antischizophr. Treat.* **213**, 167–210 (2012).
436. Staley, J. K. & Mash, D. C. Adaptive increase in D_3 dopamine receptors in the brain reward circuits of human cocaine fatalities. *J. Neurosci.* **16**, 6100 (1996).
437. Schwartz, J.-C., Diaz, J., Pilon, C. & Sokoloff, P. Possible implications of the dopamine D3 receptor in schizophrenia and in antipsychotic drug actions. *Brain Res. Rev.* **31**, 277–287 (2000).
438. Yang, P., Perlmutter, J. S., Benzinger, T. L. S., Morris, J. C. & Xu, J. Dopamine D3 receptor: A neglected participant in Parkinson Disease pathogenesis and treatment? *Ageing Res. Rev.* **57**, 100994 (2020).

439. Moraga-Amaro, R., Gonzalez, H., Pacheco, R. & Stehberg, J. Dopamine receptor D3 deficiency results in chronic depression and anxiety. *Behav. Brain Res.* **274**, 186–193 (2014).
440. Shen, H. *et al.* Involvement of dopamine D3 receptor in impulsive choice decision-making in male rats. *Neuropharmacology* **257**, 110051 (2024).
441. Elgueta, D. *et al.* Pharmacologic antagonism of dopamine receptor D3 attenuates neurodegeneration and motor impairment in a mouse model of Parkinson's disease. *Neuropharmacology* **113**, 110–123 (2017).
442. Du, F., Li, R., Huang, Y., Li, X. & Le, W. Dopamine D3 receptor-preferring agonists induce neurotrophic effects on mesencephalic dopamine neurons. *Eur. J. Neurosci.* **22**, 2422–2430 (2005).
443. Joyce, J. N., Woolsey, C., Ryoo, H., Borwege, S., & Hagner, D. Low dose pramipexole is neuroprotective in the MPTP mouse model of Parkinson's disease, and downregulates the dopamine transporter via the D 3 receptor. *BMC Biol.* **2**, 1–12 (2004).
444. Newman, A. H. *et al.* Molecular Determinants of Selectivity and Efficacy at the Dopamine D3 Receptor. *J. Med. Chem.* **55**, 6689–6699 (2012).
445. Antonini, A. *et al.* Role of Pramipexole in the Management of Parkinson's Disease. *CNS Drugs* **24**, 829–841 (2010).
446. Hubble, J. P. *et al.* Pramipexole in Patients with Early Parkinson's Disease. *Clin. Neuropharmacol.* **18**, (1995).
447. Tysnes, O.-B. & Storstein, A. Epidemiology of Parkinson's disease. *J. Neural. Transm.* **124**, 901–905 (2017).
448. Parkinson, J. An essay on the shaking palsy. *Arch. Neurol.* **20**, 441–445 (1969).
449. Sveinbjornsdottir, S. The clinical symptoms of Parkinson's disease. *J. Neurochem.* **139**, 318–324 (2016).
450. McGregor, M. M. & Nelson, A. B. Circuit mechanisms of Parkinson's disease. *Neuron* **101**, 1042–1056 (2019).
451. Politis, M. & Niccolini, F. Serotonin in Parkinson's disease. *Behav. Brain Res.* **277**, 136–145 (2015).
452. Thomas, S. D., Abdalla, S., Eissa, N., Akour, A., Jha, N. K., Ojha, S. & Sadek, B. Targeting microglia in neuroinflammation: H3 receptor antagonists as a novel therapeutic approach for Alzheimer's disease, Parkinson's disease, and autism spectrum disorder. *Pharmaceuticals* **17**, 831 (2024).
453. Balestrino, R. & Schapira, A. H. V. Parkinson disease. *Eur. J. Neurol.* **27**, 27–42 (2020).
454. Poewe, W. et al. Parkinson disease. *Nat. Rev. Dis. Primers* **3**, 1–21 (2017).
455. Schultz, W. Depletion of dopamine in the striatum as an experimental model of parkinsonism: direct effects and adaptive mechanisms. *Prog. Neurobiol.* **18**, 121–166 (1982).
456. Zheng, K. S. et al. Clinical characteristics of exacerbations in Parkinson disease. *Neurologist* **18**, 120–124 (2012).
457. Park, A. & Stacy, M. Non-motor symptoms in Parkinson's disease. *J. Neurol.* **256**, 293–298 (2009).
458. Olanow, C. W. & Stocchi, F. Levodopa: A new look at an old friend. *Mov. Disord.* **33**, 859–866 (2018).
459. Fernandez, H. H. & Chen, J. J. Monoamine Oxidase-B Inhibition in the Treatment of Parkinson's Disease. *Pharmacotherapy* **27**, 174-185 (2007).
460. Fabbri, M., Ferreira, J. J. & Rascol, O. COMT Inhibitors in the Management of Parkinson's Disease. *CNS Drugs* **36**, 261–282 (2022).
461. Chen, J. J. & Swope, D. M. Pharmacotherapy for Parkinson's Disease. *Pharmacotherapy* **27**, 161-173 (2007).
462. Vanle, B., Olcott, W., Jimenez, J., Bashmi, L., Danovitch, I., & IsHak, W. W. (2018). NMDA antagonists for treating the non-motor symptoms in Parkinson's disease. *Transl. Psychiatry*, **8(1)**, 117.

463. Eisenreich, W., Sommer, B., Hartter, S. & Jost, W. H. Pramipexole Extended Release: A Novel Treatment Option in Parkinson's Disease. *Parkinsons Dis.* **2010(1)**, 612619 (2010).
464. Barone, P. *et al.* Pramipexole for the treatment of depressive symptoms in patients with Parkinson's disease: a randomised, double-blind, placebo-controlled trial. *Lancet Neurol*. **9**, 573–580 (2010).
465. Wang, Y. *et al.* Neuroprotective effects of pramipexole transdermal patch in the MPTP-induced mouse model of Parkinson's disease. *J. Pharmacol. Sci.* **138**, 31–37 (2018).
466. Li, C. *et al.* Neuroprotection of Pramipexole in UPS Impairment Induced Animal Model of Parkinson's Disease. *Neurochem. Res.* **35**, 1546–1556 (2010).
467. Antonini, A., Tolosa, E., Mizuno, Y., Yamamoto, M. & Poewe, W. H. A reassessment of risks and benefits of dopamine agonists in Parkinson's disease. *Lancet Neurol.* **8**, 929–937 (2009).
468. Youdim, M. B. H.; Gross, A.; Finberg, J. P. M. Rasagiline [N-Propargyl-1R(+)-Aminoindan], a Selective and Potent Inhibitor of Mitochondrial Monoamine Oxidase B. *Br. J. Pharmacol.* **132(2)**, 500-506 (2001).
469. Vieira-Coelho, M. A.; Soares-da-Silva, P. Effects of Tolcapone upon Soluble and Membrane-Bound Brain and Liver Catechol-O-Methyltransferase. *Brain Res.* **821(1)**, 69–78 (1999).
470. Kornhuber, J. *et al*.P. Therapeutic Brain Concentration of the NMDA Receptor Antagonist Amantadine. *Neuropharmacol.* **34(7)**, 713–721 (1995).
471. Harwell, V., & Fasinu, P. S. Pitolisant and other histamine-3 receptor antagonists—an update on therapeutic potentials and clinical prospects. *Med.* **7**(**9**), 55 (2020).
472. Molina-Hernández, A., Nuñez, A., Sierra, J.-J. & Arias-Montaño, J.-A. Histamine H3 receptor activation inhibits glutamate release from rat striatal synaptosomes. *Neuropharmacology* **41**, 928–934 (2001).
473. Arias-Montaño, J.-A. Histamine H3 receptors and their role in basal ganglia physiology and pathophysiology. *Signal Transduct.* **7**, 364–371 (2007).
474. Xu, J. & Pittenger, C. The histamine H3 receptor modulates dopamine D2 receptor–dependent signaling pathways and mouse behaviors. *J. Biol. Chem.* **299**, (2023).
475. Zhou, Z. *et al.* Histamine and receptors in neuroinflammation: Their roles on neurodegenerative diseases. *Behav. Brain Res.* **465**, 114964 (2024).
476. Alhusaini, M., Eissa, N., Saad, A. K., Beiram, R. & Sadek, B. Revisiting Preclinical Observations of Several Histamine H3 Receptor Antagonists/Inverse Agonists in Cognitive Impairment, Anxiety, Depression, and Sleep–Wake Cycle Disorder. *Front. Pharmacol.* **13**, (2022).
477. Kornum, B. R. *et al.* Narcolepsy. *Nat. Rev. Dis. Primers* **3**, 1–19 (2017).
478. Barateau, L., Pizza, F., Plazzi, G. & Dauvilliers, Y. Narcolepsy. *J. Sleep. Res.* **31(4)**, e13631 (2022).
479. Thannickal, T. C. *et al.* Reduced Number of Hypocretin Neurons in Human Narcolepsy. *Neuron* **27**, 469–474 (2000).
480. Bassetti, C. L. A. *et al.* Narcolepsy — clinical spectrum, aetiopathophysiology, diagnosis and treatment. *Nat. Rev. Neurol.* **15**, 519–539 (2019).
481. Dauvilliers, Y. *et al.* CSF hypocretin-1 levels in narcolepsy, Kleine-Levin syndrome, and other hypersomnias and neurological conditions. *J. Neurol. Neurosurg. Psychiatry* **74**, 1667–1673 (2003).
482. Thannickal, T. C., Nienhuis, R. & Siegel, J. M. Localized Loss of Hypocretin (Orexin) Cells in Narcolepsy Without Cataplexy. *Sleep* **32**, 993–998 (2009).
483. Gerashchenko, D. *et al.* Hypocretin-2-Saporin Lesions of the Lateral Hypothalamus Produce Narcoleptic-Like Sleep Behavior in the Rat. *J. Neurosci.* **21**, 7273–7283 (2001).
484. Barateau, L., Lopez, R. & Dauvilliers, Y. Management of narcolepsy. *Curr. Treat. Options Neurol.* **18**, 1–13 (2016).

485. Peyron, C. *et al.* Neurons Containing Hypocretin (Orexin) Project to Multiple Neuronal Systems. *J. Neurosci.* **18**, 9996–10015 (1998).
486. Sakurai, T. The neural circuit of orexin (hypocretin): maintaining sleep and wakefulness. *Nat. Rev. Neurosci.* **8**, 171–181 (2007).
487. Schwartz, J.-C. The histamine H3 receptor: from discovery to clinical trials with pitolisant. *Br. J. Pharmacol.* **163**, 713–721 (2011).
488. Anderson, D. Narcolepsy: a clinical review. *JAAPA* **34**, 20–25 (2021).
489. Thorpy, M. J. & Dauvilliers, Y. Clinical and practical considerations in the pharmacologic management of narcolepsy. *Sleep Med.* **16**, 9–18 (2015).
490. Fleckenstein, A. E., Volz, T. J., Riddle, E. L., Gibb, J. W. & Hanson, G. R. New Insights into the Mechanism of Action of Amphetamines. *Annu. Rev. Pharmacol. Toxicol.* **47**, 681–698 (2007).
491. Auger, R. R. *et al.* Risks of High-Dose Stimulants in the Treatment of Disorders of Excessive Somnolence: A Case-Control Study. *Sleep* **28**, 667–672 (2005).
492. Barateau, L., Lopez, R. & Dauvilliers, Y. Treatment Options for Narcolepsy. *CNS Drugs* **30**, 369–379 (2016).
493. Kothare, S. V. & Kaleyias, J. Pharmacotherapy of Narcolepsy: Focus on Sodium Oxybate. *Clin. Med. Insights* **2**, CMT.S1087 (2010).
494. Abad, V. C. & and Guilleminault, C. New developments in the management of narcolepsy. *Nat. Sci. Sleep* **9**, 39–57 (2017).
495. Ballon, J. S. & Feifel, D. A systematic review of modafinil: Potential clinical uses and mechanisms of action. *J. Clin. Psychiatry* **67**, 554—566 (2006).
496. Baladi, M. G. *et al.* Characterization of the Neurochemical and Behavioral Effects of Solriamfetol (JZP-110), a Selective Dopamine and Norepinephrine Reuptake Inhibitor. *J. Pharmacol. Exp. Ther.* **366**, 367–376 (2018).
497. Thorpy, M. J. Recently Approved and Upcoming Treatments for Narcolepsy. *CNS Drugs* **34**, 9–27 (2020).
498. Schweitzer, P. K. *et al.* Solriamfetol for Excessive Sleepiness in Obstructive Sleep Apnea (TONES 3). A Randomized Controlled Trial. *Am. J. Respir. Crit. Care Med.* **199**, 1421–1431 (2018).
499. Malhotra, A. *et al.* Long-term study of the safety and maintenance of efficacy of solriamfetol (JZP-110) in the treatment of excessive sleepiness in participants with narcolepsy or obstructive sleep apnea. *Sleep* **43**, zsz220 (2020).
500. Carter, L. P. *et al.* A randomized, double-blind, placebo-controlled, crossover study to evaluate the human abuse liability of solriamfetol, a selective dopamine and norepinephrine reuptake inhibitor. *J. Psychopharmacol.* **32**, 1351–1361 (2018).
501. Thakkar, M. M. Histamine in the regulation of wakefulness. *Sleep. Med. Rev.* **15**, 65–74 (2011).
502. Uguen, M. *et al.* Preclinical evaluation of the abuse potential of Pitolisant, a histamine H3 receptor inverse agonist/antagonist compared with Modafinil. *Br. J. Pharmacol.* **169**, 632–644 (2013).
503. Madras, B. K. *et al.* Modafinil Occupies Dopamine and Norepinephrine Transporters in Vivo and Modulates the Transporters and Trace Amine Activity in Vitro. *J. Pharmacol. Exp. Ther.* **319 (2)**, 561–569 (2006).
504. Lingenhoehl, K. *et al.* γ-Hydroxybutyrate Is a Weak Agonist at Recombinant GABAB Receptors. *Neuropharmacol.* **38 (11)**, 1667–1673 (1999).
505. Han, D. D.; Gu, H. H. Comparison of the Monoamine Transporters from Human and Mouse in Their Sensitivities to Psychostimulant Drugs. *BMC Pharmacol.* **6 (1)**, 6. (2006).
506. Rothman, R. B.; Baumann, M. H. Monoamine Transporters and Psychostimulant Drugs. *Eur. J. Pharmacol.* **479 (1)**, 23–40 (2003).
507. Strebhardt, K. & Ullrich, A. Paul Ehrlich's magic bullet concept: 100 years of progress. *Nat. Rev. Cancer* **8**, 473–480 (2008).

508. Morphy, R., Kay, C. & Rankovic, Z. From magic bullets to designed multiple ligands. *Drug Discov. Today* **9**, 641–651 (2004).
509. Anighoro, A., Bajorath, J. & Rastelli, G. Polypharmacology: challenges and opportunities in drug discovery: miniperspective. *J. Med. Chem.* **57**(**19**), 7874–7887 (2014).
510. Zheng, H., Fridkin, M. & Youdim, M. From single target to multitarget/network therapeutics in Alzheimer's therapy. *Pharmaceuticals* **7**, 113–135 (2014).
511. Youdim, M. B. H., Kupershmidt, L., Amit, T. & Weinreb, O. Promises of novel multi-target neuroprotective and neurorestorative drugs for Parkinson's disease. *Parkinsonism Relat. Disord.* **20**, S132–S136 (2014).
512. Millan, M. J. On 'polypharmacy' and multi-target agents, complementary strategies for improving the treatment of depression: a comparative appraisal. *Int. J. Neuropsychopharmacol.* **17**(**6**), 1009–1037 (2014).
513. Morphy, R. & Rankovic, Z. Designed multiple ligands. An emerging drug discovery paradigm. *J. Med. Chem.* **48**, 6523–6543 (2005).
514. Proschak, E., Stark, H. & Merk, D. Polypharmacology by design: a medicinal chemist's perspective on multitargeting compounds. *J. Med. Chem.* **62**, 420–444 (2018).
515. Morphy, R. & Rankovic, Z. The physicochemical challenges of designing multiple ligands. *J. Med. Chem.* **49**, 4961–4970 (2006).
516. Hopkins, A. L. Network pharmacology: the next paradigm in drug discovery. *Nat. Chem. Biol.* **4**, 682–690 (2008).
517. Khanfar, M. A., Affini, A., Lutsenko, K., Nikolic, K., Butini, S. & Stark, H. Multiple targeting approaches on histamine H3 receptor antagonists. *Front. Neurosci.* **10**, 201 (2016).
518. Von Coburg, Y., Kottke, T., Weizel, L., Ligneau, X. & Stark, H. Potential utility of histamine H3 receptor antagonist pharmacophore in antipsychotics. *Bioorg. Med. Chem. Lett.* **19**, 538–542 (2009).
519. Lepailleur, A. *et al.* Dual histamine H3R/serotonin 5-HT4R ligands with antiamnesic properties: pharmacophore-based virtual screening and polypharmacology. *J. Chem. Inf. Model* **54**, 1773–1784 (2014).
520. Pala, D. *et al.* Synthesis and characterization of new bivalent agents as melatonin-and histamine H3-ligands. *Int. J. Mol. Sci.* **15**, 16114–16133 (2014).
521. Keith, J. M. *et al.* Pyrrolidino-tetrahydroisoquinolines bearing pendant heterocycles as potent dual H3 antagonist and serotonin transporter inhibitors. *Bioorg. Med. Chem. Lett.* **17**, 4374–4377 (2007).
522. Stocking, E. M. *et al.* Synthesis and biological evaluation of diamine-based histamine H3 antagonists with serotonin reuptake inhibitor activity. *Bioorg. Med. Chem. Lett.* **17**, 3130–3135 (2007).
523. Letavic, M. A. *et al.* Novel tetrahydroisoquinolines are histamine H3 antagonists and serotonin reuptake inhibitors. *Bioorg. Med. Chem. Lett.* **17**, 1047–1051 (2007).
524. Altenbach, R. J. *et al.* Diaryldiamines with Dual Inhibition of the Histamine H3 Receptor and the Norepinephrine Transporter and the Efficacy of 4-(3-(Methylamino)-1-phenylpropyl)-6-(2-(pyrrolidin-1-yl)ethoxy)naphthalen-1-ol in Pain. *J. Med. Chem.* **53**, 7869–7873 (2010).
525. Apelt, J. *et al.* Development of a new class of nonimidazole histamine H3 receptor ligands with combined inhibitory histamine N-methyltransferase activity. *J. Med. Chem.* **45**, 1128–1141 (2002).
526. Graßmann, S. *et al.* Imidazole derivatives as a novel class of hybrid compounds with inhibitory histamine N-methyltransferase potencies and histamine hH3 receptor affinities. *Bioorg. Med. Chem.* **11**, 2163–2174 (2003).
527. Khan, N. *et al.* The dual-acting H3 receptor antagonist and AChE inhibitor UW-MD-71 dose-dependently enhances memory retrieval and reverses dizocilpine-induced memory impairment in rats. *Behav. Brain Res.* **297**, 155–164 (2016).

528. Bajda, M. *et al*. Dual-acting diether derivatives of piperidine and homopiperidine with histamine H3 receptor antagonistic and anticholinesterase activity. *Arch*. *Pharm*. *(Weinheim)* **345**, 591–597 (2012).
529. Morini, G. *et al*. Synthesis and structure–activity relationships for biphenyl H3 receptor antagonists with moderate anti-cholinesterase activity. *Bioorg*. *Med*. *Chem*. **16**, 9911–9924 (2008).
530. Darras, F. H. *et al*. Synthesis, biological evaluation, and computational studies of Tri- and tetracyclic nitrogen-bridgehead compounds as potent dual-acting AChE inhibitors and hH3 receptor antagonists. *ACS Chem*. *Neurosci*. **5**, 225–242 (2014).
531. Bembenek, S. D. *et al*. Lead identification of acetylcholinesterase inhibitors–histamine H3 receptor antagonists from molecular modeling. *Bioorg*. *Med*. *Chem*. **16**, 2968–2973 (2008).
532. Bautista-Aguilera, Ó. M. *et al*. Contilisant, a Tetratarget Small Molecule for Alzheimer's Disease Therapy Combining Cholinesterase, Monoamine Oxidase Inhibition, and H3R Antagonism with S1R Agonism Profile. *J. Med*. *Chem*. **61 (15)**, 6937–6943 (2018)
533. Bertinaria, M. *et al*. [3-(1H-Imidazol-4-yl) propyl] guanidines containing furoxan moieties. *Bioorg*. *Med*. *Chem*. **7**, 1197–1205 (2003).
534. Bertinaria, M. H3 receptor ligands: new imidazole H3-antagonists endowed with NO-donor properties. *Il Farmaco* **58**, 279–283 (2003).
535. Tosco, P. *et al*. Furoxan analogues of the histamine H3-receptor antagonist imoproxifan and related furazan derivatives. *Bioorg*. *Med*. *Chem*. **13**, 4750–4759 (2005).
536. Moses, J. E. & Moorhouse, A. D. The growing applications of click chemistry. *Chem*. *Soc*. *Rev*. **36**, 1249–1262 (2007).
537. Bertozzi, C. A Special Virtual Issue Celebrating the 2022 Nobel Prize in Chemistry for the Development of Click Chemistry and Bioorthogonal Chemistry. *ACS Cent*. *Sci*. **9**, 558–559 (2023).
538. Rostovtsev, V. V., Green, L. G., Fokin, V. V. & Sharpless, K. B. A stepwise Huisgen cycloaddition process: Copper(I)-catalyzed regioselective "ligation" of azides and terminal alkynes. *Angew*. *Chem*. *Int*. *Ed*. **41**, 2596–2599 (2002).
539. Tornøe, C. W., Christensen, C. & Meldal, M. Peptidotriazoles on Solid Phase: [1,2,3]-Triazoles by Regiospecific Copper(I)-Catalyzed 1,3-Dipolar Cycloadditions of Terminal Alkynes to Azides. *J*. *Org*. *Chem*. **67**, 3057–3064 (2002).
540. Baskin, J. M. & Bertozzi, C. R. Bioorthogonal Click Chemistry: Covalent Labeling in Living Systems. *QSAR Comb*. *Sci*. **26**, 1211–1219 (2007).
541. Agard, N. J., Prescher, J. A. & Bertozzi, C. R. A Strain-Promoted [3 + 2] Azide−Alkyne Cycloaddition for Covalent Modification of Biomolecules in Living Systems. *J*. *Am*. *Chem*. *Soc*. **126**, 15046–15047 (2004).
542. Oliveira, A. B., Guo, Z. & Bernardes, G. J. L. Inverse electron demand Diels–Alder reactions in chemical biology. *Chem*. *Soc*. *Rev*. **46**, 4895–4950 (2017).
543. Blackman, M. L., Royzen, M. & Fox, J. M. Tetrazine Ligation: Fast Bioconjugation Based on Inverse-Electron-Demand Diels−Alder Reactivity. *J*. *Am*. *Chem*. *Soc*. **130**, 13518–13519 (2008).
544. Lang, K. & Chin, J. W. Bioorthogonal Reactions for Labeling Proteins. *ACS Chem*. *Biol*. **9**, 16–20 (2014).
545. Nikić, I. *et al*. Minimal tags for rapid dual-color live-cell labeling and super-resolution microscopy. *Angew*. *Chem*. *Int*. *Ed*. **53**, 2245–2249 (2014).
546. Šečkutė, J. & Devaraj, N. K. Expanding room for tetrazine ligations in the in vivo chemistry toolbox. *Curr*. *Opin*. *Chem*. *Biol*. **17**, 761–767 (2013).
547. Adhikari, K., Vanermen, M., Da Silva, G., Van den Wyngaert, T., Augustyns, K. & Elvas, F. Trans-cyclooctene—a Swiss army knife for bioorthogonal chemistry: exploring the synthesis, reactivity, and applications in biomedical breakthroughs. *EJNMMI Radiopharm*. *Chem*. **9**, 47 (2024).

548. Thalhammer, F., Wallfahrer, U. & Sauer, J. Reaktivität einfacher offenkettiger und cyclischer dienophile bei Diels-Alder-reaktionen mit inversem elektronenbedarf. *Tetrahedron Lett.* **31**, 6851–6854 (1990).
549. Bach, R. D. Ring Strain Energy in the Cyclooctyl System. The Effect of Strain Energy on [3 + 2] Cycloaddition Reactions with Azides. *J. Am. Chem. Soc.* **131**, 5233–5243 (2009).
550. Choi, S.-K., Kim, J. & Kim, E. Overview of Syntheses and Molecular-Design Strategies for Tetrazine-Based Fluorogenic Probes. *Molecules* **26**, (2021).
551. Devaraj, N. K., Hilderbrand, S., Upadhyay, R., Mazitschek, R. & Weissleder, R. Bioorthogonal turn-on probes for imaging small molecules inside living cells. *Angew. Chem. Int. Ed. Engl.* **49**, 2869—2872 (2010).
552. Comeo, E. *et al.* Ligand-Directed Labeling of the Adenosine A1 Receptor in Living Cells. *J. Med. Chem.* **67**, 12099–12117 (2024).
553. Ramil, C. P. *et al.* Spirohexene-Tetrazine Ligation Enables Bioorthogonal Labeling of Class B G Protein-Coupled Receptors in Live Cells. *J. Am. Chem. Soc.* **139**, 13376–13386 (2017).
554. Garland, S. L. Are GPCRs still a source of new targets? *J. Biomol. Screen.* **18**(**9**), 947–966 (2013).
555. Ciruela, F., Jacobson, K. A. & Fernández-Dueñas, V. Portraying G protein-coupled receptors with fluorescent ligands. *ACS Chem. Biol.* **9**, 1918–1928 (2014).
556. Soave, M., Briddon, S. J., Hill, S. J. & Stoddart, L. A. Fluorescent ligands: Bringing light to emerging GPCR paradigms. *Br. J. Pharmacol.* **177**, 978–991 (2020).
557. Lakowicz, J. R. Introduction to fluorescence. *Principles of Fluorescence Spectroscopy*, 1–23 (1999).
558. Jameson, D. M. Introduction to fluorescence. *CRC Press,* Boca Raton, USA (2025).
559. Kuder, K. & Kiec-Kononowicz, K. Fluorescent GPCR ligands as new tools in pharmacology-update, years 2008-early 2014. *Curr. Med. Chem.* **21**, 3962–3975 (2014).
560. Vernall, A. J., Hill, S. J. & Kellam, B. The evolving small-molecule fluorescent-conjugate toolbox for Class A GPCRs. *Br. J. Pharmacol.* **171**(**5**), 1073–1084 (2014).
561. Orndorff, W. R. & Hemmer, A. J. Fluorescein and some of its derivatives. *J. Am. Chem. Soc.* **49**, 1272–1280 (1927).
562. Rajasekar, M. Recent development in fluorescein derivatives. *J. Mol. Struct.* **1224**, 129085 (2021).
563. Song, L., Hennink, E. J., Young, I. T. & Tanke, H. J. Photobleaching kinetics of fluorescein in quantitative fluorescence microscopy. *Biophys. J.* **68**, 2588–2600 (1995).
564. Sjöback, R., Nygren, J. & Kubista, M. Absorption and fluorescence properties of fluorescein. *Spectrochim. Acta A Mol. Biomol. Spectrosc.* **51**, L7–L21 (1995).
565. Sun, W.-C., Gee, K. R., Klaubert, D. H. & Haugland, R. P. Synthesis of Fluorinated Fluoresceins. *J. Org. Chem.* **62**, 6469–6475 (1997).
566. Mottram, L. F., Boonyarattanakalin, S., Kovel, R. E. & Peterson, B. R. The Pennsylvania Green Fluorophore: a hybrid of Oregon Green and Tokyo Green for the construction of hydrophobic and pH-insensitive molecular probes. *Org. Lett.* **8**, 581–584 (2006).
567. Hammershøj, P., Kumar, E. K. P., Harris, P., Andresen, T. L. & Clausen, M. H. Facile Large-Scale Synthesis of 5- and 6-Carboxyfluoresceins: Application for the Preparation of New Fluorescent Dyes. *European J. Org. Chem.* **2015**, 7301–7309 (2015).
568. Loudet, A. & Burgess, K. BODIPY dyes and their derivatives: syntheses and spectroscopic properties. *Chem. Rev.* **107**, 4891–4932 (2007).
569. Banuelos, J. BODIPY dye, the most versatile fluorophore ever? *The Chem. Rec.* **16**, 335–348 (2016).
570. Boens, N., Leen, V. & Dehaen, W. Fluorescent indicators based on BODIPY. *Chem. Soc. Rev.* **41**, 1130–1172 (2012).

571. AAT Bioquest, Inc. Quest Graph™ Spectrum [BODIPY FL]. *AAT Bioquest*.https://www.aatbio.com/fluorescence-excitation-emission-spectrum-graph-viewer/bodipy_fl. (accessed 2025, May 7).
572. Macarró, R. & Hertzberg, R. P. Design and implementation of high throughput screening assays. *Mol. Biotechnol.* **47**, 270–285 (2011).
573. Chen, Y. *et al.* Review of advanced imaging techniques. *J. Pathol. Inform.* **3**, 22 (2012).
574. Fish, K. N. Total internal reflection fluorescence (TIRF) microscopy. *Curr. Protoc. Cytom.* **50**, 12–18 (2009).
575. Semwogerere, D. & Weeks, E. R. Confocal microscopy. *Encycl. Biomater. Biomed. Eng.* **23**, 1–10 (2005).
576. Galbraith, C. G. & Galbraith, J. A. Super-resolution microscopy at a glance. *J. Cell. Sci.* **124**, 1607–1611 (2011).
577. Ayoub, M. A. Resonance energy transfer-based approaches to study GPCRs. In *Methods Cell. Biol.* **132**, 255–292 (2016).
578. Sprague, B. L. & McNally, J. G. FRAP analysis of binding: proper and fitting. *Trends Cell. Biol.* **15**, 84–91 (2005).
579. Vrljic, M., Nishimura, S. Y. & Moerner, W. E. Single-molecule tracking. *Lipid Rafts* 193–219 (2007).
580. Minoshima, M. & Kikuchi, K. Photostable and photoswitching fluorescent dyes for super-resolution imaging. *JBIC J. Biol. Inorg. Chem.* **22**, 639–652 (2017).
581. Turksoy, A., Yildiz, D. & Akkaya, E. U. Photosensitization and controlled photosensitization with BODIPY dyes. *Coord. Chem. Rev.* **379**, 47–64 (2019).
582. Klymchenko, A. S. Solvatochromic and Fluorogenic Dyes as Environment-Sensitive Probes: Design and Biological Applications. *Acc. Chem. Res.* **50**, 366–375 (2017).
583. Liguori, C. et al. Pitolisant for treating narcolepsy comorbid with Parkinson's disease. *Sleep Med.* **66**, 86–87 (2020).
584. Esbenshade, T. A., Browman, K. E., Bitner, R. S., Strakhova, M., Cowart, M. D., & Brioni, J. D. The histamine H3 receptor: an attractive target for the treatment of cognitive disorders. *Br. J. Pharmacol.* **154**, 1166–1181 (2008).
585. Khanfar, M. A., Affini, A., Lutsenko, K., Nikolic, K., Butini, S., & Stark, H. Multiple targeting approaches on histamine H3 receptor antagonists. *Front. Neurosci.* **10**, 201 (2016).
586. Olanow, C. W. & Schapira, A. H. V. Therapeutic prospects for Parkinson disease. *Ann. Neurol.* **74**, 337–347 (2013).
587. Dagli, R. J., & Sharma, A. Polypharmacy: a global risk factor for elderly people. *J. Int. Oral Health* **6**(6), i (2014).
588. Schneider, E. H., Neumann, D., & Seifert, R. Histamine H_4-receptor expression in the brain?. *Naunyn-Schmiedeberg's Arch. Pharmacol.* **388**, 5–9 (2015).
589. Zhan, S. et al. Comparative efficacy and safety of multiple wake-promoting agents for the treatment of excessive daytime sleepiness in narcolepsy: a network meta-analysis. *Nat. Sci. Sleep* **217**, 217–230 (2023).
590. Wu, H. & Devaraj, N. K. Advances in Tetrazine Bioorthogonal Chemistry Driven by the Synthesis of Novel Tetrazines and Dienophiles. *Acc. Chem. Res.* **51**, 1249–1259 (2018).
591. Csoti, I., Herbst, H., Urban, P., Woitalla, D. & Wüllner, U. Polypharmacy in Parkinson's disease: risks and benefits with little evidence. *J. Neural. Transm.* **126**, 871–878 (2019).
592. Poewe, W. Treatments for Parkinson disease—past achievements and current clinical needs. *Neurology* **72**, 65–73 (2009).
593. Xu, J. & Pittenger, C. The histamine H3 receptor modulates dopamine D2 receptor–dependent signaling pathways and mouse behaviors. *J. Biol. Chem.* **299(4)**, (2023).
594. Brooks, D. J. Dopamine agonists: their role in the treatment of Parkinson's disease. *J. Neurol. Neurosurg. Psychiatry* **68**, 685–689 (2000).
595. Walter, M. & Stark, H. Histamine receptor subtypes: a century of rational drug design. *Front. Biosci.-Scholar* **4(2)**, 461–488 (2012).

596. Mierau, J. *et al*. Pramipexole binding and activation of cloned and expressed dopamine D2, D3 and D4 receptors. *Eur. J. Pharmacol. Mol. Pharmacol.* **290**(**1**), 29–36 (1995).
597. Finkelstein, H. Darstellung organischer Jodide aus den entsprechenden Bromiden und Chloriden. *Ber. Dtsch. Chem. Ges.* **43**, 1528–1532 (1910).
598. Falkenstein, M. *et al*. Histamine H3 receptor antagonists with peptidomimetic (keto) piperazine structures to inhibit Aβ oligomerisation. *Bioorg. Med. Chem.* **50**, 116462 (2021).
599. Le Chatelier, H. Sur un énoncé général des lois des équilibres chimiques. *C. R. Acad. Sci.* **99**, 786-789 (1884).
600. Hughes, E. D. & Ingold, C. K. Discussion of constitutional and solvent effects on the mechanism, kinetics, velocity and orientation of substitution. *J. Chem. Soc.*, 244 (1935).
601. Carey, F. A. & Sundberg, R. J. *Advanced Organic Chemistry: Part A: Structure and Mechanisms*. Springer Science & Business Media, Heidelberg, Germany (2007).
602. Gupta A. K. *et al*. Process for the preparation of 2-amino-4,5,6,7-tetrahydro-6-aminobenzothioles from cyclohexanes and cyclohexanones as intermediates. **WO2004026850A1** (Generics UK Ltd., 2004).
603. Smith, M. B. *March's Advanced Organic Chemistry: Reactions, Mechanisms, and Structure*. John Wiley & Sons, Hoboken, USA (2020).
604. Abdel-Magid, A. F. & Mehrman, S. J. A review on the use of sodium triacetoxyborohydride in the reductive amination of ketones and aldehydes. *Org. Process Res. Dev.* **10**, 971–1031 (2006).
605. Cordes, E. H. & Jencks, W. P. The mechanism of hydrolysis of Schiff bases derived from aliphatic amines. *J. Am. Chem. Soc.* **85**, 2843–2848 (1963).
606. McMurry, J. E. *Organic Chemistry.* **9th edn.**, Cengage Learning, Boston, USA (2015).
607. Streitwieser, A., Cohen, S. G. & Taft, R. W. *Progress in Physical Organic Chemistry* **Vol. 2**., Interscience, (1964).
608. Stark H. *et al*. Medicaments. **WO2009056811A2** (Motac Neuroscience Ltd., 2009).
609. Cordes, E. H. & Bull, H. G. Mechanism and catalysis for hydrolysis of acetals, ketals, and ortho esters. *Chem. Rev.* **74**, 581–603 (1974).
610. Volhard, J. Ueber Darstellung α-bromierter Säuren. *Justus Liebigs Ann. Chem.* **242**, 141–163 (1887).
611. Hantzsch, A. & Weber, J. H. Ueber Verbindungen des Thiazols (Pyridins der Thiophenreihe). *Ber. Dtsch. Chem. Ges.* **20**, 3118–3132 (1887).
612. Carey, F. A. & Sundberg, R. J. *Advanced Organic Chemistry: Part B: Reactions and Synthesis* **Vol. 3**. Springer US, New York, USA (2007).
613. Fife, T. H. General acid catalysis of acetal, ketal, and ortho ester hydrolysis. *Acc. Chem. Res.* **5**, 264–272 (1972).
614. Dess, D. B. & Martin, J. C. A useful 12-I-5 triacetoxyperiodinane (the Dess-Martin periodinane) for the selective oxidation of primary or secondary alcohols and a variety of related 12-I-5 species. *J. Am. Chem. Soc.* **113**, 7277–7287 (1991).
615. Omura, K. & Swern, D. Oxidation of alcohols by "activated" dimethyl sulfoxide. A preparative, steric and mechanistic study. *Tetrahedron* **34**, 1651–1660 (1978).
616. Anelli, L. P., Biffi, C., Montanari, F. & Quici, S. Fast and selective oxidation of primary alcohols to aldehydes or to carboxylic acids and of secondary alcohols to ketones mediated by oxoammonium salts under two-phase conditions. *J. Org. Chem.* **52**, 2559–2562 (1987).
617. Ho, S. K. The thermal decomposition of aliphatic aldehydes. *Proc. R. Soc. Lond. A. Math. Phys. Sci.* **276**, 278–292 (1963).
618. Nielsen, A. T. & Houlihan, W. J. The aldol condensation. *Organic reactions* **16**, 1–438 (2004).
619. Batsika, C. S. *et al*. Light-promoted oxidation of aldehydes to carboxylic acids under aerobic and photocatalyst-free conditions. *Green Chem.* **24**, 6224–6231 (2022).

620. Bell, R. P. The reversible hydration of carbonyl compounds. In *Advances in Physical Organic Chemistry* **Vol. 4**, 1–29 (Academic Press, 1966).
621. Sander, K. *et al*. First metal-containing histamine H3 receptor ligands. *Org*. *Lett*. **12**, 2578–2581 (2010).
622. Montanari, S. *et al*. Discovery of novel benzofuran-based compounds with neuroprotective and immunomodulatory properties for Alzheimer's disease treatment. *Eur. J. Med*. *Chem*. **178**, 243–258 (2019).
623. Hansen, T., Roozee, J. C., Bickelhaupt, F. M. & Hamlin, T. A. How solvation influences the SN2 versus E2 competition. *J. Org*. *Chem*. **87**, 1805–1813 (2022).
624. Lowry, T. H. & Richardson, K. S. *Mechanism and Theory in Organic Chemistry* **3rd edn**. Harper & Row, New York, USA (1987).
625. Hughes, E. D. & Ingold, C. K. Mechanism of substitution at a saturated carbon atom. Part IV. A discussion of constitutional and solvent effects on the mechanism, kinetics, velocity, and orientation of substitution. *J. Chem*. *Soc. (Resumed)* **244**, 244–255 (1935).
626. Hughes, E. D., Ingold, C. K. & Scott, A. D. The mechanism of elimination reactions. Part I. Unimolecular olefin formation from alkyl halides in sulphur dioxide and formic acid. *J. Chem*. *Soc. (Resumed)* **1271**, 1271–1277 (1937).
627. Affini, A., Hagenow, S., Zivkovic, A., Marco-Contelles, J. & Stark, H. Novel indanone derivatives as MAO B/H3R dual-targeting ligands for treatment of Parkinson's disease. *Eur. J. Med*. *Chem*. **148**, 487–497 (2018).
628. Frandsen, I. O. *et al*. Identification of Histamine H3 Receptor Ligands Using a New Crystal Structure Fragment-based Method. *Sci*. *Rep*. **7**, (2017).
629. Berlin, M., Boyce, C. W. & de Lera Ruiz, M. Histamine H3 receptor as a drug discovery target. *J. Med*. *Chem*. **54**, 26–53 (2011).
630. Gogoi, S. *et al*. Novel bivalent ligands for D2/D3 dopamine receptors: Significant cooperative gain in D2 affinity and potency. *ACS Med*. *Chem*. *Lett*. **3**, 991–996 (2012).
631. Brown, D. A., Kharkar, P. S., Parrington, I., Reith, M. E. A. & Dutta, A. K. Structurally constrained hybrid derivatives containing octahydrobenzo[g or f]quinoline moieties for dopamine D2 and D3 receptors: Binding characterization at D2/D3 receptors and elucidation of a pharmacophore model. *J. Med*. *Chem*. **51**, 7806–7819 (2008).
632. Zakharkin, L. I. & Khorlina, I. M. Reduction of esters of carboxylic acids into aldehydes with diisobutylaluminium hydride. *Tetrahedron Lett*. **3**, 619–620 (1962).
633. Pedras, M. S. C. & Montaut, S. Probing crucial metabolic pathways in fungal pathogens of crucifers: Biotransformation of indole-3-acetaldoxime, 4-hydroxyphenylacetaldoxime, and their metabolites. *Bioorg*. *Med*. *Chem*. **11**, 3115–3120 (2003).
634. Winterfeldt, E. Applications of diisobutylaluminium hydride (DIBAH) and triisobutylaluminium (TIBA) as reducing agents in organic synthesis. *Synthesis* **1975**, 617–630 (1975).
635. Lewis, G. N. Valence and Tautomerism. *J. Am*. *Chem*. *Soc*. **35**, 1448–1455 (1913).
636. Stark H. *et al*. Medicaments. **WO2009056805A1** (Motac Neuroscience Ltd., 2009).
637. Doyle, M. P., Dellaria Jr, J. F., Siegfried, B. & Bishop, S. W. Reductive deamination of arylamines by alkyl nitrites in N, N-dimethylformamide. A direct conversion of arylamines to aromatic hydrocarbons. *J. Org*. *Chem*. **42**, 3494–3498 (1977).
638. Zollinger, H. *Diazo Chemistry I: Aromatic and Heteroaromatic Compounds*. VCH, Weinheim, Germany (1994).
639. Ridd, J. H. Nitrosation, diazotisation, and deamination. *Q*. *Rev*. *Chem*. *Soc*. **15**, 418–441 (1961).
640. Kornblum, N., Cooper, G. D. & Taylor, J. E. The Chemistry of Diazo Compounds. II. Evidence for a Free Radical Chain Mechanism in the Reduction of Diazonium Salts by Hypophosphorous Acid. *J. Am*. *Chem*. *Soc*. **72**, 3013–3021 (1950).
641. Randolph, J. T. *et al*. Prodrug Strategies to Improve the Solubility of the HCV NS5A Inhibitor Pibrentasvir (ABT-530). *J. Med*. *Chem*. **63**, 11034–11044 (2020).

642. Bender, M. L. Mechanisms of catalysis of nucleophilic reactions of carboxylic acid derivatives. *Chem. Rev.* **60**, 53–113 (1960).
643. Clayden, J., Greeves, N. & Warren, S. *Organic Chemistry*. Oxford University Press, New York, USA, (2012).
644. Cipriani T. *et al.* HSP90-targeting conjugates and formulations thereof. **WO2019118830A1** (Tarveda Therapeutics Inc., 2019).
645. Montalbetti, C. A. & Falque, V. Amide bond formation and peptide coupling. *Tetrahedron* **61**, 10827–10852 (2005).
646. Okada, Y. *Peptide Chemistry 1993: Proceedings of the 31st Symposium on Peptide Chemistry, Akashi*. Protein Research Foundation (1994).
647. Sandmeyer, T. Ueber die Ersetzung der Amidgruppe durch Chlor in den aromatischen Substanzen. *Ber. Dtsch. Chem. Ges.* **17**, 1633–1635 (1884).
648. Hodgson, H. H. The Sandmeyer reaction. *Chem. Rev.* **40**, 251–277 (1947).
649. Pajouhesh, H. & Lenz, G. R. Medicinal chemical properties of successful central nervous system drugs. *NeuroRx* **2**, 541–553 (2005).
650. Leo, A., Hansch, C. & Elkins, D. Partition coefficients and their uses. *Chem. Rev.* **71**, 525–616 (1971).
651. Bissantz, C., Kuhn, B. & Stahl, M. A medicinal chemist's guide to molecular interactions. *J. Med. Chem.* **53**, 5061–5084 (2010).
652. Davis, A. M. & Teague, S. J. Hydrogen bonding, hydrophobic interactions, and failure of the rigid receptor hypothesis. *Angew. Chem. Int. Ed.* **38**, 736–749 (1999).
653. Klebe, G. *Drug Design: Methodology, Concepts, and Mode-of-Action*. Springer, Heidelberg, Germany (2013).
654. Merz Jr, K. M., Ringe, D. & Reynolds, C. H. *Drug Design: Structure- and Ligand-Based Approaches*. Cambridge Univ. Press, (2010).
655. Bennett, J. P. & Piercey, M. F. Pramipexole - A new dopamine agonist for the treatment of Parkinson's disease. *J. Neurol. Sci.* **163**, 25–31 (1999).
656. Thomas, S. D., Abdalla, S., Eissa, N., Akour, A., Jha, N. K., Ojha, S. & Sadek, B. Targeting microglia in neuroinflammation: H3 receptor antagonists as a novel therapeutic approach for Alzheimer's disease, Parkinson's disease, and autism spectrum disorder. *Pharmaceuticals* **17**, 831 (2024).
657. Olanow, C. W.; Stern, M. B.; Sethi, K. The Scientific and Clinical Basis for the Treatment of Parkinson Disease. *Neurology*, **72***,* 1–136 (2009)
658. Nuermaimaiti, M.; Oyama, G.; Kasemsuk, C.; Hattori, N. Istradefylline for Restless Legs Syndrome Associated with Parkinson's Disease. *Tremor Other Hyperkin. Mov.* **8**, 521 (2018).
659. Thorpy, M. J. Recently approved and upcoming treatments for narcolepsy. *CNS Drugs* **34**, 9–27 (2020).
660. Barateau, L. & Dauvilliers, Y. Recent advances in treatment for narcolepsy. *Ther. Adv. Neurol. Disord.* **12**, 1756286419875622 (2019).
661. Billiard, M. Narcolepsy: current treatment options and future approaches. *Neuropsychiatr. Dis. Treat.* **4**, 557–566 (2008).
662. Zhan, S. *et al.* Comparative efficacy and safety of multiple wake-promoting agents for the treatment of excessive daytime sleepiness in narcolepsy: a network meta-analysis. *Nat. Sci. Sleep* **15**, 217–230 (2023).
663. Thakrar, C. *et al.* Effectiveness and side-effect profile of stimulant therapy as monotherapy and in combination in the central hypersomnias in clinical practice. *J. Sleep Res.* **27**, (2018).
664. Pérez-Carbonell, L. *et al.* Adherence to wakefulness promoting medication in patients with narcolepsy. *Sleep Med.* **70**, 50–54 (2020).
665. Markham, A. Solriamfetol: First Global Approval. *Drugs* **79**, 785–790 (2019).
666. Kumar, R. Approved and investigational uses of modafinil: an evidence-based review. *Drugs* **68**, 1803–1839 (2008).

667. Li, S. & Yang, J. Pitolisant for treating patients with narcolepsy. *Expert. Rev. Clin. Pharmacol.* **13**, 79–84 (2020).
668. Yang, J. & Gao, J. Solriamfetol for the treatment of excessive daytime sleepiness associated with narcolepsy. *Expert Rev. Clin. Pharmacol.* **12**, 723–728 (2019).
669. Wingen, K. & Stark, H. Scaffold variations in amine warhead of histamine H3 receptor antagonists. *Drug Discov. Today: Technol.* **10**, e483–e489 (2013).
670. Köteles, I. *et al.* Determination of the Enantiomeric Purity of Solriamfetol by High-Performance Liquid Chromatography in Polar Organic Mode Using Polysaccharide-Type Chiral Stationary Phases. *Chromatographia* **83**, 909–913 (2020).
671. Salamon-Krokosz, K. *et al.* Fluorinated Olefinic Lactams: The Case of Amino Acids - Preparation and Mechanistic Studies. *Synthesis (Germany)* **54**, 3785–3792 (2022).
672. Kamble V. S. *et al.* Process for preparation of solriamfetol and intermediates thereof. **WO2021161232A1** (Lupin Ltd., 2021).
673. Staab, H. A. New methods of preparative organic chemistry IV. Syntheses using heterocyclic amides (azolides). *Angew. Chem. Int. Ed. Engl.* **1**, 351–367 (1962).
674. De Castro, S., Camarasa, M. J., Balzarini, J. & Velázquez, S. Discovery and SAR studies of a novel class of cytotoxic 1,4-disubstituted piperidines via Ugi reaction. *Eur. J. Med. Chem.* **83**, 174–189 (2014).
675. Schelhaas, M. & Waldmann, H. Protecting group strategies in organic synthesis. *Angew. Chem. Int. Ed. Engl.* **35**, 2056–2083 (1996).
676. Committee for Medicinal Products for Human Use (CHMP). Assessment report. Sunosi. **EMEA/H/C/004893/0000** (EMA, 2019).
677. Wuts P. G. M., Greene T. W. *Greene's Protective Groups in Organic Synthesis.* John Wiley & Sons, Inc., (2007).
678. Ghosh, A. K. & Brindisi, M. Organic carbamates in drug design and medicinal chemistry. *J. Med. Chem.* **58**, 2895–2940 (2015).
679. Gai, S. *et al.* The design of protozoan phosphoribosyltransferase inhibitors containing non-charged phosphate mimic residues. *Bioorg. Med. Chem.* **74**, 117038 (2022).
680. Boisnard, S., Neuville, L., Bois-Choussy, M. & Zhu, J. Asymmetric synthesis of actinoidic acid derivatives. *Org. Lett.* **2**, 2459–2462 (2000).
681. Turkyilmaz, S. & Wilcox, C. S. Asymmetric solution-phase mixture aldol reaction using oligomeric ethylene glycol tagged chiral oxazolidinones. *Tetrahedron Lett.* **58**, 2031–2033 (2017).
682. Watanabe, M. *et al.* Stereochemical diversity-oriented conformational restriction strategy. Development of potent histamine H3 and/or H4 receptor antagonists with an imidazolylcyclopropane structure. *J. Med. Chem.* **49**, 5587–5596 (2006).
683. Kovalainen, J. T. *et al.* Synthesis and in vitro pharmacology of a series of new chiral histamine H3-receptor ligands: 2-(R and S)-amino-3-(1H-imidazol-4(5)-yl)propyl ether derivatives. *J. Med. Chem.* **42**, 1193–1202 (1999).
684. Schmitt, K. C.; Reith, M. E. A. Regulation of the Dopamine Transporter. *Ann. N. Y. Acad. Sci.*, **1187 (1)**, 316–340 (2010).
685. Windhorst, A. D., Leurs, R., Menge, W. M., Timmerman, H. & Herscheid, J. D. Synthesis of radioligands for the histamine H3 receptor. In *Pharmacochemistry Library* **30**, 159–174 (1998).
686. Wijtmans, M. *et al.* Triazole Ligands Reveal Distinct Molecular Features That Induce Histamine H4 Receptor Affinity and Subtly Govern H4/H3 Subtype Selectivity. *J. Med. Chem.* **54**, 1693–1703 (2011).
687. Mayer, S. & Lang, K. Tetrazines in Inverse-Electron-Demand Diels-Alder Cycloadditions and Their Use in Biology. *Synthesis (Germany)* **49**, 830–848 (2017).
688. Giepmans, B. N. G., Adams, S. R., Ellisman, M. H. & Tsien, R. Y. The fluorescent toolbox for assessing protein location and function. *Science (1979)* **312**, 217–224 (2006).
689. Devaraj, N. K. & Weissleder, R. Biomedical applications of tetrazine cycloadditions. *Acc. Chem. Res.* **44**, 816–827 (2011).

690. Zhao, G., Li, Z., Zhang, R., Zhou, L., Zhao, H. & Jiang, H. Tetrazine bioorthogonal chemistry derived in vivo imaging. *Front. Mol. Biosci.* **9**, 1055823 (2022).
691. Devaraj, N. K., Weissleder, R. & Hilderbrand, S. A. Tetrazine-based cycloadditions: Application to pretargeted live cell imaging. *Bioconjug. Chem.* **19**, 2297–2299 (2008).
692. Mishra, A., Carrascal-Miniño, A., Kim, J. & T. M. de Rosales, R. [68Ga]Ga-THP-tetrazine for bioorthogonal click radiolabelling: pretargeted PET imaging of liposomal nanomedicines. *RSC Chem. Biol.* **5**, 622–639 (2024).
693. Eddins, A. J., Pung, A. H., Cooley, R. B. & Mehl, R. A. Tetrazine amino acid encoding for rapid and complete protein bioconjugation. *Bio-protoc.* **14**, e5048 (2024).
694. Nizi, M. G. *et al.* Potent 2,3-dihydrophthalazine-1,4-dione derivatives as dual inhibitors for mono-ADP-ribosyltransferases PARP10 and PARP15. *Eur. J. Med. Chem.* **237**, 114362 (2022).
695. Hughes, D. L. The Mitsunobu Reaction. *Org. React.* **42**, 335–656 (1992).
696. Croll, E. A. & Kwon, O. Mechanism of the Mitsunobu Reaction: An Ongoing Mystery. *Synthesis (Germany)* **56**, 1843–1850 (2024).
697. Mitsunobu, O. The use of diethyl azodicarboxylate and triphenylphosphine in synthesis and transformation of natural products. *Synthesis* **1981**, 1–28 (1981).
698. Yang, J., Karver, M. R., Li, W., Sahu, S. & Devaraj, N. K. Metal-catalyzed one-pot synthesis of tetrazines directly from aliphatic nitriles and hydrazine. *Angew. Chem. Int. Ed.* **51**, 5222–5225 (2012).
699. Cheewawisuttichai, T. & Brichacek, M. Development of a multifunctional neoglycoside auxiliary for applications in glycomics research. *Org. Biomol. Chem.* **19**, 6613–6617 (2021).
700. Sarris, A. J. C. *et al.* Fast and pH-independent elimination of trans-cyclooctene by using aminoethyl-functionalized tetrazines. *Chem. Eur. J.* **24**, 18075–18081 (2018).
701. Alghamdi, Z. S., Klausen, M., Gambardella, A., Lilienkampf, A. & Bradley, M. Solid-Phase Synthesis of s-Tetrazines. *Org. Lett.* **25**, 3104–3108 (2023).
702. Pinner, A. Ueber die Einwirkung von Hydrazin auf Imidoäther. *Justus Liebigs Ann. Chem.* **297**, 221–271 (1897).
703. García-Aznar, P. & Escorihuela, J. Computational insights into the inverse electron-demand Diels-Alder reaction of norbornenes with 1,2,4,5-tetrazines: norbornene substituents' effects on the reaction rate. *Org. Biomol. Chem.* **20**, 6400–6412 (2022).
704. Anderson, E. D. & Boger, D. L. Inverse electron demand diels-alder reactions of 1,2,3-triazines: Pronounced substituent effects on reactivity and cycloaddition scope. *J. Am. Chem. Soc.* **133**, 12285–12292 (2011).
705. Schmitt, A., Hinkeldey, B., Wild, M. & Jung, G. Synthesis of the core compound of the BODIPY dye class: 4,4'-difluoro-4-bora-(3a,4a)-diaza-s-indacene. *J. Fluoresc.* **19**, 755–758 (2009).
706. Kozma, E., Demeter, O. & Kele, P. Bio-orthogonal fluorescent labelling of biopolymers through inverse-electron-demand Diels–Alder reactions. *ChemBioChem* **18**, 486–501 (2017).
707. Evans, H. L., Carroll, L., Aboagye, E. O. & Spivey, A. C. Bioorthogonal chemistry for 68Ga radiolabelling of DOTA-containing compounds. *J. Labelled Comp. Radiopharm.* **57**, 291–297 (2014).
708. Knall, A. C. & Slugovc, C. Inverse electron demand Diels-Alder (iEDDA)-initiated conjugation: A (high) potential click chemistry scheme. *Chem. Soc. Rev.* **42**, 5131–5142 (2013).
709. Haynam, C. A., Brumbaugh, D. V. & Levy, D. H. The spectroscopy, photophysics, and photochemistry of the dimer of dimethyl tetrazine. *J. Chem. Phys.* **81**, 2282–2294 (1984).
710. Snowdon, P. J., Whiteoak, R. J. & Manley, J. D. The hydrolysis of clofentezine and related tetrazines as the basis of determination of residues in bovine tissues. *Fresenius' J. Anal. Chem.* **339**, 444–447 (1991).

711. Darko, A. *et al*. Conformationally strained trans-cyclooctene with improved stability and excellent reactivity in tetrazine ligation. *Chem. Sci.* **5**, 3770–3776 (2014).
712. Tomarchio, E. G. *et al*. Tetrazine–trans-cyclooctene ligation: Unveiling the chemistry and applications within the human body. *Bioorg. Chem.*, **107573** (2024).
713. Devi, G., Hedger, A. K., Whitby, R. J. & Watts, J. K. Double Click: Unexpected 1:2 Stoichiometry in a Norbornene-Tetrazine Reaction. *J. Org. Chem.* **88**, 5341–5347 (2023).
714. Sasse, A. *et al*. Influence of bulky substituents on histamine H3 receptor agonist/antagonist properties. *J. Med. Chem.* **45**, 4000–4010 (2002).
715. Handula, M., Chen, K. T. & Seimbille, Y. IEDDA: an attractive bioorthogonal reaction for biomedical applications. *Molecules* **26**, 4640 (2021).
716. Adhikari, S., Moscatelli, J., Smith, E. M., Banerjee, C. & Puchner, E. M. Single-molecule localization microscopy and tracking with red-shifted states of conventional BODIPY conjugates in living cells. *Nat. Commun.* **10**, 1–12 (2019).
717. Adhikari, S., Moscatelli, J. & Puchner, E. Live Cell Super-Resolution Imaging with Red-Shifted States of Conventional Bodipy Fluorophores. *Biophys. J.* **116**, 439a–440a (2019).
718. Hara, T. *et al*. Flow cytometry-based binding assay for GPR40 (FFAR1; free fatty acid receptor 1). *Mol. Pharmacol.* **75**, 85–91 (2009).
719. Urano, Y. *et al*. Evolution of fluorescein as a platform for finely tunable fluorescence probes. *J. Am. Chem. Soc.* **127**, 4888–4894 (2005).
720. Buchanan, J. L. *et al*. Discovery of 2,4-bis-arylamino-1,3-pyrimidines as insulin-like growth factor-1 receptor (IGF-1R) inhibitors. *Bioorg. Med. Chem. Lett.* **21**, 2394–2399 (2011).
721. Ueno, T. *et al*. Rational principles for modulating fluorescence properties of fluorescein. *J. Am. Chem. Soc.* **126**, 14079–14085 (2004).
722. Yang, L., Simionescu, R., Lough, A. & Yan, H. Some observations relating to the stability of the BODIPY fluorophore under acidic and basic conditions. *Dyes Pigm.* **91**, 264–267 (2011).
723. Lipinski, C. A., Lombardo, F., Dominy, B. W. & Feeney, P. J. Experimental and computational approaches to estimate solubility and permeability in drug discovery and development settings. *Adv. Drug Deliv. Rev.* **23**, 3–25 (1997).
724. Di, L. & Kerns, E. H. *Drug-like properties: concepts, structure design, and methods*. Elsevier, London, UK, (2016).
725. Schaeffer, L. The role of functional groups in drug–receptor interactions. In *The practice of medicinal chemistry*, 464–480 (Academic Press, 2008).
726. Jończyk, J., Malawska, B. & Bajda, M. Hybrid approach to structure modeling of the histamine H3 receptor: Multi-level assessment as a tool for model verification. *PLoS One* **12**, e0186108 (2017).
727. Sameiro, M. & Gonçalves, T. Fluorescent labeling of biomolecules with organic probes. *Chem. Rev.* **109**, 190–212 (2009).
728. Jablonowski, J. A. *et al*. The first potent and selective non-imidazole human histamine H4 receptor antagonists. *J. Med. Chem.* **46**, 3957–3960 (2003).
729. Ni, Y. & Wu, J. Far-red and near infrared BODIPY dyes: synthesis and applications for fluorescent pH probes and bio-imaging. *Org. Biomol. Chem.* **12**, 3774–3791 (2014).
730. Wang, J. *et al*. Self-assembled BODIPY nanoparticles for near-infrared fluorescence bioimaging. *Molecules* **28**, 2997 (2023).
731. Gao, D. *et al*. Molecular Engineering of Near-Infrared Light-Responsive BODIPY-Based Nanoparticles with Enhanced Photothermal and Photoacoustic Efficiencies for Cancer Theranostics. *Theranostics* **9**, 5315–5331 (2019).
732. Chen, D. D. *et al*. Bioactivity and structure–activity relationship of cinnamic acid derivatives and its heteroaromatic ring analogues as potential high-efficient acaricides against Psoroptes cuniculi. *Bioorg. Med. Chem. Lett.* **28**, 1149–1153 (2018).

733. Wittig, G. & Schöllkopf, U. Über Triphenyl-phosphin-methylene als olefinbildende Reagenzien (I. Mitteil.). *Chem. Ber.* **87**, 1318–1330 (1954).
734. Bensinger, D. *et al.* Virtual Screening Identifies Irreversible FMS-like Tyrosine Kinase 3 Inhibitors with Activity toward Resistance-Conferring Mutations. *J. Med. Chem.* **62**, 2428–2446 (2019).
735. Krajcovicova, S. *et al.* A Synthetic Approach for the Rapid Preparation of BODIPY Conjugates and their use in Imaging of Cellular Drug Uptake and Distribution. *Chem. - Eur. J.* **24**, 4957–4966 (2018).
736. Brückner, R. *Reaktionsmechanismen*. Springer, Heidelberg, Germany (2004).
737. Sinha, M. *et al.* Antiplasmodial activity of new 4-aminoquinoline derivatives against chloroquine resistant strain. *Bioorg. Med. Chem.* **22**, 3573–3586 (2014).
738. Wang, J., Uttamchandani, M., Li, J., Hu, M. & Yao, S. Q. "Click" synthesis of small molecule probes for activity-based fingerprinting of matrix metalloproteases. *Chem. Commun.* **(36)**, 3783–3785 (2006).
739. Seifert, R. *et al.* Paradoxical Stimulatory Effects of the "Standard" Histamine H4-Receptor Antagonist JNJ7777120: the H4 Receptor Joins the Club of 7 Transmembrane Domain Receptors Exhibiting Functional Selectivity. *Mol. Pharmacol.* **79**, 631–638 (2011).
740. Dang Q. *et al.* Heteroaromatic cyclic compound, and preparation method therefor and use thereof. **WO2024149239A1** (Shanghai Innovkong Pharmaceutical Tech Co Ltd, 2024).
741. Hoggett, J. G. *Nitration and Aromatic Reactivity*. Cambridge University Press, Cambridge, UK (1971).
742. Sharma, S. K. *et al.* Three-component reaction involving metal-free heteroannulation of N-Boc-3-amido indole, aryl aldehydes, and aromatic alkynes under microwave conditions: Synthesis of highly diversified δ-carbolines. *Tetrahedron Lett.* **51**, 6022–6024 (2010).
743. Béchamp, A. De l'action des protosels de fer sur la nitronaphtaline et la nitrobenzine; nouvelle méthode de formation des bases organiques artificielles de Zinin. *Ann. Chim. Phys.* **17**, (1854).
744. Chiba, K., Hashimoto, Y. & Yamaguchi, T. Affinity labeling with 4-azidophthalimide (AzPI): Relation between labeling rate and fluorescence intensity. *Chem. Pharm. Bull.* **65**, 994–996 (2017).
745. Kumari, S., Carmona, A. V., Tiwari, A. K. & Trippier, P. C. Amide bond bioisosteres: Strategies, synthesis, and successes. *J. Med. Chem.* **63**, 12290–12358 (2020).
746. Henderson, W. A. Jr. & Schultz, C. J. The Nucleophilicity of Amines. *J. Org. Chem.* **27**, 4643–4646 (1962).
747. Abdel-Magid, A. F., Carson, K. G., Harris, B. D., Maryanoff, C. A. & Shah, R. D. Reductive amination of aldehydes and ketones with sodium triacetoxyborohydride. Studies on direct and indirect reductive amination procedures. *J. Org. Chem.* **61**, 3849–3862 (1996).
748. Wersinger E. *et al.* H4 receptor inhibitors for treating tinnitus. **WO2013182711A1** (Sensorion, 2013).
749. Desmadryl G. & Chabbert C. Selective histamine H4 receptor antagonists for the treatment of vestibular disorders. **WO2010072829A1** (Institut National de la Santé et de la Recherche Médicale, 2010).
750. Zhang, G., Yu, H., Qin, G. & Huang, H. Rh-Catalyzed oxidative C-H activation/annulation: Converting anilines to indoles using molecular oxygen as the sole oxidant. *Chem. Commun.* **50**, 4331–4334 (2014).
751. Bunnett, J. F. & Zahler, R. E. Aromatic nucleophilic substitution reactions. *Chem. Rev.* **49**, 273–412 (1951).
752. Nunes J. J. *et al.* Substituted heterocyclic compounds and methods of use. **WO2005021551A1** (Amgen Inc., 2005).

753. Meisenheimer, J. Ueber Reaktionen aromatischer Nitrokörper. *Justus Liebigs Ann. Chem.* **323**, 205–246 (1902).
754. Eberhart, A. J. *et al.* Sulfoxide-directed metal-free ortho-propargylation of aromatics and heteroaromatics. *Chem. - Eur. J.* **21**, 7428–7434 (2015).
755. Geunes, E. P., Meinhardt, J. M., Wu, E. J. & Knowles, R. R. Photocatalytic Anti-Markovnikov Hydroamination of Alkenes with Primary Heteroaryl Amines. *J. Am. Chem. Soc.* **145**, 21738–21744 (2023).
756. Kaiser, D., Klose, I., Oost, R., Neuhaus, J. & Maulide, N. Bond-forming and-breaking reactions at sulfur (IV): sulfoxides, sulfonium salts, sulfur ylides, and sulfinate salts. *Chem. Rev.* **119**, 8701–8780 (2019).
757. Bernier, D., Wefelscheid, U. K. & Woodward, S. Properties, preparation and synthetic uses of amine N-oxides. An update. *Org. Preparations Proced. Int.* **41**, 173–210 (2009).
758. Cremlyn R. J. *An Introduction to Organosulfur Chemistry.* John Wiley & Sons Ltd, Chichester, UK (1996).
759. Smits, R. A. *et al.* Discovery of quinazolines as histamine H4 receptor inverse agonists using a scaffold hopping approach. *J. Med. Chem.* **51**, 7855–7865 (2008).
760. Wu, T. *et al.* Discovery of 2-(4-Substituted-piperidin/piperazine-1-yl)-N-(5-cyclopropyl-1 H-pyrazol-3-yl)-quinazoline-2, 4-diamines as PAK4 inhibitors with potent A549 cell proliferation, migration, and invasion inhibition activity. *Molecules* **23**, 417 (2018).
761. Cho, N. C. *et al.* Discovery of 2-aryloxy-4-amino-quinazoline derivatives as novel protease-activated receptor 2 (PAR2) antagonists. *Bioorg. Med. Chem.* **23**, 7717–7727 (2015).
762. Barbosa, M. L. D. C. *et al.* Regioselective nucleophilic aromatic substitution: Theoretical and experimental insights into 4-aminoquinazoline synthesis as a privileged structure in medicinal chemistry. *Molecules* **29**, 6021 (2024).
763. Shaikh, S. M. & Wagh, M. R. Characterization, synthesis, and antimicrobial activities of quinazoline derivatives [EMNEDAQZHO] and their metal ion complexes. *Oriental J. Chem.* **40**, 1329–1339 (2024).
764. Baluja, S. & Nandha, K. Synthesis and thermal decomposition kinetics of some pyrazolo-quinazoline derivatives. *World Sci. News* **31**, 100–110 (2016).
765. Flohr A., Groebke Zbinden K., Koerner M., & Lerner C. *Pyrrolidino Heterocycles.* **WO2013178569A1** (Hoffmann-La Roche, 2013).
766. Li, H. *et al.* Periodic mesoporous organosilica nanoparticles with BOC group, towards HIFU responsive agents. *Molecules* **25**, 974 (2020).
767. Seibold, U., Wängler, B. & Wängler, C. Rational Design, Development, and Stability Assessment of a Macrocyclic Four-Hydroxamate-Bearing Bifunctional Chelating Agent for 89Zr. *ChemMedChem* **12**, 1555–1571 (2017).
768. Sulsky, R. & Demers, J. P. Alkylation of N-benzyloxyureas and carbamates. *Tetrahedron Lett.* **30**, 31–34 (1989).
769. Nagasawa A., Arata Y., & Uneme H. *Chinazolin-Derivate, die zur Hemmung der Cytokininsignalleitung fähig sind.* **EP2100507A1** (Sumitomo Chemical Co, 2009).
770. Smits, R. A., Leurs, R. & De Esch, I. J. P. Quinazolines and related heterocyclic compounds, and their therapeutic use. **U.S. Patent No. 8,530,486** (Vereniging voor Christelijk Hoger Onderwijs Wetenschappelijk Onderzoek en Patientenzorg, 2013).
771. Wang, M. *et al.* Design, synthesis and fungicidal activity of 2-substituted phenyl-2-oxo-, 2-hydroxy- and 2-acyloxyethylsulfonamides. *Molecules* **22**, 738 (2017).
772. Vilsmeier, A. & Haack, A. über die Einwirkung von Halogenphosphor auf Alkyl-formanilide. Eine neue Methode zur Darstellung sekundärer und tertiärer p-Alkylamino-benzaldehyde. *Eur. J. Inorg. Chem.* **60**, 119–122 (1927).
773. Zhang, M., Venable, J. D. & Thurmond, R. L. The histamine H4 receptor in autoimmune disease. *Expert Opin. Investig. Drugs* **15**, 1443–1452 (2006).

774. Fulmer, G. R. *et al*. NMR Chemical Shifts of Trace Impurities: Common Laboratory Solvents, Organics, and Gases in Deuterated Solvents Relevant to the Organometallic Chemist. *Organometallics* **29**, 2176–2179 (2010).
775. ChemDraw, *Revvity Signals*. https://revvitysignals.com (accessed 2025, May 7).
776. BioRender, *BioRender.com* https://biorender.com (accessed 2025, May 7).
777. Adobe Illustrator, *Adobe Inc*. https://adobe.com (accessed 2025, May 7).
778. MestReNova, *Mestrelab Research* https://mestrelab.com (accessed 2025, May 7).
779. Prism, *GraphPad Software Inc.* https://graphpad.com (accessed 2025,May 7).
780. RCSB PDB: Protein Data Bank. https://www.rcsb.org (accessed 2025, May 7)
781. PyMOL 3.1, *Schrödinger Inc.* PyMOL | pymol.org (accessed 2025, May 7).
782. Origin, *OriginLab Corporation* https://originlab.com (accessed 2025, May 7).
783. ChatGPT, *OpenAI* https://openai.com (accessed 2025, May 7).
784. Cody – AI Coding Assistant; *Sourcegraph* https://sourcegraph.com (accessed 2025, May 7).
785. Elek, M. *et al*. Synthesis, in silico, and in vitro studies of novel dopamine D2 and D3 receptor ligands. *Arch. Pharm. (Weinheim)* **354**, 2000486 (2021).
786. Bautista-Aguilera, Ó. M. *et al*. Multitarget-directed ligands combining cholinesterase and monoamine oxidase inhibition with histamine H3R antagonism for neurodegenerative diseases. *Angew. Chem. Int. Ed.* **56**, 12765–12769 (2017).
787. Kottke, T. *et al*. Receptor-specific functional efficacies of alkyl imidazoles as dual histamine H3/H4 receptor ligands. *Eur. J. Pharmacol.* **654**, 200–208 (2011).
788. Nordemann, U. *et al*. Luciferase reporter gene assay on human, murine and rat histamine H4 receptor orthologs: correlations and discrepancies between distal and proximal readouts. *PLoS One* **8**, e73961 (2013).
789. Werner, T. *et al*. First Report on Cationic Triphenylphosphonium Compounds as Mitochondriotropic H3R Ligands with Antioxidant Properties. *Antioxidants* **13(11)**, 1345 (2024).
790. Roth, B. Assay Protocol Book *National Institute of Mental Health Psychoactive Drug Screening Program* **3** (2018).
791. Sander, K.; Kottke, T.; Weizel, L.; Stark, H. Kojic Acid Derivatives as Histamine H3 Receptor Ligands. *Chem. Pharm. Bull. (Tokyo)*, **58 (10)**, 1353–1361 (2010).